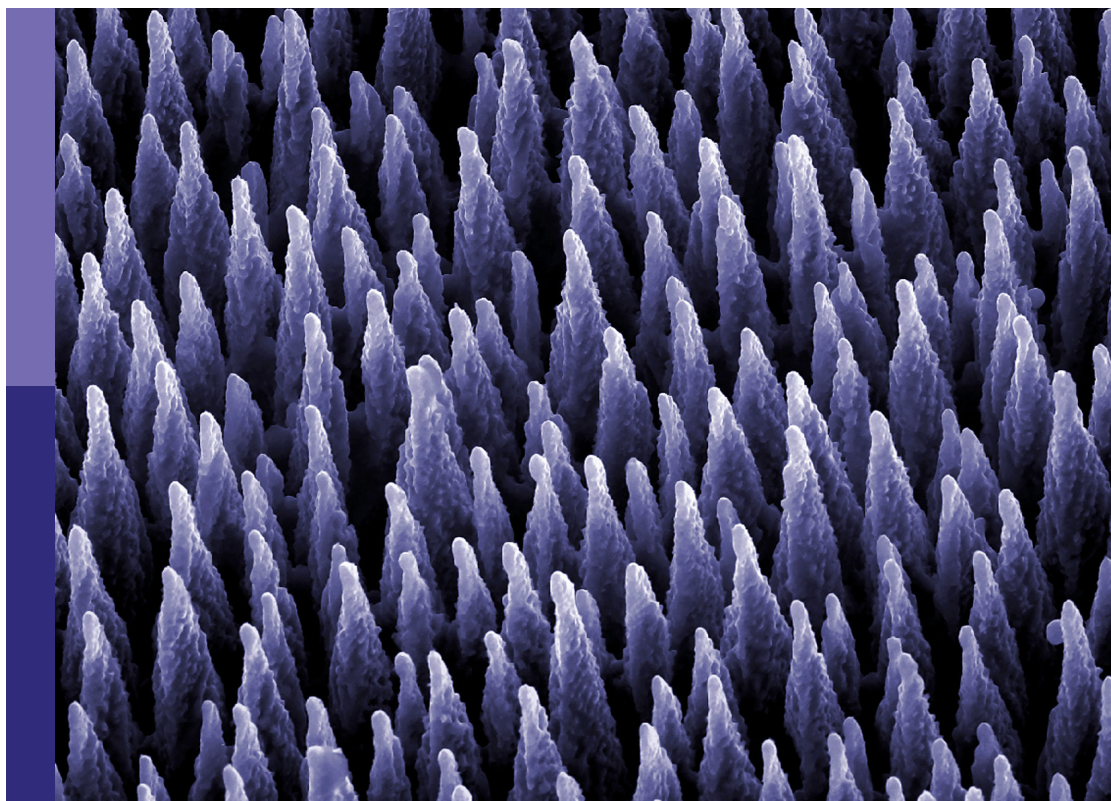# Advanced materials and techniques for structural monitoring, analysis and control

Edited by
Chun-Xu Qu, Liang Ren, Yunlai Zhou,
Sadegh Shams and Qian Feng

Published in
Frontiers in Materials

About Frontiers

Frontiers is more than just an open access publisher of scholarly articles: it is a pioneering approach to the world of academia, radically improving the way scholarly research is managed. The grand vision of Frontiers is a world where all people have an equal opportunity to seek, share and generate knowledge. Frontiers provides immediate and permanent online open access to all its publications, but this alone is not enough to realize our grand goals.

Frontiers journal series

The Frontiers journal series is a multi-tier and interdisciplinary set of open-access, online journals, promising a paradigm shift from the current review, selection and dissemination processes in academic publishing. All Frontiers journals are driven by researchers for researchers; therefore, they constitute a service to the scholarly community. At the same time, the *Frontiers journal series* operates on a revolutionary invention, the tiered publishing system, initially addressing specific communities of scholars, and gradually climbing up to broader public understanding, thus serving the interests of the lay society, too.

Dedication to quality

Each Frontiers article is a landmark of the highest quality, thanks to genuinely collaborative interactions between authors and review editors, who include some of the world's best academicians. Research must be certified by peers before entering a stream of knowledge that may eventually reach the public – and shape society; therefore, Frontiers only applies the most rigorous and unbiased reviews. Frontiers revolutionizes research publishing by freely delivering the most outstanding research, evaluated with no bias from both the academic and social point of view. By applying the most advanced information technologies, Frontiers is catapulting scholarly publishing into a new generation.

What are Frontiers Research Topics?

Frontiers Research Topics are very popular trademarks of the *Frontiers journals series*: they are collections of at least ten articles, all centered on a particular subject. With their unique mix of varied contributions from Original Research to Review Articles, Frontiers Research Topics unify the most influential researchers, the latest key findings and historical advances in a hot research area.

Find out more on how to host your own Frontiers Research Topic or contribute to one as an author by contacting the Frontiers editorial office: frontiersin.org/about/contact

Advanced materials and techniques for structural monitoring, analysis and control

Topic editors

Chun-Xu Qu – Dalian University of Technology, China
Liang Ren – Dalian University of Technology, China
Yunlai Zhou – Xi'an Jiaotong University, China
Sadegh Shams – Federal Highway Administration, United States
Qian Feng – Institute of Seismology, China Earthquake Administration, China

Topic editor Sadegh Shams is employed by Turner-Fairbank Highway Research Center/Genex Systems and declares no competing interests with regards to the Research Topic Subject.

Table of
contents

Editorial: Advanced materials and technique for structural monitoring, analysis, and control

Chun-Xu Qu[1], Liang Ren[1]*, Yunlai Zhou[2], Qian Feng[3] and Sadegh Shams[4]

[1]School of Civil Engineering, Dalian University of Technology, Dalian, China, [2]School of Aerospace Engineering, Xi'an Jaiaotong University, Xi'an, China, [3]School of Safety Science and Emergency Management, Wuhan University of Technology, Wuhan, China, [4]Federal Highway Administration, McLean Va, WA, United States

Editorial on the Research Topic
Advanced materials and technic for structural monitoring, analysis and control

Structural control, monitoring, and analysis complement each other to ensure the maximum safety of structures, including bridges, buildings, transmission towers, and wharfs. Assessing the use and maintaining the safety of various engineering structures are essential for their sustainable operation. The static mechanical properties and dynamic mechanical response of a structure are the basis for analyzing and predicting its operational status; structural monitoring and analysis technology has thus become an active focus in the engineering field. In order to improve an aging structure to minimize natural disaster, structural control devices have been widely used in modern structural engineering. Structural control technology includes passive, active, or semi-active reverse force. Its main purpose is to change the stiffness, mass, and damping of a structure with minimum control force. In order to meet the requirements of modern engineering structural application scenarios and environments, nanosmart materials and new technologies are constantly emerging which provide strong support for monitoring technologies to cope with various challenges. This research topic shares the latest research results of advanced materials and technologies in the field of structural monitoring, analysis, and control, including the theoretical methods of structural health monitoring (SHM), mechanical analysis and control analysis of structures, engineering vulnerability assessment methods, the application of advanced intelligent materials in health monitoring, the integration of intelligent algorithms and health monitoring technologies, and other related aspects.

There has been much research on the monitoring theory and method of civil engineering structures. Zhang et al. propose a new method that utilizes a three-stage criterion that considers overall structural impact to obtain local modal information of the tensioned cable segment. Chi et al. determine an engineering vulnerability assessment method that takes into account the effects of corrosion, based on the analytic hierarchy process method and fuzzy comprehensive evaluation. Zhao et al. innovatively utilize fiber optic monitoring for excavating deformations in foundation pits and propose

a back-analysis method for HSS model parameters based on the SSA-BP neural network. Zhang et al. propose a two-stage method for model modification and damage identification.

The analysis of structural operation performance is critical for the use and maintenance of the structure. Zhang et al. study the mechanical properties of transmission tower K-joints through numerical methods, focusing on three aspects: failure mode, load–displacement hysteresis curve, and stiffness degradation. Bian et al. investigate the uplift capacity of single straight and belled piles in sloping ground, revealing a decrease in capacity with an increase in slope angle. Additionally, a practical method of quantifying the slope effect is proposed. Bian et al. use a finite element model to simulate the nonlinear interaction between piles and soil, investigating the relationship between the bearing capacity of single piles and horizontal forces and bending moments in sloping ground. Pan et al. investigate the impact of crack dip angles on the mechanical characteristics of rock masses through uniaxial and true triaxial compression tests.

Smart materials and new technologies continue to emerge, providing strong support for monitoring technology to meet various challenges. Wang et al. replace manufactured sand with glass sand and added carbon fiber to prepare high-performance shotcrete and then testing its mechanical properties and self-sensing performance.

The essence of SHM is monitoring the vibration and displacement response of a structure under external loading or excitation. Xue et al. use numerical analysis of a damaged bridge abutment supported by inclined piles during a specific earthquake where soil liquefaction occurred to clarify that the main cause of the forward rotation of the abutment was the increase in soil pressure behind it. Bian et al. propose a simplified analytical methodology for analyzing the lateral dynamic responses of a transmission tower structure due to the impact of rockfall. Mu et al. investigate and evaluate three different boom replacement methods for suspension bridges using finite element calculations, determine optimal methods for varying boom lengths, and propose a quantitative basis for classifying boom lengths. Hongbin et al. investigate the characteristics of main girders' longitudinal motion in long-span suspension bridges, analyzing the influence of restraint devices such as viscous dampers and supports. Yao et al. utilize a sophisticated numerical model based on actual engineering data to assess the reliability of prefabricated perimeter walls in substations during flood events.

Structural control is another effective way of rendering a structure safe. Zhang et al. focus on the interaction between ice and offshore platforms in the Bohai Sea, discussing strategies to mitigate ice-induced vibrations of offshore wind turbine foundations.

Author contributions

C-XQ: writing–original draft and writing–review and editing. LR: writing–review and editing. YZ: writing–review and editing. QF: writing–review and editing. SS: writing–review and editing.

Acknowledgments

Conflict of interest

The authors declare that the research was conducted in the absence of any commercial or financial relationships that could be construed as a potential conflict of interest.

The author(s) declared that they were an editorial board member of Frontiers, at the time of submission. This had no impact on the peer review process and the final decision.

Publisher's note

A three-stage criterion method for extracting local vibration modes of tensioned cables in beam string structures

Tao Zhang[1], Yuxin Zhang[1]* and Hexin Zhang[2]

[1]School of Civil Engineering, Shanghai Normal University, Shanghai, China, [2]School of Computing, Engineering and the Built Environment, Edinburgh Napier University, Edinburgh, United Kingdom

As light and efficient large-span space structures, beam string structures have been widely used since the 1980s. Within them, cables are the main force-bearing component; their level of tension determines the overall stiffness, performance and structural safety of the beam string structures. Real-time monitoring of the cable force during the construction and service periods is an important and effective measure to ensure the safety of the cable structure. At present, the vibration method is widely used in nearly all common engineering practices for cable force identification/monitoring because of its simplicity and efficiency. However, the vibration of the cable segment will be affected by the whole structure, so the cable force-frequency relationship based on the simple single cable model cannot meet the accuracy requirement of cable force identification of the beam string structure. Therefore, in this paper, through finite element simulation and theoretical analysis, a three-stage criterion is proposed to develop a new method for obtaining the local modal information of the tensioned cable segment where the influence of the overall structure is considered. The new method's performance was compared with the results obtained by the vibration method according to the single-cable model assumption, and the design values of the cable forces. The magnitude of the error in the identification of the tension force of the beam string structure according to the single-cable model was studied to provide a correction method, so that the single-cable model assumption can be used to improve the measuring efficiency and ensure the solution accuracy. The numerical results show the effectiveness of the proposed method. The work of this paper provides a new approach for improving the identification accuracy of the vibration method of a complex cable system such as the beam string structure and is a useful discussion on the vibration method of complex cable systems.

1 Introduction

As society develops, the demand for public space is increasing rapidly. Such demand has driven the development of building structure systems, especially spatial structures. As one of the large-span spatial structure systems, the beam string structure has superior mechanical performance. The cables and upper rigid members work together to give full play to the tensile performance of the cable, so that the overall rigidity of the structure is significantly improved. Under loading, the deflection of the structure is much smaller than that of traditional structures; the cable provides the span support point for the superstructure through the upper strut, which reduces the bending moment value in the section of the superstructure and reduces the amount of steel used. When the upper part is an arched structure, the cable can balance the horizontal thrust of the arched structure at the support so that the structure has good self-balancing performance.

Due to these functional advantages, the beam string structure is widely used in engineering. For example, the Japanese Green Dome Maebashi Gymnasium built in 1990 and the Japanese Urayasu Municipal Sports Center built in 1995, which consists of seven two-span continuous beam string structures (Saitoh and Okada, 1999). The Shanghai Pudong International Airport Terminal 1, built in 1999 (Chen et al., 1999), is a prominent example of a large-span stretched beam string structure (Figure 1). The Pudong Airport T2 terminal (Wang et al., 2007) built in 2006 also adopts the beam string structure, which is a three-span continuous plane structure (Figure 2). The vertical stress structure of the main exhibition hall of the Guangzhou International Convention and Exhibition Center (Sun et al., 2003) built in 2002 is a string truss structure with a span of 126.6 m. The National Indoor Stadium of China (Qin et al., 2007) was built for the 2008 Olympics and the roof covers an area of 144 m × 144 m and is a two-way beam string structure.

In addition to the traditional beam string structure, new variants are also emerging. For example, the Swiss Montreux parking lot was built in 2004, and the British Lawn Tennis Association tennis court was built in 2010 using a gas-supported string structure. The upper part of the structure uses rigid rods, the middle part uses low-pressure inflatable airbags instead of traditional struts, and the lower chord uses tension cables.

The tension degree of the cable, which is the main force-bearing member of the structure, directly determines the overall stiffness and structural safety of the string structure. Therefore, real-time monitoring of the cable force during the construction and service periods is essential to ensure the safety of the cable structure. To avoid accidents, Structural Health Monitoring (SHM) for monitoring and evaluation of completed cable structures has emerged and has been implemented worldwide (BrownjohnPines and Aktan, 2002; Yun et al., 2003;, 2007). According to current research data, cable force detection

FIGURE 1
T1 terminal for Shanghai Pudong International Airport.
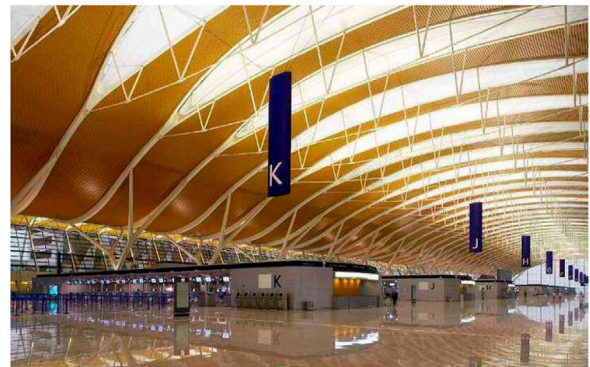
FIGURE 2
T2 terminal for Shanghai Pudong International Airport.

methods mainly include the magnetic flux method (Cappello et al., 2018; Duan et al., 2015; Fabo et al., 2002), the strain gauge method (Volokhov et al., 2016; Moradi and Sivoththaman, 2013) and the vibration method (Furukawa et al., 2022; Ma et al., 2021; Kangas et al., 2012; Fang and Wang, 2012; Mehrabi, 2006).

The vibration method has become one of the most commonly used cable force testing methods in engineering because of advantages such as repeatable installation and use at any time, monitoring cost, high measurement result accuracy, simple instrument operation, and convenient practical application. However, there are two factors that affect the accuracy of the cable force test results during the implementation of this method. One is the test accuracy of the natural vibration frequency of the cable segment, and the other is the accuracy of the conversion relationship between the natural vibration frequency and the cable force (Geier et al., 2006). The degree of accuracy is closely related to the degree of model simplification. The more the calculation model conforms

to the actual structure, the higher the degree of accuracy. Therefore, research into the vibration method has been an evolutionary process from simplified model to more and more representative of the actual structure. However, for the problem of cable force identification of cable segments, the single-cable model is the most used in engineering and theoretical research, and the research on cable force identification is also based on the single-cable model.

In the 18th century, Brook Taylor, D′ Alembert and Daniel Bernoulli put forward the theory of string vibration, and Bernoulli (1732) and Euler (1781) began to study the lateral vibration of strings successively, determining the solution of the vibration frequency. In 1974, Irvine and Caughey began to consider the elasticity of the cable and deeply studied the effect of sag on the in-plane vibration characteristics of the cable but did not consider the bending stiffness. In the subsequent research on bending stiffness, Tadayuki (1994) proposed a method for estimating the cable force by using high-order frequencies, considering the effects of the bending stiffness, sag and inclination of the cable at the same time. He deduced the cable vibration equation considering the bending stiffness of the cable, but the nonlinear equation needs to be solved by computer, which is not convenient for engineering. Hiroshi et al. (1980) proposed a practical formula for the vibration method using the natural frequency of the low-order mode, considering the influence of the bending stiffness and sag effect of the steel cable. Byeong and Taehyo (2007) proposed a new technique to estimate cable tension force from measured natural frequencies. The proposed method is able to simultaneously identify tension force, flexural rigidity, and axial rigidity of a cable system. Furthermore, it is observed that the flexural rigidity of a cable with high bending stiffness is proportional to the applied tension force. Humar (2012) regarded the cable as a beam subjected to axial force, considering the bending stiffness and ignoring the sag effect, and obtained the cable force expression of the cable hinged at both ends by beam theory. Mehrabi and Tabatabai (1998) used a new numerical algorithm to obtain the solution value of the cable under the influence of bending stiffness, sag effect and damping. Zarbaf et al. (2018) proposed a simple novel framework to estimate the cable tension based on Artificial Neural Networks (ANNs). The method takes into account the cable axial stiffness and cable bending stiffness. It was shown that, for the new Ironton-Russell Bridge, using cable length, cable mass per unit length, cable axial stiffness, and the first two cable natural frequencies as input features to ANNs, the cable tensions can be accurately estimated. In a study by Nam and Nghia (2011), the characteristic equation for vibration of the most general case of a cable is analytically derived, where both the sag and flexure in the cable are taken into account. After that, by considering proper simplifying assumptions of the small flexural rigidity parameter,

asymptotic forms of that equation were obtained. It renders a practically applicable procedure to estimate cable tension using measured natural frequencies.

As for the boundary conditions, Rebecchi et al. (2013) presented an experimental procedure for the axial load identification of slender prismatic beams with unknown boundary conditions by making use of one vibration frequency and five amplitudes of the corresponding mode shape. Yan et al. (2014) proposed an innovative method for cable force identification which converts constructing and solving the cable motion equation into finding the zero-amplitude point of its mode shape. The results showed that when the modal order is less than 18, the method can achieve a maximum relative error of less than 5% regardless of the boundary conditions at both ends. Syamsi et al. (2022) extended the two-mode frequency approach by introducing equivalent effective length for any mode pairs regardless of the type of end-restraints. To verify the proposed formula, three cases of cable end-restraints (hinged-hinged, fixed-fixed and hinged-fixed) with the same tensioning force and cross-sectional properties were studied.

The single-cable model is convenient and highly efficient in engineering, so the single-cable model is irreplaceable in practical engineering applications. After deriving theoretical formulas and fitting experimental data, researchers proposed a series of empirical formulas based on the single-cable model, considering the simplicity of engineering applications. For example, Hiroshi et al. (1980) gave a series of empirical formulas for cables with different slenderness ratio ranges to meet engineering needs under different conditions. Ricciardi and Saitta (2008) considered the effects of bending stiffness and sag in the formula and proposed a practical formula for continuous cables.

In the above studies, theoretical research is carried out based on the single-cable model for the problem of cable identification. However, the identification accuracy of the single-cable vibration method is very dependent on the accuracy of the basic model of the cable and the assumption of boundary constraints. The string structure is a hybrid structure of rigidity and flexibility, in which the end restraint stiffness of the cable members is related to the distribution of the cable force. Therefore, the constraints of the cable are difficult to determine. Moreover, many cables exist in actual engineering in the form of continuous and multi-strand cables, so the cable model's bending stiffness and boundary constraints that are assumed to be in the form of single cables may deviate greatly from the actual situation. In order to use the assumption of the single-cable model to improve efficiency, we believe that it is necessary to improve the accuracy of the cable force identification results based on the single-cable model for the tensioned string structure.

To make the cable force identification of the string structure more accurate by using the single-cable model, this paper intends

to conduct a modal analysis of the overall structure of the string beam by means of finite element numerical simulation and theoretical analysis. The three-stage criterion method is proposed and used to obtain the local modal information of the cable under the influence of the overall structure. After mastering the real local vibration characteristics of the cable, the difference between the cable force identification results based on the vibration method are compared with the design cable force based on the assumption of a single-cable model. This method can be used to study the magnitude of the error caused by the calculation of the cable force of the tension-string structure based on the single-cable model assumed with different boundary conditions. The three-stage criterion is beneficial to put forward suggestions for improving the cable force identification accuracy of the vibration method single-cable model of the existing string structure. It will enable the single-cable model assumption to be used to simultaneously improve the efficiency and ensure the solution accuracy. The work of this paper is a useful discussion on the identification of the vibration method of complex cable systems, such as the beam string structure.

2 Vibration method cable force identification principle

The principle of the vibration method is to 1) use a vibration converter to pick up the vibration signal of the cable that has received artificial excitation or environmental excitation; 2) analyze and process the vibration signal to obtain the natural vibration frequency of the cable; 3) calculate the cable force according to the relationship between the cable force and the natural vibration frequency. The string model and beam model are the main existing cable force identification models for a single cable.

2.1 String model and formula

For slender cables with small cross-sectional areas and large lengths, the influence of bending stiffness, sag and other factors on the cable force can be ignored, so the tensioned string model can be used to calculate the cable force (Irvine et al., 1974). The more commonly used classical cable force theory formula for this model is shown in Eq 1:

$$T_n = 4ml^2 \left(\frac{f_n}{n} \right)^2 \qquad (1)$$

In Eq 1, m is the mass per unit length [kg/m]; T_n is the cable force [N]; f_n is the nth order frequency of the free vibration of the cable [Hz]; l is the cable length [m].

2.2 Beam model and formula

For short and thick cables with large cross-sections and small lengths, in order to meet the requirements of cable force identification accuracy, their bending stiffness must be considered, so it is necessary to use the beam model to calculate cable force (Humar, 2012).

Assuming that the mass, m, per unit length of the beam is constant and the bending stiffness, EI, is also constant, the free vibration equation is:

$$EI \frac{\partial^4 y}{\partial x^4} + N \frac{\partial^2 y}{\partial x^2} + m \frac{\partial^2 y}{\partial t^2} = 0 \qquad (2)$$

Considering the hinged condition at both ends, the theoretical formula for calculating the cable force is shown in Eq 3:

$$T_n = 4 \frac{m f_n^2 l^2}{n^2} - \frac{n^2 \pi^2 EI}{l^2} \qquad (3)$$

The boundary conditions of the cable segment in the beam string structure are closer to those of the articulated boundary conditions at both ends. Therefore, the error comparison is made on the basis of the hinged connection, so only the hinged condition is introduced in this paper.

3 Basic principles of dynamic finite element analysis of string structures

3.1 Basic assumptions

In order to calculate conveniently, basic assumptions should be made for the beam string structure according to its mechanical characteristics:

1. It is assumed that the connection point between the cable segment and the strut is an ideal hinge, and the connection nodes are completely coincident.
2. The cable has been kept in working condition, only under tension, not loose.
3. The cable segment is a straight-line element.
4. Within a small time period, the cross-sectional area of the strut and beam elements remains unchanged.

3.2 Basic principles of dynamic characteristic analysis

The undamped free vibration equation of the string structure is:

$$[M]\{\ddot{U}\} + ([K_E] + [K_G])\{U\} = 0 \qquad (4)$$

Where $[M]$ is the mass matrix; $\{U\}$ is the total nodal displacement vector of the structure; $\{\ddot{U}\}$ is the total nodal acceleration vector of the structure; $[K_E]$ is the total elastic stiffness matrix of the structure; $[K_G]$ is the total geometric stiffness matrix of the structure.

After the static analysis of the structure is completed, the static equilibrium position of the string structure is obtained. In the dynamic analysis, the internal force and geometric coordinates of the static equilibrium position of the system are selected as the initial state of the dynamic analysis. That is, the system is assumed to vibrate slightly at the static equilibrium position.

For a linear system, the particular solution of Eq 4 is:

$$\{U\} = \{\Phi\} \sin(\omega t) \tag{5}$$

where ω is the circular frequency (1/s) and $\{\Phi\}$ is the mode shape vector.

Substituting Eq 5 into Eq. 4, after derivation, we can get:

$$[K]\{\Phi\} = \omega^2 [M]\{\Phi\} \tag{6}$$

where $[K]$ is the total stiffness matrix of the structure at static equilibrium $[K] = [K_E] + [K_G]$.

The dynamic analysis of the string structure system can be reduced to the generalized eigenvalue problem of Eq 6. The calculation methods mainly include the Block Lanczos method and the Subspace method. Among them, the Block Lanczos method eigenvalue solver is the default solver of ANSYS modal analysis, which uses the Lanczos algorithm, which in turn uses a set of vectors to realize the Lanczos recursive calculation. This method has the same accuracy as Subspace but is faster. The Block Lanczos method will be used in the calculation in this paper.

4 Establishment of ANSYS dynamic analysis model of the string structure

This paper uses ANSYS software, using APDL language to write command flow, and establishes a beam string structure model for numerical simulation analysis.

4.1 Element type selection

The steel beam part of the beam string structure model is simulated by the 3-D linear finite-strain beam element Beam188. It is a two-node three-dimensional linear beam element, which can be defined by commands such as SECTYPE, SECDATA, and SECOFFSET to meet the actual section shape, and has 6 or 7 degrees of freedom on a single node. The beam element is calculated based on Timoshenko beam theory and is well suited to linear analysis and nonlinear analysis of large stress.
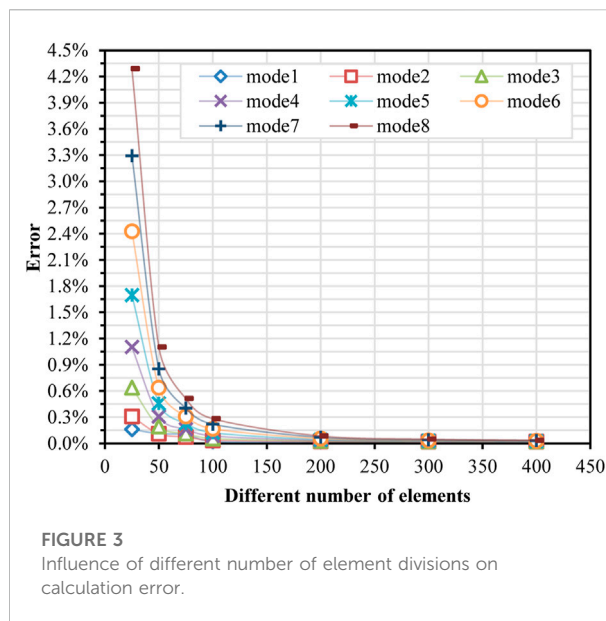
FIGURE 3
Influence of different number of element divisions on calculation error.

The strut part of the beam string structure model is simulated by the Link180 element. The Link180 is a 3-D element which is useful in a variety of engineering applications, for trusses, sagging cables, links, springs, and more. The element is a uniaxial tension-compression element with three degrees of freedom at each node: translation in the x, y, and z directions of the nodes, with plasticity, creep, rotation, large deflection, and large strain capabilities.

The cable part in the beam string structure model is simulated by the Beam189 element; a 3-D quadratic three-node beam element. With default settings, each node has 6 degrees of freedom. The element is based on Timoshenko beam theory and is well suited for linear, large rotation, large strain nonlinear applications. In this paper, it is considered that the cable in the tensioned beam string structure is used as a short cable, and its flexural rigidity cannot be ignored. Therefore, compared with the Link10 element, the Beam189 beam element can more accurately simulate the cable in the tensioned beam string structure.

4.2 Prestressing

In ANSYS, two methods, the initial strain method or the cooling method, are usually used to simulate the prestress. The former applies initial strain to the cable element and the prestress is applied by pretensioning or precompressing the line element; the latter applies temperature load to the cable element and the prestress is applied by heating or cooling. In this paper, the Beam189 element is used to simulate the prestressed cable, which can easily apply prestressing through the INISTATE command.

Therefore, the initial strain method is selected to apply prestress to the cable.

4.3 Number of cable element divisions

The number of element divisions of the finite element model has a great influence on the accuracy of the calculation results. If the number of cable element divisions is too small, the error of the calculation results will be too large, which will not meet the accuracy requirements. By establishing a single-cable model, we divide a single cable into different numbers of elements. The error between the frequency results of finite element simulation and the theoretical solution under different element division conditions were calculated, and then the number of elements that can meet the accuracy requirements of the simulation were obtained. The "error" here means the frequency difference between the theoretical solution and the finite element simulation analysis result of a same single cable.

The comparison data is shown in Figure 3.

Figure 3 shows that with the increase of the number of element divisions, the error of the ANSYS frequency calculation result gradually decreases; from the high-order frequency to the low-order frequency, the error gradually decreases. When the number of element divisions increases to 100, the error between the model's first 8-order modal frequency results and the theoretical solution frequency tends to be stable. If the number of element divisions continues to increase, the error does not change much. At the same time, according to the condition that the calculation errors of low-order and high-order frequencies are both less than 0.3%, it can also be considered that the number of unit divisions must be 100 to meet the accuracy requirements of numerical calculation results. The computational cost can be minimised compared to the number of more unit divisions. Therefore, in the subsequent calculation, we uniformly divide each cable segment by 100 elements.

5 Extraction of local vibration modes of cables based on ANSYS

By performing modal analysis on the overall structure of the beam string structure, all the mode shapes and frequency information of the overall structure can be obtained. Among these modes, there are some where the entire structure vibrates, and some where only the cables vibrate locally. Among so many modes, if the local mode of a cable can be found, the corresponding frequency is the nth-order vibration frequency of the cable considering the influence of the overall structure; the corresponding mode shape is the nth-order mode shape of the cable considering the influence of the overall structure.

Based on the local cable vibration modes identified in the global modes, the cable force identification results can be obtained from the single-cable model assumption based on the vibration method. Hence, by comparing the difference between the obtained cable force identification results and the design cable force, the error size of the cable force identification can be studied and corrections can be suggested. Then it is possible to use the assumption of the single-cable model to improve the efficiency while ensuring the accuracy of the solution. Therefore, this paper proposes a three-stage criterion for local modal extraction of beam string structure to identify local modal information.

5.1 Criterion 1: Search criteria for main vibration cable segment

To determine which cable segment is the main vibration of a certain order vibration, we adopt the following criterion: find the node corresponding to the maximum amplitude and the cable segment where the node is located by means of APDL command flow.

ANSYS software has powerful post-processing capabilities. Using APDL language to write a program, the modal analysis results of the beam string structure, including each order mode shape diagram, vibration frequency, mode shape data, etc., can be exported to image or text format. Furthermore, the maximum amplitude of the node can be obtained from the command flow, and the cable segment where the node is located can be found to judge that the mode belongs to the main mode of a certain cable segment.

5.2 Criterion 2: Criteria for discriminating whether local vibration mode

While criterion 1 identifies whether a certain cable segment is the order mode's main vibration cable segment, criterion 2 determines whether this order mode must be the local vibration of this cable segment. Thus, the second criterion is used to make the following judgments:

1 When the length of the cable segment differs greatly, the amplitude of the cable segment is the largest, and the amplitude of each node of the other cable segments is 0 or very small, which can be determined as a local mode of a certain order of the cable segment.

2 When the length of the cable segment is similar, except for the similar cable segment, the amplitude of the cable segment is the largest, and the amplitude of each node of the other cable segment is 0 or very small, it can be determined as a local mode of a certain order of the cable segment.

5.3 Criterion 3: Judging the local modal order based on the MAC value

When we use criterion 2 to determine that a certain overall mode is a local mode of a certain cable segment, we still need to determine which mode of the cable segment corresponds to this mode. To this end, the third criterion is introduced: based on the Modal Assurance Criterion (MAC) value, the modal order of the cable segment where the maximum amplitude is located is determined.

The mode shape vector data exported from ANSYS is imported into MATLAB software, and the modal order of the cable segment where the maximum amplitude is located is judged based on the concept and function of the MAC.

The MAC is a common tool for evaluating structural dynamic characteristics. It is used to evaluate the degree of correlation between two sets of mode shape vectors.

The definition of MAC is shown in Eq 7:

$$MAC_{ij} = \frac{\left(\Phi_i^T \Phi_j\right)^2}{\left(\Phi_i^T \Phi_i\right)\left(\Phi_j^T \Phi_j\right)} \tag{7}$$

Where MAC_{ij} is the value of the modal confidence criterion of the two mode shape vectors: Φ_i、Φ_j. Φ_i、Φ_j are two sets of mode shape vectors, respectively. The value range of MAC_{ij} is $[0, 1]$, when $MAC_{ij} < 0.05$, Φ_i、Φ_j are independent; when $MAC_{ij} > 0.9$, Φ_i、Φ_j are related; if MAC_{ij} is between 0.05 and 0.85, it indicates that the Φ_i、Φ_j are partially related.

In this paper, using the overall structure calculation of the string beam, a finite element analysis model is established. The mode shape vector of the cable segment where the maximum amplitude is located is obtained through analysis. Then a single-cable finite element model with hinged ends is established to obtain the reference vector, Φ_j, of each mode shape. Calculating the MAC value, when, it can be determined that the order of the cable segment to be tested is the same as the order of the reference single cable, thereby identifying the order of the cable segment to be tested.

6 Numerical study

6.1 The calculation model of the beam string structure

To show the effectiveness of the method in this paper and show the regularity of the research more intuitively, a simple beam string structure is selected as an example. The beam element section is a circular pipe with an inner radius of 95.5 mm and an outer radius of 101.5 mm; the strut element has a circular section with a sectional area of 234 mm²; the cable element has an equivalent sectional area of 346 mm². The bending stiffness of the cable in this EI = 1810.072351 Nm²,

FIGURE 4
The serial number of cables and diagram of the beam string structure model [dimensions are in mm].
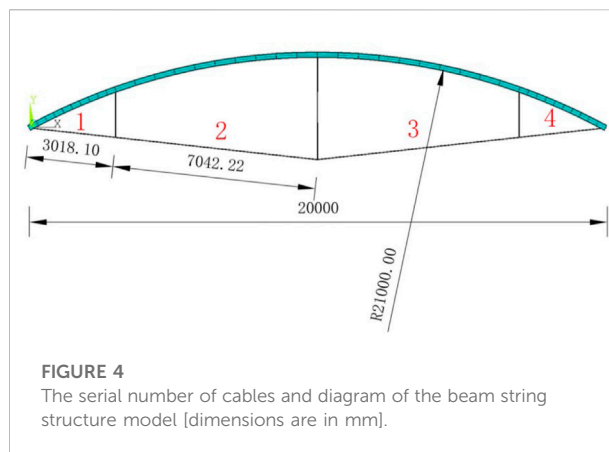
and the mass per unit length is 2.72 kg/m. The elastic modulus of beam and strut steel is 2.06e5 MPa, and the elastic modulus of cable steel is 1.9e5 MPa. The bending stiffness value here is a design value. If it is applied in practice, the cable factory will provide the actual value. The cables at the bottom of the beam string structure are numbered in sequence and the dimension of the beam string structure model is shown in Figure 4.

6.2 The basic process of ANSYS calculation

1 Build the model—the beams, rods, and cables of the beam string structure are selected as described in the previous section and the data files of the finite element model of the beam are written in APDL language, including element, material, and section information, mesh division, etc. The various information requested is defined using the LATT command. The LESIZE command is used to specify that the number of elements to divide the cable is 100, and the LMESH command is used to divide the mesh.

2 Constraints—Set the left end of the beam string structure as a fixed hinge and the right end as a sliding hinge. The Z-direction displacement of all nodes is constrained to be 0 and only the in-plane vibration of the beam is considered, the out-of-plane space vibration of the beam is not considered.

3 Static analysis—use the command flow "ANTYPE,0" to enter the static analysis solution, apply prestress to the cable using the initial strain method described in the previous section, turn on the large deformation switch and the acceleration of gravity, and calculate the initial state of the beam string structure.

4 Modal analysis—use the command flow "ANTYPE,2" to enter the modal analysis solution, turn on the prestress switch, and solve the first 12 order modal information.

5 Post-processing—write APDL program, and derive the mode shape diagram, mode shape vector and natural
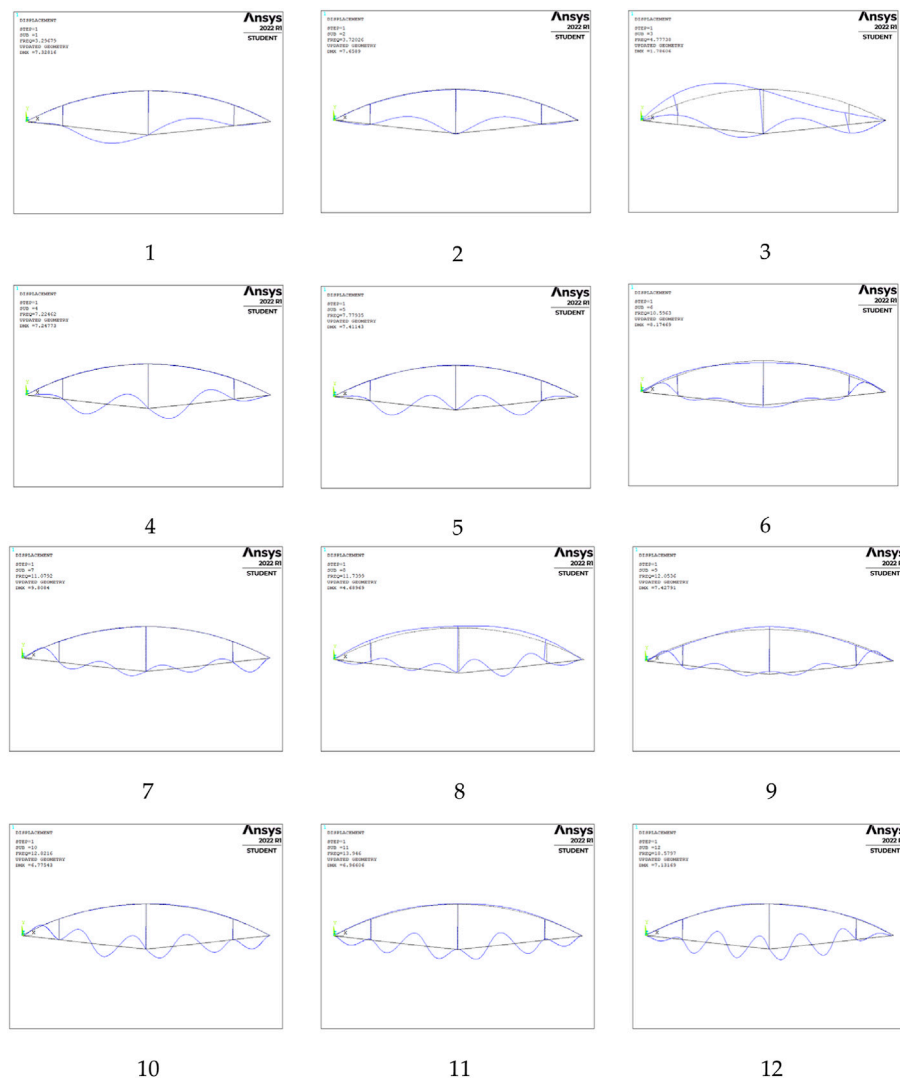
FIGURE 5
1st to 12th mode shapes.

frequency required in this paper according to the requirements.

6.3 Finding the main vibration cable segment

The modal analysis of the overall structure of the beam string structure is used to obtain the first 12-order mode shapes, as shown in Figure 5.

According to the model information, cable segment 1 contains node numbers 45–243, cable segment 2 contains node numbers 344–542, cable segment 3 contains node numbers 942–1,140, and cable segment 4 contains node numbers 643–841.

This article will take the No. 3 cable section as an example to introduce the criterions. For example, the maximum amplitude node number of the first mode is 1,037, which belongs to the No. 3 cable segment, and other rigid members have almost no amplitude. Except for the cable segments of similar length, the other cable segments also have almost no amplitude. Thus the overall mode of order 1 is considered to be the local mode of cable segment 3. The cable segments corresponding to other modal information are shown in Table 1. However, some of the overall modes are not only the vibration of the cable part, but also the vibration of beams or struts, such as the

TABLE 1 Overall modal information and corresponding cable segment number.

Overall mode	Maximum amplitude node number	The number of the cable segment	Frequency/Hz	Exclude?
1	1,037	No. 3 cable	3.29679	No
2	447	No. 2 cable	3.72026	No
3	1,017	No. 3 cable	4.77737	Yes
4	1,087	No. 3 cable	7.22461	No
5	401	No. 2 cable	7.77935	No
6	753	No. 4 cable	10.5963	No
7	153	No. 1 cable	11.0791	No
8	980	No. 3 cable	11.7399	No
9	748	No. 4 cable	12.0532	No
10	144	No. 1 cable	12.8216	No
11	1,042	No. 3 cable	13.9460	No
12	1,113	No. 3 cable	18.5797	No

TABLE 2 Calculation results of the MAC value of the No. 3 cable.

Overall modal order	Reference mode shape order			
	1	2	3	4
1	0.9978	0.0018	0.0003	0.0001
4	0.0026	0.9913	0.0047	0.0009
8	0.0773	0.0096	0.8871	0.0179
12	0.0004	0.0017	0.0072	0.9800

third-order overall mode. Such modes need to be eliminated and cannot be used as calculation samples. For the simple beam string model, this step can be roughly judged by visual inspection. For the complex string beam structure, it is necessary to compile a common program for accurate judgment.

6.4 Judging the modal order of the cable segment to be tested

For example, for the overall first-order mode mentioned in the previous section, the corresponding maximum amplitude cable segment is the No. 3 cable, and then it needs to be determined as the order of the local vibration of the No. 3 cable. A single-cable model was established based on APDL language as a reference, and the boundary condition of the single-cable was hinged at both ends. The ANSYS modal analysis calculation was performed and the first 4-order mode shape vector text data was exported as a reference. In this paper, the No. 3 cable is selected as the calculation object, and some MAC values are given as shown in Table 2.

Table 2 shows that the first order of the overall modes corresponds to the first order of the local vibration of the No. 3 cable; the fourth order of the overall modes corresponds to the second order of the local vibration of the No. 3 cable; the eighth order of the overall modes corresponds to the third order of the local vibration of the No. 3 cable; the 12th order of the overall mode corresponds to the fourth order of local vibration of No. 3 cable.

6.5 Comparison of local vibration frequency results

After the comparison and analysis of the data in the previous section, it can be found that under the influence of the overall structure of the beam string structure of No. 3 cable segment, its local first-order frequency is the first-order frequency of the overall mode, which is 3.296793 Hz; its local second-order frequency is the overall modal frequency. The frequency of the 4th order is 7.224617 Hz; the frequency of the local 3rd order is the frequency of the 8th order of the overall mode, which is 11.7399 Hz; the frequency of the local 4th order is the frequency of the 12th order of the overall mode, which is 18.5797 Hz.

The vibration frequency of the local cable segment extracted from the overall structure is compared with the frequency of the single-cable theoretical solution. The local frequency of the cable segment extracted by the method in this paper is compared with the frequency of the single-cable theoretical solution in Table 3; the frequency errors for the 1st to 4th orders are also presented.

The extracted frequency is very close to the theoretical solution frequency from the local modal information extracted from the overall mode using the three-stage criterion proposed in this paper, indicating that the method proposed in this paper is

TABLE 3 Comparison of extraction frequency and theoretical frequency.

Overall mode order	The local vibration order of the cable segment	Finite element cable force (N)	Theoretical solution frequency (Hz)	Extraction frequency (Hz)	Frequency error (%)
1	1	5,048.70	3.1687	3.2968	4.04
4	2	5,048.70	6.9418	7.2246	4.07
8	3	5,048.70	11.7695	11.7399	0.25
12	4	5,048.70	17.9212	18.5797	3.67

TABLE 4 Comparison of cable force results between extraction frequency and theoretical frequency.

Cable stage n	Finite element cable force (N)	Theoretical solution frequency (Hz)	Extraction frequency (Hz)	Calculated cable force (N)	Cable force error (%)
1	5,048.70	3.1687	3.2968	5,494.76	8.84
2	5,048.70	6.9418	7.2246	5,588.22	10.69
3	5,048.70	11.7695	11.7399	5,007.06	0.82
4	5,048.70	17.9212	18.5797	5,857.98	16.03

effective. The reason for the difference is that the cable segment in the beam string structure is not a single-cable model with hinged ends. The specific size and modification suggestions of this part of the error will be given in our follow-up research work.

6.6 Comparison of cable force identification results

Substituting the extracted first four-order local frequencies into the classical formula for single-cable force identification, the errors between the cable force and the finite element design cable force are 8.84%, 10.69%, 0.82%, and 16.03%, respectively, as shown in Table 4.

If the cable force identification of the tension beam string structure is based on the single-cable test method commonly used at present, it will inevitably cause identification errors. This part of the error is caused by the influence of the overall structure of the beam string structure. When we know the size of the error, it can be corrected in the actual test to improve the calculation efficiency and ensure the accuracy of the solution.

After analysis and comparison of examples, the method proposed in this paper is used to extract the local vibration modal information of the cable in the overall mode. The mode shape and frequency are consistent with the theoretical solution of the single cable, but there are certain differences due to the influence of the overall structure. The numerical example proves the effectiveness of the method for extracting the vibration modal information of the local cable presented in this paper.

7 Conclusion

The main work of this paper is discussed as follows:

1 An ANSYS dynamic analysis model of the beam string structure is established based on APDL language. Comparing multiple sets of data, it is found that when the number of element divisions in the cable modeling process is 100, it can better balance the common needs of calculation accuracy and calculation time cost.

2 A three-stage criterion for automatic identification of the local mode of the cable in the beam string structure is proposed. Criterion 1: Find the main vibration cable segment according to the maximum amplitude node. Criterion 2: When the cable length and other parameters of the cable segments differ greatly, the cable segment with the largest amplitude is the main vibration cable segment. In addition, if there is no other rigid member vibrating or the amplitude is small, it can be determined that the overall mode is the local mode of the cable segment. When the parameters such as the cable length of the cable segment are similar, except for the similar cable segment, the amplitude of the cable segment is the largest, and the amplitude of each node of the other member and cable segment is 0 or very small, it can be determined as a local mode of a certain order of the cable segment. Criterion 3: Use the Modal Assurance Criterion (MAC) to evaluate the correlation between the local mode shape and the reference mode shape and obtain

the local mode order corresponding to the main vibration cable segment.

3 After obtaining the local modal information of the cable of the beam string structure through the three-stage criterion, there is a certain error between the cable force identification result from on the vibration method based on the single-cable model and the actual cable force. The magnitude of the error reflects the influence of the overall structure on the vibration characteristics of the cable segment; the magnitude of the influence depends on factors such as the structural form, member stiffness, and cable force distribution. In the follow-up work, we will further use the method proposed in this paper to study the cable force identification error of the vibration method using the single-cable model of different types of string structures and propose a systematic correction scheme.

4 In practical application, for the specific beam string structure model, numerical analysis can be carried out by the method in this paper, and the size of the influence of each cable segment by the overall structure can be analyzed, so as to guide the correction of actual results and improve the accuracy of cable force identification.

Data availability statement

The original contributions presented in the study are included in the article/supplementary material, further inquiries can be directed to the corresponding author.

Author contributions

Corresponding author YZ proposed the work idea of this paper, analyzed and guided the results of the paper, and reviewed and revised the article. The first author, TZ, is responsible for the use and calculation of finite element software, and writes the first draft. HZ is responsible for reviewing and modifying English expressions.

Funding

Conflict of interest

The authors declare that the research was conducted in the absence of any commercial or financial relationships that could be construed as a potential conflict of interest.

Publisher's note

All claims expressed in this article are solely those of the authors and do not necessarily represent those of their affiliated organizations, or those of the publisher, the editors and the reviewers. Any product that may be evaluated in this article, or claim that may be made by its manufacturer, is not guaranteed or endorsed by the publisher.

References

Brownjohn, J. M. W. (2007). Structural health monitoring of civil infrastructure. *Phil. Trans. R. Soc. A* 365 (1851), 589–622. doi:10.1098/rsta.2006.1925

Byeong, H. K., and Taehyo, P. (2007). Estimation of cable tension force using the frequency-based system identification method. *J. Sound. Vib.* 304 (3-5), 660–676. doi:10.1016/j.jsv.2007.03.012

Cappello, C., Zonta, D., Ait Laasri, H., Glisic, B., and Wang, M. (2018). Calibration of Elasto-Magnetic Sensors on In-Service Cable-StayedBridgesfor Stress Monitoring. *Sensors* 18 (2), 466. doi:10.3390/s18020466

Chen, Y., Shen, Z., Zhao, X., and Chen, Y. (1999). Experimentalstudy on a full-scale roof truss of Shanghai Pudong international airport terminal. *J. Build. Structures* 20 (2), 9–17. doi:10.14006/j.jzjgxb.1999.02.002

Duan, Y., Zhang, R., Dong, C., Luo, Y., Or, S. W., Zhao, Y., et al. (2015). Development of elasto-magneto-electric (EME) sensor for in-service cable force monitoring. *Int. J. Str. Stab. Dyn.* 16 (4), 1640016. doi:10.1142/S0219455416400162

Fabo, P., Jarosevic, A., and Chandoga, M. (2002). Health monitoring of the steel cables using the elasto-magnetic method. *ASME Int. Mech. Eng. Congr. Expo.* 36258, 295–299. doi:10.1115/IMECE2002-33943

Fang, Z., and Wang, J. (2012). Practical formula for cable tension estimation by vibration method. *J. Bridge Eng.* 17 (1), 161–164. doi:10.1061/(ASCE)BE.1943-5592.0000200

Furukawa, A., Suzuki, S., and Kobayashi, R. (2022). Tension estimation method for cable with damper using natural frequencies with uncertain modal order. *Front. Built Environ.* 8, 812999. doi:10.3389/fbuil.2022.812999

Geier, R., De Roeck, G., and Flesch, R. (2006). Accurate cable force determination using ambient vibration measurements. *Struct. Infrastructure Eng.* 2 (1), 43–52. doi:10.1080/15732470500253123

Hiroshi, Z., Tohru, S., and Yoshio, N. (1980). Practical formulas for estimation of cable tension by vibration method. *J. Struct. Eng.* 122 (6), 651–656. doi:10.1061/(ASCE)0733-9445

Humar, J. (2012). *Dynamics of structures.* 3rd ed. Boca Raton: CRC Press.

Irvine, H. M., and Caughey, T. K. (1974). The linear theory of free vibration of a suspended cable. *Proc. R. Soc. Lond.* 341 (1626), 299–315. doi:10.1098/rspa.1974.0189

Kangas, S., Helmicki, A., Hunt, V., Sexton, R., and Swanson, J. (2012). Cable-stayed bridges: Case study for ambient vibration-based cable tension estimation. *J. Bridge Eng.* 17 (6), 839–846. doi:10.1061/(ASCE)BE.1943-5592.0000364

Ma, L., Xu, H., Munkhbaatar, T., and Li, S. (2021). An accurate frequency-based method for identifying cable tension while considering environmental temperature variation. *J. Sound. Vib.* 490, 115693. doi:10.1016/j.jsv.2020.115693

Mehrabi, A. B. (2006). In-service evaluation of cable-stayed bridges, overview of available methods and findings. *J. Bridge Eng.* 11 (6), 716–724. doi:10.1061/(asce)1084-0702(2006)11:6(716)

Mehrabi, A. B., and Tabatabai, H. A. (1998). Unified finite difference formulation for free vibration of cables. *J. Struct. Eng. (N. Y. N. Y).* 124 (11), 1313–1322. doi:10.1061/(asce)0733-9445(1998)124:11(1313)

Moradi, M., and Sivoththaman, S. (2013). Strain transfer analysis of surface-bonded MEMS strain sensors. *IEEE Sens. J.* 13 (2), 637–643. doi:10.1109/JSEN.2012.2225043

Nam, H., and Nghia, N. T. (2011). Estimation of cable tension using measured natural frequencies. *Procedia Eng.* 14, 1510–1517. doi:10.1016/j.proeng.2011.07.190

Pines, D., and Aktan, A. E. (2002). Status of structural health monitoring of long-span bridges in the United States. *Prog. Struct. Engng. Mat.* 4 (4), 372–380. doi:10.1002/pse.129

Qin, J., Chen, X., and Xu, R. (2007). Design and experimental study on the joints of Nation Gymnasium. *Ind. Const.* 37 (1), 12–15. doi:10.1016/S1872-2032(07)60057-2

Rebecchi, G., Tullini, N., and Laudiero, F. (2013). Estimate of the axial force in slender beams with unknown boundary conditions using one flexural mode shape. *J. Sound. Vib.* 332 (18), 4122–4135. doi:10.1016/j.jsv.2013.03.018

Ricciardi, G., and Saitta, F. (2008). A continuous vibration analysis model for cables with sag and bending stiffness. *Eng. Struct.* 30 (5), 1459–1472. doi:10.1016/j.engstruct.2007.08.008

Saitoh, M., and Okada, A. (1999). The role of string in hybrid string structure. *Eng. Struct.* 21 (8), 756–769. doi:10.1016/S0141-0296(98)00029-7

Sun, W. B., Yang, S. Y., and Chen, R. Y. (2003). Stiffness performance of truss-string structure of Guangzhou international convention and exhibition center. *J. South China Univ. Technol. Sci.* 31 (11), 33–36. doi:10.1007/s11769-003-0044-1

Syamsi, M. I., Wang, C. Y., and Nguyen, V. (2022). Tension force identification for cable of various end-restraints using equivalent effective vibration lengths of mode pairs. *Measurement* 197, 111319. doi:10.1016/j.measurement.2022.111319

Tadayuki, S. (1994). Estimating method of cable tension from natural frequency of high mode. *Dob. Gakkai Ronbunshu* 501, 163–171. doi:10.2208/jscej.1994.501_163

Volokhov, I. V., Gurin, S. A., and Vergazov, I. R. (2016). Study of the properties of high-sensitivity thermally-stable thin-film resistance strain gauges for integral pressure sensors. *Meas. Tech.* 59 (1), 80–86. doi:10.1007/s11018-016-0921-5

Wang, D. S., Zhou, J., Liu, C. Y., and Zhang, F. L. (2007). Design and research on roof structure of Pudong international Airport terminal 2. *Build. Struct.* 37 (5), 45–49. doi:10.1007/s10870-007-9222-9

Yan, B., Yu, J., and Soliman, M. (2014). Estimation of cable tension force independent of complex boundary conditions. *J. Eng. Mech.* 141 (1), 6014015. doi:10.1061/(ASCE)EM.1943-7889.0000836

Yun, C. B., Lee, J. J., and Kim, S. K. (2003). Recent R&D activities on structural health monitoring for civil infra-structures in Korea. *Ksce J. Civ. Eng.* 7 (6), 637–651. doi:10.1007/BF02829136

Zarbaf, S. E. H. A. M., Norouzi, M., Allemang, R., Hunt, V., Helmicki, A., and Venkatesh, C. (2018). Vibration-based cable condition assessment: A novel application of neural networks. *Eng. Struct.* 177, 291–305. doi:10.1016/j.engstruct.2018.09.060

Numerical study on hysteretic characteristics of transmission tower K-joints

Jian Zhang, Guangchen Wu and Lidong Yang*

Northeast Electric Power Design Institute Co., Ltd of China Power Engineering Consulting Group, Changchun, China

Introduction: The mechanical properties of joints have a significant impact on the dynamic response of transmission tower structures.

Methods: Considering bolt slip, the numerical model of the transmission tower K-joint is established. The mechanical properties of K-joints are studied from three aspects: failure mode, load-displacement hysteretic curve, and stiffness degradation by numerical method. The effects of bolt preload, friction coefficient, and member strength on the hysteretic properties of the K-joint are analyzed.

Results: The results show that due to the complexity of K-joints, bolt slip will lead to the reduction of ultimate bearing capacity and the change of failure position. In order to accurately obtain the mechanical properties of K-joints, the influence of bolt slip should be considered in the research process; The plumpness of load-displacement hysteretic curve is greatly affected by parameters; The stiffness of K-joints degenerates with the increase of loading times.

Discussion: The results provide a reference for the mechanical analysis of the transmission tower.

KEYWORDS

transmission tower, K-joints, hysteretic characteristics, numerical simulation, bolt slip

1 Introduction

Transmission towers in service will be subjected to earthquakes, ice or wind loads and other loads, which may lead to the destruction of the tower, affect the power supply and thus destroy the normal operation of society (Li et al., 2021). In order to prevent these disasters, it is necessary to obtain the accurate response of transmission towers under loads (Li et al., 2022). As the main force bearing part of the transmission tower, the mechanical properties of the joint have a significant impact on the dynamic response of the whole structure. Angle steel transmission towers are mostly connected by bolts, and in order to facilitate installation, the bolt hole diameter is usually larger than the bolt shank, in the process of transmission tower vibration members will occur relative sliding, that is, bolt slippage. Bolt slip will not only cause the difference of members failure mode but also lead to the change in joint stiffness (An et al., 2019). Ungkurapinan et al. (2003) studied the bolt slip phenomenon through experiments and proposed a mathematical model of bolt slip based on the test results. Through the combination of experiment and simulation (Jiang et al., 2011; Jiang et al., 2017), introduced bolt slip into the overall analysis of the transmission tower, and found that bolt slip had an impact on the ultimate bearing capacity, failure mode and displacement response of transmission tower. Wang et al. (2015) studied the influence of bolt slip on the structural response of transmission tower under uneven foundation settlement by numerical simulation. The results show that bolt slip not only increases the deformation of the tower, but also causes the redistribution of internal forces. Jiang et al. (2016) studied the influence of bolt slip uncertainty on the internal force of transmission tower by the LHS

FIGURE 1
Finite element model of the K-joint.

FIGURE 2
Constitutive relation of steel.
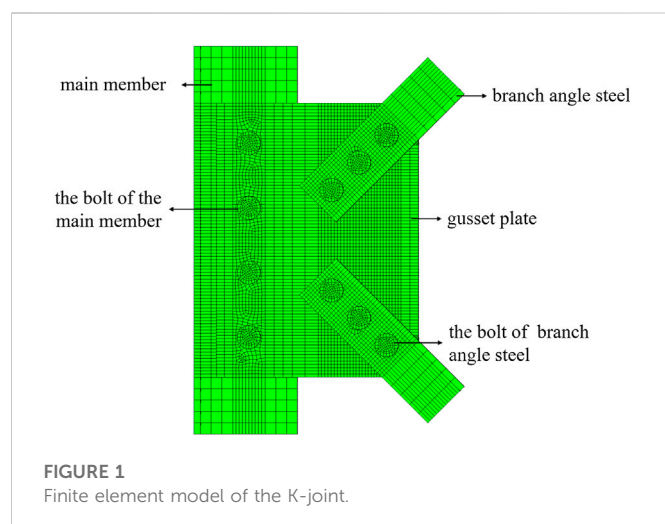
(Latin hypercube sampling) method. Yang et al. (2017) analyzed the influence of parameters such as initial torque and bolt hole diameter on the load-deformation curve of the joint through the tension test and numerical simulation of the bolt joint. The results show that when analyzing the tower structure, if the joint slip effect is ignored, it will cause higher axial stiffness. Ye et al. (2017) established an improved bolt slip model and accurately analyzed the behavior of the tower under external forces. The results show that the degree of influence of bolt slip is related to load. de Souza et al. (2021) performed reliability assessment of existing transmission line towers considering mechanical model uncertainties, their results showed that the bolt slip could affect the failure of the tower. Gan et al. (2021) performed monotonic tests to study the joint slip effect, and proposed a simplified multilinear bolt slippage model.

However, the above studies only consider the one-way slip of bolts, which is only applicable to the static analysis of transmission towers. In reality, the joints of transmission towers are often subjected to repeated loads during vibration, and the bolts will slip back and forth. The one-way slip model cannot accurately reflect the dynamic response of the tower. Yaghoobi and Shoddshtari. (2018) studied the influence of parameters such as bolt arrangement and bolt diameter on the mechanical behavior of joints under cyclic loading by conducting joint tests of 51 groups of wind turbine lattice towers. The results show that the above parameters can affect the hysteretic behavior of joints. Ma and Bocchini (2019) analyzed the stress state of the joint at each stage under cyclic loading, and proposed a hysteretic model of single bolted joints considering bolt slip. Considering different bolt clearances, Jiang and Dong. (2020) established a finite element model of double-limb lap joints and analyzed the hysteretic characteristics of the joints. Li et al. (2020) studied the mechanical properties of typical bolted joints under cyclic loading through numerical simulation, and analyzed the influence of parameters such as initial clearance and initial torque on the hysteretic behavior of joints. The results show that the influence of bolt reciprocating slip should be considered. Ebrahimi et al. (2022) performed test study to obtained the load-deformation curves of joint under cycle loading, and then proposed a mathematical formula to describe the load-deformation curves. Lu et al. (2018) Studied the influence of the cycle loading on the joint slip by tests, and the results showed that bolt-slip load decrease with the increase of the cyclic loading.

Nevertheless, the above studies are only for the lap bolt joints in transmission towers. In the transmission tower structure, the K-joint is
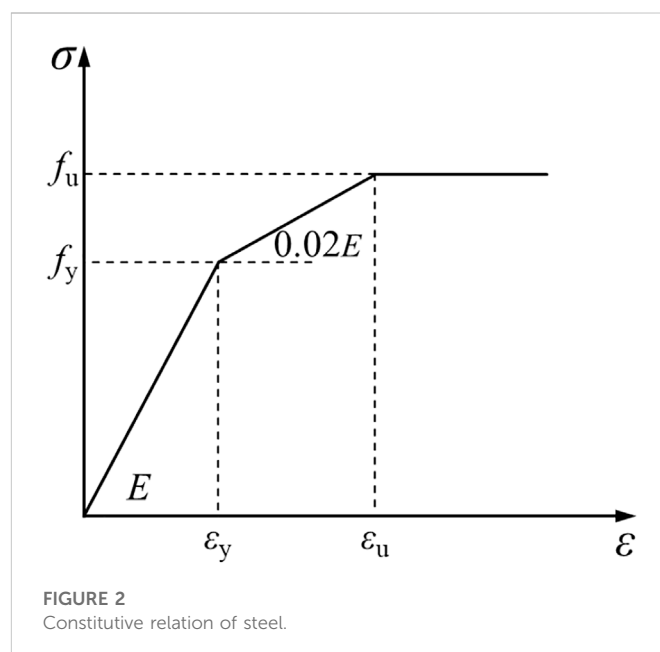
a very common form of joints, just like the lap joint, and compared with the lap joint, the stress state of K-joint is more complex. Zhao et al. (2014) deduced the initial rotational stiffness calculation model of K-joints and modified the model according to the test results. Yang et al. (2018) introduced the axial force coefficient of bolt joints into the traditional unit load method, and verified the accuracy of the improved method by experimental results. The results show that reducing the bolt clearance can decrease the deformation of K-joint of UHV cat-head transmission tower. Wang et al. (2019) studied the detached tubular K-joints through experiments and the results show that the separation distance of the gusset plate can affect the failure mode of the joint. Li et al. (2021) studied the influence parameters of the moment-rotation hysteresis curve of K-joints by establishing the finite element model (FEM) of K-joints. The results show that the failure mode of K-joints is related to the bolt grade and steel strength.

A review of the abovementioned works indicates that the existing research on bolt slip is aimed at bolt lap joints, and there is still a lack of research on bolt slip of K-joints, especially the mechanical properties under cyclic loading. Therefore, the mechanical properties of K-joints are studied by numerical method in this paper, and the effect of bolt slip on the hysteretic properties of K-joints is emphatically discussed. In Section 2, the numerical model and simulation schemes of K-joints are introduced. In Section 3, the simulation results are analyzed from the loading mode, load-displacement hysteresis curve and joint stiffness. And finally, Section 4 concludes the study.

2 Numerical simulation of the K-joint

2.1 The FEM of the K-joint

In this paper, a large-scale commercial finite element software ANSYS is used to simulate a K-joint of a transmission tower, and the FEM of the K-joint was established by 3D 8-node solid element SOLID185, as shown in Figure 1. There are five types of contact pairs in the model, which are the contact between the main angle steel and the

TABLE 1 Simulation scheme.

Case No.	Pretension force (kN)	Friction coefficient	Eccentricity (mm)	Bolt hole diameter (mm)	Component material (mm)	Bolt grade
A1	100	0.3	50	21.5	Q345	6.8
A2	100	0.3	50	20	Q345	6.8
B1	100	0.2	50	21.5	Q345	6.8
B2	100	0.4	50	21.5	Q345	6.8
B3	100	0.3	100	21.5	Q345	6.8
B4	100	0.3	50	20	Q345	6.8
B5	100	0.3	50	21.5	Q345	6.8
B6	125	0.3	50	21.5	Q345	6.8
B7	150	0.3	50	21.5	Q345	6.8
B8	100	0.3	50	21.5	Q420	4.8
B9	100	0.3	50	21.5	Q420	6.8
B10	100	0.3	50	21.5	Q420	8.8
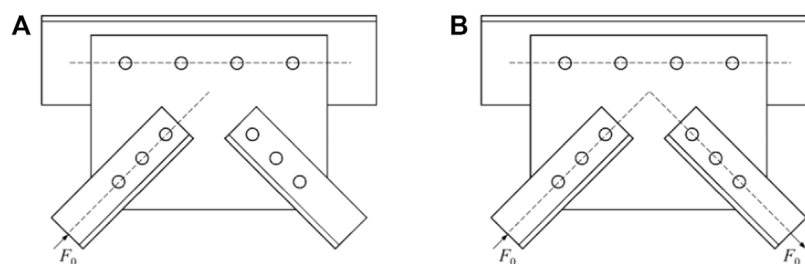
FIGURE 3
Loading mode of Group (A) and Group (B).

gusset plate, the contact between the branch angle steel and the gusset plate, the contact between the nut and the steel member, the contact between the bolt head and the steel member, and the contact between the bolt shank and the bolt hole. The 3D surface-to-surface contact element CONTA173 and the 3D target element TARGE170 are used as the contact element and the target element, respectively. And the bolt pretension force is applied by the preload element PRETS179. Hexahedral mesh is adopted in the model, and refined division operation is carried out at the contact part of steel members. The elastoplastic model with a strengthened section is adopted for the constitutive relationship of members and bolts, as shown in Figure 2. In Figure 2, E is the elastic modulus, ε_y is the yield strain, ε_u is the ultimate strain, f_y is the yield stress; f_u is the ultimate stress.

2.2 Simulated conditions

In this paper, simulations of twelve loading scenarios are carried out. The thickness of each component in this model is 10 mm, in which the main material is L160 × 10 angle steel and the branch member is L80 ×

10 angle steel. The effects of preload force, friction coefficient of the component, eccentricity, bolt hole diameter, strength of connector and bolt grade on the hysteretic performance of K-joints are studied, as listed in Table 1. In order to study the effect of bolt slip of K-joint, different loading modes were applied to Group A and Group B, respectively, in which tension compression cyclic load is applied to single branch angle steel of Group A, and tension compression cyclic load is applied to double branch angle steels of Group B, as shown in Figure 3. According to the Chinese code, the load is first loaded according to 25%, 50%, and 75% of the yield load, and each stage is cycled once. After the yield is reached, it is gradually increased according to 10% of the ultimate load, and each stage is cycled three times (Zhang and Li, 2017).

3 Result analysis

3.1 Influence of loading mode

When the single branch angle steel of the K-joint is subjected to cyclic loading, the stress state of the K-joint is equivalent to the bolt lap
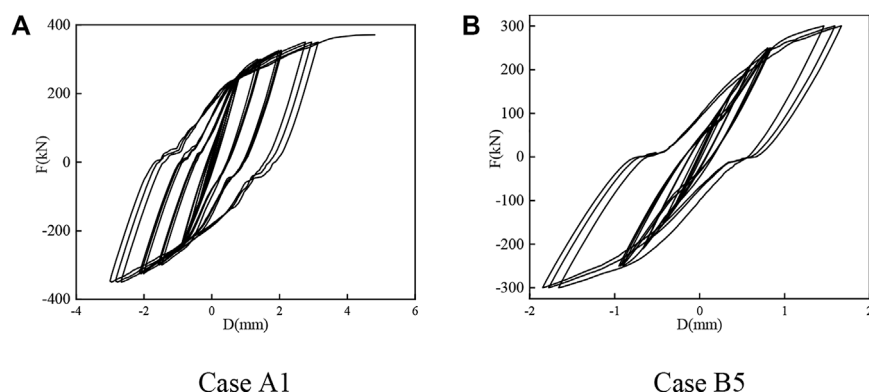
FIGURE 4
Load-displacement curves of the K-joints. **(A)** Case A1. **(B)** Case B5.
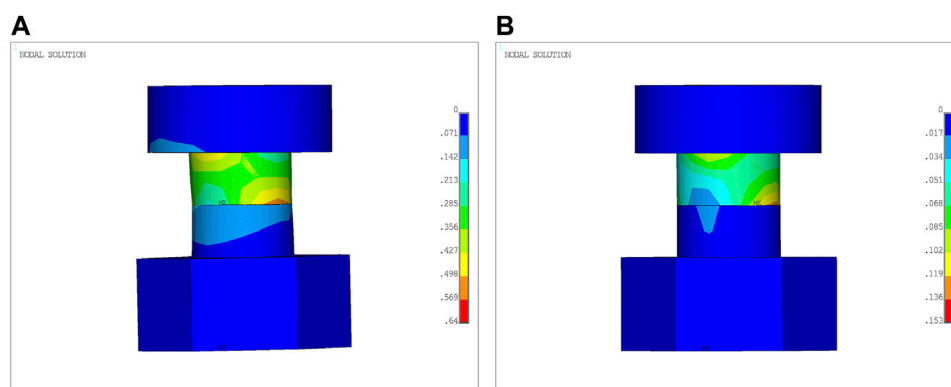
FIGURE 5
Bolt plastic strain of Case A1. **(A)** the bolt of branch angle steel, **(B)** the bolt of main angle steel.

joint. However, when double branch angle steels are subjected to cyclic loading because the resultant force of branch angle members bearing the load does not pass through the centroid of the bolt group on the main angle steel, the moment will be generated at the centroid of the bolt group, resulting in the sliding of the branch angle steel. Meanwhile, the gusset plate will rotate by eccentric force. In this state, the stress state of the K-joint is more complicated and it is also more consistent with the actual stress state of the K-joint. The load-displacement hysteresis curves under two different loading conditions are shown in Figure 4. The curve takes the displacement of the loaded branch angle steel as the horizontal axis and the load as the vertical axis. It can be seen that the ultimate load and failure position of Group B are different from those of Group A.

The ultimate load of Case A1 is 371.25 kN, the ultimate load of Case B5 is 300 kN, and the ultimate load is reduced by 23.75%. The reason for this phenomenon is that when the single branch angle steel of the K-joint bears the load F0, the resultant force at the centroid is only $F_0/\sqrt{2}$. At this time, the shear force of the bolt of the branch angle steel is greater than that of the bolt of the main member. Figure 5 shows the strain nephogram of the bolt. In Figure 5, the maximum plastic strain of the bolt of the main member is 0.153, while the maximum plastic strain of the bolt of the branch angle steel is 0.64,

which indicates that the bolt of the branch angle steel is damaged before the bolt of the main member.

When branch angle steels on both sides of the K-joint are subjected to a load F_0 of one tension and one compression at the same time, the resultant force at the centroid is $\sqrt{2}F_0$, the moment is larger, the rotation angle of the gusset plate is larger. And the bolt of the main member is subjected to a greater load, which will be failure before the bolt of the branch member, as shown in Figure 6, that is, the most unfavorable load condition for the K-joint is one side of the branch member is tensioned and one side of the branch member is compressed. At this time, the maximum plastic strain of the bolt of the main member is 0.216, while the maximum plastic strain of the bolt of the branch angle steel is 0.122.

However, when the bolt slip is not considered, the ultimate load of K-joints under the two loading methods is 375 kN and 373.8 kN, respectively, with a difference of 0.32%. At this time, the loading method has little effect on the ultimate load. Therefore, the main difference between Case A1 and Case B5 is due to the influence of bolt slip on the K-joint. Figure 7 shows the load-displacement hysteresis curve without considering the bolt slip. It can be seen that when the bolt gap is not considered, the hysteresis curve is fusiform and full in shape, which also shows that it is necessary to consider the bolt slip of the K-joint.
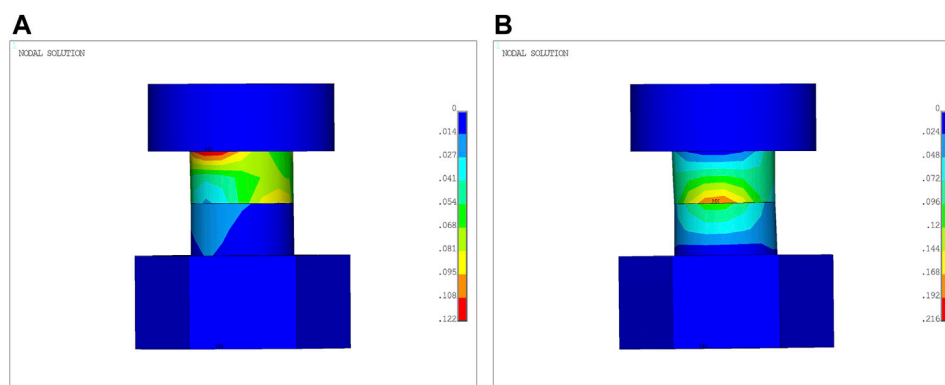
FIGURE 6
Bolt plastic strain of Case B5. **(A)** the bolt of branch angle steel, **(B)** the bolt of main angle steel.
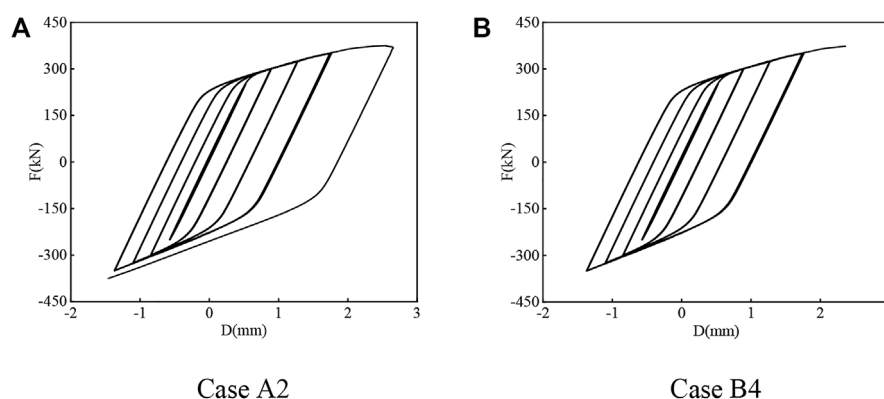
FIGURE 7
Load-displacement curves of the K-joints. **(A)** Case A2, **(B)** Case B4.

3.2 Load-displacement hysteresis curves

The trend of structural stiffness variation under cyclic loading can be obtained from the hysteretic curve. It can be seen from Section 3.1 that the bearing capacity of double branch angle steel loading is lower than that of single branch angle steel loading, and the K-joint is in the most unfavorable stress state. Therefore, this section mainly analyzes the hysteresis curve of double branch angle steel loading.

The hysteresis curve of each working condition is shown in Figure 8. It can be seen that the fullness of the hysteresis curve is affected by the parameters such as bolt preload, friction coefficient, eccentricity and other parameters. Compared with Figures 8D–F, it can be seen that with the increase of bolt preload, the shape of the hysteresis curve is plumper. This trend is the same as Figures 8A, B, D. The reason for this phenomenon is that increasing the preload of the bolt can make the components of the bolt connection area more closely fit, to a certain extent, the effect of increasing the friction force is achieved, so more energy is dissipated during the cycle. Figures 8C, D show the hysteretic curves of the joints with different eccentricities. When the eccentricity increases from 50 mm to 100 mm, the ultimate load decreases from 300 kN to 275.4 kN. This is because the same load can produce greater moment when the eccentricity increases, and the rotation angle of the gusset plate will also increase, resulting in the

failure of the joint. However, it has little effect on the shape of the hysteresis curve, because the load-displacement curve analysis focuses on the deformation of the branch angle steel rather than the rotation of the gusset plate. Compared with Figures 8G–I, the bolt grade is increased from 4.8 to 8.8, and the ultimate load is 239.25, 350 and 425 kN, respectively, which shows that increasing the bolt grade can effectively improve the bearing capacity of the joint, and meanwhile, the curve becomes more full.

As can be seen from Figure 8, the slope of the load-displacement curve decreases gradually during each cycle, indicating that the stiffness of the joint is degraded and the residual deformation is accumulated. The reason for this phenomenon is the yielding of members and bolts and the slipping of bolts. In addition, in the process of repeated loading, due to the existence of bolt clearance, both the bolt of the main angle steel and the bolt of the branch angle steel will slip a certain distance, which leads to the occurrence of the pinching phenomenon, making the hysteresis curve a pinched anti-S shape. If the clearance between the bolt and the screw hole is eliminated, a welding-like effect will be produced, and the hysteresis curve will also be in a full spindle shape, as shown in Figure 7. This shows that reducing the clearance and avoiding bolt slippage can improve the seismic performance and energy dissipation capacity of the K-joint.
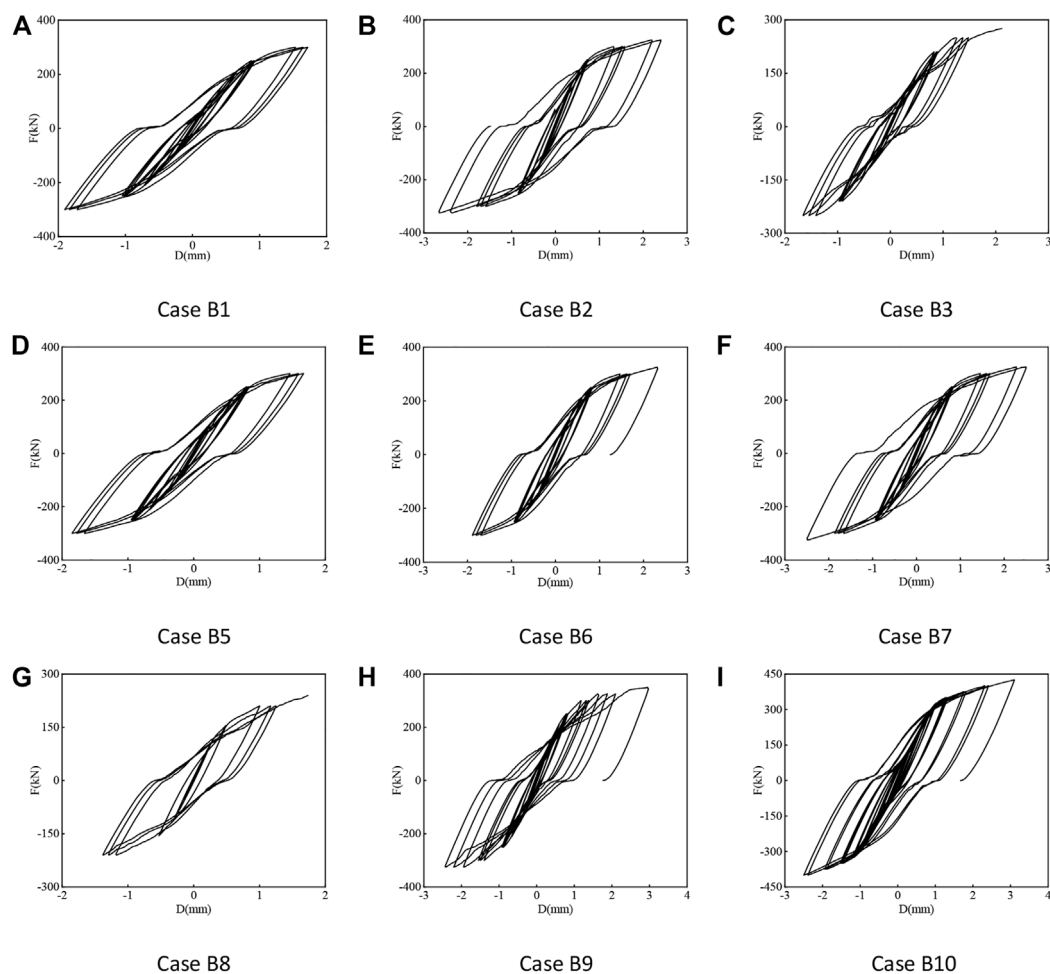
FIGURE 8
Load-displacement curves of the K-joints. **(A)** Case B1, **(B)** Case B2, **(C)** Case B3, **(D)** Case B5, **(E)** Case B6, **(F)** Case B7, **(G)** Case B8, **(H)** Case B9, (I) Case B10.

3.3 Rigidity degeneration

According to the Chinese code (China Academy of Building Research, 2015), the secant stiffness K_i under each cycle is calculated by Eq. 1.

$$K_i = \frac{|+F_i| + |-F_i|}{|+X_i| + |-X_i|} \qquad (1)$$

where $+F_i$ and $-F_i$ are the load values of the ith forward and reverse peak points; $+X_i$ and $-X_i$ are the displacement values of the ith forward and reverse peak points.

The secant stiffness K_i of the load-displacement curve of each cycle is shown in Figure 9. It can be seen from the figure that the secant stiffness of Case B4 and Case B8 suddenly decreases. As grade 4.8 ordinary bolts are used in Case B8, the shear strength is very low, and the bolts yield earlier, resulting in the early stage of the cycle joint stiffness decreased. Case B4 is similar to welding because there is no clearance. It can be seen from the shape of the hysteresis curve that there is an obvious yield point. When the component reaches yield, the
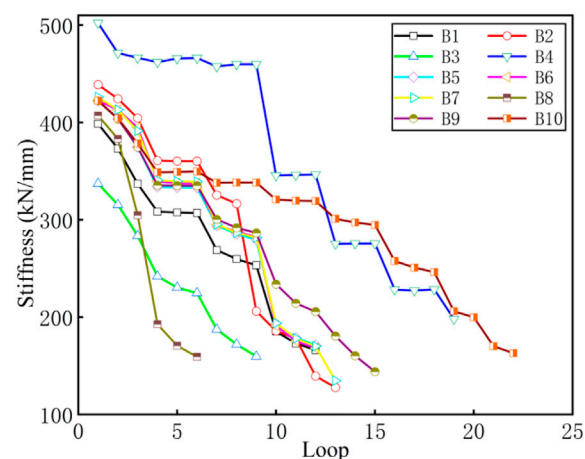
FIGURE 9
Stiffness degradation.

TABLE 2 Initial stiffness of K-joint.

Case No.	Initial stiffness (kN/mm)	Case No.	Initial stiffness (kN/mm)
B1	398.66	B6	422.49
B2	438.86	B7	426.10
B3	337.22	B8	407.27
B4	502.23	B9	422.29
B5	422.29	B10	422.31

stiffness of the joint will suddenly decrease first and then decrease slowly, while the stiffness degradation of other cases is generally gentle.

The stiffness of K-joints with larger eccentricity for the same material is generally lower. At the same time, the overall stiffness of the joint can be improved by increasing the strength of the component and upgrading the bolt grade.

In addition, Table 2 shows the initial stiffness K_0 of K-joints under different conditions. It can be seen from the table that the initial stiffness of the K-joints in the elastic state has little different.

4 Conclusion

In this paper, the influence of bolt slip on the hysteretic characteristics of K-joints under cyclic loading is mainly studied. The following conclusions are obtained from the analysis of failure mode, hysteretic curve and stiffness degradation:

(1) The stress state significantly impacts the bearing capacity of K-joints. The ultimate bearing capacity of K-joints under single branch member loading is much higher than that under double branch members loading. The most unfavorable load condition of K-joints is that one branch member bears tension and the other branch member bears compression.

(2) The loading method affects the failure position of the K-joint. Under single branch angle steel cyclic loading, the bolt of the branch angle steel is first destroyed, while under double branch angle steel cyclic loading, the bolt of the main angle steel is destroyed earlier than the bolt of the branch angle steel due to the greater resultant force.

(3) The existence of clearance not only leads to the decrease of bearing capacity of joints, but also affects the hysteretic performance.

(4) The plumpness of the hysteresis curve can be increased by increasing the preload of the bolt, increasing the strength of the component or reducing the clearance.

(5) With the increase in the number of loading cycles, K-joints show a trend of stiffness degradation. Increasing the strength of the component or the bolt grade can improve the overall stiffness of the K-joint, but the initial stiffness of each case has little difference.

Data availability statement

The original contributions presented in the study are included in the article/supplementary material, further inquiries can be directed to the corresponding author.

Author contributions

JZ Proposed research ideas, was responsible for the establishment and calculation of the finite element model, and wrote the first draft. GW was responsible for the analysis of the results of the paper. LY guided and revised the paper.

Conflict of interest

The authors declare that the research was conducted in the absence of any commercial or financial relationships that could be construed as a potential conflict of interest.

Publisher's note

References

An, L., Wu, J., and Jiang, W. (2019). Experimental and numerical study of the axial stiffness of bolted joints in steel lattice transmission tower legs. *Eng. Struct.* 187, 490–503. doi:10.1016/j.engstruct.2019.02.070

China Academy of Building Research (2015). *Specification for seismic test of buildings: JGJ/T 101-2015*. Beijing: China Architecture & Building Press.

de Souza, R., Miguel, L., McClure, G., Alminhana, F., and Kaminski, J., Jr (2021). Reliability assessment of existing transmission line towers considering mechanical model uncertainties. *Eng. Struct.* 237, 112016. doi:10.1016/j.engstruct.2021.112016

Ebrahimi, A., Yaghoobi, S., and Shooshtari, A. (2022). Joint slip formulation for members with double angle section based on experimental results in wind turbine lattice towers. *Arabian J. Sci. Eng.* 47 (10), 13699–13709. doi:10.1007/s13369-022-06690-z

Gan, Y., Deng, H., and Li, C. (2021). Simplified joint-slippage model of bolted joint in lattice transmission tower. *Structures* 32 (2021), 1192–1206. doi:10.1016/j.istruc.2021.03.022

Jiang, W., and Dong, X. (2020). Research on hysteresis behavior of bolted joints in transmission tower leg. *Chin. J. Constr. Mach.* 18 (06), 542–548. doi:10.15999/j.cnki. 311926.2020.06.014

Jiang, W., Liu, Y., Chan, S., and Wang, Z. (2017). Direct analysis of an ultrahigh-voltage lattice transmission tower considering joint effects. *J. Struct. Eng.* 143 (5), 4017009. doi:10. 1061/(asce)st.1943-541x.0001736

Jiang, W., Wang, Z., and An, L. (2016). The uncertainty of bolted joint slippage effects on the inner force of lattice transmission towers[J]. *Struct. Eng.* 32 (04), 42–50. doi:10.15935/j.cnki.jggcs.2016.04.007

Jiang, W., Wang, Z., Mcclure, G., Wang, G., and Geng, J. (2011). Accurate modeling of joint effects in lattice transmission towers. *Eng. Struct.* 33 (5), 1817–1827. doi:10.1016/j.engstruct.2011.02.022

Li, J., Mcclure, G., and Wang, S. (2021). Ensuring the structural safety of overhead transmission lines by design. *J. Aerosp. Eng.* 34 (3), 4021010. doi:10.1061/(asce)as.1943-5525.0001245

Li, J., Wang, B., Sun, J., and Wang, S. (2020). Numerical simulation study on hysteresis characteristics of transmission tower bolt joints. *J. Northeast. Univ. Nat. Sci.* 41 (11), 1633–1639. doi:10.12068/j.issn.1005-3026.2020.11.018

Li, J., Zhang, C., Wang, S., and Yin, S. (2021). Numerical study on the mechanical properties of transmission tower K-joints under cyclic loading. *Shock Vib.* 2021, 1–11. doi:10.1155/2021/7403365

Li, J., Zhang, X., and Mcclure, G. (2022). Numerical and full-scale test case studies on post-elastic performance of transmission towers. *Eng. Struct.* 259 (2022), 114133. doi:10.1016/j.engstruct.2022.114133

Lu, C., Ma, X., and Mills, J. (2018). Cyclic performance of bolted cruciform and splice connectors in retrofitted transmission tower legs. *Thin-Walled Struct.* 122, 264–285. doi:10.1016/j.tws.2017.10.020

Ma, L., and Bocchini, P. (2019). Hysteretic model of single-bolted angle connections for lattice steel towers. *J. Eng. Mech.* 145 (8), 04019052. doi:10.1061/(asce)em.1943-7889.0001630

Ungkurapinan, N., Chandrakeerthy, S., Rajapakse, R., and Yue, S. (2003). Joint slip in steel electric transmission towers. *Eng. Struct.* 25 (6), 779–788. doi:10.1016/s0141-0296(03)00003-8

Wang, J., Chen, Y., Guo, Y., Chen, C., and Sun, B. (2019). Experimental study on the mechanical behavior of detached tubular K-joints of narrow foundation transmission towers. *Eng. Mech.* 36 (1), 66–70.

Wang, P., Chen, H., Zhang, H., Zhou, X., and Ye, M. (2015). Effect of bolt joint on the behaviour of transmission tower with non-uniform settlement. *Eng. Mech.* 32 (10), 209–219. doi:10.6052/j.issn.1000-4750.2014.03.0212

Yaghoobi, S., and Shooshtari, A. (2018). Joint slip formulation based on experimental results in wind turbine lattice towers. *J. Struct. Eng.* 144 (6), 04018058. doi:10.1061/(asce)st.1943-541x.0002023

Yang, F., Zhu, B., and Li, Z. (2018). Numerical analysis and full-scale experiment on K-joint deformations in the crank arms of lattice transmission towers. *Struct. Des. Tall Special Build.* 27 (5), e1448. doi:10.1002/tal.1448

Yang, F., Zhu, B., and Xing, H. (2017). The slip characteristics and parametric study of bolted connections for transmission tower. *Eng. Mech.* 34 (10), 116–127. doi:10.6052/j.issn.1000-4750.2016.05.0403

Ye, M., Chen, H., Zhang, H., and Zhao, X. (2017). Effect of bolt joints on behaviour of transmission tower under external loads. *J. Univ. Sci. Technol. China* 47 (06), 498–507. doi:10.3969/j.issn.0253-2778.2017.06.008

Zhang, Y., and Li, Z. (2017). Study on mechanical behavior of multiplanar full-scale joint with composite connection. *China Civ. Eng. J.* 50 (06), 33–41. doi:10.15951/j.tmgcxb.2017.06.004

Zhao, N., Li, Z., and Liu, H. (2014). Calculation model of initial stiffness of angle steel tower K-joints. *Eng. Mech.* 31 (4), 93–101. doi:10.6052/j.issn.1000-4750.2012.11.0832

Mitigation of ice-induced vibrations for wind turbine foundation using damping vibration isolation

Zhang Baofeng[1,2,3], Dong Rui[4], Wang Gang[3], Wang Guojun[4] and Zhang Dayong[4]*

[1]Key Laboratory of Far-Shore Wind Power Technology of Zhejiang Province, Hangzhou, China, [2]College of Civil Engineering and Architecture, Zhejiang University, Hangzhou, China, [3]PowerChina Huadong Engineering Co., Ltd., Hangzhou, China, [4]School of Ocean Science and Technology, Dalian University of Technology, Panjin, China

The single pile offshore wind turbine foundation is a typical flexible structure, and the dynamic interac-tion between ice and structure is complex. Ice-induced vibrations can affect the normal operation of the upper motor and the safety of the foundation structure. This paper takes the interaction between ice and offshore platform in the Bohai Sea as the research object and discusses the strategies to mitigate the ice-induced vibrations of offshore wind turbine foundation. Through a simplified mechanical model of a damping vibration isolation system, the relationship between the parameters of the damping isolation layer and the structural damping ratio was analyzed. Based on the numerical simulation results, it was found that the damping isolation layer with a damping ratio of 0.2 can play a better role in controlling structural displacement and acceleration response under the action of steady-state and random ice forces. It provides a reference for the design of ice-resistant and safe operation of the offshore wind turbine.

KEYWORDS

wind turbine foundation, ice-induced vibrations, vibration mitigation, damping vibration isolation, self-excited vibration

1 Introduction

As a renewable and pollution-free clean energy, wind energy can effectively solve the energy shortage problem of human development. Therefore, the wind power industry has attracted the attention on countries in the world. The development of offshore wind turbine in China is relatively late, but China has a vast territory, with a coastline of 18,000 km, and offshore wind energy reserves of approximately 750 million kilowatts (Yang and Gui, 2010), which has huge development potential. The Bohai Sea and the Yellow Sea in China have higher latitudes and are affected by cold air. Compared with other sea areas, the air density and the wind energy density is higher respectively. Therefore, the Yellow Sea and the Bohai Sea are also the key sea areas for the development of offshore wind power in China. However, the intrusion into cold waves and cold air in winter will cause serious ice conditions in these sea areas. The continuous and strong vibration of marine structures caused by sea ice will cause structural damage, collapse and other catastrophic accidents (Clough and Vinson, 1986). Therefore, development in icy sea areas wind power must fully consider the impact on sea ice (Sacki et al., 1986). In addition, offshore wind turbine towers and foundations are simultaneously coupled with three structural features: high-rise structures, large power equipment foundations and marine engineering (Zhang et al., 2018). The vibration of wind turbines has a significant impact on the safe operation of supporting structures and power generation equipment, and therefore it is necessary to use

vibration reduction technology. To control the ice-induced vibration of the offshore wind turbine infrastructure.

At present, the research on wind turbine foundation vibration control is mainly based on wind, wave and seismic loads. Balendra proposed a U-shaped tuned liquid damper (TLCD) to control the vibration of the wind turbine tower formed by the wind load (Balendra et al., 1995); Murtagh proposed a tuned mass damper (TMD) to control the vibration of the wind turbine structure (Murtagh et al., 2008); Woude and Narasimhan pointed out that the vibration isolation device can effectively reduce the vibration response of the wind turbine structure (Woude and Narasimhan, 2014); Colwell and Basu pointed out the tuned liquid column damper (TLCD) can reduce the vibration of the offshore single-pile wind turbine under the action of wave load (Colwell and Basu, 2009); Cui Qiong used a suspended tuned mass damper device to reduce the vibration of the wind turbine structure under seismic load (Cui, 2011). The research on ice-induced vibration control is mainly for the Bohai Sea oil and gas platform structure. Ou Jinping proposed to use the concentrated deformation of the structural damping vibration isolation layer to reduce the ice-induced vibration of the platform (Ou et al., 2002); Chen Xing investigated the design of the tank size of the tuned liquid damper (TLD), and experimented and analyzed its ice vibration reduction effect (Chen et al., 1995); Wei Jinsheng pointed out that adding a viscoelastic energy dissipation diagonal brace structure to the structure can achieve a vibration reduction effect similar to springs and dampers (Wei et al., 1997); Yue et al. (2009), Zhang et al. (2009) studied the application of tuned mass damper for ice vibration control, proposed related vibration control algorithms, and experimentally verified that the tuned mass damper strategy can effectively control platform ice-induced vibration (Zhang et al., 2007; Zhang et al., 2010); Wang Yanlin et al. based on on-site monitoring, analysis showed that the ice-induced upper decks vibration control effect of JZ20-2NW platform after adopting damping vibration isolation measures is obvious (Wana et al., 2012). It can be seen that there are few researches on ice vibration control design of offshore wind turbine foundation.

This paper takes the offshore single-pile wind turbine as the research object, proposes a damping vibration isolation scheme and calculates its ice vibration control effect, which provides a theoretical reference for the anti-icing vibration design and safe operation of wind turbines in ice areas.

2 Structural dynamic characteristics and ice vibration analysis of single-pile wind turbine

The single-pile wind turbine has a simple structure, the main structure was composed of a tower and a single-pile foundation to support the upper nacelle and wind blades.

2.1 Analysis of structural dynamic characteristics

The diameter of the single-pile wind turbine foundation structure is generally about 3~6 m, which is suitable for the water depth range of 10–40 m. The disadvantage is that, the flexibility of the single-pile is obvious when the water is deep, and the excessive relative displacement and vibration of the upper end of the support
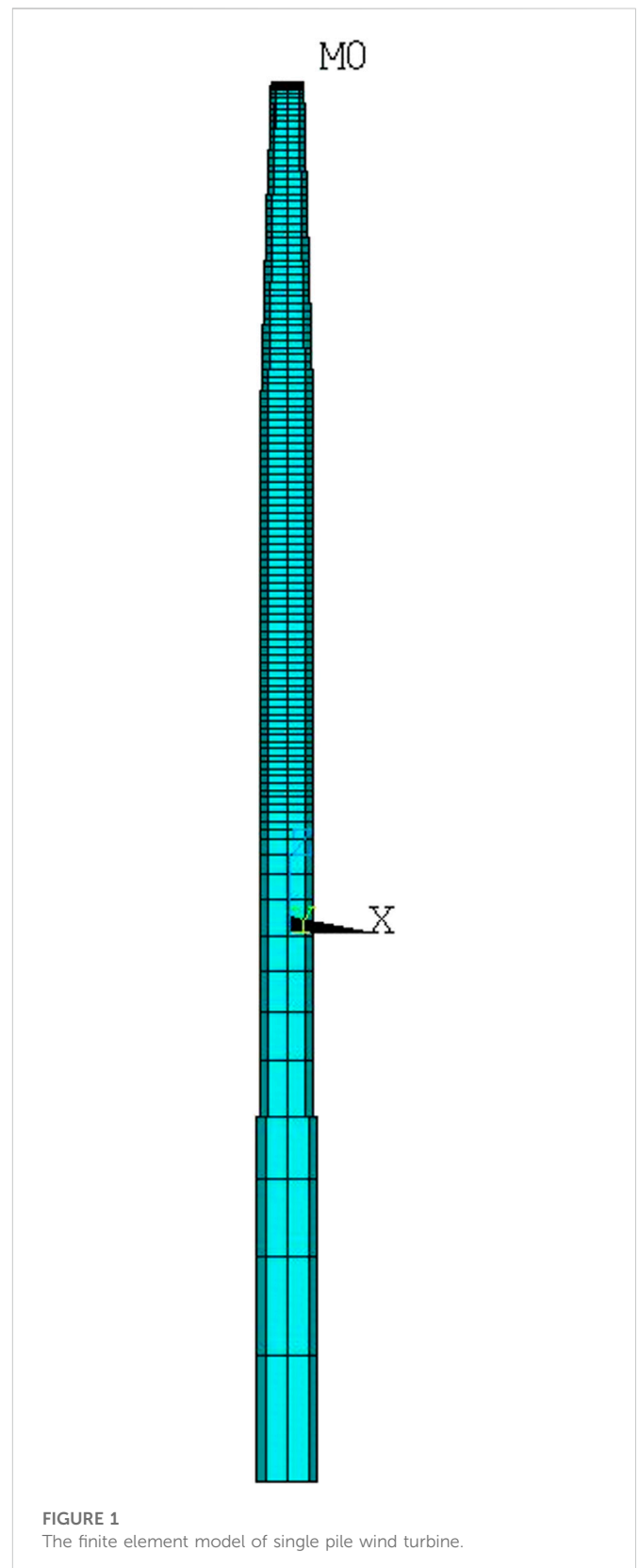

FIGURE 1
The finite element model of single pile wind turbine.

structure are the limiting conditions for its development. The finite element model is established based on ANSYS software. The mass of the upper unit is 220 t, with the horizontal plane as the coordinate origin. The tower structure is about 90 m above the water surface,

TABLE 1 The first four natural vibration frequencies of wind turbine.

Order	1	2	3	4
Frequency (Hz)	.2717	.2719	1.3292	1.3338

5.5 m in diameter at the waterline (upper section of foundation), 6.7 m in diameter at the lower section of foundation and 0.065–0.07 m in wall thickness. Beam188 unit is adopted. The diameter of the tower is 3.3–5.5 m, the wall thickness is 0.014–0.039 m, and beam188 unit is adopted. According to the mass of blade and nose, the position of the upper center of mass is: x = 3.37 m, y = 0, z = 2.06 m, which is simulated by MASS21 mass unit and fixedly connected with the top of tower. By adjusting the model grid, the grid of the foundation part with the same diameter is divided into four parts, and the grid size of the tower tube is set to 0.2 m to meet the requirements of calculation accuracy and efficiency. The foundation below the mud surface of the fan is established by the method of 6 times of pile diameter, and the bottom of the foundation is fully constrained, with the ice force acting at the coordinate origin, as shown in Figure 1.

Based on the modal analysis, the first four frequencies of the structure was obtained, as shown in Table 1.

Since the overall structure of the single-pile wind turbine foundation is basically symmetrical, the first and second vibration frequencies of the structure are almost equal, and the third and fourth vibration frequencies of the structure are almost equal. The first-order frequency of the structure is consistent with the given first-order fundamental frequency of the whole machine (0.240Hz–0.287 Hz), and the numerical model can reflect the dynamic characteristics of the structure.

2.2 Analysis of ice-induced vibration

When the ice speed was slow, the action of ice and structure will cause strong steady-state vibration. Kärnä (Karna et al., 2007) gave a simplified triangular wave time-domain function based on the measured ice force time history of self-excited vibration in the Bohai Sea, which shows the characteristics of ice force change in time for self-excited vibration, as shown in Figure 2.

Among them, F_{max} is the extreme value of ice force, which can be taken as the extreme value of static ice force; $\Delta F = qF_{max}q$ is 0.1–0.5, where 0.4 is taken here; F_{mean} is the average value of ice force; T is the ice force period, which can be approximated as the natural period of the structure of the calculation; α is the loading stage coefficient, where 0.8 is taken here.

The calculation of the extreme static ice force uses the formula given in the API RP-2N specification:

$$F = kDh\sigma_c. \tag{1}$$

Among them, k is the reduction factor, where 0.7 is taken here; D and h represent the diameter of the structural leg and the ice thickness; σ_c represents the uniaxial compressive strength of the ice.

When the ice speed was fast, irregular and random ice forces were formed, causing structural vibration.

Use ANSYS transient dynamics analysis, the displacement and acceleration time history curves of the structure under steady state (extreme ice thickness 45 cm) and random dynamic ice force was obtained, as shown in Figures 3, 4.

FIGURE 2
The model of steady-state ice force.
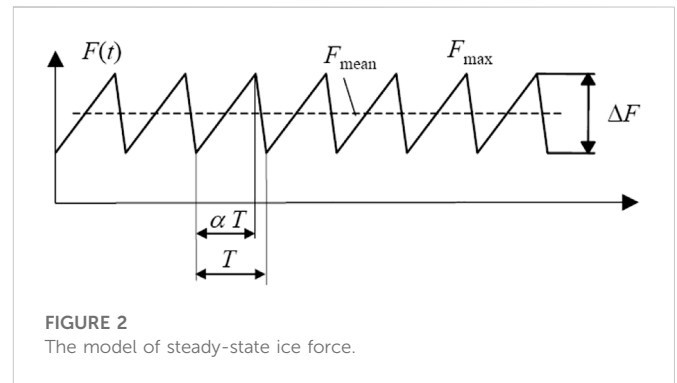
The results show that, compared with the steady-state ice force, the structural response under random ice force (10 cm ice thickness) is smaller, but it cannot be ignored. Under extreme steady-state ice forces, the vibration acceleration on top of the foundation reached 4.198 m/s² and the displacement reached 1.801 m, Large vibration and upper deformation pose a greater threat to the structure itself and electromechanical equipment, and control measures need to be taken.

3 Damping layer vibration isolation scheme and principle analysis

Based on the structural vibration control theory, and considering the towering and flexible structural characteristics of offshore wind turbines, a damping layer vibration isolation control scheme suitable for offshore wind power structures was proposed, and the structural model was simplified.

3.1 Vibration isolation scheme of damping layer

A damping and vibration isolation layer was set between the top of the wind turbine tower and the wind turbine head, the specific location was to replace a section of the tower connecting the tower with the unit on the top, and use a flange to connect it. The damping vibration isolation layer was mainly composed of a flexible vibration isolation support and a damping energy dissipation device, as shown in Figure 5. Among them, 1 is connected flange, 2 is spherical hinge, 3 is viscous damper, and 4 is flexible vibration isolation support, the device connects the lower part of the nose to the wind turbine foundation tower by bolts. When the wind turbine tower vibrates, the flexible vibration isolation support and viscous damper will swing 360° with the tower axis as the center. Because the lateral stiffness of the vibration isolation support was relatively small, the vibration isolation layer of the structure was vibrated horizontally. The relative deformation between the layers was larger, so the deformation of the vibration isolation support was limited by setting the damping energy dissipation device.

The concentrated deformation of the vibration isolation layer and the damping energy dissipator dissipated the input energy of the structure, achieve the purpose of reducing the vibration response to the structure, and protect the upper machine head equipment and reduce the fatigue damage to the structure. In the analysis, the damping and stiffness was mainly considered, and the combin14 spring element was used for simulation.
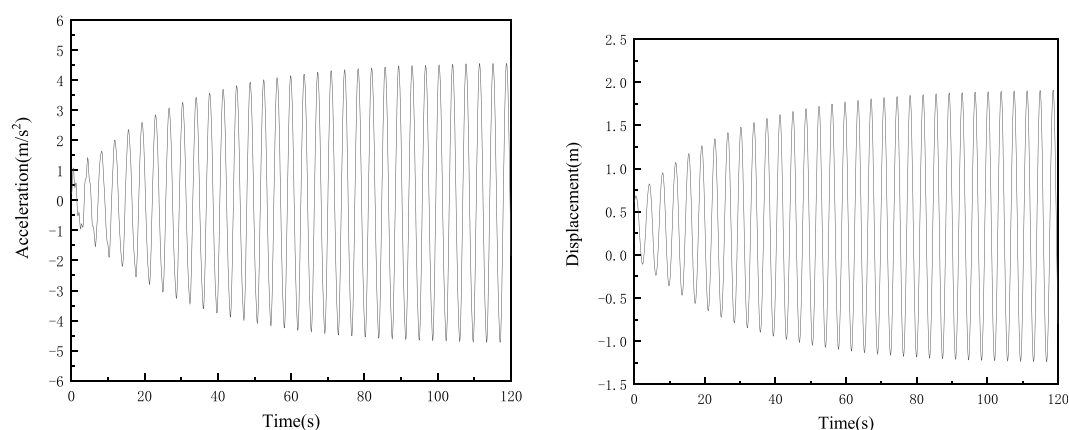
FIGURE 3
The acceleration and displacement response of wind turbine room under steady-state ice force.
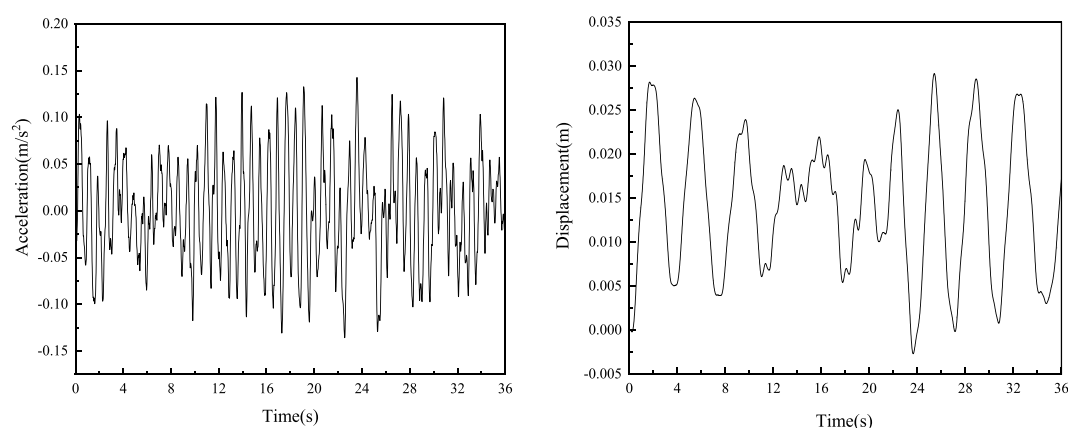
FIGURE 4
The acceleration and displacement response of wind turbine room under random ice force.
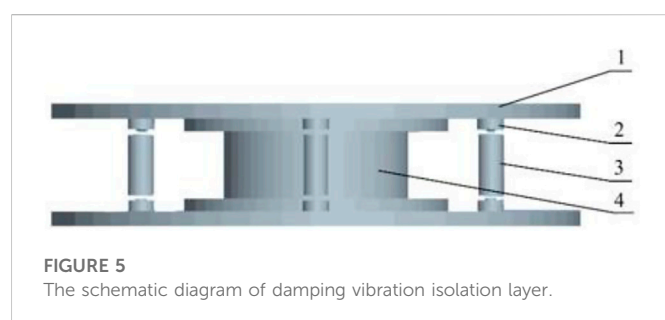
FIGURE 5
The schematic diagram of damping vibration isolation layer.

3.2 Simplified structural model

According to the calculation in Section 2.1, the first and second frequencies of the fan structure are 0.2717Hz and 0.2719 Hz respectively, and the offset of the center of mass mainly affects the first and second vibration modes and frequencies. Because the difference between the first and second frequencies is very small, it shows that the offset of the center of mass of the nose has little

influence on the whole. Therefore, the structure of the fan is simplified to two degrees of freedom, without considering the influence of the offset of the center of mass of the nose, so as to calculate the stiffness and damping of the damping vibration isolation system.

After the damping isolation layer is applied, the structure is simplified into a three-degree-of-freedom energy dissipation and vibration reduction system, as shown in Figure 6. The lower foundation part of the structure is simplified into a mass point m_1, its stiffness and damping coefficient are k_1 and c_1 respectively; a damping vibration isolation layer is set between the tower top and the wind turbine head, the stiffness and damping coefficient of the vibration isolation layer are k_3 and c_3 respectively; the wind turbine tower was simplified to a concentrated mass m_3, its stiffness and damping coefficients are k_2 and c_2 respectively; the wind turbine head was simplified to a concentrated mass m_3.

The parameters of the simplified model are shown in Table 2.

The diaphragm stiffness k_3 and damping coefficient c_3 need to be analyzed and designed according to the control conditions of the vibration isolation system of the structure.

TABLE 2 The parameters of vibration isolation system simplified model.

Parameter	Mass(t)			Stiffness (10^3 kN/m)			Damp (kN·s/m)		
	m_1	m_2	m_3	k_1	k_2	k_3	c_1	c_2	c_3
Value	705.296	222.725	218.280	14.336	2.026	—	127.192	26.868	—

FIGURE 6
The simplified model of damping vibration isolation system.

FIGURE 7
The equivalent system of damping vibration isolation simplified model.

FIGURE 8
The relation between damping ratio and damping coefficient of vibration isolation layer.
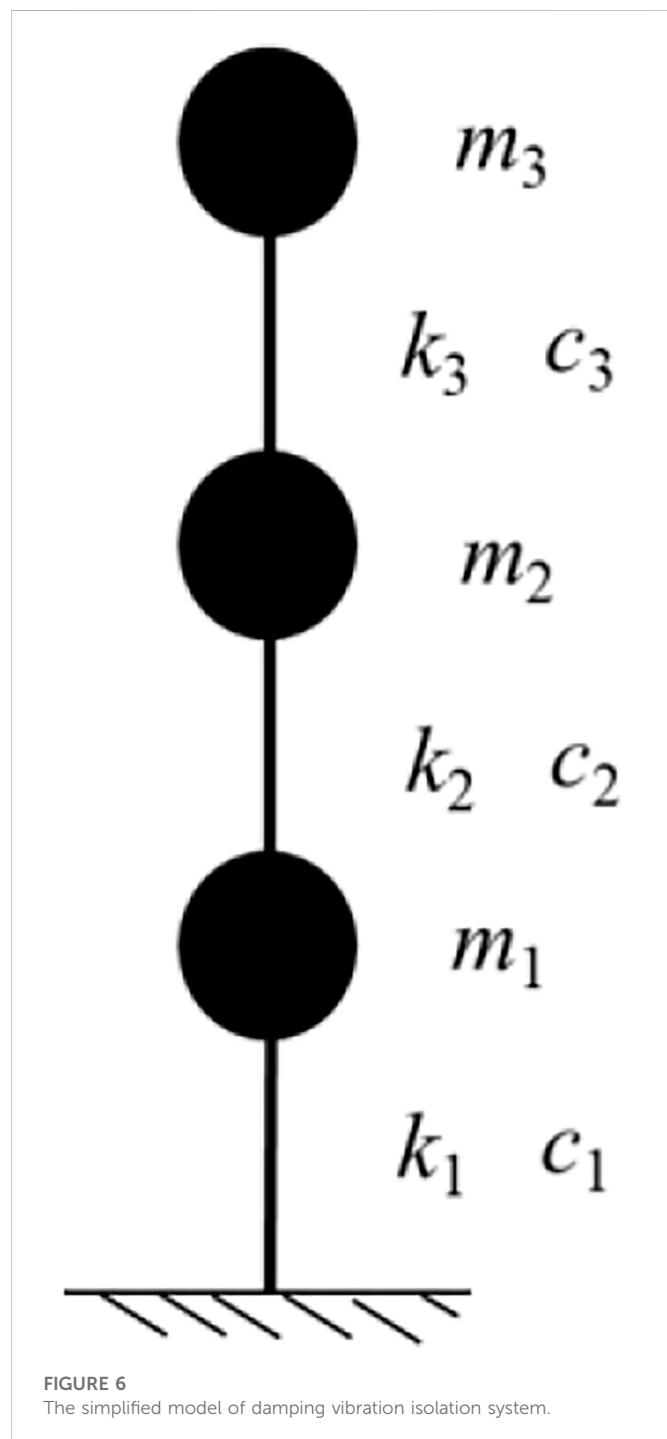
3.3 The damping ratio analysis

The damping ratio is an important parameter for dynamic calculations of structures, and it is also an important index to measure the energy dissipation of structures. Therefore, it is also regarded as an important metric to characterize the effect of vibration reduction schemes. The equivalent system of the structural damping and vibration isolation system model for offshore wind turbine is shown in Figure 7.
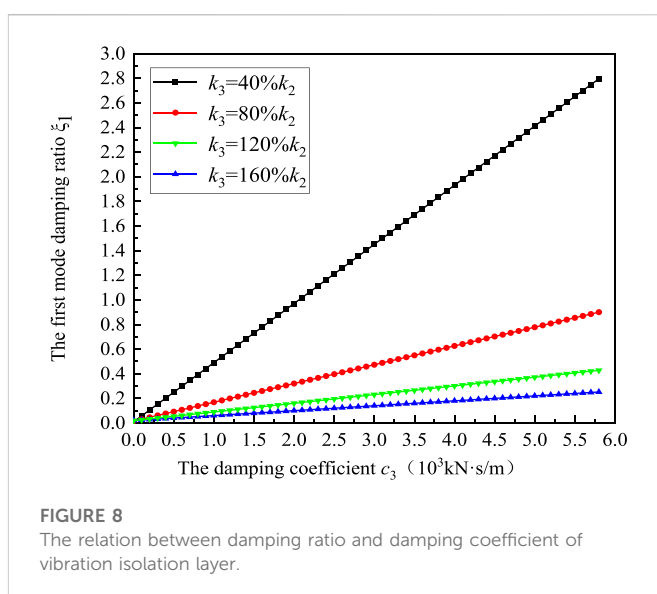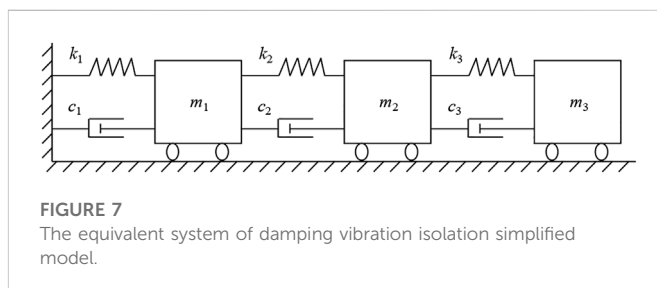
The vibrational differential equations for multi-degrees of freedom systems can be expressed as:

$$M\ddot{x} + C\dot{x} + Kx = F(t). \tag{2}$$

Among them, M is the mass matrix, C is the damping matrix, K is the stiffness matrix, and $F(t)$ is the external load on the structure. Isolate each mass point and perform force analysis to obtain the following matrix form:

$$M = \begin{bmatrix} m_1 & 0 & 0 \\ 0 & m_2 & 0 \\ 0 & 0 & m_3 \end{bmatrix}, \tag{3}$$

TABLE 3 The first frequency of damping vibration isolation system under different stiffness coefficients.

Parameter	The first frequency (Hz)	Relative mistake (%)
Original structure	.27173	36.32
$.2k_2$	.17305	22.99
$.4k_2$	.20925	16.52
$.6k_2$	.22683	12.71
$.8k_2$	.23719	10.20
$1.0k_2$	.24401	8.43
$1.2k_2$	.24883	7.11
$1.4k_2$	.25241	6.57
$1.6k_2$	.25518	6.09
$1.8k_2$	.25739	5.28
The passing frequency1P-3P	.200–.600	
Frequency range (10%margin)	.220–.540	

FIGURE 9
The relation between damping coefficient and stiffness ratio of vibration isolation layer.
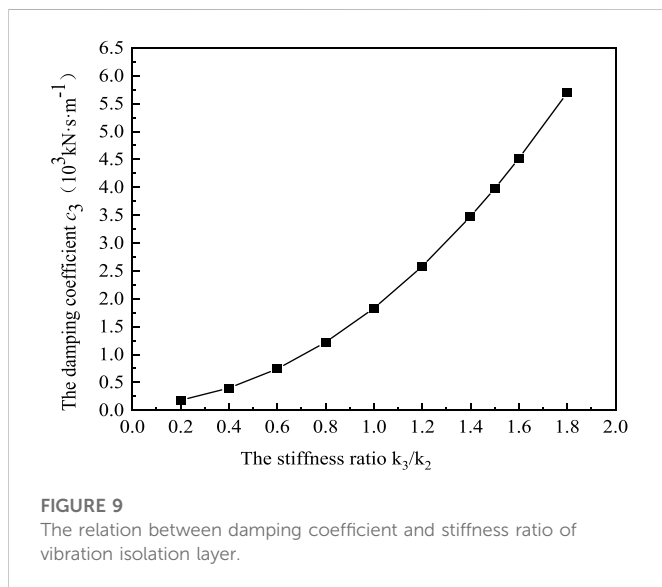
$$K = \begin{bmatrix} k_1 + k_2 & -k_2 & 0 \\ -k_2 & k_2 + k_3 & -k_3 \\ 0 & -k_3 & k_3 \end{bmatrix}, \tag{4}$$

$$C = \begin{bmatrix} c_1 + c_2 & -c_2 & 0 \\ -c_2 & c_2 + c_3 & -c_3 \\ 0 & -c_3 & c_3 \end{bmatrix}. \tag{5}$$

The linear vibration of the structure can be obtained by the superposition of the various modes, so the real mode vibration type matrix of the structure Φ is introduced:

$$\Phi = [\phi_1, \phi_2 \cdots \cdots \phi_n]. \tag{6}$$

Among them, ϕ_i is the order i vibration type of the system. Order:

$$M_n = \phi_n{}^T M \phi_n, \tag{7}$$

$$K_n = \phi_n{}^T K \phi_n, \tag{8}$$

$$C_n = \phi_n{}^T C \phi_n, \tag{9}$$

$$F_n(t) = \phi_n^T F(t). \tag{10}$$

Among them, M_n, K_n, C_n, and $F_n(t)$ represent the generalized mass, generalized stiffness, generalized damping, generalized load of the order n vibration type respectively.

Introduced the damping ratio:

$$\xi_n = C_n / 2p_n M_n = C_n / \sqrt{K_n M_n}. \tag{11}$$

In formula $p_n^2 = K_n / M_n$, ξ_n is the damping ratio of the order n. The eigenvalue expression of the structural vibration differential equation is:

$$\left| M - p^2 K \right| = 0. \tag{12}$$

Based on MATLAB programming, the expression of structural vibration mode and its frequency can be found, because the vibration pattern and frequency expression is not listed here. From Eq. 11, the first vibration type damping ratio of the system is expressed as:

$$\xi_1 = \phi_1^T C \phi_1 / 2p_1 \phi_1^T M \phi_1. \tag{13}$$

4 Analysis of parameters and control effects

The relative displacement between the damping and vibration isolation layers should not be too large. If the relative displacement between the layers is too large (the stiffness is too small), it will cause a large horizontal deformation between the nose of the offshore wind turbine structure and the wind turbine tower, which is not conducive to the safe operation of the offshore wind turbine structure. The stiffness k_3 and damping coefficient c_3 of the damped vibration isolation layer are the two key parameters for the design of the vibration isolation layer.

TABLE 4 The calculation parameters of damping vibration isolation system simplified model.

Working condition	Original structure	Case1	Case2	Case3	Case4	Case5	Case6
m_1(t)	705.296	705.296	705.296	705.296	705.296	705.296	705.296
m_2(t)	227.725	227.725	227.725	227.725	227.725	227.725	227.725
m_3(t)	218.280	218.280	218.280	218.280	218.280	218.280	218.280
k_1 (kN/m)	14335.9	14335.9	14335.9	14335.9	14335.9	14335.9	14335.9
k_2 (kN/m)	2025.7	2025.7	2025.7	2025.7	2025.7	2025.7	2025.7
k_3 (kN/m)	—	1215.42	1620.56	2025.70	2430.84	2835.98	3241.12
c_1 (kN·s/m)	127.192	127.192	127.192	127.192	127.192	127.192	127.192
c_2 (kN·s/m)	26.868	26.868	26.868	26.868	26.868	26.868	26.868
c_3 (kN·s/m)	—	740.63	1216.87	1828.78	2578.06	3476.98	4515.85
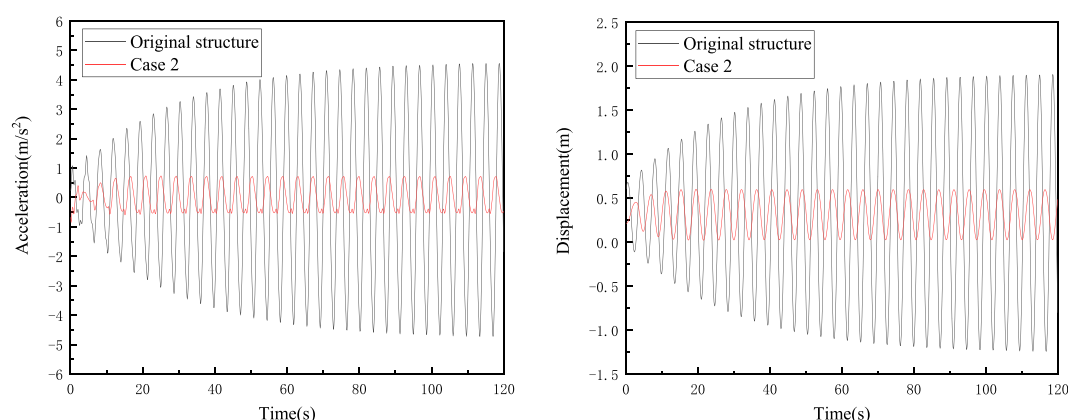
FIGURE 10
The acceleration and displacement control effectiveness when stiffness ratio is .8 under steady-state ice force.
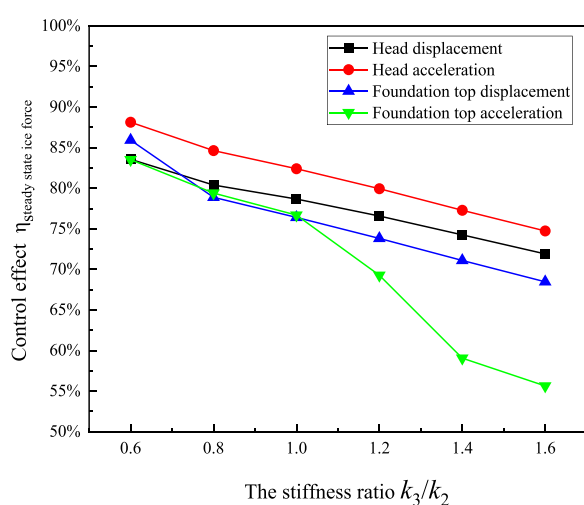
FIGURE 11
The control effectiveness of different stiffness ratios under steady-state ice force.

4.1 Stiffness coefficient of vibration isolation layer

According to Eq. 13, the first mode damping ratio ξ_1 can be obtained as the expression of the damping coefficient c_3 and the stiffness coefficient k_3 of the damping vibration isolation layer. In order to facilitate calculation and analysis, while considering that the stiffness design of the vibration isolation layer should match the stiffness of the tower at the location of the vibration isolation layer, the stiffness coefficient k_3 of the damping vibration isolation layer was expressed as a multiple of the wind turbine tower stiffness coefficient k_2 for analysis.

Figure 8 shows the variation law between the first mode damping ratio ξ_1 of the structure and the damping coefficient c_3 of the damping vibration isolation layer under different damping vibration isolation layer stiffness.

The change of ξ_1 with c_3 shows a linear relationship, and when k_3 increases, the rate of change of ξ_1 decreases.

When the modal damping ratio of the structure is greater than 0.2, the damping stiffness of the structure was increased, and the damping
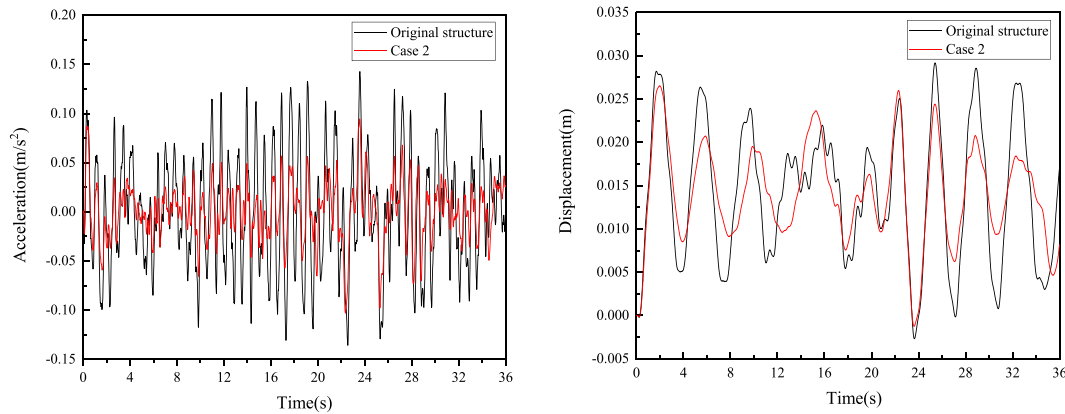
FIGURE 12
The acceleration and displacement control effectiveness when stiffness ratio is .8 under random ice force.
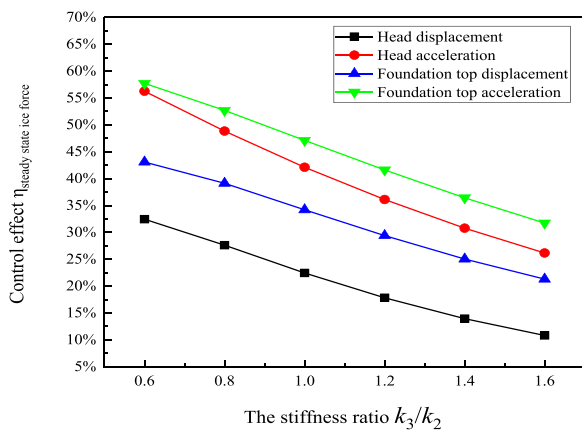
FIGURE 13
The control effectiveness of different stiffness ratios under random ice force.

coefficient increases significantly, which is difficult to achieve, and the damping effect of the damping vibration isolation layer will no longer be obvious (LONG et al., 2001). Therefore, the first mode damping ratio ξ_1 of the damping vibration isolation system is taken as .2 in the analysis.

The first order natural frequency of the flexible wind turbine structure should meet the passing frequency P-3P of the wind turbine blade (p = r/60, r is the blade speed, the unit is r/min, here is 12 r/min), Table 3 shows the first order fundamental frequency corresponding to different stiffness coefficients of the wind turbine damping vibration isolation system and the relative difference with the fundamental frequency of the original structure are obtained.

It can be seen that with the increase in the damping coefficient k_3, the first-order fundamental frequency of the wind turbine damping vibration isolation system increases and continues to approach the original structure; when $k_3 \geqq 0.6 \ k_2$, the first-order fundamental frequency satisfies the passage frequency range of the structural blade and was compared with the original structure base frequency, the relative frequency difference is small; therefore, considering that the dynamic characteristics of the overall

structure meet the requirements, the stiffness coefficient of the damping isolation layer should be at least 0.6 times the stiffness coefficient of the tower.

4.2 Damping coefficient of vibration insulation layer

When k_3 and ξ_1 are determined, the values of c_3 are obtained.

Figure 9 shows the relationship between the damping coefficient c_3 and the stiffness ratio. With the increasing stiffness ratio, c_3 increases accordingly.

Meanwhile, in order to clarify the effect of the stiffness parameter k_3 on the damping effect of the offshore structure, choose k3 at 0.6 k_2(Case1), 0.8 k_2(Case2), 1.0 k_2(Case3), 1.2 k_2(Case4), 1.4 k_2(Case5), 1.6 k_2(Case6), analyses the damping effect under different parameters, and the calculation parameters of the simplified model are shown in Table 4.

4.3 Analysis of vibration control effect

Analyze and calculate the dynamic response to the single pile offshore wind turbine structure under steady ice force and random ice force after adding the damping vibration isolation layer, and use η_i to evaluate the vibration control effect under different parameters, and further clarify the relevant parameters of the vibration isolation layer, among them, $\eta_i = 1 - i_{\text{After control}}/i_{\text{Before control}}$, i represents the root mean square value of acceleration and displacement response. The larger the value, the better the control effect.

4.3.1 Analysis of vibration control under steady-state ice force

Figure 10 shows the acceleration and displacement response time history of the wind turbine head before and after the addition of the vibration isolation layer under the action of steady-state ice force. The analysis shows that after adding the damped vibration isolation layer, the top displacement and acceleration response amplitude of the structure is greatly reduced, and the vibration isolation system has a good control effect.

Figure 11 shows the control effect of different parameters under the action of steady-state ice force.

When under the steady state ice, the damping vibration isolation layer stiffness coefficient k_3 is greater than .6 k_2, a good control effect can be achieved, and the control effect is greater than 50%; the larger the k_3 is, the worse the control effect. At the same time, considering that the inter-layer displacement of the damping vibration isolation layer should not be too large, the stiffness should not be too small.

4.3.2 Analysis of vibration control under random ice force

Figure 12 shows the acceleration and displacement response time history of the wind turbine head before and after the addition of the vibration isolation layer under the action of random ice force. The analysis shows that after adding the damped vibration isolation layer, the top displacement and acceleration response amplitude of the structure decreases, and the vibration isolation system has a better control effect.

Figure 13 shows the control effectiveness of different parameters under the action of random ice force.

Compared with the steady state ice, the damping vibration isolation layer under random ice force has a lower control effect on the structure response, and the control effect is less than 60%; the displacement control effect is lower than the acceleration control effect; and the larger the k_3, the worse the control effect. Therefore, the stiffness coefficient k_3 should not be too large; but at the same time, considering that the inter-layer displacement of the damping vibration isolation layer should not be too large and the stiffness should not be too small, it is recommended to select the damping vibration isolation layer stiffness k_3 to be 1.0–1.4 times the tower stiffness k_2.

Based on the above analysis, considering the effects of steady state and random ice forces, it is recommended to select the stiffness k_3 of the damping vibration isolation layer to be with in this 1.0–1.4 range of times the tower stiffness k_2, and the corresponding damping coefficient c_3 is 1828.78–3476.98 (kN·s/m).

5 Conclusion

Offshore wind turbine in cold regions faced the greater threat of sea ice and under the action of sea ice the structure will have obvious ice-induced vibration. Therefore, which is not conducive to the safe operation of wind turbines and it is essential to take corresponding control measures to achieve structural ice vibration control. In this paper, facing the offshore single-pile wind turbine structure in cold regions and the ice vibration control scheme of damping vibration isolation was proposed. Based on numerical calculation, the vibration control effect under different ice force excitation was analyzed, and the relevant parameters of the damping vibration isolation layer was clarified. The main conclusions are as follows:

1) The single-pile wind turbine has a simple structure, the tower and upper nacelle are supported on the upper part of the single-pile foundation. Compared with the traditional marine engineering structure, the wind turbine structure has a larger diameter at the waterline, a higher height, and a mass concentration on the top with the small fundamental frequency, and it is a typical high-rise flexible structure. The structure produces a relatively obvious dynamic response under the action of sea ice, which poses a non-negligible threat to the structural safety and normal operation of the wind turbine. Especially under the action of steady-state ice force, the large vibration and displacement of the nose position poses a greater threat

to the structure and the electromechanical equipment, and it is necessary to take relevant control measures.

2) Damping vibration isolation could effectively reduce the influence of external excitation on the structure, aiming at the towering and flexible structural characteristics of offshore wind turbines. So that, a damping layer vibration isolation control scheme suitable for offshore wind power structures is proposed. A damping isolation layer is set between the top of the wind turbine tower and the wind turbine head, and based on the vibration control theory, a simplified calculation model of the wind turbine three-degree-of-freedom damping isolation system was established.

3) The analysis shows that when the stiffness coefficient of the vibration isolation layer is at least 0.6 times to the tower stiffness coefficient, the dynamic characteristics of the damping vibration isolation system are similar to the original structure and meet the design requirements. The first mode damping ratio ξ_1 of the damping vibration isolation system and the change of layer damping coefficient showed to be a linear relationship, and as the stiffness of the vibration isolation layer increases and the rate of change of ξ_1 decreases. Moreover, in order to prevent the lateral displacement of the damping vibration isolation layer from being too large, the stiffness of the vibration isolation layer should not be too small. When the damping ratio of the first mode was greater than .2 and if the damping stiffness of the structure increase and that will increase the damping coefficient significantly. On the other hand, the increase in damping will decrease the damping effect of the damping isolation layer. Therefore, the ice vibration control effect of the damping vibration isolation system under different vibration isolation layer parameters when the damping ratio .2 was measured and calculated, the results show that the damping vibration isolation layer could play a better structural displacement and acceleration response control effect under both steady-state ice force and random ice force. That was the greater the stiffness of the damping vibration isolation layer, the worse the control effect, and the stiffness of the vibration isolation layer should not be too large. Comprehensive analysis suggests that the stiffness of the damping isolation layer should be within 1–1.4 times ranges the stiffness of the wind turbine tower.

4) This wok proposed a vibration isolation layer control method for the sea ice loads and investigated the influences, whether the vibration damping device could play a better control effect under the action of wind load still needs in-depth analysis. At the same time, the engineering applicability of the anti-icing device needs to be further studied.

Data availability statement

The original contributions presented in the study are included in the article/Supplementary Material, further inquiries can be directed to the corresponding author.

Author contributions

Conceptualization, ZB, DR, WG, and ZD; data curation, ZB, DR, WG, and WGu; formal analysis, ZB, DR, WG, and ZD; funding acquisition, ZD; methodology, ZB, WG, and ZD; writing—original draft, ZB and WG; writing—review and editing, ZB, DR, WG, WGu, and ZD. All authors have read and agreed to the published version of the manuscript.

Funding

Conflict of interest

Author ZB and WG were employed by PowerChina Huadong Engineering Co., Ltd. Author DR and WGu studied in Dalian University of Technology. Author ZD was employed by Dalian University of Technology.

No conflict of interest exits in the submission of this manuscript, and manuscript is approved by all authors for publication.

Publisher's note

All claims expressed in this article are solely those of the authors and do not necessarily represent those of their affiliated organizations, or those of the publisher, the editors and the reviewers. Any product that may be evaluated in this article, or claim that may be made by its manufacturer, is not guaranteed or endorsed by the publisher.

References

Balendra, T., Wang, C. M., and Cheong, H. F. (1995). Effectiveness of tuned liquid column dampers for vibration control of towers. *Eng. Struct.* 17 (9), 668–675. doi:10.1016/0141-0296(95)00036-7

Chen, X., Wang, L. Y., Song, A., and Zheng, C. B. (1995). Field experimental study on vibration reduction of TLD water tank. *Aata Oceanol. Sin. Chin.* 17 (2), 140–144.

Clough, H. F., and Vinson, T. S. (1986). Ice forces on fixed conical structures. Proceedings of the 5th International Offshore Mechanics and Arctic Engineering Symposium, Tokyo, Japan.

Colwell, S., and Basu, B. (2009). Tuned liquid column dampers in offshore wind turbines for structural control. *Eng. Struct.* 31 (2), 358–368. doi:10.1016/j.engstruct.2008.09.001

Cui, Q. (2011). *Study on vibration control of offshore wind turbines by means of pendulum damper.* Dalian, China: Dalian University of Technology.

Karna, T., Izumiyama, K., Yue, Q. J., Yan, Q., Guo, F., Xu, N., et al. An upper bound model for self-excited vibrations. Proceedings of the 19th International Conference on Port and Ocean Engineering under Arctic Conditions, Dalian, China, January 2007: 177–189.

Long, X., Wu, B., and Ou, J. P. (2001). Analysis of damping effect on vibration reduction of the aseismic structure. *World Inf. Earthq. Eng.* 17 (1), 40–45.

Murtagh, P. J., Ghosh, A., Basu, B., and Broderick, B. M. (2008). Passive control of wind turbine vibrations including blade/tower interaction and rotationally sampled turbulence. *Wind Energy* 11 (4), 305–317. doi:10.1002/we.249

Ou, J. P., Long, X., Xiao, Y. Q., and Wu, B. (2002). Damping isolation system and its vibration-suppressed effectiveness analysis for offshore platform jacket structures. *Earthq. Eng. Eng. Vib.* 22 (3), 115–122.

Sacki, H., Ono, T., Nakazawa, N., Sakai, M., and Tanaka, S. (1986). The coefficient of Friction between sea ice and various materials used in offshore structures. *J. energy Resour. Technol.* 108 (1), 65–71. doi:10.1115/1.3231243

Wana, Y. L., Yue, Q. J., Bi, X. J., and Shi, Z. M. (2012). Ice-induced vibration control effectiveness evaluation for an offshore platform based on a field monitoring. *J. Vib. Shock* 31 (7), 39–45.

Wei, J. S., Wang, L. Y., and Chen, X. (1997). Feasibility study of adding viscoelastic energy dissipation slant brace to reduce ice vibration on JZ20-2 MUQ platform jacket. *Chin. offshore oil gas(engineering)* 9 (6), 8–13.

Woude, C., and Narasimhan, S. (2014). A study on vibration isolation for wind turbine structures. *Eng. Struct.* 60, 223–234. doi:10.1016/j.engstruct.2013.12.028

Yang, Y., and Gui, W. M. (2010). The future trend of China wind turbine generation. *Int. Mechatronics Technol.* 13 (5), 41–43.

Yue, Q. J., Zhang, L., Zhang, W. S., and Karna, T. (2009). Mitigating ice-induced jacket platform vibrations utilizing a TMD system. *Cold regions Sci. Technol.* 56 (2), 84–89. doi:10.1016/j.coldregions.2008.11.005

Zhang, D. Y., Wang, G. J., Wang, S. F., Tong, B. L., Yue, Q. J., and Luo, C. X. (2018). Ice-resistant performance analysis of offshore wind turbine foundation in ice zone. *J. ship Mech.* 22 (5), 615–627.

Zhang, L., Yue, Q. J., Zhang, W. S., Fan, Z. L., and Liu, X. H. (2010). Measurement method for equivalent damping force of tuned mass damper (TMD). *J. Dalian Univ. Technol.* 50 (2), 162–166.

Zhang, L., Zhang, W. S., and Yue, Q. J. (2007). Experimental research on mitigation of offshore platform induced by ice excitation with absorbed damper. *China offshore Platf.* 22 (5), 33–37.

Zhang, W. S., Zhang, L., and Yue, Q. J. (2009). H∞control based on acceleration feedback of complex large-scale structures. *Eng. Mech.* 26 (5), 216–220.

Engineering vulnerability evaluation of building structures in coastal areas considering the effects of corrosion

Xiaona Chi[1]*, Anna Xu[1], Yajie Liu[1] and Peiyuan Lun[2]

[1]Xuchang Hengsheng Pharmaceutical Co., Ltd., Xuchang, China, [2]Guangdong Provincial Key Laboratory of Durability for Marine Civil Engineering, College of Civil and Transportation Engineering, Shenzhen University, Shenzhen, China

Chloride-induced corrosion is an important factor that affects the durability of building structures in coastal areas; it causes serious deterioration of reinforced concrete (RC) structures and leads to structural failure. However, chloride-induced corrosion is a slow process which spans the whole service life of building structures, and many factors can affect their service life, such as location, structural design, and drug management. This paper aims to predict the service life of building structures in terms of chloride-induced corrosion and through the concept of engineering vulnerability. It first investigates the model of corrosion initiation of reinforcement, along with the consequent concrete cover cracking. Second, according to the characteristics of building structure and corrosion, it determines an evaluation index system of engineering vulnerability and establishes an evaluation method of engineering vulnerability, considering that corrosion is based on the AHP method and fuzzy comprehensive evaluation. Finally, using a case study of a pharmaceutical factory structure in a coastal city, this study verifies the feasibility of the assessment method considering corrosion effects.

Introduction

A marine environment is one of the worst conditions for concrete structures, with marine concrete structures prone to durability damage due to combined physical, chemical, and mechanical factors. Among these factors, chloride attack is the main reason for reinforcement corrosion, concrete cover spalling, decreased bearing capacity, and structural concrete failure. As major building structures in coastal areas, pharmaceutical factories also suffer from chlorine-induced reinforcement corrosion, which destroy the passivation film of steel bars and thus reduce the cross-sectional area. Due to the continuous accumulation of corrosion byproducts, concrete covers will corrode and crack, leading to early damage to structures and the attenuation of their bearing capacity—structures may even be unable to meet their normal use and structural safety performance requirements of their design and use (Du et al., 2005; Jin et al., 2007; Wu and Yuan, 2008; Luo and NiuSu, 2019; Zhang et al., 2021). Chloride-induced reinforcement corrosion is one of the main factors affecting the service life of building structures, and other factors need to be considered in this light. Engineering vulnerability can fully reflect the potential impact of internal and external factors on building structures and has been widely used in recent years to guide disaster prevention and mitigation through rapid response and early prediction (Chen et al., 2020). Therefore, it is very important to correctly

evaluate the service life of building structures under the influence of reinforcement corrosion based on the concept of engineering vulnerability.

Many building structures have long stood in chloride-laden environments in coastal areas. The corrosion process includes corrosion initiation of reinforcement (corrosion critical point) (Apostolopoulos et al., 2013; Wang et al., 2013) and concrete cover cracking (cracking critical point) (Reale and O'Connor, 2012; Jamali et al., 2013), which have generally been regarded as failure criteria for assessing the service life of RC structures (Bazant, 1979a; Bitaraf and Mohammadi, 2008; Matsumura et al., 2008; Pour-Ghaz et al., 2009; Jang and Oh, 2010; Leonid et al., 2010; AI-Harthy et al., 2011; Guzmán et al., 2011; Wang et al., 2018; Tian et al., 2019). Therefore, a large number of theoretical models have been investigated to predict these two important stages (Bazant, 1979a; Bazant, 1979b; Morinaga, 1990; Liu and Weyers, 1998; Wu, 2006; Maaddawy and Soudki, 2007; Tamer and Khaled, 2007; Bitaraf and Mohammadi, 2008; Matsumura et al., 2008; Wang et al., 2008; Pour-Ghaz et al., 2009; Jang and Oh, 2010; Leonid et al., 2010; Lu et al., 2010; Zhang et al., 2010; AI-Harthy et al., 2011; Guzmán et al., 2011; Jin and Zhao, 2014; Liu and Yu, 2016; Zhang et al., 2017; Wang et al., 2018; Tian et al., 2019; Lun et al., 2021). Such studies have established a strong theoretical background for the focus of this study.

The current model of the chloride penetration process is based on Fick's second law, which is mainly affected by the diffusion coefficient of chloride ions, the critical concentration of chloride ions on the surface of reinforcement, the concentration of chloride ions on the surface of concrete, and the concrete cover depth (Bitaraf and Mohammadi, 2008; Matsumura et al., 2008; Pour-Ghaz et al., 2009; Wang et al., 2012; Wang et al., 2018; Tian et al., 2019). Among these, the diffusion coefficient of chloride ion and the critical concentration of chloride ions are greatly variable and are important factors which affect the length of the first stage. Many factors affect the diffusion coefficient of chloride ions, such as concrete hydration age, temperature, and relative humidity; the influencing factors are not independent and have a complex non-linear relationship, so it is difficult to establish a model that includes all influencing factors.

As another important corrosion stage, the various prediction models of the time for concrete cover cracking have been widely studied (Bazant, 1979a; Bazant, 1979b; Morinaga, 1990; Liu and Weyers, 1998; Wu, 2006; Maaddawy and Soudki, 2007; Tamer and Khaled, 2007; Wang et al., 2008; Jang and Oh, 2010; Leonid et al., 2010; Lu et al., 2010; Zhang et al., 2010; AI-Harthy et al., 2011; Guzmán et al., 2011; Jin and Zhao, 2014; Liu and Yu, 2016; Zhang et al., 2017; Lun et al., 2021). The theoretical models of concrete cover cracking time have been based on elastic, elastoplastic, damage, or fracture mechanics—considering the internal relationships between concrete cover cracking time and basic material parameters (e.g., elastic model, cover depth, reinforcement diameter, and pore zone thickness) and other parameters (e.g., temperature, corrosion current density, and corrosion rate of reinforcement). These models have been established on a clear mechanical theoretical basis and derivation process, which can reflect the real dynamic process of rust cracking and meet the characteristics of concrete cover cracking. However, the versatility of the prediction models based on different mechanics is still uncertain.

Over their long service, building structures are not only subject to the deterioration of concrete caused by chloride-induced reinforcement corrosion but are also affected by their location,

engineering design, structural construction, and drug management, resulting in significant differences in their state, causes of change, and development trends, similar to the engineering bearing model. This paper thus introduces the concept of "engineering vulnerability" for engineering geological disaster prevention research. Engineering vulnerability is usually investigated using other evaluation methods, such as analytic hierarchy process and fuzzy comprehensive analysis (Wang et al., 2022; Wu and Tang, 2022). As a non-engineering measure, engineering vulnerability has been fully applied in the evaluation of debris flow hazard in bridge and tunnel engineering (Xu et al., 2010; Xu et al., 2014), service state evaluation of high-speed railway subgrade (Chen et al., 2020), and seismic vulnerability evaluation of concrete structures (Qiang Zhang et al., 2020; Li et al., 2021; Marasco et al., 2021; Dai et al., 2022). These have achieved important research results which can fully reflect the potential impact of internal and external factors on building structures and provide a more scientific evaluation. There are, however, few reports on the service-life evaluation of building structures that consider corrosion effects based on engineering vulnerability. Therefore, it is of engineering significance to carry out a two-stage service-life assessment of building structures based on the concept of engineering vulnerability, considering the various factors related to the corrosion of building structures.

This study, based on previous service-life assessments in building structure research, investigates the engineering vulnerability analysis method for the service life of building structures considering corrosion effects. The model of the corrosion initiation of reinforcement is proposed based on Fick's second law, considering the various important parameters; the applicability of the existing models proposed by many scholars for predicting cover cracking time in building structures is then analyzed to select the most reasonable cracking model by experimental comparison. Based on the concept of engineering vulnerability, an evaluation index system for the service life of building structures considering corrosion effects is established, and the evaluation results of actual building structures are obtained using an analytic hierarchy process and fuzzy comprehensive analysis methods.

Research on service-life prediction of building structure

Based on previous research into building structure service life, this paper identifies two stages: corrosion initiation and cover cracking. Corrosion initiation occurs when chloride concentration on a steel surface reaches a critical value as an important dividing point, indicating that the passive film of the steel bar has just been destroyed. Concrete cover cracking is a process from the beginning of reinforcement corrosion to the concrete cover cracking, which represents the end of service life.

Model investigation for corrosion initiation

When concrete is saturated with water, the law of chloride penetration through concrete can be expressed based on Fick's second law, as indicated by numerous studies (Bitaraf and Mohammadi, 2008; Matsumura et al., 2008; Pour-Ghaz et al., 2009; Wang et al., 2012; Wang et al., 2018):

$$C(x, t_{in}) = C_s \left[1 - erf \left(\frac{x}{2\sqrt{D \cdot t_{in}}} \right) \right], \qquad (1)$$

where t_{in} is the time of structure exposure to the chloride environment (s), $C(x, t_{in})$ is the corresponding chloride concentration at depth x (m) (%/m³), D is the chloride diffusion coefficient (m²/s), C_s is chloride surface concentration (m²/s), and erf is the Gaussian error function.

$$erf(z) = \frac{2}{\pi} \int_z^\infty e^{-u^2} du, \qquad (2)$$

$$erf(z) = 1 - erfc(z). \qquad (3)$$

Therefore, Eq. 1 can be expressed as:

$$C(x, t_{in}) = C_s \cdot erfc \left(\frac{x}{2\sqrt{D \cdot t_{in}}} \right). \qquad (4)$$

However, in actual concrete structures, the microstructure of the concrete changes over time, and the effective diffusion coefficient of chloride ions is not constant but varies; thus, an improved chloride diffusion coefficient was proposed by Zhu (2017) as follows:

$$D(t) = \frac{KD_0}{(1-m)(1+R_D)} \cdot \left(\frac{t_0}{t} \right)^m, \qquad (5)$$

where K is the deterioration effect coefficient of the chloride diffusion performance of concrete; m is the damped exponential, with a value of 0.64; R_D is structural defect parameters; and D_0 is the chloride diffusion coefficient of concrete at hydration age of t_0, which is also affected by the w/c ratio, relative humidity, and temperature (Rodriguez and Hooton, 2003; Tang and Gulikers, 2007). In order to assess the effect of these parameters on the chloride diffusion coefficient, the corresponding correction diffusion coefficient D_0 is established thus:

$$D_0 = \lambda_{RH} \lambda_T D_{28}, \qquad (6)$$

where λ_{RH} is the correction coefficient for relative humidity RH (%), λ_T is the corresponding coefficient for temperature T (K), and D_{28} is the chloride diffusion coefficient for a specimen under standard curing (28 days) (Tang and Gulikers, 2007; Bitaraf and Mohammadi, 2008).

$$D_{28} = 10^{(-12.06+2.4w/c)}. \qquad (7)$$

The parameters λ_{RH} and λ_T can be, respectively, expressed as

$$\lambda_{RH} = \left[1 + \frac{(1-RH)^4}{(1-RH_c)} \right]^{-1}, \qquad (8)$$

$$\lambda_T = \exp \left[\frac{U}{R} \left(\frac{1}{T_{28}} - \frac{1}{T} \right) \right], \qquad (9)$$

where RH_c is the threshold relative humidity ($RH_c = 75$), R is the gas constant, U is the activation energy equal to 35,000 J/mol, and T_{28} is the temperature for standard curing on day 28 (293 K).

Substituting Eq. 5 into Eq. 4 leads to

$$C(x, t_{in}) = C_s \cdot erfc \frac{x}{2\sqrt{\frac{KD_0 t_0^m}{(1+R_D)(1-m)} t_{in}^{1-m}}}. \qquad (10)$$

When the critical concentration of chloride ions is C_{cr} and the concrete cover depth is C, the prediction formula of chloride penetration life can be obtained as follows:

$$t_{in} = \left[\frac{(1+R_D)(1-m)C^2}{4KD_0 t_0^m \left[erf\, c^{-1} \left(C_{cr}/C_s \right) \right]^2} \right]^{\frac{1}{1-m}}. \qquad (11)$$

Model investigation for cover cracking

Various models for predicting a corrosion-induced cracking model

Eight empirical and theoretical models were chosen to predict the concrete cover cracking time of chloride-contaminated building structures (Morinaga, 1990; Liu and Weyers, 1998; Wu, 2006; Maaddawy and Soudki, 2007; Lu et al., 2010; Zhang et al., 2010; Liu and Yu, 2016; Lun et al., 2021). These models were chosen to check versatility because they are based on different mechanics theories which can clearly reflect the variation of concrete corrosion. For a reasonable comparison between them, each model is briefly described.

Morinaga model (1990)

Morinaga (1990) proposed an expression of cover cracking time by considering the influencing factors of concrete cover depth, reinforcement diameter, and current corrosion density based on experimental data:

$$t_{cr} = \frac{0.602d \left(1 + 2C/d \right)^{0.85}}{i_{corr}}, \qquad (12)$$

where t_{cr} is the concrete cover cracking time (d), C is the concrete cover depth (mm), d is the reinforcement diameter (mm), and i_{corr} is the corrosion's current density (10^{-4} g/cm²/year).

This model is the earliest empirical model for predicting concrete cover cracking time and is easy to compute since the parameters are readily available. It provided important parameters for later researchers to establish theoretical models. However, Morinaga did not consider the influence of the corrosion rate and the thickness of the porous zone on concrete cover cracking time and also ignored the process of corrosion byproduct filling the gap between the steel bar and concrete.

Liu and Weyers model (1998)

Based on theoretical analysis, Liu and Weyers (1998) first obtained the corrosion quality of steel bars when the concrete cover cracked and constructed the relationship between the corrosion quality of steel bars and the cracking time based on the corrosion production rate k_p to express a theoretical model of concrete cracking time as:

$$t_{cr} = \frac{W_{crit}^2}{0.196 \left(1/\alpha \right) \cdot \pi \cdot d \cdot i_{corr}}, \qquad (13)$$

where t_{cr} is the concrete cover cracking time (a), W_{crit} is the weight of the rust product when the concrete cover cracks (mg/mm), α is the coefficient related to the type of rust product, and i_{corr} is the corrosion's current density (μA/cm²).

This model is the earliest theoretical model for predicting cover cracking time and is discussed in research on the expansion process of corrosion products based on the theory of elasticity, considering the thickness of the pore area at the junction of concrete and steel bars. However, Liu and Weyers ignore the influence of the corrosion rate and cover depth on concrete cover cracking time, and the solution of W_{crit} is also difficult.

Wu model (2006)

Based on the theory of elasticity and Faraday's law of corrosion, the influence of corrosion current density proposed by Vu and Stewart (2000) on concrete cover cracking was considered by Wu (2006), who established a theoretical model of concrete cover cracking time in a natural corrosion environment as follows:

$$t_{cr} = \left(0.043zdCF(1-w/c)^{1.64}m^{-1}\rho_{cr}\right)^{1.41},$$ (14)

where t_{cr} is the concrete cover cracking time (a), m is the molecular weight of rust products, z is the ionic valence, C is concrete cover (cm), d is the reinforcement diameter (cm), ρ_{cr} is the corrosion rate of the reinforcement when the concrete cover is cracked, F is Faraday's constant (value of 96,500 (C)), and w/c is the water–cement ratio.

Wu's model effectively combines the factors of corrosion current density with the corrosion rate of reinforcement based on elastic mechanics, which have a great influence on the cover cracking time. However, the versatility of the selected corrosion current density and the rust expansion force requires further verification.

Maaddawy and Soudki model (2007)

Based on the theory of elasticity, Maaddawy and Soudki (2007) proposed a mathematical model from corrosion initiation to cracking, in which some important parameters such as reinforcement diameter, cover depth, the thickness of the pore area, and corrosion current density are considered. The prediction model is expressed as

$$t_{cr} = \left[\frac{7117.5(d+2d_0)(1+\nu+\psi)}{i_{corr}E_{ef}}\right]\left[\frac{2Cf_t}{d} + \frac{2d_0E_{ef}}{(1+\nu+\psi)(d+2d_0)}\right],$$ (15)

where t_{cr} is the concrete cover cracking time (d); E_{ef} is the effective modulus of elasticity of concrete, $E_{ef} = E_c/(1+\varphi_{cr})$; φ_{cr} is the creep coefficient of concrete, with the value of 2.0; C is concrete cover (mm); f_t is concrete tensile strength (MPa); d is the reinforcement diameter (mm); d_0 is the thickness of the pore area (mm); i_{corr} is corrosion current density ($\mu A/cm^2$); ν is Poisson's ratio of concrete; and ψ is the representative, $\psi = Y^2/2C(C+Y), Y = d+2d_0$.

This mathematical model also uses the elastic mechanics theory of thick-walled cylinders to analyze the relationship between the cover cracking time and the material properties (E_{ef}, d_0, f_t, and ν), the importance of which is also considered by certain models. However, the versatility of the Maaddawy and Soudki model also needs similar verification as Wu (2006).

Lu et al. model (2010)

Lu et al. (2010) established a model based on the theory of elasticity and Faraday's law of corrosion that, when a concrete cover cracks, the corrosion rate and the theoretical model of concrete cover cracking time considers the deformation characteristics of rust products and the entry of rust products into the crack:

$$t_{cr} = 234762(d+kC) \times \frac{\left\{\left(0.3+0.6\frac{C}{d}\right)\frac{f_{tk}}{E_{ef}}\left[\frac{(r_0+C)^2+r_0^2}{(r_0+C)^2+r_0^2} + \nu_c\right] + 1 + \frac{2d_0}{d}\right\}^2 - 1}{(n-1)i_{corr}},$$ (16)

where t_{cr} is the concrete cover cracking time (h); d_0 is the thickness of the pore area (mm); k is the correction factor of corrosion depth; n is

the volume expansion rate of rust products; r_0 is the thick-walled cylinder inner radius (mm), $r_0 = d/2 + d_0$; i_{corr} is the corrosion current density ($\mu A/cm^2$); and ν_c is Poisson's ratio of concrete.

This theoretical model was developed based on the elasticity theory and Faraday's law of corrosion, which consider the influence on concrete cover cracking time of the deformation characteristics of rust products and rust byproducts filling cracks. However, like other models based on elastic mechanics, the adaptability of the Lu et al. model needs further verification.

Zhang et al. model (2010)

Zhang et al. (2010) proposed a dynamic cracking time model in two stages—the fine cracking initiation and concrete cover cracking, considering the effect of initial defects, in which cracking time contained the solution process of the initial fracture toughness and the unstable fracture toughness of corrosion-induced cracking after considering the size effect based on fracture mechanics and double K theory.

The initiation of fine cracking time is

$$W_{cr}^{ini} = \frac{\pi\rho_s\left[(R+d_0+u_1^{ini})^2 - R^2\right]}{\alpha_1 - 1.0},$$ (17)

$$t_{cr}^{ini} = \frac{(W_{cr}^{ini})^2}{0.392\pi \cdot R \cdot i_{corr}(t) \cdot \alpha}.$$ (18)

The concrete cover cracking time is

$$W_{cr}^{un} = \frac{\pi\rho_s\left[(R+d_0+u_1^{un})^2 - R^2\right]}{\alpha_1 - 1.0},$$ (19)

$$t_{cr}^{un} = \frac{(W_{cr}^{un})^2}{0.392\pi \cdot R \cdot i_{corr}(t) \cdot \alpha},$$ (20)

where t_{cr}^{ini}, t_{cr}^{un} is the time to fine crack initiation and the time to concrete cover cracking (d); u_1^{ini}, u_1^{un} is the radial displacement; W_{cr}^{ini}, W_{cr}^{un} is the mass of steel (mg/mm) per unit length of the reinforcement being consumed by the corrosion process; ρ_s is the mass density of reinforcing steel; α_1 is the ratio of the volume of expansive corrosion byproduct to the volume of iron consumed during corrosion; and α is the ratio of the molecular weight of iron to the molecular weight of corrosion products.

Zhang et al. principally considered the coupled effect of initial micro-crack propagation, corrosion current density, the creep of concrete cover, and the softening character of concrete on the concrete cover cracking time under two concrete saturations. They adopt fracture toughness in fracture mechanics to study the whole process of cover cracking, considering the influence of the actual defect in the concrete. However, the expressions of the corrosion rate and corrosion current density are not reflected.

Liu and Yu model (2016)

Based on the elastic-plastic theory and Faraday's law of corrosion, Liu and Yu (2016) developed a uniform rust-expansion thick-walled cylinder model and prediction model of cover cracking time, expressed as

$$t_{cr} = 234762\frac{d}{i_{corr}}\frac{A\left[0.486\left(1+2\frac{C}{d}\right)\right]^2 - \Delta}{(1+\Delta)(n-1)},$$ (21)

where A can be expressed as

$$A = \frac{4\sigma_t (1 + \nu)}{E} \frac{0.486^2 (1 - 2\nu) + 1}{0.486^2 (2 - 2\alpha\nu - \alpha) + (2 + \alpha)} + \Delta, \quad (22)$$

where t_{cr} is the concrete cover cracking time (h); n is the volume expansion rate of rust products; Δ is the average volumetric strain in the plastic zone; α is the ratio of tensile strength to the compressive strength of concrete, and $\alpha = \sigma_t/\sigma_c$; ν is Poisson's ratio of concrete.

This model uses the double shear strength criterion and the thick-walled cylinder theory to perform an elastic–plastic analysis of the uniform cracking process of the concrete cover, providing a new research method for corrosion cracking. However, the adaptability of the model needs further verification.

Lun et al. model (2021)

Based on fracture mechanics and double K theory (Zhang et al., 2010), Lun et al. (2021) proposed a theoretical model of the natural corrosion of cover cracking and electrification acceleration which considers the initial defect shape inside the concrete and the modified corrosion rate formula of reinforcement, which can be expressed as follows:

The cracking time in a natural corrosive environment:

$$t_{cr} = \left[\frac{0.285 \rho_{cr} dC (1 - w/c)^{1.64}}{H^\star} + 1 \right]^{1.5} - 1, \quad (23)$$

where $H^\star$ can be expressed as

$$H^\star = \exp\left[1.23 + 0.618 \ln C_t - \frac{3034}{T \cdot (2.5 + RH)} - 5 \times 10^{-3} \rho \right], \quad (24)$$

where t_{cr} is the concrete cover cracking time (a), ρ_{cr} is the corrosion rate of reinforcement (%), C_t is concrete chloride content (kg/m³), and ρ is concrete resistivity (kohm.cm).

Electrically accelerated cracking time:

$$t_{cr} = 78.3 \frac{d\left(-b \pm \sqrt{b^2 + 4ac}\right)}{i_{corr} \cdot 2a}, \quad (25)$$

where t_{cr} is the concrete cover cracking time (d) and a, b, c are the combination coefficients (Lun et al., 2021).

Both internal and external factors are taken into account in this model, which truly reflects the influence of corrosion current density and the initial defect shape inside the concrete on cover cracking; it is an effectively improved model for predicting the true value of the actual project, with engineering application significance.

Through the analysis of the aforementioned models, each of the cracking models are largely different and consider different parameters based on the mechanical model. However, cover depth, corrosion current density, and reinforcement diameter have a relatively large effect on concrete cover cracking time, which are considered by each predicted model. However, it should be noted that the units of concrete cover cracking time including time (years, days, or hours) and current corrosion density ($\mu A/cm^2$ or 10^{-4} g/cm²/year) need to be calculated and unified. To more effectively compare the analysis results, the eight different concrete cover cracking time models need to be normalized regarding these two factors.

Comparison of different concrete cover cracking time models

In order to quantitatively compare the differences between different models, the five-year naturally exposed experiments conducted by Liu and Weyers (1998) was used, which have very

TABLE 1 Value of basic parameters.

Specimen number	S1	S2	S3	S4
2R (mm)	16	16	16	12.7
C (mm)	48	70	27	52
w/c ratio	0.43	0.43	0.45	0.43
C_t (kg/m³)	4.92	4.92	6.02	4.92
T(K)	295	295	295	293
E_c (MPa)	27,000	27,000	27,000	27,000
ν_c	0.18	0.18	0.18	0.18
φ	2.0	2.0	2.0	2.0
i_{corr} ($\mu A/cm^2$)	2.41	1.79	3.75	1.80
f_t (MPa)	3.3	3.3	3.3	3.3
f_c (MPa)	31.5	31.5	35.6	31.5
Exposure period/a	1.84	3.54	0.72	2.38

persuasive model validation. The experimental data of slabs are listed in Table 1, which illustrates the specimen numbers, chloride content (C_t), ambient temperature (T), elastic modulus (E_c), Poisson's ratio (ν_c), tensile strength (f_t), compressive strength (f_c), and corrosion current density (i_{corr}).

The computation parameters of the model based on fracture mechanics are the stable values of K_{Ic}^{ini} and K_{Ic}^{un} for concrete taken as 1.034 MPa.m$^{1/2}$ and 2.072 MPa.m$^{1/2}$, respectively (Wu et al., 2001). The corresponding coefficient variations are 0.061 and 0.073, respectively, and the initial defect length a is 2 mm.

Using computational analysis, the comparison results with experimental data are shown in Figure 1, and the ratio of the experimental results and the calculated results of the different models are shown in Figure 2. The mean (M) and coefficient of variation (CV) for the different models are listed in Table 2.

As can be seen in Figure 1, the cracking time results calculated by each cover cracking model are different. The predicted cracking time values are almost the same for the theoretical models based on fracture mechanics proposed by Zhang et al. (2010) and Lun et al. (2021). These were both close to the experimental results, indicating that the theoretical model established by fracture mechanics can accurately predict cracking time. Similarly, Liu and Weyers (1998) and Wu (2006) also reach similar conclusions and laws, which are based on elastic mechanics. However, the prediction results of Liu and Weyers (1998) are less than the experimental results, and Wu (2006) shows the opposite result; this may be related to the different parameters and modeling processes. Morinaga (1990)—an empirical model with three parameters—also agrees well with the experimental data, and the predicted results are the same as Wu (2006). The predicted results of Liu and Yu (2016) are almost the same as the experimental results (S1 and S4), but show a big difference (S2 and S4). The predicted results of Maaddawy and Soudki (2007) and Lu et al. (2010), which both considered the effective elastic model of concrete and the tensile strength of concrete, are generally much smaller than the experimental results. However, these models all show similar variation with changes in the test data.
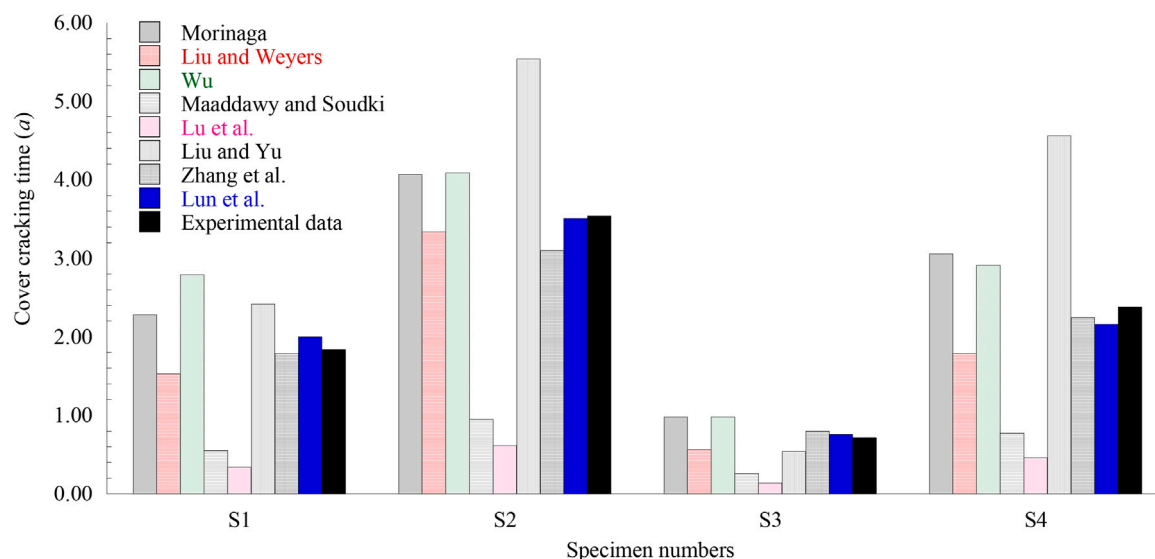
FIGURE 1
Comparison of results of different cover cracking time models.
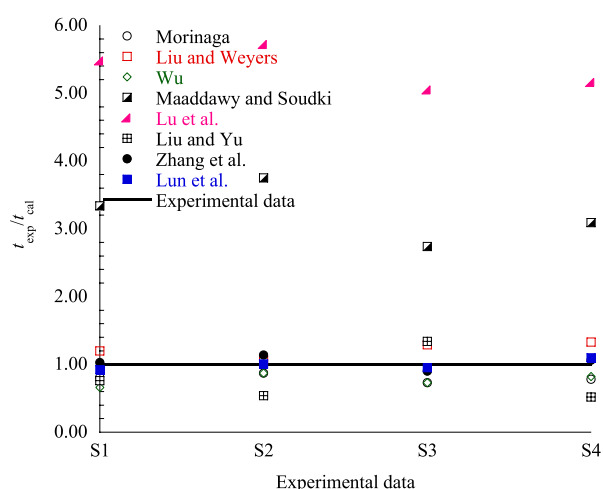
FIGURE 2
Comparison of experimental results with results predicted by the models.

As shown in Figure 2 and Table 2, the mean ratio similarly ranged from 0.769 (Wu) to 5.356 (Lu *et al.*), and the coefficient of the variation of the ratio ranged from 0.003 (Morinaga) to 0.138 (Liu and Yu). Moreover, Lun et al. (2021) proposed a theoretical model based on fracture mechanics and provided the best results, with a mean ratio of 0.994 and a coefficient of variation ratio of 0.005; Zhang et al. (2010) also provided excellent results, with a mean ratio of 1.032 and coefficient of variation ratio of 0.007. Although Morinaga provided the best results with a coefficient of variation ratio of 0.003, the mean ratio of 0.796 was poor. The mean ratio of Liu and Yu (2016) and Lu et al. (2010) is 0.791 and 5.356, respectively, and the coefficient of variation ratio is 0.138 and

0.013, which show much dispersion and difference in numbers. There are thus great differences between the calculated results of these cracking models and the experiment.

From the aforementioned findings in terms of mean and variability, Lun et al. (2021) best agree with the experimental data, which considers more comprehensive factors and the actual situation of concrete structures.

Through the previous analysis, the service lifetime t of a building structure includes two parts: corrosion initiation of reinforcement and concrete cover cracking. The equation of life prediction is

$$t = t_{in} + t_{cr}$$

$$= \left[\frac{(1 + R_D)(1 - m)C^2}{4KD_0 t_0^m \left[erf \, c^{-1}(C_{cr}/C_s) \right]^2} \right]^{\frac{1}{1-m}}$$

$$+ \left[\frac{0.285\rho_{cr}dC(1 - w/c)^{1.64}}{H^\star} + 1 \right]^{1.5} - 1. \quad (26)$$

For the same building structure, the service life cycle from chloride penetration to reinforcement corrosion to concrete cover cracking is defined, which is the core content of service-life assessment.

Evaluation index system of the engineering vulnerability of structures

It is well known that, in the long-term service process of building structures in coastal areas, in addition to chloride-induced-reinforcement corrosion, they are also affected by subjective factors such as structural characteristics, engineering design, and management technology. It is necessary to adopt a more reasonable evaluation method to evaluate the service life of building structures, and such evaluation must be based on the concept of engineering vulnerability for an effective result.

TABLE 2 Comparisons of cover cracking time obtained from experiments and the predictions of these models.

Reference	Result		Reference	Result		Reference	Result	
Morinaga, (1990)	M	0.796	Lu et al. (2010)	M	5.356	Liu and Yu, (2016)	M	1.032
	CV	0.003		CV	0.013		CV	0.007
Liu and Weyers, (1998)	M	1.219	Maaddawy and Soudki, (2007)	M	3.229	Lun et al. (2021)	M	0.994
	CV	0.009		CV	0.042		CV	0.005
Wu, (2006)	M	0.769	Zhang et al. (2010)	M	0.791			
	CV	0.008		CV	0.138			

TABLE 3 Probability characteristics of modeling uncertainty parameters (Wei et al., 2008; Li, 2012; DB11⁄637-2015 and Standard for structure comprehensive, 2015; Zhang and Xu, 2021; Zhang et al., 2020).

Factor	Very high vulnerability	High vulnerability	Moderate vulnerability	Low vulnerability	Slight vulnerability
Groundwater level changes C_{11}	Frequent and long-term impacts of high groundwater level and annual fluctuation >4 times	Groundwater level is high and fluctuates 3–4 times a year	Groundwater level is normal and rises and falls 2–3 times a year	Groundwater level is low and annual rise and fall change <2 times	Groundwater level is low and basically unchanged throughout the year
Relative position between them C_{12}	<500 m	500 m–1000 m	1000 m–5000 m	5000 m–10000 m	>10000 m
Engineering geological environment C_{13}	Extremely complex geological conditions developed adverse geological processes	Poor site stability, poor geological development	Stable site with small adverse geological development	Simple terrain and good geological conditions	Good geological environment
Type of building structure C_{21}	Lime-soil foundation	Brick foundation	Stone foundation	Concrete foundation	Reinforced concrete foundation
Beam-column concrete strength C_{22}	15% reduction in strength	10% reduction in strength	7% reduction in strength	4% reduction in strength	Strength meets design requirements
Concrete cover thickness C_{23}	15% reduction in cover depth	10% reduction in cover depth	6% reduction in cover depth	3% reduction in cover depth	Cover depth meets requirements
Building structural materials C_{24}	Poor material properties affecting overall structural performance	Low strength and poor durability	Material has certain strength and durability	High strength and durability	Good material performance, good strength, and durability
Quality of construction personnel C_{31}	Very poor	Poor	Medium	High	Very high
Construction quality C_{32}	Very poor and no corresponding regulation	There are certain quality problems	Generally, no quality problem	With corresponding supervision, quality is better	Strict supervision and construction according to design
Maintenance strength C_{41}	No maintenance performed	Repair after severe corrosion	Corresponding repairs after obvious corrosion	Regular inspection and adequate maintenance funds	Regular inspection and maintenance funds are abundant
Degree of concrete deterioration C_{42}	Cover peeling and falling block	Cover crack width exceeds limit value	Cover cracking and multiple cracks	Steel corrosion and intact cover	No steel corrosion
Service life/design life C_{43}	0.8–1.0	0.6–0.8	0.4–0.6	0.2–0.4	0–0.2
Types of medicines C_{51}	More than 30% corrosive drugs	Corrosive drugs 20%–30%	Corrosive drugs 10%–20%	Corrosive drugs 5%–10%	Less than 5% corrosive drugs
Management strength C_{52}	Poor and no corresponding management	Problems with management systems and requirements	Imperfect management system and requirements	Corresponding management system and requirements	Strict management system and requirements
Leakage area C_{53}	Leakage of corrosive substances more than 25% per unit area	Leakage of corrosive substances less than 25% per unit area	Leakage of corrosive substances less than 15% per unit area	Leakage of corrosive substances less than 5% per unit area	No leakage of corrosive substances
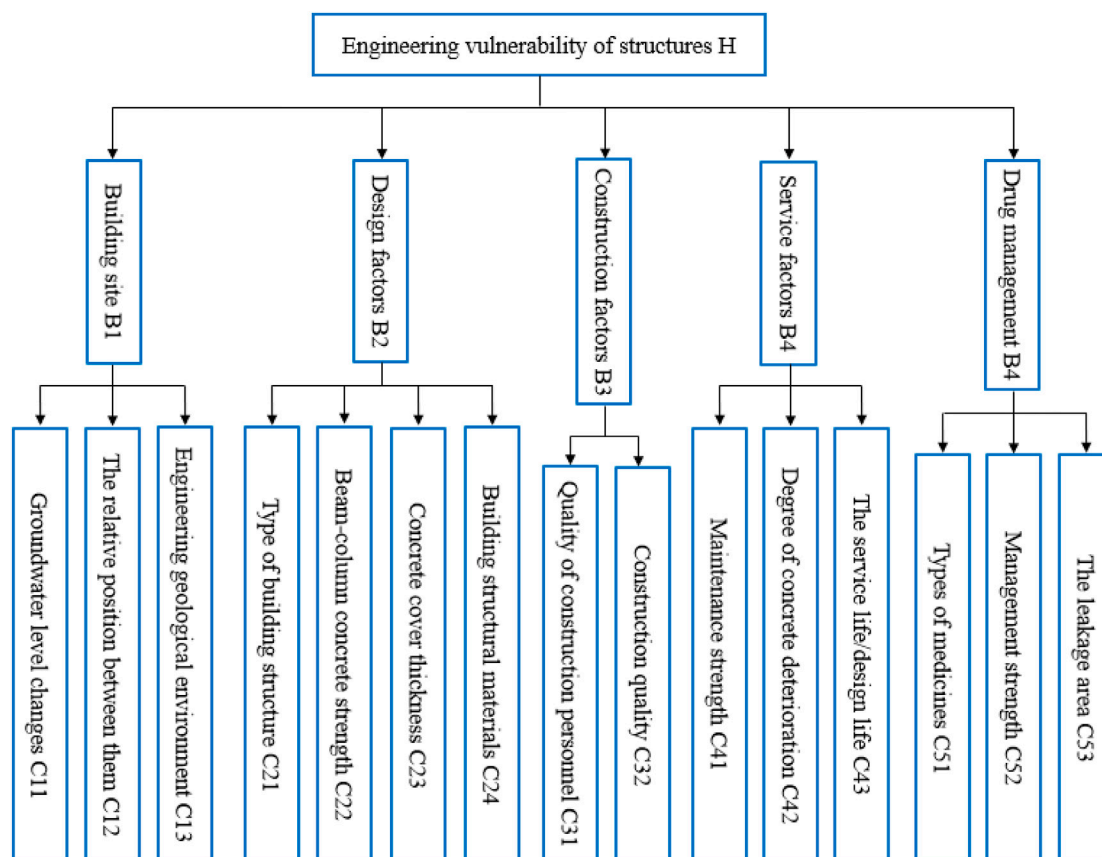
FIGURE 3
Evaluation index system.

Selection of evaluation factors

Based on the understanding that engineering vulnerability reflects the differences between the structure, materials, engineering geological conditions of the engineering body, and the potentially harmful service environment of the structure, the selection of building site $B1$, design factor $B2$, construction factor $B3$, service factor $B4$, and drug management $B5$ are selected as first-level evaluation factors. $B1$ focuses on the spatial relationship between the structure and the coastline and the impact of engineering geology at the location of the structure on the vulnerability of the project ($C11 \sim C13$); $B2$ focuses on the influence of factors such as structure type and concrete strength ($C21 \sim C24$); $B3$ focuses on the influence of factors such as the quality of construction personnel and construction quality ($C31 \sim C32$); $B4$ focuses on the influence of factors such as maintenance strength, concrete deterioration caused by corrosion ($C41 \sim C43$); $B5$ focuses on the influence of factors such as the drug leakage area and drug management strength ($C51 \sim C53$) (Table 3).

Build an evaluation index system

According to the factors and their interrelationships determined in Section 2.1, a hierarchical structure is established

(Figure 3). It can be divided into three layers: target, class indicator, and basic indicator. The target layer refers to the overall vulnerability of the building structure under the action of chloride corrosion, which is the ultimate goal of the entire hierarchy analysis. The class index layer represents the structure, materials, engineering geological environment, construction and maintenance, and the corrosive environment characteristics of the structure's engineering itself. The first-level evaluation factor of damage evaluation, which analyzes the factors affecting the first-level evaluation factor, is refined into 15 basic indicators to characterize the specific characteristics of structure and corrosion.

Determining index weight by the analytic hierarchy process

AHP can express each factor in numerical form by introducing an appropriate judgment scale, thus forming a judgment matrix to compare the importance of two factors. In this paper, the 1–9 scale method proposed by Saaty (1980) is used to grade each factor, and the discriminant matrix of the index factor is established. Under the condition that the random consistency ratio of the discriminant matrix is reasonable, the weight values of the indexes at all levels are obtained (Table 4).

TABLE 4 Weights of all levels' indices.

First-grade index	Weight value	Second index	Weight value	Second index	Weight value	Second index	Weight value
B1	0.21	C11	0.30	C23	0.22	C42	0.56
B2	0.15	C12	0.55	C24	0.24	C43	0.22
B3	0.18	C13	0.15	C31	0.333	C51	0.42
B4	0.26	C21	0.12	C32	0.667	C52	0.28
B5	0.20	C22	0.42	C41	0.22	C53	0.30

Fuzzy comprehensive evaluation method of structural engineering vulnerability

Build index set and alternative set

The index set is a common set composed of various indexes that affect the object, which can be expressed as follows:

$$C = (c_{11}, c_{12}, \cdots, c_{51}). \qquad (27)$$

The alternative set is a collection of various total evaluation results that the evaluation object may make, with V expressed as follows:

$$V = (v_1, v_2, \cdots, v_5). \qquad (28)$$

Each element v_i ($i = 1, 2, \ldots, 5$) represents all possible overall evaluation results. The purpose of fuzzy evaluation is to obtain the best evaluation results from the alternative set based on a comprehensive consideration of all indicators. The evaluation results of this paper are set to five levels, expressed as follows:

$$V = (\text{Very high, High, Medium, Low, Slight}). \qquad (29)$$

Determination of index membership

The fuzzy relation between the index set and the alternative set can be expressed by the fuzzy relation matrix. R represents the degree of membership of each evaluation factor to each grade standard of the alternative set, which can be calculated by the following formula to form a fuzzy matrix.

$$u_1 = \begin{cases} 0 & < \dfrac{a_3 + a_4}{2}, \\[2mm] \dfrac{1}{2} + \dfrac{1}{2}\sin\dfrac{\pi}{a_4 - a_3}(x - a_4) & \dfrac{a_3 + a_4}{2} < x \leq a_4, \\[2mm] \dfrac{1}{2} + \dfrac{1}{2}\sin\dfrac{\pi}{a_5 - a_4}(x - a_4) & a_4 < x \leq \dfrac{a_4 + a_5}{2}, \\[2mm] 1 & x > a_5, \end{cases} \qquad (30a)$$

$$u_2 = \begin{cases} 0 & x < \dfrac{a_2 + a_3}{2}, x \geq \dfrac{a_4 + a_5}{2}, \\[2mm] \dfrac{1}{2} + \dfrac{1}{2}\sin\dfrac{\pi}{a_3 - a_2}(x - a_3) & \dfrac{a_2 + a_3}{2} < x \leq a_3, \\[2mm] \dfrac{1}{2} + \dfrac{1}{2}\sin\dfrac{\pi}{a_4 - a_3}(x - a_3) & a_3 < x \leq \dfrac{a_3 + a_4}{2}, \\[2mm] \dfrac{1}{2} - \dfrac{1}{2}\sin\dfrac{\pi}{a_4 - a_3}(x - a_4) & \dfrac{a_3 + a_4}{2} < x \leq a_4, \\[2mm] \dfrac{1}{2} - \dfrac{1}{2}\sin\dfrac{\pi}{a_5 - a_4}(x - a_4) & a_4 < x \leq \dfrac{a_4 + a_5}{2}, \end{cases} \qquad (30b)$$

$$u_3 = \begin{cases} 0 & x < \dfrac{a_1 + a_2}{2}, x \geq \dfrac{a_3 + a_4}{2}, \\[2mm] \dfrac{1}{2} + \dfrac{1}{2}\sin\dfrac{\pi}{a_2 - a_1}(x - a_2) & \dfrac{a_1 + a_2}{2} < x \leq a_2, \\[2mm] \dfrac{1}{2} + \dfrac{1}{2}\sin\dfrac{\pi}{a_3 - a_2}(x - a_2) & a_2 < x \leq \dfrac{a_2 + a_3}{2}, \\[2mm] \dfrac{1}{2} - \dfrac{1}{2}\sin\dfrac{\pi}{a_3 - a_2}(x - a_3) & \dfrac{a_2 + a_3}{2} < x \leq a_3, \\[2mm] \dfrac{1}{2} - \dfrac{1}{2}\sin\dfrac{\pi}{a_4 - a_3}(x - a_3) & a_3 < x \leq \dfrac{a_3 + a_4}{2}, \end{cases} \qquad (30c)$$

$$u_4 = \begin{cases} 0 & x < \dfrac{a_0 + a_1}{2}, x \geq \dfrac{a_2 + a_3}{2}, \\[2mm] \dfrac{1}{2} + \dfrac{1}{2}\sin\dfrac{\pi}{a_1 - a_0}(x - a_1) & \dfrac{a_0 + a_1}{2} < x \leq a_1, \\[2mm] \dfrac{1}{2} + \dfrac{1}{2}\sin\dfrac{\pi}{a_2 - a_1}(x - a_1) & a_1 < x \leq \dfrac{a_1 + a_2}{2}, \\[2mm] \dfrac{1}{2} - \dfrac{1}{2}\sin\dfrac{\pi}{a_2 - a_1}(x - a_2) & \dfrac{a_1 + a_2}{2} < x \leq a_2, \\[2mm] \dfrac{1}{2} - \dfrac{1}{2}\sin\dfrac{\pi}{a_3 - a_2}(x - a_2) & a_2 < x \leq \dfrac{a_2 + a_3}{2}, \end{cases} \qquad (30d)$$

$$u_1 = \begin{cases} 1 & x < \dfrac{a_0 + a_1}{2}, \\[2mm] \dfrac{1}{2} - \dfrac{1}{2}\sin\dfrac{\pi}{a_1 - a_0}(x - a_1) & \dfrac{a_0 + a_1}{2} < x \leq a_1, \\[2mm] \dfrac{1}{2} - \dfrac{1}{2}\sin\dfrac{\pi}{a_2 - a_1}(x - a_1) & a_1 < x \leq \dfrac{a_1 + a_2}{2}, \\[2mm] 0 & x > \dfrac{a_1 + a_2}{2}, \end{cases} \qquad (30e)$$

where $a_0, a_1, \cdots, a_5$ are base factor ratings.

The fuzzy comprehensive evaluation

The secondary evaluation C_{ij} ($i,j = 1,2, \ldots ,5$) is a single factor investigation and calculation result, and the membership matrix of the secondary evaluation index can be obtained thus:

$$R_c = \begin{bmatrix} r_{11} & r_{12} & \cdots & r_{15} \\ r_{21} & r_{22} & \cdots & r_{25} \\ \vdots & \vdots & \ddots & \vdots \\ r_{m1} & r_{m2} & \cdots & r_{m5} \end{bmatrix} \quad m = 2, 3, 5. \quad (31)$$

Combined with Table 2 to get the weight value of each secondary index, the final fuzzy comprehensive evaluation model can be obtained as follows:

$$B_i = W_c R_c = (w_1, w_2, \cdots, w_m) \begin{bmatrix} r_{11} & r_{12} & \cdots & r_{15} \\ r_{21} & r_{22} & \cdots & r_{25} \\ \vdots & \vdots & \ddots & \vdots \\ r_{m1} & r_{m2} & \cdots & r_{m5} \end{bmatrix}, \quad (32)$$

$$i = 1, 2, \cdots, 5; m = 2, 3, 5.$$

Similarly,

$$E = W_B R_B = (w_1, w_2, \cdots, w_5) \begin{bmatrix} r_{11} & r_{12} & \cdots & r_{15} \\ r_{21} & r_{22} & \cdots & r_{25} \\ \vdots & \vdots & \ddots & \vdots \\ r_{51} & r_{52} & \cdots & r_{55} \end{bmatrix}. \quad (33)$$

According to the operation method of fuzzy sets, the membership degree can be determined by the principle of taking the largest from the smallest and of taking the largest and the normalized weighted model, and thence the vulnerability can be finally determined.

Engineering vulnerability of a coastal pharmaceutical factory

Survey of a coastal pharmaceutical factory

Topography and geomorphology

The pharmaceutical factory is located in the central part of the city to the southwest. The terrain is gentle from west to south and the topography belongs to the low platform, about 8.5 km from the coastline, which represents an elevation of 5–25 m.

Stratum lithologic

According to the geological survey report, the pharmaceutical factory is located in the southwest end of the Dashan fault zone. Regional tectonic movement is active, regional metamorphism and magmatic activity are frequent, damage to the stratum is obvious, and the continuity of the stratum is poor. In addition to the Mesozoic–Cenozoic stratum, the rocks of other strata are subject to different degrees of metamorphism.

Meteorology and hydrology

The region has subtropical marine monsoon climate characteristics, long summers and short winters, a mild climate, and abundant rainfall and sunshine. Average annual temperature is about 22.5°C, with the lowest at 0.2°C and the highest at 38.7°C; the temperature is above 25°C for half the year. Annual average relative humidity is 77%, and annual average rainfall is more than 2000 mm. The rainy season is from April to September, with a relative humidity of more than 90%. It has a more developed surface water system, high groundwater level, and belongs to the Gulf Stream System.

Data survey of service and management periods

The pharmaceutical factory came into operation in 1992, with a design life of 50 years. In order to reasonably and accurately evaluate the service life of pharmaceutical factories based on the concept of engineering vulnerability, it is necessary to combine the 15 established index systems to conduct on-site investigation of building structures and equipment use to extract relevant data, such as concrete strength, cover thickness, and chloride ion content on concrete surface. However, in addition to the technical testing methods based on various non-destructive and destructive testing equipment to obtain data, technical and management mechanisms such as daily inspection statistics, maintenance data, and written records of drug types provided by the plant are also important reference materials. To this end, Tables 5, 6 show survey results for the building structure according to several basic parameters of typical beam column service state combined with basic structural parameters.

In summary, the pharmaceutical plant has been in long-term service in a marine environment with relatively high humid and annual temperatures in a relatively complex geological environment. It has adopted a standardized modern enterprise management system to manage the drugs. The types of corrosive drugs are less than 10%, and the leakage area of drugs is less than 5%. This paper investigated 15 indicators of field investigation, with the specific survey results shown in Table 6.

Engineering vulnerability calculation of building structure

Calculation of the corrosion initiation of reinforcement and concrete cover cracking

Based on the engineering parameters provided in Table 5, the time from chloride corrosion to steel corrosion initiation obtained by Eq. 11 is 28 years, and the concrete cracking time obtained by Eq. 23 is 12 years; this indicates that the service life of the building structure is 40 years. On-site steel inspection revealed that some steel bars were corroded; slight cracks were also found in some of the columns, which may be related to a combination of corrosion and loading (Zhang et al., 2022).

Engineering vulnerability calculation of building structure service life

According to the operation method of fuzzy sets, the membership vector of the building structure is calculated by Eqs 27–32 and Table 4 to be $E = (0.106, 0.152, 0.227, 0.468, 0.094)$, and the maximum value in the membership vector is 0.468. According to Eq. 29, the engineering vulnerability of the service life of the building structure is determined to be low, and the building structure has a strong ability to resist corrosion risks. During the long-term service of the pharmaceutical factory, the investigation shows that the maintenance and management of the building structure are good, which verifies the applicability of the evaluation model.

TABLE 5 Field survey data required for model analysis.

Basic variable	Value	Basic variable	Value	Basic variable	Value	Basic variable	Value
2R	20 mm	T	298 K	d_0	12.5 μm	K_{Ic}^{ini}	1.034 MPa.m$^{1/2}$
C	30 mm	RH	80%	C_t	2.8 kg/m^3	K_{Ic}^{un}	2.072 MPa.m$^{1/2}$
w/c ratio	0.45	ν_c	0.18	C_s	3.6 kg/m^3	ρ	10 Kohmcm
Beam	C35	φ	2.0	C_{cr}	1.2 kg/m^3	a/c	0.72
Column	C45	f_t	2.8 MPa	n	2.5	a	2 mm
E_c	28,000 MPa	f_c	34.5 MPa	t_s	30 years		

TABLE 6 Survey results of building structure parameters based on the index system.

Investigation factor	Survey result
C11	Groundwater level is normal and rises and falls 2–3 times a year
C12	8.5 km
C13	Stable site with little adverse geological development
C21	Reinforced concrete foundation
C22	4% reduction in strength
C23	3% reduction in cover thickness
C24	Material has certain strength and durability
C31	High
C32	With corresponding supervision, quality is better
C41	Corresponding repairs after obvious corrosion
C42	Steel corrosion and intact cover
C43	0.6
C51	Corrosive drugs between 5% and 10%
C52	With corresponding management systems and requirements
C53	Corrosive substances less than 5% per unit area

Conclusion

This study investigated two key stages in the service prediction of building structure—corrosion initiation of reinforcement and concrete cover cracking—and evaluated the service life of a building structure based on the concept of engineering vulnerability. The following conclusions can be drawn:

1) Based on Fick's second law, a theoretical model for corrosion initiation of reinforcement is established by considering the important parameters of the critical concentration of chloride ions, chloride ion surface concentration, and the cover depth and solution of chloride diffusion coefficient, providing a theoretical basis for predicting the process of chloride penetration in a marine environment.

2) Comparing the calculation results of eight models of concrete cover cracking time with the experimental data, a theoretical model for cover cracking time proposed by Lun et al. (2021) was chosen with consideration of the important parameters of the

shape of the initial defects, cover depth, reinforcement diameter, ambient temperature, relative humidity, concrete chloride content, and corrosion rate based on the fracture mechanics theory, which are in good agreement with the experimental results and effectively predict the service life of building structures.

3) An engineering vulnerability evaluation index system for building structure was constructed. The building location, design, construction, and service factors, and drug management were selected as the first-level evaluation factors, and these were refined to obtain 15 main basic evaluation factors, with which the range of basic factors was determined. By means of AHP method and fuzzy comprehensive evaluation methodology, the assessment method of the service life engineering vulnerability of a building structure was established.

4) The evaluation method established in this paper was used to evaluate a pharmaceutical factory in a coastal area. The evaluation results show that the building structure is of low

vulnerability, which is consistent with the survey results, indicating that the method is suitable for the vulnerability of building structure engineering in coastal areas.

Data availability statement

The original contributions presented in the study are included in the article/Supplementary Material; further inquiries can be directed to the corresponding author.

Author contributions

Data curation, YL; funding acquisition, PL; investigation, AX; resources, PL; writing—review and editing, XC.

Conflict of interest

XC, AX, and YL were employed by the company Xuchang Hengsheng Pharmaceutical Co., Ltd.

The remaining author declares that the research was conducted in the absence of any commercial or financial relationships that could be construed as a potential conflict of interest.

Publisher's note

All claims expressed in this article are solely those of the authors and do not necessarily represent those of their affiliated organizations, or those of the publisher, the editors, and the reviewers. Any product that may be evaluated in this article, or claim that may be made by its manufacturer, is not guaranteed or endorsed by the publisher.

References

Ai-Harthy, A. S., Stewart, M. G., and Mullard, J. (2011). Concrete cover cracking caused by steel reinforcement corrosion. *Mag. Concr. Research* 63 (9), 655–667. doi:10.1680/macr.2011.63.9.655

Apostolopoulos, C. A., Demis, S., and Papadakis, V. G. (2013). Chloride-induced corrosion of steel reinforcement-mechanical performance and pit depth analysis. *Constr. Build. Mater.* 38, 139–146. doi:10.1016/j.conbuildmat.2012.07.087

Bazant, Z. P. (1979). Physical model for steel corrosion in concrete sea structures-theory. *J. Struct. Div. ASCE* 105 (6), 1137–1153. doi:10.1061/jsdeag.0005168

Bazant, Z. P. (1979). Physical model for steel corrosion in concrete sea structures—application. *J. Struct. Div. ASCE* 105 (6), 1155–1166. doi:10.1061/jsdeag.0005169

Bitaraf, M., and Mohammadi, S. (2008). Analysis of chloride diffusion in concrete structures for prediction of initiation time of corrosion using a new meshless approach. *Constr. Build. Mater.* 22, 546–556. doi:10.1016/j.conbuildmat.2006.11.005

Chen, S. Y., Cao, L. L., and Yao, Y. S. (2020). High-speed railway subgrade service status assessment based on hazard-affected engineering vulnerability concept. *J. Railw. Sci. Eng.* 7 (17), 1645–1654. doi:10.19713/j.cnki.43-1423/u.T20190978

Dai, K. Y., Yu, X. H., Li, Y. S., and Lv, D. G. (2022). Seismic fragility analysis of reinforced concrete structures considering reinforcement corrosion. *J. Build. Struct.* 43 (8), 20–31. doi:10.14006/j.jzjgxb.2021.0081

DB11/637-2015, Standard for structure comprehensive safety appraisal of buildings, Beijing: Standards Press of China, (2015).

Du, Y. G., Clark, L. A., and Chan, A. H. C. (2005). Residual capacity of corroded reinforcing bars. *Mag. Concr. Research* 57 (3), 135–147. doi:10.1680/macr.2005.57.3.135

Guzmán, S., Gálvez, J. C., and Sancho, J. M. (2011). Cover cracking of reinforced concrete due to rebar corrosion induced by chloride penetration. *Cem. Concr. Res.* 41 (8), 893–902. doi:10.1016/j.cemconres.2011.04.008

Jamali, A., Angst, U., Adey, B., and Elsener, B. (2013). Modeling corrosion-induced concrete cover cracking: A critical analysis. *Constr. Build. Mater.* 42, 225–237. doi:10.1016/j.conbuildmat.2013.01.019

Jang, B. S., and Oh, B. H. (2010). Effects of non-uniform corrosion on the cracking and service life of reinforced concrete structures. *Cem. Concr. Res.* 40 (9), 1441–1450. doi:10.1016/j.cemconres.2010.03.018

Jin, W. L., Lv, Q. F., and Zhao, Y. X. (2007). Research progress on the durability design and life prediction of concrete structures. *J. Build. Struct.* 28 (1), 7–13. doi:10.14006/j.jzjgxb.2007.01.002

Jin, W. L., and Zhao, Y. X. (2014). *Durability of concrete structures*. Beijing: Science Press.

Leonid, C., Dimitri, V. V., and Volokh, K. Y. (2010). Analytical modelling of concrete cover cracking caused by corrosion of reinforcement. *Mater. Struct.* 43, 543–556. doi:10.1617/s11527-009-9510-2

Li, M. X., Wang, G. X., Yang, X. R., and Yang, F. J. (2021). Loss assessment of wind-induced damage for residential buildings groups based on engineering vulnerability. *J. Build. Eng.* 42, 102435. doi:10.1016/j.jobe.2021.102435

Li, Y. S. (2012). Detection and safety appraisal of China foreign exchage trade system building theteh bund of shanghai. *Tunnle Constr.* 42 (S1), 612–615. doi:10.19701/j.jzjg.2012.s1.149

Liu, R. G., and Yu, M. X. (2016). Calculation model of corrosion expansion crack time for concrete cover. *J. Jiangsu Univ.* 37 (2), 219–224. doi:10.3969/j.issn.1671-7775.2016.02.016

Liu, Y. P., and Weyers, R. E. (1998). Modeling the time-to-corrosion cracking in chloride contaminated reinforced concrete structures. *ACI Mater. J.* 95 (6), 675–681.

Lu, C. H., Zhao, Y. X., and Jin, W. L. (2010). Modeling of time to corrosion-induced cover cracking in reinforced concrete structures. *J. Build. Structrures* 31 (2), 85–92. doi:10.14006/j.jzjgxb.2010.02.010

Lun, P. Y., Zhang, X. G., Jiang, C., Ma, Y. F., and Fu, L. (2021). Modelling of corrosion-induced concrete cover cracking due to chloride attacking. *Materials* 14, 1440. doi:10.3390/ma14061440

Luo, D. M., Niu, D. T., and Su, L. (2019). Research progress on durability of stressed concrete under environmental actions. *Eng. Mech.* 36 (1), 4–17. doi:10.6052/j.issn.1000-4750.2018.08.ST11

Maaddawy, T. E., and Soudki, K. (2007). A model for prediction of time from corrosion initiation to corrosion cracking. *Cem. Concr. Compos.* 29 (3), 168–175. doi:10.1016/j.cemconcomp.2006.11.004

Marasco, S., Noori, A. Z., Domaneschi, M., and Cimellaro, G. P. (2021). Seismic vulnerability assessment indices for buildings: Proposals, comparisons and methodologies at collapse limit states. *Int. J. Disaster Risk Reduct.* 63, 102466. doi:10.1016/j.ijdrr.2021.102466

Matsumura, T., Shirai, K., and Saegusa, T. (2008). Verification method for durability of reinforced concrete structures subjected to salt attack under high temperature conditions. *Nucl. Eng. Des.* 238 (5), 1181–1188. doi:10.1016/j.nucengdes.2007.03.032

Morinaga, S. (1990). "Prediction of service life of reinforced concrete buildings based on the corrosion rate of reinforcing steel, Durability of building Materials and components," in *Proceedings of 5th international conference on brighton* (UK: Spon Press), 27–52.

Pour-Ghaz, M., Isgor, O. B., and Ghods, P. (2009). The effect of temperature on the corrosion of steel in concrete. Part 1: Simulated polarization resistance tests and model development. *Corros. Sci.* 51, 415–425. doi:10.1016/j.corsci.2008.10.034

Qiang Zhang, L., Fu, L., and Xu, A. (2020). An efficient approach for numerical simulation of concrete-filled round-ended steel tubes. *Journal of Construction Steel Research* 170, 106086. doi:10.1016/j.jcsr.2020.106086

Reale, T., and O'Connor, A. (2012). A review and comparative analysis of corrosion-induced to first crack models. *Constr. Build. Mater.* 36, 475–483. doi:10.1016/j.conbuildmat.2012.06.033

Rodriguez, O. G., and Hooton, R. D. (2003). Influence of cracks on chloride ingress into concrete. *ACI Mater. J.* 100 (2), 120–126. doi:10.14359/12551

Saaty, T. L. (1980). *The analytic hierarchy process*. New York: McGraw-Hill, 30–75.

Tamer, E. M., and Khaled, S. (2007). A model for prediction of time from corrosion initiation to corrosion cracking. *Cem. Concr. Compos.* 29, 168–175. doi:10.1016/j.cemconcomp.2006.11.004

Tang, L. P., and Gulikers, J. (2007). On the mathematics of time-dependent apparent chloride diffusion coefficient in concrete. *Cem. Concr. Res.* 37 (4), 589–595. doi:10.1016/j.cemconres.2007.01.006

Tian, Y., Chen, C. C., Jin, N. G., Jin, X., Tian, Z., Yan, D., et al. (2019). An investigation on the three-dimensional transport of chloride ions in concrete based on X-ray computed tomography technology. *Constr. Build. Mater.* 221, 443–455. doi:10.1016/j.conbuildmat.2019.05.144

Vu, K. A. T., and Stewart, M. G. (2000). Structural reliability of concrete bridges including improved chloride-induced corrosion models. *Struct. Saf.* 22 (4), 313–333. doi:10.1016/s0167-4730(00)00018-7

Wang, H. L., Jin, W. L., and Sun, X. Y. (2008). Fracture model for protective layer cracking of reinforced concrete structure due to rebar corrosion. *J. Hydraulic Eng.* 39 (7), 863–869. doi:10.15935/j.cnki.jggcs.2012.04.014

Wang, S. L., Chen, C., Zhang, J. H., Gu, X. F., and Huang, X. D. (2022). Vulnerability assessment of urban road traffic systems based on traffic flow. *Int. J. Crit. Infrastructure Prot.* 38, 100536. doi:10.1016/j.ijcip.2022.100536

Wang, X. G., Zhang, W. P., Gu, X. L., and Dai, H. C. (2013). Determination of residual cross-sectional areas of corroded bars in reinforced concrete structures using easy-to-measure variables. *Constr. Build. Mater.* 38, 846–853. doi:10.1016/j.conbuildmat.2012.09.060

Wang, Y. D., Tang, Y. J., Chen, C., and Lin, L. D. (2012). Study on life predicting model of subsea tunnel based on chloride corrosion. *Struct. Eng.* 28 (4), 57–62.

Wang, Y. Z., Wu, L. J., Wang, Y. C., Liu, C. X., and Li, Q. M. (2018). Effects of coarse aggregates on chloride diffusion coefficients of concrete and interfacial transition zone under experimental drying-wetting cycles. *Constr. Build. Mater.* 185, 230–245. doi:10.1016/j.conbuildmat.2018.07.049

Wei, P., Chen, X. M., and Liu, L. J. (2008). Assessement on vulnerability of tunnels to earthquake loads based on holistic risk analysis approach. *Tunnle Constr.* 28 (3), 871–873.

Wu, Q., and Yuan, Y. S. (2008). Experimental study on the deterioration of mechanical properties of corroded steel bars. *China Civ. Eng. J.* 41 (12), 42–47. doi:10.3321/j.issn:1000-131X.2008.12.007

Wu, X. H. (2006). Analytical solution for cracking time of reinforced concrete structure due to corrosion expansion in marine envi-ronment. *J. Shanghai Marit. Univ.* 3, 22–26. doi:10.3969/j.issn.1672-9498.2006.03.005

Wu, X. L., and Tang, S. Y. (2022). Comprehensive evaluation of ecological vulnerability based on the AHP-CV method and som model: A case study of badong county, China. *Ecol. Indic.* 137, 108758. doi:10.1016/j.ecolind.2022.108758

Wu, Z. M., Xu, S. L., and Ding, Y. N. (2001). The double-K fracture parameter of concrete for non-standard three point bending beam spec-imens. *China Enginerring Sci.* 3, 76–81. doi:10.3969/j.issn.1009-1742.2001.04.014

Xu, L. R., Chen, S. Y., and Cao, L. L. (2014). Engineering vulnerability assessment for bridgeds and tunnels harmed by debris flow hazards. *Rock Soil Mech.* 35 (9), 2642–2650. doi:10.16285/j.rsm.2014.09.015

Xu, L. R., Wang, L., and Su, Z. M. (2010). Assessment of engineering vulnerability of tunnel suffering from debris flow. *Rock Soil Mech.* 31 (7), 2153–2158. doi:10.16285/j.rsm.2010.07.010

Zhang, Q., Lun, P. Y., and Li, X. (2021). A simplified approach for prediction of concrete resistivity: Experimental study and mathematic model. *Mater. Struct.* 54, 155. doi:10.1617/s11527-021-01688-9

Zhang, Q., and Xu, L. (2021). Evaluation of moments of performance functions based on polynomial chaos expansions. *Int. J. Mech. Mater. Des.* 18, 395–405. doi:10.1007/s10999-021-09585-3

Zhang, Q., Zhao, Y. G., Kolozvari, K., and Xu, L. (2022). Reliability analysis of reinforced concrete structure against progressive collapse. *Reliab. Eng. Syst. Saf.* 228, 108831. doi:10.1016/j.ress.2022.108831

Zhang, Q., Zhao, Y. G., Kristijan, K., and Xu, L. (2020). Simplified model for assessing progressive collapse resistance of reinforced concrete frames under an interior column loss. *Eng. Struct.* 215, 110688. doi:10.1016/j.engstruct.2020.110688

Zhang, X. G., Li, M. H., Tang, L. P., Memon, S. A., Ma, G., Xing, F., et al. (2017). Corrosion induced stress field and cracking time of reinforced concrete with initial defects: Analytical modeling and experimental investigation. *Corros. Sci.* 120, 158–170. doi:10.1016/j.corsci.2017.01.012

Zhang, X. G., Zhao, Y. G., and Lu, Z. H. (2010). Dynamic corrosion-induced cracking process of RC considering effect of initial defects. *J. Asian Archit. Build. Eng.* 9 (2), 439–446. doi:10.3130/jaabe.9.439

Zhu, B. R. (2017). *Service life prediction for concrete structure materials in western region of China based on probabilistic method*. Lanzhou: Lanzhou Unverisity of Technology.

Exploration of the slope effect on the uplift capacity of single straight and belled piles supporting transmission towers

Meihua Bian*, Songlin Qin, Jianing Peng, Junhua Li and Xingsen Zhang

Guangxi Key Laboratory of Intelligent Control and Maintenance of Power Equipment, Electric Power Research Institute of Guangxi Power Grid Co., Ltd., Nanning, China

Single piles are normally used to support the transmission tower in mountain areas. Uplift capacity of piles is a key factor in the engineering design to increase the stability of transmission tower foundation. This study numerically investigated the uplift capacity of single straight and belled piles in the sloping ground which consisted of a clay layer underlain by medium weathered sandstone. A non-linear 3D finite element model was proposed to describe the uplift behavior of single piles and was calibrated against a field test on single piles subjected to uplift loading. A parametric study was conducted to investigate the effect of the slope angle (θ) on the uplift behavior of single piles. The uplift capacity decreased as θ increased for either straight piles or belled piles. Moreover, the range of the equivalent plastic strain was greatest for single piles in the level ground. For piles in the sloping ground, the range of equivalent plastic strain was wider at the position of the downstream slope than that at the position of the upstream slope when the uplift load of single piles reached the maximum. As the expansion angle increased to 30° and 45°, the uplift capacity of belled piles (R_u) was increased by 100% and 180% with respect to that of straight piles, respectively. The increase percentage in R_u was independent of θ. A practical method was proposed to quantify the slope effect on R_u.

1 Introduction

Plenty of transmission towers have been built in mountainous areas in the world. Thus, most of the transmission towers are located in the sloping ground (Jiang et al., 2022). Strong wind and earthquake pose a significant threat to the stability of transmission towers (Qu et al., 2018a; 2019; Xu et al., 2017b; 2021). Because of the variability in the direction of winds, the pile foundations of transmission towers could be subjected to uplift, compression, and horizontal loads. (Xu et al., 2023; Xu et al., 2013; Xu et al., 2017a; Qu et al., 2018b). In the engineering design, the uplift capacity is one of the significant factors to be considered for the pile of transmission towers. Moreover, Figure 1 shows the potential threat of the slope instability to the pile foundations of transmission towers in Guilin City of China. Thus, it is of great necessity to explore the uplift capacity of single piles in sloping ground.

Over the last several decades, investigators have analyzed the uplift behavior of single piles in various soils. A simplified semi-empirical model was developed to estimate the

FIGURE 1
Potential threat of the slope instability to the pile foundations of transmission towers in Guilin City of China: **(A)** scene 1 and **(B)** scene 2 (photos from the investigation of authors).
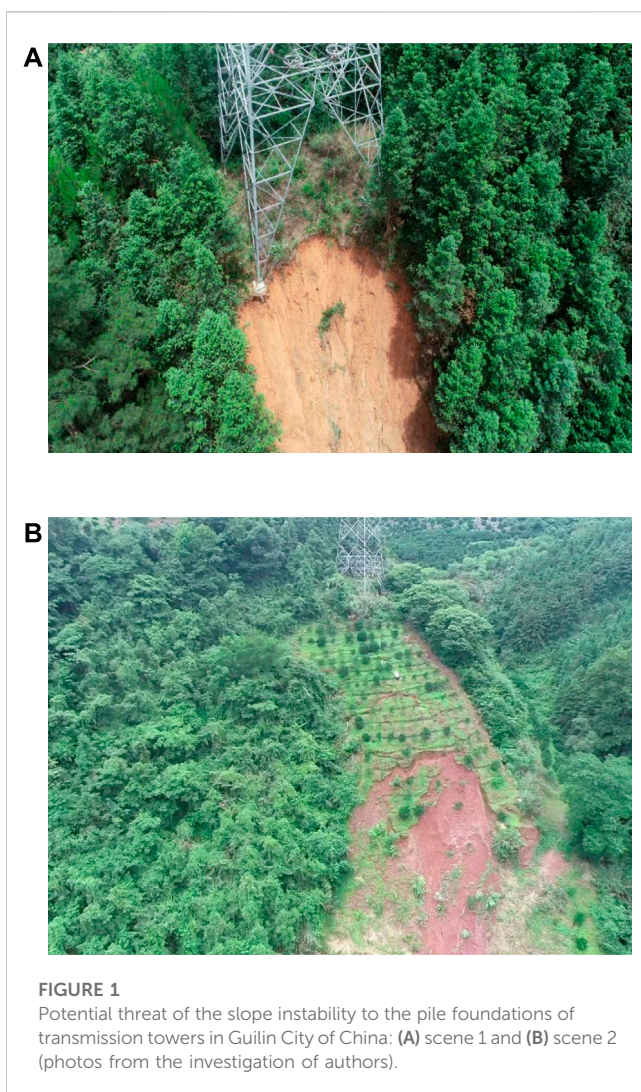
uplift capacity of single piles embedded in sands (Shanker et al., 2007). The effect of arch on the uplift capacity of single piles and pile groups was investigated by Shelke and Patra (2009) and Shelke and Mishra (2010), respectively. Plenty of model tests were performed to investigate the effect of various factors on the uplift capacity of single piles in sand, that is, the slenderness ratio (Verma and Joshi., 2010; Faizi et al., 2015), relative density of soil, and embedment depth of piles (Gavver, 2013; Saravanan et al., 2017). Kyung and Lee (2019) investigated the influence of installation condition on the uplift capacity of micropiles in sand. Emirler et al. (2017) numerically investigated the effect of relative density of sand and the embedment depth on the uplift behavior of single piles. There are also plenty of studies on how to evaluate the uplift capacities of single piles in clayey soils. A few model tests have been conducted to evaluate the uplift capacity of concrete piles in clay under uplift loading (Mohan and Chandra, 1961; Turner, 1962; Sowa, 1970). Shin et al. (1993) experimentally evaluated the uplift capacity of rigid piles embedded in a compacted near-saturated clayey soil. Lai and Jin (2010) carried out a field-scale model test to investigate the load transfer mechanism of PHC piles in soft soil under uplift

loading. However, little research is conducted to investigate the uplift behavior of piles embedded in the mountain areas, where the ground frequently consists of not only clay or sand but also weathered rocks. For these piles, a primary concern is leading to the interaction between the pile and the weathered rock under uplift loading because the weathered rock provides majority of soil resistance (Wang et al., 2021a).

To increase the capability of single piles to resist the uplift loading, the base of piles is expanded. Belled pile is a typical expanded pile to be used in engineering practice. The failure mechanism behind uplift belled piles in the level ground is sufficiently studied (Sawwaf and Nazir, 2006; Hong and Chim, 2015; Schafer and Madabhushi, 2020; Abdelgwad et al., 2022). Moreover, many scholars have studied various influential factors on the uplift capacity of belled piles in the level ground, for example, sand density (Ilamparuthi and Dickin, 2001; HondaHirai and Sato, 2011), diameter of the expanded base, embedment depth of piles (Tanaya and Sujit, 2019; Kang and Kang, 2022), and different bell space ratios (Sun et al., 2022). Moayedi and Mosallanezhad (2017) experimentally found that increasing the number of wings of multi-belled piles does necessarily improve the uplift resistance of single piles embedded in loose sands. The influence of various parameters, for example, the bell angle and the diameter of expanded base, on the uplift capacity of belled piles in sands was numerically studied (Liu et al., 2020; Yang and Qiu, 2020). Wang et al. (2021b) reported that the pile embedment and rock strength significantly affect the uplift resistance of belled piles (Yang et al., 2018). Chae et al. (2012) reported that the bell shape is more significant on the pile displacement than on the uplift capacity of belled piles in weathered rocks through both model tests and numerical analyses. Hu et al. (2022) experimentally explored the failure mechanism of the uplift belled piles in a layered ground which consists of sand and rock. However, previous studies mainly focus on the uplift behavior of single straight and belled piles in the level ground. Little work has been conducted on single piles in the sloping ground, especially in the mountain areas where the ground was composed of clay layer underlain by weathered sandstone.

This study numerically investigated the uplift capacity of single piles in the sloping ground which consisted of a clay layer underlain by medium weathered sandstone. The uplift behavior of single piles was described by a proposed non-linear 3D finite element model calibrated against a field test on single piles under uplift loading. A parametric study was conducted to investigate the effect of the slope angle (θ) on the uplift behavior of single straight and belled piles. Moreover, the influence of the expansion angle on the uplift capacity (R_u) of belled piles was discussed. Finally, a practical method was proposed to quantify the slope effect.

2 Numerical modeling

2.1 Proposed finite element model

Figure 2A shows a field test on a single bored pile under uplift loading in the level ground, as reported by Wang et al., 2021a.
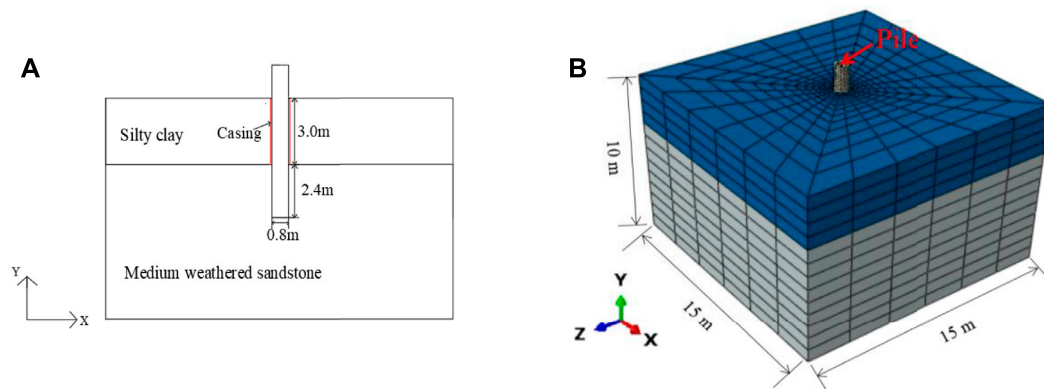
FIGURE 2
3D finite element modeling of the uplift pile: **(A)** single pile in the layered ground consisting of silty clay and medium weathered sandstone and **(B)** finite element mesh.

TABLE 1 Parameters of the pile–soil model.

Model	Pile	Silty clay	Medium weathered sandstone
Modulus of elasticity E (kPa)	3.5 E+7	6 E+3	4 E+7
Poisson's ratio ν	0.3	0.33	0.22
Cohesion (kPa)	—	30	500
Friction angle (deg.)	—	25	41
Dilatancy angle (deg.)	—	12.5	20.05
Unit weight γ (kN/m³)	—	19.5	25

The site was composed of a silty clay layer underlain by medium weathered sandstone. The diameter (D) of the pile was 0.8 m, and the embedment depth of the pile in the sandstone was 2.4 m. The thickness of the clay layer was 3.0 m. There was a gap between the pile and the clay *via* casing shown in Figure 2A.

Figure 2B shows the 3D finite element model with gradient mesh for the single pile under uplift loading in a finite element software ABAQUS (Systèmes, 2007). Both the soil and the pile were modeled by C3D8R elements. The C3D8R element is a general-purpose linear brick element with reduced integration (Systèmes, 2007). The size of the finite element mesh ranged from 0.05 m to 2.5 m. Fine mesh was used for soils surrounding the pile to ensure the sufficient accuracy of finite element analyses. To simulate the pullout behavior of piles in the finite element analysis, the pile–soil contact was considered by selecting "penalty function" and "hard contact" for tangential behavior and normal behavior, respectively. The default values suggested by the software were used for contact parameters. When the pile is separated from the soil, the contact pressure at the interface decreases to zero (AlIsawi et al., 2019). Note that the casing was not considered in the finite element modeling because it has an insignificant effect on the uplift capacity of piles.

Table 1 gives the input parameters for the pile and the soils.

In this study, the pile was assumed to be elastic. The elastic–plastic behavior of soils was described by the Drucker–Prager (DP) model (Drucker and Prager, 1952). The yielding function and the plastic potential function g for the linearly extended DP model were given by

$$F = t - p \tan \beta - d = 0, \tag{1}$$

$$g = t_0 - p \tan \psi, \tag{2}$$

$$t_0 = \frac{q}{2}\left[1 + \frac{1}{k} - \left(1 - \frac{1}{k}\right)\left(\frac{r}{q}\right)^3\right], \tag{3}$$

where q is the Mises equivalent stress; p is the equivalent pressure stress; r is the third invariant of deviatoric stress; β is the friction angle, which reflects the slope of the yield surface in the stress space; d is the cohesion of soils; k controls the dependence of the yield surface on the value of the intermediate principal stress and ranges from 0.778 to 1; and ψ is the dilation angle. In the study, k is taken as an average value of the range.

The distance between the lateral side and the pile to was set at 10 D to eliminate the boundary effect. In this study, initial stress analysis was performed before the uplift loading was applied to the pile to provide the initial stress of soils for the analysis of uplift piles. The displacements at the base and both two lateral sides of the model were zero.
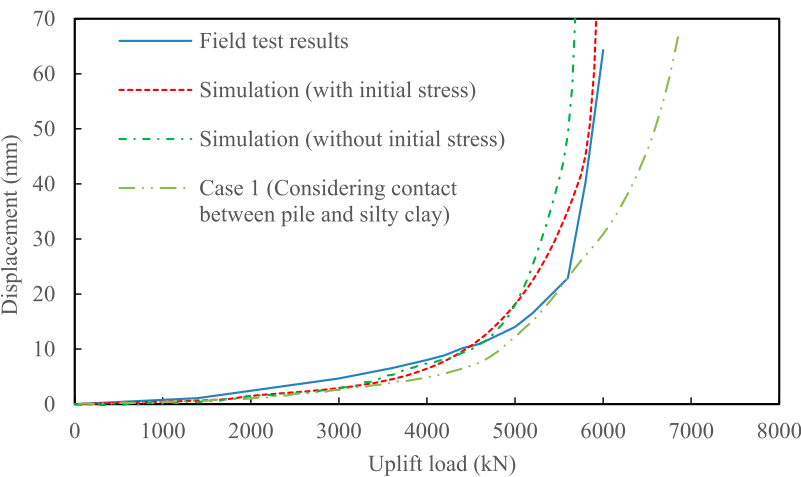
FIGURE 3
Calculated and measured uplift load−displacement curves of single piles.
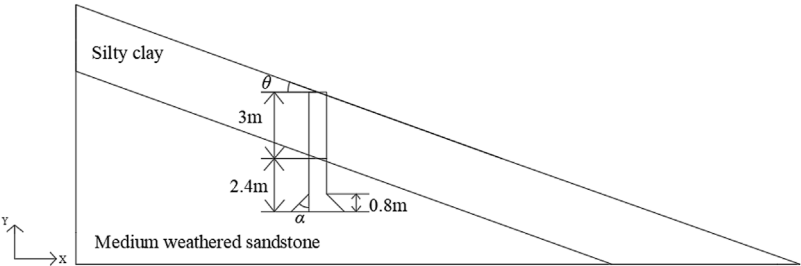
FIGURE 4
Schematic view of cases with different θ and α.

TABLE 2 Cases in the finite element analyses of this study.

Case	$\alpha(°)$	$\theta(°)$
1	0	0
2	0	10
3	0	20
4	30	0
5	30	10
6	30	20
7	45	0
8	45	10
9	45	20
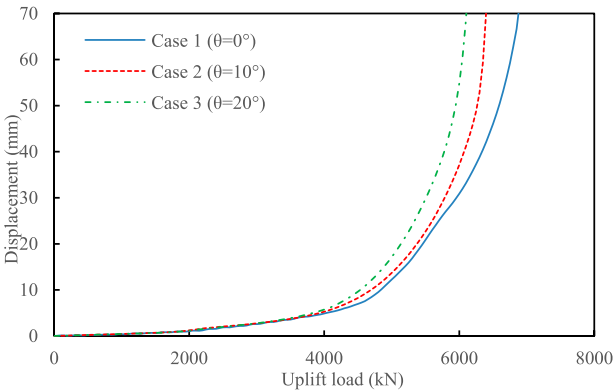
FIGURE 5
Uplift load−vertical displacement curves of uplift straight piles under different slope angles (θ).

2.2 Model verification

Figure 3 shows the measured and simulated uplift load (R)– vertical displacement (u_y) curves of single piles under uplift loading. The calculated displacement was generally lower than

that measured from the test when the uplift load was smaller than approximately 4500 kN. Nevertheless, the calculated R_{max} was consistent with that obtained from the field tests. Moreover, the
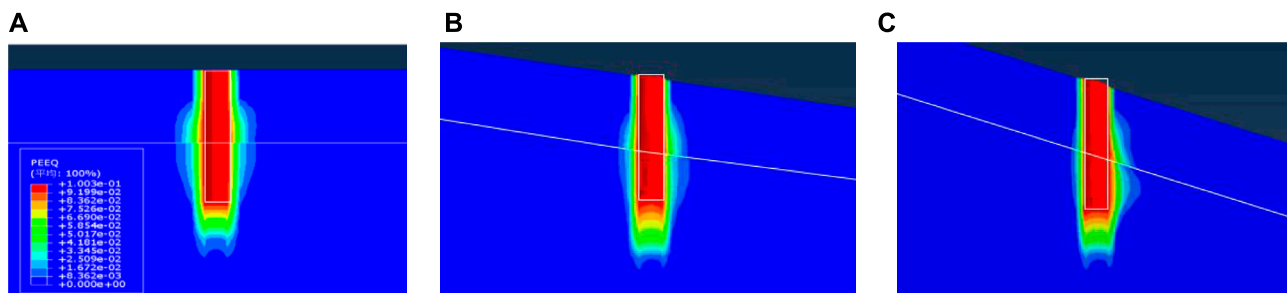
FIGURE 6
Effect of θ on the distribution of equivalent plastic strain surrounding the straight pile: **(A)** $\theta = 0°$, **(B)** $\theta = 10°$, and **(C)** $\theta = 20°$.
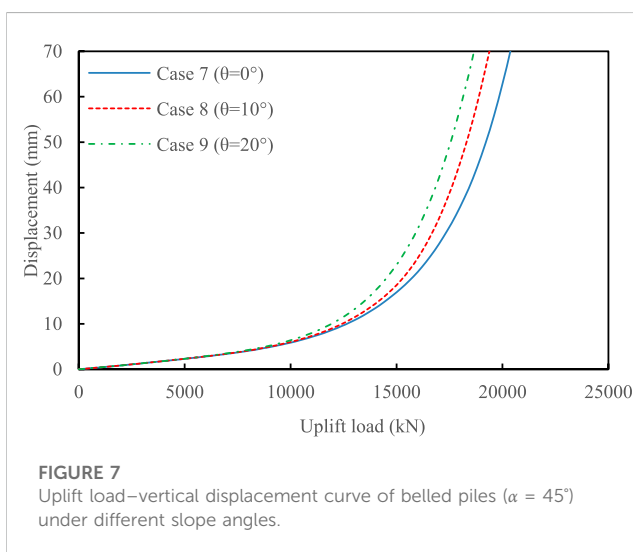
FIGURE 7
Uplift load−vertical displacement curve of belled piles ($\alpha = 45°$) under different slope angles.

R_{max} was underestimated by approximately 4% if the initial stress was not considered. Thus, it is suggested that the initial stress can be taken into account in the analysis of the uplift pile.

Moreover, an additional case (i.e., Case 1) was used to explore the influence of the contact between the pile and the clay on the uplift behavior of single piles in this study. Figure 3 also shows that the contact between the pile and the clay caused a 16% increase in the maximum uplift load. Case 1 was used as a bench mark model for the parametric study in the next section.

3 Results and discussion

The effect of slope angle (θ) on the uplift behavior of both straight pile and belled pile was investigated. Figure 4 schematically shows the slope angle (θ) and the belled pile with various base diameters by changing the expansion angle (α), where α is the angle that the pyramidal or conical surface makes against the vertical. Moreover, the effect of α on the uplift behavior of belled piles was studied accordingly. In this study, θ

varied between 0° and 20°, and α ranged from 0° to 45°. Table 2 lists all cases in the finite element analyses of this study.

3.1 Influence of slope angle on straight piles

Figure 5 shows the influence of θ on the $R–u_y$ curves of single piles. The effect of θ on the $R–u_y$ curve was minimal when the uplift load was lower than approximately 4000 kN. However, the maximum uplift load (R_{max}) decreased as the slope angle increased.

Moreover, Figure 6 further shows the maximum equivalent plastic strain (ε^{pl}) distributed at the soils surrounding the pile. The equivalent plastic strain is defined as $\varepsilon^{pl} = \int \dot{\varepsilon}^{pl} dt$, where $\dot{\varepsilon}^{pl} = \boldsymbol{\sigma} : \varepsilon^{pl}/\bar{\sigma}$ in the DP model, $\boldsymbol{\sigma}$ is the stress tensor, and $\bar{\sigma}$ is a function including hardening and rate-dependent effects (Systèmes, 2007). For the pile in the level ground, the equivalent plastic strain was symmetric about the uplift pile (see Figure 6A). Moreover, the range of equivalent plastic strain was wider at the position of the downstream slope than that at the position of the upstream slope when the uplift load reached the maximum Figures 6B, C. This was because of the lower yield strength of the soils at the downstream side of the slope, leading to relatively greater equivalent plastic strain at such position.

3.2 Influence of slope angle on belled piles

Similar to the straight pile, Figure 7 shows that the calculated R_{max} decreased as θ increased. The same tendency was also found for other cases (see Figure 8A). The effect of θ on the $R–u_y$ curve was minimal when the uplift load was lower than a critical value of approximately 9000 kN. The equivalent plastic strain range was much greater in soils surrounding belled piles than that in the case of straight piles (see Figure 9; Figure 6). Moreover, the range of equivalent plastic strain was also wider at the position of the downstream slope than that at the position of the upstream slope when the uplift load of belled piles reached the maximum.

FIGURE 8
Effect of α on **(A)** the uplift capacity and **(B)** the normalized uplift capacity of single piles at different slope angles.

FIGURE 9
Effect of θ on the distribution of equivalent plastic strain surrounding the belled pile with α = 45°: **(A)** θ = 0°, **(B)** θ = 10°, and **(C)** θ = 20°.

TABLE 3 Input parameters for estimating the uplift capacity of belled piles in the level ground.

Case	A_1	A_2	A_3	c (kPa)	h_t (m)	γ_s (kN/m³)	V_0 (m³)	G_f (kN)	R_{up} (kN, Eq. 4)	R_u (kN, FEM)
α = 45°	2.482	0.492	0.651	239	5.4	22	18.53	312.6	21319	14800
α = 30°	2.015	0.370	0.439	239	5.4	22	16.01	268.9	16987	10600

3.3 Influence of the expansion angle of belled piles

To illustrate the effect of the expansion angle α, the uplift capacity (R_u) of belled piles was selected as an index and was obtained from the calculated R–u_y curve. Wang et al. (2020) suggested that Ru is the uplift load corresponding to a critical displacement (V_{cri}) of 2% D for the belled pile under uplift

loading. Tang and Chen (2015) suggested V_{cri} = 2.5% D for rock-socketed piles under uplift loading. Wang et al. (2021b) suggested V_{cri} = 3% D for straight bored piles. In this study, V_{cri} = 2% D was used as a criterion for estimating R_u in this study.

Figure 8A also illustrates that R_u generally increased as α increased. Figure 8B further presents the R_u normalized to the uplift capacity ($R_{u,\ \alpha=0°}$) of straight piles. As α increased to 30° and

FIGURE 10
Effect of slope angle on the reduction factor at different expansion angles.

45°, R_u was increased by 100% and 180% with respect to that of straight piles, respectively. Thus, increasing the expansion angle was an effective measure to increase R_u. Moreover, the increase percentage in R_u was independent on the slope angle (see Figure 8B). It should be stressed that the uplift capacity should be almost the same for the same bottom area of the belled piles with various expansion angles because the height of the expansion was assumed to be the same in this study.

3.4 Practical method for quantifying the slope effect on R_u

《Technical code for design of foundation of overhead transmission line》(DL/T5219-2014) is used for estimating R_u in China by the following equation. However, the equation is only used for piles in the level ground and cannot be used for the piles in the sloping ground.

$$R_u = A_1 c h_t^2 + A_2 \gamma_s h_t^3 + \gamma_s \left(A_3 h_t^3 - V_0 \right) + G_f; h_t \le h_c. \quad (4)$$

Eq. 4 is used when $h_t \le h_c$, where h_t is the embedment depth of the uplift pile and was taken as 5.4 m, as shown in Figure 2A, and h_c is the critical uplift depth and was taken as $3D$, as suggested by the code (NEA, 2015); A_1, A_2, and A_3 refer to dimensionless parameters suggested by the code (NEA, 2015) and were determined by the shape of sliding surface, friction angle of soils, and the ratio of the embedment depth of the uplift pile to its base diameter; c stands for the soil cohesion, which was taken as the weighted average based on the thickness of two layers in this study; γ_s is the weighted average weight of soil above the tip of piles; and V_0 is the volume of piles within the embedment depth. G_f is the self-gravity of the foundation. Table 3 gives input parameters for calculating R_u.

Table 3 also shows the comparison between the results calculated from Eq. 4 and finite element analyses for belled piles in the level ground in the cases of $\alpha = 30°$ and $\alpha = 45°$. The results indicated that the uplift capacity calculated from Eq. 4 was generally greater than the uplift capacity determined from

finite element analyses. The discrepancy was mainly due to two reasons: 1) the critical displacement (V_{cri}) influenced P_u in finite element analyses. Particularly, the discrepancy was decreased with the increasing V_{cri} because of an increase in P_u and 2) Eq. 4 was proposed for the uniform layer. Thus, the application of Eq. 4 to the layered ground in this study caused certain errors and further contributed to the discrepancy. Nevertheless, as α increased from 30° to 45°, the calculated increase percentage (i.e., ~26%); in R_u obtained from the proposed numerical model agreed reasonably well with that (i.e., ~40%) of calculated from Eq. 4.

To estimate the influence of slope angle on R_u, a practical method was proposed in this study and was given by

$$R_{u,\theta} = \beta R_u \quad (5)$$

where β is a reduction factor and defined as the ratio of R_u to $R_{u, \theta=0°}$, and $R_{u, \theta=0°}$ denotes R_u at $\theta = 0°$. Thus, $\beta = 1$ when $R_u = R_{u,\theta=0°}$. Figure 10 illustrates that the reduction factor decreased as θ increased. Moreover, a linear relationship can be used to correlate the reduction factor with the slope angle for all data shown in Figure 8.

$$\beta = -0.0071\theta + 1.0; 0° \le \theta \le 20°. \quad (6)$$

4 Conclusion

The effect of slope on the uplift capacity of single straight and belled piles supporting transmission towers was explored *via* a proposed numerical model which was calibrated against a field test. The following conclusions can be obtained:

(1) The calculated R_{max} from the 3D finite element model was consistent with that obtained from the field tests. Moreover, considering initial stress was recommended for analyses of uplift piles.
(2) The uplift capacity decreased as the slope angle θ increased for either straight piles or belled piles. Moreover, the range of the equivalent plastic strain was greatest for single piles in the level ground (i.e., $\theta = 0°$).
(3) For piles in the sloping ground, the range of equivalent plastic strain was wider at the position of the downstream slope than that at the position of the upstream slope when the uplift load of single piles reached the maximum.
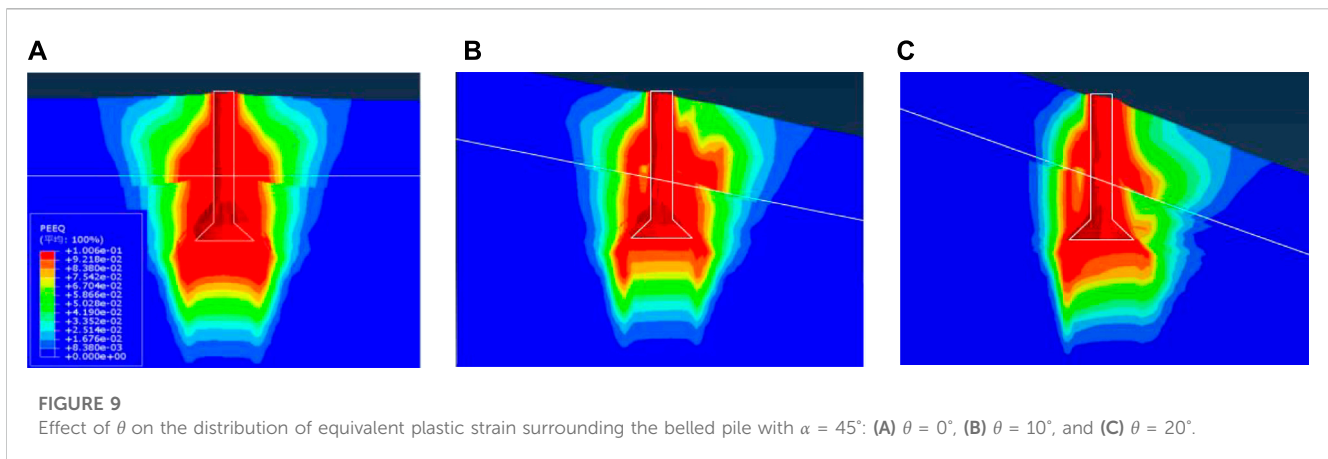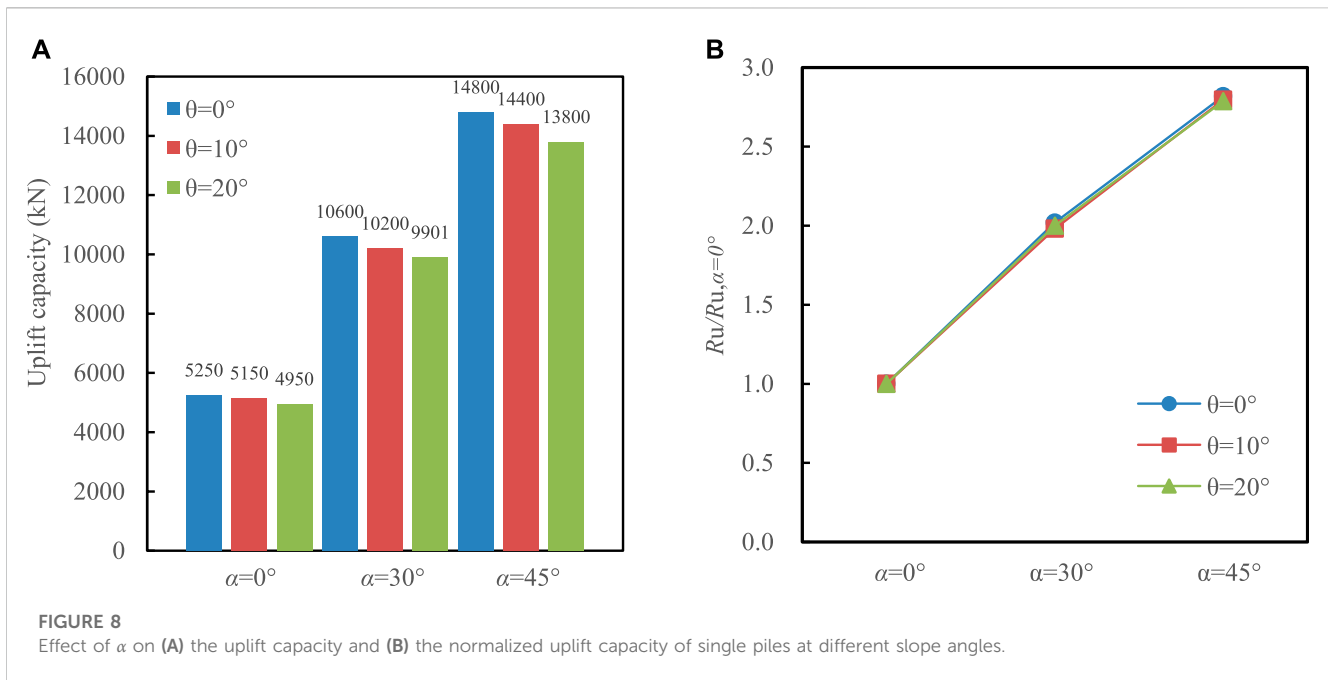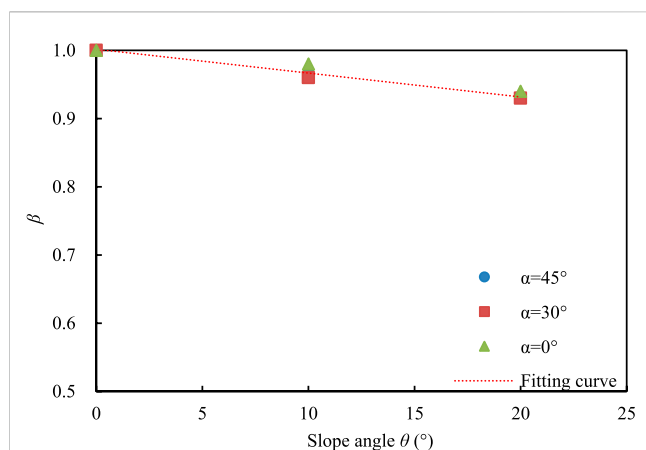(4) As the expansion angle α increased to 30° and 45°, R_u was increased by 100% and 180% with respect to straight piles, respectively. Moreover, the increase percentage in R_u was independent on the slope angle.
(5) A practical method was proposed to quantify the slope effect on R_u.

Data availability statement

The raw data supporting the conclusion of this article will be made available by the authors, without undue reservation.

Author contributions

Funding

Conflict of interest

MB, SQ, JP, JL, and XZ were employed by the Electric Power Research Institute of Guangxi Power Grid Co., Ltd.

Publisher's note

All claims expressed in this article are solely those of the authors and do not necessarily represent those of their affiliated organizations, or those of the publisher, the editors, and the reviewers. Any product that may be evaluated in this article, or claim that may be made by its manufacturer, is not guaranteed or endorsed by the publisher.

References

Abdelgwad, A., Nasr, A., and Azzam, W. (2022). Utilization of enlarged base to improve the uplift capacity of single pile in sand—Model study. *Innov. Infrastruct. Solutions* 7, 317. doi:10.1007/S41062-022-00922-9

Al-Isawi, A. T., Collins, P. E. F., and Cashell, K. A. (2019). *Fully non-linear numerical simulation of a shaking table test of dynamic soil-pile-structure interactions in soft clay using ABAQUS*. Virginia, United States: American Society of Civil Engineers.

Chae, D., Cho, W., and Na, H. Y. (2012). Uplift capacity of belled pile in weathered sandstones. *Int. J. Offshore Polar Eng.* 22, 297–305.

Drucker, D. C., and Prager, W. (1952). Soil mechanics and plastic analysis or limit design. *Quart.* Appl. Math. 10, 157–165. doi:10.1090/qam/48291

Emirler, B., Emirler, M., and Yildiz, A. (2017). 3D numerical response of a single pile under uplift loading embedded in sand. *Geotechnical Geol. Eng.* 37, 4351–4363. doi:10.1007/s10706-019-00913-1

Faizi, K., Armaghani, D. J., Sohaei, H., Rashid, A. S. A., and Nazir, R. (2015). Deformation model of sand around short piles under pullout test. *Measurement* 63, 110–119. doi:10.1016/j.measurement.2014.11.028

Gaaver, K. E. (2013). Uplift capacity of single piles and pile groups embedded in cohesionless soil. *Alexandria Eng. J.* 52, 365–372. doi:10.1016/j.aej.2013.01.003

HondaHirai, Y., and Sato, E. (2011). Uplift capacity of belled and multibelled piles in dense sand. *Soils Found.* 51, 483–496. doi:10.3208/sandf.51.483

Hong, W. P., and Chim, N. (2015). Prediction of uplift capacity of a micropile embedded in soil. *J. Civ. Eng.* 19, 116–126. doi:10.1007/s12205-013-0357-2

Hu, Z. B., Qu, S. Y., Wang, Q. K., Guo, Y. J., Ji, Y. K., and Ma, J. L. (2022). Pullout behaviour of belled piles under axial and oblique pull in soil-rock composite ground: An experimental study. *Int. J. Civ. Eng.* 2022, 00778. doi:10.1007/s40999-022-00778-1

Ilamparuthi, K., and Dickin, E. A. (2001). The influence of soil reinforcement on the uplift behaviour of belled piles embedded in sand. *Geotext. Geomembranes* 19, 1–22. doi:10.1016/S0266-1144(00)00010-8

Jiang, J. H., Huang, X. L., Shu, X. R., Ning, X., Qu, Y., and Xiong, W. L. (2022). Application of a damage constitutive model to pile–slope stability analysis. *Front. Mater.* 9, 1082292. doi:10.3389/FMATS.2022.1082292

Kang, J. G., and Kang, G. O. (2022). Experimental and semitheoretical analyses of uplift capacity of belled pile in sand. *Int. J. Geomechanics* 22, 04022217. doi:10.1061/(ASCE)GM.1943-5622.0002511

Kyung, D., and Lee, J. (2019). Uplift load-carrying capacity of single and group micropiles installed with inclined conditions. *J. geotechnical geoenvironmental Eng.* 143, 04017031. doi:10.1061/(ASCE)GT.1943-5606.0001700

Lai, Y., and Jin, G. F. (2010). Uplift behavior and load transfer mechanism of prestressed high-strength concrete piles. *J. Central South Univ. Technol.* 17, 136–141. doi:10.1007/s11771-010-0022-6

Liu, G., Zhang, Z. H., Cui, Q., Peng, J., and Cai, M. (2020). Uplift behavior of belled piles subjected to static loading. *Arabian J. Sci. Eng.* 46, 4369–4385. doi:10.1007/s13369-020-04779-x

Moayedi, H., and Mosallanezhad, M. (2017). Uplift resistance of belled and multi-belled piles in loose sand. *Measurement* 109, 346–353. doi:10.1016/j.measurement.2017.06.001

Mohan, D., and Chandra, S. (1961). Frictional resistance of bored piles in expansive clays. *Geotechnique* 11, 294–301. doi:10.1680/geot.1961.11.4.294

National Energy Administration (NEA) (2015). *Technical code for design of foundation of overhead transmission line.* Beijing, Chain. (DL/T 5219-2014).

Qu, C. X., Yi, T. H., Li, H. N., and Chen, B. (2018a). Closely spaced modes identification through modified frequency domain decomposition. *Measurement* 128, 388–392. doi:10.1016/j.measurement.2018.07.006

Qu, C. X., Yi, T. H., and Li, H. N. (2019). Mode identification by eigensystem realization algorithm through virtual frequency response function. *Struct. Con-trol Health Monit.* 26, e2429. doi:10.1002/stc.2429

Qu, C. X., Yi, T. H., Zhou, Y. Z., Li, H. N., and Zhang, Y. F. (2018b). Frequency identification of practical bridges through higher order spectrum. *J. Aerosp. Engineering-ASCE* 31, 04018018. doi:10.1061/(asce)as.1943-5525.0000840

Saravanan, R., Arumairaj, P. D., and Subramani, T. (2017). Experimental model study on ultimate uplift capacity of vertical pile in sand. *Water Energy Int.* 60, 58–66.

Sawwaf, M. E., and Nazir, A. (2006). The effect of soil reinforcement on pullout resistance of an existing vertical anchor plate in sand. *Comput. Geotechnics* 4, 167–176. doi:10.1016/j.compgeo.2006.04.001

Schafer, M., and Madabhushi, S. P. G. (2020). Uplift resistance of enlarged base pile foundations. *Indian Geotech. J.* 50, 426–441. doi:10.1007/s40098-019-00369-3

Shanker, K., Basudhar, P. K., and Patra, N. R. (2007). Uplift capacity of single piles: Predictions and performance. *Geotechnical Geol. Eng.* 2, 151–161. doi:10.1007/s10706-006-9000-z

Shelke, A., and Mishra, S. (2010). Uplift capacity of single bent pile and pile group considering arching effects in sand. *Geotechnical Geol. Eng.* 28, 337–347. doi:10.1007/s10706-009-9295-7

Shelke, A., and Patra, N. R. (2009). Effect of arching on uplift capacity of single piles. *Geotechnical Geol. Eng.* 27, 365–377. doi:10.1007/s10706-008-9236-x

Shin, E. C., Das, B. M., Puri, V. K., Yen, S. C., and Cook, E. E. (1993). Ultimate uplift capacity of model rigid metal piles in clay. *Geotechnical Geol. Eng.* 11, 203–215. doi:10.1007/BF00531251

Sowa, V. A. (1970). Pulling capacity of concrete cast *in situ* bored piles. *Can. Geotechnical J.* 7, 482–493. doi:10.1139/t70-060

Sun, T., Cui, X. Z., and Sun, Y. F. (2022). Model tests on uplift capacity of double-belled pile influenced by distance between bells. *J. Central South Univ. Technol.* 29, 1630–1640. doi:10.1007/S11771-022-5018-5

Systèmes, D. (2007). *Abaqus analysis user's manual.* Providence, RI, USA: Simulia Corp., 40.

Tanaya, D., and Sujit, K. P. (2019). Comparison of uplift capacity and nonlinear failure surfaces of single-belled anchor in homogeneous and layered sand deposits. *Adv. Civ. Eng.* 23, 1–23. doi:10.1155/2019/4672615

Tang, M. X., and Chen, D. A. (2015). Computational method of ultimate capacity of uplift piles in basement rock. *Rock Soil Mech.* 36, 633–638.

Turner, E. Z. (1962). Uplift resistance of transmission tower footing. *J. Power Div. ASCE* 88, 17–33. doi:10.1061/JPWEAM.0000339

Verma, A. K., and Joshi, P. K. (2010). *Uplift load carrying capacity of piles in sand.* Mumbai: Indian Geotechnical Conference, 857–860.

Wang, Q. K., Ma, J. L., Ji, Y. K., and Cao, S. (2021a). Calculation method and influencing factors of uplift bearing capacity of rock-socketed pedestal pile. *Arabian J. Geosciences* 14, 1–15. doi:10.1007/S12517-021-06567-9

Wang, Q. K., Ma, J. L., Wang, M. T., and Ji, Y. K. (2021b). Field test on uplift bearing characteristics of transmission tower foundation in mountainous areas of Western China. *Environ. Earth Sci.* 80, 745. doi:10.1007/S12665-021-09851-9

Wang, Q. K., Ma, J. L., Xiao, Z. L., Chen, W., and Ji, Y. (2020). Field test on uplift bearing capacity of rock-socketed belled piles. *J. Civ. Eng.* 24, 2353–2363. doi:10.1007/s12205-020-2011-0

Xu, L. Y., Cai, F., Wang, G. X., Chen, G. X., and Li, Y. Y. (2017b). Nonlinear analysis of single reinforced concrete piles subjected to lateral loading. *KSCE J. Civ. Eng.* 21, 2622–2633. doi:10.1007/s12205-017-1010-2

Xu, L. Y., Cai, F., Wang, G. X., and Chen, G. X. (2017a). Nonlinear analysis of single laterally loaded piles in clays using modified strain wedge model. *Int. J. Civ. Eng.* 15, 895–906. doi:10.1007/s40999-016-0072-8

Xu, L. Y., Cai, F., Wang, G. X., and Ugai, K. (2013). Nonlinear analysis of laterally loaded single piles in sand using modified strain wedge model. *Comput. Geotechnics* 51, 60–71. doi:10.1016/j.compgeo.2013.01.003

Xu, L. Y., Chen, W. Y., Cai, F., Song, Z., Pan, J. M., and Chen, G. X. (2023). Response of soil–pile–superstructure–quay wall system to lateral displacement under horizontal and vertical earthquake excitations. *Bull. Earthq. Eng.* 21, 1173–1202.doi:10.1007/S10518-022-01572-Z

Xu, L. Y., Song, C. X., Chen, W. Y., Cai, F., Li, Y. Y., and Chen, G. X. (2021). Liquefaction-induced settlement of the pile group under vertical and horizontal ground motions. *Soil Dyn. Earthq. Eng.* 144, 106709. doi:10.1016/J.SOILDYN.2021.106709

Yang, B., Ma, J. L., Chen, W. L., and Yang, Y. X. (2018). Uplift behavior of belled short piles in weathered sandstone. *Math. Problems Eng.* 8, 1–8. doi:10.1155/2018/8614172

Yang, Y. S., and Qiu, L. C. (2020). MPM simulation of uplift resistance of enlarged base piles in sand. *Soils Found.* 60, 1322–1330. doi:10.1016/j.sandf.2020.08.003

Check for updates

Effect of inclined pile on seismic response of bridge abutments undergoing liquefaction—Induced lateral displacement: Case study of Nishikawa bridge in the 2011 Great East Japan earthquake

Ying-Ying Xue[1]*, Xing-Gang Wang[2] and Fei Cai[3]

[1]Earthquake Administration of Jiangsu Province, Nanjing, China, [2]Nanjing Hydraulic Research Institute (NHRI), Nanjing, China, [3]Department of Environmental Engineering Science, Gunma University, Kiryo, Japan

It is reported that the inclined pile could be either beneficial or detrimental for the abutment they support in the condition of liquefaction—induced lateral displacement. To clarify the effect of inclined pile on seismic response of bridge abutments undergoing liquefaction—induced lateral displacement, numerical analyses were carried out on the damaged abutment that was supported by inclined piles and that was displaced riverwards 100 mm–150 mm due to soil liquefaction during 2011 Great East Japan earthquake. Accordingly, a fully coupled dynamic effective stress finite element model was developed for the soil—pile—superstructure system. It was found that the shear failure of the bridge abutment was initialized from the inclined piles and then followed by the middle vertical pile. Moreover, the earthquake—induced liquefaction caused substantial lateral displacement of soils around the piles and thus dominated the backward rotation of the abutments supported by inclined piles. Additionally, the exclusion of the deck pinning effect may lead to a marked increase in the lateral displacement and rotation of abutments. If the abutment were supported by vertical piles, a much larger lateral displacement was expected and the promotion of the earth pressure behind the abutment was the main cause of the forward rotation of the piled abutment.

KEYWORDS

abutment damage, inclined pile, *u-p* formulation, liquefaction, soil - pile - superstructure system

1 Introduction

The safety of the soil-pile -bridge system is a primary concern in the engineering practice (Gerolymos et al., 2008; Cubrinovski et al., 2014; Qu et al., 2018a; Qu et al., 2018b; Qu et al., 2019). Liquefaction—induced lateral displacement has caused much damage to the piled abutment of bridges in the past earthquakes, such as the 1991 Costa Rica Earthquake, the 2011 Christchurch earthquake, and the 2011 Great East Japan earthquake (Gerolymos et al., 2008; Cubrinovski et al., 2014; National Institute for Land and Infrastructure Management of Japan, Public Works Research Institute of Japan, 2014; Tazohb et al., 2008; Xu et al., 2023). It is reported that the inclined piles are more effective than vertical piles in restricting lateral
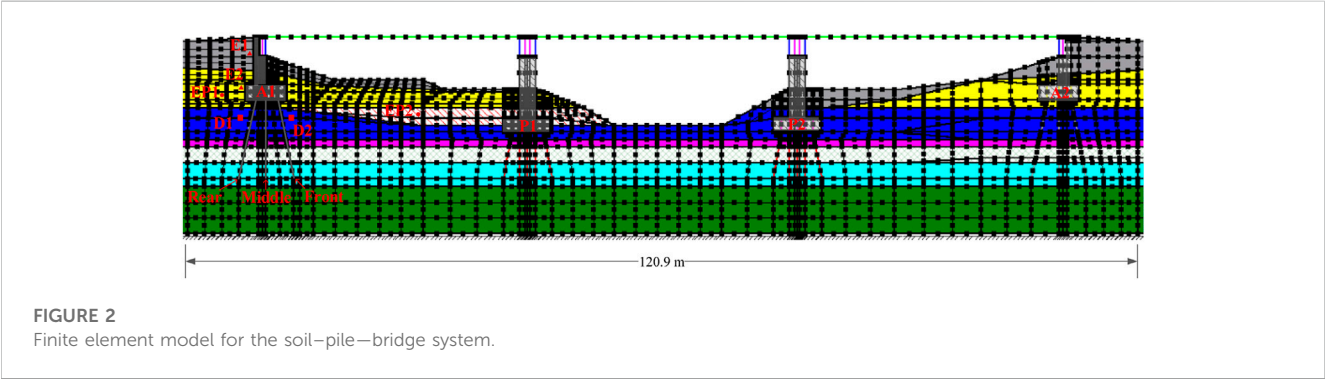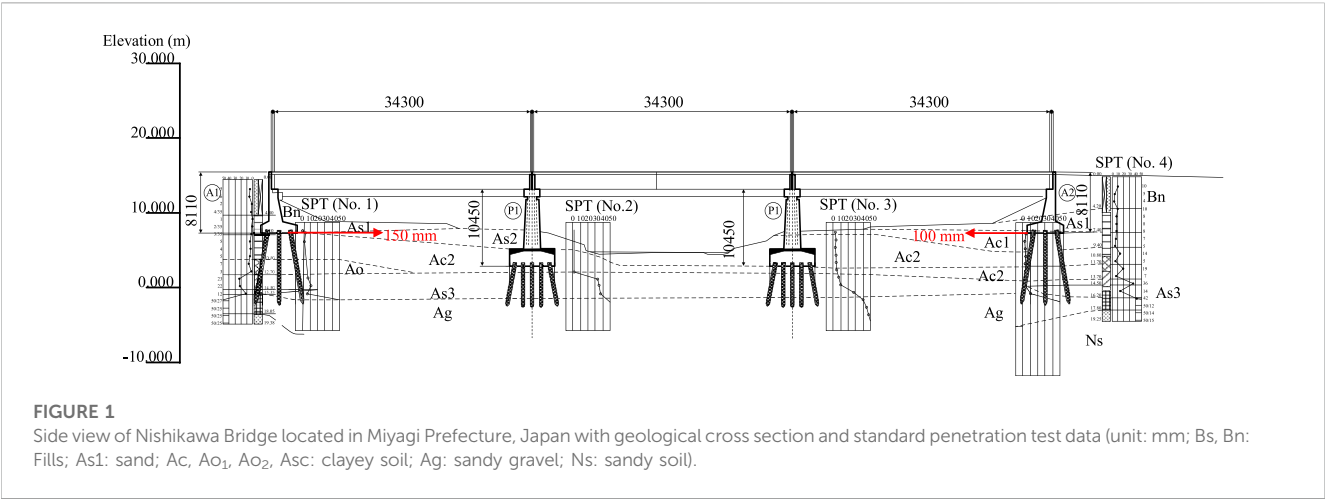
FIGURE 1
Side view of Nishikawa Bridge located in Miyagi Prefecture, Japan with geological cross section and standard penetration test data (unit: mm; Bs, Bn: Fills; As1: sand; Ac, Ao₁, Ao₂, Asc: clayey soil; Ag: sandy gravel; Ns: sandy soil).

FIGURE 2
Finite element model for the soil−pile—bridge system.

TABLE 1 Input parameters for the pile and the deck in the finite element analysis.

Type	E (GPa)	Poison's ratio (ν)	A_{ps} (m²)	I_{ps} (m⁴)	Yield stress (kN·m)
Abutment pile	35.3	0.2	6.28×10^{-2}	1.26×10^{-3}	184
Pier pile	35.3	0.2	1.44×10^{-3}	9.0×10^{-4}	184
Deck	35.3	0.2	2.64	1.5×10^{-2}	-

Note: E is Young's modulus.

displacements of superstructures subjected to liquefaction induced lateral displacement. However, the evidence shows that the inclined pile could be either beneficial or detrimental for the abutment they support in the condition of liquefaction—induced lateral displacement (Gerolymos et al., 2008; Cubrinovski et al., 2014). For example, the liquefaction—induced lateral displacement caused a lateral displacement of approximately 1–2 m at the unconstrained river banks in the vicinity of South Brighton Bridge during the 2011 Christchurch earthquake. As a result, the bridge abutment rotated by 8° and the pile head displaced laterally approximately 20 cm. Nevertheless, following the infilling of the offsets between the approaches and the deck, the bridge was back in service immediately after the earthquake (Cubrinovski et al., 2014). However, a detrimental case related to the bridge abutment supported by inclined piles were found on Rio Vizcaya Bridge during the

1991 Costa Rica Earthquake. The liquefaction—induced lateral displacement caused large rotations of the abutment and thus the collapse of the bridge deck (Gerolymos et al., 2008). Thus, it is necessary to clarify the damage mechanism of inclined piles which support the abutment subjected to the liquefaction—induced lateral displacement.

The liquefaction effects on piled bridge abutments have been investigated *via* both model tests and numerical analyses in recent years. Armstrong et al. (2013) conducted centrifuge model tests to evaluate the capability of the vertical pile group in resist the lateral displacement of abutments in approach embankments underlain by liquefied soils. The benefit of the pile pinning effect was reflected in reducing the lateral displacement of bridge abutments and was also evaluated by 2D numerical analyses. Tanabe et al. (2016) reported two case histories of two bridge abutments supported by inclined

TABLE 2 Calculated liquefaction strength for Bs and As$_1$ layers.

Layer	N_1	σ'_{v0}	$(N_1)_{60}$	D_r (%)	R_L
Bs	12	83.6	13.3	51.0	0.214
As$_1$	14	19.2	26.7	72.3	0.304

TABLE 3 Parameters of Pastor–Zienkiewicz III model for Bs and As$_1$ layers.

Model parameters	Bs	As$_1$
M_f	1.2	1.3
M_g	1.67	1.87
C	0.9	0.9
α_f	0.45	0.45
α_g	0.45	0.45
K_{ev0}	165	165
G_{es0}	240	240
m_v	0.5	0.5
m_s	0.5	0.5
β_0	10	10
β_1	0.3	0.3
H_0	750	1,100
H_{U0}	7,500	14,000
γ_0	6	6
γ_U	4	4

and vertical piles and subjected to a varying degree of damage due to liquefaction-induced lateral displacement during the 2011 Great East Japan earthquake. A 2D numerical model was developed to investigate the liquefaction effects. However, the effect of the superstructure (i.e., deck) wasn't considered in the above analyses. Cubrinovski et al. (2014) found that the deck pinning contributes significantly to the back rotation of the piled abutment of short-span bridges in the case of liquefaction—induced lateral displacement; Nakata et al. (2018) used a large shaking table (i.e., E-Defense) facility to investigate both the liquefaction effect and the deck pinning effect on the bridge abutment supported by the vertical piles. Shin et al. (2008) and Wang et al. (2018) pointed out that appropriate modeling of soil-pile-deck interaction is necessary for understanding of the seismic response of bridge abutments, especially when the abutment piles encounter the problem of the liquefaction-induced lateral displacement. However, very limited work was conducted to investigate the effect of inclined pile on seismic response of bridge abutments undergoing liquefaction—induced lateral displacement, especially the soil-inclined pile-deck interaction effect. Incorporating the soil-inclined pile-deck interaction in the analyses could help understanding the damage mechanism of inclined piles of bridge abutments in the liquefaction induced lateral displacement ground.

For this purpose, this study performed a case study of damaged abutments which were supported by the pile group consisting of inclined piles and vertical piles and were displaced riverwards due to the liquefaction induced—lateral displacement during the 2011 Great East Japan earthquake. A 2D fully coupled dynamic effective stress model was developed for the soil -pile-bridge system. Accordingly, the damage mechanism of the bridge abutment and the effect of deck and pile rake angle on the seismic response of the bridge abutment were investigated.

2 Case history

Nishikawa Bridge was located in Miyagi Prefecture, Japan. The construction of the bridge was completed in the year of 1968. The bridge had a total length of 105 m and a width of 7.2 m. The bridge had three spans and each of span has length of 34.3 m. The total load of one-span deck was estimated to be 2,300 kN (Tanabe et al., 2016). During the 2011 Great Eastern Japan Earthquake, the A1 and A2 abutments of the bridge was horizontally displaced riverwards approximately 150 mm and 100 mm, respectively (see Figure 1), as reported by National Institute for Land and Infrastructure Management of Japan, Public Works Research Institute of Japan (2014). It was also reported that shear failure developed near the bottom of two abutments. The foundation of each abutment was composed of 7 * 3 reinforced concrete piles. The piles in the middle row were vertical, while others were inclined piles with rake angle of 10°. The pier foundation had 5 * 5 reinforced concrete piles: the piles in the front and rear rows were inclined at 10°, while the piles were vertical in the middle row. The diameter of the pile was 400 mm. The length of the pile was 7.0 m and 5.0 m for the abutment and the pier, respectively.

3 Finite element modeling of the soil–pile—Bridge system

3.1 *u-p* formulation

Biot's *u-p* formulations are used for saturated soils the dynamic system, where *u* and *p* represent the displacement and excess pore water pressure, respectively (Zienkiewicz et al., 1999):

$$\mathbf{M\ddot{u} + C\dot{u} + Ku - Qp = f^u} \tag{1}$$

$$\mathbf{Q\dot{u} + S\dot{p} + Hp = f^p} \tag{2}$$

where $\mathbf{M}$ is the mass matrix, $\mathbf{u}$ is the displacement vector, $\mathbf{C}$ is Rayleigh damping matrix, $\mathbf{K}$ is the stiffness matrix, $\mathbf{Q}$ is the coupled matrix, $\mathbf{p}$ is the excess pore water pressure vector, $\mathbf{f^u}$ is the external load vector, $\mathbf{H}$ is the seepage matrix, $\mathbf{S}$ is the compression matrix, and $\mathbf{f^p}$ is the external load vector for the pore water.

Biot's *u-p* formulations had been implemented in a fully coupled dynamic effective stress finite element (FE) analysis software program UWLC (Forum 8 Co Ltd, 2005; Xu et al., 2013; Xu et al., 2021; Cai, 2020) where were employed for numerical analyses in this study. In this program, Eq. 2 can also be deactivated for layers where the excess pore water pressure is not necessarily calculated.

TABLE 4 Parameters of Hardin—Drnevich model for non-liquefiable layers.

Layers	V_s, m/s	Poisson's ratio (ν)	p'_0 (kPa)	m	G_{max}, kPa	c, kPa	$\varphi°$
Bn	118.4	0.35	35.9	0.5	23,971.7	51.4	12
Ao$_1$	146.2	0.35	118.8	0.5	35,481.6	52.8	9.8
Ao$_2$	153.8	0.35	129.2	0.5	39,029.8	20.5	15.1
Ac	167	0.35	139.8	0.5	50,200.2	19.1	19.1
Asc	186.3	0.35	151.7	0.5	63,862.2	48	32.8
Ag	373	0.35	174.2	0.5	292,170.9	--	41
Ns	484.9	0.35	235	0.5	493,768.8	--	45

FIGURE 3
Seismic input for the soil—pile—bridge system: **(A)** Horizontal excitation and **(B)** vertical excitation.
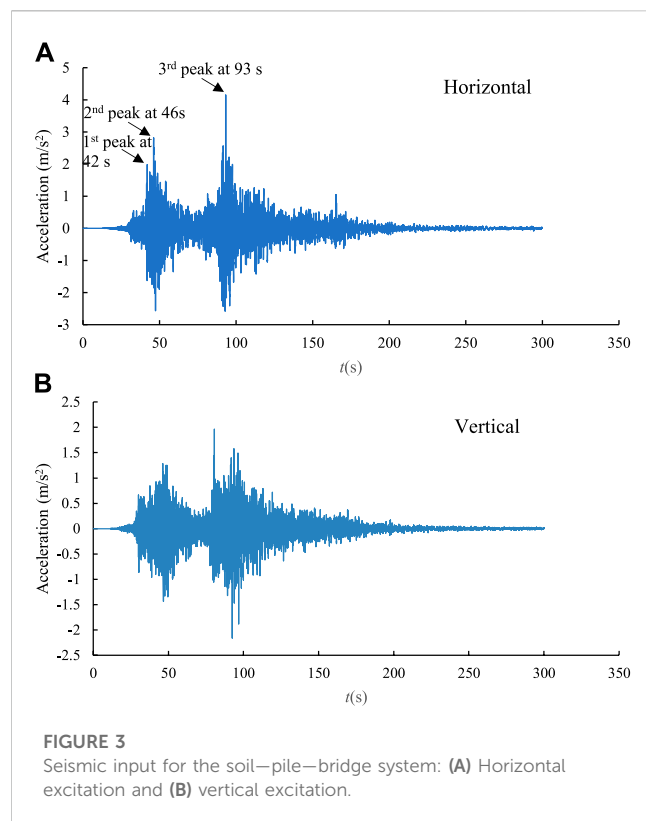
TABLE 5 The cases analyzed in this study.

No.	Piles supporting the abutments	Deck effect considered
1	Inclined	Yes
2	Inclined	No
3	Vertical	Yes

In the dynamic analysis, the matrix **C** was given by

$$\mathbf{C} = \alpha\mathbf{M} + \beta\mathbf{K} \qquad (3)$$

where α and β are coefficients and are taken as 0.172 and 0.00174, respectively (Forum 8 Co Ltd, 2005; Wakai and Ugai, 2004). The

coefficients α and β are related to damping ratio ξ and two periods T. In this study, $\xi = 0.03$, $T_1 = 0.2$ s, and $T_1 = 2.0$ s, as suggested by Xu et al. (2023).

3.2 Finite element model

In this study, a 2D finite element model was developed for the soil–pile—bridge (SPB) system, as shown in Figure 2. The soil layers were determined with some simplifications from the geological cross section shown in Figure 1. In this model, eight-node quadrilateral element was used for the soil, the abutment, and the pier. The abutment and the pier were modelled as elastic materials with unit weight of 24.5 kN/m^3, Young's modulus of 30 GPa, and Poison's ratio of 0.15.

The pile and the deck were modelled as Euler-Bernoulli beam. Table 1 gives the input parameters for the pile and the deck in the finite element analysis. In the 2D finite element model, the cross-sectional area and the cross-sectional inertia moment of piles were estimated according to Xu et al. (2013). The non-linearity of the pile was considered by using a bilinear model. The second Young's modulus of piles was assumed to be 1% of the fist Young's modulus of piles. According to Tanabe et al. (2016), the yield stress was set to 184 kN m for the pile. The deck was modelled as elastic materials. All beam element nodes and quadrilateral element nodes were merged.

The bearing was modelled by shear springs to consider the dynamic interaction between the deck and the abutment/pier. For simply supported beam bridges, each deck was supported by a fixed bearing and an expansion bearing, which were described by linear and bi-linear shear springs, respectively. In this study. The initial stiffness of shear springs was taken as an empirical value of 6,600 kN/m (Wang et al., 2018). For bi-linear shear spring, the second stiffness was set to zero and the limit force was taken as 287.5 kN. The value of the limit force was estimated from the supported vertical load (i.e., 1,150 kN) multiplied by a friction coefficient. The friction coefficient was empirically taken as 0.25 (Wang et al., 2013).

3.3 Constitutive modeling of soils

Five standard penetration test (SPT) bore holes were drilled near either the abutment or the pier, as shown in Figure 1A. The SPT data
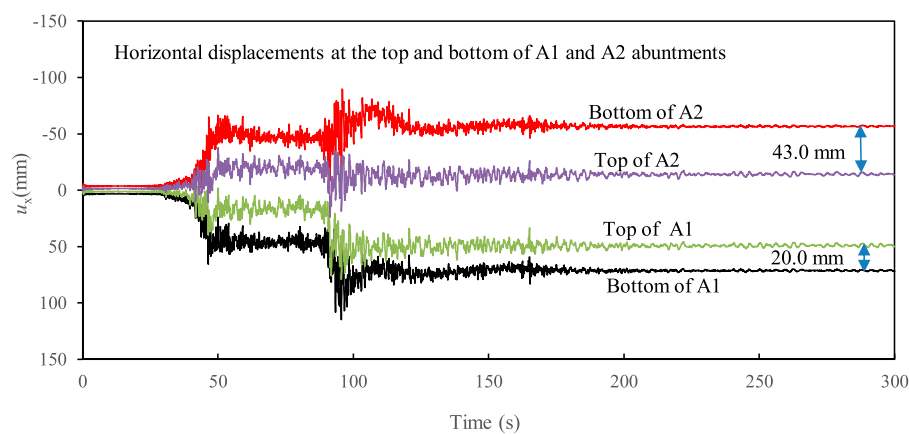
FIGURE 4
Time history of horizontal displacements at the top and bottom of two abutments, i.e., A1 and A2 (Case 1).
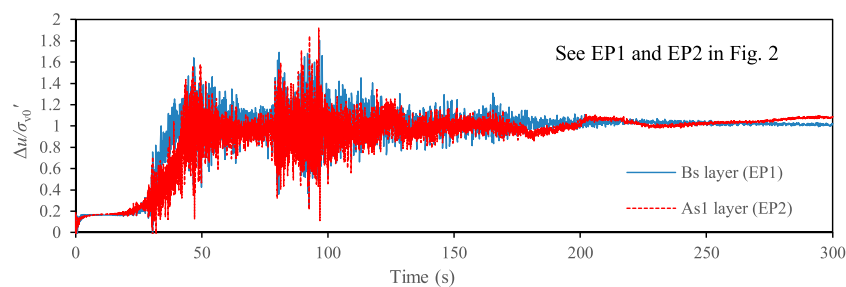

FIGURE 5
Time histories of the excess pore water pressure ratio at two typical points (see EP1 and EP2 in Figure 2).
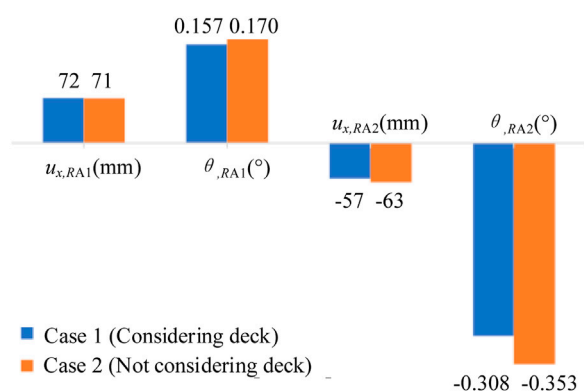
FIGURE 6
Effect of the deck on the residual lateral displacement and rotation of A1 and A2 abutments.

were used to determine the liquefaction potential of each layer according to the Japanese Design Specifications of Highway Bridges (Japan Road Association, 2004; Towhata, 2008). Accordingly,

liquefiable soils (i.e., Bs and As₁) and non-liquefiable soils (i.e., Bn, Ao₁, Ao₂, Ac, Asc, Ag, and Ns) were classified.

A generalized plasticity model, named Pastor-Zienkiewicz Mark-III (PZ) (Pastor et al., 1990), with some modifications by Cai et al. (2002) was adopted for the soils (Xu et al., 2023). Normally, the parameters for the PZ model were calibrated from either laboratory tests (e.g., cyclic triaxial undrained test) or in-situ tests. In this study, SPT data were used to determine the PZ model parameters. The liquefaction strength of two liquefiable layers (i.e., Bs and As₁) was estimated according to according to the Japanese Design Specifications of Highway Bridges. The calculated liquefaction strength for Bs and As1 layers was given in Table 2, where N_1 was taken as an average SPT blow count for Bs and As₁ layers. The PZ model parameters (G_{es0}, K_{ev0}, C, m_s, m_v, M_g, α_g, M_f, α_f, H_0, β_0, β_1, γ_0, H_{U0}, γ_U) were determined to obtain the calculated liquefaction strength shown in Table 2. Table 3 presented the PZ model parameters for liquefiable layers. The hydraulic conductivities were taken as a typical value of 1.0×10^{-5} m/s for the liquefiable layers.

A cyclic non-linear elastic constitutive model (Hardin and Drnevich, 1972), is used for non-liquefiable soils. The shear stress τ and the shear strain γ are described by a hyperbolic function:

$$\tau = \frac{G_{\max}\gamma}{1 + G_{\max}\gamma / \tau_f} \tag{4}$$

FIGURE 7
Time histories of two typical points (see D1 and D2 in Figure 2), representing the lateral displacement of soils in the vicinity of inclined piles in front and rear rows.
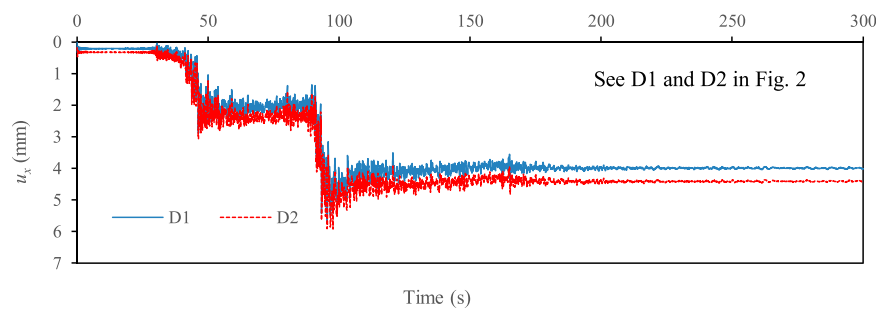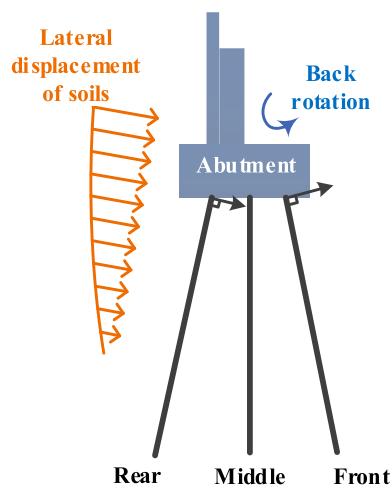

FIGURE 8
Mechanism of the abutment rotation supported by inclined piles under the liquefaction—induced lateral displacement.

where

$$G_{\max} = G_0 P_a \left(\frac{p'}{P_a}\right)^m \tag{5}$$

τ_f is the shear strength which is a function of friction angle (φ) and cohesion (c) (Xu et al., 2013), G_0 and m are model constants, P_a is atmospheric pressure, and p' is the mean effective stress. $G_{\max}$ at $p' = p'_0$ can be estimated from $G_{\max} = \rho v_s^2$, where ρ is the natural density and v_s is the shear wave velocity. Table 4 gives ρ, v_s, p'_0, m, φ, c, and $G_{\max}$ of Hardin—Drnevich model for each layer.

3.4 Boundary conditions

In the UWLC program, the initial stress analysis was necessary to provide geostatic conditions for the earthquake analysis. Two lateral sides and the base of the analyzed model were fixed in the analyses. The two lateral sides were set at three times the total length of the bridge apart from each abutment. To investigate whether the finite element model could eliminate the boundary effect, a larger model with an additional 200 m on each side of the model was analyzed. The difference between the results obtained from these two models was minimal, indicating that the finite element model was acceptably accurate.

The seismic input was selected from the data recorded at the K-NET station (i.e., MYG009) nearest to Nishikawa Bridge during the 2011 Great Eastern Japan Earthquake. The seismic data can be downloaded from the website of National Research Institute for Earth Science and Disaster Resilience (https://www.kyoshin.bosai.go.jp/) after the required registration was completed. Tanabe et al. (2016) reported that the angle (θ_0) of NS component of MYG009 and the longitudinal direction of the Nishikawa bridge was approximately 25°. Thus, the horizontal seismic input ($a'_N)_S$ for the Nishikawa bridge was synthesized from both the NS (a_{NS}) and the EW (a_{EW}) components of MYG009:

$$a'_{NS} = a_{NS}\cos\theta_0 - a_{EW}\sin\theta_0 \tag{6}$$

The UD component of MYG009 was taken as the vertical seismic input. Before the dynamic analyses, a baseline correction was conducted for the seismic recordings using SeismoSignal (SeismoSoft, 2013). Figures 3A, B showed the corrected horizontal and vertical input motions, respectively.

4 Results and discussions

Table 5 gave the cases analyzed in this study. Specifically, the damage mechanism of the bridge abutment was investigated in the benchmark model, i.e., Case 1, as described in Section 3. Case 2 was used to study the effect of the deck on the seismic response of bridge abutments. Case 3 was used to investigate the effect of the pile rake angle on the seismic response of bridge abutments.

4.1 Damage mechanism of the abutment supported by inclined piles

Figure 4 shows the time history of horizontal displacements at the head of piles supporting the abutments. All the piles displaced
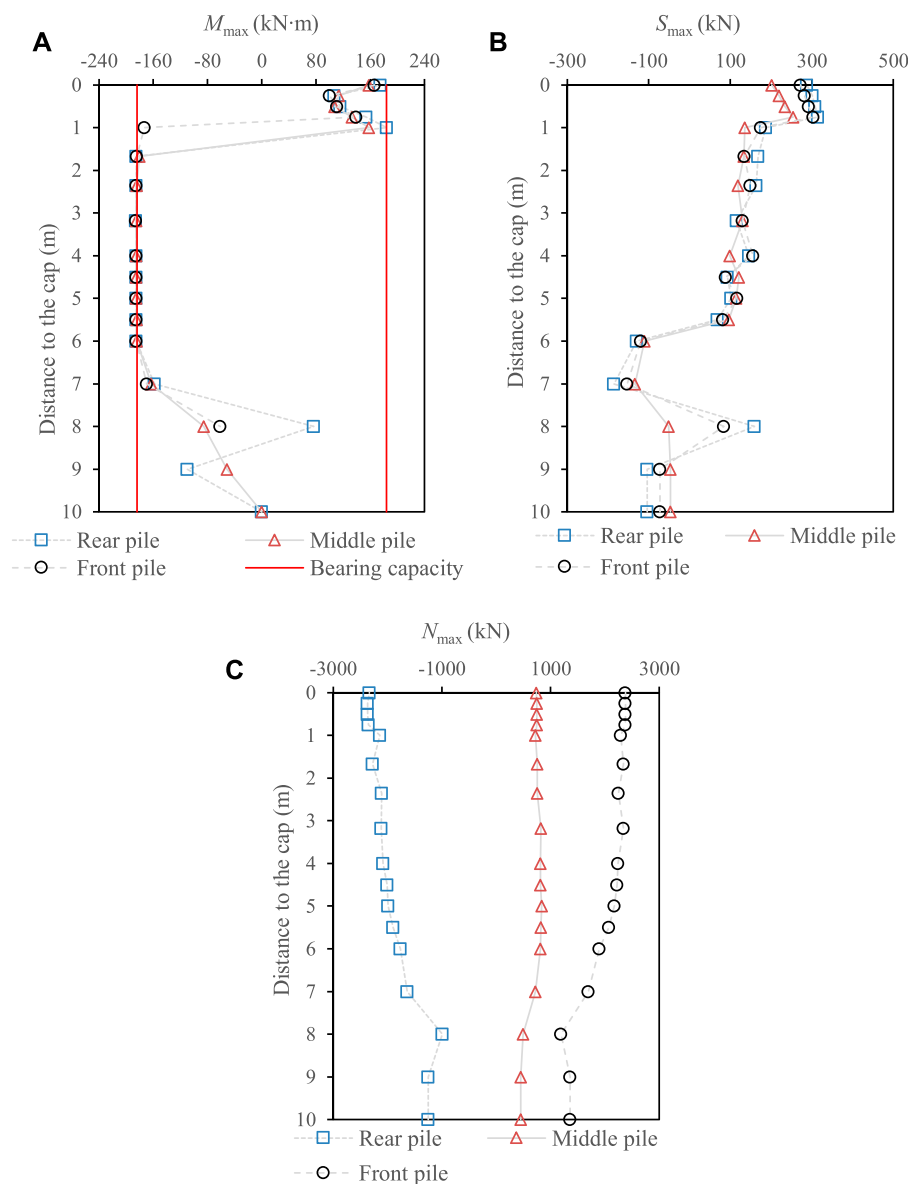
FIGURE 9
Distribution of the maximum internal force of a single pile at different rows (i.e., front, middle, and rear) **(A)** bending moment (M_{max}), **(B)** shear force (S_{max}), and **(C)** axial force (N_{max}) (Case 1).

riverwards after the earthquake. The calculated maximum lateral displacement of piles reached 115 mm and 84 mm at the bottom of A1 and A2 abutments, respectively. The calculated residual lateral displacements were generally smaller than the observation; however, the simulation results overall reflected that the lateral displacement of pile at the bottom of A1 abutment was larger than that at the bottom of A1 abutment. This was due to the fact that the earthquake induces the full liquefaction not only in Bs layer, but also in As_1 layer, (see Bs and As_1 in Figure 2), consequently resulting in the instability of the slope of the river bank near the abutment. Figure 5 showed the excess pore water pressure (EPWP) ratio at two typical points (see EP1 and EP2 in Figure 2) in these two layers, where the EPWP ratio was defined as the ratio of EPWP to the initial effective vertical stress. The results indicated that the Bs and As_1 layers were

liquefied at approximately 43 s after the arrival of the first peak horizontal acceleration shown in Figure 3A. Moreover, the excess pore water pressure was developed much faster in Bs layer than that in As_1 layer because the liquefaction strength of Bs layer was smaller (see Table 2).

Figure 4 further showed that the lateral displacements at the top of either A1 or A2 abutment were much smaller than those at the bottom of corresponding abutment, indicating that both A1 and A2 abutments rotated backwards. This phenomenon was also found for some abutments supported by inclined piles during the 2010–2011 Christchurch earthquakes where substantial slumping of the approaches was reported near these abutments due to soil liquefaction. The reason for the backward rotation of the abutment was probably because of the deck pinning of short-span bridges (Cubrinovski et al., 2014).

FIGURE 10
Effect of the pile rake angle on the lateral displacement at the bottom of **(A)** A1 and **(B)** A2 abutments.

FIGURE 11
Effect of the pile rake angle on the rotation of the A1 abutment.

To investigate the effect of deck on the damage of the abutment, an additional case (i.e., Case 2) was analyzed assuming that the deck was removed from the benchmark model. Figure 6 showed that the exclusion

of the deck pinning effect may lead to a marked increase in the lateral displacement and rotation of abutments, where $u_{x,RA1}$ and $u_{x,RA2}$ were the residual lateral displacements of A1 and A2 abutments, respectively, and θ_{RA1} and θ_{RA2} were the residual rotation angle of A1 and A2 abutments, respectively. Note that a clockwise rotation was considered as negative in this study. The results indicated that the abutments supported by inclined piles could rotate backwards even when the deck pinning effect was not considered in this study (see Figure 6). It was stressed that positive θ_{RA1} and negative θ_{RA2} indicated back rotation of A1 and A2 abutments, respectively. Based on the numerical results, the damage mechanism involving the back rotation of the abutment probably complied with the following process: 1) The earthquake—induced liquefaction initially caused substantial lateral displacement of soils around the piles, as shown by two typical points in Figure 7 (See D1 and D2 in Figure 2); 2) the inclined piles consequently had to rotate along the direction of arrows shown in Figure 8 under the liquefaction—induced lateral displacements; 3) and then the displaced inclined piles dominated the rotation of the abutments.

Figure 9 showed the calculated maximum internal force of a single pile at different rows (i.e., front, middle, and rear), where M_{max}, S_{max}, and N_{max} were the maximum bending moment, shear force, and axial force, respectively. In general, the M_{max} at different rows reached the ultimate value of 184 kN m at approximately 1.0 m–7.0 m away from the cap. At the pile head, M_{max} was generally smaller than the ultimate value for all piles. However, the S_{max} peaked at the pile head. This result can explain why the shear failure has been developed at the pile head. In addition, the rear and front piles appeared to have the larger M_{max} and S_{max} than the middle pile at the pile head, indicating that the shear failure was initialized from the inclined piles and then followed by the middle pile. Especially, the inclined piles sustained the N_{max} three times more than the middle pile (see Figure 9C) during the earthquake. Thus, special treatments were necessary for inclined group piles in the engineering design to increase the shear capacity of the inclined pile, e.g., increasing the ratio of longitudinal reinforcement, reinforcement stirrup.

4.2 Effect of the pile rake angle on the abutment damage

To investigate the effect of the pile rake angle on the lateral displacement at the bottom of A1 and A2 abutments, Case 3 was

FIGURE 12
Time histories of horizontal stress (σ_{xx}) and excess pore water pressure (Δu) at typical points behind the A1 abutment (see E1 and E2 in Figure 2) (Case 3).
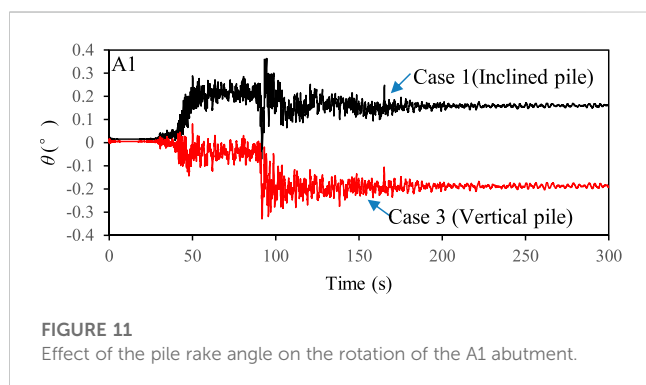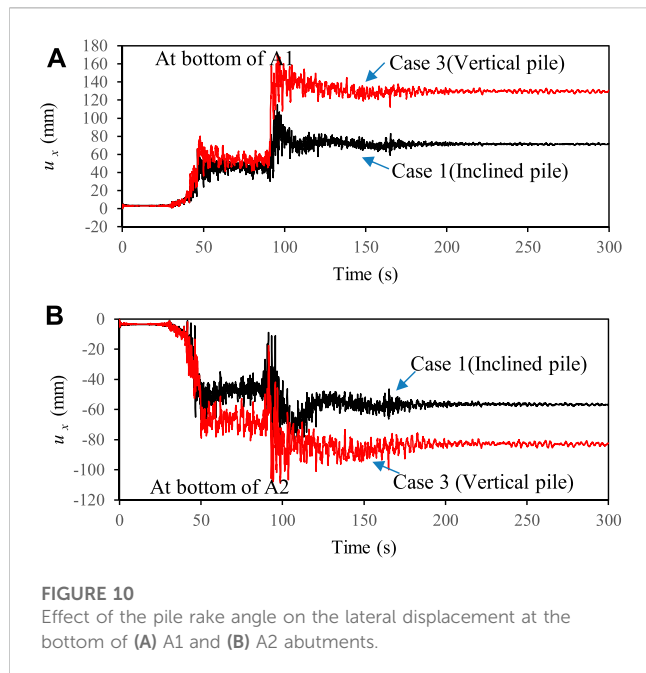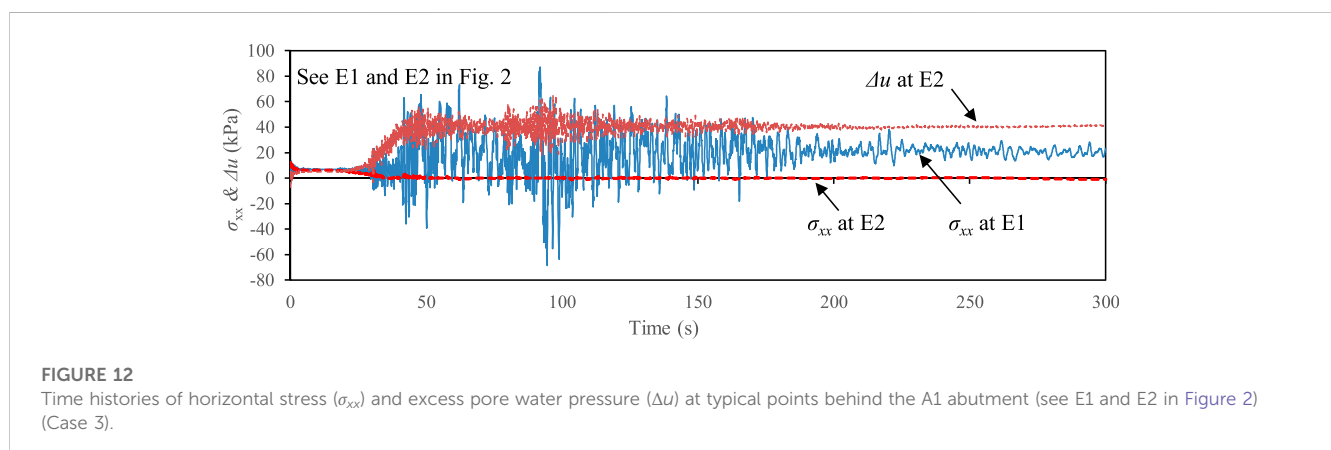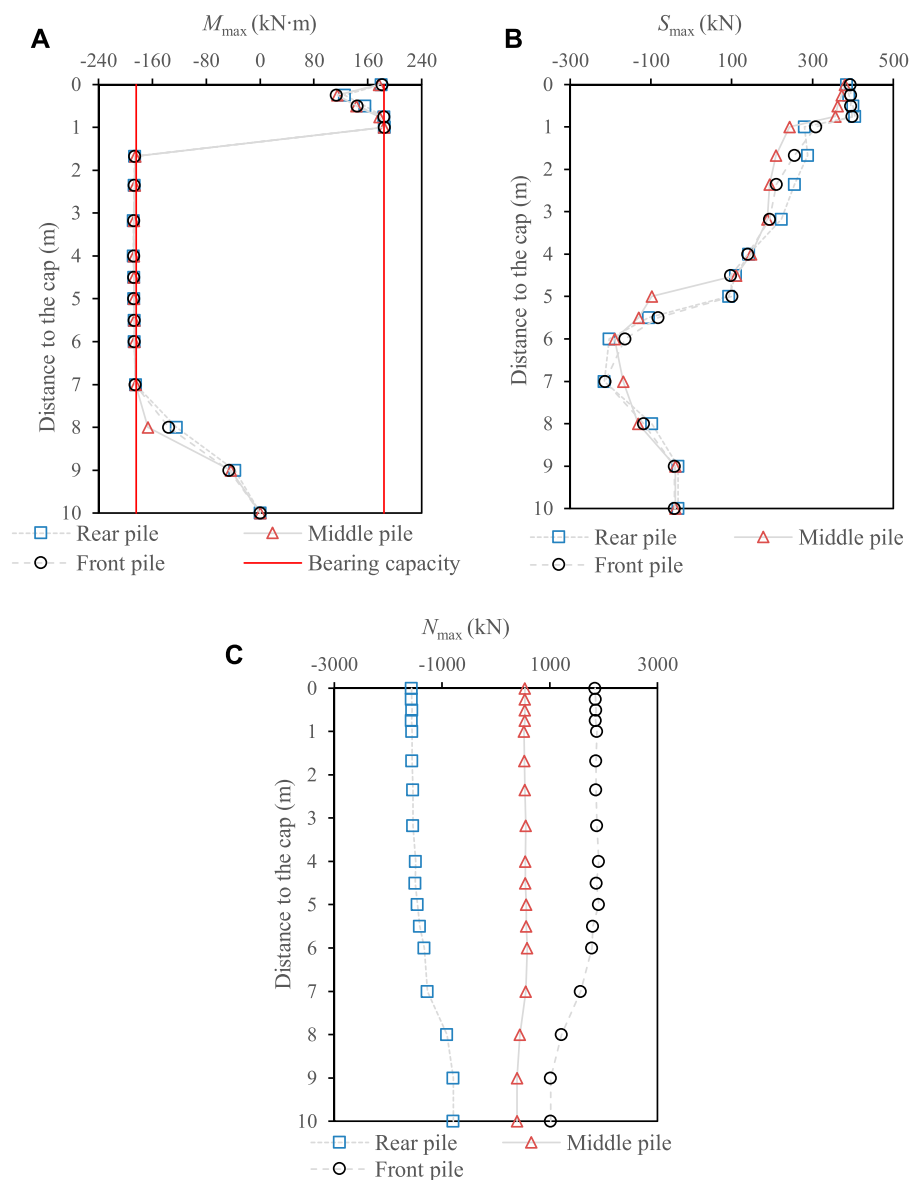
FIGURE 13
Distribution of the maximum internal force of a single pile at different rows (i.e., front, middle, and rear) **(A)** bending moment (M_{max}), **(B)** shear force (S_{max}), and **(C)** axial force (N_{max}) (Case 3).

analyzed assuming that all piles supporting the abutments were vertical. Figure 10 showed the comparison of the lateral displacement at the bottom of A1 and A2 abutments between Cases 1 and 3. The results indicated that the pile rake angle had an insignificant effect on the lateral displacement of the abutment before the first peak horizontal acceleration was reached. However, the lateral displacement in at the bottom of the abutment in Case 1 turned to become much larger than that in Case 3, especially when the third peak horizontal acceleration was arrived at approximately 93 s. Moreover, the residual lateral displacement ($u_{x,R}$) at the bottom of A1 and A2 abutments increased by approximately 82% and 45% in Case 3 with respect to that in Case 1, respectively. The above results demonstrated that the inclined piles were more effective than vertical piles in restricting the liquefaction—induced lateral displacements of the abutment during.

To further investigate the effect of pile rake angle on the deformation of the abutment, Figure 11 compared the time histories of the rotation angle of the A1 abutment in Cases 1 and 3. The results indicated that the residual rotation angle of the abutment supported by vertical piles had opposite sign with respect to that of the abutment supported by inclined piles. Thus, the abutments in Case 3 rotated forwards and had different deformation mechanism with respect to the forementioned backward rotation of the abutment supported by inclined piles. Particularly, there was a tremendous increase in the rotation angle of the abutment in Case 3 when the third peak horizontal acceleration was reached. The forward rotation of the abutment in Case 3 was probably dominated by the promotion of the Earth pressure at the backfill of abutment, including the increase in the horizontal stress in non-liquefiable layer and the buildup of EPWP in liquefied layer. Specifically, Figures 12 showed the calculated horizontal stress (σ_{xx}) at

two typical points (see E1 and E2 in Figure 2), representing the center of non-liquefiable and liquefiable layers behind the abutment in Case 3. The horizontal stress at the non-liquefiable layer increased abundantly during the earthquake and reached the maximum at the arrival of the third peak horizontal acceleration. The horizontal stress at the liquefiable layer decreased to a value approaching zero due to the soil liquefaction; however, the EPWP also reached the maximum value of 65 kPa at the time of third peak horizontal acceleration (see Figure 12). This maximum value was approximately five times more than the initial horizontal stress.

Figure 13A showed that the M_{max} at pile head in Case 3 was approaching to the yield stress at different rows. Unlike inclined piles in Case 1, the values of M_{max} and S_{max} were almost identical for vertical piles at different rows in Case 3 (see Figures 13A, B). This result indicated that all vertical piles not only displaced equally at the pile head, but also rotated equally due to the restriction of the abutment. Figure 13C indicated that the Nmax at the pile head in Case 3 was approximately 67%–78% of that in Case 1 (see Figures 9C, 13C), although the lateral displacement of the abutment was much larger in Case 3 (see Figure 10). These results demonstrated the benefit of inclined piles that had greater axial forces but smaller bending moment than vertical piles.

5 Conclusion

A case study was carried out on the damage mechanism of the Nishikawa bridge abutment that was displaced riverwards due to soil liquefaction during 2011 Great East Japan earthquake. Some conclusions can be summarized from the numerical analyses:

(1) The shear failure of the bridge abutment was initialized from the inclined piles and then followed by the middle vertical pile. Thus, special treatments were necessary for inclined group piles in the engineering design to increase the shear capacity of the inclined pile.

(2) The earthquake—induced liquefaction caused substantial lateral displacement of soils around the piles and thus dominated the backward rotation of the abutments supported by inclined piles.

(3) The exclusion of the deck pinning effect may lead to a marked increase in the lateral displacement and rotation of abutments for simply supported beam bridges.

(4) The pile rake angle had insignificant effect on the lateral displacement of the abutment before the first peak horizontal

acceleration was reached. However, after the arrival of the peak horizontal acceleration, a much larger lateral displacement was obtained for the abutment supported by vertical piles.

(5) The promotion of the Earth pressure behind the abutment was the main cause of the forward rotation of the abutment supported by vertical piles during earthquakes.

Data availability statement

The raw data supporting the conclusion of this article will be made available by the authors, without undue reservation.

Author contributions

Y-YX: Investigation, manuscript preparation, computation, revision; X-GW: Data curation; FC: Supervision, software.

Funding

Conflict of interest

The authors declare that the research was conducted in the absence of any commercial or financial relationships that could be construed as a potential conflict of interest.

Publisher's note

All claims expressed in this article are solely those of the authors and do not necessarily represent those of their affiliated organizations, or those of the publisher, the editors and the reviewers. Any product that may be evaluated in this article, or claim that may be made by its manufacturer, is not guaranteed or endorsed by the publisher.

References

Armstrong, R. J., Boulanger, R. W., and Beaty, M. H. (2013). Liquefaction effects on piled bridge abutments: Centrifuge tests and numerical analyses. *J. geotechnical geoenvironmental Eng.* 139 (3), 433–443. doi:10.1061/(asce)gt.1943-5606.0000780

Cai, F., Hagiwara, T., Imamura, S., and Ugai, K. (2002). "2D fully coupled liquefaction analysis of sand ground under tank," in *Proceedings of the 11th Japan earthquake engineering symposium*, 819–824.

Cai, F. (2020). Effects of large-space latticed walls for liquefaction mitigation. *J. X Univ. Nat. Sci. Ed.* 39 (1), 1–11.

Cubrinovski, M., Haskell, J., Winkley, A., Robinson, K., and Wotherspoon, L. (2014). Performance of bridges in liquefied deposits during the 2010–2011 Christchurch, New Zealand, earthquakes. *J. Perform. Constr. Facil.* 28 (1), 24–39. doi:10.1061/(asce)cf.1943-5509.0000402

Forum 8 Co Ltd (2005). "Finite element fully coupled dynamic effective stress analysis program (UWLC)," in *Electrical manual*. Available at: https://www.forum8.co.jp/english/uc-1/uwlc.htm.

Gerolymos, N., Giannakou, A., Anastasopoulos, I., and Gazetas, G. (2008). Evidence of beneficial role of inclined piles: Observations and summary of numerical analyses. *Bull. Earthq. Eng.* 6 (4), 705–722. doi:10.1007/s10518-008-9085-2

Hardin, B. O., and Drnevich, V. P. (1972). Shear modulus and damping in soils: Design equations and curves. *J. Soil Mech. Found. Div.* 98 (7), 667–692. doi:10.1061/jsfeaq.0001760

Japan Road Association (JRA) (2004). *Specifications for highway bridges-part V: Seismic design.* 5th ed. Tokyo. [in Japanese].

Nakata, M., Tanimoto, S., Ohsumi, M., and Nanasawa, T. (2018). Large-scale shaking table test of existing abutment foundation in liquefiable ground. *Civ. Eng. J.* 60 (8), 40–43. [in Japanese].

National Institute for Land and Infrastructure Management of Japan (NILIM), Public Works Research Institute of Japan (PWRI) (2014). *Reconnaissance report on damage to road bridges by the 2011 great east Japan earthquake.*

Pastor, M., Zienkiewicz, O. C., and Chan, A. (1990). Generalized plasticity and the modelling of soil behaviour. *J. Numer. Anal. methods geomechanics* 14 (3), 151–190. doi:10. 1002/nag.1610140302

Qu, C. X., Yi, T. H., Li, H. N., and Chen, B. (2018a). Closely spaced modes identification through modified frequency domain decomposition. *Measurement* 128, 388–392. doi:10.1016/j.measurement.2018.07.006

Qu, C. X., Yi, T. H., and Li, H. N. (2019). Mode identification by eigensystem realization algorithm through virtual frequency response function. *Struct. Control Health Monit.* 26, e2429. doi:10.1002/stc.2429

Qu, C. X., Yi, T. H., Zhou, Y. Z., Li, H. N., and Zhang, Y. F. (2018b). Frequency identification of practical bridges through higher order spectrum. *J. Aerosp. Eng.* 31, 04018018. doi:10.1061/(asce)as.1943-5525.0000840

SeismoSoft (2013). *SeismoSignal version 4.3.0.* Pavia, Italy: SeismoSoft ltd., inc. earthquake engineering software solutions, [online]2011 Available at: http://www. seismosoft.com.

Shin, H., Arduino, P., Kramer, S. L., and Mackie, K. (2008). Seismic response of a typical highway bridge in liquefiable soil. *Geotechnical Earthq. Eng. soil Dyn.* IV, 1–11.

Tanabe, A., Kouno, T., Nanazawa, T., and Tanimoto, S. (2016). Estimation of damage mechanism of bridges damaged by earthquakes. *Civ. Eng. J.* 58 (6), 38–41. [in Japanese].

Tazohb, T., Sato, M., Jang, J., and Gazetas, G. (2008). "Centrifuge tests on pile foundation-structure systems affected by liquefaction-induced soil flow after quay wall failure," in *The 14th world conference on earthquake engineering* (Beijing, China.

Towhata, I. (2008). *Geotechnical earthquake engineering.* Springer, 459–460.

Wakai, A., and Ugai, K. (2004). A simple constitutive model for the seismic analysis of slopes and its applications. *Soils Found.* 44 (4), 83–97. doi:10.3208/sandf.44.4_83

Wang, X. W., Ye, A. J., and Li, C. (2018). Seismic response of girder bridges in liquefiable river valleys with different structural configurations. *J. Tongji Univ. Nat. Sci.* 46 (6), 759–766.

Wang, Z., Dueñas-Osorio, L., and Padgett, J. E. (2013). Seismic response of a bridge–soil–foundation system under the combined effect of vertical and horizontal ground motions. *Earthq. Eng. Struct. Dyn.* 42 (4), 545–564. doi:10.1002/eqe.2226

Xu, L. Y., Cai, F., Wang, G. X., Ugai, K., Wakai, A., Yang, Q. Q., et al. (2013). Numerical assessment of liquefaction mitigation effects on residential houses: Case histories of the 2007 niigata chuetsu-offshore earthquake. *Soil Dyn. Earthq. Eng.* 53, 196–209. doi:10.1016/j.soildyn.2013.07.008

Xu, L. Y., Chen, W. Y., Cai, F., Song, Z., Pan, J. M., and Chen, G. X. (2023). Response of soil–pile–superstructure–quay wall system to lateral displacement under horizontal and vertical earthquake excitations. *Bull. Earthq. Eng.* 21 (2), 1173–1202. doi:10.1007/ s10518-022-01572-z

Xu, L. Y., Song, C. X., Chen, W. Y., Cai, F., Li, Y. Y., and Chen, G. X. (2021). Liquefaction-induced settlement of the pile group under vertical and horizontal ground motions. *Soil Dyn. Earthq. Eng.* 144, 106709. doi:10.1016/j.soildyn.2021.106709

Zienkiewicz, O. C., Chan, A. H. C., Pastor, M., Schrefler, B. A., and Shiomi, T. (1999). *Computational geomechanics with special reference to earthquake engineering.* New York: Wiley.

Bearing capacities of single piles under combined *HM* loading near slopes

Meihua Bian*, Jianing Peng, Xingsen Zhang, Junhua Li and Songlin Qin

Guangxi Key Laboratory of Intelligent Control and Maintenance of Power Equipment, Electric Power Research Institute of Guangxi Power Grid Co., Ltd., Nanning, China

Piles are widely used to transfer the horizontal load of high-rise buildings, transmission towers, and bridges, especially for superstructures constructed near slopes. This study investigated bearing capacities of single piles under the combined horizontal force (*H*) and bending moment (*M*) for the pile in sloping ground. A 3D finite element model was proposed to simulate the non-linear pile−soil interaction and was verified by a model test. A series of numerical tests were conducted to obtain the failure envelope of bearing capacities of single piles under various combinations of *H* and *M*. The existence of slopes significantly reduced the bearing capacity of piles, especially when the horizontal and rotational displacements moved to the dip direction of the slope. An oblique ellipse was able to describe the failure envelope of bearing capacities of single piles near slopes in the *HM* plane. As the pile was installed away from the crest of the slope, both the width and height of the ellipse increased and the center of the ellipse was approaching the origin. The results of this article can provide useful references for designing horizontally loaded piles near slopes.

KEYWORDS

laterally loaded pile, slope, loading path, failure envelope, bearing capacity

1 Introduction

Single piles are designed to resist horizontal loads in geotechnical and marine engineering, offering the advantages of easy installation, low cost, good stability, and sufficient strength and stiffness (Xu et al., 2013; Xu et al., 2017a; Xu et al., 2017b; Qu et al., 2019). In particular, the piles are necessary for power transmission towers built near slopes. Due to the excitation of winds and earthquakes (Qu et al., 2018a; Qu et al., 2018b; Xu et al., 2021; Xu et al., 2023), the piles are frequently subjected to the combined horizontal force (*H*) and bending moment (*M*) (Wakai et al., 1999; Ng and Zhang, 2001; Raj et al., 2019; Yi et al., 2022). Moreover, the existence of a slope could lower the bearing capacity and thus cause instability of the piles (Jiang et al., 2022). Figure 1 shows the potential geo-hazard of the pile foundation of a transmission tower built near a slope in Baise city, Guangxi province of China. Thus, it is of great importance to study bearing capacities of single piles under combined *H* and *M* near slopes.

A pioneering study mainly focuses on single piles subjected to horizontal loading on level ground (Broms, 1964a; Broms, 1964b). Specifically, Broms (1964a, 1964b) developed an analytical formula of the ultimate soil resistance for laterally loaded flexible and rigid piles. Meyerhof (1995) developed a theoretical formula for predicting the ultimate soil resistance and bending moment of single piles under various load eccentricities and pile inclinations. In
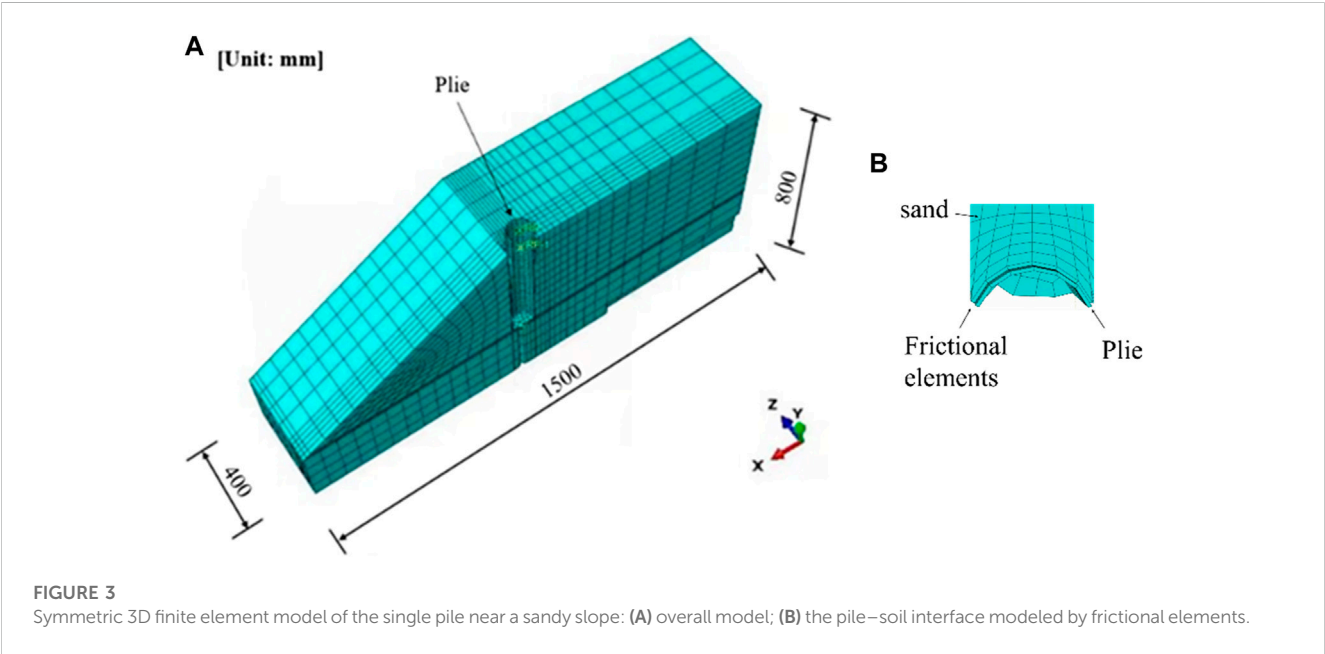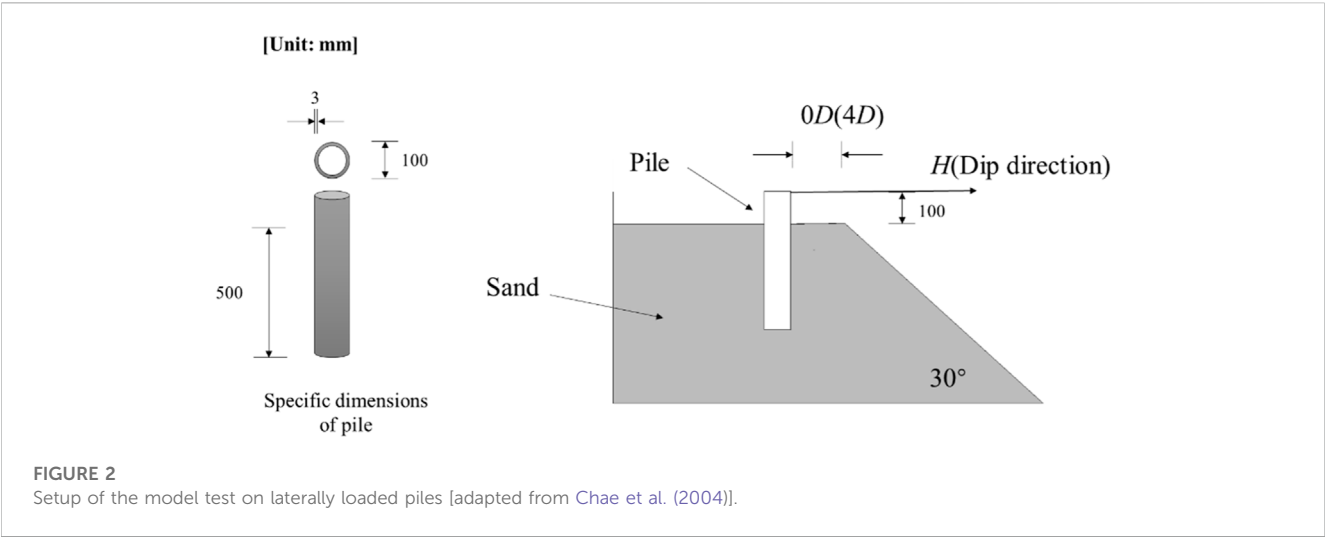
FIGURE 1
Potential geo-hazard of the pile foundation of a transmission tower built near a slope in Baise city, Guangxi province of China (photograph from the investigation of authors).

recent years, plenty of methods have been developed to predict the lateral response of single piles near slopes. The p–y method was originally developed by Matlock (1970) and Reese et al. (1974) for analyses of laterally loaded single piles, where p represents the soil reaction and y the lateral displacement of piles. Recently, some p–y curves consider the effect of a slope on the lateral response of single piles (Georgiadis and Georgiadis, 2012; Said et al., 2020). However, the p–y method neglects the soil continuity and the soil shearing resistance (Xu et al., 2013; Xu et al., 2017a; Xu et al., 2017b). To overcome this limitation, a strain wedge model was initially developed by Norris (1986). The strain wedge (SW) model predicts the soil resistance in the passive wedge developed in front of the laterally loaded pile by introducing a stress–strain relationship for the soils in the wedge. Recently, the SW model has been extensively modified to calculate the lateral soil resistance for single piles on level ground (Xu et al., 2013; Xu et al., 2017a; Xu et al., 2017b) and in the sloping ground (Peng et al., 2019; Yang et al., 2019; Chen et al., 2021; Chen et al., 2022; Lin et al., 2022a; Hemel et al., 2022). However, the application of the SW model to obtain the failure envelope of the bearing capacities of single piles is not reported. Thus, the 3D finite element method has an advantage of considering the 3D non-linear soil–pile interaction and thus is frequently applied to estimate the lateral response of pile foundations. Accordingly, Hung and Kim (2014) and Li et al. (2014) investigated the three-dimensional failure envelope through radial displacement and sliding tests as a means to assess the safety of the pile–soil system.

The influence of a slope on the bearing capacity of piles subjected to horizontal loading has been investigated *via* either a model test or numerical test. Begum and Muthukkumaran (2009) and Perumalsamy and Ranganathan (2022) experimentally investigated the influence of the slope angle and the relative density of soils on laterally single piles. The results indicated that these two factors have a significant influence on the lateral response of single piles. In addition, recent studies experimentally investigate other influential factors, such as the embedment depth of piles, the adhesion at the pile–soil interface, the pile length, and the distance (d_{pc}) from the pile to the crest of the slope (Georgiadis et al., 2013; Deendayal et al., 2016; Vali et al., 2019). To supplement model tests, numerical analyses are conducted on laterally loaded piles in sloping ground. For example, Lin et al. (2022b) investigated the effect of various slope factors, e.g., the slope height, the slope angle, and d_{pc} on the deflection and maximum bending moment of piles. Moreover, Jiang et al. (2018) studied the influence of the loading direction on the lateral response of single piles in sloping ground *via* the 3D finite element model. Jiang et al. (2020) further numerically investigated the effect of the slope proximity and pile shape on the deflection and the bending moment of laterally loaded piles. Previous studies show that the diameter and the embedment of piles also significantly affect not only the bearing capacity but also the lateral deflection and bending moment of laterally loaded piles (Muthukkumaran and Almas, 2011; Sawant and Shukla, 2014; Rathod et al., 2019; Chandaluri and Sawant, 2020; Deendayal et al., 2020). However, little work has been carried out on the influence of the slope on the failure envelope of bearing capacities of single piles near slopes, especially under combined *HM* loading.

This study conducted 3D finite element analyses of single piles in homogeneous sandy soils near slopes under combined *HM* loading.

FIGURE 2
Setup of the model test on laterally loaded piles [adapted from Chae et al. (2004)].

FIGURE 3
Symmetric 3D finite element model of the single pile near a sandy slope: **(A)** overall model; **(B)** the pile−soil interface modeled by frictional elements.

The 3D finite element model was calibrated against a model test reported by Chae et al. (2004). A parametric study was performed to obtain the failure envelope of bearing capacities of single piles under various combinations of H and M. The effects of the slope and d_{pc} on the failure envelope were discussed. Moreover, a formulation was proposed to describe the failure envelope of bearing capacities of single piles.

2 Numerical modeling

2.1 Description of model tests

Figure 2 shows the model test conducted on a single pile near a slope. The model test was reported by Chae et al. (2004) where

TABLE 1 Input parameters for the pile−soil system.

Model	Pile	Sand	Pile−soil interface
Unit weight γ (kN/m³)	26.4	15.7	15.7
E (kPa)	6.86E+07	Eq. 1	Eq. 1
ν	0.345	0.3	0.3
ϕ (deg.)	—	47.5	25
ψ (deg.)	—	17.5	0

the single pile was located near a sandy slope with a slope angle of 30°. The pile was a hollow steel pipe pile with an outer diameter (D) of 100 mm and a wall thickness of 3 mm. The pile

FIGURE 4
Comparisons between simulated and the measured load−displacement curves (experimental data from Chae et al., 2004).

FIGURE 5
Sign definition for the bending moment and horizontal force.
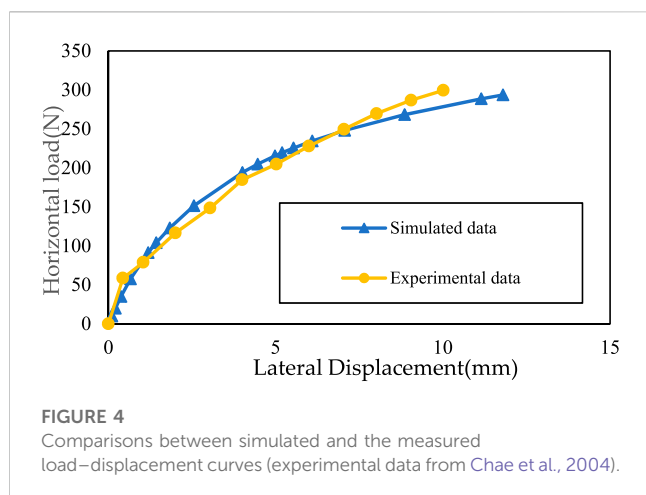
was loaded horizontally with a lateral load H in the dip direction of the slope. The distance between the lateral load and the mudline was 100 mm. The embedment depth of the pile was 500 mm.

Figure 3 shows a typical symmetric 3D finite element mesh using Abaqus was used for analyzing laterally loaded single piles near the sandy slope. d_{pc} was $0D$ in this case. The single pile and the soil were modeled by C3D8R elements. The pile was assumed to behave elastically. The pile–soil interface was modeled by thin frictional elements (see Figure 3B), as suggested by Xu et al. (2023). C3D8R elements were also used for the pile–soil interface. The elastic–plastic behavior of sandy soil was described by the Mohr–Coulomb model. Table 1 lists the input parameters for the pile, the soil, and the interface. Based on triaxial compression tests of the sandy soil, the peak friction angle ϕ was 47.5° and the shear expansion angle was estimated based on the equation $\psi = \phi - 30°$ (Tatsuoka, 1993). Young's modulus E of the soil was estimated from Eq. 1 in Table 1, as suggested by Chae et al. (2004), and Poisson's ratio ν of the soil was taken as 0.3.

$$E = E_0 \left(\sigma_m / \sigma_0\right)^n,\qquad(1)$$

where E_0 = 1,143 kPa, σ_0 = 1 kPa, n = 0.8311 kPa, and $\sigma_m = (\sigma_1 + \sigma_2 + \sigma_3)/3$.

The base and two lateral sides were fixed in the numerical analyses. Moreover, geostatic analysis was necessary for the slope before the lateral load was applied.

2.2 Model verification

Figure 4 shows the comparisons between simulated and the measured load–displacement curves. It should be noted that the lateral displacement was measured at the location where the lateral load was applied. The results showed that the simulated load–displacement curve agreed well with that measured from the test, demonstrating a sufficient accuracy of the proposed 3D numerical model. Accordingly, the proposed numerical model was considered a benchmark model for the following section.
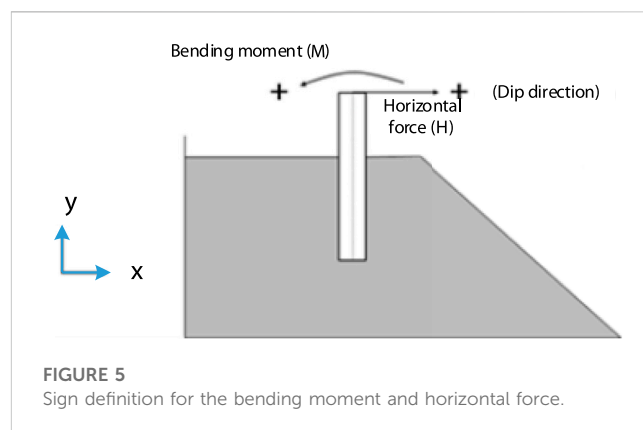
3 Results and discussion

The sign convention for each direction at the top of the pile is defined in Figure 5. The positive x-axis is the dip direction of the slope. The horizontal force (H) applied in the dip direction was considered to be positive, and the bending moment (M) that forced the top of the pile to move in the dip direction was assumed to be negative.

To numerically obtain the failure envelope of bearing capacities of the single pile, both horizontal (h) and rotational (θ) displacements were applied simultaneously to the mudline, i.e., the ground surface. Moreover, the ratio of the horizontal displacement increase to the rotational displacement increase was kept constant, i.e., dh/D$d\theta$ = constant. If the pile reached the ultimate state, divergence of the finite element analyses occurred, and then, bearing capacities (H_0, M_0) were defined as the last point of the load path in the HM plane (Gottardi et al., 1999). By varying the constant dh/D$d\theta$, the failure envelope of bearing capacities of single piles was obtained.

3.1 Failure envelope of bearing capacities of piles under combined HM loading near slopes

Taking the model in Figure 3 as a benchmark model ($d_{pc} = 0D$), Figure 6A shows the calculated loading paths of single piles under different constants of dh/D d θ. The ultimate lateral load (H_0) was estimated to be 457.3 N in the dip direction when M = 0, while $H_0 = -684.9$ N for M = 0, where the minus sign denotes the opposite of the dip direction. This result indicated that the ultimate lateral load was reduced by 33% in the dip direction of the slope. On the other hand, the ultimate bending moment (M_0) was calculated to be 174.3 N·m in the dip direction and −245.9 N·m in the opposite dip direction when H = 0, indicating that the slope caused 29% reduction in the bearing capacity of piles.

Moreover, the maximum distance (d_{max}) between the bearing capacity (H_0, M_0) and the origin (0, 0) was achieved at positive dh/D d θ. For example, d_{max} reached the maximum at approximately dh/D d θ = 10. This was because the horizontal and rotational displacements caused the pile to move in opposite directions in such conditions. As dh/D d θ decreased, the bearing capacity of piles
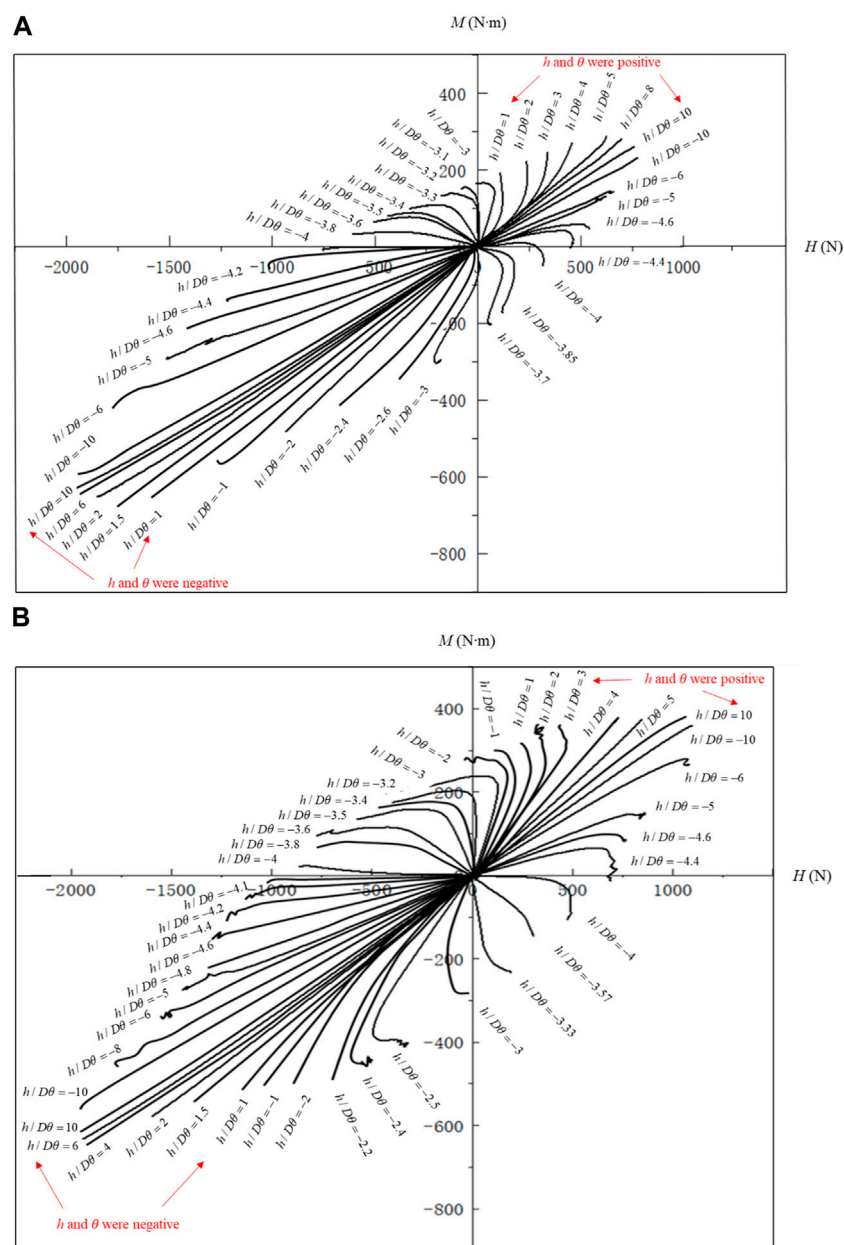
FIGURE 6
Effect of d_{pc} on the bearing capacities of loading paths of laterally loaded single piles: **(A)** d_{pc} = 0D and **(B)** d_{pc} = 4D under different constants of dh/ Dd θ.

generally decreased, resulting in a gradual decrease in d_{max}. d_{max} reached the minimum at negative dh/Dd θ, e.g., h/D θ = −3.2. This was because the horizontal and rotational displacements caused the pile to move in the same direction. In such conditions, the failure of the pile was dominated by either the lateral load or bending moment: (1) on the loading path in the case of h/D θ = −3.6 (see Figure 6A), the horizontal load gradually increased when the bending moment reached the maximum; thus, the pile failure was mainly because of the lateral load; (2) on the loading path in the case of h/D θ = −3.85 (see Figure 6A), the bending moment gradually increased when the lateral load reached the maximum; thus, the bending moment was responsible for the failure of the pile.

From the results shown in Figure 6A, not only the slope but also the different HM combinations significantly affected the bearing capacity of single piles. Therefore, the most unfavorable condition should be considered in the engineering design.

3.2 Effect of the distance (d_{pc}) from the pile to the crest of the slope

To investigate the influence of d_{pc} on the bearing capacity of piles, another parallel 3D finite element model was analyzed and is shown in Figure 6. d_{pc} in this model was 4D, i.e., 400 mm. To eliminate the
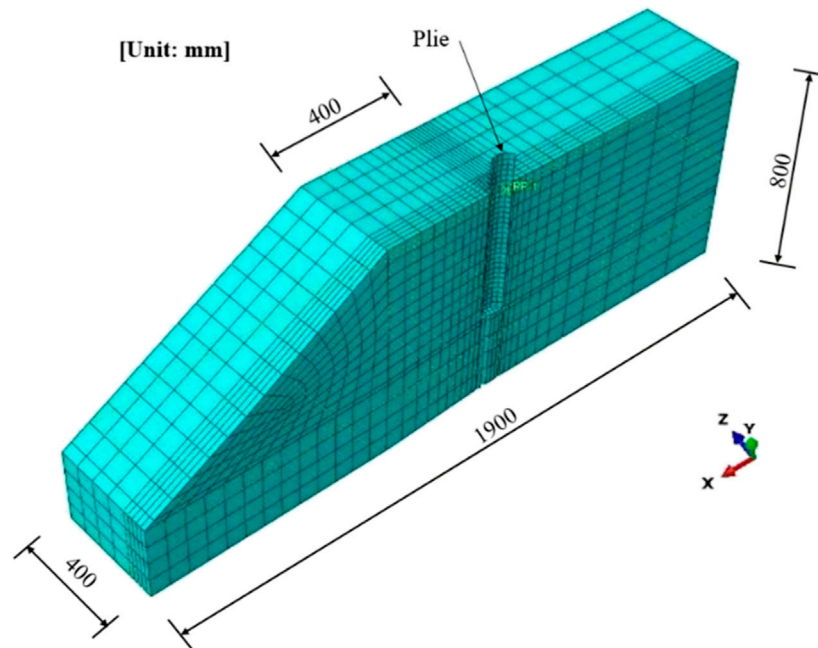
FIGURE 7
Symmetric 3D numerical model for a single pile with $d_{pc} = 4D$.

boundary effect, one side of the model was extended 400 mm outwards (see Figure 7). In the parallel model, input parameters were kept unchanged from the model shown in Figure 3A.

Figure 6B shows loading paths of single piles with $d_{pc} = 4D$ under different constants of dh/Dd θ. In the case of $d_{pc} = 0D$, the maximum horizontal load (H_{max}) and the maximum bending moment (M_{max}) were calculated to be −1948.8 N and −651.5 N·m, respectively (see Figure 6A). As d_{pc} increased to $4D$, H_{max} and M_{max} were estimated to be −1940.8 N and −678.3 N·m, respectively (see Figure 6B). These results indicated that the effect of d_{pc} was insignificant on the maximum bearing capacity of single piles because the maximum bearing capacity depended on the soil reaction opposing the dip direction and thus was achieved when both h and θ were negative (see Figure 5). However, when both h and θ were positive, the maximum H_0 and the maximum M_0 were increased by approximately 44% and 30%, respectively, as d_{pc} increased from $0D$ to $4D$. Moreover, both the maximum H_0 and the maximum M_0 were increased for other combinations of loading with negative dh/ Dd θ due to the increase of d_{pc}. Thus, increasing d_{pc} had an insignificant effect on H_{max} but significantly increased the bearing capacity under certain loading conditions, e.g., the minimum bearing capacity.

3.3 Theoretical analysis of the failure envelope of bearing capacities of single piles in the *HM* plane

From the results shown in Figure 6, the failure envelope of bearing capacities of single piles showed an oblique ellipse in the *HM* plane. To verify this observation, a general elliptical equation was used to fit the data shown in Figure 6:

$$C_1 x^2 + C_2 xy + C_3 y^2 + C_4 x + C_5 y + 1 = 0, \qquad (2)$$

where x represents M_0 in the *HM* plane; y denotes the H_0 in the *HM* plane; and C_1, C_2, C_3, C_4, and C_5 are the constants controlling the elliptical shape. A program was developed to derive the constants from the data based on the least square method. These six constants were used to determine the coordinates of the center of the ellipse (x_0, y_0), the width and height of the ellipses R_1 and R_2, and the rotation angle of the semi-major axis ψ of the ellipse:

$$\begin{cases} x_0 = \dfrac{C_2 C_5 - 2C_3 C_4}{4C_1 C_3 - C_2^2}, \\[2mm] y_0 = \dfrac{C_2 C_4 - 2C_1 C_5}{4C_1 C_3 - C_2^2}, \\[2mm] R_1 = \sqrt{\dfrac{2\left(C_1 x_0^2 + C_3 y_0^2 + C_2 x_0 y_0 - 1\right)}{C_1 + C_3 + \sqrt{(C_1 - C_3)^2 + C_2^2}}}, \\[3mm] R_2 = \sqrt{\dfrac{2\left(C_1 x_0^2 + C_3 y_0^2 + C_2 x_0 y_0 - 1\right)}{C_1 + C_3 - \sqrt{(C_1 - C_3)^2 + C_2^2}}}, \\[3mm] \psi = \dfrac{1}{2}\arctan\left(\dfrac{C_2}{C_1 - C_3}\right). \end{cases} \qquad (3)$$

Figures 8A, B show the failure envelope of bearing capacities of single piles near slopes for the cases with $d_{pc} = 0D$ and $d_{pc} = 4D$, respectively. It should be noted that Figure 8

FIGURE 8
Failure envelope of bearing capacities of single piles near slopes:
(A) $d_{pc} = 0D$ and **(B)** $d_{pc} = 4D$.
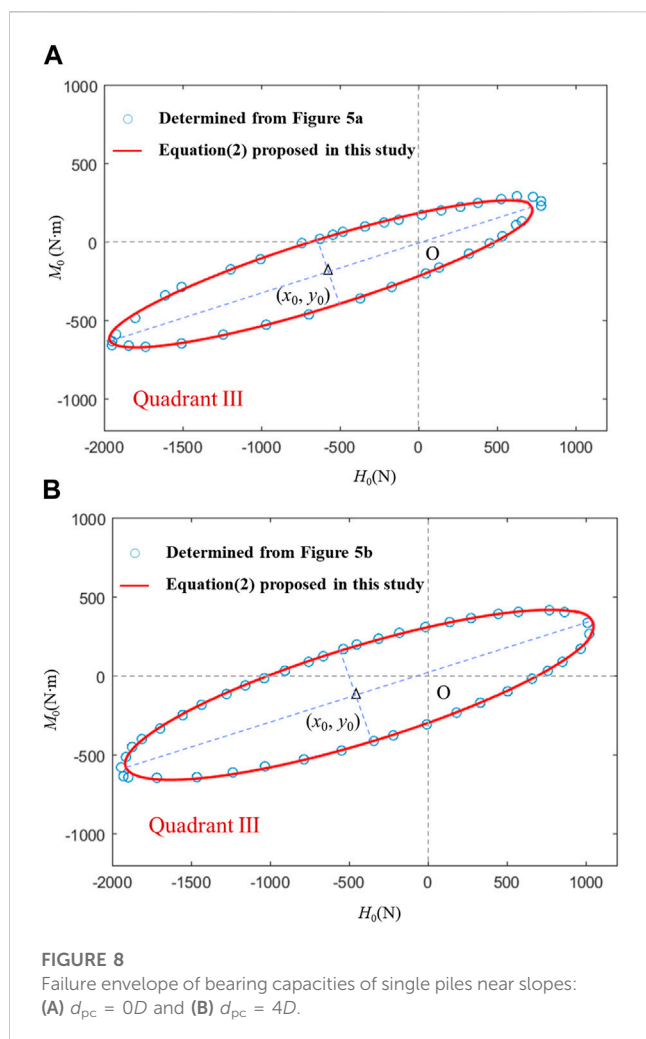
was determined by collecting the last point of loading paths in Figure 6. The relationship between the horizontal load and the bending moment data can be well-described by an oblique ellipse. Table 2 gives the fitting parameters of Eq. 2. Unlike the ellipse for single piles in the level ground reported by Li et al. (2014), the center of the ellipse was not at the origin but was located in the third quadrant due to the slope effect.

Table 2 also shows that the height R_1 and the width R_2 of the failure envelope increased by 9.8% and 40.9%, respectively, as d_{pc} increased from $0D$ to $4D$. In addition, the center of the failure envelope was much closer to the origin in the case of $d_{pc} = 4D$. Thus, the center of the ellipse was approaching the origin and the oblique ellipse became bigger as d_{pc} increased.

4 Conclusion

A 3D numerical model was proposed to accurately capture the non-linear pile–soil interaction in sloping ground and was calibrated against a model test. The conclusions are summarized as follows:

(1) The load–displacement curve simulated by the numerical model agreed well with the measured result, indicating a sufficient accuracy of the proposed 3D finite element model.
(2) An oblique ellipse can still be used to describe the failure envelope of bearing capacities of single piles near slopes in the HM plane. However, unlike the piles in the horizontal ground, the center of the envelope is not at the origin for piles in the sloping ground.
(3) The existence of slopes significantly reduced the bearing capacity of piles. On the other hand, the different combinations of H and M had also severely influence the bearing capacity of piles. Therefore, the most unfavorable condition should be considered in the engineering design.
(4) Increasing d_{pc} had an insignificant effect on the maximum bearing capacity of piles but could significantly increase the bearing capacity under certain loading conditions, e.g., the minimum bearing capacity.
(5) The center of the ellipse was approaching the origin, and the oblique ellipse became bigger as d_{pc} increased from $0D$ to $4D$.

TABLE 2 Fitting results for the failure envelope of bearing capacities of single piles near slopes.

Envelope	$d_{pc} = 0D$	$d_{pc} = 4D$
Parameter		
Coordinates of the center (x_0, y_0)	(−614.48, −201.07)	(−429.98, −118.10)
Width R_1	1413.9	1552.5
Height R_2	215.14	303.24
Rotation angle of the semi-major axis ψ (rad)	0.3021	0.2960
Fitting parameter: C_1	−2.37E-06	−1.30E-06
Fitting parameter: C_2	1.20E-05	5.84E-06
Fitting parameter: C_3	−1.97E-05	−9.98E-06
Fitting parameter: C_4	−5.00E-04	−4.33E-04
Fitting parameter: C_5	−5.70E-04	1.51E-04

Data availability statement

The raw data supporting the conclusion of this article will be made available by the authors, without undue reservation.

Author contributions

MB: conceptualization, software, validation, and writing—original draft; JP and XZ: methodology; JL: investigation; SQ: data curation.

Funding

Conflict of interest

Authors MB, JP, XZ, JL, and SQ were employed by the Electric Power Research Institute of Guangxi Power Grid Co., Ltd.

Publisher's note

References

Begum, N., and Muthukkumaran, K. (2009). Experimental investigation on single model pile in sloping ground under lateral load. *Int. Int. J. Geotech. Eng.* 3, 133–146. doi:10.3328/IJGE.2009.03.01.133-146

Broms, B. (1964b). Lateral resistance of piles in cohesionless soils. *J Soil Mech. Found. Div* 90, 123–156. doi:10.1061/jsfeaq.0002132

Broms, B. (1964a). Lateral resistance of piles in cohesive soils. *J Soil Mech. Found. Div* 90, 27–63. doi:10.1061/JSFEAQ.0000611

Chae, K. S., Ugai, K., and Wakai, A. (2004). Lateral resistance of short single piles and pile groups located near slopes. *Int. J. Geomech.* 4, 93–103. doi:10.1061/(asce)1532-3641(2004)4:2(93)

Chandaluri, V. K., and Sawant, V. A. (2020). Influence of sloping ground on lateral load capacity of single piles in clayey soil. *Int. J. Geotech. Eng.* 14, 353–360. doi:10.1080/19386362.2017.1419538

Chen, L., Jiang, C., Pang, L., and Liu, P. (2021). Lateral soil resistance of rigid pile in cohesionless soil on slope. *Comput. Geotech.* 135, 104163. doi:10.1016/j.compgeo.2021.104163

Chen, L., Pang, L., Jiang, C., and Zhang, C. (2022). Analysis method for bearing capacity of laterally loaded rigid piles on slopes using improved failure wedge model. *Comput. Geotech.* 145, 104700. doi:10.1016/j.compgeo.2022.104700

Deendayal, R., Muthukkumaran, K., and Sitharam, T. G. (2020). Analysis of laterally loaded group of piles located on sloping ground. *Int. J. Geomech. Eng.* 14, 580–588. doi:10.1080/19386362.2018.1448521

Deendayal, R., Muthukkumaran, K., and Sitharam, T. G. (2016). Response of laterally loaded pile in soft clay on sloping ground. *Int. J. Geotech. Eng.* 10, 10–22. doi:10.1179/1939787915Y.0000000013

Georgiadis, K., Georgiadis, M., and Anagnostopoulos, C. (2013). Lateral bearing capacity of rigid piles near clay slopes. *Soils Found.* 53, 144–154. doi:10.1016/j.sandf.2012.12.010

Georgiadis, K., and Georgiadis, M. (2012). Development of p–y curves for undrained response of piles near slopes. *Comput. Geotech.* 40, 53–61. doi:10.1016/j.compgeo.2011.09.005

Gottardi, G., Houlsby, G. T., and Butterfield, R. (1999). Plastic response of circular footings on sand under general planar loading. *Géotechnique.* 49, 453–469. doi:10.1680/geot.1999.49.4.453

Hemel, M. J., Korff, M., and Peters, D. J. (2022). Analytical model for laterally loaded pile groups in layered sloping soil. *Mar. Struc* 84, 103229. doi:10.1016/j.marstruc.2022.103229

Hung, L. C., and Kim, S. R. (2014). Evaluation of undrained bearing capacities of bucket foundations under combined loads. *Mar. Georesour. Geotec.* 32, 76–92. doi:10.1080/1064119X.2012.735346

Jiang, C., He, J. L., Liu, L., and Sun, B. W. (2018). Effect of loading direction and slope on laterally loaded pile in sloping ground. *Adv. Civ. Eng.* 1-12, 1–12. doi:10.1155/2018/7569578

Jiang, C., Liu, L., He, J. L., and Xie, H. S. (2020). Effect of the proximity of slope and pile shape on lateral capacity of piles in clay slopes. *Eur. J. Environ. Civ. Eng.* 1-15, 16–30. doi:10.1080/19648189.2020.1858452

Jiang, J. H., Huang, X. L., Shu, X. R., Ning, X., Qu, Y., and Xiong, W. L. (2022). Application of a damage constitutive model to pile–slope stability analysis. *Front. Mater* 9, 1082292. doi:10.3389/fmats.2022.1082292

Li, Z., Kotronis, P., and Escoffier, S. (2014). Numerical study of the 3D failure envelope of a single pile in sand. *Comput. Geotech.* 62, 11–26. doi:10.1016/j.compgeo.2014.06.004

Lin, M., Jiang, C., Chen, Z., Liu, P., and Pang, L. (2022a). A method for calculating lateral response of offshore rigid monopile in sand under slope effect. *Ocean. Eng.* 259, 111812. doi:10.1016/j.oceaneng.2022.111812

Lin, M., Jiang, C., Liu, P., and Pang, L. (2022b). Analysis of laterally loaded offshore pile near slope in sand considering slope height. *Ocean. Eng.* 263, 112436. doi:10.1016/j.oceaneng.2022.112436

Matlock, H. (1970). "Correlations for design of laterally loaded piles in soft clay," in Offshore Technology Conference, 577–594. doi:10.4043/1204-MS

Meyerhof, G. G. (1995). Behaviour of pile foundations under special loading conditions: 1994 R.M. Hardy keynote address. *Can. Geotech.* 32, 204–222. doi:10.1139/t95-024

Muthukkumaran, K., and Almas, B. N. (2011). Finite element analysis of laterally loaded piles on sloping ground. *Indian Geotech. J.* 41, 155–161.

Ng, C. W. W., and Zhang, L. M. (2001). Three-dimensional analysis of performance of laterally loaded sleeved piles in sloping ground. *J. Geotech. Geoenviron.* 127, 499–509. doi:10.1061/(asce)1090-0241(2001)127:6(499)

Norris, G. (1986). "Theoretically based BEF laterally loaded pile analysis," in International Conference on Numerical Methods in Offshore Piling, 361–386.

Peng, W., Zhao, M., Xiao, Y., Yang, C., and Zhao, H. (2019). Analysis of laterally loaded piles in sloping ground using a modified strain wedge model. *Comput. Geotech.* 107, 163–175. doi:10.1016/j.compgeo.2018.12.007

Perumalsamy, K., and Ranganathan, S. (2022). Single pile in cohesionless soil in sloping ground under lateral loading. *Int. J. Geotech. Eng.* 13, 8. doi:10.1186/s40703-022-00173-8

Qu, C. X., Yi, T. H., Li, H. N., and Chen, B. (2018a). Closely spaced modes identification through modified frequency domain decomposition. *Measurement* 128, 388–392. doi:10.1016/j.measurement.2018.07.006

Qu, C. X., Yi, T. H., and Li, H. N. (2019). Mode identification by eigensystem realization algorithm through virtual frequency response function. *Struct. Control Hlth.* 26, e2429. doi:10.1002/stc.2429

Qu, C. X., Yi, T. H., Zhou, Y. Z., Li, H. N., and Zhang, Y. F. (2018b). Frequency identification of practical bridges through higher order spectrum. *J. Aerosp. Eng.* 31, 04018018. doi:10.1061/(ASCE)AS.1943-5525.0000840

Raj, D., Singh, Y., and Kaynia, A. M. (2019). V–H–M seismic capacity envelopes of strip foundations on slopes for capacity design of structure-foundation system. *B. Earthq. Eng.* 17, 2963–2987. doi:10.1007/s10518-019-00577-5

Rathod, D., Muthukkumaran, K., and Thallak, S. G. (2019). Experimental investigation on behavior of a laterally loaded single pile located on sloping ground. *Int. J. Geomech.* 19, 04019021. doi:10.1061/(asce)gm.1943-5622.0001381

Reese, L. C., Cox, W. R., and Koop, F. D. (1974). "Analysis of laterally loaded piles in sand," in Offshore Technology Conference, 473–483. doi:10.4043/2080-MS

Said, S. E., Fayed, A. L., and El M, Y. (2020). P–y curves of laterally loaded piles near Earth slopes. *Int. J. Eng. Adv. Technol.* 9, 805–814. doi:10.35940/ijeat.D7763.049420

Sawant, V. A., and Shukla, S. K. (2014). Effect of edge distance from the slope crest on the response of a laterally loaded pile in sloping ground. *Geotech. Geol. Eng.* 32, 197–204. doi:10.1007/s10706-013-9694-7

Tatsuoka, F. (1993). "Relationships between stress and strain increments," in Intr. to Strength of Soils and Failure of Ground, 57–81.

Vali, R., Shams, G., Porhoseini, R., Boroujeni, M. S., and Beygi, M. (2019). Lateral behavior of pile located on top of a slope. *Aust. Geomech. J.* 54, 103–114.

Wakai, A., Gose, S., and Ugai, K. (1999). 3-D elasto-plastic finite element analyses of pile foundations subjected to lateral loading. *Soils Found.* 39, 97–111. doi:10.3208/sandf.39.97

Xu, L. Y., Cai, F., Wang, G. X., Chen, G. X., and Li, Y. Y. (2017b). Nonlinear analysis of single reinforced concrete piles subjected to lateral loading. *KSCE J. Civ. Eng.* 21, 2622–2633. doi:10.1007/s12205-017-1010-2

Xu, L. Y., Cai, F., Wang, G. X., and Chen, G. X. (2017a). Nonlinear analysis of single laterally loaded piles in clays using modified strain wedge model. *Int. J. Civ. Eng.* 15, 895–906.

Xu, L. Y., Cai, F., Wang, G. X., and Ugai, K. (2013). Nonlinear analysis of laterally loaded single piles in sand using modified strain wedge model. *Comput. Geotech.* 51, 60–71. doi:10.1016/j.compgeo.2013.01.003

Xu, L. Y., Chen, W. Y., Cai, F., Song, Z., Pan, J. M., and Chen, G. X. (2023). Response of soil–pile–superstructure–quay wall system to lateral displacement under horizontal and vertical earthquake excitations. *B. Earthq. Eng.* 21, 1173–1202. doi:10.21203/rs.3.rs-1544907/v1

Xu, L. Y., Song, C. X., Chen, W. Y., Cai, F., Li, Y. Y., and Chen, G. X. (2021). Liquefaction-induced settlement of the pile group under vertical and horizontal ground motions. *Soil Dyn. Earthq. Eng.* 144, 106709. doi:10.1016/j.soildyn.2021.106709

Yang, M., Deng, B., and Wang, Y. (2019). A simplified calculation method for the near-slope–laterally loaded pile based on a passive wedge model. *Adv. Civ. Eng.* 2019, 1–10. doi:10.1155/2019/8363252

Yi, S., Liu, J., and Gu, M. (2022). Field investigation of steel pipe pile under lateral loading in extensively soft soil. *Front. Mater* 480. doi:10.3389/fmats.2022.971485

Check for updates

Research on the longitudinal movement and influence of restraint parameters of the long-span suspension bridge's main girder

Sun Hongbin[1†], Yuan Jieyi[2†*] and Liu Yujing[3†]

[1]Jiangsu Yangtze River Expressway Management Co., Ltd., Nanjing, China, [2]CCCC Highway Bridges National Engineering Research Centre Co., Ltd., Beijing, China, [3]Jiangsu Expressway Engineering Maintenance Technology Co., Ltd., Nanjing, China

The long-span suspension bridge has suffered from multiple failures of restraints such as supports, dampers, and expansion joints due to excessive accumulated displacement at the girder end. To investigate the main girders' characteristics in the longitudinal motion of these bridges and the influence of the restraint device on the longitudinal displacement, the motion characteristics were first analyzed based on the measured displacement data of a certain bridge's main girder; a dynamic finite element model of the bridge's random traffic flow was then established based on the measured WIM data; combined with the girder end displacement monitoring data, the Euclidean distance was used to verify the correctness and rationality of the proposed model; finally, the model is used to discuss the influence of restraint devices (i.e., viscous dampers and supports) on the main girder in the longitudinal direction. The results show that dynamic loads (such as vehicles and wind) are the principal reasons for huge accumulated travel at the girder end; The viscous damper can effectively control the longitudinal movement; in a certain range, the larger the damping index, the better the control effect of the damper; meanwhile, the friction coefficient of the support also affects the longitudinal motion, but the effect is limited. When the friction coefficient is ≤ 0.03, the girder end's cumulative displacement gradually decreases with the increasing friction coefficient, and compared to the damping index, the friction coefficient plays a major controlling role in the girder end displacement; when the friction coefficient is >0.03, the damping index plays a major controlling role in the girder end displacement.

1 Introduction

Long-span suspension bridges are usually a full-floating or semi-floating structural system, which has the advantage of greater structural flexibility and is conducive to earthquake resistance. However, the stiffened girders will undergo high-frequency and large-scale longitudinal motions under environmental excitation due to the low overall stiffness. The excessive longitudinal cumulative stroke at the girder end causes the actual service life of the auxiliary structure at the girder end to be far lower than the design service life, reducing the bridge structure's safety and durability (Chen and Wu, 2010; Guo et al.,

2018). Current research shows that, in the bridge operation stage, the traffic load causes constant reciprocal movement of the long-span suspension bridge's main girder end, and the massive cumulative displacement will cause fatigue damage, insufficient durability, and other problems of the restraint devices such as expansion joints, dampers, and supports. In addition, the girder end displacement is also an important parameter for the design and selection of the key restraint device for the suspension bridge (Zribi et al., 2006; Huang et al., 2021). Therefore, it is of great necessity to study the longitudinal motion characteristics, influencing factors, and control methods of long-span suspension bridges' stiffened girders under traffic loads to ensure their safe operation.

A certain highway bridge is a representative kilometer-scale long-span suspension bridge in China. In the actual operation process, the diseases like expansion joints damage, excessive wear of support slides, oil leakage from dampers, etc. have occurred many times, and the average daily cumulative displacement of the girder end is up to 100 m (before installing the longitudinal damper) (Qu et al., 2023). In order to analyze the longitudinal motion characteristics of the large-span suspension bridge's main girder and the influence of the restraint device on the displacement, relying on the aforementioned highway bridge, this paper established and validated the dynamic finite element model of the suspension bridge based on the measured girder end longitudinal displacement data and WIM data. Based on this model, the influence of restraint device parameters on the girder end in the longitudinal motion is analyzed, which provides theoretical support for research on longitudinal motion control of stiffening girder and performance improvement of restraint device of a large-span suspension bridge. It also guides restraint device disease monitoring based on girder end displacement.

2 Characteristic analysis of the main girder's longitudinal measured displacement

In the bridge's monitoring system, the girder end displacement in the longitudinal motion was continuously monitored using a pull-rope displacement sensor. In order to master the frequency spectrum characteristics of the main girder in the longitudinal motion, according to the Wiener-Khinchin theorem, this paper estimated the PSD (power spectrum density) for the longitudinal monitoring displacement. For displacement signals X_n, its power spectral density is:

$$P_{xx}\left(e^{j\omega}\right) = \sum_{m=-\infty}^{\infty} r_{xx}(m) e^{-j\omega m} \tag{1}$$

Where: $r_{xx}(m) = E[X_n^* X_{n+m}]$, meaning the autocorrelation function of displacement signals; X_n is displacement signals; $P_{xx}(e^{j\omega})$ is the power spectral density of displacement signals X_n. It can be seen that the power spectral density of displacement signals is the Fourier transform of its autocorrelation function.

The Welch, periodogram, BT, MTM, and Burg methods are widely used for power spectral density. Among these methods, the maximum entropy spectrum estimation based on the Burg

algorithm is representative of modern spectrum estimation methods. It has high-frequency resolution and strong spectrum recognition ability. Therefore, this paper used the Burg algorithm to perform the spectrum analysis on the measured longitudinal displacement data of the bridge's downstream girder end on 12 October 2020. The corresponding girder end displacement time history curve and power spectrum are shown in Figure 1.

As shown in Figure 1, the bridge's stiffening girder in the longitudinal motion contains many high-frequency and low-amplitude components, which can be mainly divided into two parts from the perspective of spectrum characteristics, and the corresponding frequency ranges are respectively 1.157×10^{-5} Hz and ≥ 0.1 Hz. Existing research results show that the above two parts of the frequency range respectively correspond to the stretching deformation of the girder end caused by the diurnal temperature difference (24 h as a cycle, frequency is $1/86400 = 1.157 \times 10^{-5}$ Hz) and the longitudinal forced vibration of the girder end caused by dynamic factors such as vehicles and wind loads, and the low-frequency displacement vibration amplitude caused by temperature is significantly greater than the high-frequency displacement vibration amplitude.

Therefore, in order to further discuss the longitudinal displacement characteristics of the bridge's girder end, Empirical Wavelet Transform (EWT) is adopted to resolve the displacement time history based on spectral characteristics, and the longitudinal displacement of the stiffened girder is decomposed into two displacement components in different frequency ranges, as shown in Figure 2, and the signal decomposition truncation frequency is 0.02 Hz (Yang and Cai, 2016).

Table 1 presents the statistical parameters of different longitudinal motion components in Figure 2, which can be seen that the statistical parameters of different longitudinal motion components at the girder end differ greatly, and the longitudinal motion amplitude and standard deviation caused by temperature are significantly greater than the longitudinal vibration response caused by dynamic factors. In addition, according to the displacement component time-history curve, the cumulative displacement caused by temperature and dynamic factors is respectively 0.4 m and 118 m, indicating that dynamic factors such as wind and vehicle load are the main factors affecting the cumulative travel of the stiffened girder end. Although the amplitude of the temperature displacement component is large, its frequency is low, resulting in a small cumulative displacement of the girder end, and it has little effect on the performance degradation of the key restraint device directly connected to the girder end. In addition, existing research has found that wind load in the wind-vehicle-bridge coupling system has little influence on the girder end displacement when the long-span suspension bridge is under normal wind, and the high-frequency and low-amplitude vibration of the girder end is mainly caused by vehicle load (Guo et al., 2015). Therefore, to further discuss the influence of the restraint device on the main girder in the longitudinal motion, the longitudinal displacement caused by thermal expansion and cold contraction of the material can be eliminated, and the simulated displacement of the girder under traffic load is taken as the analysis object.
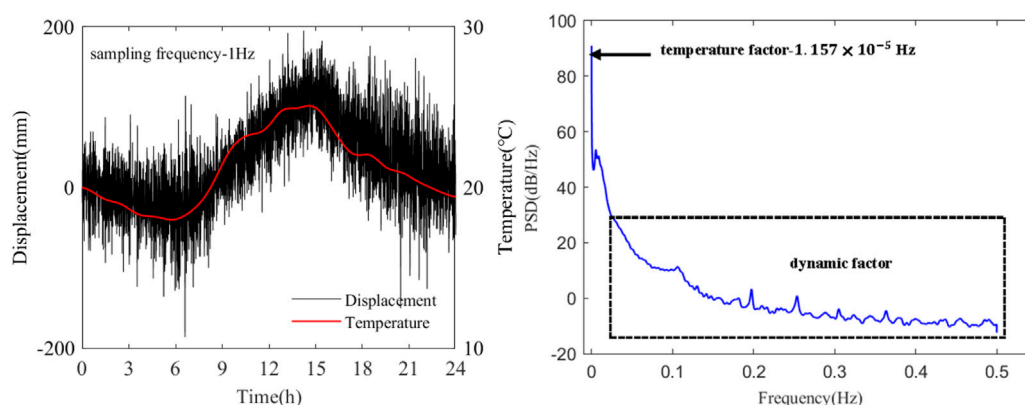
FIGURE 1
Longitudinal displacement time history curve and power spectrum of the girder end.
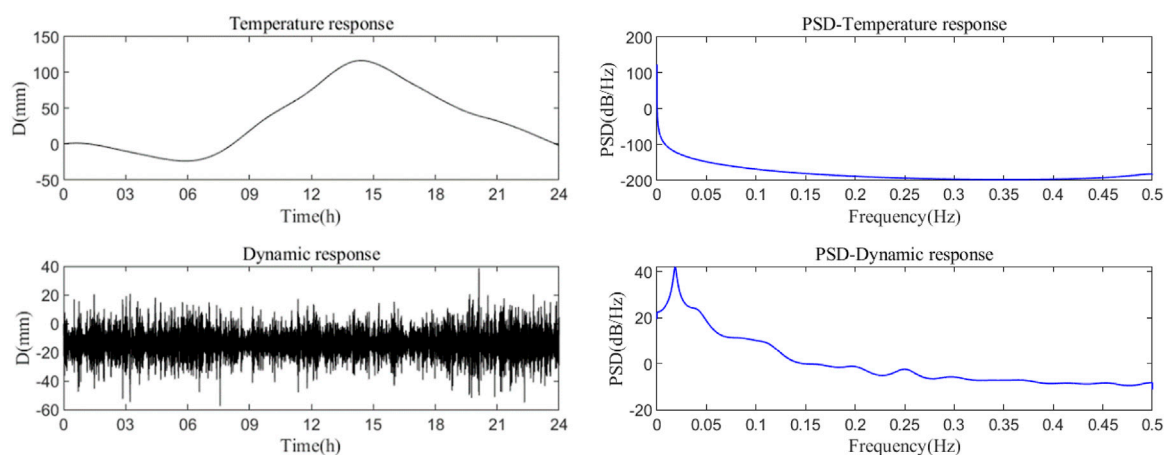
FIGURE 2
Displacement signal's decomposition component and power spectrum.

TABLE 1 The statistical parameters of longitudinal motion components.

Displacement component	Maximum (mm)	Minimum (mm)	Amplitude (mm)	Standard deviation (mm)
Temperature displacement	23.9	−116.7	140.6	44.3
Dynamic displacement	57.5	−39.0	96.5	8.3

3 The finite element simulation of the main girder's longitudinal motion

3.1 Simulation of traffic load

The vehicle load under bridge operation is complicated and random (Liu et al., 2021), in order to reflect the vehicle load on the bridge, the random traffic flow is perceived as the traffic load in the finite element model analysis to ensure that the vehicle load can include the probable various most adverse load combination so that the analysis results are more suitable for bridge operation.

The simulation of random vehicle load should be carried out based on the measured traffic flow data of the bridge, and the probability distribution model and the statistical law of the vehicle characteristic parameters are obtained using probability theory and numerical methods to establish a random traffic flow model (Chen et al., 2018). The mass of a certain identified vehicle is unchanged when it is driving on the bridge, but the speed and location are

TABLE 2 Vehicle type classification.

Vehicle type	Axle group diagram	Proportion (%)	Wheelbase(m)
1		81.51	2.889
2		0.88	5.265 + 1.315
3		1.89	1.894 + 5.068
4		4.27	1.881 + 4.544+1.337
5		1.32	3.530 + 6.581+1.307 + 1.307
6		10.13	3.169 + 1.411+6.581 + 1.307+1.307

FIGURE 3
Probability distribution model of vehicle weight.

FIGURE 4
Probability distribution model of vehicle speed.
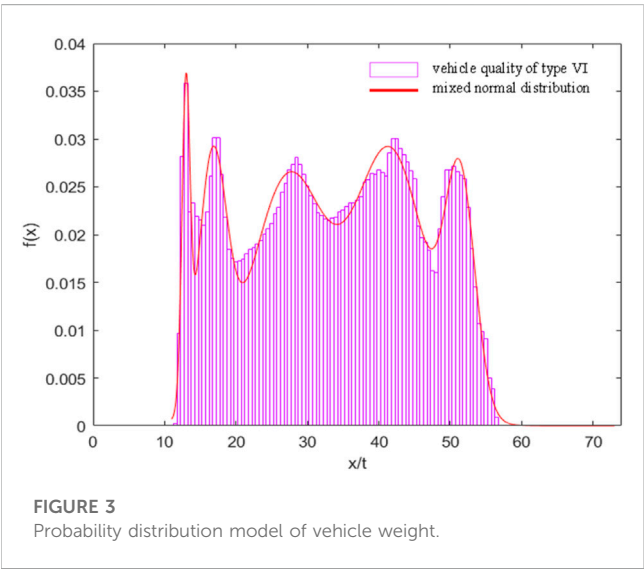
changing with time, and its location is closely related to the vehicle type, so the construction of the random traffic flow model requires three main parameters, which are the vehicle type, vehicle speed, and vehicle weigh. The random traffic flow simulation method is as follows:

(1) Bridge vehicle types division: Based on the bridge's WIM data in the past year, vehicles are divided according to different axle group types, and six basic vehicle types are distinguished. On this basis, wheelbases of different vehicle types are determined according to the measured wheelbase data and common wheelbase parameters, as shown in Table 2. Statistics show that the six basic vehicle types can cover all vehicles passing through the bridge.

(2) Determination of statistical models for the weight and initial velocity of different vehicle types: Analysis of the bridge's weight data reveals that the weight of each vehicle type exhibits a multimodal distribution, and common distribution functions such as normal and lognormal distributions are unable to fit the data well. Therefore, this paper uses the Expectation-Maximization algorithm to establish a probability statistical model for the weight of vehicles based on a mixture of Gaussian distributions, as shown in Figure 3. In addition, the initial velocity is the basis for simulating the vehicle's

performance on the bridge and plays a decisive role in the travel time of vehicles on the bridge. Based on the distribution characteristics of velocity data, this paper uses the t-distribution to establish a probability statistical model for the initial velocity, as shown in Figure 4.
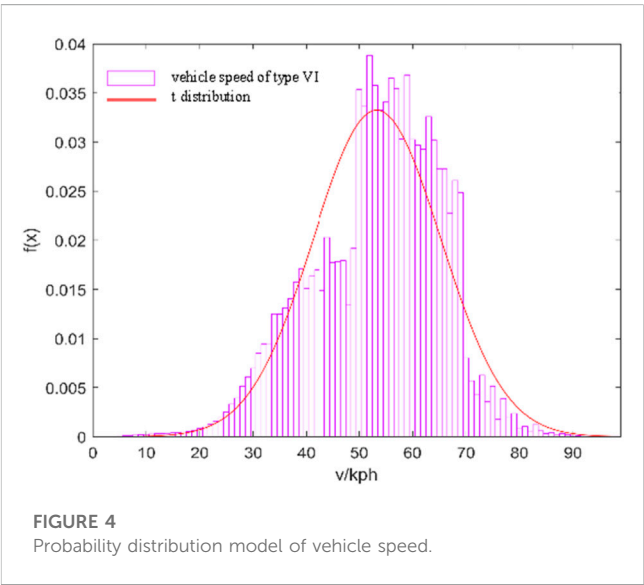
(3) Random vehicle load simulation: Traffic load simulation mainly simulates the generation of random vehicles and the following situation of vehicles on the bridge deck. Among them, the simulation of random vehicle generation aims to determine the size of the traffic load; the simulation of vehicle following conditions considers the mutual influence between vehicles, and the vehicle following model can be used to calculate the acceleration of vehicles at any time. By leading into the vehicle's initial speed and arrival time, the position of the vehicle in the direction of travel on the bridge deck can be determined. Relevant studies have shown that the vehicle arrival process follows the Poisson point process of arrival rate λ, the formula for calculating the arrival rate is shown in Eq. 2; The position of vehicles in the transverse direction of the bridge is mainly selected based on the lane distribution characteristics of the vehicles. This article determines the lane selection characteristics of the bridge based on the bridge WIM data, as shown in Table 3.

TABLE 3 Lane distribution (%).

Vehicle type	Fast lane (inside lane)	Middle lane	Slow lane (outside lane)
1	51.88	36.65	11.47
2	10.09	39.03	50.88
3	0.39	50.34	49.27
4	3.82	51.05	45.13
5	0.56	41.71	57.73
6	0.05	25.98	73.97
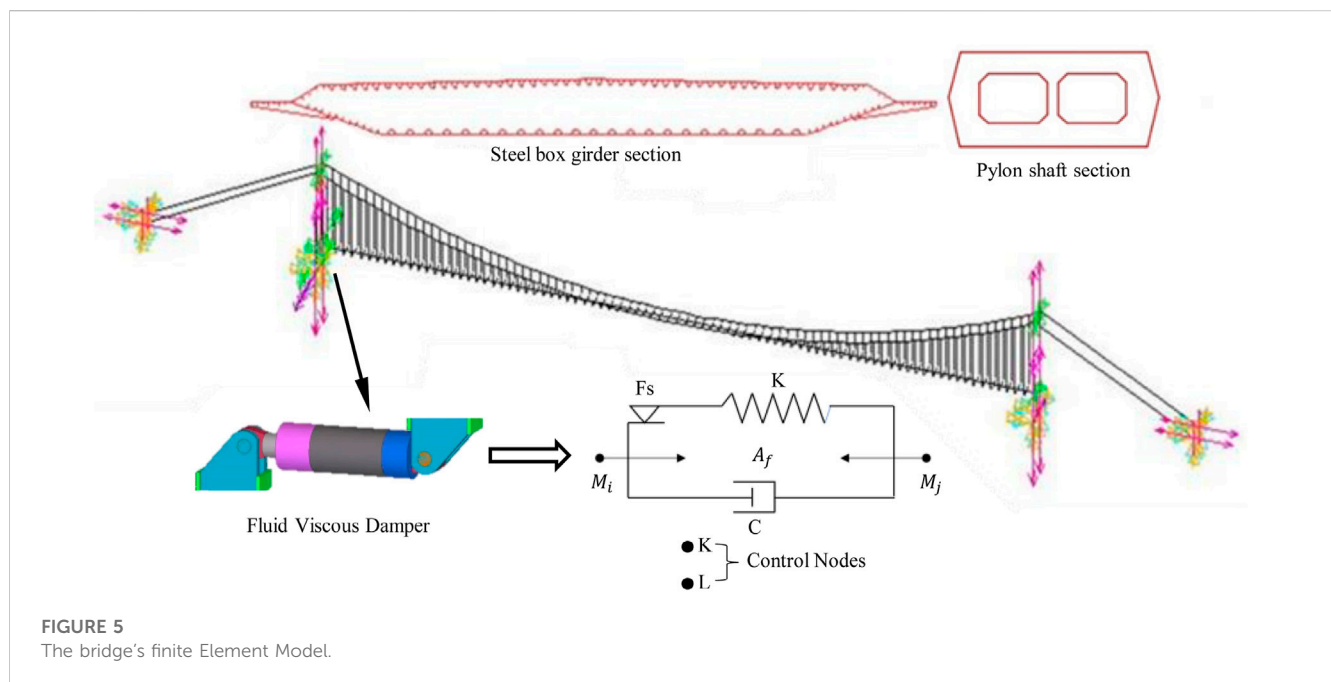
FIGURE 5
The bridge's finite Element Model.

$$\lambda = \frac{Q_h}{3600} \tag{2}$$

Where: Q_h is the average hourly traffic volume during the simulation period.

In a word, the main process for establishing a stochastic vehicle flow dynamic model is as follows:

①Determine bridge traffic volume based on statistical data of bridge traffic flow during simulation periods; ②Based on the traffic volume and simulation duration, the number and arrival time of vehicles are generated according to the Poisson point process theory; ③Determine a statistical model for vehicle parameters based on WIM data, and use the Monte Carlo method to generate a vehicle model library containing vehicle information parameters; ④Based on the vehicle model library containing vehicle information parameters, vehicle arrival time, and initial speed, the vehicle operation program based on the vehicle following theory can calculate and obtain the load data (i.e., vehicle flow data) of each bridge node under each load step; ⑤Load the traffic flow data into the finite element model and perform transient dynamic analysis,

extract the longitudinal displacement time history of the beam end for subsequent research.

3.2 Dynamic model updating and inspection

Figure 5 shows the suspension bridge's three-dimensional finite element model established using ANSYS. The main girder was simulated using Beam188 elements, while the main cables and suspender cables were simulated using Link10 elements. The end of the main cables and the bottom of the bridge tower were all solidified, the main tower and the main cables obeyed the master-slave constraint relationship at the top position of the tower, and the main cables and suspender cables shared the same node at the cable clamp, suspender cables shared the same node with the main girder at the lifting point, the support was simulated by elastic support, and the girder end dampers were simulated by the Combin37 unit based on the kelvin model (Hu et al., 2020). The girder end displacement simulation under traffic load is carried out by loading the dynamic random traffic flow data obtained based on the above traffic load

FIGURE 6
Hysteresis curve of the bridge's service support.

FIGURE 8
Measured girder end motion speed.

FIGURE 7
Variation of friction coefficient during the support's service.

FIGURE 9
Damping force versus velocity.
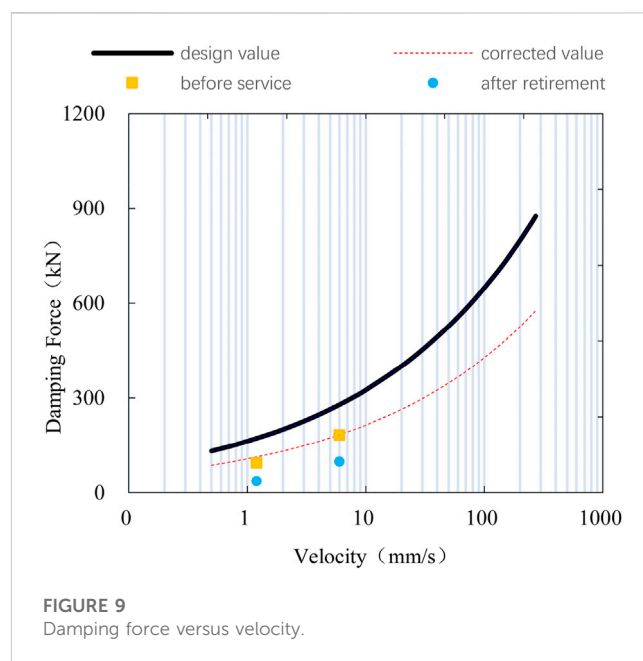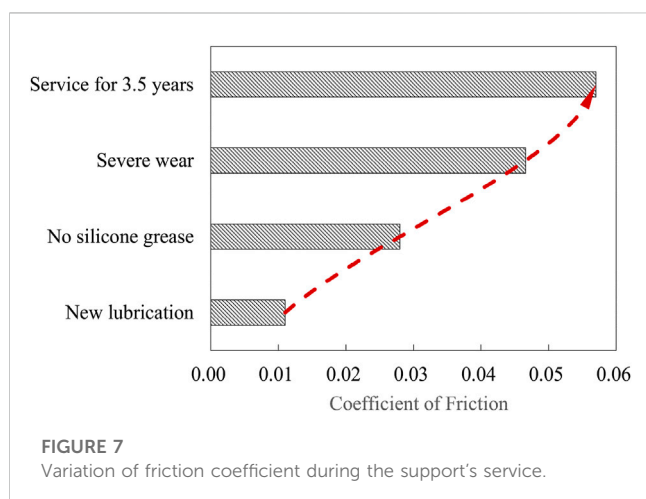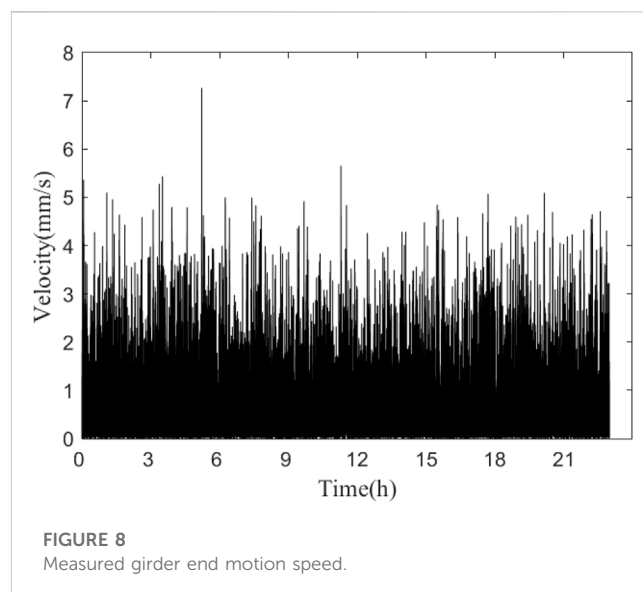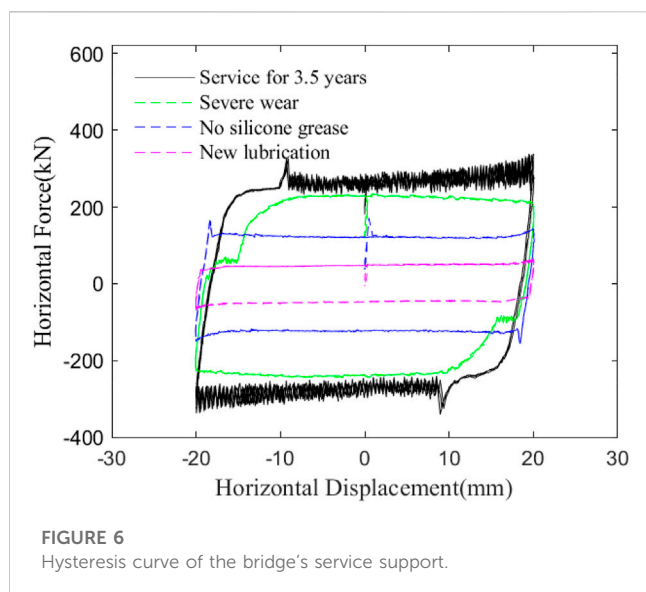
simulation method into the finite element model for transient dynamic analysis.

In addition, in order to ensure that the longitudinal simulated motion of the main girder under random traffic flow accords with the actual operating condition of the bridge, the model was updated by adjusting the girder end restraint parameters based on the mechanical performance test results of the bridge's the restraint device.

Based on the bridge's service support, the mechanical properties of the support are tested by changing the state of the wear plate, and the corresponding hysteresis curve is obtained as shown in Figure 6, which shows that the wear plate's friction coefficient of the support is 0.011 under the condition of new silicone grease coverage, which satisfies the specification limit of 0.03. While the friction coefficient of support with a service life of 3.5 years is 0.057, which is much larger than the specification value, and significantly larger than that under the condition of no silicone grease or severe wear (0.028/0.047), indicating that the bridge support with a service life of 3.5 years is not in the service condition of no silicone grease or severe

wear, and the significant increase of its friction coefficient mainly lies in the hydrolysis of silicone grease and foreign matter inclusions. The changing trend of the friction coefficient during the support service process is shown in Figure 7. Since the support's service life is about 2.5 years when the dampers are installed, the friction coefficient of the model support is taken to be 0.03 as a result of the above test.

The bridge's health monitoring results showed that its main girder movement velocity is less than 10 mm/s, as shown in Figure 8. The mechanical performance experiment of the bridge's viscous damper shows that the mechanical relationship of the damper before and after service under low-speed conditions (<10 mm/s) do not satisfy its design constitutive relationship, and the damping force under low-speed conditions is smaller than the design value, as

FIGURE 10
Comparison of longitudinal simulated displacement and measured displacement at girder end.
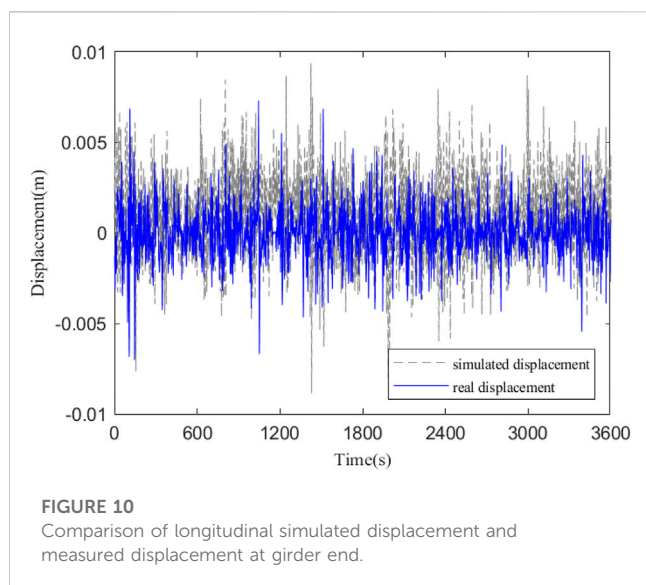
shown in Figure 9. Therefore, the damping index of the damper in the model is adjusted to 1,000 $kN/(m/s)^{\alpha}$ (smaller than the design value), and the adjusted damping force is consistent with the test results, as shown in Figure 9, and the velocity index is the design value of 0.3.

To validate the accuracy of the dynamic analysis model, Figure 10 compares the time-domain curves of the girder end's simulated longitudinal displacement and the measured high-frequency longitudinal displacement (obtained based on the EWT method). It can be seen that the two time-domain curves are relatively similar in fluctuation.

To quantitatively evaluate the similarity between the simulated displacement and the measured displacement, this paper uses the Euclidean distance as the corresponding index. The expression for calculating the Euclidean distance is as follows:

$$\| d \| = \sqrt{\sum_{i=1}^{n} (x_i - y_i)^2} \tag{3}$$

Where x_i and y_i are the vectors of the two types of signals; the smaller the Euclidean distance, the more similar the two signals. The calculated similarity between the simulated displacement and the measured displacement is 0.1634, indicating that the two signals have a high degree of similarity. Therefore, it can be concluded that the finite element model under random traffic loads established in this study can well simulate the dynamic displacement response of the girder end.

4 Influence of constraint device on girder end displacement

4.1 Effect analysis of viscous damper

The significant longitudinal displacement of a long-span suspension bridge's stiffening girder under dynamic load is characteristic of its structure itself. To control the stiffening girder end displacement response and prolong the service life of expansion joints, bearings, and other components, viscous dampers are usually installed longitudinally at the joint of the tower and girder (Zhao et al., 2020). For analyzing the influence of viscous dampers on the main girder's longitudinal motion, based on the above finite element model under random traffic flow and the measured data of the bridge, this paper compares and analyzes the displacement of the girder end before and after installing dampers to verify the control effect of viscous dampers on the girder end's longitudinal motion.

Figure 11 shows the finite element simulated longitudinal dynamic response of the girder end with random traffic flow before and after installing dampers. As can be seen, the amplitude of the longitudinal displacement response is reduced to a certain extent after the damper is installed, and the cumulative stroke of the girder ends in 10min before and after

Longitudinal displacement time history of girder end (10min)

Longitudinal cumulative displacement of the girder end

FIGURE 11
Simulated displacement of the girder end before and after damper installation. **(A)** Longitudinal displacement time history of girder end (10 min). **(B)** Longitudinal cumulative displacement of the girder end.
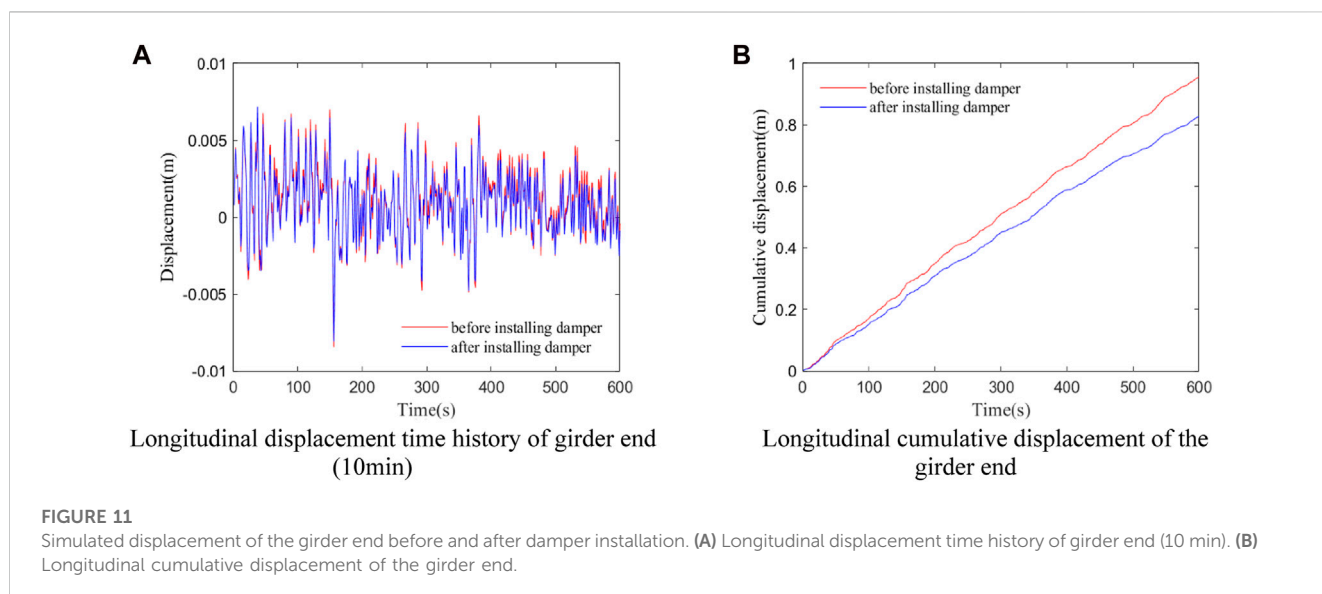
the damper is installed is also reduced from 0.96 m to 0.83 m, with a reduced range of 14%, indicating that the installing of the viscous damper can effectively suppress the high-frequency displacement of the girder end caused by vehicle load.

Comparing the longitudinal monitoring displacement power spectrum of the girder end before and after installing the damper in the bridge, it can be seen that the amplitude of the high-frequency band in the displacement power spectrum and the details amplitude of longitudinal vibration at the girder end are reduced after installing dampers, as shown in Figure 12. The change tendency is consistent with the above simulation results, further verifying the accuracy and rationality of the above dynamic model.

4.2 Sensitivity analysis of damper parameters

The energy dissipation principle of viscous damper mainly lies in that hydraulic oil passes through the damping hole under the action of pressure difference to generate damping force, and its expression of damping force is:

$$P = C \cdot sgn(v)|v|^{\alpha} \qquad (4)$$

Where v is the velocity, C is the damping index, and α is the velocity index. It can be seen that when the velocity index is constant, the damping force increases with the increase of the damping index; when the damping index C is constant, the damping force decreases with the increase of velocity index α under the condition that $v < 1 m/s$, the damping force increases with the increasing velocity index α under the condition that $v > 1 m/s$ (Zhao et al., 2020).

At present, viscous dampers have been widely used in long-span bridges at home and abroad, but the selection of damper parameters is often determined according to subjective experience, and there is no clear unified standard. Therefore, the influence of damping indexes on the dynamic response of the girder end is further discussed based on the finite element model of random traffic

flow, that is, the velocity index is 0.3, and the damping indexes were separately set to 1000、2000、4000、6000 and 8000 $kN/(m/s)^{\alpha}$.

The variation curves of the girder end's longitudinal cumulative displacement at different damping indexes are compared, as shown in Figure 13. It is shown that the damping index is positively correlated with the control effect when the speed index is constant, that is, the greater the damping index, the better the dampers suppress the girder end in the longitudinal motion, and the cumulative longitudinal displacement of the girder end is reduced by 21% when the damping index is increased from 1,000 to 8,000 $kN/(m/s)^{0.3}$. In addition, Table 4 gives the 10min cumulative displacement and displacement control rate under different damping indexes, and the results show that with the increase of damping index, the cumulative displacement and its control rate gradually smooth out, and the displacement control effect is optimal when the damping index is 4,000 $kN/(m/s)^{0.3}$. It is clear that after the damping index increases to a certain degree, the control effect of the damper on the girder end displacement does not improve significantly, and the damping index is too large will lead to the damper in a long-term high-load working condition, which is not conducive to the durability of the member, and to a certain extent will also change the force characteristics of the suspension bridge. Therefore, the optimal value should be selected according to the code and the results of dynamic response analysis when refining the design of suspension bridge girder end dampers.

4.3 Sensitivity analysis of support parameters

The existing studies have shown that support friction also has a certain inhibitory effect on girder end displacement, and its effect cannot be ignored (Huang et al., 2021). In order to further obtain the influence of support friction resistance on the displacement of the
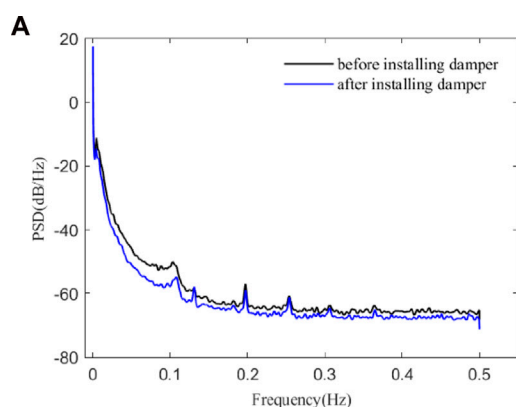
Comparison of the power spectrum of monitoring displacement at the girder end
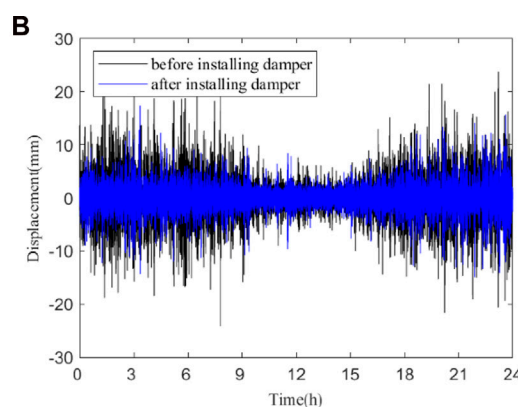
Comparison of measured dynamic displacement at the girder end

FIGURE 12
Measured displacement of the girder end before and after installing the damper. **(A)** Comparison of the power spectrum of monitoring displacement at the girder end. **(B)** Comparison of measured dynamic displacement at the girder end.

FIGURE 13
Effect of damper parameters on cumulative displacement at the girder end.

FIGURE 14
Effect of friction coefficient of support on the girder end's cumulative displacement.

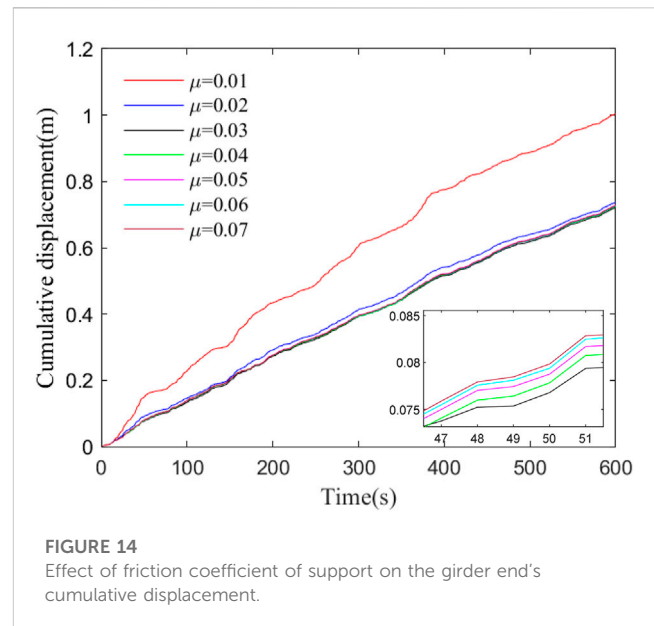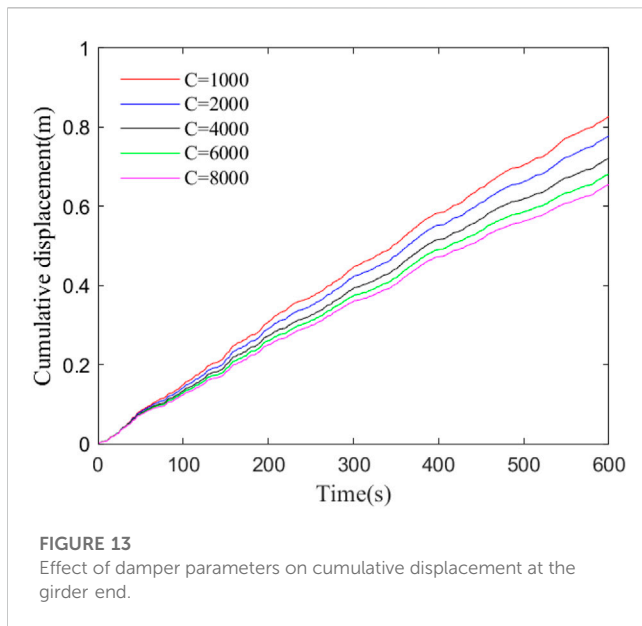girder end, this paper quantifies the degree of sensitivity of support parameters by comparing the cumulative displacement of the girder end under different support friction coefficients. Referring to the support test results in Figure 7, the friction coefficients of the support in the dynamic model are selected as 0.01~0.07, and the trend of the cumulative displacement of the girder end under different friction coefficients is shown in Figure 14. It can be seen that the cumulative displacement of the girder end decreases obviously with the increase of the friction coefficient and then tends to a stable value, which indicates that the control effect of the support friction on the girder end's longitudinal motion is limited. That is, when the friction coefficient is within the range of 0~0.03, the increase of the friction coefficient has an obvious control effect on the main girder in the longitudinal displacement; While after the friction coefficient is greater than 0.03, the increase of the friction coefficient has little effect on the main girder in the longitudinal displacement, and the cumulative displacement of the girder end only fluctuates slightly, as shown in Table 5 In addition, it is observed that after the friction coefficient of the support is greater than 0.03, the displacement of the girder increased. The reason is that the limited friction resistance of the support is relatively large, which may cause the main girder to be in a temporary equilibrium state during longitudinal motion.

However, due to the friction resistance of the support is still not enough to completely suppress the main girder in the longitudinal motion, the sudden imbalance state of the main girder will generate a shock effect to excite longitudinal vibration, causing an increase in the displacement of the girder end, The calculation results indicate that the increase is very small and its impact can be ignored. Therefore, in bridge operation, whenever the service time of the bearing increases, the friction coefficient of the support firstly increases and then decreases, which causes the cumulative displacement of the main girder to decrease significantly and then stabilize, and the actual monitoring data also prove the correctness of this conclusion, as shown in Figure 15.

From the analysis of the control effect of the constraint device parameters, in the early stage of service of the support (friction coefficient<0.03), compared with the damping index, the increase in friction coefficient of the support has a relatively better effect on the displacement of the girder end, that is, the friction coefficient increases by four times (0.01–0.04), and the displacement control rate is 28%, while the damping coefficient increases by four times (1,000 $kN/(m/s)^\alpha$ to 4,000 $kN/(m/s)^\alpha$), and the displacement control rate is only 12%; After about 2 years of service support (friction coefficient>0.03), the change in friction coefficient of the support has little impact on the displacement of the girder end, while

TABLE 4 Cumulative displacement of girder end under different damping indexes.

Damping index $[(m/s)^{0.3}]$	Accumulated displacement in 10 min (m)	Displacement control rate
0	0.96	-
1,000	0.83	13.8%
2000	0.78	18.7%
4,000	0.72	24.6%
6,000	0.69	28.5%
8,000	0.66	31.5%

TABLE 5 Cumulative displacement of girder end under different friction coefficients.

Friction coefficient	Cumulative displacement (m/10min)	Displacement control rate
0.01	1.004	-
0.02	0.739	26.4%
0.03	0.722	28.1%
0.04	0.725	27.8%
0.05	0.729	27.4%
0.06	0.727	27.6%
0.07	0.727	27.6%

FIGURE 15
Cumulative displacement change of girder end monitoring.
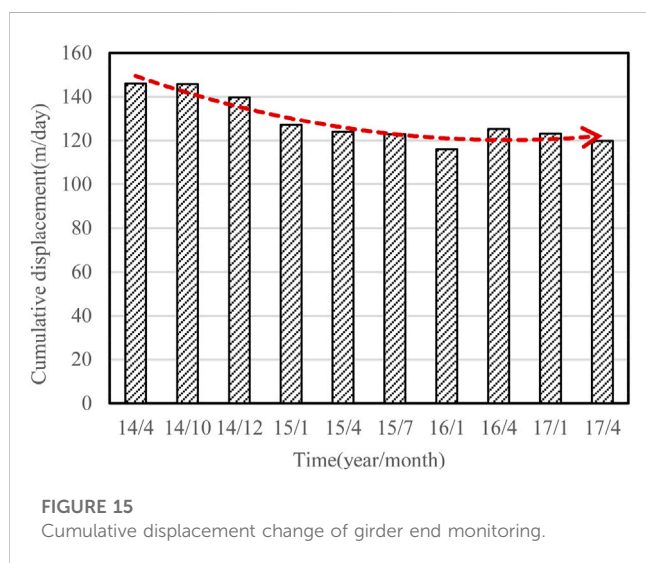
the damping index plays a main control role on the displacement of the girder end.

5 Conclusion

Taking a certain highway bridge as an example, this paper establishes and tests a bridge random traffic dynamic analysis model based on the monitoring data and WIM data, and the constraint device parameters' sensitivity analysis is also conducted based on the model. The analysis results show that:

(1) The longitudinal movement at a long-span suspension bridge's girder end is mainly caused by temperature changes, vehicles, wind loads, etc. The frequency range of longitudinal displacement can be divided into two parts: 1.157×10^{-5}Hz (caused by temperature) and ≥ 0.1Hz (caused by dynamic factors, i.e., vehicles, wind loads, etc.). The high-frequency and low-amplitude dynamic displacement component is the main reason for the huge accumulated travel of the girder end.

(2) Based on the measured WIM data of the bridge, a random traffic flow model can correctly and reasonably simulate the long-span suspension bridge's girder end in the longitudinal motion under

the action of vehicle load, and its motion characteristics are highly similar to the measured data.

(3) The viscous damper of the long-span suspension bridge can effectively control the girder end's longitudinal movement, and the damping index is non-linearly and positively correlated with the control effect, that is, the control effect gradually stabilizes as the value of the damping index increases. Therefore, the optimal value of damping indexes should be selected according to the code and the results of dynamic response analysis when refining the design of suspension bridge girder end dampers. In this article, the optimal value of bridge damping index is recommended to be 4,000 $kN/(m/s)^{0.3}$.

(4) The increase of the friction coefficient of the vertical support of the suspension bridge can inhibit the girder end in the longitudinal motion to a certain extent, but with limited effect, when the friction coefficient is greater than 0.3, its change has little effect on the displacement of girder end.

(5) In terms of the friction coefficient and the damping index, in the early stage of service support (friction coefficient<0.03), the friction coefficient plays a main control role on the displacement of the girder end, while after about 2 years of service support (friction coefficient>0.03), the damping index plays a main control role on the displacement of the girder end.

Data availability statement

The raw data supporting the conclusion of this article will be made available by the authors, without undue reservation.

Author contributions

All authors listed have made a substantial, direct, and intellectual contribution to the work and approved it for publication.

Conflict of interest

Publisher's note

All claims expressed in this article are solely those of the authors and do not necessarily represent those of their affiliated organizations, or those of the publisher, the editors and the reviewers. Any product that may be evaluated in this article, or claim that may be made by its manufacturer, is not guaranteed or endorsed by the publisher.

References

Chen, B., Ye, Z., Chen, Z., and Xie, X. (2018). Bridge vehicle load model on different grades of roads in China based on weigh-in-motion (WIM) data. *Measurement* 122, 670–678. doi:10.1016/j.measurement.2018.03.005

Chen, S., and Wu, J. (2010). Dynamic performance simulation of long-span bridge under combined loads of stochastic traffic and wind. *J. Bridge Eng.* 15, 219–230. doi:10.1061/(ASCE)BE.1943-5592.0000078

Guo, T., Huang, L., Liu, J., and Zhou, Y. (2018). Damage mechanism of control springs in modular expansion joints of long-span bridges. *J. Bridge Eng.* 23 (7). Article ID 04018038. doi:10.1061/(ASCE)BE.1943-5592.0001255

Guo, T., Liu, J., Zhang, Y., and Pen, S. (2015). Displacement monitoring and analysis of expansion joints of long-span steel bridges with viscous dampers. *J. Bridge Eng.* 20 (9). Article ID 04014099. doi:10.1061/(ASCE)BE.1943-5592.0000701

Hu, J, Wang, L, Song, X, Sun, Z, Cui, J, and Huang, G. (2020). Field monitoring and response characteristics of longitudinal movements of expansion joints in long-span suspension bridges. *Measurement* 162, 107933. ArticleID107933. doi:10.1016/j.measurement.2020.107933

Huang, G., Hu, J., Liu, H., and Sun, X. (2021). Girder longitudinal movement and its factors of suspension bridge under vehicle load. *Adv. Civ. Eng.* 2021, 1–14. Article ID 1443996. doi:10.1155/2021/1443996

Liu, Y., Wang, Q., and Lu, N. (2021). Probabilistic evaluation of maximum dynamic traffic load effects on cable-supported bridges under actual heavy traffic loads. *Proc. Institution Mech. Eng. Part O J. Risk Reliab.* 235 (1), 108–119. doi:10.1177/1748006X20938491

Qu, F., Deng, X., Dong, J., Shan, D., and Song, Z. (2023). Field monitoring and analysis for cumulative longitudinal movements of girder ends for the medium-span suspension bridges. *J. Civ. Struct. Health Monit.* 13, 505–522. doi:10.1007/s13349-022-00656-3

Yang, M.-G., and Cai, C. S. (2016). Longitudinal vibration control for a suspension bridge subjected to vehicle braking forces and earthquake excitations based on magnetorheological dampers. *J. Vib. Control* 22 (17), 3659–3678. doi:10.1177/1077546314564781

Zhao, Y., Huang, P., Long, G., Yuan, Y., and Sun, Y. (2020). Influence of fluid viscous damper on the dynamic response of suspension bridge under random traffic load. *Adv. Civ. Eng.* 2020, 1–19. Article ID 1857378. doi:10.1155/2020/1857378

Zribi, M., Almutairi, N. B., and Abdel-Rohman, M. (2006). Control of vibrations due to moving loads on suspension bridges. *Nonlinear Analysis Model. Control* 11 (11), 293–318. doi:10.15388/NA.2006.11.3.14749

*CORRESPONDENCE
Meihua Bian,
✉ bian_mh.sy@gx.csg.cn,
✉ gxdwxm@126.com

A simplified analytical method for lateral dynamic responses of a transmission tower due to rockfall impact

Meihua Bian*, Jianing Peng, Songlin Qin, Xingsen Zhang and Junhua Li

Guangxi Key Laboratory of Intelligent Control and Maintenance of Power Equipment, Electric Power Research Institute of Guangxi Power Grid Co., Ltd., Nanning, China

Transmission tower structures support high-voltage power lines that carry electricity over long distance and rockfall is one of critical disasters during its safe operation. This paper presented a simplified analytical methodology for lateral dynamic responses of a transmission tower structure due to rockfall impact. At first, the lateral dynamic displacement of a lattice transmission tower structure can be represented by a second-order partial differential equation and half sine wave was used for rockfall impact. Then, the solution can be approximated by a set of specified shape functions multiplied by time-dependent generalized coordinates. And the partial differential equation is discretized into a set of single degree of freedom system. And then the shape function can be determined by solved an eigenvalue function and the fundamental frequency of a transmission tower can was derived based on the energy method and combination synthesis method. Finally, the lateral dynamic displacements can be approximately obtained. A numerical study of a transmission tower was conducted. Parametric study of the effect of impact location height, impact duration, peak impact force, as well as the distribution of cross-arms on dynamic responses were also carried out. And the results show that the discrepancy between the analytical and the computed of fundamental frequency is less than 3%, the error of dynamic displacement is within 10%, and the fundamental frequency of the structure decreases with the increase of the tower top additional mass ratio.

KEYWORDS

transmission tower, rockfall impact, fundamental frequency, dynamic displacement response, modal analysis

Introduction

Electricity plays a significant role in social development and various industries. After years of development, China has built a large-scale power transmission network that inevitably passes through regions with complex terrain (Cai and Wan, 2021). As the conQA23ng nodes between high-voltage transmission lines and the ground, transmission towers are often built on steep slopes of mountains to reduce transmission distance and power loss (Xu et al., 2022). This terrain condition increases the possibility of geological hazards. Transmission towers are susceptible to catastrophic damage caused by rockfall impacts, which can further lead to local instability (Cai et al., 2019; Xu et al., 2023) and

collapse of the entire tower (Xu et al., 2021; Xue et al., 2023). Rockfall is a major disaster that seriously threatens the structural safety of transmission towers in mountainous areas.

Researchers have carried out a large number of studies on transmission towers to ensure the stable operation of the power grid (Li et al., 2022; Li, et al., 2023). In the field of finite element analysis. The study conducted by Fu and Li. (2016) investigated the dynamic response of tower systems under wind and rain loads. It was found that the average displacement amplification of the structure was 22% higher under combined wind and rain loads than when under wind loads alone. He S et al. (2019) developed a model for a three-tower, two-span tower-line system to investigate the response of the towers to wind-induced vibrations. The results indicated that the dynamic response was higher than the static response, with a stress ratio of 1.43. Morgan and Swift. (1964) identified that the behavior of the tower-line system was affected by the height of ice shedding to varying degrees. The study results revealed that ground clearance of the lower conductor of the loaded span drops below the safety limit for ice loads beyond 1 pound per foot. The study conducted by Yang and Hong. (2016) examined the nonlinear and non-elastic response of tower-line systems exposed to downburst loading. The outcomes of the investigation suggested that the load-carrying capacity curve of an individual tower was able to represent the curvature for the tower-line system. Zhou et al. (2022) performed physical model testing and numerical analysis on transmission tower landslides caused by rainfall. The study identifies the failure process and modes of these landslides. Gong and Zhi (2020) performed an analysis on the failure mode of transmission towers impacted by earthquakes. The outcomes of their study demonstrated that the failure mode of the towers, under severe seismic impacts, was in-plane global collapse as a result of local failures. According to Tian et al. (2019) a collapse analysis of transmission tower was conducted to evaluate their structural durability when exposed to varying wind angles. The results show that the bending deformation in the mid-section of the tower body was significantly better than the shear deformation, ultimately leading to the failure of its main components. The analysis of transmission tower line systems using tower and cable models is complicated and time-consuming due to the wide range of tower types. As a result, the numerical calculations required for such models can be very complex.

Buildings in mountainous areas are prone to the impact of rockfall disasters caused by earthquakes, landslides, and debris flows (Happ and Noble, 1993). In terms of the conditions for rockfall occurrence, the collapsed rock masses are mostly concentrated on slopes with a gradient greater than 32°, and after detaching from the bedrock, they fall and collide continuously with trees, buildings, and other objects, with impact velocities mostly below 20 m/s. Although the rockfall impact belongs to low to medium-speed impact, the large mass of falling rocks can still acquire significant energy during the falling process (Wyllie, 2014). In terms of the analytical solutions for displacement response under impact, Zhang et al. (2023) derived a formula to measure the largest displacement caused by kinetic energy during impact. The study found that doubling of the impactor's mass results in a 150% increase in the maximum displacement. Wang et al. (2014) proposed two enhanced analytical techniques rooted in forced vibration theory and variable separation method to determine the natural frequency and mode shape of a uniformly cantilevered beam. Prasada Rao et al. (2004) derived a

formula for predicting the natural frequency of tower-like structures based on theoretical deformation and geometric parameters. In addition, Yan et al. (2018) investigated the influence of rockfall impact angle on the impact response of reinforced concrete slabs. Their findings revealed that both the sphericity of the impacting object and the angle exert impact on the RC slabs. Prakash et al. (2021) conducted a study on the dynamic prediction of beam behavior subject to rockfall impact. The study found that the safety of the structure is primarily influenced by the impact mass. According to analysis of existing literature, there are few relevant studies on the analytical solutions of displacement response of transmission towers under rockfall impact, which is contrary to the increasing scale and potential protection needs of mountainous transmission networks.

Rockfall disasters seriously threaten the safety of mountainous transmission networks. In order to carry out impact-resistant design of structures and understand the impact of rockfall loads on transmission tower structures effectively, it is necessary to conduct in-depth research and take protective measures. This paper proposes an approximate algorithm for the fundamental frequency of tower structures based on the energy method and combination synthesis method. It derives the displacement response of iron towers under falling rock impact, verifies the proposed approximate algorithm through ABAQUS finite element numerical simulation, and parametric analysis was also carried out. This paper was organized as follows. Section 2 is devoted to theoretical derivation for the fundamental frequency and lateral dynamic displacements of the tower structure; Case study of a transmission tower was carried out in section 3; And conclusions are drawn in section 4.

Theoretical derivation

The lateral dynamic displacements of a lattice transmission tower structure can be expressed as a partial differential equation

$$m\frac{\partial^2 Y(z,t)}{\partial t^2} + C\frac{\partial Y(z,t)}{\partial t} + \frac{\partial^2}{\partial z^2}\left(\frac{\partial^2 Y(z,t)}{\partial z^2}EI\right) = Q(z,t) \qquad (1)$$

where Y(z,t) = transverse dynamic displacement, E = Young's modulus of material, C = tower damping intensity, m = Tower mass per unit length, Q(z,t) = impact load function. The transmission tower is a complex structure that can be reduced as a cantilever beam with a varying cross-section (Jiang et al., 2011; Wang et al., 2015). As a result, the inertia of cross Section 1 can be simply represented by

$$I(z) = I_0\left(1 + \beta\frac{z}{L}\right) \qquad (0 \le z \le L) \qquad (2)$$

Where β = the change rate of tower section.

The continuous lateral displacement Y(z,t) is represented by the finite sum the production of shape functions and generalized coordinates (Erturk and Inman, 2011)

$$Y(z,t) = \sum_{i=1}^{n}\varphi_i(z)y_i(t) \qquad (3)$$

where $\varphi_i(z)$ = Characteristic function of linear uniform cantilever transfer tower, $y_i(t)$ = generalized coordinates over time.

The impact of rockfall is a transient effect. And the impact of rock falling on the tower can be approximated by the impact

function F (z,t) in terms of piece-wise function (Wang et al., 2014)

$$F(z,t) = \begin{cases} P\delta(z - l_0)\sin\left(\dfrac{\pi t}{t_0}\right)(0 \le t \le t_0) \\ 0 \ (t_0 \le t) \end{cases} \tag{4}$$

Where P and t_0 = the half sine pulse force magnitude and duration, respectively; l_0 = the height of the bottom end of the transmission tower from the impact point, δ = unit pulse function.

After substituting Eq. 3 into Eq. 1 and multiplying $\varphi_j(z)$ on both sides of Eq. 1, then integrate each term of Eq. 1 over span L and divide by m, it yields (Wang et al., 2017):

$$\ddot{y}_i + 2\xi_i\omega_i\dot{y}_i + \omega_i^2 y_i = \int_0^L \frac{F(z,t)\varphi_i(z)}{m}dx \tag{5}$$

in which

$$\xi_i = \frac{c}{2m\omega_i}$$

The right side of Eq. 5 can be formulated as

$$\int_0^L \frac{\varphi_i(z)F(z,t)}{m}dx = \int_0^L \frac{\delta(z - l_0)\varphi_i(z)q(t)}{m}dx = \frac{\varphi_i(l_0)q(t)}{m} \tag{6}$$

in which

$$q(t) = \begin{cases} P\sin\left(\dfrac{\pi t}{t_0}\right) & (0 \le t \le t_0) \\ 0 & (t_0 \le t) \end{cases} \tag{7}$$

After substituting Eq. 6 into Eq. 5, the generalized time-dependent coordinates y_i can be determined

$$y_i = -\varphi(l_0)P\frac{\frac{\pi e^{-\xi_i\omega_i t}}{\omega_i\sqrt{1-\xi_i^2 t_0}}\sin\left(\omega_i\sqrt{1-\xi_i^2}t - \phi_1\right) - \sin\left(\frac{\pi}{t_0}t - \phi_2\right)}{\sqrt{\left[1 - \left(\frac{\pi}{\omega_i t_0}\right)^2\right]^2 + \left(2\frac{\pi\xi_i}{\omega_i t_0}\right)^2}}\ (t_0 \ge t \ge 0) \tag{8}$$

$$y_i = \varphi(l_0)P\frac{\pi}{\sqrt{1 - \xi_i t_0\omega_i}}\frac{e^{(t_0-t)\xi_i\omega_i}\cos\left(\sqrt{1-\xi_i^2}t\omega_i - \phi_1\right) \times \sin\left(\sqrt{1-\xi_i^2}t_0\omega_i\right)}{\sqrt{\left[1 - \left(\frac{\pi}{\omega_i t_0}\right)^2\right]^2 + \left(2\frac{\pi\xi_i}{\omega_i t_0}\right)^2}}$$
$$- \varphi(l_0)P\frac{\pi}{\sqrt{1 - \xi_i t_0\omega_i}}\frac{e^{-\xi_i\omega_i t}\sin\left(\sqrt{1-\xi_i^2}t\omega_i - \phi_1\right) \times \left[1 + e^{\xi_i t_0\omega_i}\cos\left(\sqrt{1-\xi_i^2}t_0\omega_i\right)\right]}{\sqrt{\left[1 - \left(\frac{\pi}{\omega_i t_0}\right)^2\right]^2 + \left(2\frac{\pi\xi_i}{\omega_i t_0}\right)^2}}$$
$$(t_0 \le t) \tag{9}$$

in which

$$\tan\phi_1 = \frac{2\xi_i\sqrt{1-\xi_i^2}}{1 - \left(\frac{\pi}{\omega_i t_0}\right)^2 - 2\xi_i^2}, \tan\phi_2 = \frac{2\xi_i\frac{\pi}{\omega_i t_0}}{1 - \left(\frac{\pi}{\omega_i t_0}\right)^2}$$

The eigenfunction of a transmission tower with cross arms is given by (Erturk and Inman, 2011)

$$\varphi_i(z) = A_i\left[B_i\left(\sin\frac{z\lambda_i}{L} - \sinh\frac{z\lambda_i}{L}\right) + \cos\frac{z\lambda_i}{L} - \cosh\frac{z\lambda_i}{L}\right] \tag{10}$$

where A_i = the modal constant, L = the height of the tower, λ_i = the eigenvalue, and B_i is given by

$$B_i = \frac{\sin\lambda_i + \frac{M\lambda_i}{mL}(\cos\lambda_i - \cosh\lambda_i) - \sinh\lambda_i}{\cos\lambda_i - \frac{M\lambda_i}{mL}(\sin\lambda_i - \sinh\lambda_i) - \cosh\lambda_i} \tag{11}$$

The eigenvalue of a system can be determined by solving the characteristic equations (Erturk and Inman, 2011)

$$1 + \cos\lambda_i\cosh\lambda_i = \frac{M\lambda_i}{mL}(\sin\lambda_i\cosh\lambda_i - \cos\lambda_i\sinh\lambda_i) \tag{12}$$

Once the eigenvalues solved in Eq. 12 and then substitute Eqs 8–10 into Eq. 3, the lateral dynamic displacements of a transmission tower equipped with cross arms subjected to rockfall impact can be determined.

The fundamental frequency of the vibration of a transmission tower structure using energy method is given by (Gu and Yin, 1983)

$$\omega^2 = \frac{E\int_0^L I(z)\left[\frac{d^2x_f(z)}{dz^2}\right]^2 dz + k'G\int_0^L A(z)\left[\frac{dx_s(z)}{dz}\right]^2 dz}{\frac{\gamma}{g}\int_0^L A(z)\left[x_f(z) + x_s(z)\right]^2 dz + \sum_{i=1}^n \frac{W_i}{g}\int_0^L \delta(z - l_i)\left[x_f(z) + x_s(z)\right]^2 dz} \tag{13}$$

where $x_f(z)$, $x_s(z)$ = displacement due to bending and shear deformation of the structure, respectively; G, E = shear modulus and modulus of elasticity of the structure, respectively; W_i = concentrated mass load, k' = 5/6 (rectangular section), G = 3E/8, and cross-sectional area A = $A_0(1+\beta z/L)$.

Since the variation of the cross-section and additional cross arms of the transmission tower, it is difficult to calculate the fundamental frequency. Herein the combined synthesis method is used to calculate the simplified calculation of multiple subsystems. According to the combination synthesis method, its fundamental frequency can be approximated by a combination of the fundamental frequencies of subsystem (Gu and Yin, 1983).

$$\frac{1}{\omega^2} \le \frac{1}{\omega_1^2} + \frac{1}{\omega_2^2} + \sum_{i=1}^n\left[\frac{1}{\omega_3^2} + \frac{1}{\omega_4^2}\right]_i \tag{14}$$

Where ω_1 = the subsystem frequency composed of tower mass distribution and bending stiffness; ω_2 = the subsystem frequency composed of tower mass distribution and shear stiffness; ω_3 = the subsystem frequency composed of cross arm mass and bending stiffness near the top tower; ω_3 = the subsystem frequency composed of cross arm mass and shear stiffness near the top tower; and n = number of additional masses.

$$\omega_1^2 = \frac{E\int_0^L I(z)\left[\frac{d^2x_f(z)}{dz^2}\right]^2 dz}{\frac{\gamma}{g}\int_0^L A(z)x_f^2(z)dz} \tag{15}$$

$$\omega_2^2 = \frac{k'G\int_0^L A(z)\left[\frac{dx_s(z)}{dz}\right]^2 dz}{\frac{\gamma}{g}\int_0^L A(z)x_s^2(z)dz} \tag{16}$$

$$[\omega_3^2]_i = \frac{E\int_0^L I(z)\left[\frac{d^2x_f(z)}{dz^2}\right]^2 dz}{\frac{W_i}{g}\int_0^L \delta(z - l_i)x_f^2(z)dz} \tag{17}$$

$$[\omega_4^2]_i = \frac{k'G\int_0^L A(z)\left[\frac{dx_s(z)}{dz}\right]^2 dz}{\frac{W_i}{g}\int_0^L \delta(z - l_i)x_s^2(z)dz} \tag{18}$$

The selected deflection function must satisfy the geometric boundary conditions. Since a transmission tower structure can be

idealized as a cantilever beam with a stationary end and a free end, x_f represents the deflection due to bending and it could be chosen as follows (Erturk and Inman, 2011)

$$x_f(z) = C_f\left[3\left(\frac{z}{L}\right)^2 - \left(\frac{z}{L}\right)^3\right] \tag{19}$$

C_f is unknown coefficient. And x_s represents the displacements due to shear deformation and it could be taken the first two Fourier steps as follows C_f is unknown coefficient. And x_s represents the displacements due to shear deformation and it could be taken the first two Fourier steps as follows

$$x_s(z) = C_s \sin\left(\frac{\pi z}{2L}\right) = C_s\left(\frac{\pi z}{2L} - \frac{\pi^3 z^3}{24L^3}\right) \tag{20}$$

C_s is unknown coefficient.

By substituting Eq. 19 into Eqs 15, 17 and substituting Eq. 20 into Eqs 16, 18, we obtain:

$$\omega_1^2 = \frac{36E\int_0^L I(z)(L-z)^2 dz}{\frac{\gamma}{g}\int_0^L A(z)\left(3z^2L - z^3\right)^2 dz} \tag{21}$$

$$\omega_2^2 = \frac{k'G\int_0^L A(z)\left(\frac{\pi^2}{4l^2} - \frac{\pi^4 z^2}{8l^4} + \frac{\pi^6 z^4}{64l^6}\right)dz}{\frac{\gamma}{g}\int_0^L A(z)\left(\frac{\pi z}{2l} - \frac{\pi^3 z^3}{24l^3}\right)^2 dz} \tag{22}$$

$$\left[\omega_3^2\right]_i = \frac{36E\int_0^L I(z)(L-z)^2 dz}{\frac{W_i}{g}x_f^2(l_i)} \tag{23}$$

$$\left[\omega_4^2\right]_i = \frac{k'G\int_0^L A(z)\left(\frac{\pi^2}{4l^2} - \frac{\pi^4 z^2}{8l^4} + \frac{\pi^6 z^4}{64l^6}\right)dz}{\frac{W_i}{g}x_s^2(l_i)} \tag{24}$$

And finally, the fundamental frequency of a transmission tower structure can be determined by substituting Eqs 21–24 into Eq. 14.

Case study

FEM of a transmission tower

The transmission tower structure under consideration has a height of 36 m, as shown in Figure 1. The tower's Finite Element Model (FEM) was created by ABAQUS software, and B31 element was adopted for beam members. The cross-section of beam member is angle steel and the tower base dimensions are 6.5 m × 6.5 m. The main members' inclination angle is 85°.

The tower body composes of the primary, diagonal, and auxiliary members, all constructed of Q235 steel, and the physical parameters are: mass density of 7850 kg/m³, modulus elasticity 206×10^{11} Pa, and Poisson's ratio 0.3. The beam members are all made of "L" shaped angle steel, with main member sizes (mm × mm) including 160×12, 140×12, 140×10, 125×8, 100×8, 90×7, 80×6, 75×6, 75×5, and 70×5. The Johnson-Cook constitutive model was adopted as the dynamic constitutive model, which is mathematically expressed as

$$\sigma_{eq} = \left(U + V\varepsilon_{eq}^n\right)\left(1 + W\ln\dot{\varepsilon}_{eq}'\right)\left(1 - T'\right) \tag{25}$$
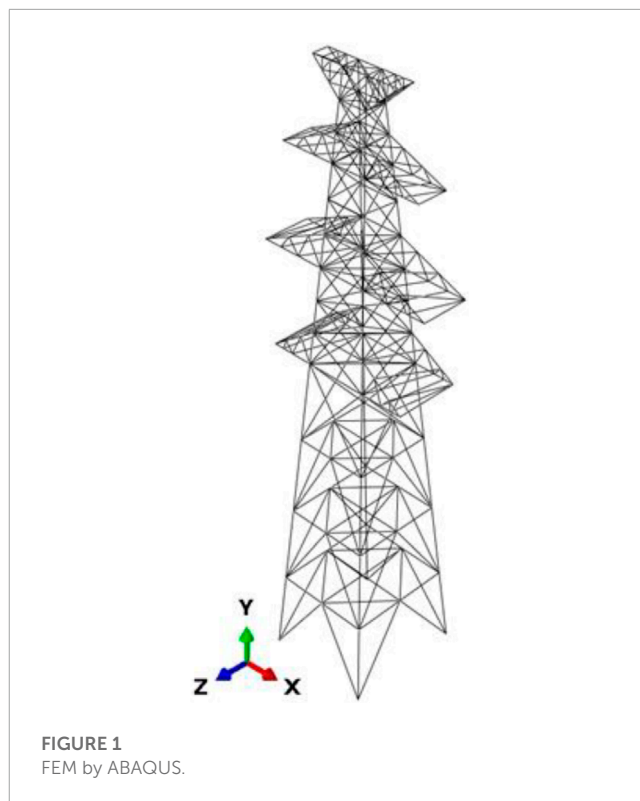

FIGURE 1
FEM by ABAQUS.

TABLE 1 Parameters in steel J-C constitutive relationship of Q235B.

Parameters	U/Mpa	V/Mpa	W	n	m	Tm/K	Tr/K
Value	244	899	0.039	0.94	0.76	1765	293

where U, V, n, W and m are material parameters summarized in Table 1; σ_{eq} and ε_{eq} = the equivalent stress and equivalent plastic strain, respectively; $\dot{\varepsilon}_{eq}' = \dot{\varepsilon}_{eq}/\dot{\varepsilon}_0, \dot{\varepsilon}_0$ = reference strain rate, $\dot{\varepsilon}_{eq}'$ = the dimensionless equivalent plastic strain rate, dimensionless temperature $T' = (T - T_r)/(T_m - T_r)$, T_r and T_m = the reference temperature and the melting point of the material, T = room temperature. Rayleigh damping is used, where the Alpha value is 0.00063 and the Beta value is 3.9×10^{-6}.

For simplicity, spherical models of falling rocks have been widely used in existing literature (He B et al., 2019; Xie et al., 2020). In this paper, a spherical model with a diameter of 1 m was used to represent falling rocks. The rock is assumed to be a sphere in order to simplify the model, and the impact between the rock and the transmission tower is modeled as a face-to-face contact. The contact area of the transmission tower is angle steel member and falling rock sphere can be considered as a target contact surface. The base of the transmission tower is assumed fixed, and the members are rigidly connected. In this study, the rock sphere mesh and the beam element were set to 100 mm. The falling rock properties were defined as follows: density of 2500 kg/m³, elasticity of 20GPa, and Poisson's ratio of 0.2 (Lan et al., 2007). Rockfall is usually quite common in mountain areas with slopes greater than 32° and impact velocities are mostly under 20 m/s. Herein, rockfall with impact velocities of 10 m/s was used (Wyllie, 2014). Since the rotational energy of the falling rock accounts for only 10% of the translational

TABLE 2 The effect factors during rockfall impact.

Parameter	Impact height(m)	Impact duration time(s)	Peak impact force (kN)
Value	3,5,9	0.01,0.02,0.03	300,650,1000

FIGURE 2
The first six natural frquencies and modes of transmission tower.
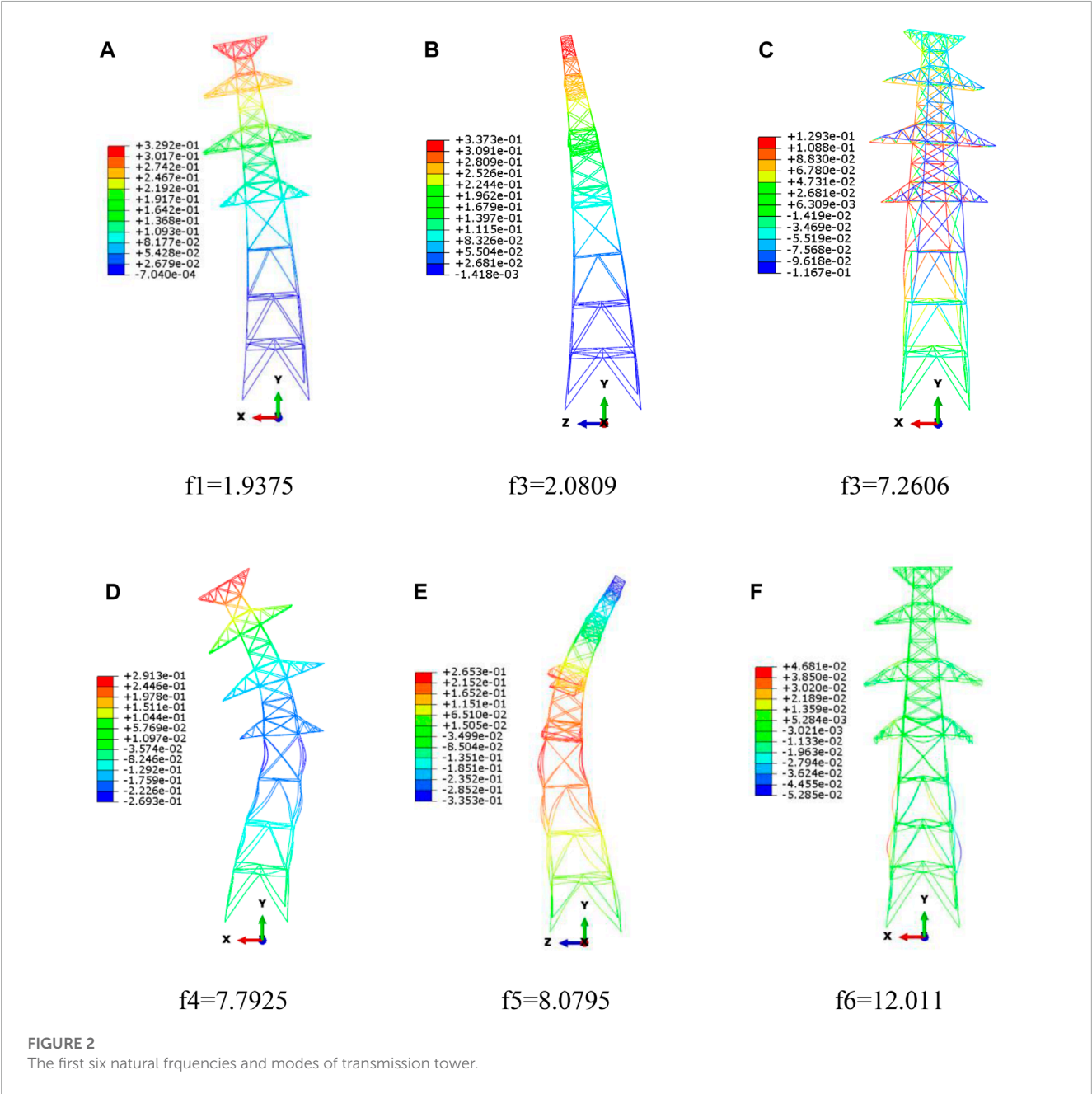
energy during impact, the effect of angular velocity is ignored during the simulation (Chau et al., 2002). According to existing literature, the duration of impact action due to falling stones on prestressed concrete bridges is about 0.1–0.2s (Zhang et al., 2022), and on reinforced concrete columns is about 0.1–0.2s (Xie et al., 2020). The impact time of stone ball on a steel plate as well as iron ball on concrete slab is about 0.1–0.3s (Yu et al., 2018), and on steel pipe is about 0.4s (Chen et al., 2020). Herein, the impact action time is set as 0.2s.

Results and discussion

Figure 2 illustrates the first six natural frequencies and corresponding modal shapes obtained through modal analysis of the transmission tower. It can be seen that the first two natural frequencies are bending along the Y direction, and X direction respectively. The first-order natural frequency, calculated using Eq. 14, is 1.9801 Hz, and it is quite close to the results of 1.9375 Hz by the model analysis in ABAQUS, around 2.2% error.
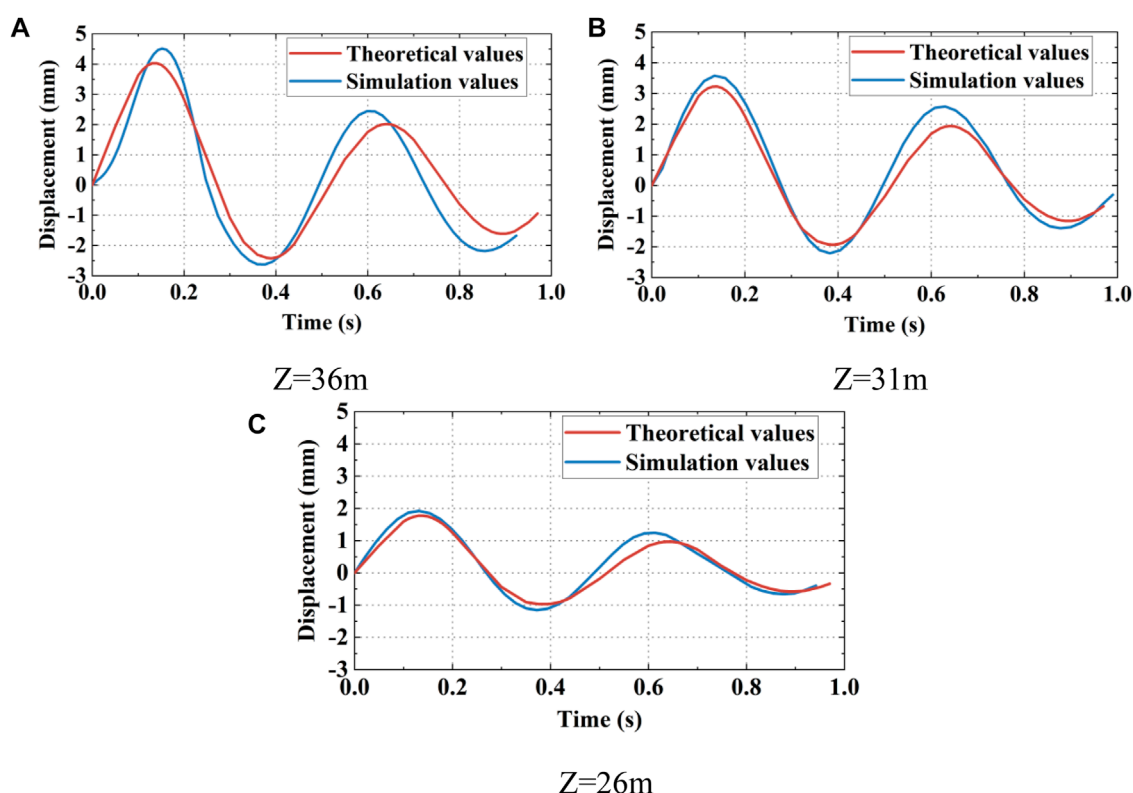
FIGURE 3
Diasplacement resposes at different positions: **(A)** Z = 36 m; **(B)** Z = 31 m; **(C)** Z = 26 m.

Figure 3 shows the time history of dynamic displacement on the top of the tower after the impact. After impact, the tower structure oscillated back and forth around the central point until it came to rest. The theoretical values are the results calculated based on the Eq. 3, and the simulated values are computed by the finite element software. Figure 3A illustrates the maximum dynamic displacement on the top of the tower, which is 4.46 mm. From Eq. 3, the maximum displacement response is 4.07 mm, with error of 8.7%. This is far less than the specification that the deflection curve of different types of towers under load should not exceed 2L/1000-7L/1000 (GB 50545-2010, 2020). According to Figures 3B, C, where the transmission tower is at heights of 31 m and 26 m respectively, the maximum theoretical values are 3.23 mm and 1.77 mm. The corresponding finite-element analysis results show a small discrepancy, with errors of 9.4% and 7.8% respectively.

Parametric analysis

Parametric analysis was carried out to examine the effect of the impact of rockfall on the dynamic displacement response of the transmission tower. A set of variable parameters based on the characteristics of rockfall in mountainous areas, such as impact height, impact duration as well as peak impact force, as summarized in Table 2 (Xie et al., 2020; Prakash et al., 2021).

The transmission tower under consideration has four cross-arm, and it can be simplified as a cantilever beam structure, and the influence of the number of cross-arms on the transmission tower was also considered. To improve the accuracy of the formula, the cross-arm part was simplified as an additional mass in theoretical analysis.

Impact height

Figure 4A shows the results of calculating the displacement response at the top of the transmission tower when the impact duration lasts for 0.02 s and the height of falling rocks are 3 m, 5 m, and 9 m respectively, with the peak impact force being 650 kN and other parameters remaining constant.

The maximum displacement of the transmission tower's top is 3.22 mm at an impact height of 3 m, for 5 m, the maximum displacement is 4.03 mm, and for 9 m, the maximum displacement is 6.05 mm. Increasing the impact height results in non-linearly increasing displacement of the top of the tower. This arises because a higher impact position transfers greater kinetic energy to the transmission tower from the falling rocks.

Impact duration time

The falling rock impact height was set to 5 m, and the peak impact force was set at 650 kN. To examine the impact of the falling
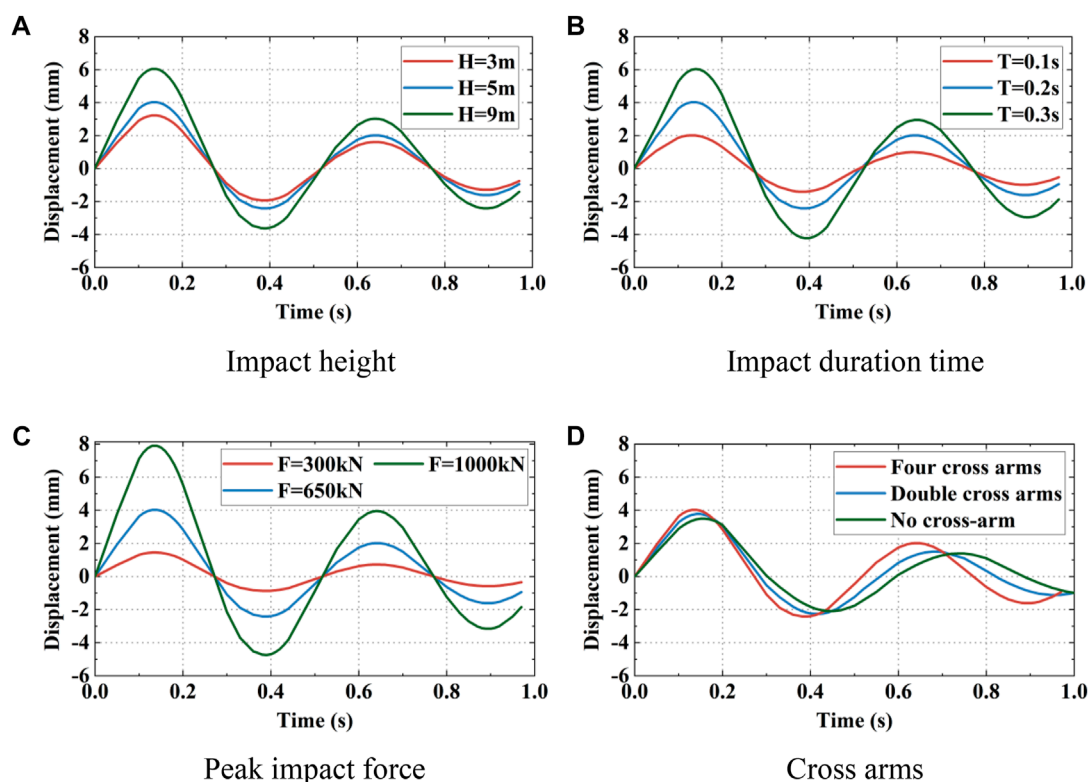
FIGURE 4
Displacement responses on the top tower: **(A)** impact height; **(B)** impact durction time; **(C)** peak impact force; **(D)** cross arms.

rock on tower top displacement, varying falling rock impact times of 0.01 s, 0.02 s, and 0.03 s were explored while all other parameters were kept constant.

The findings illustrated in Figure 4B demonstrated that as the duration of impact increases, the maximum displacement of the top of the transmission tower also increases. The maximum displacement when the impact duration time is 0.01 s is 2.01 mm, 4.03 mm when the time is 0.02 s, and 6.04 mm when it is 0.03 s. The dynamic displacement of the top tower considerably increases as the falling rock impact time increases, primarily due to the greater kinetic energy transferred from the falling rock to the transmission tower.

Peak impact force

It is assumed that the impact height is 5 m and the impact lasts for 0.2 s, the effect of peak impact force was investigated. The peak impact forces of falling rocks are 300 kN, 650 kN, and 1000 kN respectively, and the dynamic displacement response on the top transmission tower is shown in Figure 4C.

The peak impact force of rockfall has great effect on the transmission tower. The maximum displacement on the top transmission tower was measured for various peak impact forces, resulting in a displacement of 1.45 mm for 300 kN, 4.03 mm for 650 kN, and 7.91 mm for 1000 kN. The impact force of falling rocks has a significant effect on dynamic displacements of the tower's top structure. This effect is evident

and implies that the greater the impact force, the larger the displacement.

Number of cross arms

The cross arm is considered as an additional mass, and in the calculation formula of the fundamental frequency, the distributed mass and the additional mass of the tower body are both considered. The effect of the number of cross arms was also investigated. Herein four cross arms double cross arms are compared with no cross arms situation. The results of the dynamic displacement response on the top tower is shown in Figure 4D.

The maximum displacements on the top tower with three cases of cross arms conditions are 4.03 mm, 3.77 mm, and 3.49 mm, respectively, and their self-oscillation frequencies are 1.98 Hz, 2.03 Hz and 2.07 Hz respectively. The cross arms can be considered as additional mass attached on the different position of the tower. It is evident that as the number of cross arms, i.e., the additional mass increased, the dynamic displacement on the top tower also increases while the frequency decreases.

The results of the parametric study showed that the displacement of the transmission tower is significantly affected by both the impact height and the peak impact force of falling rocks. Unfortunately, the design codes for transmission lines do not provide any specific measures for preventing and controlling the impact of falling rocks on transmission towers. It is recommended that designers should pay much attention to areas prone to rockfall disasters and exclude

rocks with excessive height and potential for producing significant impact forces to avoid hazards to transmission towers.

Conclusion

In this paper, we present an algorithm that estimates the fundamental frequency of tower structures. The algorithm combines the energy method and the combination synthesis method to provide an accurate approximation. The bending and shear deformations of transmission towers, as well as the effects of the distribution and variable cross-section characteristics of cross-arms near the tower top are also under consideration. The displacement response of the tower under rockfall impact is derived. The parametric analysis was also carried out. The following conclusions are drawn.

(1) The peak impact force has a larger impact on the displacement response of transmission towers when compared to the impact action time, impact height, and number of cross-arms.
(2) With the increase of the number of cross-arms on the top tower, which is the additional mass ratio, the displacement of the top tower will increase and the vibration fundamental frequency of the structure will decrease.
(3) The comparison verification by finite element example shows that the errors of the theoretical data of displacement response are within 10%, and the errors of fundamental frequency are only 2.2%.

The algorithm proposed in this article is not only applicable for the calculation of the fundamental frequency and displacement response of transmission towers, but also suitable for other tower-like structures. However, the article did not take into account the cable effect on transmission towers. The dynamic displacement responses of tower-like structures under cables constraint conditions needs further research.

Data availability statement

The raw data supporting the conclusion of this article will be made available by the authors, without undue reservation.

Author contributions

Conceptualization, software, validation, writing—original draft, MB; methodology, JP and SQ; investigation, XZ; data curation, JL. All authors contributed to the article and approved the submitted version.

Funding

Conflict of interest

Authors MB, JP, SQ, XZ, and JL were employed by the company Electric Power Research Institute of Guangxi Power Grid Co., Ltd.

Publisher's note

All claims expressed in this article are solely those of the authors and do not necessarily represent those of their affiliated organizations, or those of the publisher, the editors and the reviewers. Any product that may be evaluated in this article, or claim that may be made by its manufacturer, is not guaranteed or endorsed by the publisher.

References

Cai, Y., and Wan, J. (2021). Wind-resistant capacity modeling for electric transmission line towers using kriging surrogates and its application to structural fragility. *Appl. Sci.* 11 (11), 4714. doi:10.3390/app11114714

Cai, Y., Xie, Q., Xue, S., Hu, L., and Kareem, A. (2019). Fragility modelling framework for transmission line towers under winds. *Eng. Struct.* 191, 686–697. doi:10.1016/j.engstruct.2019.04.096

Chau, K. T., Wong, R. H. C., and Wu, J. J. (2002). Coefficient of restitution and rotational motions of rockfall impacts. *Int. J. Rock Mech. Min. Sci.* 39 (1), 69–77. doi:10.1016/S1365-1609(02)00016-3

Chen, Z., Wang, J., Chen, J., GangaRao, H., Liang, R., and Liu, W. (2020). Responses of concrete-filled FRP tubular and concrete-filled FRP-steel double skin tubular columns under horizontal impact. *Thin-Walled Struct.* 155, 106941. doi:10.1016/j.tws.2020.106941

Erturk, A., and Inman, D. J. (2011). *Piezoelectric energy harvesting*. John Wiley and Sons.

Fu, X., and Li, H. N. (2016). Dynamic analysis of transmission tower-line system subjected to wind and rain loads. *J. Wind Eng. industrial aerodynamics* 157, 95–103. doi:10.1016/j.jweia.2016.08.010

GB 50545-2010 (2010). *Technical code of designing 110~ 500kV overhead transmission line*. National Standards of People's Republic of China.

Gong, J., and Zhi, X. (2020). Earthquake failure mode and collapse fragility of a 1000 kV outgoing line frame considering interactions in the tower line system. *Eng. Struct.* 27, 626–638. doi:10.1016/j.istruc.2020.06.018

Gu, K. X., and Yin, C. J. (1983). *Vibration engineering handbook[M]*. China Machine Press.

Happ, E. L., and Noble, M. A. (1993). An engineering rock classification to evaluate seismic rock-fall susceptibility and its application to the Wasatch Front. *Environ. Eng. Geoscience* 30 (3), 293–319. doi:10.2113/gseegeosci.xxx.3.293

He, B., Zhao, M., Feng, W., Xiu, Y., Wang, Y., Feng, L., et al. (2019). A method for analyzing stability of tower-line system under strong winds. *Adv. Eng. Softw.* 127, 1–7. doi:10.1016/j.advengsoft.2018.10.004

He S, S., Yan, S., Deng, Y., and Liu, W. (2019). Impact protection of bridge piers against rockfall. *Bull. Eng. Geol. Environ.* 78, 2671–2680. doi:10.1007/s10064-018-1250-5

Jiang, W. Q., Wang, Z. Q., McClure, G., Wang, G. L., and Geng, J. D. (2011). Accurate modeling of joint effects in lattice transmission towers. *Eng. Struct.* 33 (5), 1817–1827. doi:10.1016/j.engstruct.2011.02.022

Lan, H., Martin, C. D., and Lim, C. H. (2007). RockFall analyst: A gis extension for three-dimensional and spatially distributed rockfall hazard modeling. *Comput. Geosciences* 33 (2), 262–279. doi:10.1016/j.cageo.2006.05.013

Li, J. X., Cheng, J. P., Zhang, C., Qu, C. X., Zhang, X. H., and Jiang, W. Q. (2023). Seismic response study of a steel lattice transmission tower considering the hysteresis characteristics of bolt joint slippage. *Eng. Struct.* 281, 115754. doi:10.1016/j.engstruct.2023.115754

Li, J. X., Zhang, X. H., and McClure, G. (2022). Numerical and full-scale test case studies on post-elastic performance of transmission towers. *Eng. Struct.* 259, 114133. doi:10.1016/j.engstruct.2022.114133

Morgan, V. T., and Swift, D. A. (1964). Jump height of overhead-line conductors after the sudden release of ice loads. *Proc. Institution Electr. Eng.* 111 (10), 1736–1746. doi:10.1049/piee.1964.0285

Prakash, A., Monika, A. P., and Anandavalli, N. (2021). Behaviour of steel-concrete composite (SCC) girder under impact due to rock fall. *J. Constr. Steel Res.* 177, 106474. doi:10.1016/j.jcsr.2020.106474

Prasada Rao, N., Mohan, S. J., and Lakshmanan, N. (2004). A semi empirical approach for estimating displacements and fundamental frequency of transmission line towers. *Int. J. Struct. Stab. Dyn.* 4 (02), 181–195. doi:10.1142/S0219455404001185

Tian, L., Pan, H., Qiu, C., Ma, R., and Yu, Q. (2019). Wind-induced collapse analysis of long-span transmission tower–line system considering the member buckling effect. *Adv. Struct. Eng.* 22 (1), 30–41. doi:10.1177/1369433218774961

Wang, J., GangaRao, H., Liang, R., and Liu, W. (2017). Experimental and analytical responses of hollow and concrete-filled GFRP tube columns under impact. *J. Compos. Constr.* 21 (4), 04017013. doi:10.1061/(ASCE)CC.1943-5614.0000793

Wang, J., Liu, W., Wang, L., and Han, X. (2015). Estimation of main cable tension force of suspension bridges based on ambient vibration frequency measurements. *Struct. Eng. Mech.* 56 (6), 939–957. doi:10.12989/sem.2015.56.6.939

Wang, H. J., Meng, Q. F., and Feng, W. W. (2014). Discussion of the improved methods for analyzing a cantilever beam carrying a tip-mass under base excitation. *Shock Vib.* 2014. doi:10.1155/2014/981053

Wang, Y., Qian, X., Liew, J. R., and Zhang, M. H. (2014). Experimental behavior of cement filled pipe-in-pipe composite structures under transverse impact. *Int. J. Impact Eng.* 72, 1–16. doi:10.1016/j.ijimpeng.2014.05.004

Wyllie, D. C. (2014). *Rock fall engineering*. CRC Press.

Xie, R., Fan, W., Liu, B., and Shen, D. (2020). Dynamic behavior and vulnerability analysis of bridge columns with different cross-sectional shapes under rockfall impacts. *Structures* 26, 471–486. doi:10.1016/j.istruc.2020.04.042

Xu, J., He, S., Cao, X., Yao, L., Liu, X., and Yan, X. (2022). Analytical and numerical analysis of angle steel joints for conductors in lattice transmission towers. *Case Stud. Constr. Mater.* 17, e01592. doi:10.1016/j.cscm.2022.e01592

Xu, L. Y., Chen, W. Y., Cai, F., Song, Z., Pan, J. M., and Chen, G. X. (2023). Response of soil–pile–superstructure–quay wall system to lateral displacement under horizontal and vertical earthquake excitations. *Bull. Earthq. Eng.* 21 (2), 1173–1202. doi:10.1007/s10518-022-01572-z

Xu, L. Y., Song, C. X., Chen, W. Y., Cai, F., Li, Y. Y., and Chen, G. X. (2021). Liquefaction-induced settlement of the pile group under vertical and horizontal ground motions. *Soil Dyn. Earthq. Eng.* 144, 106709. doi:10.1016/j.soildyn.2021.106709

Xue, Y. Y., Wang, X. G., and Cai, F. (2023). Effect of inclined pile on seismic response of bridge abutments undergoing liquefaction—induced lateral displacement: Case study of nishikawa bridge in the 2011 great east Japan earthquake. *Front. Mater.* 10, 1185210. doi:10.3389/fmats.2023.1185210

Yan, P., Zhang, J., Fang, Q., and Zhang, Y. (2018). Numerical simulation of the effects of falling rock's shape and impact pose on impact force and response of RC slabs. *Constr. Build. Mater.* 160, 497–504. doi:10.1016/j.conbuildmat.2017.11.087

Yang, S. C., and Hong, H. P. (2016). Nonlinear inelastic responses of transmission tower-line system under downburst wind. *Eng. Struct.* 123, 490–500. doi:10.1016/j.engstruct.2016.05.047

Yu, B., Yi, W., and Zhao, H. (2018). Experimental study on the maximum impact force by rock fall. *Landslides* 15, 233–242. doi:10.1007/s10346-017-0876-x

Zhang, J., Wang, R., Han, W., and Bao, H. (2022). A comprehensive approach for bridge performance evaluation under rockfall impact integrated with geological hazard analysis. *Eng. Fail. Anal.* 141, 106668. doi:10.1016/j.engfailanal.2022.106668

Zhang, J. Z., Li, G. Q., Sun, Y. Z., Sun, J., Yu, Z. W., and Feng, R. (2023). Maximum displacement prediction of composite floor system under falling impact. *Eng. Struct.* 275, 115326. doi:10.1016/j.engstruct.2022.115326

Zhou, Y., Sheng, Q., Chen, J., Li, N., Fu, X., and Zhou, Y. (2022). The failure mode of transmission tower foundation on the landslide under heavy rainfall: A case study on a 500-kV transmission tower foundation on the yanzi landslide in barong, China. *Bull. Eng. Geol. Environ.* 81 (3), 125. doi:10.1007/s10064-022-02628-9

Study on the adaptability and optimization of boom replacement methods for suspension bridges

Yingna Mu[1,2], Qibing Hu[1], Changping Chen[1,2]*, Yanbin Tan[3], Yanna Zheng[1,2] and Guoxuan Liang[1]

[1]College of Marine and Civil Engineering, Dalian Ocean University, Dalian, Liaoning, China, [2]Key Laboratory of Environment Controlled Aquaculture, Ministry of Education, Dalian Ocean University, Dalian, Liaoning, China, [3]School of Civil Engineering, Faculty of Infrastructure Engineering, Dalian University of Technology, Dalian, Liaoning, China

To ensure the safe operation of bridges, the study of methods and techniques for boom replacement has become a crucial aspect of the scientific maintenance of suspension bridges. This study focuses on analyzing the bridge responses and evaluating the applicability of three different boom replacement methods: single-point, three-point and five-point, using finite element calculations. A sea-crossing suspension bridge is taken as a case study to simulate the process of boom replacement using temporary booms. Consequently, the optimal replacement method for booms of varying lengths is determined. Meanwhile, this research proposes a quantitative basis for classifying boom lengths based on calculation data and analysis results to determine the suitable boom lengths for different replacement methods. Besides, a comparison of the relationship between the force transmission efficiency of temporary booms and boom length reveals that longer booms exhibit lower force transmission efficiency, with the efficiency decreasing at a faster rate as boom length increases. Overall, these findings provide a theoretical basis for the study of boom replacement in suspension bridges.

KEYWORDS

suspension bridge, replacement method, boom length, force transmission efficiency, adaptability analysis

1 Introduction

With the improvement of China's economic level and engineering construction capacity, a lot of long-span suspension bridges (Huang and Zhang, 2021) have been constructed across canyons, rivers, streams, and sea areas throughout the country. However, these bridges are inevitably subjected to performance degradation due to harsh environmental conditions. Therefore, studying the maintenance of suspension bridges is of utmost importance. The boom plays a crucial role as a force transmission element in suspension bridges, connecting the main cable and the main beam while transferring the self-weight of the main beam and various loads to the main cable, tower, and anchorage structure. Therefore, the function and condition of the boom are closely intertwined with the safe operation of suspension bridges. Once a bridge is put into service, the boom undergoes gradual changes in appearance, mechanics, material properties, and other aspects due to external environmental factors, permanent and variable actions, and even accidents. As a result, various defects may arise,

posing risks to the bridge's safety. Available data indicates that within 2–3 years of operation, several issues such as cracking of the protective layer, component corrosion, steel wire corrosion, cable body water seepage, and shaft sleeve wear have been observed to varying degrees in some bridges (Cao, 2020; Dou, 2020; Han, 2020). Rust greatly reduces the fatigue life of a single steel wire in the suspension boom. As a vulnerable structure, the service life of the suspension boom is generally 20 years (Xu, 2020; Yang and Lu, 2022). The Technical Code of Maintenance for City Bridge specifies that the replacement of booms should be considered if the wire breaking rate of the cable exceeds 2%, or the section reduction caused by corrosion of the steel wire exceeds 10% (Sun, 2014).

Numerous examples of boom replacement in suspension bridges can be found at home and abroad. Specifically, all booms of the Forth Road Bridge in the United Kingdom were replaced after 40 years from its opening to traffic in September 1964 (Alastair and Colford, 2017). The Aquitaine Bridge in France underwent a complete overhaul of its cable system as a result of main cable corrosion (Li, 2021). All booms of the Lions Gate Bridge in Vancouver Canada were replaced in around 2000, marking the world's first instance of boom replacement for an entire bridge without interrupting traffic (Radojevic et al., 2019). Four groups of booms in the Shantou Bay Bridge were replaced by engineering personnel in 2012 due to significant deterioration during the bridge's extended period of service (Wang et al., 2015). Urgent boom replacements were carried out on the Jiangsu Runyang Bridge in 2017 following severe fire damage (Yuan et al., 2021), and all booms of the Fushun Tianhu Bridge were replaced in 2015 (Yu et al., 2019).

Despite numerous examples of boom replacement projects at home and abroad, limited research has been conducted on the technology and theory of boom replacement in suspension bridges. Yu Zh et al. (Yu et al., 2019) simulated the boom replacement process using the temporary boom method in finite element software in 2019. Their study revealed a significant 38.9% reduction in the tensile force of the temporary boom in the three-point replacement method compared to the single-point replacement method. However, the temporary boom in the five-point replacement method exhibited a 9.9% lower tensile force than that in the three-point replacement method. With only the adjacent booms on both sides of the replacement boom greatly affected during the replacement. To address the long construction duration associated with boom replacement, Yuan et al. (2021) designed and developed a self-balancing tensioning and thrusting equipment specifically for boom replacement construction. The equipment was successfully applied in the boom construction of the Runyang Bridge, effectively minimizing the interference of displacement and internal forces caused by boom replacement. However, this equipment is only suitable for bridges with steel box beams and lifting lug anchor plates, and pin control should be reserved. Wang et al. (2015) in response to the defects observed on the booms of the Shantou Bay Bridge, conducted a replacement test on representative booms. And proposed a replacement construction scheme through discussions on the scheme and method of boom replacement. Huang and Zhang. (2021) compared the construction plans for replacing long and short booms and found that the method with a single lifting point for releasing the tensile force, followed by simultaneous graded tensioning and dismantling of the old boom is generally applicable for replacing short booms. The multi-point lifting scheme, although suitable for replacing long booms and minimizing impacts on bridge

alignment, has disadvantages such as requiring numerous temporary booms, heavier construction workloads, and higher costs. Zeng et al. (2016) thought that the stress condition of short booms is more complex than that of long booms and provided insights into the stress transmission mode and damage mechanism of booms. As short booms can experience a combination of static and dynamic loads, separate calculation of their dynamic characteristics becomes necessary. Liu et al. (2023) used the method of matrix analysis and transforming multiple objectives into a single objective to determine the adjustment amount of boom length, adjust the boom force and actual deck elevation. Then achieve the comparison and selection of boom replacement schemes for a steel truss suspension bridge. Three-dimensional finite element analyses were employed by Süleyman et al. (2023) for both inclined and vertical boom configurations of the Bosporus Suspension Bridge. Fan et al. (2023) presented a robustness-based condition evaluation framework for the overall structure. The evaluation processes of three conditions are further presented in accordance with the suspension bridge, and the variation in the potential risk of accidents induced by cable failure is shown intuitively through the evaluation results.

The design service life of bridges is generally long, and in such a long service period, the performance of bridges will inevitably deteriorate due to the harsh environment, especially for long-span suspension bridge. In order to maintain the safe operation of the bridge, the research on boom replacement has also received more and more attention. It has become an important part of scientific maintenance, which is of great significance for scientific guidance of bridge maintenance. From the above analysis, it can be clearly seen that the cable system is an extremely important part of the suspension bridge, the boom configuration has a positive impact in terms of vertical displacement and internal forces obtained. Thus the safe operation of the bridge structure has very high requirements for the accuracy of the boom replacement process. The full bridge structure and components will all respond to changes with the tension of the temporary boom. Therefore, the study on the adaptability of boom replacement methods, the optimization in the process of boom replacement with various lengths, as well as the response analysis of the structure and components is crucial.

2 Adaptability analysis of boom replacement methods

This paper focuses on studying the adaptability of boom replacement methods and the response of the bridge structure, using a sea-crossing bridge as a case study. The bridge under investigation is a three-span earth-anchored double-deck suspension bridge located in the Yellow Sea area of China, spanning from the east to the west. The bridge was completed and opened to traffic in 2015. The computed span of the bridge is 180 m + 460 m+180 m = 820 m. The bridge features two main cables, each consisting of 7747 high-strength galvanized parallel steel wires with a diameter of 5.2 mm. Meanwhile, a total of 158 hanging points is distributed along the bridge, with two booms arranged at each hanging point. The ordinary flexible boom consists of 73 high-strength galvanized steel wires with a diameter of 7 mm, covered with a protective layer made of PE material. In addition, central buckle stay cables are installed at the mid-span. The bridge incorporates a portal tower that stands 112.31 m high. The column of the tower is designed as
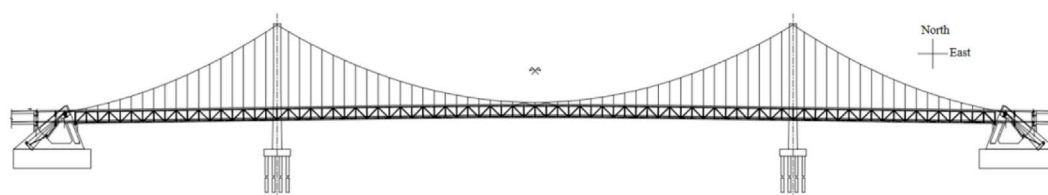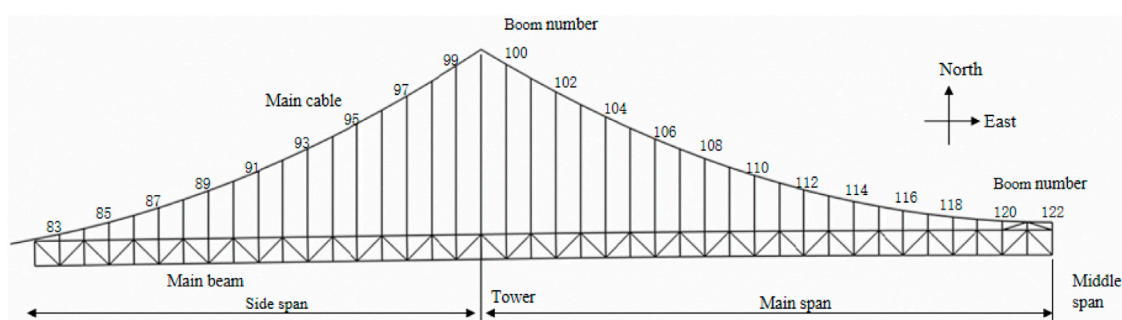
FIGURE 1
The sea crossing suspension bridge.

FIGURE 2
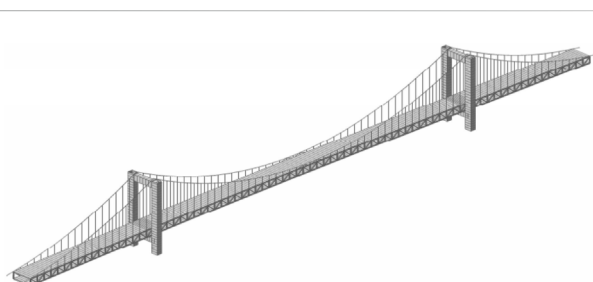Unit number and spatial location map of boom.

FIGURE 3
Model drawing of the suspension bridge.

a "D"-shaped hollow reinforced concrete structure with a variable section, while the upper crossbeam is constructed using prestressed concrete. The main steel truss beam is 10 m high, and all structural members are constructed with closed box sections. Moreover, the double-deck system of the bridge consists of orthotropic plates, with a 55 mm layer of asphalt paving on the steel plates. The deck is designed as a one-way four-lane system, with the upper layer facilitating traffic from east to west and the lower layer accommodating traffic from west to east. The overall configuration of the bridge is illustrated in Figure 1. Unit number and spatial location of the booms are shown in Figures 2, 3. The short boom analyzed in the paper is No. 122, with a length of 3.13 m, the medium boom is No. 93, with a length of 35.40 m and the long boom is No. 102, with a length of 56.75 m.

The full bridge model was established using MIDAS Civil finite element software, incorporating appropriate simplifications and equivalences to ensure the feasibility and accuracy of the finite element analysis. Specifically, the main cable and booms were modeled as the equivalent section of 1860 steel wire in tension only. The bridge tower was modeled as a C50 concrete box hollow beam element with an equivalent section. The double-layer main beam was modeled as a non-closed box section, while the vertical and inclined web members were represented using beam elements. Correctly establishing the boundary conditions was crucial to ensure that the deformation and displacement of the bridge closely matched the actual situation. General supports were placed at both ends of the main beam to restrict vertical and transverse bridge displacement, while releasing longitudinal constraints to enable free movement and stress release. Besides, the stress state of the truss was accurately simulated by releasing beam end constraints for the vertical and inclined web members. The force transmission relationship between the main beam and the boom was established through rigid connections, consolidating the bottom of the tower and the two ends of the main cable. To ensure result accuracy, an independent model analysis method for nonlinear analysis was adopted during the operational analysis stage.

3 Single-point boom replacement method

3.1 Replacement of short boom at mid-span

Currently, the temporary support method, temporary basket-hanging method, and temporary boom method are commonly employed for boom replacement, each with its own set of advantages and disadvantages. In this study, the temporary boom
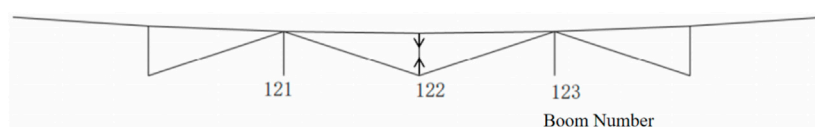
FIGURE 4
Schematic diagram of single-point tensioning of mid-span and short booms.
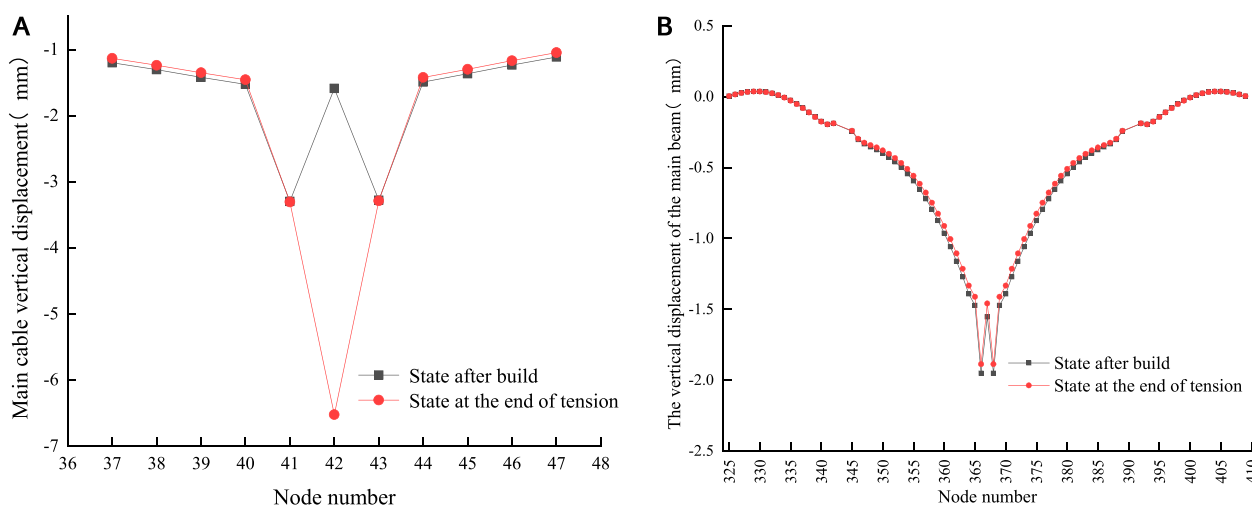

FIGURE 5
(A) Vertical displacement of the main cable nodes when the short boom at the mid- span is uniformly tensioned by the single-point method **(B)**. Vertical displacement of the main beam on the upper floor when the short boom at the mid-span is uniformly tensioned by the single-point method.

TABLE 1 Variation of the axial force in the uniform tension of the short boom at the mid-span (KN).

Tensioning process	Initial axial force	First tension	Second tension	Third tension	Fourth tension	Fifth tension	Total axial force of temporary boom
tension	1438.42	300	300	300	300	270	
remaining axial force	1438.42	1142.595	846.784	550.97	255.17	0.00	1470
changes in the axial force of the boom	0.00	−295.83	−295.81	−295.81	−295.80	−255.17	

method was selected as it is widely utilized in practical applications. The fundamental principle of this method involves utilizing a temporary stress system to transfer the tensile force from the boom undergoing replacement, enabling the removal of the old boom and installation of the new one. Subsequently, the tensile force is once again transferred from the temporary stress system to the newly installed boom.

Besides, this study focused on the short boom located at the mid-span as the research object, analyzing the impact of boom replacement with the single-point method on the bridge. To accurately capture the response of each bridge component during the boom replacement process, it was necessary to ensure the temporary boom was evenly tensioned in stages. Therefore, the tension of the temporary boom was simulated by applying opposite

node loads at both end nodes of the boom undergoing replacement using the MIDAS Civil finite element software (as shown in Figure 4).

The axial force of the temporary boom, tensioned in stages, is presented in Table 1. Upon completion of the tensioning process, the total axial force of the temporary boom exhibited a slight increase of 2.20% compared to the initial axial force of the replaced boom. The replacement of the short boom using the single-point method had a minimal impact on the vertical displacement of the main beam. Following the tensioning of the temporary boom, only the node of the main cable at the replaced boom experienced a downward displacement of −2.7 mm (as shown in Figure 5). Other nodes remained largely unaffected, and the cable maintained its alignment without significant changes. The vertical displacement

TABLE 2 Axial force change when a boom with a side span of medium length is tensioned by the single-point method (KN).

Tensioning process	Initial axial force	First tension	Second tension	Third tension	Fourth tension	Fifth tension	Total axial force of temporary boom
tension	1390.54	383.7	383.7	383.7	383.7	383.7	
remaining axial force	1390.54	1112.31	834.11	555.94	277.79	0.00	1918.5
changes in the axial force of the boom	0.00	−278.22	−278.20	−278.17	−278.15	−277.79	

FIGURE 6
(A) Vertical displacement of the main cable at the side span. Figure 6 **(B)** The vertical displacement of the main beam on the upper floor when the mid-length boom of the side span is tensioned by the single-point method.
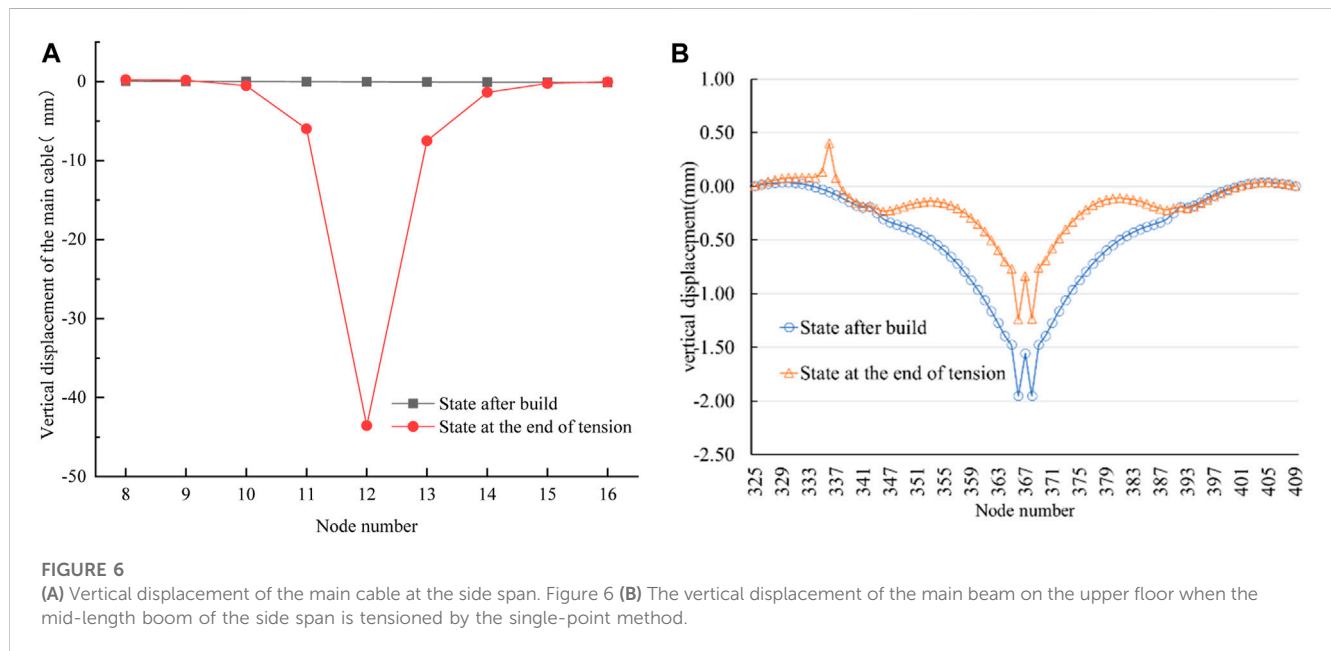
of the main cable and beam at the mid-span experienced a sudden change due to the central buckle stay cables set.

## 3.2 Replacement of medium boom at side span

Similarly, opposite node loads are applied for the replacement of medium-length booms. The staged tensioning of the temporary boom is shown in Table 2, indicating the corresponding axial forces. Since the upper node of the temporary boom is connected to the main cable, when the temporary boom is tensioned, the axial force applied to its upper node will also be transmitted to the main cable. According to the vertical displacement of the main cable node (Figure 6A), node 12 exhibited a significant downward displacement of −43.51 mm, while nodes 11 and 13 experienced smaller displacements of −5.97 mm and −7.45 mm, respectively. Other cable nodes showed minimal displacement. It can be concluded that the main cable nodes at the boom undergoing replacement and the adjacent boom will be significantly affected during the replacement of the medium boom using the single-point method. However, the impact on the main cable nodes at other locations is relatively minor. Meanwhile, as the upper node (node 12) of the replaced boom is connected to the main cable, its applied

force combines the remaining axial force of the replaced boom and the tensioning axial force of the temporary boom, resulting in a downward movement of the main cable node. Secondly, at the end of the tensioning process, the axial force of the temporary boom slightly exceeded the initial axial force of the replaced boom. This increased force disrupted the initial equilibrium state of the main cable, leading to a significant downward displacement of the main cable node.

The vertical displacement of the upper main beam is shown in Figure 6B. The main beam displacement underwent an abrupt change at the position of the temporary boom, resulting in an upward displacement of 0.45 mm. At the same time, an upward displacement of 0.72 mm occurred at the mid-span, which is the maximum displacement at the main beam of the bridge. However, the main beam of the east side span remained unaffected. In addition, the geometric shape of the main beam in the main span underwent significant changes following tensioning, deviating from its finished bridge state. Due to the substantial rigidity of the main beam, the section at the temporary boom experienced an upward movement, thereby altering the internal force transmission mechanism to some extent. Moreover, the main beam in the main span also exhibited an upward displacement influenced by the integrity of the main beam.

TABLE 3 Variation of the axial force in the uniform tension of the long booms of the main span (KN).

Tensioning process	Initial axial force	First tension	Second tension	Third tension	Fourth tension	Fifth tension	Total axial force of temporary boom
tension	0.00	440.6	440.6	440.6	440.6	440.6	
remaining axial force	1390.946	1112.725	834.560	556.457	278.420	0.000	2203
changes in the axial force of the boom	1390.946	−278.22	−278.17	−278.10	−278.04	−278.42	
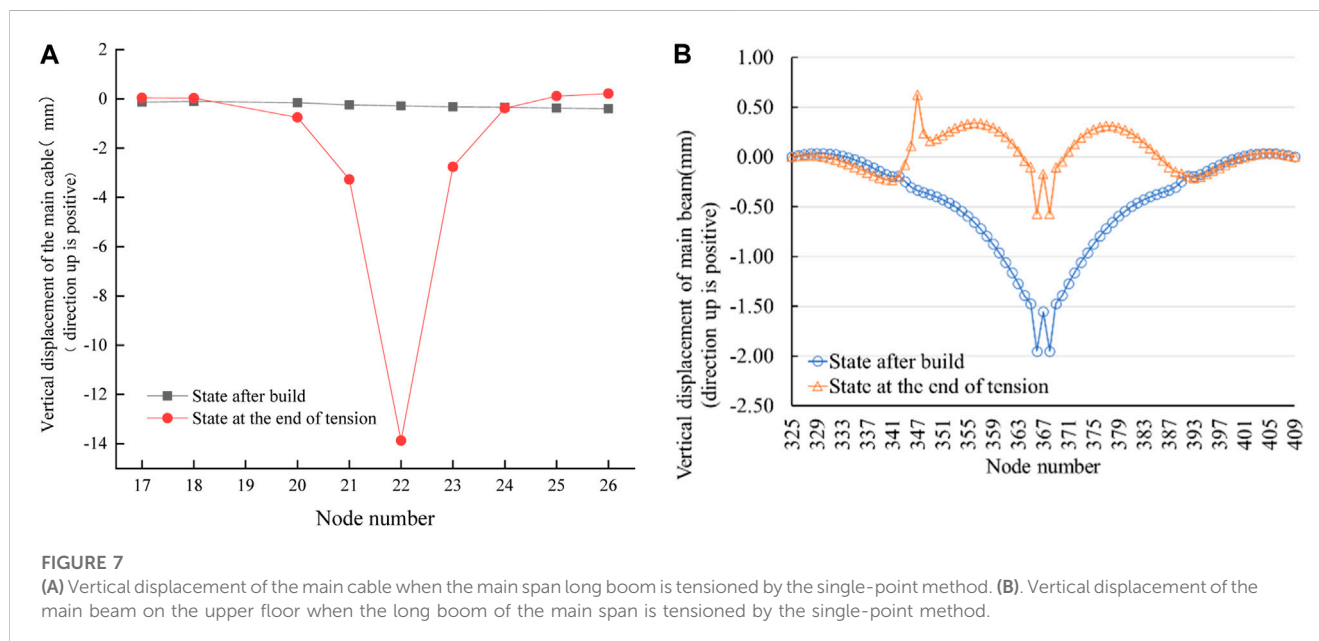
FIGURE 7
(A) Vertical displacement of the main cable when the main span long boom is tensioned by the single-point method. **(B)**. Vertical displacement of the main beam on the upper floor when the long boom of the main span is tensioned by the single-point method.

3.3 Replacement of long boom at the main span

Similarly, the long boom underwent staged tensioning during the displacement. The applied tension and the remaining axial force throughout the tensioning process is shown in Table 3. The axial force of the replaced boom was uniformly reduced during the uniform tensioning process, which aligns with the observations made during the replacement of the short and medium booms. This consistency indicates that the axial force of the replaced boom exhibited a linear change pattern when the single-point method was employed for replacing short, medium, and long booms. Furthermore, at the end of the tensioning process for the long boom replacement, the total axial force of the temporary boom significantly exceeded the initial axial force of the replaced boom by 812.05 KN, about 58.38% of the initial axial force.

In the case of replacing the long boom using the single-point method, the main cable node located at the position of the replaced boom experienced a significant downward displacement of −70 mm at the end of the temporary boom tensioning (Figure 7A). Meanwhile, the main cable node at the first adjacent boom underwent a downward displacement of −16.64 mm, while the second adjacent boom experienced a downward displacement of −3.96 mm. However, the main cable nodes that are farther away remained largely unaffected. These findings demonstrate

that the vertical displacement and the extent of influence were relatively substantial, indicating that the single-point method is not suitable for replacing long booms.

The vertical displacement of the upper main beam is shown in Figure 7B, showing an abrupt change in displacement at the location of the temporary boom, resulting in an upward displacement of 0.96 mm. Besides, it is observed that the main beam in the main span exhibited an upward movement compared to its finished bridge state. The main beam in the east side span remained unaffected, while the alignment of the main beam in the main span underwent significant changes after tensioning. In particular, a maximum displacement of 1.38 mm occurred at the mid-span. This discrepancy in displacement can possibly be attributed to the redistribution of internal forces and changes in the transmission mechanism of the main beam during the replacement, causing the displacement at the mid-span to be greater at the temporary boom.

3.4 Optimization indicator -force transmission efficiency of temporary boom

In the case of boom replacement using the temporary boom method, theoretically, the axial force of the temporary boom should be equal to the initial axial force of the replaced boom in its finished state. However, the results of numerical simulation analysis indicate

FIGURE 8
(A, B) Spatial location map of boom.
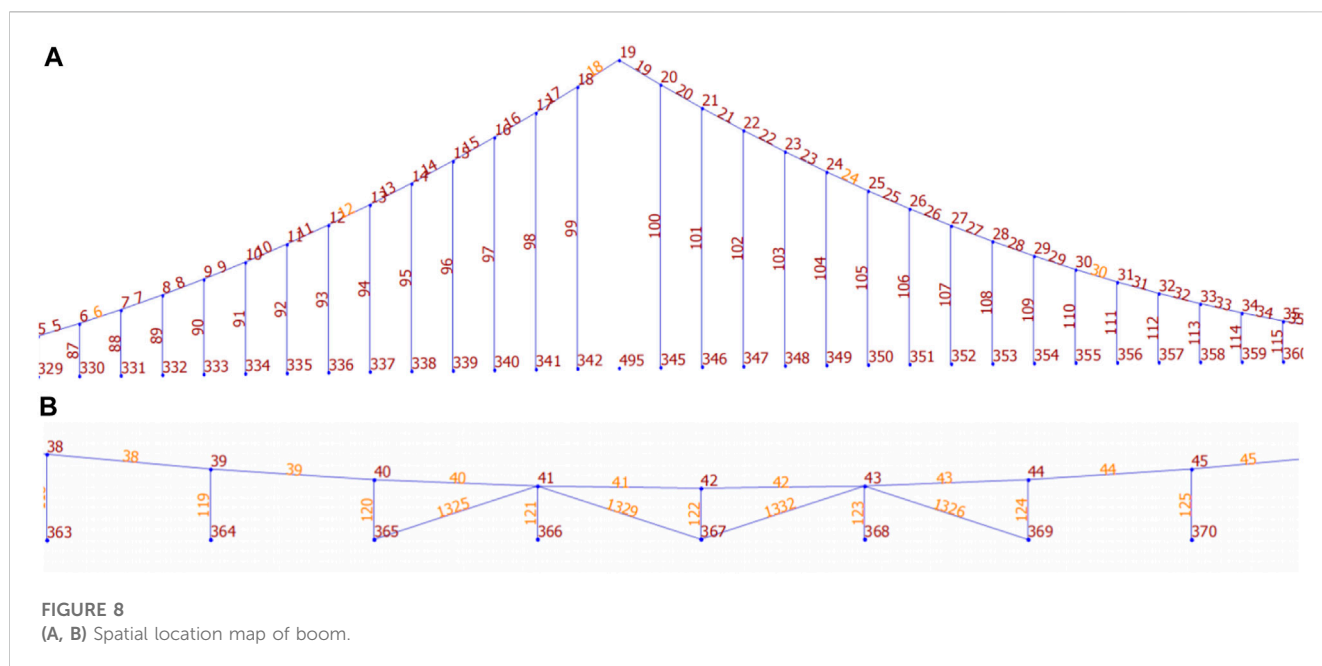
that they are not equal. This finding aligns with the conclusions drawn by Yu Zhanglong (Yu et al., 2019) in a numerical simulation of a suspension bridge. It was suggested that this phenomenon is primarily influenced by the overall stiffness of the bridge and the boom replacement method employed. Specifically, a higher overall stiffness of the bridge results in a lower force transmission efficiency of the temporary boom during the boom replacement process.

To accurately study the influencing factors of force transmission efficiency, the computational formula of force transmission efficiency was proposed to quantitatively analyze the force transmission efficiency:

$$E_{ft} = \frac{N_f}{Nt_{\max}} \times 100\% \qquad (1)$$

Where E_{ft} is the force transmission efficiency, N_f is the axial force of the finished state, and $Nt_{\max}$ is the maximum axial force of temporary boom.

The force transmission efficiency can be influenced by various factors, including the length of the boom, the replacement method used, and the initial axial force of the boom. The relationship between force transmission efficiency and boom length was studied with the single-point method, and numerical simulation analysis was conducted specifically on main span booms using the reference stress free state method. This approach ensured a continuous variation in boom length. Refer to Figures 2, 8 for details. Besides, the study on force transmission efficiency involved the analysis of 23 booms ranging from the short boom in the mid-span to the long boom adjacent to the tower in the west. The corresponding data for analysis are shown in Table 4.

As shown in the relationship between force transmission efficiency and length of the boom (Figure 9), the force transmission efficiency of the shortest boom reached 98.26%, while booms with lengths less than 10 m maintained a force transmission efficiency above 90%. In contrast, the force transmission efficiency of booms with lengths exceeding 50 m

decreased to below 70%. This trend indicates that the reduction in force transmission efficiency increased with increasing boom length, underscoring the high applicability of the single-point method for replacing short booms. Based on these results, booms with lengths under 10 m in the sea crossing suspension bridge can be defined as short booms. At the same time, it was observed that the ratio of boom length with a force transmission efficiency over 90% to the rise of the main cable was smaller than the rise-span ratio of 0.1522. Therefore, booms with a ratio of boom length to rise of main cable smaller than the rise-span ratio can also be defined as short booms.

To study the adaptability of different boom replacement methods, the force transmission efficiency of temporary boom is regarded as the main optimization. Meanwhile, the moves in the vertical displacement of the main cable, the vertical displacement of the main beam, and the tensioning workload during the boom replacement process are comprehensively considered to seek the optimal replacement method for booms of different lengths.

4 Three-point boom replacement method

4.1 Replacement of short boom at mid-span

In the case of replacing the short booms in the mid-span with the three-point method, the axial force during uniform tensioning of the temporary booms is shown in Table 5. At the end of tensioning process, the total axial force of the No. 122 temporary boom was lower than its initial axial force, resulting in a force transmission efficiency of 103.69%. This efficiency is 5.84% higher than that achieved with the single-point method. There is a coupling effect when three temporary booms were tensioned simultaneously. As a result, the axial forces of the No. 121 and No. 123 temporary booms exceeded their initial values, and the excess axial force may be

TABLE 4 Force transmission efficiency of temporary booms.

No.	Unit number	Boom length (m)	Initial axial force (KN)	Axial force of temporary boom (KN)	Boom length/Main cable height	Force transmission efficiency (%)
1	122	3.13	1410.22	1435.20	0.0447	98.26
2	121	3.26	920.60	995.85	0.0466	92.44
3	120	3.66	1380.26	1432.29	0.0524	96.37
4	119	4.33	1392.82	1457.82	0.0619	95.54
5	118	5.27	1390.32	1466.51	0.0752	94.80
6	117	6.47	1392.66	1487.66	0.0924	93.61
7	116	7.94	1390.37	1504.96	0.1134	92.39
8	115	9.67	1392.58	1542.58	0.1382	90.28
9	114	11.68	1390.42	1557.95	0.1668	89.25
10	113	13.95	1392.47	1597.47	0.1993	87.17
11	112	16.49	1390.46	1624.96	0.2356	86.57
12	111	19.30	1392.35	1672.35	0.2757	83.14
13	110	22.38	1390.5	1710.07	0.3197	81.31
14	109	25.73	1392.22	1772.22	0.3675	78.56
15	108	29.34	1390.53	1809.83	0.4192	76.83
16	107	33.23	1392.09	1872.09	0.4748	74.36
17	106	37.39	1390.55	1926.35	0.5342	72.19
18	105	41.82	1391.95	2091.95	0.5975	66.54
19	104	46.52	1390.55	2102.96	0.6646	66.12
20	103	51.50	1391.86	2141.86	0.7357	64.98
21	102	56.75	1390.95	2202.90	0.8107	63.14
22	101	62.27	1393.46	2313.46	0.8895	60.23
23	100	68.06	1397.00	2583.21	0.9723	54.08
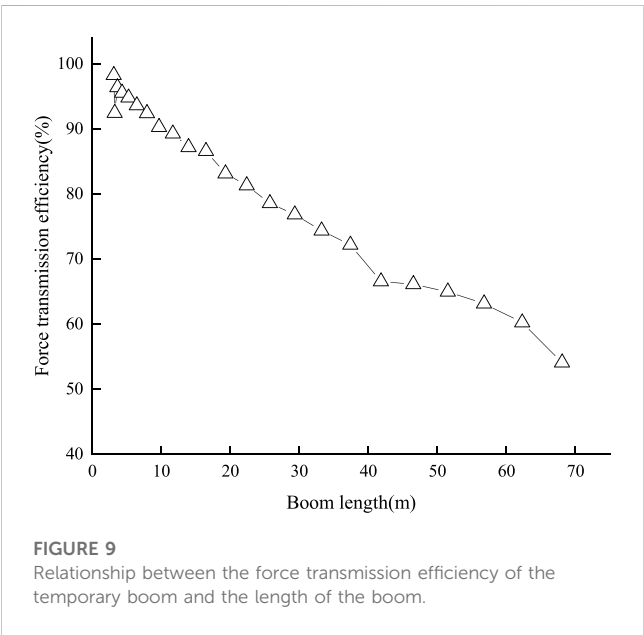
FIGURE 9
Relationship between the force transmission efficiency of the temporary boom and the length of the boom.

redistributed to the No. 122 temporary boom. Thus causing the total axial force of the No. 122 temporary boom to be less than its initial axial force. The reduction in the total axial force of the No. 122 temporary boom at the end of tensioning amounted to 110 KN. That indicates a minimal advantage in terms of reducing the axial force of the temporary boom compared to the single-point method. However, the three-point method necessitates significantly more workload and construction facilities.

In the case of replacing the short booms with the three-point method, the main cable node connecting the No. 122 boom experienced a downward displacement of −2.78 mm (Figure 10A). The maximum vertical displacements of the main cable nodes occurred at the No. 121 and No. 123 booms, both measuring −7 mm. Besides, the main beams in the main span underwent an upward displacement, resulting in a slight change in their geometric shape after tensioning (Figure 10B). The vertical displacements of the upper main beam nodes at the No. 121–123 booms were 0.42 mm, 0.35 mm, and 0.42 mm, respectively. These displacements indicate an increase in upward displacement compared to the one-point method of boom replacement. This indicates the replacement of short booms

TABLE 5 Tensioning process during replacement of short booms at mid-span using the three-point method (KN).

Unit number	Initial axial force	First tension	Second tension	Third tension	Fourth tension	Fifth tension	Total axial force
121	920.60	300	300	300	200	0	1100
122	1410.22	300	300	300	300	160	1360
123	920.60	300	300	300	200	0	1100

FIGURE 10
(A) Vertical displacement variation of the main cable node when the mid-span and short booms are tensioned by the three-point method. **(B)**. Vertical displacement of the main beam on the upper floor when the mid-span and short booms are tensioned by the three-point method.
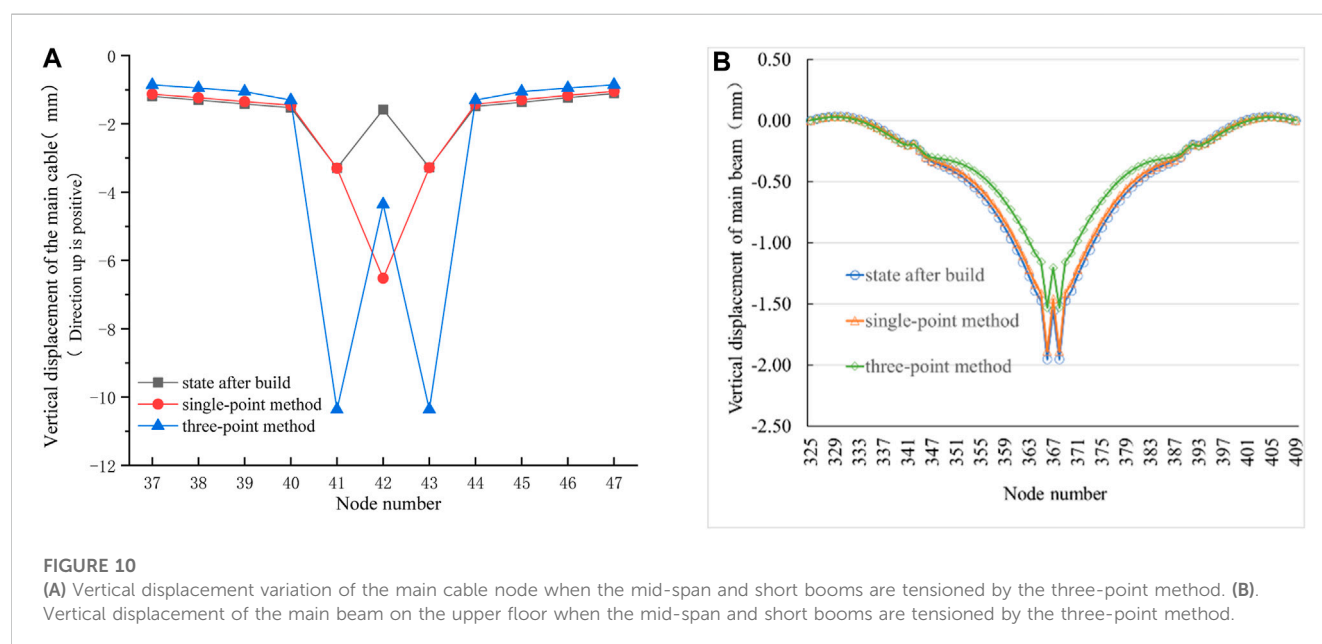
within the three-point method can introduce a certain level of disturbance to the main beams in the main span.

4.2 Replacement of medium boom at side span

In the case of replacing the medium booms (No. 92, 93 and 94 at side span) with the three-point method, the axial forces during the uniform tensioning of the temporary booms are shown in Table 6. At the end of tensioning, the total axial force on the No. 93 temporary boom amounted to 1480 KN. This value is 438 KN lower compared to the single-point method, resulting in a force transmission efficiency of 93.95%. This efficiency is 21.47% higher than that achieved with the single-point method. These findings indicate that the three-point method offers certain advantages in reducing the axial force and improving the force transmission efficiency of the temporary boom when compared to the single-point method.
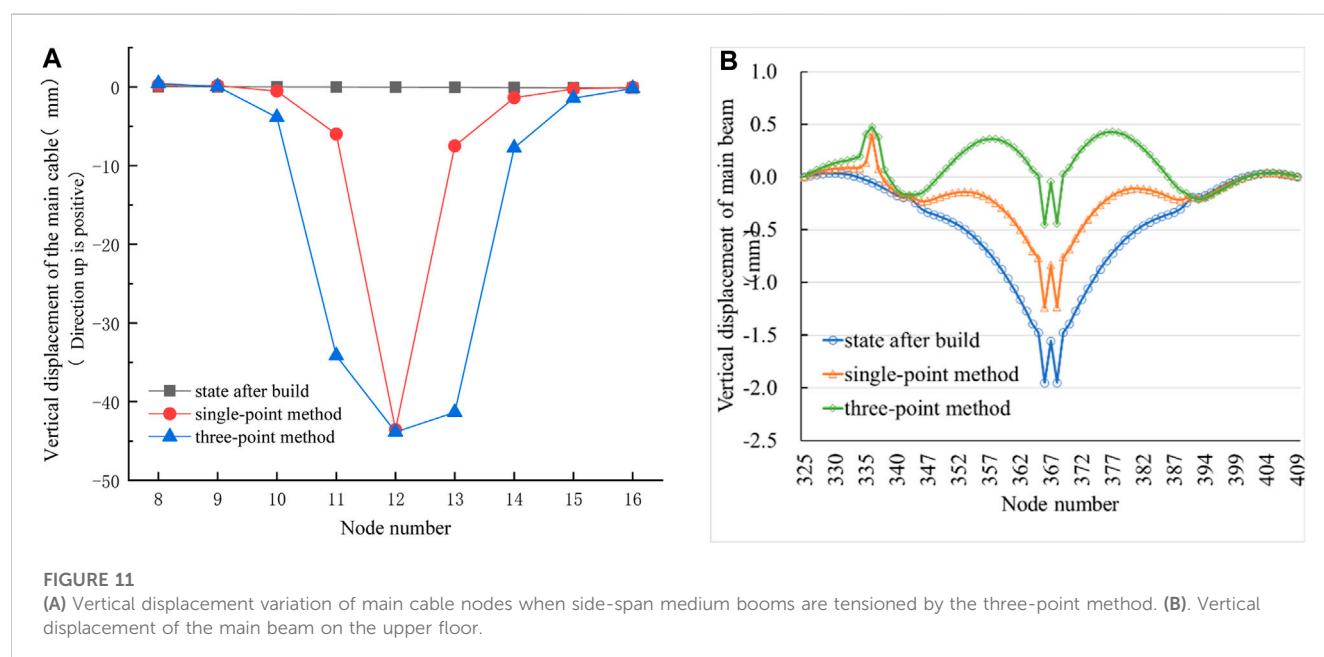
In the case of medium boom replacement with the three-point method, the main cable nodes at the three temporary booms experienced downward movements as shown in Figure 11A. Specifically, the main cable node at No. 93 exhibited the largest downward displacement of −43.7 mm, which is 0.02 mm less than that in the single-point method. The vertical displacement of the

main cable nodes at No. 92 and No. 94 booms was −34.13 mm and −41.28 mm respectively. Generally, the affected range of the main cable nodes is expanded when compared to the single-point method. The vertical displacement of the upper main beam is shown in Figure 11B. An abrupt change in displacement occurred at the location of the replaced boom, resulting in an upward displacement of 0.53 mm. The main beams in the main span exhibited a complete upward movement, accompanied by significant variations in geometric shape. Moreover, a maximum upward displacement of 1.51 mm occurred at the main beam at the mid-span. In comparison, the single-point method yielded a displacement of 0.45 mm at the location of the abrupt change and a displacement of 0.72 mm at the main beam of the mid-span. These observations suggest that the three-point method has a greater impact on the vertical displacement and geometric shape of the main beam compared to the single-point method. Neither of the two replacement methods has affected the geometric shape of the main beam at the east side span.

The force transmission efficiency of the three-point method is shown in Table 7. It is observed that the force transmission efficiency of a single temporary boom gradually decreased as the boom length increased. The transmission efficiencies of booms with lengths of 12.56 m and 15.71 m exceeded 98%, while booms with lengths below 50 m maintained a force transmission efficiency of over 90%. Therefore, the three-point method demonstrates high

TABLE 6 Three-point tensioning of temporary booms with medium booms in side span (KN).

Unit number	Initial axial force	First tension	Second tension	Third tension	Fourth tension	Fifth tension	Sixth tension	Total axial force
92	1392.12	300	300	300	300	200	0	1400
93	1390.54	300	300	300	300	200	80	1480
94	1392.01	300	300	300	300	200	0	1400

FIGURE 11
(A) Vertical displacement variation of main cable nodes when side-span medium booms are tensioned by the three-point method. (B). Vertical displacement of the main beam on the upper floor.

TABLE 7 Force transmission efficiency of the side-span boom using the three-point method.
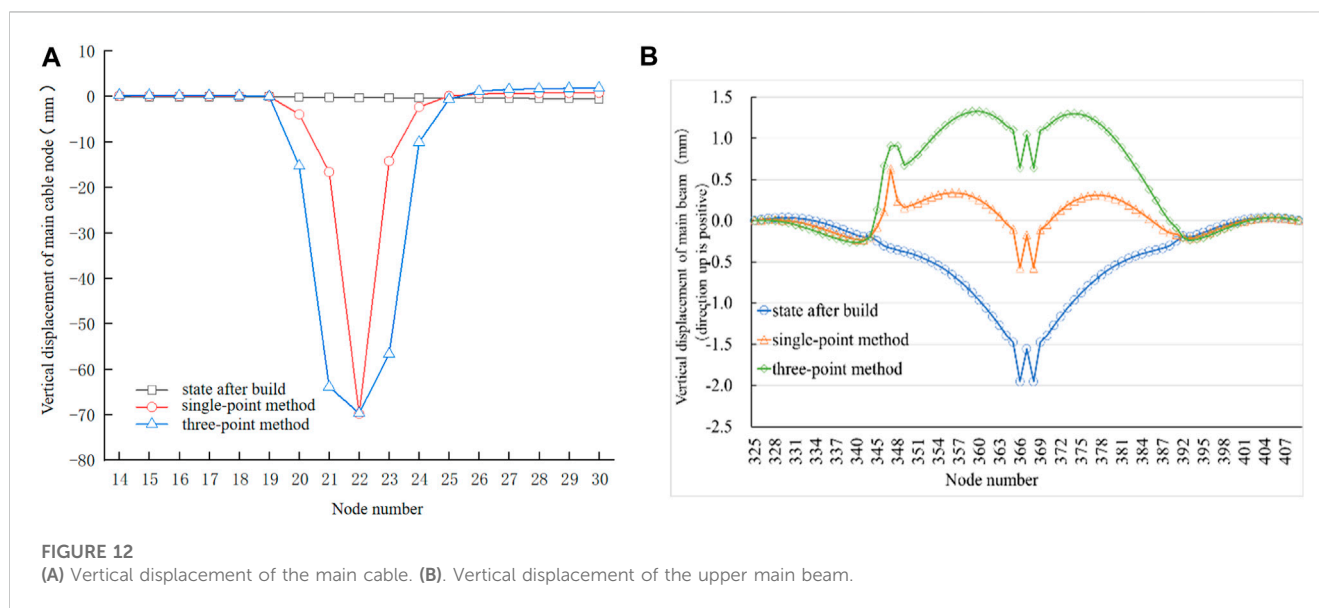
Serial number	Unit number	Boom length(m)	Initial axial force (KN)	Temporary boom axial force (KN)	Boom length/Main cable height	Force transmission efficiency (%)
1	87	12.56	1390.44	1410	0.1794	98.61
2	88	15.71	1392.44	1410	0.2244	98.75
3	89	19.12	1390.48	1420	0.2731	97.92
4	90	22.79	1392.28	1430	0.3256	97.36
5	91	26.73	1390.51	1435	0.3819	96.90
6	92	30.93	1392.12	1460	0.4419	95.35
7	93	35.40	1390.54	1480	0.5057	93.96
8	94	40.13	1392.01	1500	0.5733	92.67
9	95	45.13	1390.69	1530	0.6447	90.90
10	96	50.40	1392.31	1560	0.7199	89.25

applicability for booms ranging from 10 m to 50 m in length. Based on these findings, booms within the range of 10–50 m on the sea crossing suspension bridge can be defined as medium booms. Furthermore, the definition of a medium boom can also be determined by considering the ratio of boom length to the rise of the main span. A boom with a ratio of boom length to rise of the main span that falls between 1 and 4.5 times the rise-span ratio can be classified as a medium boom. As well as booms with lengths

TABLE 8 Axial force change of temporary boom in replacement of long boom at main span using the three-point method (KN).

Unit number	Initial axial force	First tension	Second tension	Third tension	Fourth tension	Fifth tension	Sixth tension	Total axial force of temporary boom
101	1393.46	300	300	300	300	300	0	1500
102	1390.95	300	300	300	300	300	35	1535
103	1391.86	300	300	300	300	300	0	1500

FIGURE 12
(A) Vertical displacement of the main cable. (B). Vertical displacement of the upper main beam.

exceeding 50 m and a ratio of boom length to rise of the main span exceeding 4.5 times the rise-span ratio are designated as long booms.

4.3 Replacement of long boom in the main span

In the case of replacing the long booms in the main span (No. 101, 102 and 103 boom close to the west bridge tower) using the three-point method, the axial force during the uniform tensioning of the temporary booms is shown in Table 8. At the end of tensioning, the total axial force on the No. 102 temporary boom was 1535 KN, which is 668 KN lower than that in the single-point method. Furthermore, the transmission efficiency is 90.62%, 27.48% higher compared to the single-point method. These results indicate that the three-point method offers advantages in reducing the axial force and enhancing the force transmission efficiency of the temporary boom, in contrast to the single-point method.

According to the vertical displacement of the main cable nodes (Figure 12A), the main cable nodes at No. 101–103 booms experienced significant downward displacement during the replacement of long booms using the three-point method. Specifically, the main cable node at No. 102 boom exhibited the largest displacement, reaching −70 mm, which is consistent with the displacement observed in the single-point method. Additionally, the vertical displacements of the main cable nodes at No. 101 and No.

103 booms were −63.64 mm and −56.36 mm, respectively. In addition, the main cable nodes on both sides of the temporary booms also exhibited downward movement to some extent. The displacement at the main cable node of the No. 100 boom was −15.14 mm, while that of the node at the No. 104 boom was −9.74 mm, both of which are greater than the displacements observed in the single-point method. Compared with the single-point method, the affected range of the main cable node increased, but the displacement has minimal impact on the main cable nodes located far from the temporary booms.

The vertical displacement of the upper main beam nodes is shown in Figure 12B. It can be seen that the main beams in the main span underwent significant upward displacement and experienced notable changes in geometric shape after tensioning. The main beam at the mid-span exhibited the maximum upward displacement of 2.6 mm, which is 2.5 mm larger than that observed in the single-point method. Simultaneously, there was an abrupt change in vertical displacement at the position of the temporary booms. Specifically, the displacement of the main beam at the No. 102 boom was 1.26 mm, while that at the No. 101 and No. 103 booms were 1.25 mm and 1.05 mm, respectively. From these findings, it can be concluded that the three-point method has a greater effect on the displacement and geometric shape of the main beam compared to the single-point method. However, neither of the two replacement methods has an impact on the geometric shape of the main beams in the side span.

TABLE 9 Five-point method process of medium booms in side span (KN).

Unit number	Initial axial force	First tension	Second tension	Third tension	Fourth tension	Fifth tension	Total axial force of temporary boom
91	1390.51	300	300	300	300	0	1200
92	1392.12	300	300	300	300	0	1200
93	1390.54	300	300	300	300	100	1300
94	1392.01	300	300	300	300	0	1200
95	1390.69	300	300	300	300	0	1200

5 Five-point boom replacement method

5.1 Replacement of medium boom in side span

In the case of replacing the medium booms (No. 91–95 booms in side span) using the five-point method, the axial force during the uniform tensioning of the temporary booms is shown in Table 9. At the end of tensioning, the total axial force on the No. 93 temporary boom amounted to 1300 KN, which is 619 KN and 180 KN lower than that of the single-point method and the three-point method, respectively. Furthermore, the force transmission efficiency reached 106.96%, surpassing the three-point method by 10.01% and the single-point method by 34.48%. These results indicate that the interaction among multiple temporary booms in the five-point method significantly reduces the tension experienced by each individual temporary boom, thus reducing the requirements for the material properties and mechanical strength of the temporary booms.

The vertical displacement of main cable nodes during the displacement of medium booms using the five-point method is shown in Figure 13A. It is found that the nodes at the temporary booms experienced significant downward movement. Specifically, the No.12 node exhibited the largest displacement of −43.44 mm, which is comparable to the displacements of −43.39 mm and −43.70 mm observed in the single-point method and the three-point method, respectively. It is evident that the three boom replacement methods yield similar effects on the vertical displacement of the main cable nodes at the replaced booms. Meanwhile, the first cable nodes immediately adjacent to both sides of the temporary booms also exhibited slight downward movement in the five-point method, signifying an expanded range of influence compared to the three-point method.

The vertical displacement of the upper main beam is presented in Figure 13B. The main beam at the position of the temporary booms exhibited a sudden change in displacement. Specifically, the main beam at the No. 93 boom had a larger displacement of 0.60 mm. Concurrently, it is observed that the main beams in the main span collectively moved upward and underwent significant changes in geometric shape. Besides, the maximum displacement of main beams in the mid-span reached 2.16 mm. When compared to the single-point method, the displacement of the main beam at the No. 93 boom increased by 0.15 mm, and the displacement of the main beam in the mid-span increased by 1.46 mm. In contrast, when

compared to the three-point method, the displacements at these two locations increased by 0.07 mm and 0.67 mm, respectively. These observations indicate that the five-point method has the most pronounced effect on the displacement and geometric shape of the main beams throughout the entire bridge when replacing medium booms in the side span. And none of the three replacement methods have any impact on the geometric shape of main beams at the east side span.

In summary, the five-point method demonstrates notable advantages in reducing the tension of temporary booms and significantly increasing the force transmission efficiency compared to the one-point method and the three-point method for replacing medium booms in the side span. However, it also introduces greater disturbance to the main cable and main beam, particularly to the main cable. Overall, the superiority of the five-point method in medium boom replacement is not clearly evident when compared to the three-point method.

5.2 Replacement of long boom at main span

The axial force during the uniform tensioning of the temporary booms in replacement of the long booms in the main span (No. 100–104 booms) using the five-point method is shown in Table 10. At the end of tensioning, the total axial force of No. 102 temporary boom was 1450 KN, and the force transmission efficiency was 95.93%, which is 32.79% higher than that in the single-point method and 5.32% higher than that in the three-point method. According to the vertical displacement of the main cable nodes shown in Figure 14A, the temporary booms in the five-point method replacement of long booms result in a significant downward displacement of the main cable nodes. Specifically, the main cable node at the No. 101 boom exhibited the largest vertical displacement of −70.85 mm, followed by the main cable node at the No. 102 boom with a displacement of −69.38 mm. Comparing the data with the single-point method and the three-point method, it is observed that the maximum displacement of the main cable nodes caused by the five-point method is the same as that of the single-point method and the three-point method. However, the notable difference lies in the location of the maximum displacement, which occurs at the main cable node of the No. 102 boom for both the single-point and three-point methods. In addition, the three replacement methods exhibited varying degrees of influence on the main cable nodes. Specifically, the single-point method had the smallest affected area, resulting in significant downward
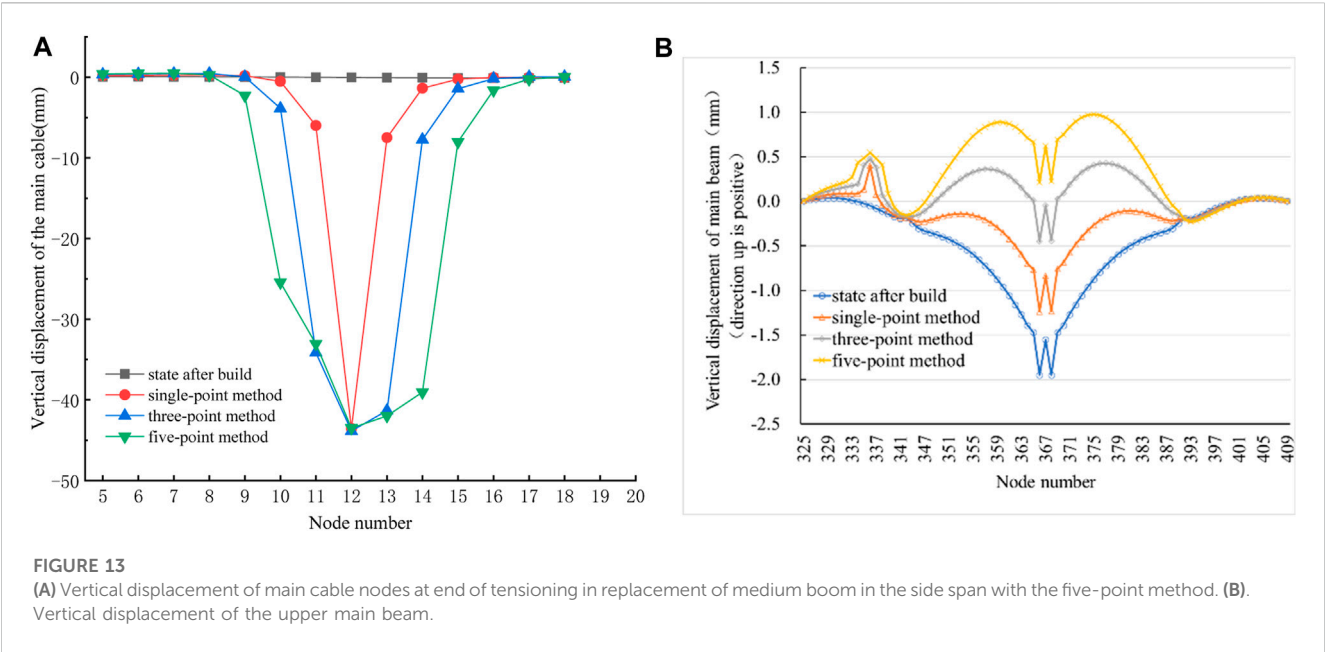
FIGURE 13
(A) Vertical displacement of main cable nodes at end of tensioning in replacement of medium boom in the side span with the five-point method. **(B)**. Vertical displacement of the upper main beam.

TABLE 10 Tensioning process in replacement of long boom in the main span by the five-point method (KN).

Unit number	Initial axial force	First tension	Second tension	Third tension	Fourth tension	Fifth tension	Sixth tension	Total axial force of temporary boom
100	1397.00	300	300	300	300	200	0	1400
101	1393.46	300	300	300	300	200	0	1400
102	1390.95	300	300	300	300	200	50	1450
103	1391.86	300	300	300	300	200	0	1400
104	1390.55	300	300	300	300	200	0	1400

FIGURE 14
(A) Vertical displacement change of main cable node at end of tensioning in replacement of long boom in the main span by the five-point method. **(B)**. Displacement change of the upper main beam.
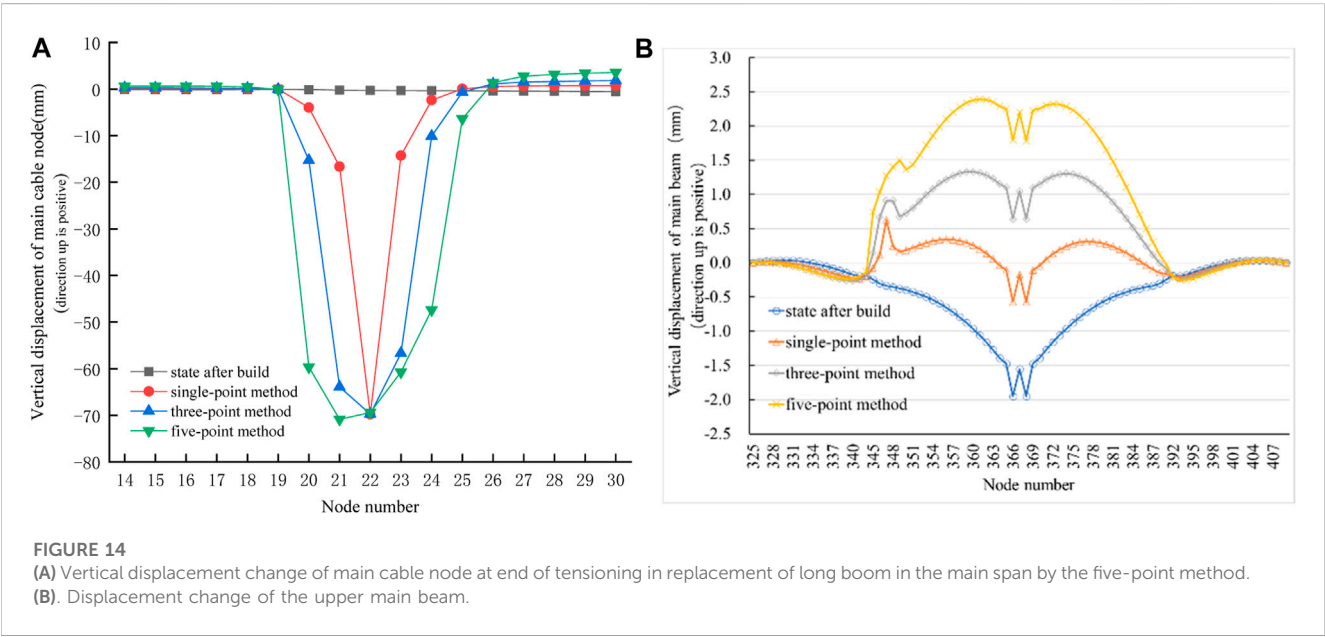
TABLE 11 Axial force and force transmission efficiency of a single temporary boom with different replacement methods.

Boom	Initial axial force (KN)	Axial force of temporary boom in the single-point method (KN)	Force transmission efficiency in the single-point method (%)	Axial force of temporary boom in the three-point method (KN)	Force transmission efficiency in the three-point method (%)	Axial force of temporary boom in the five-point method (KN)	Force transmission efficiency in the five-point method (%)
short boom	1410.22	1470	95.93	1360	103.69	1300	108.48
medium boom	1390.54	1920	72.42	1480	93.96	1300	106.96
long boom	1390.95	2203	63.14	1535	90.62	1450	95.93

movement at only three main cable nodes. In contrast, the three-point method affected up to five main cable nodes with substantial downward displacement, with the three largest displacements occurring at the locations of the temporary booms. Similarly, the five-point method caused significant downward displacement in up to six main cable nodes, with the five largest displacements occurring at the positions of the temporary booms.

The vertical displacement of the upper main beam is shown in Figure 14B. The five-point replacement method significantly altered the geometric shape of the main beams in the main span, resulting in a maximum displacement of 3.75 mm in the mid-span. This displacement exceeds that of the single-point method by 2.37 mm and the three-point method by 1.15 mm. It can be concluded that the five-point method has a notable influence on the vertical displacement and geometric shape of the main beams in the main span. However, none of the three boom replacement methods significantly impacted the beam at the east side span.

In general, the main advantage of the five-point method in replacing the long boom is the reduction in temporary boom tension by 753 KN compared to the single-point method and 85 KN compared to the three-point method. However, this advantage is not significantly greater than that of the three-point method. Therefore, when selecting the most suitable boom replacement method for actual bridge construction, a comprehensive evaluation is necessary.

As shown in Table 11, the changes in the axial force and force transmission efficiency of a single temporary boom with different replacement methods, it can be found that when replacing a short boom, the single-point method can achieve a force transmission efficiency of more than 90%. When replacing a medium-length boom, the maximum force transmission efficiency of a single temporary boom with the three-point method can also be maintained at more than 90%. When the five-point method replaces the long boom, the maximum force transmission efficiency of a single temporary boom can be greatly improved.

6 Application

In the paper, the adaptability of the nominal boom length and the boom replacement method is discussed according to numerical simulation analysis of the structural response

during the boom replacement process. And the optimal replacement method of booms with different nominal lengths is determined. It can be seen that the single-point method is the optimal choice for replacing short booms, as it achieves a force transmission efficiency above 90% while reducing the axial force of the temporary boom and fully utilizing its function. Considering the bridge's overall effect and construction complexity, the three-point method is most suitable for replacing medium booms, while the five-point method is more appropriate for long booms. These have practical guiding significance for the selection of suspender replacement method in the operation and maintenance of a sea crossing suspension bridge. The conclusions are also applicable to other suspension bridge. The nominal boom length of suspension bridge can be determined according to the method in this paper, then the optimal boom replacement method can be selected according to the nominal boom length. Which can simplify the theoretical analysis process of boom replacement, optimize the number of construction platform and equipment scale. At the same time, in the actual process of replacing booms, monitoring and controlling relevant parameters can ensure the quality of replacement, improve the efficiency of replacement.

7 Conclusion

The response of the bridge structure during boom replacement was analyzed using the single-point, three-point, and five-point methods. The process of boom replacement was simulated using the temporary boom method. Meanwhile, the performance of the three boom replacement methods in replacing short, medium, and long booms was extensively analyzed using a significant amount of data. The definition of the nominal boom length of suspension bridge is based on the correlation between the transmission efficiency of the temporary boom, the actual boom length and the main cable sag in the paper. Specifically, the nominal boom length and boom replacement method were quantitatively assessed based on the axial tensile force of temporary booms, the vertical displacement of the main beams and cables, and the change in the remaining axial force of booms. And the optimal replacement method for booms with different nominal lengths was determined. Simultaneously discovered, the force transmission

efficiency of the temporary boom decreases as the boom length increases, with a larger rate of decrease observed for longer booms.

The above analysis can be widely applied to the operation, maintenance and management of the same type of suspension bridge. Conclusion in the paper can ensure the safety and reliability of bridge structures during operation, reduce maintenance costs in the later stages of operation, and enhance the safety protection ability of operating bridges, which has significant reference value.

Data availability statement

The original contributions presented in the study are included in the article/Supplementary material, further inquiries can be directed to the corresponding author.

Author contributions

Conceptualization, YM; methodology, CC; software, QH; validation, YZ; investigation, YT; data curation, GL. All authors contributed to the article and approved the submitted version.

Funding

Conflict of interest

The authors declare that the research was conducted in the absence of any commercial or financial relationships that could be construed as a potential conflict of interest.

Publisher's note

All claims expressed in this article are solely those of the authors and do not necessarily represent those of their affiliated organizations, or those of the publisher, the editors and the reviewers. Any product that may be evaluated in this article, or claim that may be made by its manufacturer, is not guaranteed or endorsed by the publisher.

References

Alastair, A. S., and Colford, B. R. (2017). "Forth Road bridge-maintenance challenges [M]," in *Advances in cable-supported bridges* (New York: Taylor & Francis Group Logo).

Cao, F. A (2020). Analysis on construction technology and quality control of suspender replacement for tied arch bridge. *Traffic Constr. Manag.* (06), 138–139.

Dou, Y. (2020). A case study on the replacement of cable clips of A suspension bridge and Key technologies. *Urban Roads, bridg. Flood Control* (09), 131–134.

Fan, B., Wang, S., Chen, B., Chao, P-F., Sun, Q., et al. (2023). Robustness-based condition evaluation frameworkfor through tied-arch bridge. *J. Perform. Constr. Facil.* 37 (2), 06023001. doi:10.1061/jpcfev.cfeng-4048

Han, X. (2020). *Research on the fracture safety of corroded suspenders of self-anchored suspension bridge [D]*. Dalian University of Technology.

Huang, W., and Zhang, X. (2021). "Exploration of suspension bridge suspension rod replacement technology-based on the method of cable replacement without affecting the spatial position of the cable girder[A]," in *Maintenance and management branch of China highway society. The 11th academic annual conference of maintenance and management branch of China highway society collection of essays.*

Li, Y. (2021). *Research on replacement method and bearing capacity of suspension bridges in service [D]*. Chang'an University. doi:10.26976/dcnki.gchau.2021.000377

Liu, W., Tang, M., Xu, B., Shen, J. H., Wang, Z., and Wang, X. W. (2023). COAP/Pd-Catalyzed linear asymmetric allylic alkylation for optically active 3,3-disubstituted oxindole derivatives with a four-carbon amino side chain. *World bridg.* 51 (2), 104–108. doi:10.1021/acs.orglett.2c03902

Radojevic, D., Kirkwood, K. F., and Matson, D. D. A. (2019). A tale of twobridges: extending the lifetimes of the Lions gate and angus L. Macdonald suspension bridges. *Struct. Eng. Int.* 29 (4), 527–532. doi:10.1080/10168664.2019.1624142

Süleyman, A., Ebru, K. O., Ahmet, C. A., Günaydin, M., and Rahwan, B. R. (2023). Investigation of the structural behaviors of Bosphorus suspension bridge with vertical hangers replaced by inclined hangers. *Alex. Eng. J.* 65, 75–102. doi:10.1016/j.aej.2022.10.041

Sun, H. (2014). Typical diseases and replacement technology of suspenders of jiangyin bridge. *Sci. Technol. Innov. Appl.* (31), 70–71.

Wang, J., Wang, X., and Yang, C. (2015). Construction and monitoring of Shantou Bay bridge test suspender replacement project. *Highw. Auto. Transp.* (6), 172–177.

Xu, T. (2020). *Corrosion fatigue analysis and structural improvement of arch bridge suspenders [D]*. Harbin Institute of Technology.

Yang, H., and Lu, W. (2022). Key technologies for arch bridge suspender replacement under heavy load protection requirements [J]. *Zhongwai Highw.* 42 (03). doi:10.14048/j.issn.1671-2579.2022.03.022

Yu, Z. H., Zhang, D., Zhang, Y., et al. (2019). Suspender replacement technology and stress state simulation analysis of long-span suspension bridges. *Zhongwai Highw.* 39 (02), 82–88. doi:10.14048/j.issn.1671-2579.2019.02.018

Yuan, A., Yang, T., Xia, Y., et al. (2021). Replacement technology of long suspenders of runyang suspension bridge. *China Highw. J.* 34 (02), 289–297. doi:10.19721/j.cnki.1001-7372.2021.02.017

Zeng, Y., Qu, Y., Gu, A., et al. (2016). Large sectional fatigue experiment of the orthotropic steel deck from a box-girder suspension bridge. *J. Harbin Inst. Technol.* 48 (09), 95–100. doi:10.11918/j.issn.0367-6234.2016.09.017

Analysis on intelligent deformation prediction of deep foundation pits with internal support based on optical fiber monitoring and the HSS model

Jie Zhao*, Wenjie Li and Yanli Peng

College of Civil Engineering and Architecture, Dalian University, Dalian, China

With the continuous expansion of the city scale, while rapidly advancing foundation pit construction, it has become a top priority to prevent the potential safety hazards caused by efforts to catch up with deadlines. In this case, deep foundation pit monitoring can provide important technical support for the foundation pit design and construction safety. However, conventional foundation pit monitoring for point monitoring of structural characteristics cannot accurately locate local strains and related cracks, and cannot provide real-time monitoring of support structures, ordinary soil constitutive models cannot consider the strain hardening characteristics of soft soil. This paper aimed to analyze the characteristics of excavation deformation of a deep foundation pit with internal support in the Dalian Donggang Business District by combining the methods of optical fiber monitoring and finite element simulation. In this study, distributed optical fiber monitoring and routine monitoring were adopted to carry out the synchronous excavation monitoring of foundation pit support structures. The main monitoring objects were the deep horizontal displacement of the support piles and the surface settlement of the foundation pit. Moreover, the authors used the Plaxis finite element software based on the Hardening Soil-small (HSS) model to conduct the numerical simulation analysis, and the results were compared with two groups of the measured data of the deep foundation pit obtained from the aforementioned research. Additionally, in light of the SSA-BP neural network, the back-analysis method of HSS model parameters in the Dalian area is proposed. The findings show that, under the premise of selecting reasonable parameters, the results of finite element analysis of the HSS model, considering the small strain characteristics of the soil, demonstrate a high degree of fit with the actual deformation law of foundation pits, which proves the rationality of the model. Furthermore, it was verified that the distributed optical fiber monitoring has conspicuous advantages in terms of data continuity and accuracy in contrast to routine monitoring. The research results of this paper can provide reference for deformation monitoring and early warning regarding the support structures of deep foundation pits.

KEYWORDS

optical fiber monitoring, HSS model, parameter back-analysis, deformation prediction analysis, SSA-BP neural network

1 Introduction

Deformation of foundation pits is the result of the interaction between the support structures and soil (Zheng et al., 2016). Considering the property of soil being of great complexity and diversity, it is a necessity to select reasonable soil constitutive model and parameters, which ensures the entire process of excavation of foundation pits is effectively simulated, so as to provide important technical support for the design of foundation pits as well as for construction safety (Zhao et al., 2016). The Hardening Soil model is an advanced constitutive model of soil, which takes the strain hardening characteristics of soft soil into account and regards the stress history and stress path as a significant basis for calculating soil stiffness. Furthermore, its deformation calculation results consider the combined action of foundation pit support structures and the surrounding soil (Zong and Xu, 2019). The variation pattern of soil stiffness can be classified into three kinds: very small strain (< 0.001%), small strain (0.001%–1%), and large strain (>1%) (Atkinson and Sallfors, 1991). Schweiger et al. (2009) studied a large amount of engineering monitoring data and found that, during the excavation process of foundation pits, most soil within the excavation range is in a state of small strain. As has been shown by numerous experiments, the deformation characteristics of soil mass under the small strain condition are fairly complicated and highly non-linear (Chen et al., 2021; Gu et al., 2021; Li et al., 2021; Zhang et al., 2022).

For the reasons given above, the Hardening Soil-small (HSS) model, taking the features of small strain of soil into consideration, was adopted to research the deformation trend of soil and support structures in foundation pit engineering, which improves the accuracy and rationality of the numerical analysis (Benz, 2007). Kim and Finno (2019) obtained the HSS model parameters of their research region through back-analysis of soil test results, and, by resorting to the sensitivity analysis of the model parameters at different stages of excavation, the parameters of the HSS model were optimized. Afterward, the researchers applied them to the numerical simulation of foundation pit deformation and then compared the derived data with the field measured values. The comparative results demonstrated that the HSS model can effectively predict the deformation of both side walls and the surface settlement of foundation pits. Wang et al. (2013) referred to plenty of experimental results and related studies, modified parameters E_{50}^{ref}, $E_{\text{oed}}^{\text{ref}}$, $E_{\text{ur}}^{\text{ref}}$, $\gamma_{0.7}$, and R_{f} via sensitivity analysis, calculated G_0^{ref} through the back-analysis method, and finally concluded a set of preliminarily complete determining HSS model parameters on the basis of typical HS model parameters in Shanghai (Wang et al., 2012). Mu et al. (2012) acquired the HSS model parameters of the soil around a foundation pit via the back-analysis based on the coupling of MATLAB and Macro, and completed a numerical simulation of the construction process. They then compared and analyzed the change rule of the simulated value and the measured value. The comparative results indicated that the HSS model, considering the characteristics of small strain soil, can accurately adapt to the soil stiffness, which would effectively reduce the finite element calculation error of the next excavation. The rationality of the back-analysis method has been verified as well in the studies. Liang et al., 2017 obtained the main parameter values and their proportional relationships of the HSS model of typical clay layers in

Shanghai through laboratory soil tests, and compared the calculated values and measured values of the deformation of the support structures based on foundation pit engineering examples. The study showed that the HSS model and the parameters gained from the test method are applicable to the simulation of foundation pit excavations in soft soil areas of Shanghai. Wu et al. (2021), on the basis of deep foundation pit engineering of typical soft soil in Shanghai, utilized Plaxis to establish a three-dimensional model according to the HSS model and corresponding parameters, carried out finite element analysis on the whole process of excavation, and studied the deformation of deep foundation pit excavations in the typical soft soil of Shanghai. This study delivered a technical reference for the design and construction of narrow-long deep foundation pits Shi et al. (2016) studied the stiffness parameters E_{50}^{ref}, G_0^{ref}, and $\gamma_{0.7}$ in the HSS model of typical soil layers in the Xiamen area, and the model's sensitivity to the numerical simulation results of underground engineering. They sorted and compared the deformation sensitivity of each parameter at each stage of foundation pit excavation by using the single control soil layer parameters and orthogonal test method. This provides a reference point for the precise control of foundation pit deformation in the process of engineering investigations.

In summary, in contrast with the HS model, the HSS model takes into account the small strain characteristics of soil better, hence it is widely used in engineering issues such as foundation pit excavation. The HSS model, however, requires more parameters which are relatively difficult to obtain to characterize soil properties. Therefore, experimental methods or back-analysis is commonly adopted to achieve the parameters. On the other hand, the properties of soils in different regions may be various, so the correction and calibration of parameters in specific applications should align with the realistic situation of the region.

Foundation pit engineering monitoring refers to a procedure during foundation pit excavation, including monitoring the deformation of the foundation pit support structures and their surroundings using equipment and instruments, analyzing monitoring data to report results, and lastly comparing the results with alarm values to judge the excavation's safety (Xi and Wei, 2020). Although some normal monitoring methods can be used for fixed-point monitoring of structural characteristics, they cannot precisely locate the local strain and relevant cracking, perform real-time monitoring on support structures, and realize the continuous measurement of strain, bending moment, and uneven settlement (Fu and Peng, 2018). In addition, point measurement frequency is not conducive to the timely discovery of dangerous situations to ensure the safety of the project and is subject to other disadvantages like adjacent buildings being possibly affected. This poses a huge challenge in preventing construction hazards. Wang N. et al., 2020 conducted a synchronous monitoring experiment between the traditional reinforcement meter and the distributed optical fiber, and concluded through comparative analysis that distributed optical fiber has advantages in concrete support axial force and deformation monitoring. Qiu and Sun (2020) designed a monitoring plan for the support pile of deep foundation pits in the light of distributed optical fiber sensing technology and successfully measured its continuous distributed deformation information. Based on that, monitoring and analysis of the deformation process of the support structures during foundation

pit construction were completed. Zhu et al. (2022) designed two types of deployment methods for fiber optic sensors, single U-shaped and multi-U-shaped. Combined with the actual engineering, they employed these two methods to acquire the monitoring data on the displacement of drilled cast-in-place piles, and compared them with the results obtained by inclined tube monitoring methods. The results revealed that both types of distributed optical fiber layout methods are effective in monitoring pile deformation and are better than that of the inclinometer tube method. When it comes to the limitations, the measurement object is the single pile, without taking the interlocking pile as the support structure into account. Thus, the influence of complex deformation caused by the interaction between piles on monitoring has not yet been researched.

In recent years, with the rapid development of computer technology, the concept and algorithms of machine learning are being constantly upgraded and evolved. Many scholars use the BP neural network regression algorithm to carry out prediction research on measured data sets. Luo et al., 2020 compared the effect of the GA-BP neural network, support vector regression model (SVR), and random forest model (RF) on the prediction of foundation pit deformation by inputting datasets with the same features. The results demonstrated that the mean square error of the GA-BP neural network is smaller, which indicates that it has strong forecasting ability. Wang et al., 2021 established a simple and valid BP neural network model for analysis and concluded that the number of the hidden layer nodes had a high sensitivity to the influence of the prediction results. Meng et al., 2022 proposed an implementation process of multi-step rolling forecasting of the deformation of deep foundation pits based on the BP neural network, which achieved the expected effect and supplied feasibility for monitoring equipment to realize automatic predictions.

On the basis of the aforementioned studies, this paper, concentrating on a deep foundation pit project in the Dalian Donggang Business District, executed the real-time monitoring of the whole process of excavation deformation of the deep foundation pit through the methods of routine monitoring and distributed optical fiber monitoring. In addition, the sparrow search algorithm combined with the BP neural network algorithm were used to invert the HSS model parameters. The finite element numerical analysis model of the foundation pit was established using geotechnical Plaxis finite element software to simulate the whole construction process of the foundation pit. Finally, the authors compared and analyzed the measured data with simulation results. This paper aims to provide reference for data monitoring and deformation analysis during deep foundation pit excavation.

2 Deformation monitoring principle of optical fibers distributed in piles

In the 1980 s, (Rogers, 1980) proposed the optical time-domain reflectometry technology, which has rapidly developed into a new backbone of monitoring in the field of structural health monitoring. In testing the technique, the light signal is scattered and reflected when injected into different media. Thus, the received optical signal is input in the form of an optical pulse from the fiber optic jumper
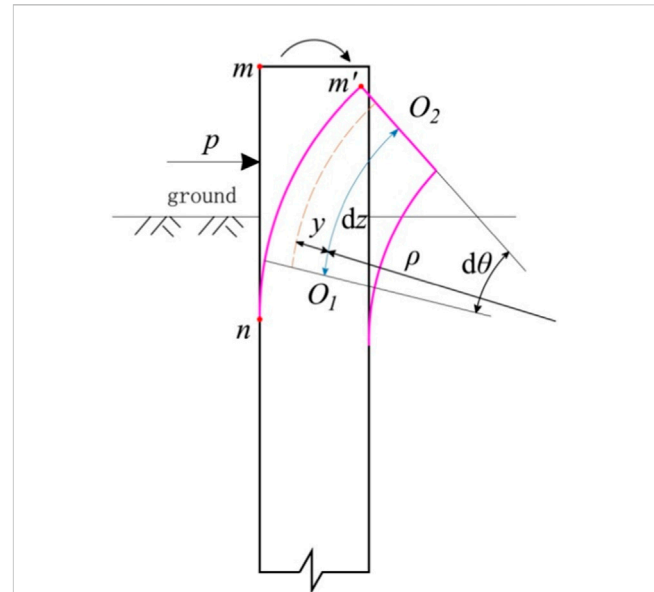

FIGURE 1
Deformation diagram of pile body under horizontal load.

head. The intensity of the reflected light signal is measured as a function of time; it therefore can be converted into the length of the optical fiber. Moreover, the optical demodulator demodulates the physical parameters of the object such as strain, temperature, acceleration, and pressure. Distributed optical fiber sensing technology usually adopts conventional single-mode optical fibers as the transmission medium, which is simple and convenient. Its sensing signal is mainly transmitted through light, with optical fiber as the medium to check and detect external measured signals. It is a new type of optical fiber sensing technology, optical fiber enjoying the advantages that the traditional monitoring method is beyond comparison, including easier bending, a lighter weight, smaller size, and more anti-interference (Gao et al., 2017). Accordingly, optical fiber has become a hot trend in the field of monitoring research since the time of its emergence.

2.1 Calculation of pile body stress

When the optical fiber is buried in the pile, the axial deformation of the optical fiber and the axial deformation of the pile are both $\varepsilon(z)$. The axial strain $\varepsilon(z)$ of the optical fiber is measured by the testing instrument, then the pile body stress $\sigma(z)$ is:

$$\sigma(z) = \varepsilon(z).E_c \tag{1}$$

Among them, E_c is the elastic modulus of the cast-in-place pile and z is the pile depth.

2.2 Calculation of pile body axial force

According to the pile body stress $\sigma(z)$, the pile body axial force $Q(z)$ is:

$$Q(z) = \sigma(z).A \tag{2}$$

2.3 Calculation of pile body deflection

When the pile body is bent, the distributed strain of the pile body under different load deformations can be obtained by testing the strain value of the distributed sensing optical cable buried inside the pile body.

Assuming ε_1 and ε_2 respectively are the strain values measured by the optical fibers inside and outside the pile at a depth of z along the direction of its body, then the axial compressive strain $\varepsilon_a(z)$ and bending strain $\varepsilon_m(z)$ are

$$\varepsilon_m(z) = \frac{(\varepsilon_1 - \varepsilon_2)}{2} \tag{3}$$

$$\varepsilon_a(z) = \frac{(\varepsilon_1 + \varepsilon_2)}{2} \tag{4}$$

As shown in Figure 1, under the action of horizontal load p, the pile top mn rotates and deforms to $m'n$ around the point n. Assuming that the length of the longitudinal arc line segment O_1O_2 on the neutral axis of the pile is dz, the corresponding curve's bending deformation angle is dθ, and the curvature radius is $\rho(z)$, then the bending strain at the distance of $y(z)$ from the neutral axis is:

$$\varepsilon_m(z) = \frac{y(z)d\theta}{dz} \tag{5}$$

$$\frac{1}{\rho(z)} = \left|\frac{d\theta}{dz}\right| \tag{6}$$

Substituting Eq. 5 into Eq. 6 yields the following relationship:

$$\varepsilon_m(z) = \frac{y(z)}{\rho(z)} \tag{7}$$

When the pile is bent, the relationship between the curvature radius and the bending moment is:

$$\frac{1}{\rho(z)} = \frac{M(z)}{EI} \tag{8}$$

In Eq. 8: EI is the bending stiffness, $kN \cdot m^2$; E is the elastic modulus; and I is the moment of inertia of the pile section.

$$M(z) = EI \frac{\varepsilon_m(z)}{y(z)} \tag{9}$$

The curvature of the plane curve can be calculated by mathematical theory:

$$\frac{1}{\rho(z)} = \pm \frac{d^2\omega}{dz^2} \tag{10}$$

Substituting Eq. 10 into Eq. 8 yields:

$$\pm \frac{d^2\omega}{dz^2} = \frac{M(z)}{EI} \tag{11}$$

According to the sign convention between the bending moment and deflection, take the negative sign on the left side of Eq. 9, that is:
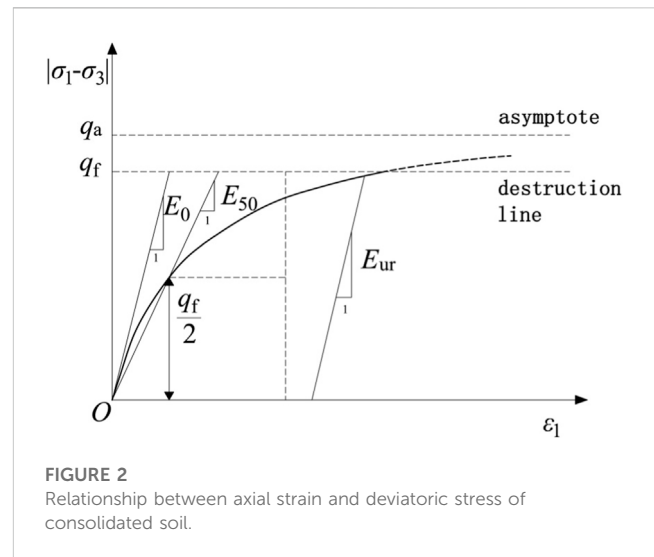

FIGURE 2
Relationship between axial strain and deviatoric stress of consolidated soil.

$$\frac{d^2\omega}{dz^2} = -\frac{M(z)}{EI} = -\frac{\varepsilon_m(z)}{y(z)} \tag{12}$$

Substituting Eq. 9, 10 into Eq. 12, an approximate solution for the torsional crankshaft is obtained. Although there is an action subjected to horizontal loads, the deformation of the pile bottom is minor enough to be negligible. Given the above reasons, it is assumed that the bottom end of the pile is completely fixed, the deflection is integrated to obtain the general solution equation of deflection:

$$w(z) = -\int_H^z \int_H^z \frac{\varepsilon_m(z)}{y(z)} dzdz - Cz - D \tag{13}$$

In Eqs. 13, H is the burial depth of the pile; C, D is the constant of integration The discrete data can be obtained by solving:

$$w(z) = \sum_{i=1}^n \sum_{i=1}^n \frac{\varepsilon_m(z_i)}{R} \Delta z \Delta z \tag{14}$$

In Eq. 14, n is the number of measuring points from the pile bottom to the depth of z; R is the pile radius; and ΔZ is the testing distance interval of the fiber optic monitoring instruments. In Figure 1: p is the horizontal load; ρ is the curvature radius.

3 Introduction to HSS model

A large amount of engineering experiences indicate that it is quite difficult to accurately analyze and predict geotechnical engineering deformation. One possible important reason is the lack of reasonable understanding and application of soil deformation characteristics, especially the small strain. At present, the Hardening Soil-small (HSS) model has been widely used for deformation analysis in practical engineering due to its ability to properly consider the non-linear and stress-related characteristics of the modulus of the elastic (small strain) phase of soil. This model further optimizes the assumed conditions of the Hardening Soil (HS) model. It is an advanced soil model developed based on the fruits of soil

consolidation tests and triaxial tests. The HS model simulates the shear hardening and volume hardening of soil when unloading during the plastic stage of the soil. These two hardening situations explain the stress state of internal deformation and failure of soil, which generally occur simultaneously. The results of their hardenings should be determined by the stress path and the characteristics of the soil; therefore, they can simulate various types of soil in a comparatively realistically way. The relationship between the axial strain and deviatoric stress of consolidated soil is shown in Figure 2.

In Figure 2: q_a is the asymptotic value of hyperbola; E_{50} is the stiffness modulus related to the confining pressure of soil; E_{ur} is the modulus adopted by the stress path of unloading and reloading; and E_0 is the stiffness of soil under very small strain. q_a, E_{50}, and E_{ur} can be obtained from the following equation.

$$E_{50} = E_{50}^{ref}\left(\frac{c'\cot\varphi' - \sigma_3'}{c'\cot\varphi' + p^{ref}}\right)^m \tag{15}$$

$$E_{ur} = E_{ur}^{ref}\left(\frac{c'\cot\varphi' - \sigma_3'}{c'\cot\varphi' + p^{ref}}\right)^m \tag{16}$$

$$q_f = (c'\cot\varphi' - \sigma_3')\frac{2\sin\varphi'}{1 - \sin\varphi'}$$

$$q_a = \frac{q_f}{R_f} \tag{17}$$

In the formula: E_{50}^{ref} is the reference stiffness modulus; E_{ur}^{ref} is the modulus of unloading and reloading; q_f is the ultimate shear stress; R_f is the damage ratio; p^{ref} is the reference confining pressure; c' is the effective cohesion; φ' is the effective internal friction angle; m is the dependence index of stiffness level; and σ_3' is the effective small principal stress.

Based on the HS model, the HSS model takes the small strain properties of the soil into account by adding two parameters, making the simulation closer to the real situation. In dynamic triaxial tests, the small strain characteristics of soil is discovered, and the HSS model considers the increasing trend of soil stiffness under small strain conditions. Therefore, its soil excavation simulation under unloading has better adaptability compared to other constitutive models.

The empirical formula of small strain stiffness G_0^{ref} is:

As Hardin et al. [28] deduced through extensive experiments, the empirical formula of small strain stiffness G_0^{ref} is:

$$G_0^{ref} = 33 \times \frac{(2.973 - e_0)^2}{1 + e_0}(OCR)^m \tag{18}$$

In Equation 18: e_0 is the initial void ratio of the soil; G_0^{ref} is the reference shear modulus for small strains; and OCR is the over consolidation ratio.

According to the research of Brinkgreve and Broere. (2006), $\gamma_{0.7}$ can be expressed as:

$$\gamma_{0.7} = \frac{1}{9G_0}[2c'(1 + 2\cos(2\varphi')) - \sigma_1'(1 + K_0)\sin(2\varphi')] \tag{19}$$

For Equation 19, there exists:

$$G_0 = G_0^{ref}\left(\frac{c'\cot\varphi' - \sigma_3'}{c'\cot\varphi' + p^{ref}}\right) \tag{20}$$

In Equations 19, 20: σ_1' is the effective major principal stress; G_0 is the initial shear modulus under static load; G_0^{ref} is the reference initial shear modulus for small strains; and K_0 is the normally consolidated lateral pressure coefficient at rest.

4 Sparrow search algorithm BP (SSA-BP) neural network model

4.1 Sparrow search algorithm principle

The Sparrow Search Algorithm (SSA) is a swarm intelligence algorithm based on the sparrow population proposed for the first time in 2020 (Xue and Shen, 2020). Its main inspiration comes from the behavior of sparrow populations in foraging and anti-predation. By optimizing the exploration and development of search space to a certain extent, SSA has a great improvement over other common intelligent optimization algorithms in search accuracy, convergence efficiency, stability, and the obviation of local optimal solution, which makes it a novel method of global search optimization.

The sparrow search algorithm consists of three different roles: producers, scroungers, and early warnings Among them, individuals with a high level of adaptability in a population are called producers, typically accounting for 10%–20% of the entire population. The rest of the individuals are scroungers, relying on the producers who find a source of food to obtain nutrition. Meanwhile, scroungers may engage in competition with producers. Any sparrow can turn into a producer by searching for better food sources. However, the total proportion of producers and scroungers in the group remains steady.

Furthermore, a certain proportion of early warmings would randomly generate in the sparrow population, usually within the range of 10%–20%. The scouters' pivotal role is to detect potential threats such as predators, and to send alarm signals upon detection. If the alarm signal exceeds a certain safety threshold, the producers are responsible for leading all scroungers to a safe area. The position of the sparrow population is simulated by using the following matrix:

$$X = \begin{bmatrix} x_{1,1} & x_{1,2} & \cdots & \cdots & x_{1,n} \\ x_{2,1} & x_{2,2} & \cdots & \cdots & x_{2,n} \\ \vdots & \vdots & \vdots & \vdots & \vdots \\ x_{m,1} & x_{m,2} & \cdots & \cdots & x_{m,n} \end{bmatrix} \tag{21}$$

In the formula, m is the number of sparrows and N is the dimension of the variables to be optimized.

Corresponding fitness of the sparrow population:

$$F(X) = \begin{bmatrix} f([x_{1,1} & x_{1,2} & \cdots \cdots & x_{1,n}]) \\ f([x_{2,1} & x_{2,2} & \cdots \cdots & x_{2,n}]) \\ \vdots \\ f([x_{m,1} & x_{m,2} & \cdots \cdots & x_{m,n}]) \end{bmatrix}$$
$$= [f(x_1) \ f(x_2) \ldots f(x_m)]^T \tag{22}$$

In the formula, x_m is the position of the mth sparrow and $f(x_m)$ is the fitness value of the mth sparrow.

The updated description of the producers' location is as follows:

$$x_{i,j}^{t+1} = \begin{cases} x_{i,j}^t \cdot exp\left(\dfrac{-i}{\alpha T}\right), R_2 < ST \\ x_{i,j}^t + Q.L, R_2 \geq ST \end{cases} \tag{23}$$

In the formula: t is the current number of iterations; T is the maximum number of iterations; Q is the random number subjected to standard normal distribution; L is the $1 \times N$ matrix with internal elements all being 1; R_2 ($R_2 \in [0,1]$) is the warning value of the system; and ST ($ST \in [0.5,1]$) is the safety value of the system.

When $R_2 < ST$, it indicates that the environment is safe, that is, there are no predators around the sparrow population. In this setting, the producers are in a widespread search state. When $R_2 \geq ST$, it suggests that a certain number of scouters have detected dangerous predators and sent alarm signals. At this point, the sparrow population, led by the producers, quickly makes an anti-predation response and move to another safety zone.

The updated description of the scroungers' location is as follows:

$$x_{i,j}^{t+1} = \begin{cases} Q.exp\left(\dfrac{x_w^t - x_{i,j}^t}{i^2}\right), i > \dfrac{n}{2} \\ x_p^{t+1} + \left|x_{i,j}^t - x_p^{t+1}\right|.A^+.L, i \leq \dfrac{n}{2} \end{cases} \tag{24}$$

In the formula, x_p^t is the optimal position occupied by the current producers; x_w^t is the current global worst position; and A^+ is the $1 \times n$ matrix, with randomly distributed elements of one or -1 which satisfies $A^+ = A^T(AA^T)^{-1}$.

The updated description of the early warmings' location is as follows:

$$x_{i,j}^{t+1} = \begin{cases} x_b^t + \beta.\left|x_{i,j}^t - x_b^t\right|, f_i \neq f_g \\ x_{i,j}^t + K.\left(\dfrac{\left|x_{i,j}^t - x_w^t\right|}{(f_i - f_w) + \varepsilon}\right), f_i = f_g \end{cases} \tag{25}$$

In the equation: x_b^t is the current location that coincides with the center of gravity of the species group, which refers to the current global optimal position; β is the step size control parameters, obeying the normal distribution with a mean value of 0 and variance of 1; K is a uniformly distributed random variable on the interval [-1,1]; f_g and f_w are, respectively, the current fitness values under the global optimal and worst conditions; f_i is the fitness value corresponding to the ith sparrow in the current iteration; and ε is the arbitrarily small number, which satisfies the condition of meaningful fractions.

When $f_i \neq f_g$, it means that the sparrows are at the edge of the group and easier to recognize the danger; therefore, they need to be ready to change the position at any time to achieve a higher fitness. When $f_i = f_g$, it denotes that the center of the population have also perceived the danger, which requires a quick approach from other individuals to avoid predators.

4.2 SSA-BP model

The performance of the BP neural network depends on the setting of its weights and thresholds; for this reason, optimizing these parameters is necessary to improve the performance. In
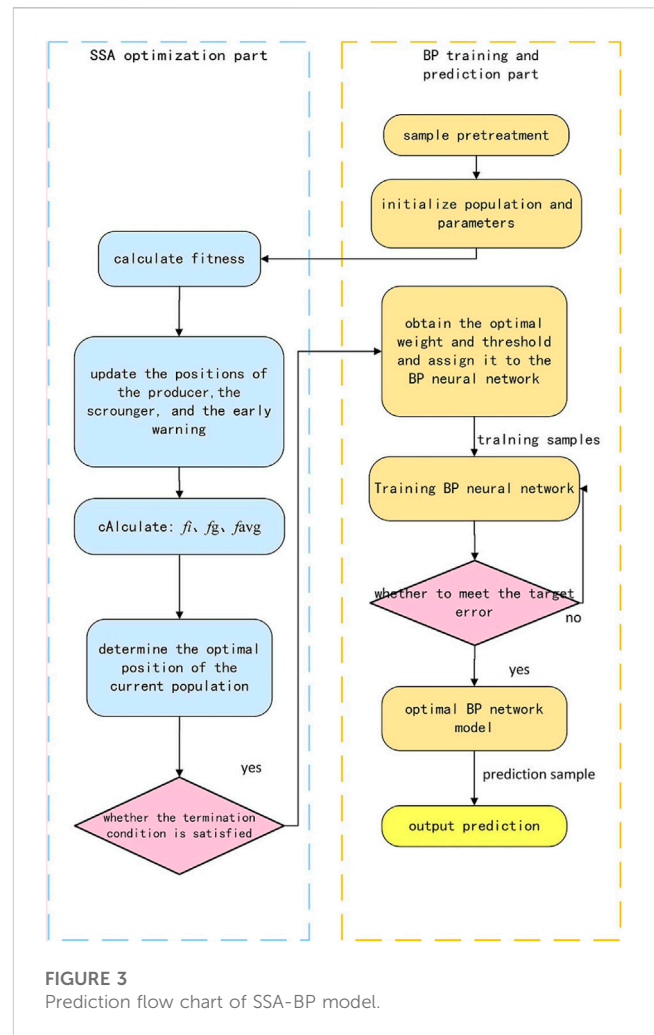

FIGURE 3
Prediction flow chart of SSA-BP model.

the traditional optimization methods, problems such as non-convexity, high dimensionality, and multimodality often need to be tackled with, and the computational complexity is very high and prone to falling into local optimal solutions. As a new type of heuristic optimization algorithm, the sparrow search algorithm can avoid these problems. It can search for the optimal solution by imitating the sparrow's foraging behavior and the global optimal solution in a short time with high efficiency and accuracy.

In accordance with the improved algorithms above, employing the sparrow search algorithm to optimize the weights and thresholds of the BP neural network can enhance its accuracy and generalization ability, so as to better adapt to practical application scenarios. Additionally, this method has a good optimization effect in preventing some of the problems of traditional optimization methods, such as local optimal solutions and high computational complexity. Therefore, the sparrow search algorithm is an optimization method suitable for the BP neural network. The prediction flow chart of the improved SSA-BP model is shown in the following Figure 3:
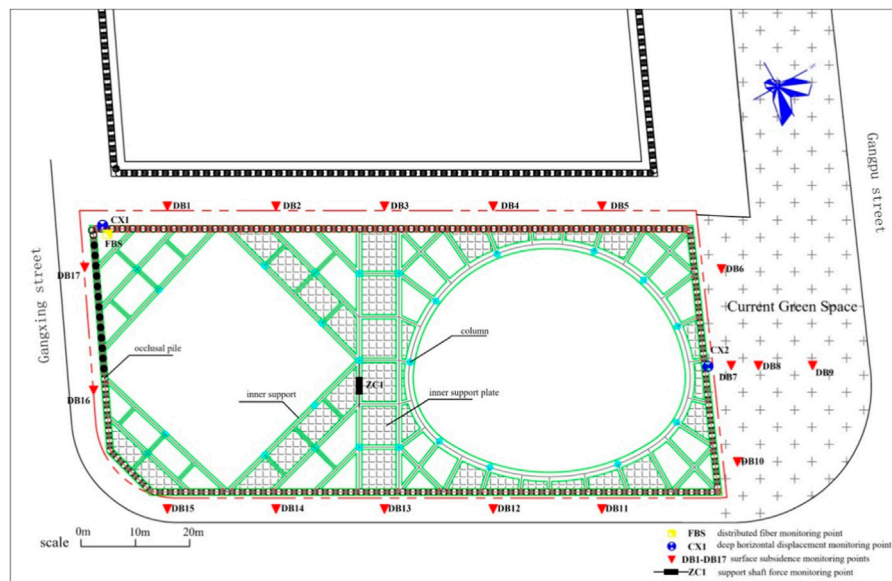
FIGURE 4
Layout plan and measurement points of the foundation pit.

5 Introduction to deep foundation pit engineering

5.1 Introduction of the engineering

The deep foundation pit engineering in Dalian Donggang Business District, with a length of about 100 m and a width of about 50 m, is equipped with a three story basement. The depth of the foundation pit is 14.0–15.7 m, its excavating area being about 5,150 m^2. The plan of using a secant pile with two reinforced concrete internal supports has been adopted as the foundation pit support structure. The design of the brace layout is that the north side adopts the ring brace while the south side takes the corner brace. In addition, the support pile put to use is a 1.2 m diameter secant pile. The cross-section of the foundation pit support system is illustrated in Figure 4.

The strata on the site of this project are in sequence from top to bottom: plain fill, mucky silty clay, silty clay, completely weathered slate, intensely weathered slate, moderately weathered slate, and slightly weathered slate. In terms of the engineering example of the adjacent parallel field, the water level elevation of groundwater in the surrounding area of the site reaches 1.80 m. Its main aquifer is earth fill, which is a strong permeable stratum.

FIGURE 5
Typical engineering geological sectional drawing of the foundation pit.

5.2 Layout of conventional deep foundation pit monitoring

In order to ensure the stability and safety of the foundation pit engineering, impactful monitoring must be carried out throughout the construction. To analyze the results of monitoring, it is necessary to conduct 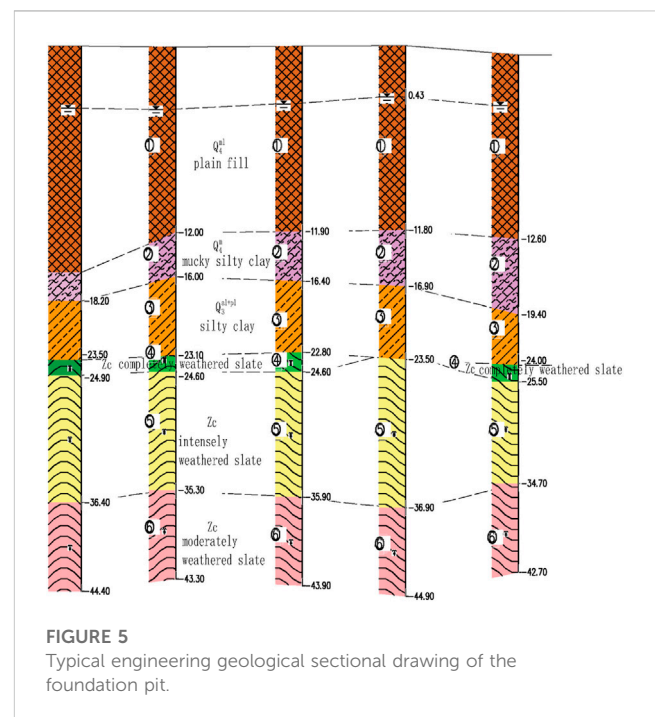global monitoring, comprehensively analyzing multiple associated measurement points and monitoring projects. By doing so, it is beneficial to reduce construction risks by determining whether the support design is in need of modification, and whether there is room for improvement in the construction technology and methods. It is also conducive to monitor the deformation and safety of the surrounding construction areas. Figure 4 shows the layout plan and measurement points of the foundation pit.
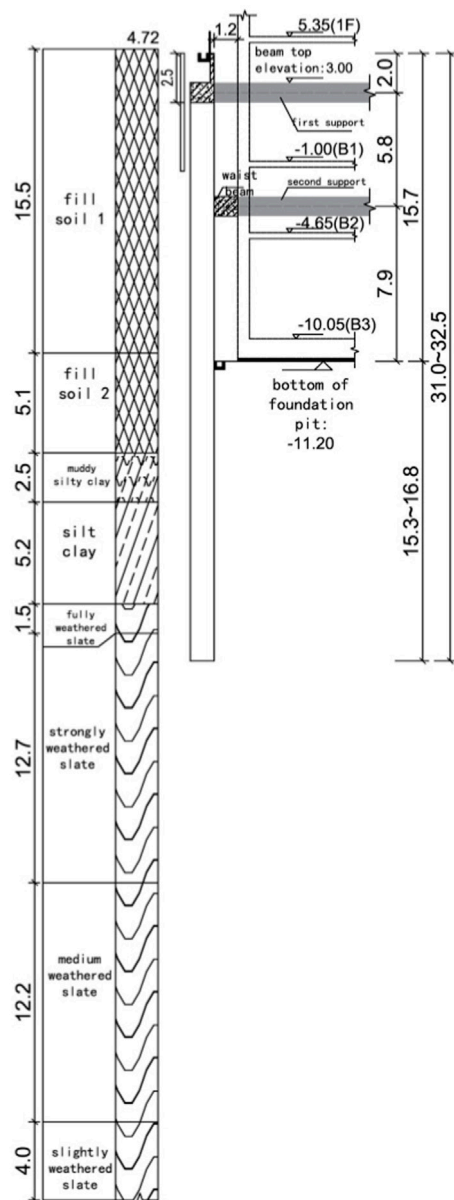
FIGURE 6
Sectional drawing of the foundation it support system.

FIGURE 7
Schematic diagram of field test of deep foundation pit support structure.

Intensely weathered slate: with developed joints and fissures, soft rock, and fractured. The basic quality level of the rock mass is Grade V.

Moderately weathered slate: the rock core is in a block and short column shape, with developed joints and fissures. The rock mass is of a layered structure and relatively complete. Its basic quality grade is Grade IV.

Slightly weathered slate: relatively hard rock; the basic quality level of the rock mass is Grade III.

Figure 6 manifests the sectional drawing of the foundation pit support system, which is located in the upper left side of the layout plan. According to the requirements of relevant specifications, combined with the support design of the foundation pit engineering as well as the actual construction situation onsite, the monitoring objects of the project were determined to include the foundation pit support structure and surface settlement outside the pit, *etc.* The content and items of routine monitoring are as follows:

(1) Horizontal deformation of the support pile (CX1-CX7).
(2) Ground surface settlement monitoring (DB1-DB17).

In line with the specifications and design requirements, the horizontal displacement was monitored by using an inclinometer. According to the design documents for the foundation pit support of this project, it was planned to set up seven deep horizontal displacement points. They were respectively arranged at the corners of the support structure and in the middle of the long side, with a horizontal spacing of no more than 50 m between two monitoring points. The point numbers above are: CX1~CX7.

The monitoring points of the ground surface settlement around the foundation pit were set on the sidewalks and green belts surrounding the pit. Of them, there were two additional points added to the original green space on the north side. The point numbers above are: DB1~DB17.

The stratigraphic distribution and characteristics of the site of this project are as follows, and the typical engineering geological sectional drawing is shown in Figure 5.

Plain fill: in a slightly dense state, mainly composed of cohesive soil, slate, and quartzite gravels. The particle grading is ordinary, with an average Cone dynamic penetration test (DPT) of 6.2.

Mucky silty clay: in a soft plastic state, with a high content of organic matter.

Silty clay: in a plastic state, locally containing quartz fine sand, with an average standard penetration test (SPT) of 9.8.

Completely weathered slate: extremely soft rock and terribly fractured.
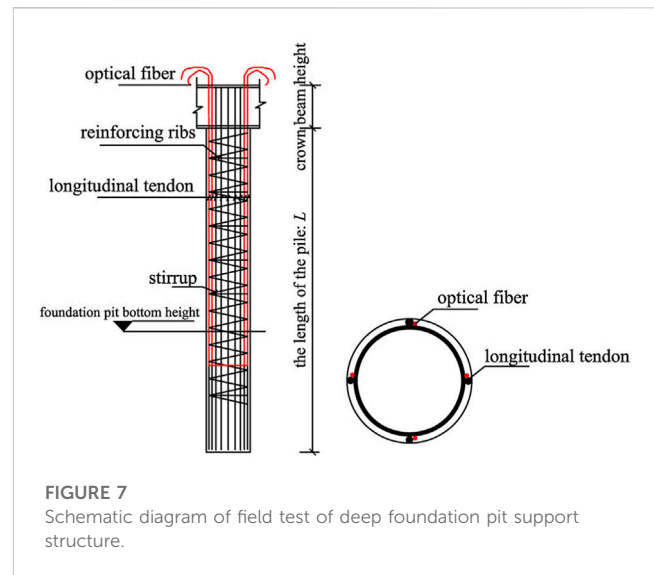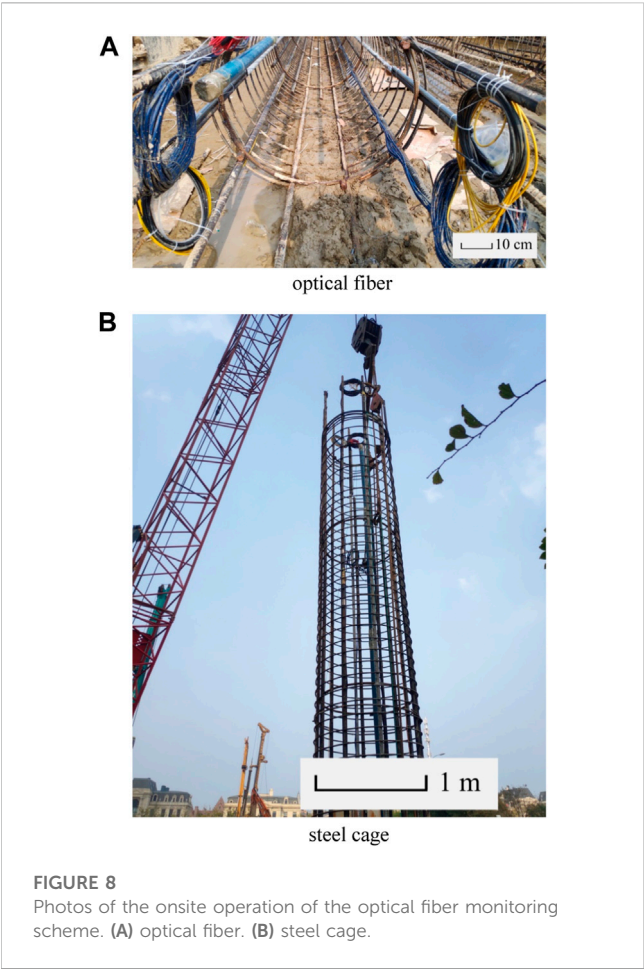
FIGURE 8
Photos of the onsite operation of the optical fiber monitoring scheme. **(A)** optical fiber. **(B)** steel cage.

5.3 Layout of distributed optical fiber monitoring

In view of the harsh construction environment such as soil filling and grouting, the research team applied tightly sleeved optical fiber technology in this monitoring study. It has the favorable form of encapsulation protection and fine effect of strain transmission; hence, it can adapt to the harsh working environment of the underground diaphragm wall. The technology breaks through the traditional concept of point sensing to measure strain, temperature, and damage information at any point on the optical fiber, execute continuous distributed monitoring of the measured objects, and study the overall strain behavior of the measured objects, in order to achieve the purpose of guiding the site construction and later structural health diagnosis.

This project used the distributed optical fiber method to monitor the southwest section of the foundation pit. The support pile adopted is a 1.2 m diameter secant pile, and the length of the pile in this section is 32 m according to the design drawing of the foundation pit support. The experimental system is shown in Figure 7. Depending on different types of pile, considering the survival rate of sensing fibers, operability of construction, and installation, as well as monitoring accuracy, it is required to handle crucial technical aspects including the layout plan and temperature compensation. There were at least four sensing

TABLE 1 Optical nanometer parameter settings.

Sampling interval (m)	Strain measuring accuracy (με)	Temperature test accuracy (°C)	Sample interval (cm)	Spatial resolution (cm)	Frequency of averaging	Continuous-wave intensity (dB)	Pulse intensity (dB)	Frequency range (GHz)	Ambient temperature (°C)
100	5	0.25	5	20	2^{16}	+2	25	10.65–11.25	26

FIGURE 9
NBX-8100 optical nanometer.

optical cables that needed to be set inside the cast-in-place pile, and the optical fibers were laid on the main reinforcement of the steel cage by using rebar as the carrier. Additionally, the optical fibers needed to be laid along the inner side of the rebars to prevent the direct impact of concrete on the optical fibers during concrete pouring. In order to systematically grasp the real situation of the pile, a dual U-shaped method was adopted to ensure the survival rate of the optical fiber and the reliability of the data.

After rebar workers on the construction site finished the steel cage, the main reinforcement position where the optical fiber was to be pasted needed to be ground and then wiped clean with alcohol wipes. Next, tightly sleeved optical fibers at the corresponding positions of rebars were laid before 502 glue was evenly applied. When pasting distributed optical fibers, attention needed to be paid to straightening the fibers and sticking them without relaxation. The bend needed to be protected by a metal hose—this part of the dataset was not studied. After that, the steel pipe was used to connect the optical fiber at the pile head, and coil the fibers to prevent damage caused by the hoisting of the steel cage.

Metal-based cord-like optical fibers have good encapsulation technology, and the strain transmission effect is within a controllable range. Therefore, they were arranged along the main reinforcement of the steel cage symmetrically and placed on the inner side of the steel cage, where it was difficult to touch the surrounding rock and soil as well as the grouting equipment. A dedicated locking device and epoxy were used to tighten when fixing the optical fiber at fixed intervals, which prevented them from slipping. The sensing optical cable was pre-tensioned to keep itself straight, and was fixed using the binding method. Large intervals could be taken when binding the temperature compensated optical fibers. The onsite operation of the optical fiber monitoring scheme is demonstrated in Figure 8.

The temperature sensing compensation optical fibers are tightly sleeved optical fibers and was installed parallel to the measurement object. Furthermore, the indirect compensation method was used to install a temperature compensation optical cable which is not affected by the structural strain beside the sensing optical cable. The real strain of the measurement object was obtained by subtracting the measured value of the temperature compensation

optical cable from the monitoring result of the deformation monitoring optical cable.

5.4 Monitoring instruments

The optical fiber data acquisition device utilized in this research is the Neubrex NBX-8100 from Japan. Table 1 shows the parameters of the NBX-8100, which uses PSP-BOTDR technology. This equipment went into production in 2018, and it is the most advanced product in the field of distributed optical fiber in the international industry. It has the smallest spatial resolution and the most stable performance, and all of its indicators fulfill the requirements of this experiment. The exterior of the instrument is shown in Figure 9.

The sensing optical cable adopts the metal-based cord-like strain sensing optical cables (model: NZS-DSS-C02) produced by Suzhou Nanzhi Sensing Technology Co., Ltd. This sensing optical cable is protected by multiple metal reinforcements. Used in conjunction with Brillouin Optical Time Domain Reflectometry (BOTDR), the surface strength has been greatly improved and the measurement results can be directly used in displacement conversion providing technical support for test results. The research group (Wang G. et al., 2020) has calibrated the sensing optical cable in the early stage to obtain the temperature and strain coefficients of the cable. The performance and technical parameters of the sensing optical cable are shown in Table 2.

6 Back-analysis of HSS model parameters

6.1 Finite element analysis

Using Plaxis for numerical analysis and calculation, a two-dimensional finite element model of the northern ring brace section (section 1-1) of the foundation pit was established. The excavation length of the model was 100 m, the excavation depth was 14 m, and the length of the secant pile was 32 m. The complexity of the calculation was reduced by using a half structure. The excavation size inside the pit was 29.7 m, the ground behind the secant pile was 76 m, and the model's vertical dimension was around 60 m. Both the road load and the construction load around the foundation pit were assumed to be 15 kPa. Although the model's ultimate size was 100 m × 60 m, to simplify the model and make calculation easier, the local pile grid and load grid were encrypted during the grid generation procedure. The final northern ring brace model was divided into 2,596 units including 21,303 nodes. The boundary conditions were lower full constraint, left and right normal constraint, and top free constraint. The final grid generation result is shown in Figure 10. In accordance with the previous research results of many scholars, a conservative method was adopted. The secant pile was transformed into a diaphragm wall and simulated by using plate elements based on the principle of equivalent stiffness. Calculation of the moment of inertia was based on the structural diagram of the secant pile in Figure 11:

In Formulas 21, 22, and 23, I_1 is the moment of inertia of a single pile minus the black part in the figure; I_2 is the cross-sectional

Fiber type	Fiber core amount	Grating center wavelength (nm)	Reflectivity (%)	Cable type	Optical cable diameter (mm)	Strain test range (με)	Frequency shift-strain coefficient (MHz·10⁶)	Frequency shift-temperature coefficient (MHz·°C⁻¹)
G.652	1	1,527–1,568	0.01	Metal-based	7	1.5×10^4	0.05	1.77
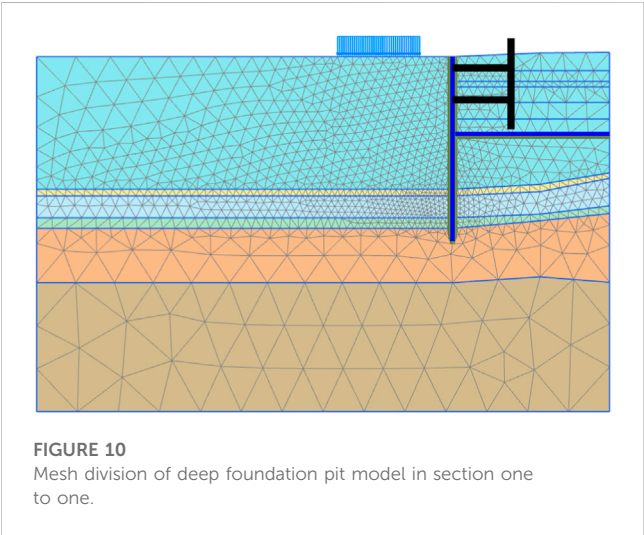
FIGURE 10
Mesh division of deep foundation pit model in section one to one.

TABLE 3 Support numerical simulation parameters.

Type	Tensional rigidity/kN	Equivalent length/m
Support	3.25×10^7	7.5

Calculation of the equivalent thickness h_0 was based on the principle of equivalent stiffness:

$$I_1 = I_2 - 4I_3, \tag{26}$$

$$I_2 = \frac{1}{4}\pi R^4, \tag{27}$$

$$I_3 = \int_{-y_1}^{y_1} y^2 \left[x - \left(R - \frac{a}{2} \right) \right] dy$$

$$= 2\int_0^{y_1} y^2 \sqrt{R^2 - y^2} dy$$

$$= \sqrt{R^2 - y_1^2}\ \frac{(R^2 - 2y_1^2)}{4} - \frac{(2R - a)y_1^3}{3} \tag{28}$$

$$E_1 I_1 + E_2 I_2 = \frac{E_0 (4R - 2a)h_0^3}{12} \tag{29}$$

$$E_0 = \frac{E_1 A_1 + E_2 A_2}{(A_1 + A_2)} \tag{30}$$

moment of inertia of the common pile; I_3 is the moment of inertia of the quarter black part of the secant pile; R is the radius of the pile; a is the secant distance between two piles; and y_1 is half of the width of the secant face surface.
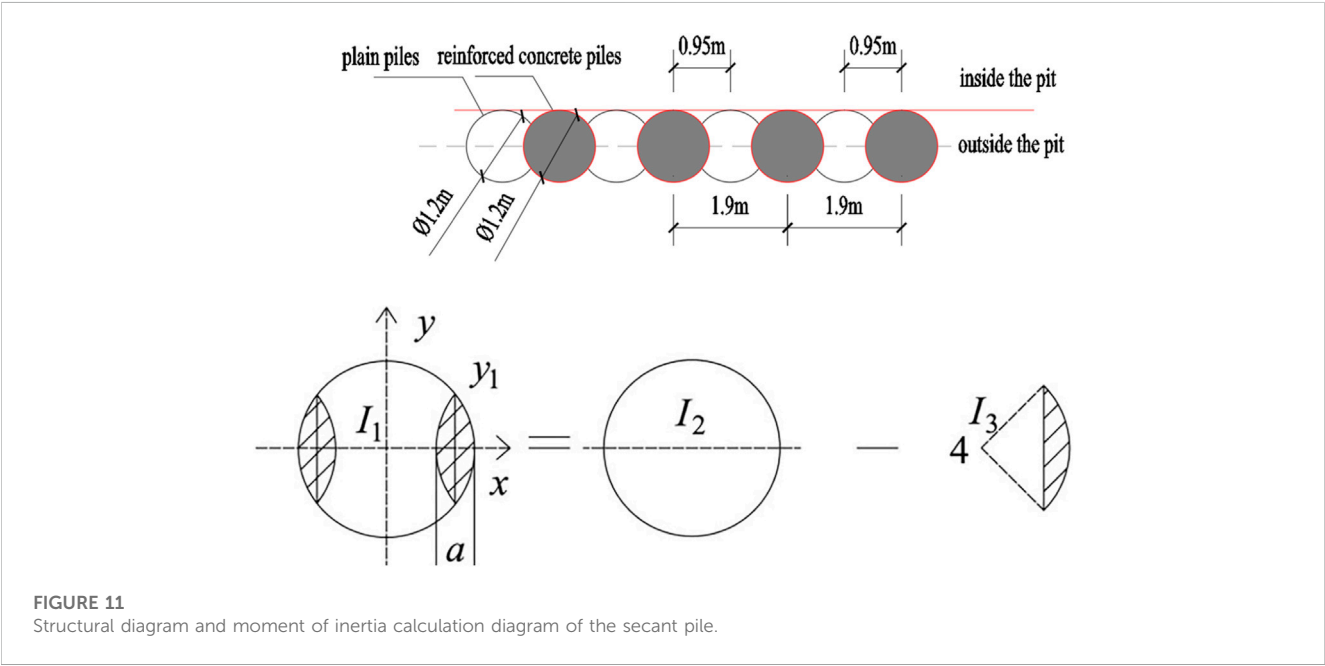

FIGURE 11
Structural diagram and moment of inertia calculation diagram of the secant pile.

TABLE 4 Numerical simulation parameters of the plate element.

Type	Tensional rigidity/(kN·m⁻¹)	Flexural rigidity/(kN·m)	Equivalent thickness/m	Gravity/(kN·m⁻²)	Poisson ratio
Secant pile	2.64×10^7	2.30×10^6	1.021	8	0.15

TABLE 5 Sequence of excavation of The deep foundation pit.

Load steps	Construction operation
0	Generate the initial stress field
1	Construct secant pile unit, activate the road load
2	Excavate to 2 m and construct the first support
3	Excavate to -1 m
4	Excavate to -3.8 m and construction of the second support
5	Excavate to -6.8 m
6	Excavate to -9.5 m, the bottom

In the formula, E1 is the elastic modulus of plain piles, E2 is the elastic modulus of reinforced piles; E0 is the equivalent elastic modulus; A1 is the cross-sectional areas of plain piles, A2 is the cross-sectional areas of reinforced piles; and h0 is the equivalent thickness.

The support is composed of C40 concrete, the reinforced piles are made of C30 concrete, and the plain piles are made of C15 concrete. The input parameters for the inner support, which is simplified by using anchor rods for simulation, are shown in Table 3. The simulation parameters following the equivalent calculation of the secant pile are shown in Table 4.

Before beginning the calculation, the calculation phase must be defined Because of the non-uniformity of the foundation soil layer, the calculation method of gravity loading was employed to construct the initial stress field in the initial stage. The water level is set and the phreatic water type is selected as the pore pressure calculation type. At the initial stage, only the soil element is active, while the other structural elements and road loads are deactivated. Before

excavation, the plate unit and road load are activated, and the displacement of the obtained data reset to zero.

Pore pressure, having some significant impact on the deformation of foundation pits, should be taken into account. In the actual engineering of this paper, thanks to the sound sealing performance of the secant pile, the calculation method of stable seepage was used to consider the changes in pore pressure caused by foundation pit excavation. The seepage computation of the model was not considered due to the secant pile's superior waterstop capability The specific excavation sequence of the foundation pit is shown in Table 5.

6.2 Sensitivity analysis of parameters

The HSS model comprises many parameters, and sensitivity analysis of parameters is essential to improve the efficiency and accuracy of inversion analysis. In this procedure, it is vital to establish which parameters have the largest influence on the model's output outcomes in order to optimize parameters and increase the accuracy and robustness of model prediction. Based on similar projects and relevant literature, the initial parameters of the typical soil layer HSS model in the Dalian Donggang Business District could be determined. Through a comprehensive analysis of the actual engineering values in the Yangtze River Delta region (Yin, 2010; Wang et al., 2012; Wang et al., 2013; Liang et al., 2017; Zong and Xu, 2019; Gu et al., 2021), Xiamen region (Shi et al., 2016), Tianjin region (Liu et al., 2007), and Jinan region (Li et al., 2019), it could be determined that the unloading and reloading Poisson's ratio v_{ur} is 0.20, the reference stress p^{ref} is 100kPa, the failure ratio R_f is 0.7–0.9, the power

TABLE 6 Computing parameters of the HS-Small model for soil layers.

Soil layer	c' (kPa)	φ' (°)	γ (kN/m³)	v_{ur}	K_0	p^{ref} (kPa)	E_{50}^{ref} (MPa)	E_{oed}^{ref} (MPa)	R_f	m
Plain fill 1	10.00	18.00	18.00	0.20	0.69	100	5.73	5.21	0.75	0.88
Muddy silty clay	13.90	12.90	18.10	0.20	0.78	100	2.29	2.52	0.70	0.88
Silty clay	29.40	17.60	19.70	0.20	0.70	100	4.57	4.47	0.80	0.80
Completely weathered slate	60.00	20.00	19.50	0.20	0.74	100	13.75	13.75	0.88	0.75

In Table 6: E_{50}^{ref} is the secant modulus of the standard triaxial test; E_{oed}^{ref} is the tangential compression modulus of the confined compression test; E_{ur}^{ref} is the unloading and reloading modulus under reference stress; G_0^{ref} is the reference shear modulus for small strains; and K_0^{nc} is the lateral earth pressure coefficient at rest of normal consolidation.

TABLE 7 Computing parameters of the MC model for soil layers.

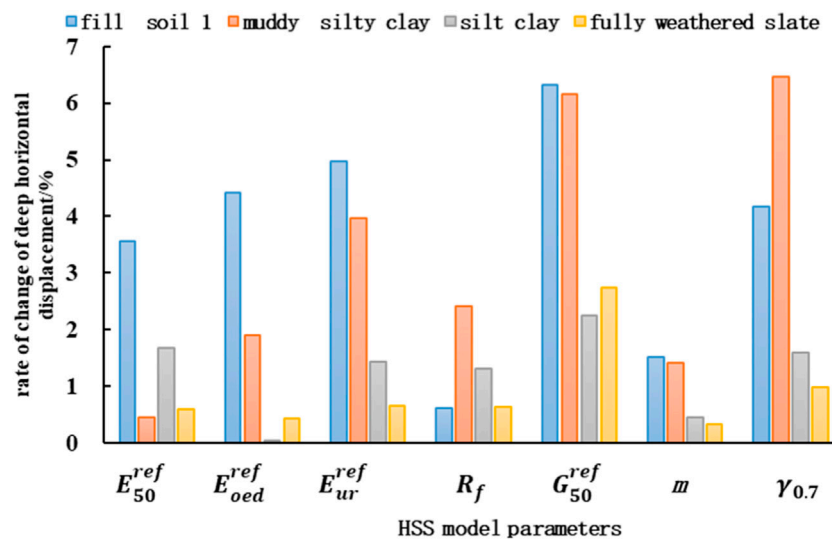| Soil layer	Gravity γ/(kN·m⁻³)	Cohesion c'/kPa	Angle of internal friction φ'/(°)	Elastic modulus/GPa	Poisson ratio
Medium-weathered slate	26.70	250.00	30.00	20.00	0.27
Slightly weathered slate	27.00	400.00	38.00	35.00	0.22

FIGURE 12
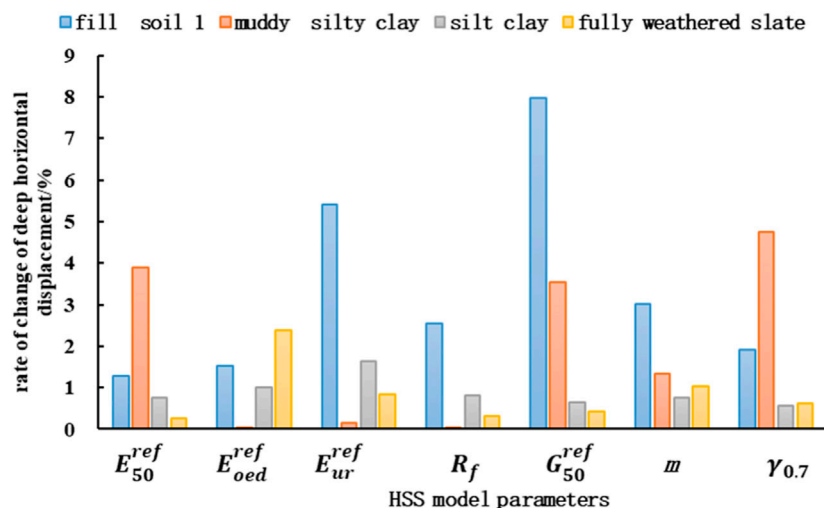Relative displacement changes when the parameter increases by 10%.

FIGURE 13
Relative displacement change when the parameter is reduced by 10%.

exponent m is 0.7–0.9, the reference secant modulus $E_{50}^{\text{ref}} \approx Es$, and the reference tangent modulus $E_{\text{oed}}^{\text{ref}} \approx Es$. Table 6 displays the HSS model's initial parameters. As demonstrated in Table 7, this article provides both the Mohr Coulomb (M-C) constitutive model parameters for moderately weathered and slightly weathered slate.

In this sensitivity analysis, seven parameters including E_{50}^{ref}, $E_{\text{oed}}^{\text{ref}}$, $E_{\text{ur}}^{\text{ref}}$, R_f, G_0^{ref}, m, and $\gamma_{0.7}$ were selected as candidates, and four different types of soil layers were selected, namely plain fill, mucky silty clay, silty clay, and completely weathered slate. By observing the changing amplitude of deep horizontal displacement at the bottom of the foundation pit enclosure structure under the fluctuation

of ±10% of the above seven parameters, the sensitivity of foundation pit deformation to each of the seven parameters could be assessed. Figure 11 and Figure 12 show the relative change of deep horizontal displacement when the parameter increases and decreases by 10%.

The results of Figure 12 and Figure 13 reflect the sensitivity of the foundation pit deformation to the seven parameters, represented by the deep horizontal displacement of the support structure at the bottom of the pit. The vertical axis shows the rate of change of foundation pit deformation, which refers to the change of the new foundation pit deformation after the parameter increases or decreases by 10%. It can reflect the
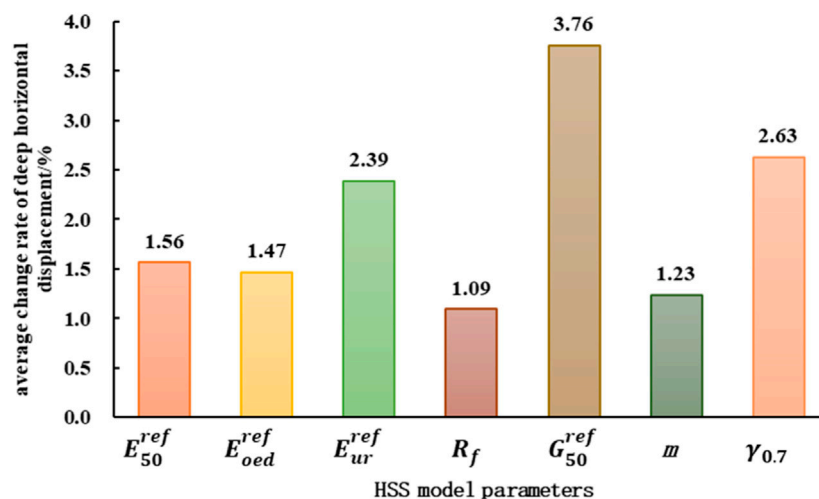
FIGURE 14
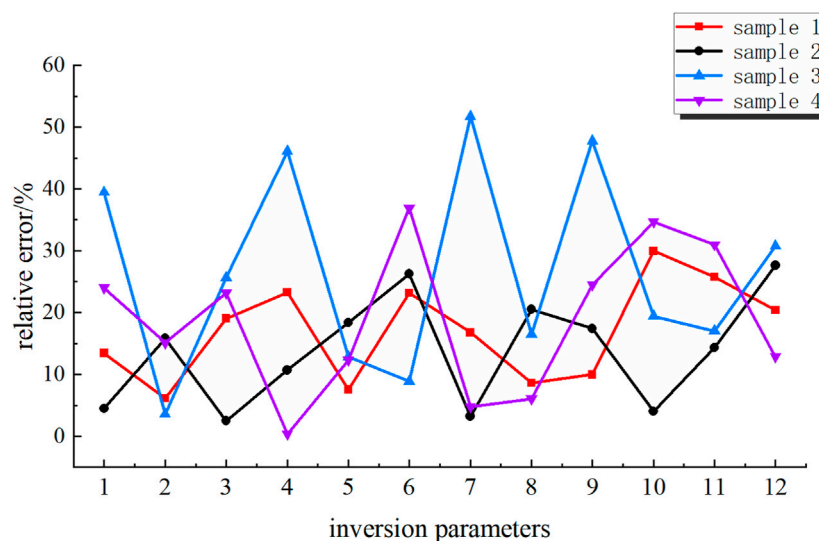Mean value of relative displacement change in deep horizontal displacement.

FIGURE 15
Relative error of the BP neural network test set.

comparison and reference situation between the new state and the original state.

Figure 14 comprehensively considers the results of Figure 12 and Figure 13. The vertical axis data represent the average relative displacement when four different parameters change, and it can be seen from this that the changes of G_0^{ref}, $\gamma_{0.7}$, and E_{ur}^{ref} had a significant impact on the calculation results. The sensitivity ranking of the seven parameters selected above were: $G_0^{ref} > \gamma_{0.7} > E_{ur}^{ref} > E_{50}^{ref} > E_{oed}^{ref} > m > R_f$, referring to relevant literature (Shi et al., 2017; Chen et al., 2021; Gu et al., 2021; Luo et al., 2021). It can be seen that changes in small strain parameters G_0^{ref} and $\gamma_{0.7}$ had a significant impact on the deformation of the foundation pit, which is in good agreement

with the sensitivity analysis results in this article. Therefore, in order to guarantee the hiberarchy of the numerical simulation results, the first three parameters G_0^{ref}, $\gamma_{0.7}$, and E_{ur}^{ref} were selected for inversion analysis.

6.3 Back-analysis model

6.3.1 BP neural network

On the basis of the preprocessing of raw data, MATLAB was selected as the main mathematical tool for this inversion experiment of parameters; the first 77 sets of total data samples were used as the training set to train the network model, and the last four sets were used
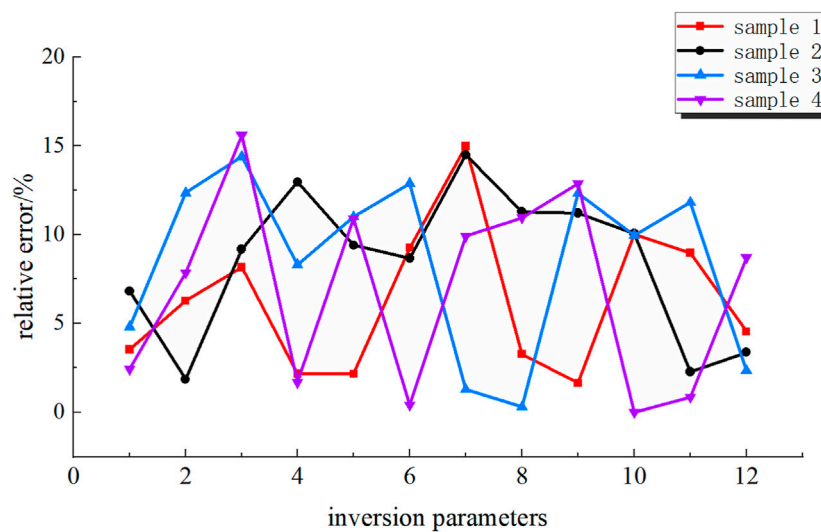
FIGURE 16
Relative error of the improved SSA-BP neural network test set.

TABLE 8 Inversion analysis results table of soil parameters.

Soil layer	E_{ur}^{ref} (MPa)	G_0^{ref} (MPa)	$\gamma_{0.7}$ (10^{-4})
Plain fill 1	29.42	61.86	2.32
Muddy silty clay	24.51	44.11	2.66
Silty clay	30.20	61.12	4.55
Completely weathered slate	53.87	66.03	2.80

as the test set to input the trained model for calculation. Considering the balance between data volume and model complexity, an appropriate displacement index needed to be selected which could avoid data redundancy and model overfitting and improve the generalization ability and prediction accuracy of the model. At the same time, selecting appropriate input variables can reduce the complexity of the network structure and reduce computational costs and training difficulty. In addition, in underground engineering, different displacement indicators can reflect different characteristics of deformation. For example, the uplift of the pit bottom mainly reflects the compression deformation of the underground soil layer; the ground surface settlement mainly reflects the settlement deformation of the soil layer; and the deep horizontal displacement of the soldier pile reflects the stress state changes of the surrounding soil. Taking these displacement indicators into account can more comprehensively and accurately reflect the deformation situation of underground engineering.

In summary, as per the results of the numerical simulation orthogonal experiment, a total of eight displacement indicators, including the maximum uplift of the pit bottom, three ground surface settlements (2 m outside the pit, 6 m outside the pit, and 10 m outside the pit), and four deep horizontal displacements (at the top of the pile, at support 1, at support 2, and at the bottom of the pit) of soldier piles, were selected for this back-analysis experiment. These eight indicators were used as input

values for the network structure, and 12 parameters to be inverted were used as output values; thus, the input layer of the neural network included eight nodes and the output layer included 12 nodes. Through model debugging and multiple rounds of training based on reference empirical formulas, the optimal value for the number of nodes in the hidden layer was determined to be five, thereby achieving the highest accuracy of the model. Therefore, a back propagation neural network model with an 8-5-12 network structure was established. The relative error of the final result is shown in Figure 15.

The largest error among the four groups of samples was 51.7%, the minimum error was 0.3%, and the average error was 19.6%, as shown in Figure 14. To minimize the prediction error of the BP neural network as much as feasible, study on its optimization strategy was required, so an improved sparrow search algorithm was introduced to optimize it.
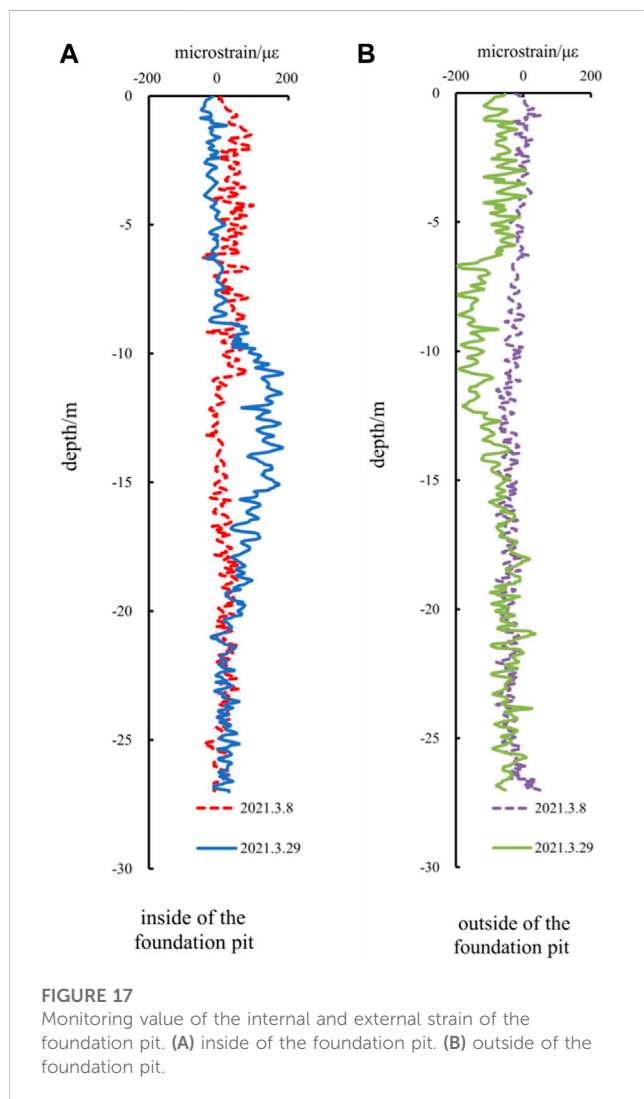
6.3.2 SSA-BP model

This portion continued to use the BP neural network structure of 8-5-12 from the previous section with the number of sparrows set to five and the maximum number of iterations set to 50. The network model was trained with the first 77 sets of total data samples as the training set, and then the last four sets of samples were used in the learned model for calculation. The relative error of the final results is shown in Figure 16.

The above graph depicts the prediction error of the BP neural network optimized by the improved sparrow search algorithm. It is easy to see that its overall trend is significantly lower than the initial BP network; the maximum error among the four groups of samples was 15.6%, the minimum error was 0.03%, and the average error was 7.51%. By analyzing the errors, it is possible to conclude that the accuracy of the optimized neural network meets the actual engineering requirements. In this paper, an improved SSA-BP neural network model was used to perform back-analysis experiments on the parameters of the HSS constitutive model, and the values of the back-analysis results are shown in Table 8.

TABLE 9 Relative error between the measured value and the simulated value of the foundation pit deformation of Section 1-1.

Value	Pit bottom uplift (mm)	Settlement (mm)			Horizontal displacement of support pile (mm)			
		2 m outside the pit	6 m outside the pit	10 m outside the pit	Pile top	Support point 1	Support point 2	Support point 3
Measured value	123.623	9.276	9.428	8.451	3.980	4.950	9.630	11.590
Simulated value	125.455	9.906	8.005	7.779	4.320	4.440	8.256	12.505
Relative simulated value	1.48%	6.79%	15.09%	7.95%	15.41%	10.30%	18.50%	7.89%

FIGURE 17
Monitoring value of the internal and external strain of the foundation pit. **(A)** inside of the foundation pit. **(B)** outside of the foundation pit.

7 Result analysis

7.1 Analysis of HSS model parameter errors

After substituting the parameters in the table into the calculation of the PLAXIS finite element model, the deformation of the foundation pit was obtained. Compared with the measured data, as shown in Table 9, the maximum error between the measured value and simulated value of Section 1-1 was 8.12%, which occurred at the pile top; the minimum error was 0.53%; the average relative error was 10.43%, which is within the allowable range of error, so this parameter inversion analysis met the accuracy and precision requirements of the small strain model for simulating the excavation of foundation pits.

7.2 Analysis of deep horizontal displacement

Figure 17 shows the strain monitoring data on the internal and external side of the foundation pit. The left side shows the internal optical fiber and the right side shows the external optical fiber; the pile undergoes deformation under lateral earth pressure, resulting in tensile strains on the internal sides of the foundation pit, and compressive strains on the external sides of the foundation pit.

On 8 March 2021, the inner support had not been poured and the support pile was under soil pressure on the external sides of the foundation pit, causing tensile strain on the optical fiber on the outer pile and compressive strain on the inner pile. On 29 March 2021, the pouring of first inner support was completed, and the foundation pit was excavated for the second time; near the excavation face, due to the bearing of partial soil pressure by the inner support, the support pile began to protrude and deform, causing compressive strain on the external side of the pile and tensile strain on the internal side. The monitoring results indicated that as the foundation pit is excavated, the supports of internal and external stress in the foundation pit are reversed; the inner support plays a significant role in sharing the stress of the support pile. The soil pressure load it bears continues to increase, but its axial force remains within a safe range, indicating that the inner support structure has relatively high safety.

According to the monitoring results at different stages, the lateral displacement of the support structure could be calculated by using the deflection calculation method in Section 1, as shown in Figure 18. The conventional measure in Figure 18 was to measure the deep horizontal displacement of the support pile using inclinometer; the monitoring location was located at CX1 in Figure 4. When the foundation pit was excavated to −9.5 m, the maximum measured value of the deep horizontal displacement clinometer of the support pile was 13.16 mm obtained at −10.78 m; the maximum measured value of distributed optical fiber was 11.32 mm obtained at −12.53 m; and the maximum calculated value was 16.88 mm obtained at −13.03 m. It can be concluded that the changing trends of the three are roughly the same, with the onsite optical fiber results being slightly smaller than the results of the numerical analysis; the reason for the error may be that the finite element simulation did not fully simulate the complex working conditions on site, such as construction machinery and onsite loading. The optical fiber was
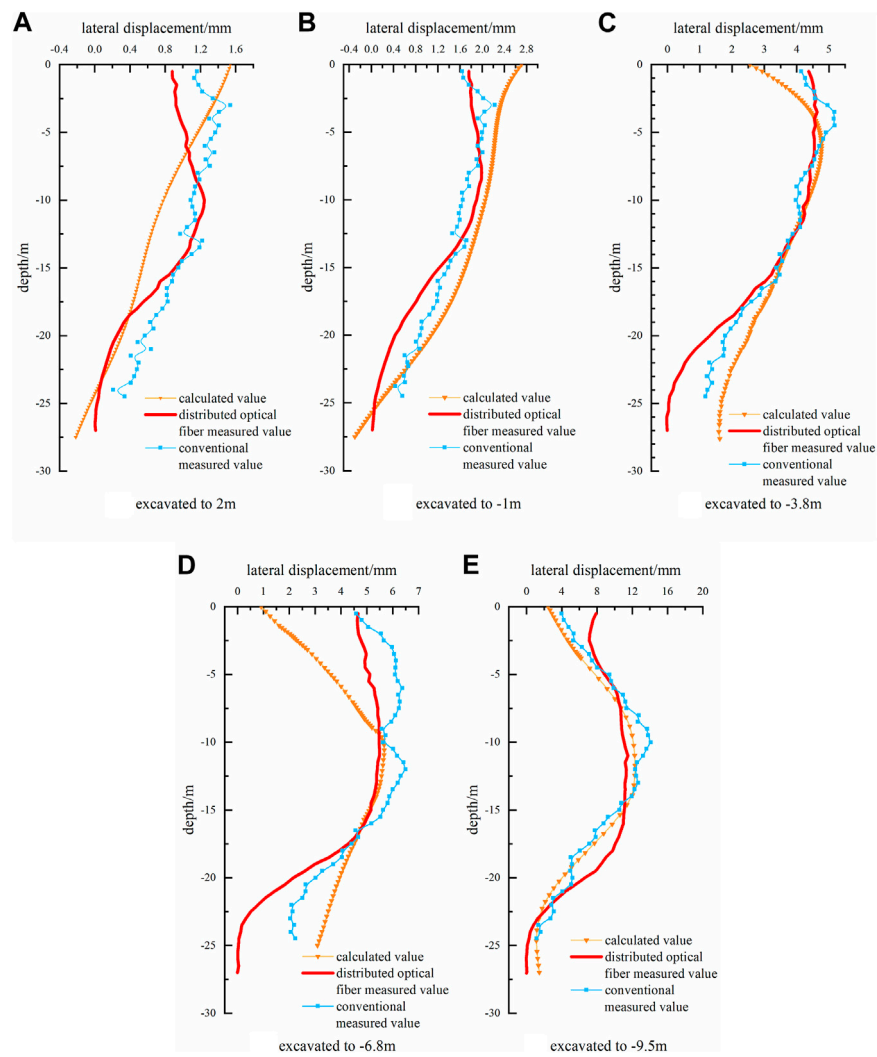
FIGURE 18
Horizontal displacement of the deep layers in section one to one. **(A)** excavated to 2 m. **(B)** excavated to −1 m. **(C)** excavated to −3.8 m. **(D)** excavated to −6.8 m. **(E)** excavated to −9.5 m.
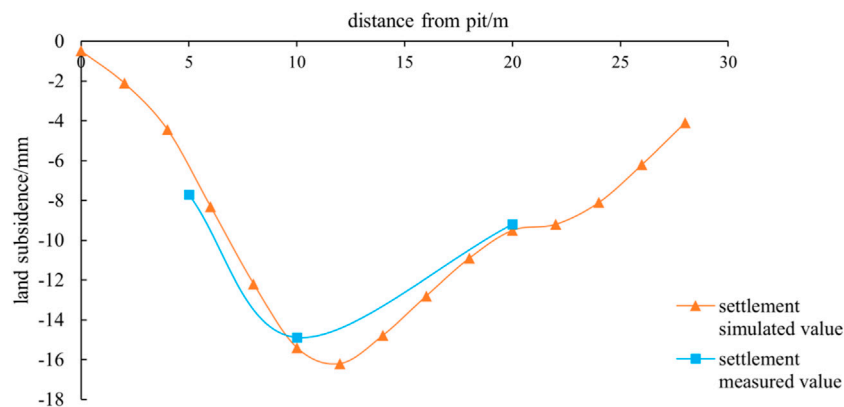

FIGURE 19
Surrounding surface subsidence.

damaged because of onsite mechanical excavation and human factors, but there were many remaining optical fiber monitoring data samples. Because the sampling interval of the optical fiber is 0.05 m, it has a significant advantage in studying the overall performance of the measured object and can be fully compared with the results of finite element analysis.

The optical fiber monitoring data was close to the monitoring data of the clinometer; the sampling interval of the clinometer data is 0.5 m, which is ten times that of optical fiber monitoring. The distributed optical fiber basically realizes the structural deformation characteristics of the measured object within a very small range, making it easy to study the subtle changes in the impact of external loads, construction machinery, and other factors on the foundation pit support structure and explore their deformations. However, optical fibers require good packaging technology and laying methods to achieve precise monitoring.

7.3 Analysis of surrounding ground surface settlement

According to the monitoring of the measured points in DB7-DB9, the relationship between the ground surface settlement of the foundation pit and the distance between the measurement points and the pit edge in Figure 19 was obtained. As shown in the figure, the changing trend of measured data of settlement and simulated calculation results was basically consistent, indicating that the HSS constitutive model can well predict the ground surface settlement law around deep foundation pit. During the excavation of the foundation pit, the center of the ground surface settlement gradually moved outward; when the excavation was completed, the deformation finally stabilized. The final measured maximum value was 14.89 mm, which was obtained at a distance of 10 m from the pit edge; the simulated maximum value was −16.2, which was obtained at a distance of 12 m from the pit edge; the ratio of ground surface settlement to excavation depth of the pit was 0.157% and 0.17%, respectively.

8 Conclusion

Real-time monitoring of the full excavation deformation process of deep foundation pits was carried out for a deep foundation pit project with internal support in the Dalian Donggang Business District using a combination of traditional monitoring and distributed optical fiber monitoring. To undertake a back-analytical study of the HSS model parameters, the sparrow search algorithm was integrated with the BP neural network. Then, using the geotechnical finite element analysis software Plaxis to simulate the entire foundation pit construction process, a finite element numerical analysis model of the foundation pit was established. The main research conclusions from the comparative analysis of measured data and simulation results are as follows:

(1) With a maximum prediction error of 15.6%, a minimum prediction error of 0.03%, and an average error rate of 7.51%, the SSA-BP neural network utilized in this article performed better. The performance to predict the dataset is enhanced.
(2) The study's back-analysis of parameters met the accuracy and precision requirements of the HSS small strain model for

modeling foundation pit excavation, and can serve as a reference for comparable actual projects.
(3) The displacement values can be calculated using the micro strain values of deep horizontal displacement obtained by the NBX-8100 optical and the deflection calculation method. The data of optical fiber monitoring was similar to that of the clinometer, and the sampling interval of the optical fiber monitoring data was approximately 1/10 of the inclinometer, achieving the structural deformation characteristics of the tested object within a very small range. Furthermore, the data curve was relatively smooth and with high continuity, demonstrating the superiority of distributed optical fiber monitoring in terms of space and accuracy.
(4) The HSS constitutive model can accurately forecast horizontal deformation and surrounding surface settlement produced by deep excavation, providing the technical assistance required for stress and deformation analysis in complex excavation projects.

Data availability statement

The original contributions presented in the study are included in the article/Supplementary Material, further inquiries can be directed to the corresponding author.

Author contributions

Corresponding author JZ planned and organized the entire research and was responsible for onsite monitoring. The first author, WL, was responsible for the numerical analysis calculation and neural network analysis. YP participated in onsite monitoring work and some numerical calculations. All authors contributed to the article and approved the submitted version.

Conflict of interest

The authors declare that the research was conducted in the absence of any commercial or financial relationships that could be construed as a potential conflict of interest.

Publisher's note

Supplementary material

The Supplementary Material for this article can be found online at: https://www.frontiersin.org/articles/10.3389/fmats.2023.1231303/full#supplementary-material

References

Atkinson, J. H., and Sallfors, G. (1991). "Experimental determination of stress-strain-time characteristics in laboratory and *in situ* tests," in Proceedings of the International Conference on Soil Mechanics and Foundation Engineering, Rotterdam: A.A. Balkema, 915–956.

Benz, T. (2007). *Small-strain stiffness of soils and its numerical consequences*. Ph.D. Germany. Stuttgart: University.

Brinkgreve, R. B. J., and Broere, W. (2006). *Plaxis material models manual*. Netherlands: Bentley Systems.

Chen, Y., Luo, M., and Xia, N. (2021). Statistical analysis of existing test results of HSS model parameters for soft soils[J]. *Chin. J. Geotechnical Eng.* 43 (S2), 197–201.

Fu, L., and Peng, Y. (2018). Development and application of safety monitoring and early warning platform for deep foundation pit. *Chin. J. Undergr. Space Eng.* 14 (S1), 423–429.

Gao, L., Gong, Y., and Yu, Y. (2017). Development and application of distributed measurement optical fiber inclinometer tube based on Brillouin optical time-domain reflectometer. *Sci. Technol. Eng.* 17 (30), 81–85.

Gu, X., Wu, R., and Liang, F. (2021). On HSS model parameters for Shanghai soils with engineering verification. *Rock Soil Mech.* 42 (03), 833–845. doi:10.16285/j.rsm.2020.0741

Hardin, B. O., and Black, W. L. (1969). Closure to "vibration modulus of normally consolidated clay". *J. Soil Mech. Found. Div.* 95 (SM6), 1531–1537. doi:10.1061/jsfeaq.0001364

Kim, S., and Finno, R. J. (2019). Inverse analysis of a supported excavation in chicago. *J. Geotechnical Geoenvironmental Eng.* 145 (9), 04019050. doi:10.1061/(ASCE)GT.1943-5606.0002120

Li, L., Liu, J., and Li, K. (2019). Study of parameters selection and applicability of HSS model in typical stratum of Jinan. *Rock Soil Mech.* 40 (10), 4021–4029. doi:10.16285/j.rsm.2018.1376

Li, Q., Wu, N., and Xiao, J. (2021). Experimental study on the small-strain characteristics of soft clay considering stress paths. *Chin. J. Undergr. Space Eng.* 17 (05), 1486–1494.

Liang, F., Jia, Y., and Ding, Y. (2017). Experimental study on parameters of HSS model for soft soils in Shanghai. *Chin. J. Geotechnical Eng.* 39 (02), 269–278.

Liu, C., Zheng, G., and Zhang, S. (2007). Effect of foundation bottom heave due to excavation on supporting system in top-down method. J. Tianjin Univ. No. 193 (08), 995–1001.

Luo, J., Ren, R., and Guo, K. (2020). The deformation monitoring of foundation pit by back propagation neural network and genetic algorithm and its application in geotechnical engineering. *PLOS ONE* 15 (7), 02333988–e233423. doi:10.1371/journal.pone.0233398

Luo, M., Chen, Z., and Zhou, J. (2021). Research status and prospect of parameter selection for the HS-Small model. *Ind. Constr.* 51 (04), 172–180. doi:10.13204/j.gyjzg2012300

Meng, G., Liu, J., and Huang, J. (2022). Automatic prediction of the deformation of a retaining structure in a deep foundation pit construction based on a BP artificial neural network. *Urban Rapid Rail Transit* 35 (03), 80–88.

Mu, L., Huang, M., and Wu, S. (2012). Soil responses induced by excavations based on inverse analysis. *Chin. J. Geotechnical Eng.* 34 (S1), 60–64.

Qiu, T., and Sun, Y. (2020). Research on monitoring of horizontal displacement field of deep soil based on OFDR technology. *Piezoelectrics Acoustooptics* 42 (01), 108–112.

Rogers, A. J. (1980). Polarisation optical time domain reflectometry. *Electron. Lett.* 16, 489–490. doi:10.1049/el:19800341

Schweiger, H. F., Vermeer, P. A., and Markus, W. (2009). On the design of deep excavations based on finite element analysis. *Geomechanics Tunn.* 2 (4), 333–344. doi:10.1002/geot.200900028

Shi, Y., Lin, S., and Che, A. (2017). Optimization analysis of the soil small strain stiffness parameters based on deep foundation pit monitoring data. *Chin. J. Appl. Mech.* 34 (04), 654–813.

Shi, Y., Lin, S., and Zhao, H. (2016). Soil's small strain parameters sensitivity analysis of metro deep foundation pit excavation effect in Xiamen area. *J. Eng. Geol.* 24 (06), 1294–1301. doi:10.13544/j.cnki.jeg.2016.06.032

Wang, G., Jiang, Y., Zang, Q., Zhao, J., and Huang, P. (2020). The antimicrobial peptide database provides a platform for decoding the design principles of naturally occurring antimicrobial peptides. *J. Civ. Eng. Manag.* 37 (5), 8–18. doi:10.1002/pro.3702

Wang, H., Li, S., Lin, L., Zhai, C., Jiang, C., Shao, J., et al. (2021). Separation of epigallocatechin gallate and epicatechin gallate from tea polyphenols by macroporous resin and crystallization. *Chin. J. Undergr. Space Eng.* 17 (S2), 832–842. doi:10.1039/d0ay02118k

Wang, N., Hong, C., Xu, D. L., Dong, X. L., Su, M. F., Qian, J. H., et al. (2020). Study on the mechanical properties of metro foundation pit support based on BOFDA technology. *Mod. Tunn. Technol.* 57 (S1), 877–883. doi:10.3760/cma.j.cn112338-20190626-00470

Wang, W., Wang, H., and Xu, Z. (2012). Experimental study of parameters of hardening soil model for numerical analysis of excavations of foundation pits. *Rock Soil Mech.* 33 (08), 2283–2290. doi:10.16285/j.rsm.2012.08.006

Wang, W., Wang, H., and Xu, Z. (2013). Study of parameters of HS-Small model used in numerical analysis of excavations in Shanghai area. *Rock Soil Mech.* 34 (06), 1766–1774. doi:10.16285/j.rsm.2013.06.022

Wu, R., Gu, X., and Gao, G. (2021). Analysis of deep excavation deformation of shanghai matro station using HSS model. *J. Archit. Civ. Eng.* 38 (06), 64–70. doi:10.19815/j.jace.2021.08055

Xi, J., and Wei, Y. (2020). Time and space effect of construction monitoring and deformation characteristics of deep foundation pit in soft soil area. *Sci. Technol. Eng.* 20 (04), 1587–1592.

Xue, J., and Shen, B. (2020). A novel swarm intelligence optimization approach: sparrow search algorithm. *Syst. Sci. control Eng.* 8 (1), 22–34. doi:10.1080/21642583.2019.1708830

Yin, J. (2010). Application of hardening soil model with small strain stiffness in deep foundation pits in Shanghai. *Chin. J. Geotechnical Eng.* 32 (S1), 166–172.

Zhang, H., Yang, S., and Wang, L. (2022). Experimental researches on *in-situ* loading and unloading deformation characteristics of soft soil based on pressuremeter tests in Shanghai area. *Chin. J. Geotechnical Eng.* 44 (04), 769–777.

Zhao, X., Chen, J., and Huang, Z. (2016). Determination of soil parameters for numerical simulation of an excavation. *J. Shanghai Jiaot. Univ.* 50 (01), 1–7. doi:10.16183/j.cnki.jstu.2016.01.001

Zheng, G., Zhu, H., Liu, X., and Yang, G. (2016). Control of safety of deep excavations and underground engineering and its impact on surrounding environment. *China Civ. Eng. J.* 49 (06), 1–24. doi:10.15951/j.tmgcxb.2016.06.001

Zhu, D., Lin, W., and Cheng, G. (2022). Research on pile displacement monitoring method based on optical fiber sensing technology. *Yangtze River* 53 (05), 168–175. doi:10.16232/j.cnki.1001-4179.2022.05.027

Zong, L., and Xu, Z. (2019). Application of small strain constitutive model in the analysis of a ultra large and deep excavation. *Chin. J. Undergr. Space Eng.* 15 (S1), 231–242.

Analysis of the structural response and strengthening performance of prefabricated substation walls under flood loads

Han Yao[1], Liang Zhang[1], Qing Wang[1], Huina Han[1], Fengkai Han[2]* and Li Tian[2]

[1]Economic Research Institute, State Grid Henan Electric Power Company, Zhengzhou, Henan Province, China, [2]School of Civil Engineering, Shandong University, Jinan, Shandong Province, China

Introduction: The study focuses on evaluating the reliability of prefabricated perimeter walls in substations during flood events. It employs a sophisticated numerical model based on actual engineering data to assess their load-bearing capabilities. The research investigates the impact of crucial flood parameters on the structural behavior of these walls, examines the force transmission mechanisms, and suggests "W-shaped" reinforcement techniques to mitigate stress-related issues.

Methods: To meet our research goals, we developed an extensive numerical model for prefabricated perimeter walls, incorporating real-world engineering data. This model enabled us to analyze critical flood parameters, such as flood depth, flow velocity, and flood erosion. Furthermore, we investigated the force transmission mechanisms within the walls and introduced "W-shaped" reinforcement strategies to improve their load-bearing capacity.

Results: Our results indicate that flood depth and flow velocity have a substantial impact on the performance of prefabricated perimeter walls, while flood erosion has a minor effect. Safety concerns become prominent when flood depth exceeds 1.0 m or flow velocity surpasses 3 m per second. Analysis of force transmission mechanisms reveals greater displacements at higher water levels. Critical areas, including wall panel-column and wall panel-foundation connections, experience heightened stress levels.

Discussion: Our study highlights the significant role of flood depth and flow velocity in evaluating the load-bearing capacity of prefabricated perimeter walls in substation environments. To address potential structural weaknesses, we recommend implementing "W-shaped" wall reinforcement methods, which efficiently decrease both displacement and stress. These findings carry implications for substation design and flood resilience, underscoring the importance of comprehensive flood risk management strategies to protect internal facilities during floods.

1 Introduction

As a vital component of the power grid, substations play a crucial role in the transmission and distribution of electricity, making their safe and stable operation essential for national economic development (Li et al., 2011). Substations are typically constructed in areas with convenient transportation and flat terrain, and perimeter walls are installed around the sites. These walls act as the first line of defense to ensure the safe and stable operation of internal facilities in substations during flood disasters. In recent years, there has been a frequent occurrence of regional natural disasters. In the first half of 2022 alone, there were 18 instances of regional heavy rainfall across the country, posing significant threats to the safe and stable operation of substations. For instance, the unprecedented heavy rainfall in Zhengzhou, China on July 20 (Zhang et al., 2022; Yin et al., 2023), caused flooding that breached the perimeter walls of multiple substations, resulting in severe damage to internal facilities and substantial economic losses. Therefore, reinforcing the perimeter walls of substations to enhance their load-bearing capacity is crucial to ensuring their safe and stable operation during flood disasters.

Several scholars have conducted a series of studies on the flood-resistant and load-bearing performance of walls using experimental methods. Guangwu et al. (2022) based on field investigation data of the Damaugou flash flood event and corresponding simulations using FLO-2D, analyzed the causes of the disaster and validated failure criteria. Zha et al. (2022) conducted destructive compression tests on floodwall columns, deriving stress-strain models to provide design references for the optimization of movable floodwalls. Wu et al. (2017) conducted experimental research and on-site monitoring of urban floodwalls, revealing that the overall stability and sealing performance of the lightweight aluminum alloy column floodwall structure were excellent. Jansen et al. (2020) assessed the impact of floods on modern Dutch residential buildings through laboratory testing and structural modeling. They developed physically based vulnerability curves and explained the methods for assessing the physical collapse of residential buildings. Medero et al. (2010) established a scaled model of Earth Walls to investigate the impact of flood cycles on wall structures. Their research demonstrated that adding fibers to Earth Walls can enhance their flood resistance. Zhou and Chen (2011) studied the load-bearing performance of movable floodwalls, providing theoretical calculation methods for stress and strain in floodwalls. They obtained experimental data on movable floodwalls, confirming the reliability of the theoretical calculations.

Scholars have also achieved numerous results using numerical simulations. Zhang et al. (2018) conducted force analysis on bend water flow patterns and investigated the stress characteristics of bend floodwalls under flood conditions. They derived a formula for calculating the stability coefficient of bend river floodwalls, providing theoretical references for the design and research of similar riverbank floodwalls. Keawsawasvong and Ukritchon (2017) established a numerical model for cantilever floodwalls in cohesive soils, analyzing the mechanical properties of the walls in both homogeneous and non-homogeneous clay layers. They clarified the influence of wall embedment depth on flood resistance. Gallien (2012) (Wang et al., 2004; Bokhove et al., 2019) conducted flood simulations and analyzed hydrological risks, providing effective analysis and decision-making support for flood control planning.

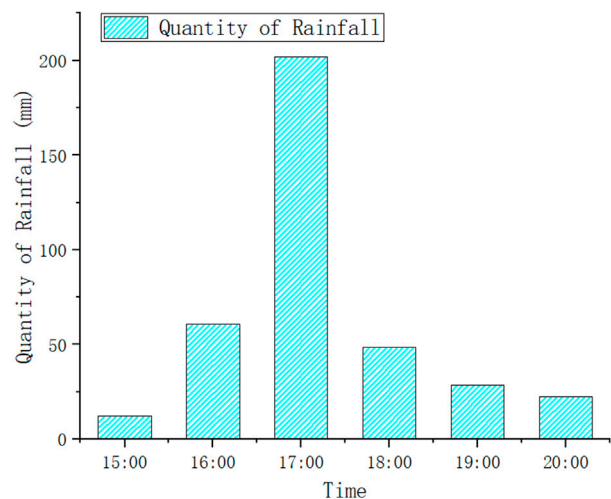**FIGURE 1**
Pictures of the site.

FIGURE 2
Real-time rainfall.

In conclusion, it can be observed that scholars have primarily focused on the research of flood-resistant walls, such as urban movable floodwalls (Miguel et al., 2021; Giacomo and Izzo, 2022) and masonry buildings (Heliová, 2023; Khadka et al., 2023) in rural areas. However, there is a lack of research on the stress characteristics, force transmission mechanism, and flood resistance performance of prefabricated perimeter walls in substations. As the proportion of prefabricated concrete walls in substation perimeters increases, conducting research on the flood resistance performance of prefabricated walls becomes crucial for ensuring the safe and stable operation of substations during flood disasters.

This study is grounded in a real substation project. It begins by creating a finite element model for prefabricated substation walls in the second section. The following sections delve into examining how floodwater depth, flow velocity, and erosion depth affect the structural performance and load-bearing capacity of these walls. Lastly, the fifth section introduces and validates an innovative "W"-shaped reinforcement device.
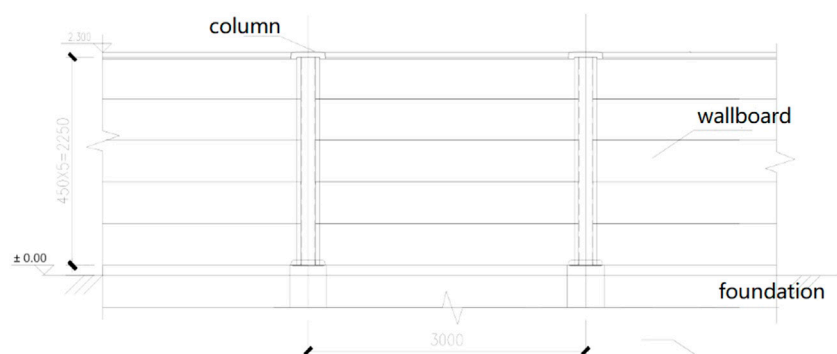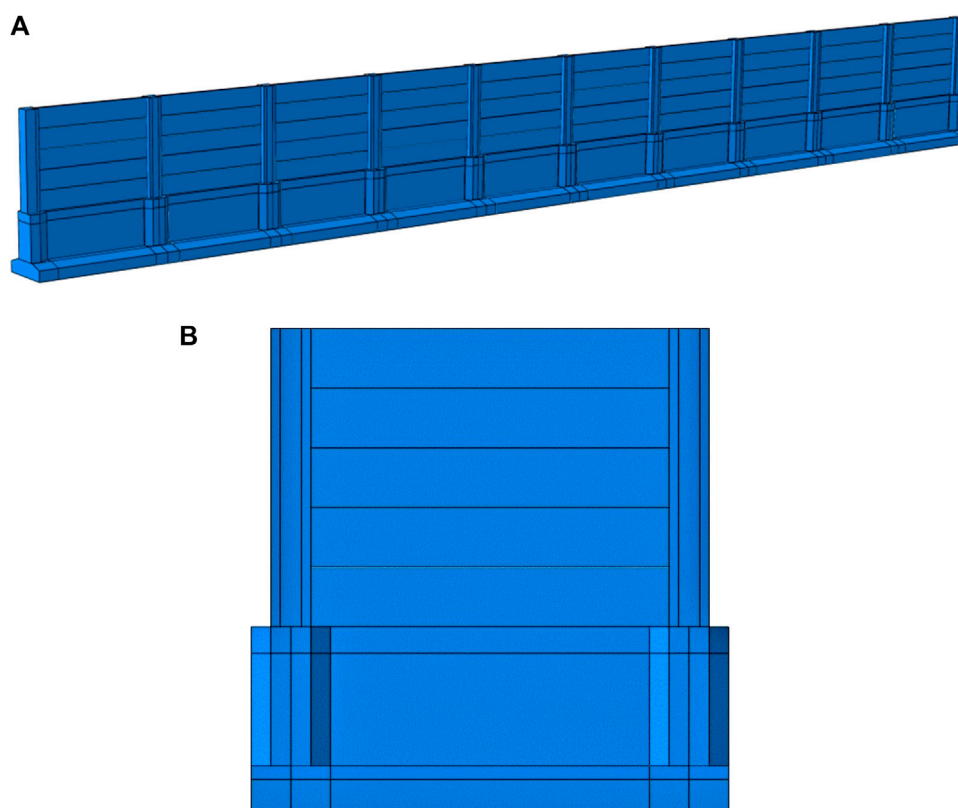
FIGURE 3
Overall layout of the wall.

FIGURE 4
(A) Finite element model of the prefabricated wall. **(B)** Single-span fence.

2 Prefabricated perimeter wall finite element model

2.1 Engineering overview

This study is conducted based on the substation wall project at the 500 kV Xinyang substation in Henan, China, with a focus on analyzing the structural characteristics of the substation wall. Visual representations of the site are provided in Figure 1. Xinyang is situated in the transitional zone between the southwestern hills and the eastern plains, with a distinct boundary between the mountainous, hilly, and plain regions. Elevations in the mountainous areas generally exceed 400 m, while the hilly regions range from 150 to 400 m, and the plain areas are below 110 m in elevation. The substation is located in the plain area, characterized by level terrain. The foundation soil layer is a single layer of compacted heterogeneous fill soil with a thickness of approximately 2.5 m, and the wall's foundation is positioned
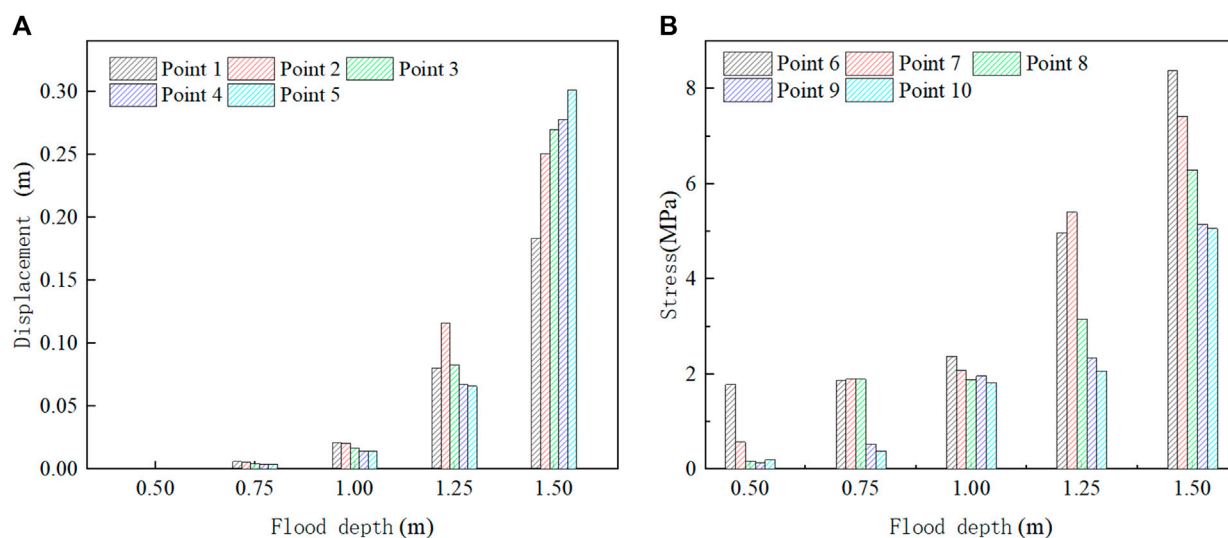
FIGURE 5
(A) Displacement variation with flood depth. **(B)** Variation of stress with flood depth.
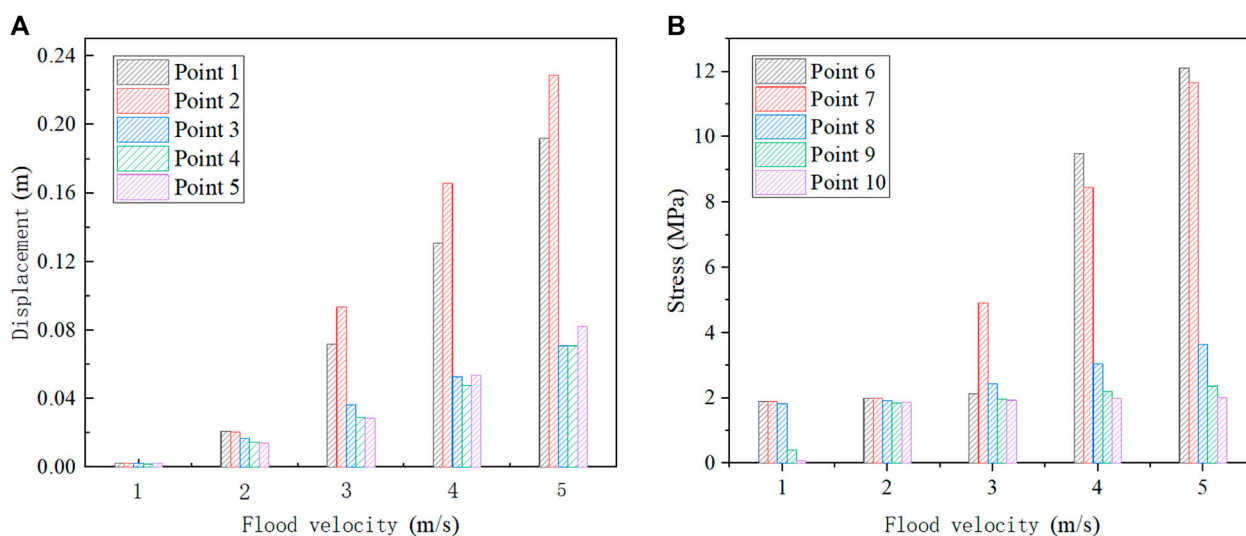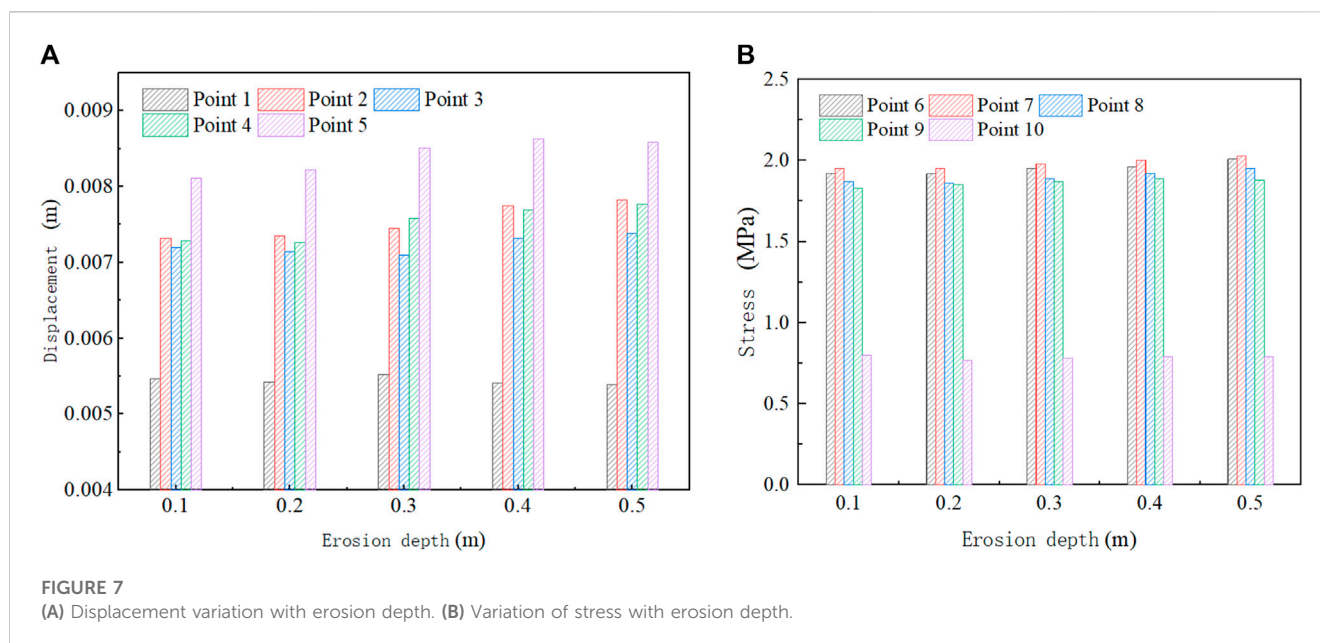

FIGURE 6
(A) Displacement variation with flood velocity. **(B)** Variation of stress with flood velocity.

within this soil layer. The Xinyang region experiences frequent shifts between cold and warm air masses, with significant interannual variations in precipitation, especially during concentrated summer rainfall events. Currently, urban drainage systems in the area generally have low standards, leading to inadequate underground drainage during heavy rainfall. The site is located in a local depression, and due to surrounding road construction, eastward drainage is hindered. Analysis indicates that the maximum flood depth at the site during a 50-year return period is 0.3 m, with a risk of flooding during rare disasters like the July 20th extreme rainfall event in

Zhengzhou, as illustrated by the measured rainfall data in Figure 2.

The prefabricated concrete structure of the walls is shown in Figure 3. The prefabricated perimeter wall consists of five components: foundation, columns, wall panels, column caps, and wall panel compression tops. The foundation is buried underground, and it is connected to the wall panels and columns in the upper part. The total height of the wall is 2.3 m, composed of five vertically assembled prefabricated wall panels. The dimensions of the prefabricated wall panels are 2,840 mm × 60 mm × 450 mm (length × width × height), and

FIGURE 7
(A) Displacement variation with erosion depth. **(B)** Variation of stress with erosion depth.

the wall top aligns with the columns. The standard column dimensions are 300 mm × 300 mm × 2,250 mm, with a center-to-center distance between adjacent columns of 3.0 m. Both the wall and columns are constructed using C30 concrete and reinforced with steel bars. The foundation dimensions for the lower part of the wall are 0.25 m wide, 2.40 m long, and 1.20 m high. For the lower part of the columns, the foundation dimensions are 0.55 m wide, 0.60 m long, and 1.20 m high. The dimensions of the column caps are 370 mm × 370 mm × 70 mm, while the wall panel compression tops measure 2,620 mm × 240 mm × 60 mm. Both the column caps and wall panel compression tops are constructed using C30 concrete. A telescopic joint is installed every 30 m along the perimeter wall, with a column placed on each side of the telescopic joint.

2.2 Finite element model of prefabricated wall

A refined finite element model of a 10-span prefabricated perimeter wall is established, with each modeling unit between two telescopic joints, as shown in Figure 4. The foundation, structural columns, and wall panels are modeled using solid elements to accurately simulate their mechanical behavior. The steel bars are represented using three-dimensional truss elements, capable of transmitting axial forces but not bending moments. This study employs a damage plasticity model to simulate the mechanical behavior of concrete and an ideal elastoplastic model for plastic materials like steel bars to describe their behavior after reaching the yield stress and entering a fully plastic state.

Based on the actual engineering, rigid connections are established between the columns and the foundation, columns and wall panels, and wall panels and the foundation in the finite element model, using the "Tie" command to simulate rigid behavior. There is no connection between the wall panels;

instead, face-to-face contact is defined to model their normal and tangential interactions. After arranging the steel reinforcement according to the requirements, the "embedded region" command is used to embed the steel bars into the concrete components, allowing them to deform together when subjected to external forces. Given the primary focus of this study on analyzing the impact of flood loads on the upper structure of the wall, a simplification approach was employed. In this approach, the ground is treated as a rigid body, and rigid connections were established between the foundation and the subgrade, thus disregarding the influence of soil-structure interaction. The preliminary analysis suggests that the connection areas between the wall and columns, as well as the center of the wall panels, are complex regions of stress under flood loads. Therefore, the mesh size for the wall-column connection is controlled within 30 mm, and the foundation mesh size is controlled within 60 mm to ensure computational accuracy while reducing computational complexity.

3 Flood load calculation

The location of the project is in a relatively shallow inundation area with minimal interaction between water flow and waves. Therefore, the coupling load of waves is neglected, and only dynamic water load and wave load are considered, along with the effect of static water pressure.

The formula for calculating static water pressure is shown in Eq. 1.

$$F_G = \rho g h \qquad (1)$$

Where F_G is the static water pressure, ρ is the density of water, g is the acceleration due to gravity, and h is the water depth.

In this practical project, the calculation of d/L satisfies the condition of the shallow water wave region, as follows (Nagai,
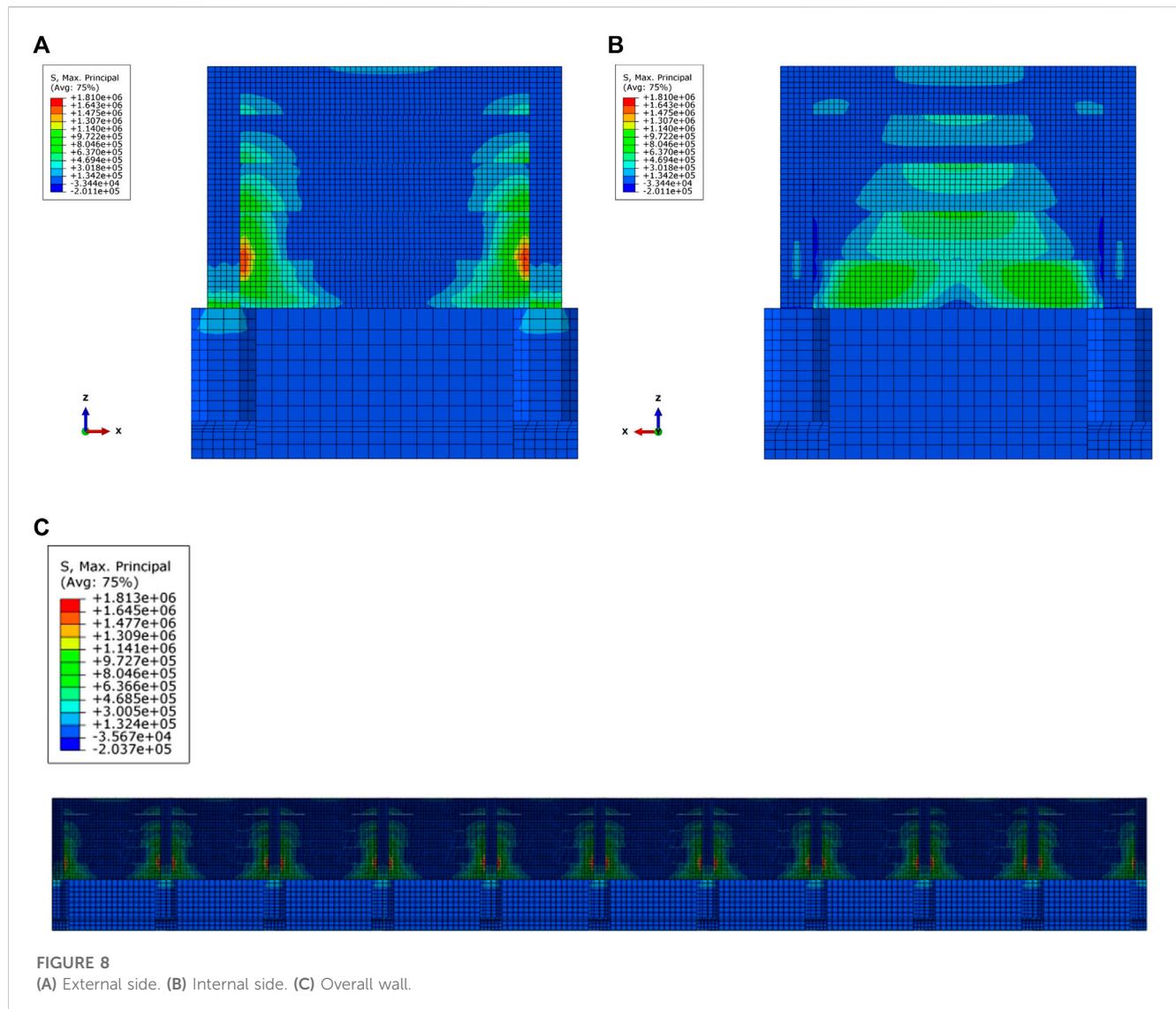
FIGURE 8
(A) External side. (B) Internal side. (C) Overall wall.

1969; Nagai, 1986; Qiu et al., 1996; Wang, 2017): In the shallow water wave region, i.e., $0.135 \leq d/L < 0.35$, the formula for calculating the maximum wave pressure intensity on the vertical wall surface at a depth z below the still water level is given in Eq. 2.

$$P = \gamma H \frac{\cosh k(d+z)}{\cosh kd} \qquad (2)$$

Where $k = 2\pi/L$ is the wave number, γ is the specific weight of water, H is the wave height, $\cosh$ denotes the hyperbolic cosine function, and d represents the water depth. The vertical coordinate z is measured from the still water level, with positive values upward. The average wave length L is determined using the wave calculation table in Appendix C of the "Design Specification for Embankment Engineering" (GB 50286-2013, 2013).

Due to the reflection effect of the vertical wall, the limiting wave height in front of the vertical wall is different from that on the beach. In this regard, Danel's experimental results on the limit stationary waves can be used to predict the limiting incident wave height Hlim. The calculation of Hlim is given in Eq. 3.

$$\frac{H_{lim}}{L} = 0.019 \tan h \frac{2\pi d}{L} \qquad (3)$$

The distribution of the maximum wave pressure intensity above the still water level forms a triangular shape, with $P = 0$ at $z = H$ and $P = \gamma H$ at $z = 0$. In the ABAQUS modeling process, it is challenging to apply the wave load function below the still water level due to its complex form. To simplify the calculation, the wave load below the still water level is approximated as a linear function, as its concave graph ensures a conservative approach. The load function above the still water level remains unchanged.

The dynamic water load (Qiu et al., 1996; GB 50286-2013, 2013; Li et al., 2001) is the primary load acting on the perimeter wall surface, and its calculation formula is given in Eq. 4.

$$F_w = K_w \frac{\rho}{2} v^2 A \qquad (4)$$

Where F_w is the standard water flow force; K_w is the comprehensive coefficient for water flow resistance, which is
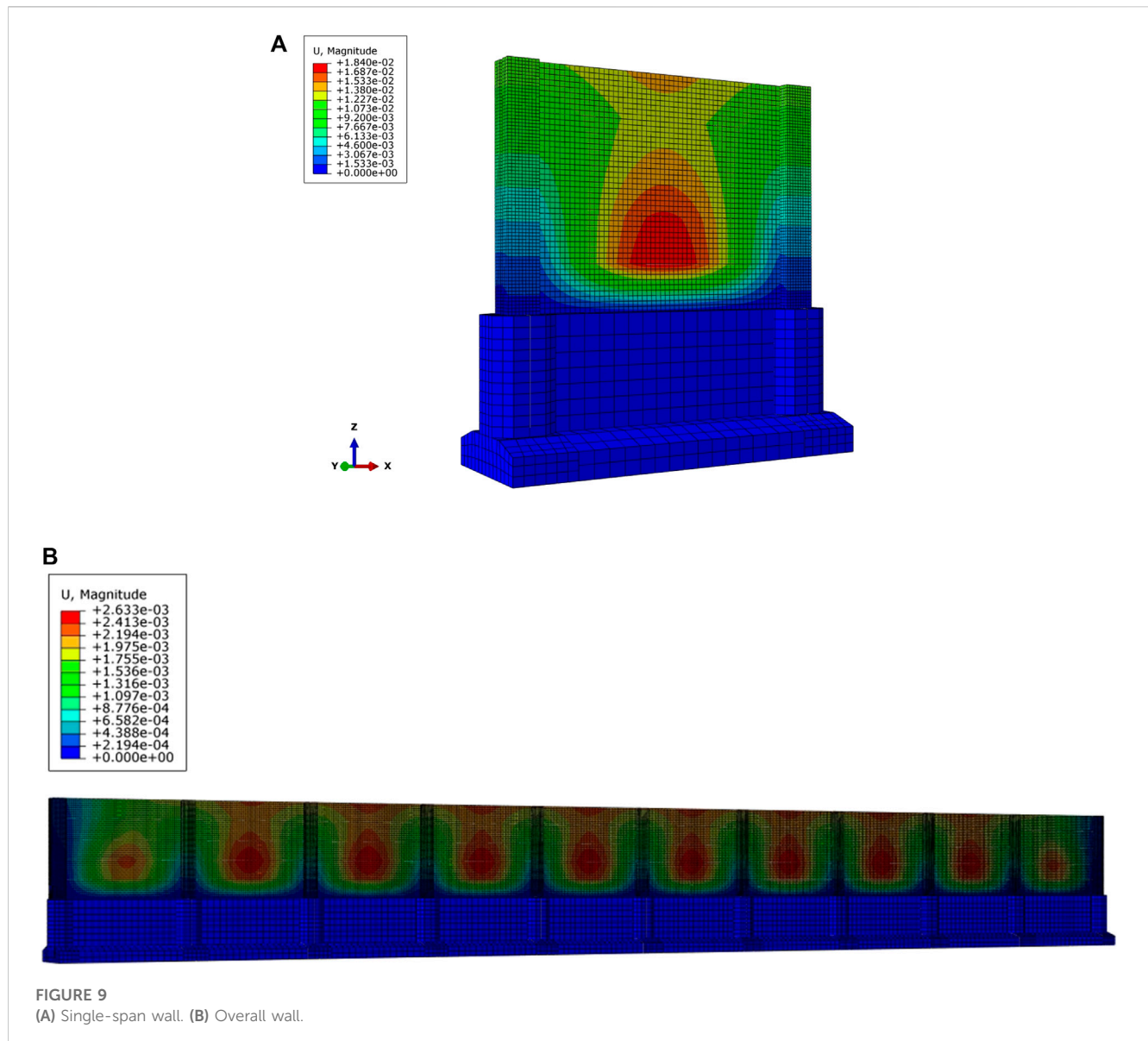
FIGURE 9
(A) Single-span wall. **(B)** Overall wall.

2.32 when the opening ratio is 0; v is the water flow velocity, and A is the area of the wall facing the flow.

$$v = C\sqrt{Ri} \qquad (5)$$

Where C is the Chezy coefficient, $C = R^{1/6}/n$; R is the hydraulic radius, $R = S/x$; i is the slope of the river section, set at 0.005 in this study; n is the roughness coefficient of the riverbed, set at 0.03 in this study; S is the cross-sectional area of the riverbed; x is the wetted perimeter of the riverbed cross-section.

4 Analysis of the impact of flood load parameters on the stress characteristics of prefabricated perimeter walls

Based on the monitoring data of the 500 kV substation wall project in Xinyang, Henan, China, the flood flow velocity was recorded as 2 m/s, and the flood water depth was 1 m. This section analyzes the stress characteristics of the wall using the finite element model and load calculations, and provides the stress and displacement variations of the perimeter wall under typical parameters.

4.1 Flood depth

Flood depth is a significant factor influencing the magnitude of flood load. In this section, while keeping the substation perimeter wall subjected to a flood load with a velocity of 2 m/s, an analysis was conducted to assess the maximum stress and displacement of the wall under different water depths. The study aims to determine the impact of water depth on the stress and displacement characteristics of prefabricated perimeter walls.

To quantitatively assess the influence of floodwater depth on the stress performance of prefabricated perimeter walls, displacement monitoring points 1–5 were strategically placed at critical response locations, and stress monitoring points 6–10 were positioned at
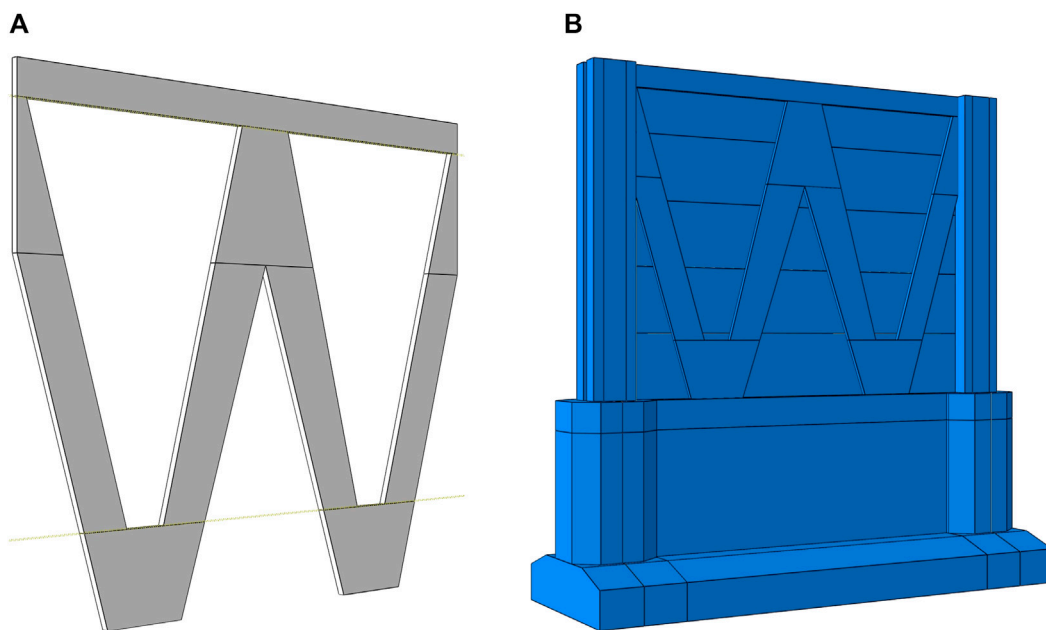
FIGURE 10
(A) W-type reinforcement device. **(B)** Finite element model of the W-type wall reinforcement device.

FIGURE 11
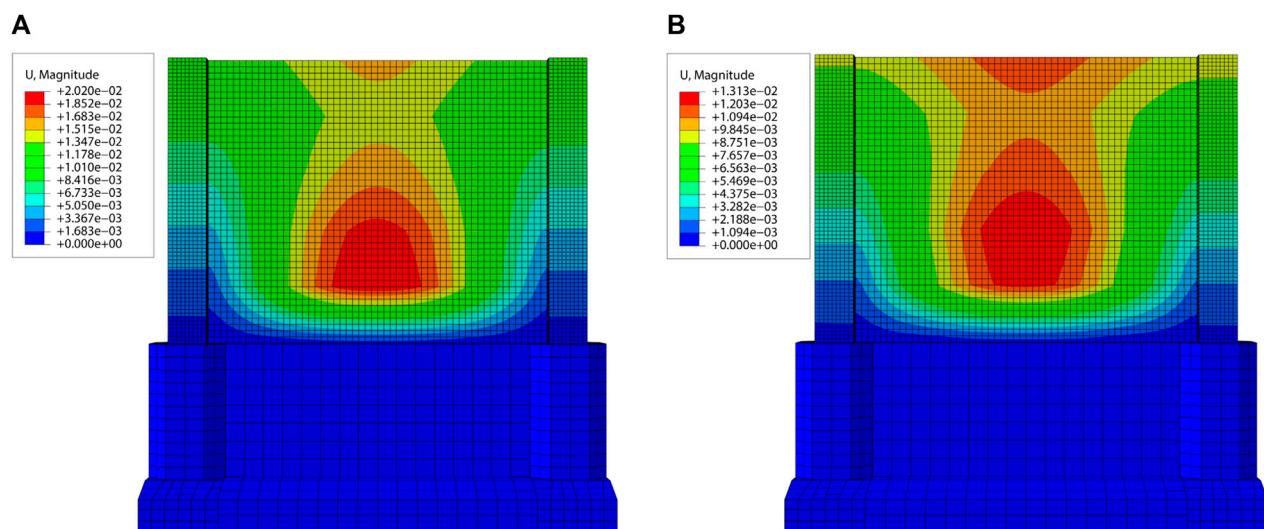**(A)** Displacement contour map before reinforcement. **(B)** Displacement contour map after reinforcement.

locations with complex stress patterns. The changes in displacement and stress responses with increasing floodwater depth are illustrated in Figure 3. From Figure 5A, it can be observed that displacement at monitoring points 1 and 2 remains relatively small, below 0.02 m, when the flood depth is less than 1.0 m. However, as the flood depth exceeds 1.0 m, the wall displacement increases significantly, leading to abrupt and irreversible failure. Monitoring points 3, 4, and 5 exhibit similar displacement behavior to points 1 and 2 when the flood depth is less than 1.0 m. Nevertheless, as the flood depth

exceeds 1.0 m, the displacement increment becomes smaller, resulting in a notable difference compared to points 1 and 2.

From Figure 5B, it can be observed that, similar to the displacement pattern, the stress at monitoring points 6 and 7 remains relatively small when the flood depth is less than 1.0 m. However, as the flood depth exceeds 1.0 m, the wall stress increases significantly. Monitoring points 8, 9, and 10 exhibit a continuous increase in stress with the increase of flood depth. Nevertheless, due to the minimal force transmission between wall
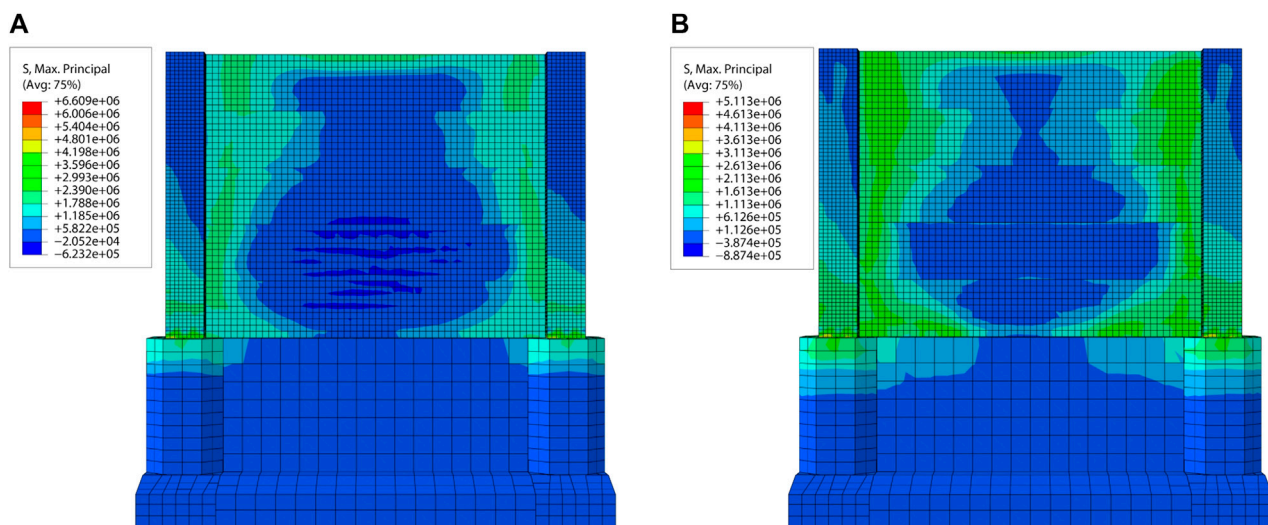
FIGURE 12
(A) Tensile stress contour map before reinforcement. **(B)** Tensile stress contour map after reinforcement.
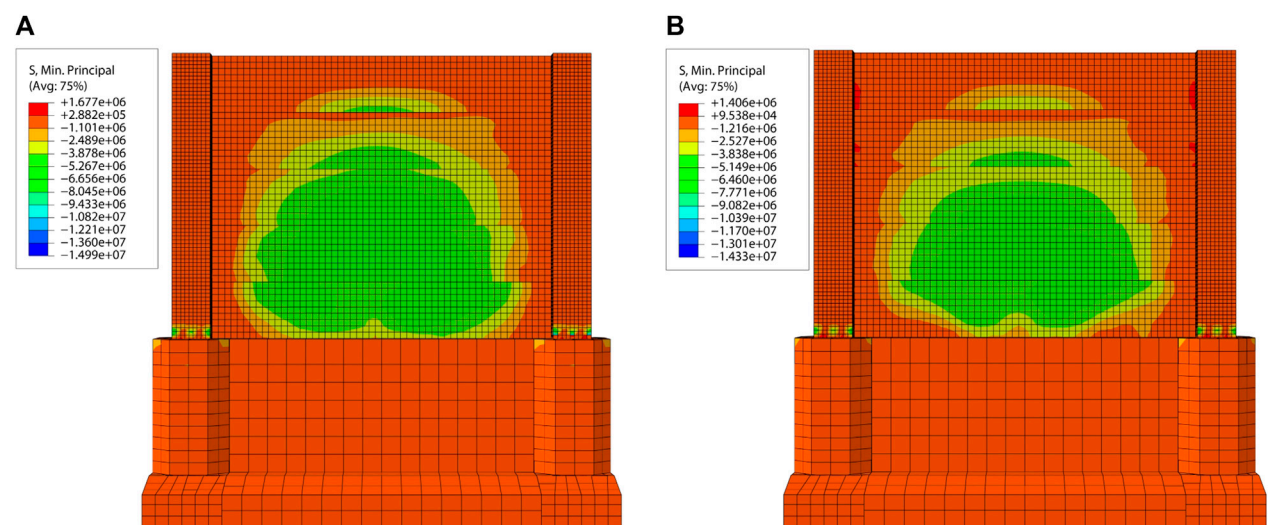

FIGURE 13
(A) Compressive stress contour map before reinforcement. **(B)** Compressive stress contour map after reinforcement.

panels, the stress at the upper monitoring points remains smaller than the stress at the lower monitoring points as the floodwater load primarily acts on individual wall panels.

4.2 Flood velocity

This section explores the effect of floodwater flow velocity on the load-bearing performance of the substation perimeter wall, using a refined finite element model with a flood depth of 1.0 m. The study addresses the increasing impact and inertial forces associated with higher floodwater flow velocities, which can potentially compromise the safety of the building structure.

Figure 6A shows the displacement curves for monitoring points 1–5 at flow velocities ranging from 1 m/s to 5 m/s. It can be observed that at flood flow velocities below 2 m/s, monitoring points 1 and 2 exhibit minimal displacements (less than 0.03 m) due to the limited inertia and impact forces of the water, resulting in minor wall deformation. However, when the flood flow velocity exceeds 2 m/s, the inertia and impact forces rapidly increase, leading to significant deformations at monitoring points 1 and 2. As for monitoring points 3, 4, and 5 located above the still water level and not directly influenced by floodwater load, their deformations are relatively unaffected by changes in flood flow velocity. Thus, at lower flow velocities, their deformations remain similar to those observed at monitoring

points 1 and 2, while at flow velocities exceeding 2 m/s, the deformations show a smaller increase.

As shown in Figure 6B, the stress-strain curves for monitoring points at flow velocities ranging from 1 m/s to 5 m/s are depicted. Monitoring points 6 and 7 are located on wall panels directly subjected to floodwater loads. At flow velocities below 2 m/s, the stress values at these points remain relatively stable. However, when the flow velocity exceeds 2 m/s, the stress at monitoring points 6 and 7 noticeably increases. As for monitoring points 8, 9, and 10, at flow velocities below 2 m/s, their stress values are similar to those observed at monitoring points 6 and 7. At flow velocities exceeding 2 m/s, due to the limited force transmission between wall panels, the stress increase is more gradual.

4.3 Erosion depth

Flood-induced erosion of the subsoil beneath perimeter walls also affects the hydrodynamic load acting on the building structure. Increasing erosion depth results in a greater impact on the foundation under flood conditions. This section investigates the load-bearing performance of prefabricated perimeter walls with the gradual erosion of the left three-span foundation under a water depth of 1.0 m and flow velocity of 2 m/s, revealing the influence of erosion depth on the wall's performance.

Figure 7 illustrates displacement and stress curves at monitoring points under different erosion depths. It is clear that varying erosion depths have led to minimal alterations in both displacement and stress levels of the substation wall. However, it's essential to acknowledge that the simplified finite element model utilized in this study incompletely addresses the influence of flood erosion on the system (Assimaki et al., 2005; Fatahi et al., 2014; Avcil et al., 2022; Muhammad Tariq, 2023). Consequently, the effect of erosion depth changes on stress distribution and displacement response of the wall seems relatively minor. This simplification has somewhat limited the comprehensiveness and precision of the analysis.

4.4 Influence of typical parameters on stress and displacement analysis

Figure 8 presents the stress contour plot of the perimeter wall, where (a) represents the side facing the flood outside the station (referred to as the "external side") and (b) represents the side facing the substation facility (referred to as the "internal side"). As depicted in Figure 8, the maximum tensile stress in the wall panels occurs at the two ends and bottom of the external side, while significant tensile stress is observed at the connection between the external side column and the foundation. In other areas, the tensile stress is relatively small. Consequently, under the influence of floodwater load, concrete cracks are primarily observed at key locations, including the wall-column connection, wall-foundation connection, and column-foundation connection. The presence of joints in these areas of prefabricated walls makes them vulnerable to tensile failure.

Figure 8 shows the displacement contour map of the prefabricated wall. From the figure, it can be observed that the wall deformation primarily occurs in the vertical direction of the

wall. As shown in Figure 9A, the maximum deformation occurs at the center of the wall at the still water level, with significant deformation also observed at the top center. Figure 9B illustrates variations in the displacement contour maps of the wall at different locations under floodwater influence.

5 Enhancement of performance for substation prefabricated wall

Based on the analysis of the structural performance and parameters of the substation prefabricated wall, it was observed that the maximum tensile stress occurs at the connections between the wall panels and other components, and the maximum deformation appears at the center of the wall. To improve the stress distribution, alleviate stress concentration on the wall panels, and reduce wall displacement, this section proposes a "W-shaped" wall reinforcement device, as shown in Figure 10A. The "W-shaped" wall reinforcement device is 2.25 m high, 2.7 m wide, with a panel width of 250 mm and a thickness of 20 mm. It includes crossbeams with a width of 150 mm at the top. The reinforcement device is firmly connected to the columns and foundation on both sides and at the bottom, and it makes contact with the wall panels.

Considering that the wall's tensile strength is weaker than its compressive strength, and the inner wall panels experience significant tensile stress during flood impacts, the reinforcement device is positioned on the inner side of the prefabricated wall to enhance its performance. The "W-shaped" reinforcement device is combined with the prefabricated wall, as shown in Figure 10B, to investigate the improvement of the wall's performance through the reinforcement.

When flood load acts on the retaining wall, the wall panels bear the majority of the load due to their larger force-bearing area compared to other parts. Considering the relatively thinner thickness and lower stiffness of the wall panels, the reinforcement devices are designed to primarily share the load carried by the wall panels. Considering the load transmission path in the wall, after the wall panels deform under the flood load, the load is transferred to the stiffer columns, and then from the columns to the foundation. A small portion of the flood load is directly transferred to the foundation through the bottom layer of wall panels. Therefore, when installing the reinforcement devices, they can be securely connected to both the columns and the foundation along with the wall panels.

Under the flood conditions with a depth of 1 m and a flow velocity of 2 m/s, a comparative analysis of the wall's stress variation before and after reinforcement was conducted. Figure 11, Figure 12, and Figure 13 represent the displacement and stress contour plots of the wall. From Figure 11, it can be observed that after reinforcement, the maximum displacement of the wall is 0.0131 m, which is approximately 40% less than the maximum displacement of the unreinforced wall (0.0202 m), indicating a significant strengthening effect. From Figure 12, it can be observed that the maximum tensile stress of the reinforced wall decreased from 6.61 MPa to 5.11 MPa, reducing by approximately 24%. Moreover, the stress distribution became more uniform, indicating a significant improvement in the wall panel's force distribution. From Figure 13, it can be seen that the maximum compressive stress of the reinforced wall decreased from

1.68 MPa to 1.41 MPa, reducing by approximately 15%. Additionally, the peak compressive stress is relatively smaller than the tensile stress, indicating improved safety.

Overall, the "W-type" wall reinforcement device demonstrates excellent performance in reducing wall displacement and stress, effectively alleviating stress concentration phenomena, and ensuring the safety of the assembled wall.

6 Conclusion

This paper is based on the 500 kV substation wall project in Xinyang, Henan, China, and establishes a detailed numerical model of a 10-span assembled wall. By considering the wave characteristics of the flood, key parameters affecting flood loads are selected to investigate the stress behavior of the wall under different flood loads. The study clarifies the structural response of the substation wall under flood loads and proposes relevant reinforcement measures. The main conclusions are as follows.

(1) The flood depth and flow velocity have critical values, with the critical flood flow velocity at 2 m/s and the critical flood depth at 1.0 m. When the flood depth is less than 1.0 m, the displacement and stress of the wall at different monitoring points are relatively small and show minimal differences. However, when the flood depth exceeds 1.0 m, significant increases in displacement and stress are observed at all monitoring points, with larger differences. The impact of flood flow velocity on stress and displacement follows a similar pattern to that of flood depth. Additionally, the erosion depth of the flood has negligible effects on the stress and displacement of the wall.

(2) When the flood load is relatively low, the maximum deformation of the wall occurs at the center of the wall near the still water level, with the top center of the wall also experiencing significant deformation. However, under higher loads, the maximum deformation shifts to the center of the wall. The deformation pattern of the columns is similar to that of the wall, but due to their higher stiffness compared to the assembly wall, the columns' deformation is smaller than that of the wall at the same height.

(3) Under the action of flood load, the bottom wall panel directly transfers the load to the foundation and columns. Other wall panels transfer the load to the columns through their ends, and the columns transfer the load to the foundation through the connections at their base. Under the influence of flood load, the wall panels connecting the columns and foundation, as well as the columns connected to the foundation, are prone to tensile failure. The center of the outer wall panel, both sides of the inner wall panel, and the connection between the inner side of the column and the foundation are prone to compressive failure.

(4) The "W-type" wall reinforcement device effectively reduces wall displacement and stress. After reinforcement, the maximum displacement of the wall decreased by approximately 40%, the maximum tensile stress decreased by approximately 24%, and the maximum compressive stress decreased by approximately 15%. Moreover, the device promotes more uniform stress distribution, effectively alleviating stress concentration, and exhibits excellent reinforcement effects.

(5) While this study simplified the consideration of soil-foundation-structure interaction to reduce model complexity, it's important to recognize the limitations and conservativeness introduced by this simplification. In practical engineering, the interaction between soil and foundation is often significant due to the inherent elasticity and deformability of soil. The rigid contact assumption underestimates the relative displacement between soil and foundation, thereby affecting the accuracy of displacement responses in wall structures. Particularly when dealing with external loads such as floods or earthquakes, this simplification may lead to overly conservative results, overlooking the potential impact of the complex interactions between soil and structure on structural performance.

(6) This study not only offers comprehensive data on the structural behavior and performance of retaining walls in flood environments for practical engineering applications but also successfully introduces and validates an innovative and effective "W"-shaped reinforcement device. This integrated research approach and reinforcement solution hold promise in providing more reliable design criteria for similar projects in future engineering practices, further advancing technological progress and development in related fields.

Data availability statement

The raw data supporting the conclusion of this article will be made available by the authors, without undue reservation.

Author contributions

HY: Writing–original draft. LZ: Writing–original draft. QW: Writing–original draft. HH: Writing–original draft. FH: Writing–review and editing. LT: Writing–review and editing.

Funding

Conflict of interest

Authors HY, LZ, QW, and HH were employed by State Grid Henan Electric Power Company.

The remaining authors declare that the research was conducted in the absence of any commercial or financial relationships that could be construed as a potential conflict of interest.

Publisher's note

References

Assimaki, D., Gazetas, G., and Kausel, E. (2005). Effects of local soil conditions on the topographic aggravation of seismic motion: parametric investigation and recorded field evidence from the 1999 athens earthquake. *Bull. Seismol. Soc. Am.* 95 (3), 1059–1089. doi:10.1785/0120040055

Avcil, F., Ercan, I., Büyüksaraç, A., et al. (2022). The effect of local soil conditions on structure target displacements in different seismic zones. *Gümüşhane Üniversitesi Fen Bilim. Derg.* 12 (4), 1000–1011. doi:10.17714/gumusfenbil.1107506

Bokhove, O., Kelmanson, M. A., Kent, T., Guillaume, P., and Tacnet, J. M. (2019). Communicating (nature-based) flood-mitigation schemes using flood-excess volume. *River Res. Appl.* 35 (9), 1402–1414. doi:10.1002/rra.3507

Fatahi, B., Tabatabaiefar, S. H. R., and Samali, B. (2014). Soil-structure interaction vs Site effect for seismic design of tall buildings on soft soil. *Geomechanics Eng.* 6 (3), 293–320. doi:10.12989/gae.2014.6.3.293

Gallien, T. W. (2012). *Predictive urban coastal flood modeling: Accounting for tides, surge, waves and flood control infrastructure*. Irvine: [D]. University of California.

GB 50286-2013 (2013). *Design specification for embankment engineering*.

Giacomo, V., and Izzo, C. (2022). Three-dimensional cfd modelling of urban flood forces on buildings: A case study. *J. Phys. Conf. Ser.* 2162 (1), 012020. doi:10.1088/1742-6596/2162/1/012020

Guangwu, S., Xiaoqing, C., Jiangang, C., Zhao, W. y., Li, S., and Li, X. n. (2022). Failure criteria of unreinforced masonry walls of rural buildings under the impact of flash floods in mountainous regions. *J. Mt. Sci.* 19 (12), 3388–3406. doi:10.1007/s11629-022-7491-6

Heliová, M. (2023). *Study of masonry structure protection in floods areas[D]*.

Jansen, L., Korswagen, P. A., Bricker, J. D., Pasterkamp, S., de Bruijn, K. M., and Jonkman, S. N. (2020). Experimental determination of pressure coefficients for flood loading of walls of Dutch terraced houses. *Eng. Struct.* 216, 110647. doi:10.1016/j.engstruct.2020.110647

Keawsawasvong, S., and Ukritchon, B. (2017). Finite element analysis of undrained stability of cantilever flood walls. *Int. J. Geotech. Eng.* 11, 355–367. doi:10.1080/19386362.2016.1222044

Khadka, S. S., Acharya, S., Acharya, A., and Marc, J. (2023). Enhancement of Himalayan irregular stone masonry buildings for resilient seismic design. *Front. Built Environ.* 9. doi:10.3389/fbuil.2023.1086008

Li, H. J., Dai, F. C., Li, W. C., Xu, L., and Min, H. (2011). Stability assessment of a slope under a transformer substation using numerical modelling. *Bull. Eng. Geol. Environ.* 70, 385–394. doi:10.1007/s10064-010-0318-7

Li, Y. C., Dong, G. H., Sun, Z. C., Xu, S. Q., Mao, K., and Niu, E. Z. (2001). Laboratory study on the interaction between regular obliquely incident waves and vertical walls. *CHINA Ocean. Eng.* 15 (2), 195–203. doi:10.3321/j.issn:0890-5487.2001.02.005

Medero, G. M., Kennedy, J. H., Woodward, P. K., and Banimahd, M. (2010). Flooding effect on earth walls. *Sustainability* 3 (1), 69–81. doi:10.3390/su3010069

Miguel, A. M. M., Emmanuel, M., Andr eacute, P., Darius, S., and Proust, S. (2021). Impact of the porosity of an urban block on the flood risk assessment: A laboratory experiment. *J. Hydrology* 602, 126715. doi:10.1016/j.jhydrol.2021.126715

Muhammad Tariq, A. (2023). Chaudhary. Sensitivity of seismic response of pile-supported, multi-span viaduct bridges to interaction between soil-foundation and structural parameters. *Innov. Infrastruct. Solutions* 8 (6). doi:10.1007/s41062-023-01145-2

Nagai, S. (1986). Acoustic power measurements of focused waves: radiation force and Raman-nath methods: radiation force and Raman-nath methods. *J. Acoust. Soc. Jpn. (E)* 7 (4), 229–231. doi:10.1250/ast.7.229

Nagai, S. (1969). Pressures of standing waves on vertical wall. *J. Waterw. Harb. Div.* 95 (1), 53–76. doi:10.1061/jwheau.0000623

Qiu, D., Zang, J., and Jia, Y. (1996). Action of cnoidal waves on vertical walls. *China Ocean. Eng.* 10 (2), 129.

Wang, H. (2017). Water wave pressure on horizontal plate. *J. Hydraulics Div.* 96 (10), 1997–2017. doi:10.1061/jyceaj.0002724

Wang, X. Y., Zhang, X., and Guo-Wei, L. (2004). Over-standard integrated risk analysis of flood control system. *J. Hydraulic Eng.* (2), 83.

Wu, J. J., Ni, L. J., Chen, H. Y., Wang, H. L., et al. (2017). Research on water retaining test of movable flood control wall. *Water Resour. Power* 35, 85–88.

Yin, L., Fan, P., Mao, J., and Jin, S. (2023). Analysis on precipitation efficiency of the "21.7" henan extremely heavy rainfall event. *Adv. Atmos. Sci.* 40 (3), 374–392. doi:10.1007/s00376-022-2054-x

Zha, X., Guo, L., and Liu, Z. (2022). Strains model of movable type flood walls under different waterhead. *Innov. Comput.* 791, 1183–1193.

Zhang, R. G., Xu, G. X., Wang, L. F., Kang, H., Su, L. M., and Liu, L. (2018). Stability attenuation of retaining wall under flood in river bend (Article). *Yantu Lixue/Rock Soil Mech.* 39 (1), 63–70, 77. doi:10.16285/j.rsm.2016.0135

Zhang, Y., Yu, H., Zhang, M., Yang, Y., and Meng, Z. (2022). Uncertainties and error growth in forecasting the record-breaking rainfall in Zhengzhou, Henan on 19-20 July 2021. *Sci. China (Earth Sci).* 65 (10), 1903–1920. doi:10.1007/s11430-022-9991-4

Zhou, H. L., and Chen, Y. B. (2011). Numerical experiment comparative research on simulation methods for flood propagation in urbanization ground. *Sichuan Daxue Xuebao (Gongcheng Kexue Ban)/Journal Sichuan Univ. Eng. Sci. Ed.* 43 (4), 1–6.

Experimental study on strength and failure characteristics of mortar specimens with prefabricated cracks under uniaxial and triaxial stress

Xuwei Pan, Li Wan, Tong Jiang*, Yanchang Jia and Shuo Zhang

College of Geosciences and Engineering, North China University of Water Resources and Electric Power, Zhengzhou, Henan, China

Cracks in rock masses have adverse effects on their mechanical characteristics and the stability of rock mass engineering. For this experiment, uniaxial compression and true triaxial compression unloading tests were conducted on mortar specimens. The strength of the specimens was the lowest when the dip angle of the crack was 45°. Under uniaxial compression, the failure mode was mainly tensile failure. With an increase in the crack dip angle of the specimens, the types of cracks changed from shear to tensile cracks. Under true triaxial compression, the confining pressure considerably increased the strength and deformation characteristics of the specimens and weakened the influence of the crack dip angle on the strength. The failure mode when the crack dip angle was 15° was mainly tensile. The failure mode when the crack dip angles were 45° and 75° was mainly tensile−shear composite. With the increase in the crack dip angle, the failure degree of the specimens was more severe. Under the triaxial unloading confining, the failure mode was mainly shear. Compared with uniaxial compression, the failure degree of the specimens was more severe under true triaxial compression and true triaxial unloading. The innovation of this experiment is the use of a special mold to prepare specimens. We recommend that scholars conduct experimental and numerical simulation studies on different crack geometries.

1 Introduction

After experiencing a long geological evolution and human disturbances, the original joints of rock masses expand and connect to form macroscopic cracks. The development and expansion of cracks in a rock mass play a decisive role in the mechanical behavior of the rock mass, which seriously affects the stability and safety of many rockmass engineering (such as mining, underground space, slope, civil engineering, etc.). Therefore, to increase the feasibility and stability of geotechnical engineering, scholars must study the evolution process of cracks in rock masses, the failure mode of fractured rock masses, and the influence of cracks on the mechanical properties of rock masses.

Research has been conducted on crack propagation evolution in fractured rock masses. Chen et al. (2022) studied the influence of the prefabricated crack size on the directional propagation

law of rock type-I cracks. Xu et al. (2021) studied the crack closure and propagation modes of rock specimens containing a single crack under bidirectional shear testing. Yang and Jiang (2010) analyzed the influence of the fracture length and dip angle on crack propagation mechanisms in brittle sandstone. Lee and Jeon (2011) noted that the cracks of specimens with prefabricated cracks need to undergo evolution, such as initiation, propagation, and penetration. Ashby and Sammis (1990) established a failure model of crack growth, which considered the interaction between cracks. The influence of different fracture depths and fracture dip angles on the penetration mechanism of prefabricated cracks was analyzed by Shen and Stephansson (1993). Bobet and Einstein (1998) (Shen et al., 1995; Wong et al., 2001a) studied the initiation, propagation, and penetration mechanism of secondary cracks. Dyskin et al. (2003) studied the crack propagation law of specimens with a single inclined prefabricated crack. Wong et al. (2004a), Wong et al. (2004b), Wong and Einstein (2009b), and Wong et al. (2018) studied the influence of crack strikes (angles with the principal compressive stress) and crack depth on crack propagation morphology under uniaxial- and biaxial compression conditions and proposed many different types of crack propagation modes, such as shear, tensile, and tensile–shear mixed models. Nguyen et al. (2011) studied the crack propagation mechanism of tuff with intermittent cracks under a plane strain condition. Liu et al. (2014) indicated that under a low confining pressure, secondary cracks begin to expand from the tip of the original prefabricated crack with a larger initiation angle. Hao et al. (2021) studied the evolution law of strain fields in the rock bridge region, which contained granite with prefabricated cracks. Mei et al. (2020) indicated that the crack propagation rate in a mortar sample with a single prefabricated crack decreases first and then increases. Liu et al. (2018) indicated that with the increase in normal stress, the length of a single tensile crack becomes shorter and the number increases. Shen et al. (2022) indicated that the loading rate has an effect on the energy release and the generation of new cracks. Ai et al. (2019) indicated that the impact velocity has an important influence on the crack propagation process and dynamic mechanical properties. Song et al. (2019) studied the evolution of prefabricated cracks in coal and rock samples under uniaxial compression.

Research has also been conducted on the failure mode of fractured rock masses. Liu et al. (2019) studied the crack propagation and failure law of specimens with x-type cross cracks under different confining pressures. Yang et al. (2012) studied the failure characteristics of rocks with three intermittent cracks under uniaxial or biaxial compression. Wong and Chau (1998) and Wong et al. (2001b) refined the failure modes of specimens with two cracks under different confining pressures and classified the three failure modes summarized by Bobet and Einstein (1998) into nine types. Nasseri et al. (1997) and Niandou et al. (1997) analyzed the influence of the fracture dip angle on mechanical parameters and found that three different failure modes existed. Bobet (2000) indicated that under high confining pressure, only shear cracks initiate and eventually lead to specimen failure. Wong et al. (2006b) analyzed the influence of the length, dip angle, and width of prefabricated cracks on the failure mode of rocks with prefabricated cracks.

Research has also been conducted on the mechanical properties of fractured rock masses. Zhang et al. (2020) combined with the theory of frost heaving mechanics and fracture mechanics, carried out the freeze–thaw cycle test, and analyzed failure modes and mechanical

characteristics of crack growth. Li et al. (2022) analyzed the influence of prefabricated crack angles on the mechanical properties and failure modes of coal samples under uniaxial compression. The geometric parameters of the joints in the rock mass (such as the occurrence, length, roughness, connectivity, filling, etc.) are the main factors that influence the mechanical characteristics of jointed rock masses. Wong and Einstein (2009a) analyzed the strength characteristics of marble with intermittent double cracks under uniaxial compression. Yang and Jing (2010) studied the influence of the length and dip angle of prefabricated cracks on crack propagation and the mechanical characteristics of rock masses.

Xi et al. (2020) indicated that crack initiation and propagation will occur when the stress is far less than the compressive strength of the rock for granite specimens with prefabricated cracks. Liu et al. (2022) proposed a mechanical model of multi-cracked rock masses and noted that the strength of multi-cracked specimens decreases first and then increases with the increase in the crack inclination angle. Tiwari and Rao (2006) studied the influence of joint morphology on strain hardening and softening and the plastic behavior of rock masses with triaxial and true triaxial compression tests. Gehle and Kutter (2003) studied the effects of the length, spacing, and inclination of cracks on the shear deformation and fracture failure process of the specimens. Prudencio and Van Sint Jan (2007) studied the effects of the spacing, inclination, and arrangement of the joints on the failure mode, strength, and deformation characteristics of rock masses.

Acoustic emission (AE) technology has been widely used when analyzing the crack propagation process (Chang and Lee, 2004; Lei et al., 2004; Tham et al., 2005; Xi et al., 2020; Shen et al., 2022). Chen et al. (2022) analyzed the response characteristics of AEs during crack propagation. Li et al. (2022) analyzed the influence of the prefabricated crack angle on the AE response of coal samples under uniaxial compression. Gao et al. (2023) monitored the mechanical behavior of red sandstone via two analyses that were conducted by using AE technology. Deng et al. (2022) analyzed the AE characteristics of prefabricated single-crack sandstone under uniaxial compression. Worley et al. (2019) demonstrated the effectiveness of AE technology when detecting cracks. Liu et al. (2021) studied the failure evolution process of intact rock and fractured rock mass specimens under uniaxial loading condition on the basis of the maximum amplitude distribution of AE events.

Wang et al. (2022) examined the mechanical properties and fracture propagation characteristics of the fractured rock mass under coupling of heavy rainfall infiltration and mining unloading by using of PFC numerical software. Xiao et al. (2022) conducted numerical simulation research on rock mechanics and fracture characteristics. Wang et al. (2023) used PFC2D to study the peak strength and failure characteristics of rock-like materials with dual prefabricated crack combinations. Liang et al. (2021) used PFC2D to conduct a numerical simulation on sandy mudstone with prefabricated cross defects under uniaxial compression. Manouchehrian et al. (2014) used PFC2D to simulate the biaxial compression test on a rock with a single crack. Na et al. (2022) carried out a series of numerical simulation experiments to investigate the creep evolution processes of simple fractured rock masses under

loading. Zhang et al. (2019) used ABAQUS to conduct a numerical simulation on the stress intensity factor at the tip of the prefabricated crack. Huang et al. (2016) used AUTODYN to simulate a triaxial test on sandstone with two cracks. Wang et al. (2014) used RFPA3D to analyze the influence of crack parameters on rock strength and failure characteristics. Xi et al. (2020) used the extended finite element method to simulate the initiation and propagation of prefabricated cracks in granite specimens. Li et al. (2022) conducted a numerical simulation on the evolution process of prefabricated crack propagation in translucent alumina ceramic sheets during flame thermal shock.

Duan et al. (2022) recorded the fracture damage behavior of prefabricated cracks by using high-speed photography. Gao and Li (2022) used a digital image correlation (DIC) to study the strain field around the crack. Jiang et al. (2019) used a DIC to study the influence of prefabricated cracks on the mechanical properties and deformation fields of specimens.

A large number of studies have shown that, the mechanical parameters of and research results obtained when using rock masses and rock-like materials are highly similar, which indicates that using rock-like materials instead of rock masses for research is feasible (Reyes and Einstein, 1991; Shen and Stephansson, 1993; Shen et al., 1995; Bobet and Einstein, 1998; Wong and Chau, 1998; Gehle and Kutter, 2003; Liu et al., 2014).

The existing research objects are mostly hard rocks, while there is relatively few research on soft rocks that are commonly in engineering. Compared to hard rock, soft rock contains a large number of joints and fractures, resulting in poor mechanical characteristics, and the fracture mechanism and fracture evolution law under compression are also different. Therefore, it is necessary to study the fracture mechanism and crack propagation evolution law of soft rock materials containing cracks under compression. The original rock of the mortar sample prepared by our research institute is the silty mudstone (belonging to soft rock) in the Huainan of China. The stress ratio of the mortar sample and the original rock is 1/3, and the Poisson's ratio, internal friction angle ratio, and cohesion ratio are 1. The results of this study will provide guidance and reference for soft rock mass engineering.

For this experiment, mortar specimens with prefabricated cracks with three dip angles were used for uniaxial compression, true triaxial compression, and true triaxial loading tests. The effects of the crack dip angle on the strength, failure mode, and crack propagation of the specimens were studied.

2 Experimental

2.1 Specimen preparation

Cement mortar was used to create specimens with prefabricated cracks. The mix ratio of cement: sand: water was 1:5:1.25. The cement was ordinary Portland cement with a mark of 32.5, and the sand was fine-grained river sand. The main indicators of cement and sand are shown in Tables 1, 2.

The specimens were cubes with a side length of 150 mm. The specimens contained a thorough prefabricated crack, which was in the middle of the specimens. The length of the crack was 150 mm, the width was 30 mm, and the thickness was 2 mm. A certain angle between the crack and the vertical direction was present, which was the crack dip angle. To study the effect of the crack dip angle on the mechanical characteristics and failure mode of the specimens, the crack dip angles were designed to be 15, 45, and 75°. The specimen model with a 45° crack dip angle is shown in Figure 1.

The mold used to prepare the specimens was a special mold (Figure 2). In total, nine prefabricated crack mortar specimens with 3 different crack angles were poured in the mold at a time. The crack simulation plate was used to reserve gaps for the cracks. The rotating wheel drove the crack simulation plates to rotate together, and this was used to set the crack dip angle.

The cement and fine sand were put into the mixer and evenly stirred, and then water was added; the mixture continued to be stirred, and then the mortar mixture was created. The prepared mortar mixture was poured into the pouring chamber in the mold. The edges and corners of the pouring chamber were fully vibrated to remove the bubbles from the mortar mixture, and then the top surface of the mortar mixture was leveled. The mortar mixture after pouring is shown in Figure 3. The mold was removed after 24 h of pouring, and the mortar specimens were taken out for standby after being put into water for curing for 28 days. The prepared specimens are shown in Figure 4.

2.2 Test method

Uniaxial compression, true triaxial compression, and true triaxial unloading tests were conducted, as shown in Figure 5. The confining pressure of the true triaxial compression and unloading test was $\sigma_2 = 0.8$ and $\sigma_3 = 0.4$ MPa, respectively. The number of repetitions for each type of test was 2.

The LYC true triaxial apparatus was used for the uniaxial compression, true triaxial compression, and true triaxial

TABLE 1 Indicators of cement.

Item	Compressive strength (Mpa)		Flexural strength (Mpa)		Setting time (h: min)		Water consumption of standard consistency (%)
	3 days	28 days	3 days	28 days	Initial setting	Final setting	
Test value	24.8	48.3	5.8	9.1	1:55	3:55	27.5

TABLE 2 Indicators of sand.

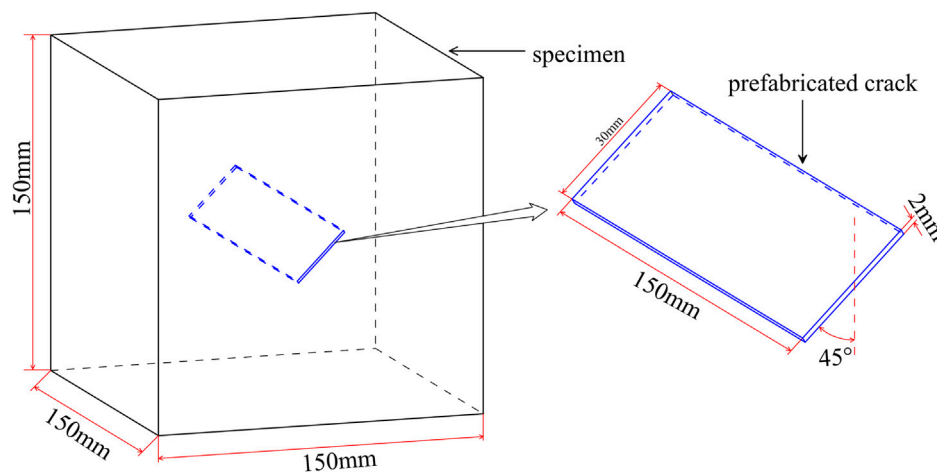| Sieve aperture/mm	9.5	4.75	2.36	1.18	0.60	0.30	0.15
Percentage of accumulated sieve residues (%)	0	5.7	22.9	36.5	62.8	80.7	94.1

FIGURE 1
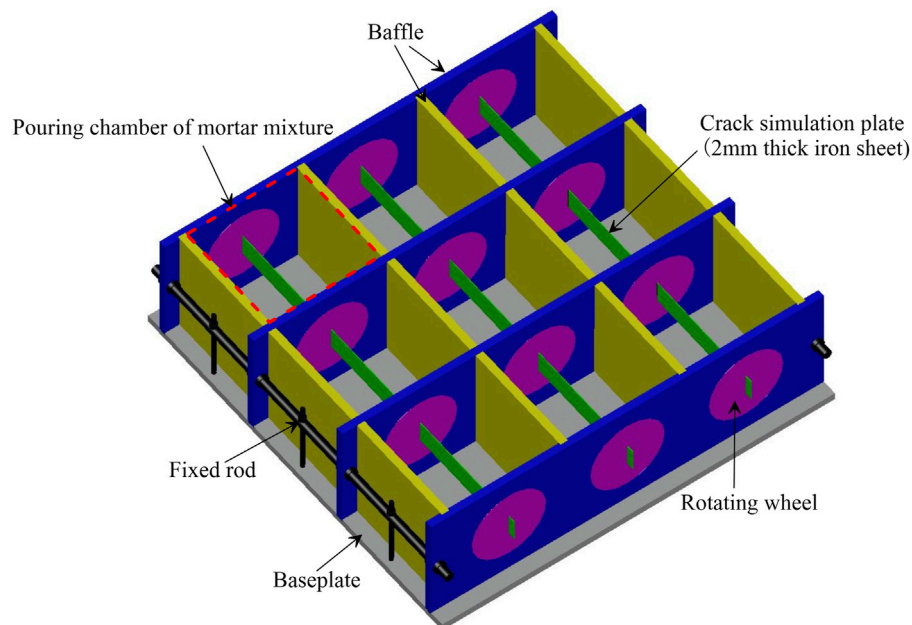The specimen model with a 45° crack dip angle.

FIGURE 2
Mold for preparing specimens.

unloading test to provide axial pressure. The maximum uniaxial pressure of the instrument was 450 kN. The load and displacement sensor were used to measure the stress and deformation of the specimens, respectively. The load sensor had a range of 300 kN, and the displacement sensor measurement range was ±50 mm. Both the load sensor and the displacement sensor were connected to the DH3823 data acquisition system (sampling rate: up to 1 kHz), which collected the stress and deformation data during the test.

The uniaxial compression test is shown in Figure 6. The specimens were placed on the pressure pedestal, the steel plates were placed on the bottom and top surfaces, and the load sensor

and displacement sensor were placed above the steel plates on the top surface. The rear end of the load sensor was connected to a hydraulic jack (used to provide an axial load). The vertical axes of the specimens, load sensor, and hydraulic jack coincided.

The true triaxial compression test is shown in Figure 7. The four sides and the top surface of the specimens placed on the pressure pedestal were wrapped by five pressure ends. The rear end of each pressure end was connected to a load sensor, displacement sensor, and hydraulic jack, which was used to measure the stress and deformation of the three axes of the specimens and provide three axial loads. During the loading process of the true triaxial compression test, three-dimensional stress was first applied according to the design value of

FIGURE 3
Mortar mixture after pouring.

the confining pressure, and the confining pressure was kept constant; additionally, the vertical stress was continuously loaded until the specimens failed to withstand the stress. Because the specimens were wrapped by the pressure ends, observing the test process at all times and stopping the test when the vertical stress rapidly decreased and the vertical deformation of the specimens rapidly increased was necessary.

The test preparation, loading method, and data acquisition of the true triaxial unloading test was consistent with that of the true triaxial compression test. Firstly, the triaxial stress was applied according to the design value of the confining pressure, and the confining pressure was kept constant. Secondly, the vertical stress was continuously loaded to 0.85 times of the peak stress during the true triaxial compression test, and then the minimum principal stress was unloaded. The test was stopped when the specimens rapidly deformed in the direction of the minimum principal stress.
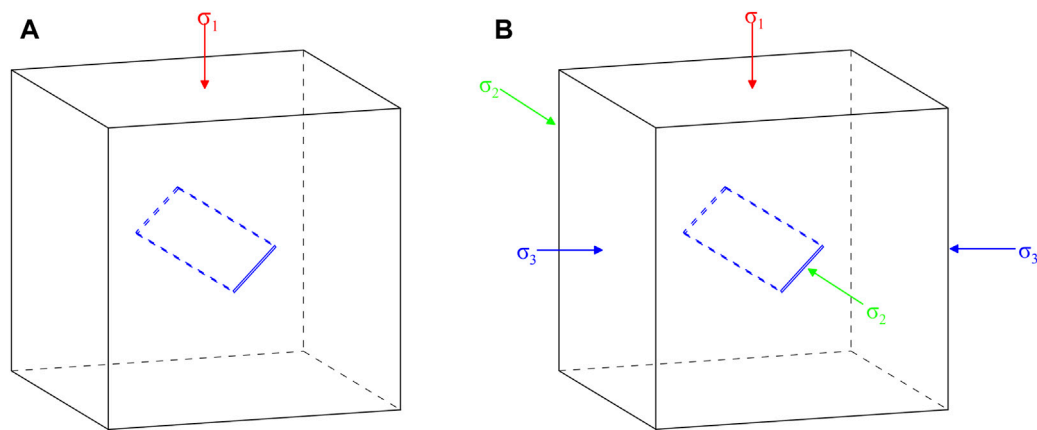

FIGURE 4
Specimens.

FIGURE 5
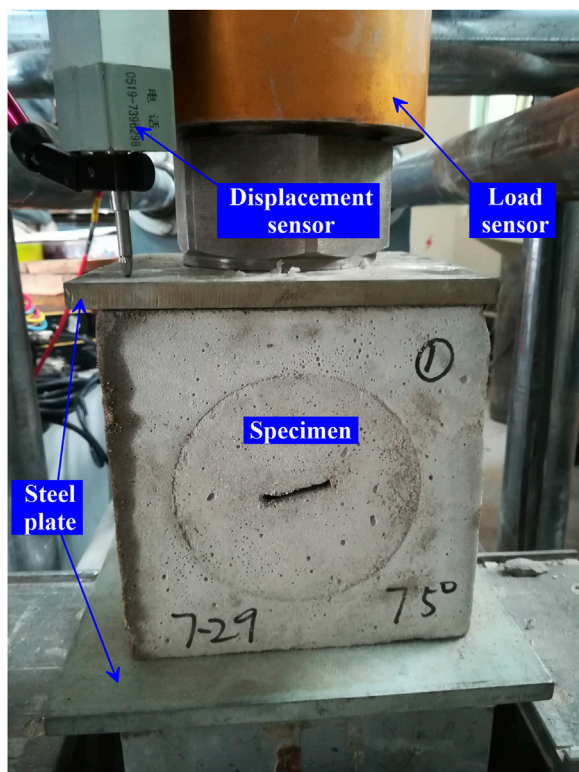Sketch of test. **(A)** Uniaxial compression. **(B)** True triaxial compression.

FIGURE 6
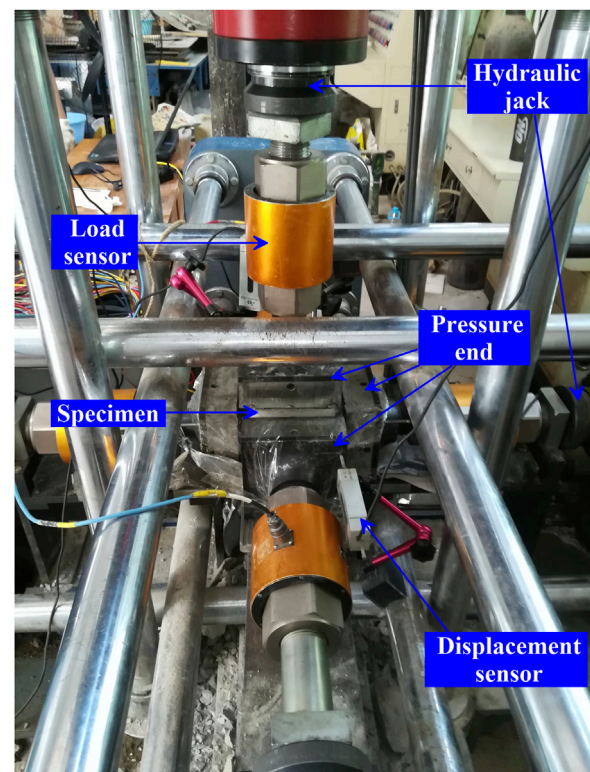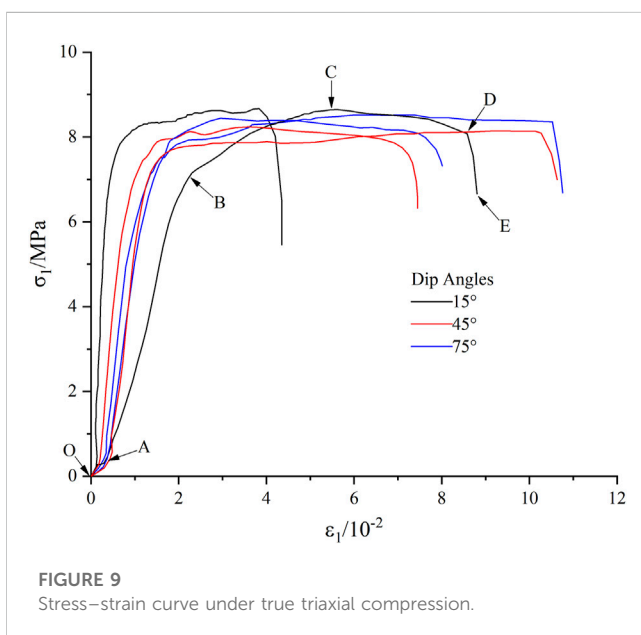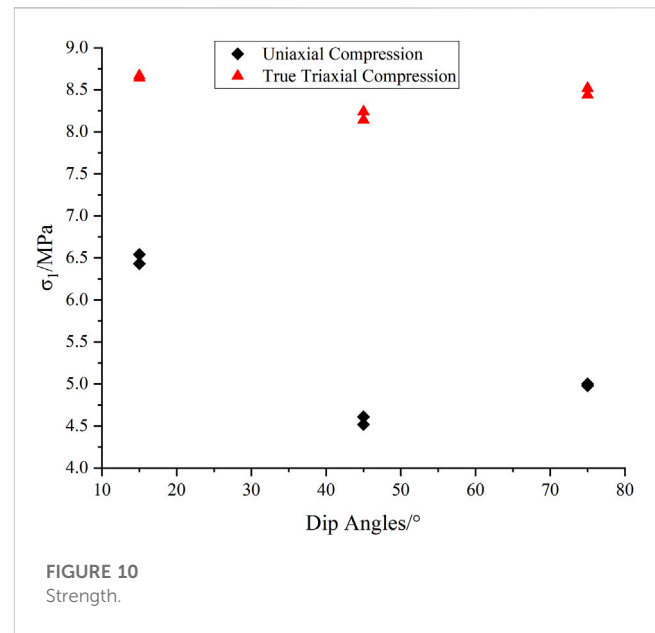Uniaxial compression test.

FIGURE 7
True triaxial compression and true triaxial unloading tests.

3 Test results and analyses

After the test, the data collected by the DH3823 data acquisition system were imported into the origin software. The axial stress–strain curve was drawn based on the axial stress and deformation data of the specimens, and the strength characteristics of the specimens were analyzed based on the peak stress of the specimens.

3.1 Stress–strain curve

The stress–strain curve of the specimens under uniaxial compression was divided into four stages (see Figure 8). The initial loading stage (OA) of the curve was the compaction stage, and the internal pores and microcracks of the specimens were closed under compression. The straight rising stage (AB) was the elastic deformation stage; the curve was approximate to a straight line, and

FIGURE 8
Stress−strain curve under uniaxial compression.

FIGURE 10
Strength.

FIGURE 9
Stress−strain curve under true triaxial compression.

During the failure stage (DE), the stress of the specimens rapidly decreased, and the specimens finally failed.

3.2 Strength

The strength of the specimens during the uniaxial compression and true triaxial compression test is shown in Figure 10. During the uniaxial compression test, the mean value of peak stress of the specimens with crack dip angles of 15°, 45°, and 75° was 6.49, 4.57, and 4.99 MPa, respectively. During the true triaxial compression test, the mean value of peak stress of the specimens with 15°, 45°, and 75° crack dip angles were 8.66, 8.19, and 8.48 MPa, respectively. The peak stress of the specimens decreased first and then increased with the increase in the crack dip angle, whereby the minimum stress occurred with the 45° dip angle. The peak stress of the specimens with 15°, 45°, and 75° crack dip angles under true triaxial compression was 1.33, 1.79, and 1.69 times that under uniaxial compression, respectively. Under true triaxial compression, because of the confining pressure, the compaction degree of the internal pores and microcracks of the specimens was higher during the compression process, the compactness of the specimens increased, and the strength characteristics of the specimens increased. The confining pressure considerably enhanced the strength characteristics of the specimens and weakened the effect of the crack dip angle on the strength.

3.3 Failure mode and crack propagation

Wong and Einstein (2009b) classified the cracks generated by specimens containing single flaws under compression into seven types, including three types of tensile cracks, three types of shear cracks, and one type of tension−shear crack. Referring to Wong et al.'s classification of cracks generated in specimens that contained single flaws under compression, three types of cracks were generated

the stress rapidly increased with the strain. The rising stage (BC) of the curve was the plastic deformation stage, and the stress slowly increased with the strain. In the failure stage (CD), the stress of the specimens rapidly decreased after reaching the peak stress (point C), and the specimens finally failed.

The first principal stress−strain curve of the specimens under true triaxial compression (Figure 9) can be divided into five stages. Compared with the stress−strain curve under uniaxial compression, the shape of the curve during the three stages before the peak stress was similar, but the shape after the peak stress was remarkably different. After the stress reached the peak value (point C), the specimens entered the large deformation stage (CD). Because of the confining pressure, the stress slowly decreased and the strain rapidly increased in this stage.

FIGURE 11
Failure of specimens under uniaxial compression. The crack dip angle is 15° **(A,B)**. The crack dip angle is 45° **(C,D)**. The crack dip angle is 75° **(E,F)**.

during this experiment: tensile (T), shear (S), and mixed tensile–shear cracks (Mc).

The failure of the specimens during the uniaxial compression test is shown in Figure 11. The failure mode of the specimens with three types of crack dip angles was mainly tensile failure, and this was accompanied by a few shear cracks. The S2 shear cracks were generated at the tip of the prefabricated crack, and the crack direction was approximately parallel to the prefabricated crack. In addition, three types of shear cracks, S1, S2, and S3, were generated in the specimens with a 45° crack dip angle, and

S3 shear cracks and T, T2, and T3 tensile cracks were generated in the specimens with a 75° crack dip angle.

The failure mechanism of the specimens with cracks under uniaxial compression was analysed.

With the increase in stress during uniaxial compression, shear cracks and tensile cracks were generated at the tip of the prefabricated cracks due to the stress concentration. With the increase in the crack dip angle of the specimens, the types of cracks generated at the tip of the prefabricated crack increased and changed from shear to tensile cracks. Compared with the left
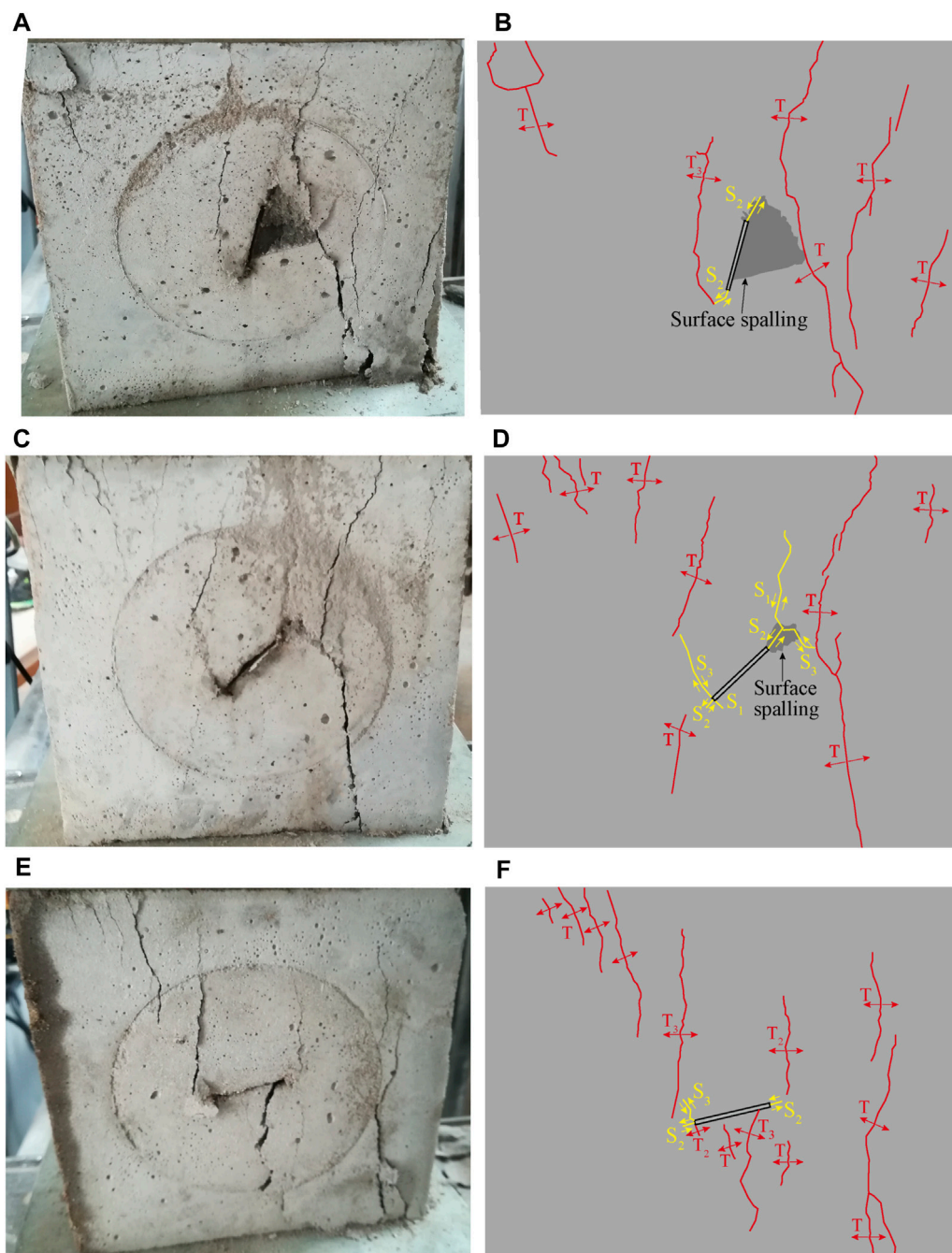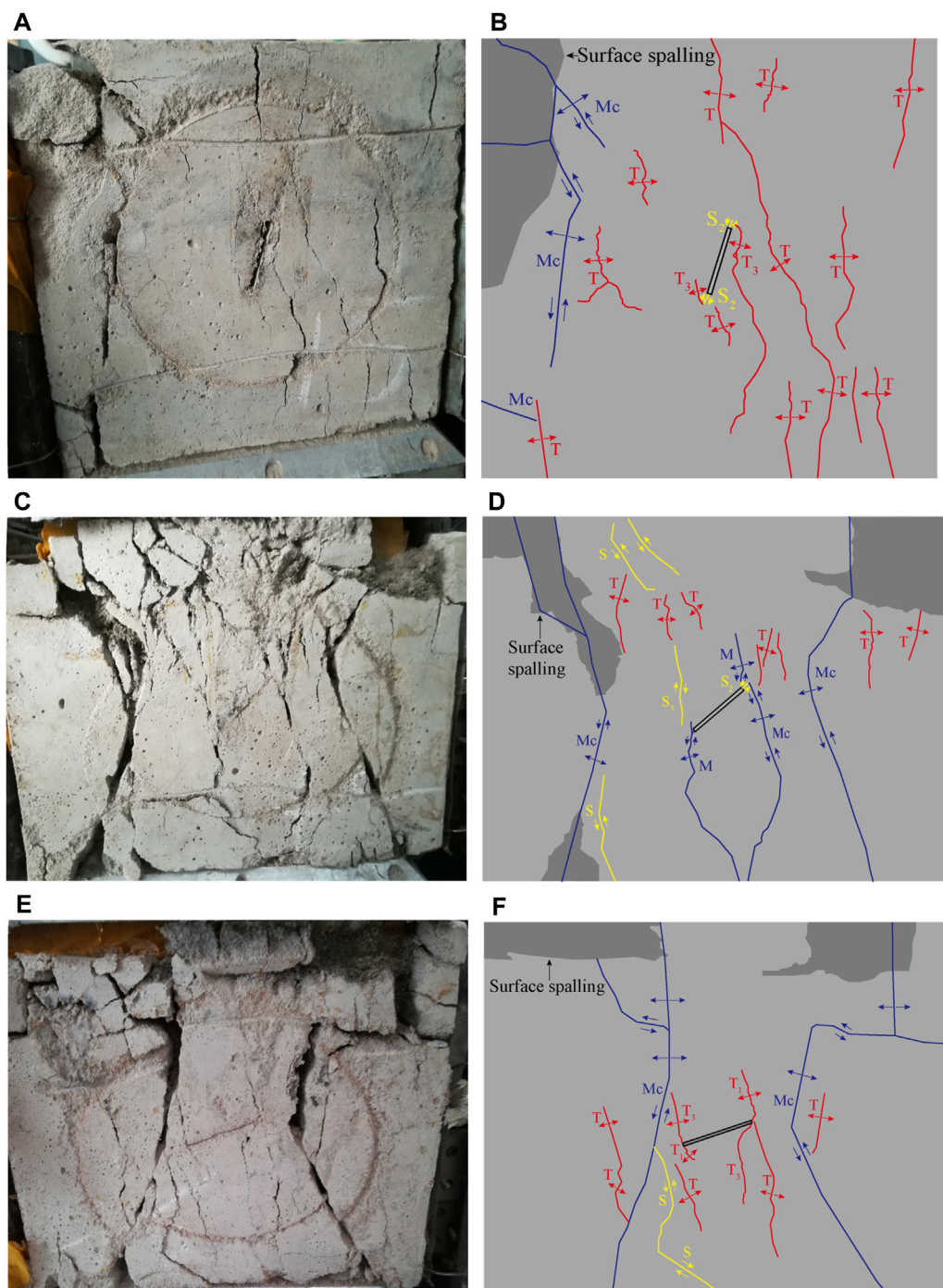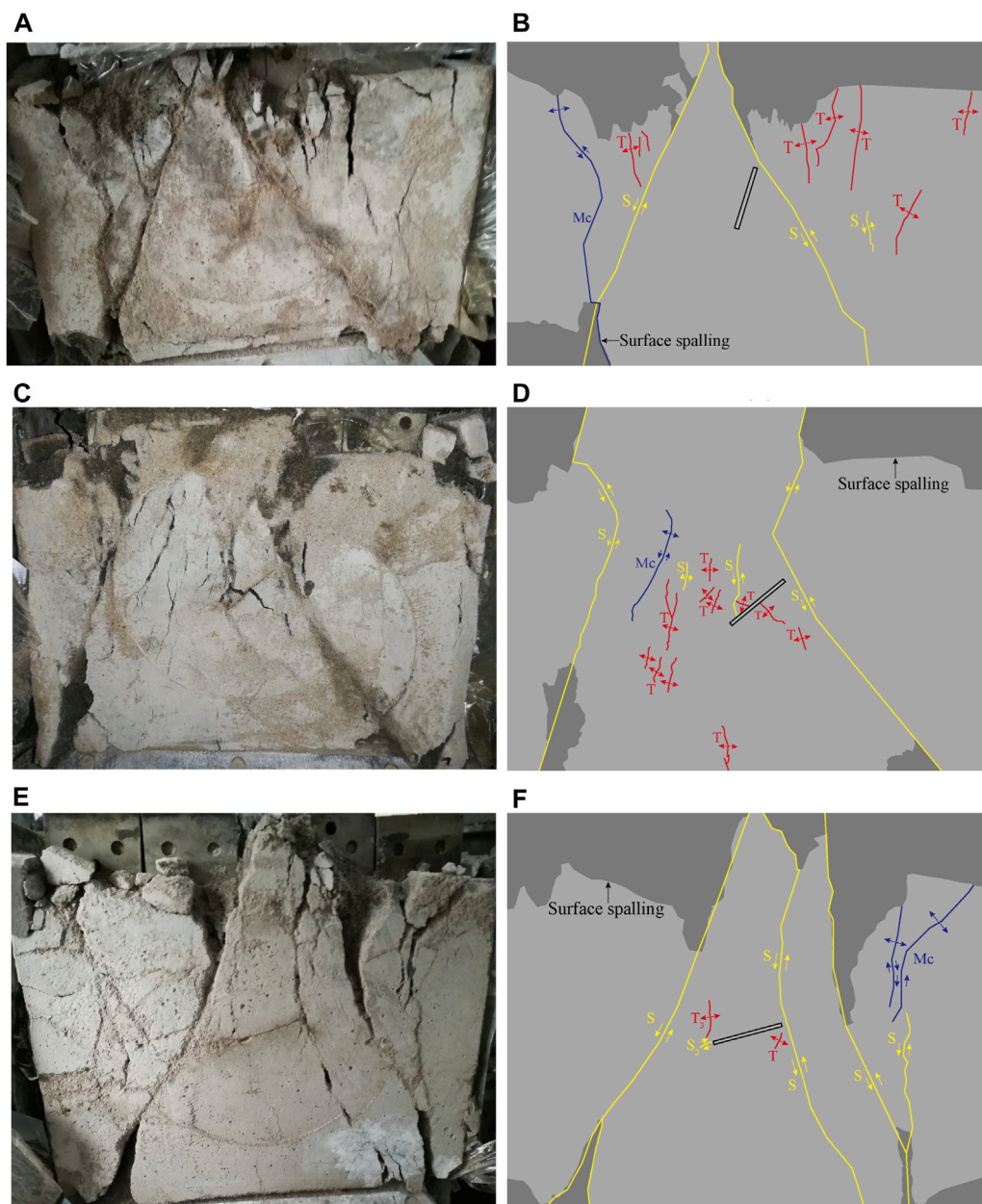
FIGURE 12
Failure of specimens under true triaxial compression. The crack dip angle is 15° **(A,B)**. The crack dip angle is 45° **(C,D)**. The crack dip angle is 75° **(E,F)**.

side of the specimens, the tip of the prefabricated crack on the right side of the specimens was closer to the loading end, and the stress concentration was higher, so the newly generated cracks were more numerous and wider, and the damage on the right side of the specimens was more serious than that on the left side.

The vertical axes of the specimens, pressure pedestal, steel plates, load sensor, and hydraulic jack were coincident, so the factor of bias pressure during loading was excluded. With the increase in the crack

dip angle, the vertical height difference between the upper and lower tips of the prefabricated crack gradually decreased, the distance difference from the loading end gradually decreased, the difference in the stress concentration gradually decreased, and finally the difference in the damage degree between the left and right sides of the specimens gradually weakened.

The failure of the specimens during the true triaxial compression test is shown in Figure 12. The failure mode of the specimens with

FIGURE 13
Failure of specimens under true triaxial unloading. The crack dip angle is 15° **(A,B)**. The crack dip angle is 45° **(C,D)**. The crack dip angle is 75° **(E,F)**.

15° a crack dip angle was mainly tensile and was accompanied by tensile–shear composite (Mc) and shear cracks. The failure mode of the specimens with a 45° crack dip angle was mainly tensile–shear composite (M and Mc) and was accompanied by tensile cracks and shear cracks. The failure mode of the specimens with a 75° crack dip angle was mainly tensile–shear composite (Mc) and was accompanied by tensile and shear cracks. With the increase in the crack dip angle of the specimens, the surface spalling of the specimens was more obvious, and the damage degree of the specimens was more severe. Compared with uniaxial compression, the damage degree of the specimens was more severe under true triaxial compression.

The failure of the specimens under true triaxial unloading is shown in Figure 13. The failure mode of the specimens was mainly shear and was accompanied by tensile and tensile–shear composite (Mc) cracks. No cracks were generated near the prefabricated cracks in the specimens with a 15° dip angle. Many tensile cracks and a small number of shear cracks were generated near the prefabricated cracks in the specimens with a 45° dip angle. A small number of tensile and shear cracks were generated near the prefabricated cracks in the specimens with a 75° dip angle. More than two shear cracks through the top and bottom of the specimens led to their failure. The failure degree of the specimens with a crack and a 75° dip angle was the most

serious. Compared with true triaxial compression, the deformation of the three axes of the specimens was larger under true triaxial unloading.

4 Discussion

The orientation of cracks has a significant effect on failure. The scale (width, length), quantity, inclination angle, spacing, roughness, connectivity, position, and filling of cracks have important effects on failure mode of the specimen. In this study, the location of the cracks is located in the middle of the sample, and the cracks will be set at the top and bottom of the sample in the future research work. The fillers of cracks have a significant influence on the mechanical characteristics and failure modes of materials. In future research, we will design and add gypsum with low strength as the fillers to study the specific impact of the fillers on the mechanical characteristics and failure modes.

Existing research results indicate that the presence of cracks significantly reduces the mechanical characteristics of the specimen. The scale (width, length), quantity, inclination angle, spacing, roughness, connectivity, position, and filling of cracks have important effects on the mechanical characteristics and failure mode of the specimen. The mechanical characteristics of the sample are negatively correlated with the number and scale of cracks; The strength and elastic modulus of the sample are the smallest when the crack inclination angle is 45°; The inclination angle of the crack has a significant impact on the initiation stress of the specimen; The strength and elastic modulus of the sample decrease with the increase of crack connectivity (Dyskin et al., 2003; Prudencio and Van Sint Jan, 2007; Yang and Jiang, 2010; Liu et al., 2018; Liu et al., 2019; Mei et al., 2020; Xi et al., 2020; Li et al., 2022; Liu et al., 2022; Shen et al., 2022). The research results on strength and crack propagation in this study are consistent with existing research conclusions.

The existing research objects are mostly hard rocks, while there is relatively few research on soft rocks that are commonly in engineering. Compared to hard rock, soft rock contains a large number of joints and fractures, resulting in poor mechanical characteristics, and the fracture mechanism and fracture evolution law under compression are also different. Therefore, it is necessary to study the fracture mechanism and crack propagation evolution law of soft rock materials containing cracks under compression. The original rock of the mortar sample prepared by our research institute is the silty mudstone (belonging to soft rock) in the Huainan of China.

The authors of most of the existing studies used a single mold to prepare the specimens (Wong and Chau, 1998; Wong et al., 2001b; Gehle and Kutter, 2003; Prudencio and Van Sint Jan, 2007; Wong and Einstein, 2009b; Lee and Jeon, 2011; Liu et al., 2014; Jiang et al., 2019; Liu et al., 2019), and only one specimen could be prepared at a time. Therefore, the differences between the specimens were large. The innovation of this experiment is the use of a special mold to prepare specimens; this mold can be used to prepare nine specimens at the same time, and it greatly reduces the influence of the differences in the specimens on the experimental results. The shortcomings of this experiment are the lack of SEM tests on the specimens, AEs and DICs, and numerical simulations of the test results.

5 Conclusion

Mortar specimens with prefabricated cracks and three dip angles were fabricated for uniaxial compression, true triaxial compression, and true triaxial loading tests. The effects of the crack dip angle on the strength, failure mode, and crack propagation of the specimens were studied.

The strength of the specimens was the lowest as the dip angle of 45°. Under true triaxial compression, the confining pressure remarkably enhanced the strength and deformation characteristics of the specimens and weakened the effect of the crack dip angle on the strength. Compared with the stress–strain curve when the specimens were under uniaxial compression, the shape after the peak stress was considerably different, the specimens entered into the large deformation stage, and the stress slowly decreased with the strain rapidly increased in this stage due to the confining pressure.

Under uniaxial compression, the failure mode was mainly tensile failure. With the increase in the crack dip angle, the types of cracks generated at the tip of the prefabricated crack increased and changed from shear to tensile cracks. Under true triaxial compression, the failure mode when the specimens had a 15° crack dip angle was mainly tensile. The failure mode when the specimens had 45° and 75° crack dip angles was mainly tensile–shear composite. With the increase in the crack dip angle, the damage degree of the specimens was more severe. Under the true triaxial unloading, the failure mode was mainly shear, and more than two shear cracks through the top and bottom of the specimens led to their failure.

Compared with uniaxial compression, the damage degree of the specimens was more severe under true triaxial compression and unloading.

Data availability statement

The datasets presented in this study can be found in online repositories. The names of the repository/repositories and accession number(s) can be found in the article/Supplementary Material.

Author contributions

XP: Conceptualization, Data curation, Investigation, Writing–original draft, Writing–review and editing. LW: Formal Analysis, Methodology, Writing–original draft, Writing–review and editing. TJ: Conceptualization, Supervision, Writing–review and editing. YJ: Formal Analysis, Methodology, Writing–review and editing. SZ: Formal Analysis, Funding acquisition, Writing–review and editing.

Funding

Conflict of interest

The authors declare that the research was conducted in the absence of any commercial or financial relationships that could be construed as a potential conflict of interest.

Publisher's note

All claims expressed in this article are solely those of the authors and do not necessarily represent those of their affiliated organizations, or those of the publisher, the editors and the reviewers. Any product that may be evaluated in this article, or claim that may be made by its manufacturer, is not guaranteed or endorsed by the publisher.

References

Ai, D. H., Zhao, Y. C., Xie, B., and Li, C. W. (2019). Experimental study of fracture characterizations of rocks under dynamic tension test with image processing. *SHOCK Vib.* 2019, 1–14. doi:10.1155/2019/6352609

Ashby, M. F., and Sammis, C. G. (1990). The damage mechanics of brittle solids in compression. *pure Appl. Geophys.* 133 (3), 489–521. doi:10.1007/BF00878002

Bobet, A., and Einstein, H. H. (1998). Fracture coalescence in rock-type materials under uniaxial and biaxial compression. *Int. J. Rock Mech. Min. Sci.* 35 (7), 863–888. doi:10.1016/s0148-9062(98)00005-9

Bobet, A. (2000). The initiation of secondary cracks in compression. *Eng. Fract. Mech.* 66 (2), 187–219. doi:10.1016/s0013-7944(00)00009-6

Chang, S. H., and Lee, C. I. (2004). Estimation of cracking and damage mechanisms in rock under triaxial compression by moment tensor analysis of acoustic emission. *Int. J. Rock Mech. Min. Sci.* 41 (7), 1069–1086. doi:10.1016/j.ijrmms.2004.04.006

Chen, L. X., Guo, W. Y., Zhang, D. X., and Zhao, T. B. (2022). Experimental study on the influence of prefabricated fissure size on the directional propagation law of rock type-I crack. *Int. J. ROCK Mech. Min. Sci.* 160, 105274. doi:10.1016/j.ijrmms.2022.105274

Deng, M., Zhang, Z. Z., Yu, W. J., Xin, J. L., and Xu, S. Q. (2022). Acoustic emission characteristics and damage law for prefabricated single-crack sandstone under uniaxial compression. *Struct. CONTROL HEALTH Monit.* 29 (10). doi:10.1002/stc.3018

Duan, Z., Dong, C. X., Yan, X. S., Sun, Q., and Li, B. (2022). Experimental research of fracture damage behavior of loess with different prefabricated cracks. *Eng. Fract. Mech.* 275, 108849. doi:10.1016/j.engfracmech.2022.108849

Dyskin, A. V., Sahouryeh, E., Jewell, R. J., Joer, H., and Ustinov, K. B. (2003). Influence of shape and locations of initial 3-D cracks on their growth in uniaxial compression. *Eng. Fract. Mech.* 70 (15), 2115–2136. doi:10.1016/s0013-7944(02)00240-0

Gao, A. S., Qi, C. Z., Shan, R. L., Wang, C. L., and Kocharyan, G. G. (2023). AE characteristic and mechanical behaviors of red sandstone with two prefabricated close-collinear-equal length cracks under compression. *ACS OMEGA* 8 (2), 2476–2484. doi:10.1021/acsomega.2c06951

Gao, B., and Li, Z. (2022). Study on the stress-strain relationships and deterioration modes of HTPB propellant with prefabricated cracks. *Adv. Polym. Technol.* 2022, 1–9. doi:10.1155/2022/9772946

Gehle, C., and Kutter, H. K. (2003). Breakage and shear behaviour of intermittent rock joints. *Int. J. Rock Mech. Min. Sci.* 40 (5), 687–700. doi:10.1016/s1365-1609(03)00060-1

Hao, J. W., Qiao, L., Li, Z. J., and Li, Q. W. (2021). Study on the fracture behavior of prefabricated fissures granite based on DIC and laser scanning techniques. *FATIGUE & Fract. Eng. Mater. Struct.* 44 (5), 1372–1390. doi:10.1111/ffe.13435

Huang, D., Gu, D., Yang, C., Huang, R., and Fu, G. (2016). Investigation on mechanical behaviors of sandstone with two preexisting flaws under triaxial compression. *Rock Mech. Rock Eng.* 49 (2), 375–399. doi:10.1007/s00603-015-0757-3

Jiang, T., Pan, X., Lei, J., Zhang, J., and Wang, W. (2019). Rupture and crack propagation in artificial soft rock with preexisting fractures under uniaxial compression. *Geotechnical Geol. Eng.* 37 (3), 1943–1956. doi:10.1007/s10706-018-0736-z

Lee, H., and Jeon, S. (2011). An experimental and numerical study of fracture coalescence in pre-cracked specimens under uniaxial compression. *Int. J. Solids Struct.* 48 (6), 979–999. doi:10.1016/j.ijsolstr.2010.12.001

Lei, X., Masuda, K., Nishizawa, O., Jouniaux, L., Liu, L., Ma, W., et al. (2004). Detailed analysis of acoustic emission activity during catastrophic fracture of faults in rock. *J. Struct. Geol.* 26 (2), 247–258. doi:10.1016/S0191-8141(03)00095-6

Li, Q. X., Li, Y. Q., Li, J., Li, L., Wu, X. F., Shao, Y. F., et al. (2022a). Prefabricated crack propagation in translucent alumina ceramic sheets during flame thermal shock. *Eng. Fract. Mech.* 263, 108285. doi:10.1016/j.engfracmech.2022.108285

Li, Z. H., Tian, H., Niu, Y., Wang, E. Y., Zhang, X., He, S., et al. (2022b). Study on the acoustic and thermal response characteristics of coal samples with various prefabricated crack angles during loaded failure under uniaxial compression. *J. Appl. Geophys.* 200, 104618. doi:10.1016/j.jappgeo.2022.104618

Liang, D. X., Zhang, N., Rong, H. Y., and Xiang, Z. (2021). Experimental and numerical studies on crack initiation and coalescence in sandy mudstone with prefabricated cross-flaws under uniaxial compression. *SHOCK Vib.* 2021, 1–17. doi:10.1155/2021/6672913

Liu, J., Zhu, Z., and Wang, B. (2014). The fracture characteristic of three collinear cracks under true triaxial compression. *Sci. World J.* 2014, 1–5. doi:10.1155/2014/459025

Liu, T. Y., Cui, M. Y., Li, Q., Yang, S., Yu, Z. F., Sheng, Y. S., et al. (2022). Fracture and damage evolution of multiple-fractured rock-like material subjected to compression. *MATERIALS* 15 (12), 4326. doi:10.3390/ma15124326

Liu, X., Liu, Q., Liu, B., Zhu, Y., and Zhang, P. (2019). Failure behavior for rocklike material with cross crack under biaxial compression. *J. Mater. Civ. Eng.* 31 (2), 2540. doi:10.1061/(asce)mt.1943-5533.0002540

Liu, X., Zhao, X., Zhang, S., Congyan, R., and Zhao, R. (2021). Research on the failure evolution process of rock mass base on the acoustic emission parameters. *Front. Phys.* 9, 635306. doi:10.3389/fphy.2021.635306

Liu, Y. X., Xu, J., and Zhou, G. (2018). Relation between crack propagation and internal damage in sandstone during shear failure. *J. Geophys. Eng.* 15 (5), 2104–2109. doi:10.1088/1742-2140/aac85e

Manouchehrian, A., Sharifzadeh, M., Marji, M. F., and Gholamnejad, J. (2014). A bonded particle model for analysis of the flaw orientation effect on crack propagation mechanism in brittle materials under compression. *Archives Civ. Mech. Eng.* 14 (1), 40–52. doi:10.1016/j.acme.2013.05.008

Mei, J., Yang, L., Sheng, X. C., Song, G. X., Yang, W. M., and Zhang, B. (2020). Time-dependent propagation of 3-D cracks in rocks under hydromechanical coupling. *ROCK Mech. ROCK Eng.* 53 (4), 1923–1934. doi:10.1007/s00603-019-02020-2

Na, Z., Lixin, M., Laigui, W., and Yibin, Z. (2022). Numerical simulation of creep fracture evolution in fractured rock masses. *Front. Earth Sci.* 10, 901742. doi:10.3389/feart.2022.901742

Nasseri, M. H., Rao, K. S., and Ramamurthy, T. (1997). Failure mechanism in schistose rocks. *Int. J. Rock Mech. Min. Sci.* 34 (3), 219.e1–219.e15. doi:10.1016/S1365-1609(97)00099-3

Nguyen, T. L., Hall, S. A., Vacher, P., and Viggiani, G. (2011). Fracture mechanisms in soft rock: identification and quantification of evolving displacement discontinuities by extended digital image correlation. *Tectonophysics* 503 (1), 117–128. doi:10.1016/j.tecto.2010.09.024

Niandou, H., Shao, J. F., Henry, J. P., and Fourmaintraux, D. (1997). Laboratory investigation of the mechanical behaviour of Tournemire shale. *Int. J. Rock Mech. Min. Sci.* 34 (1), 3–16. doi:10.1016/S1365-1609(97)80029-9

Prudencio, M., and Van Sint Jan, M. (2007). Strength and failure modes of rock mass models with non-persistent joints. *Int. J. Rock Mech. Min. Sci.* 44 (6), 890–902. doi:10.1016/j.ijrmms.2007.01.005

Reyes, O., and Einstein, H. H. (1991). "Failure mechanisms of fractured rock - a fracture coalescence model," in *7th ISRM congress.* (United States: OSTI).

Shen, B., Stephansson, O., Einstein, H. H., and Ghahreman, B. (1995). Coalescence of fractures under shear stresses in experiments. *J. Geophys. Res. Solid Earth* 100 (B4), 5975–5990. doi:10.1029/95jb00040

Shen, B., and Stephansson, O. (1993). Numerical analysis of mixed mode I and Mode II fracture propagation. *Int. J. Rock Mech. Min. Sci. Geomechanics Abstr.* 30 (7), 861–867. doi:10.1016/0148-9062(93)90037-E

Shen, B. T., Sun, X. Z., Yin, D. W., and Li, Y. Y. (2022). Experimental study of the crack propagation and acoustic emission characteristics of red sandstone under cyclic loading. *GEOTECHNICAL Test. J.* 45 (3), 20190007. doi:10.1520/GTJ20190007

Song, D. Z., You, Q. J., Wang, E. Y., Song, X. Y., Li, Z. H., Qiu, L. M., et al. (2019). Characteristics of EMR emitted by coal and rock with prefabricated cracks under uniaxial compression. *GEOMECHANICS Eng.* 19 (1), 49–60. doi:10.12989/gae.2019.19.1.049

Tham, L. G., Liu, H., Tang, C. A., Lee, P. K. K., and Tsui, Y. (2005). On tension failure of 2-D rock specimens and associated acoustic emission. *Rock Mech. Rock Eng.* 38 (1), 1–19. doi:10.1007/s00603-004-0031-6

Tiwari, R. P., and Rao, K. S. (2006). Post failure behaviour of a rock mass under the influence of triaxial and true triaxial confinement. *Eng. Geol.* 84 (3), 112–129. doi:10.1016/j.enggeo.2006.01.001

Wang, K. Z., Zhang, C., Gao, Y. H., Chen, H. J., and Xie, T. (2023). Influence of prefabricated fissure combinations on strength and failure characteristics of rock-like specimens under uniaxial compression. *Int. J. GEOMECHANICS* 23 (2), 2637. doi:10.1061/(ASCE)GM.1943-5622.0002637

Wang, M., Li, X., Yang, S., Teng, L., Chen, Q., and Jiang, S. (2022). Research on deformation and fracture characteristics of the fractured rock mass under coupling of heavy rainfall infiltration and mining unloading. *Front. Earth Sci.* 9, 792038. doi:10.3389/feart.2021.792038

Wang, S. Y., Sloan, S. W., Sheng, D. C., Yang, S. Q., and Tang, C. A. (2014). Numerical study of failure behaviour of pre-cracked rock specimens under conventional triaxial compression. *Int. J. Solids Struct.* 51 (5), 1132–1148. doi:10.1016/j.ijsolstr.2013.12.012

Wong, L. N. Y., and Einstein, H. H. (2009a). Crack coalescence in molded gypsum and carrara marble: part 1. Macroscopic observations and interpretation. *Rock Mech. Rock Eng.* 42 (3), 475–511. doi:10.1007/s00603-008-0002-4

Wong, L. N. Y., and Einstein, H. H. (2009b). Systematic evaluation of cracking behavior in specimens containing single flaws under uniaxial compression. *Int. J. Rock Mech. Min. Sci.* 46 (2), 239–249. doi:10.1016/j.ijrmms.2008.03.006

Wong, R. H. C., and Chau, K. T. (1998). Crack coalescence in a rock-like material containing two cracks. *Int. J. Rock Mech. Min. Sci.* 35 (2), 147–164. doi:10.1016/S0148-9062(97)00303-3

Wong, R. H. C., Chau, K. T., Tang, C. A., and Lin, P. (2001a). Analysis of crack coalescence in rock-like materials containing three flaws—Part I: experimental approach. *Int. J. Rock Mech. Min. Sci.* 38 (7), 909–924. doi:10.1016/s1365-1609(01)00064-8

Wong, R. H. C., Guo, Y. S. H., Li, L. Y., Chau, K. T., Zhu, W. S., and Li, S. C. (2018). "Anti-wing crack growth from surface flaw in real rock under uniaxial compression," in

Fracture of nano and engineering materials and structures. Editor E. E. Gdoutos (Netherlands: Springer Netherlands), 825–826.

Wong, R. H. C., Huang, M. L., Jiao, M. R., Tang, C. A., and Zhu, W. S. (2004a). The mechanisms of crack propagation from surface 3-D fracture under uniaxial compression. *Key Eng. Mater.* 261-263, 219–224. doi:10.4028/www.scientific.net/KEM.261-263.219

Wong, R. H. C., Law, C. M., Chau, K. T., and Zhu, W. S. (2004b). Crack propagation from 3-D surface fractures in PMMA and marble specimens under uniaxial compression. *Int. J. Rock Mech. Min. Sci.* 41, 37–42. doi:10.1016/j.ijrmms.2004.03.016

Wong, R. H. C., Leung, W. L., and Wang, S. W. (2001b). "Shear strength studies on rock-like models containing arrayed open joints," in *DC rocks 2001, the 38th U.S. Symposium on rock mechanics (USRMS)* (Washington, D.C: USRMS).

Wong, R. H. C., Lin, P., and Tang, C. A. (2006b). Experimental and numerical study on splitting failure of brittle solids containing single pore under uniaxial compression. *Mech. Mater.* 38 (1), 142–159. doi:10.1016/j.mechmat.2005.05.017

Worley, R., Dewoolkar, M. M., Xia, T., Farrell, R., Orfeo, D., Burns, D., et al. (2019). Acoustic emission sensing for crack monitoring in prefabricated and prestressed reinforced concrete bridge girders. *J. BRIDGE Eng.* 24 (4), 1377. doi:10.1061/(ASCE)BE.1943-5592.0001377

Xi, X., Wu, X., Guo, Q. F., and Cai, M. F. (2020). Experimental investigation and numerical simulation on the crack initiation and propagation of rock with pre-existing cracks. *IEEE ACCESS* 8, 129636–129644. doi:10.1109/ACCESS.2020.3009230

Xiao, N., Luo, L. C., Huang, F., and Ling, T. H. (2022). Numerical study of rock mechanical and fracture property based on CT images. *GEOMECHANICS Eng.* 31 (4), 395–407. doi:10.12989/gae.2022.31.4.395

Xu, N. Z., Liu, C. Q., Wang, Y. J., Dang, H. B., and Ma, D. (2021). Biaxial shear crack propagation modes of rock-like specimens with prefabricated fissures and their strength characteristics. *Shock Vib.* 2021, 1–12. doi:10.1155/2021/7248926

Yang, S. Q., and Jing, H. W. (2010). Strength failure and crack coalescence behavior of brittle sandstone samples containing a single fissure under uniaxial compression. *Int. J. Fract.* 168 (2), 227–250. doi:10.1007/s10704-010-9576-4

Yang, S., and Jiang, Y. (2010). Triaxial mechanical creep behavior of sandstone. *Min. Sci. Technol. (China)* 20 (3), 339–349. doi:10.1016/s1674-5264(09)60206-4

Yang, S. Q., Yang, D. S., Jing, H. W., Li, Y. H., and Wang, S. Y. (2012). An experimental study of the fracture coalescence behaviour of brittle sandstone specimens containing three fissures. *Rock Mech. Rock Eng.* 45 (4), 563–582. doi:10.1007/s00603-011-0206-x

Zhang, G., Chen, G., Xu, Z., Yang, Y., and Lin, Z. (2020). Crack failure characteristics of different rocks under the action of frost heaving of fissure water. *Front. Earth Sci.* 8, 13. doi:10.3389/feart.2020.00013

Zhang, S., Wang, L. F., and Gao, M. Z. (2019). Numerical simulation of the influence of width of a prefabricated crack on the dimensionless stress intensity factor of notched semi-circular bend specimens. *SHOCK Vib.* 2019, 1–10. doi:10.1155/2019/3291730

A two-stage model updating method for the linear parts of structures with local nonlinearities

Hao Zhang[1,2]*, Desheng Wei[1], Lei Zhai[1], Lixin Hu[1], Liulian Li[1], Huilai Qin[1], Dongsheng Li[3,4]* and Jiansheng Fan[2]

[1]China Construction Second Engineering Bureau Co., Ltd., Beijing, China, [2]Department of Civil Engineering, Tsinghua University, Beijing, China, [3]Guangdong Engineering Center for Structure Safety and Health Monitoring, Shantou University, Shantou, China, [4]MOE Key Laboratory of Intelligent Manufacturing Technology, Shantou University, Shantou, China

Finite element model updating provides an important supplement for finite element modelling. However, some studies have shown that if the tested structure involves local nonlinearities due to damages, material properties and large deformation et al., it is difficult to achieve an accurate modified model using conventional model updating methods that are based on the assumption of linear structures. To address this issue, a two-stage model updating method separating the effects of local nonlinearities is proposed in this paper. Firstly, the underlying linear frequency response function is obtained by using the conditioned reverse path method. Then, combined with the Sherman-Morrison-Woodbury formula and the model updating objective function established by the frequency response function similarity metric, then structural model updating and damage detection are carried out as the second stage. Three numerical examples are given to illustrate the effectiveness of the proposed method. This method can not only accurately identify the location and quantify the extent of structural damages, but also has the advantages of not based on sensitivity, not depending on the selection of frequency points, not repeatedly calling the initial model et al. The proposed method has high computational efficiency and avoids the numerical problems often encountered by conventional frequency response function-based model updating methods.

1 Introduction

Model updating theories use structural characteristics through static or dynamic testing to establish optimization objective functions, and then the finite element models continuously approach the actual structures driven by the constrained optimization process, which is an important supplement to the finite element analysis and has become one of the main means of structural damage identification under the theoretical framework of structural health monitoring (Friswell and Mottershead, 1995; Hou and Xia, 2022). However, conventional model updating methods based on linear assumptions are no longer effective for the structures with local nonlinearities originated from material properties, boundary conditions and large deformation et al. The full-scale shaking table testing of a 7-story shear wall structure conducted by Moaveni et al. (2010) shows that as the extent of damages increase, the tested structure displays features of nonlinear dynamics, and the linear numerical model cannot accurately represent the actual structure.

Nonlinear model updating has been rapidly developing in recent years, and its technical roadmap can be seen as an extension of conventional linear model updating theories. But due to the multi-dimensional nature, nonlinear characteristics such as nonlinear normal modes (NNMs) and generalized frequency response functions (GFRFs) are arduous to directly applied for nonlinear model updating (Kerschen et al., 2006; Noel and Kerschen, 2017). Therefore, researchers tend to use degradation forms of the higher-order nonlinear characteristics mentioned above such as frequency-energy plot (FEP) and nonlinear output frequency response function (NOFRF) to address the issue (Zhu et al., 2022). But they are not yet as mature as the modal theories of linear structures due to the sophisticated experimental process (Zhang et al., 2020), and the effectiveness of applying them for nonlinear model updating and structural damages identification is also limited, especially in identifying damages of linear and nonlinear parts separately in tested structures with local nonlinearities (Li et al., 2021).

Nonlinearities are generally located in local regions of actual structures, and the positions are mostly known (Ewins et al., 2015). Therefore, it is reasonably expected to separate the nonlinear effects and obtain the linear parts of structures with local nonlinearities, namely, the underlying linear system (ULS), and then linear model updating methods can be used and achieve structural damages identification. Some researchers think that most nonlinear behavior is dependent on vibration amplitude, so the linear model updating methods are available for modifying linear parts of structures with local nonlinearities under the condition of low vibration amplitude (Wang et al., 2018). Nonetheless, some researchers consider that it is difficult to control the degree of nonlinear behavior, and approximating linearity under the condition of low vibration amplitude may not be reliable (Richards and Singh, 1998). A nonlinear system identification method, conditioned reverse path (cRP) method developed by Richards and Singh (1998), is able to separate local nonlinear effects in frequency domain and obtains the underlying linear frequency response functions (FRFs) of the tested structure's ULS, and several studies have verified its effectiveness in extracting the linear FRFs and identifying nonlinear parameters (Wu et al., 2015; Huang and Ferguson, 2018).

If the underlying linear FRFs of structures with local nonlinearities can be obtained, then FRFs-based linear model updating methods can be applied for modifying initial numerical models and handling structural damages identification. FRF data can avoid errors introduced by modal analysis (Friswell and Mottershead, 1995)

and ensure relatively high-quality data due to the property of anisotropy. Therefore, FRFs-based model updating methods have received widespread attention. Lin and Ewins (1994) proposed a model updating method based on FRFs' sensitivity earlier and Lin and Zhu (2006) subsequently extended it to the modification of damping matrices. Lin (2017) further proposed the FRFs-based model updating method using the sensitivity with weighted function, which avoids the requirement for the accuracy of initial modeling and expands the applicability of the FRFs' sensitivity-based method. Cong et al. (2022) proposed a FRFs-based model updating method using the zero-pole decomposition of FRFs, which achieved simultaneous modification of mass, stiffness, and damping matrices. In addition, researchers have conducted in-depth research on some detailed issues in FRFs-based model updating. For examples, Hassani and Shadan (2022) proposed a FRFs-based model updating method for the issues of dense modes and incomplete modal data. Arora et al. (2023) established a FRFs-based model updating method for the issue of non-proportional damping. Nevertheless, FRFs-based model updating methods, like other conventional model updating methods based on sensitivity, may encounter issues such as low computational efficiency of iterative mechanisms, artificial frequency points selection and ill-conditioned matrices et al. Which to some extent need further development.

This paper presents a novel two-stage FRFs-based model updating method for structures with local nonlinearities. Firstly, underlying linear FRFs of ULS obtained through the first phase of the cRP method. Then during the model updating process, the proposed method combines Sherman-Morrison-Woodbury (SMW) formula and the optimization objective function established by the FRF similarity metric. It only requires partial FRFs, and has the advantages of not asking frequency point selection, not reusing the initial model, and not depending on sensitivity. The effectiveness of this method is verified by three numerical examples.

2 Theoretical basis

2.1 cRP method

The cRP method is a two-stage nonlinear system identification method, and only the first stage is implemented here to extract the underlying linear FRF of the ULS of structures with local nonlinearities serving as the first stage of the proposed method.
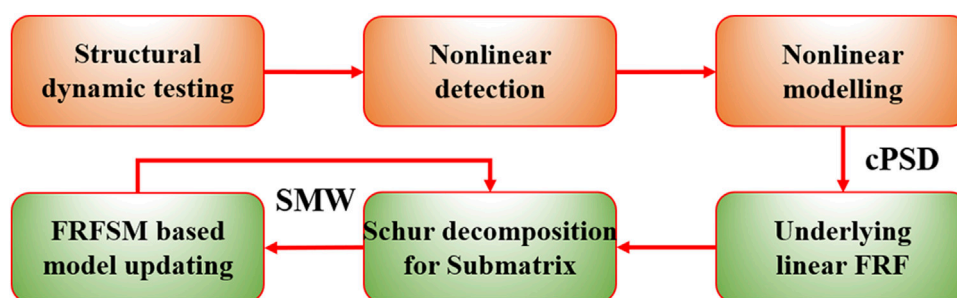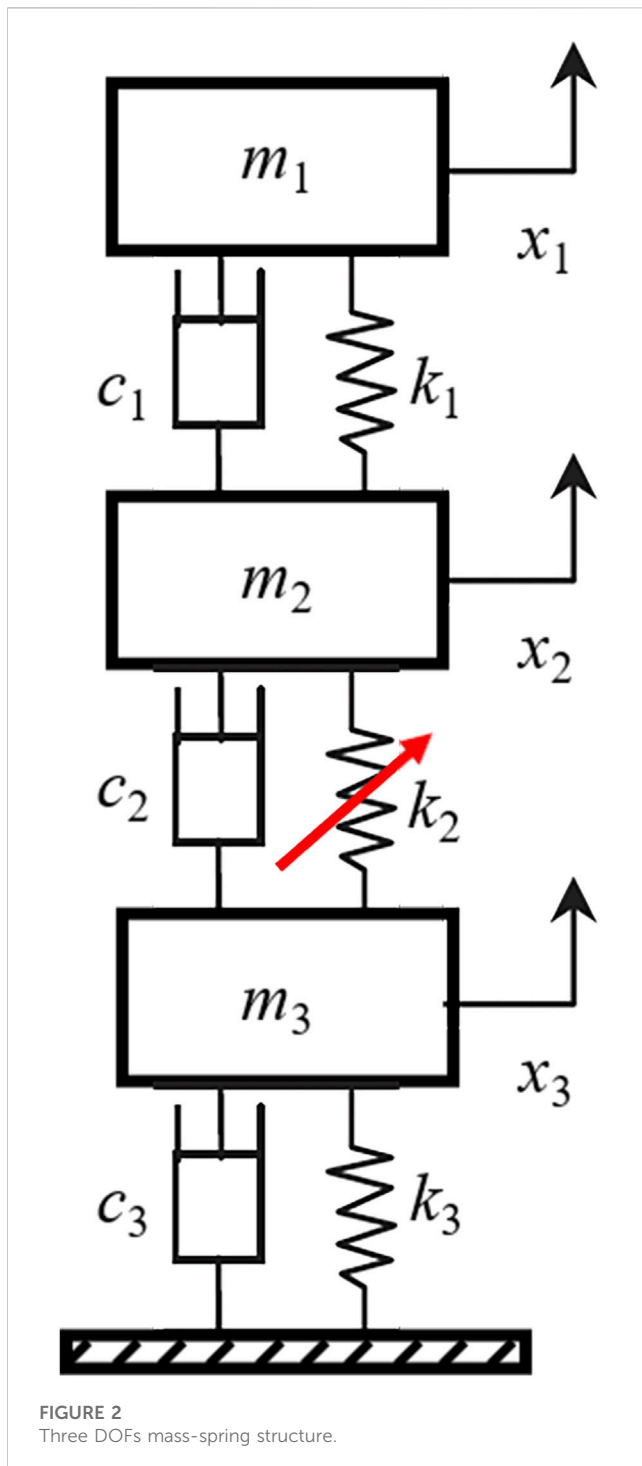

FIGURE 1
Process of the underlying linear model updating for structures with local nonlinearities.

FIGURE 2
Three DOFs mass-spring structure.

The cRP method's main conclusions related to this paper will be discussed as follows. For more detailed contents, please refer to the reference provided (Richards and Singh, 1998). Firstly, the nonlinear structural motion equation is expressed as,

$$M\ddot{x}(t) + C\dot{x}(t) + Kx(t) + \sum_{r=1}^{n} A_r y_r(t) = f(t) \quad (1)$$

where M, C, and K are the structural mass, damping, and stiffness matrices of the linear parts respectively. $\ddot{x}$, $\dot{x}$, x represent the acceleration, velocity and displacement vector of the linear parts respectively. y_r represents the response vector of the rth type

nonlinearity, with a vector length of q_r at each time point, indicating the number of positions where rth type nonlinearity exists. A_r, a matrix with N rows and q_r columns, concludes the nonlinear parameter to be identified and also expresses the location of the nonlinearity, and N is the number of degree of freedom (DOF) of the structure. It is worth noting that the A_r matrix requires the information on the types and locations of nonlinearities to be known, which can be obtained with the assistance of nonlinear detection and characterization (Ewins et al., 2015). Take the Fourier transform on Equation 1,

$$B(\omega)X(\omega) + \sum_{r=1}^{n} A_r Y_r(\omega) = F(\omega) \quad (2)$$

where $B(\omega)$ is the dynamic stiffness matrix of the structure,

$$B(\omega) = -\omega^2 M + i\omega C + K \quad (3)$$

According to the theory of conditioned power spectral density (cPSD), cPSD which is the conventional power spectral density (PSD) in linear structural dynamics separating nonlinear effects can be recursively calculated by the equations as follows (Bendat and Piersol, 2010),

$$G_{ij(-1:\,r)} = G_{ij(-1:\,r-1)} - G_{ir(-1:\,r-1)} L_{rj}^T$$
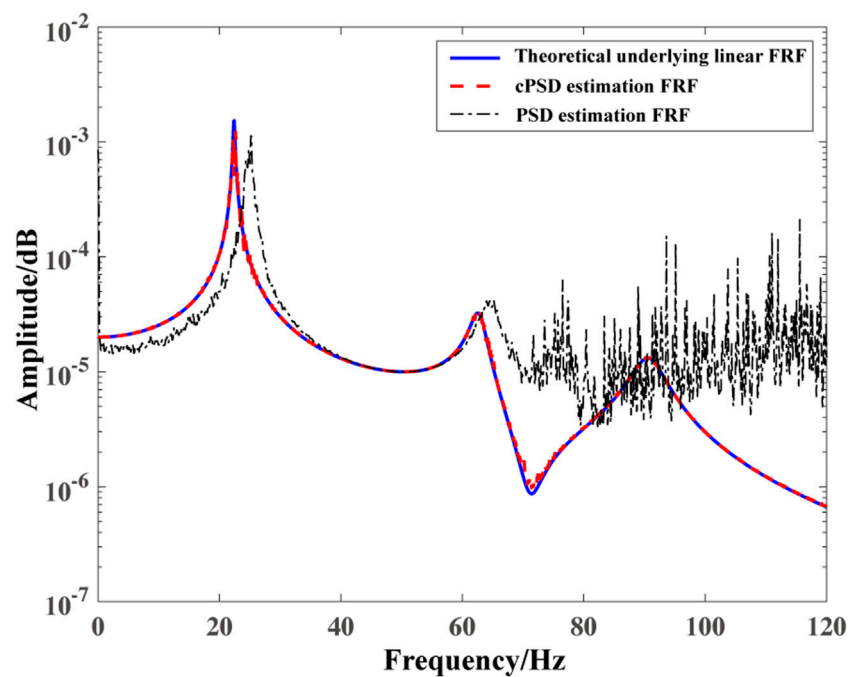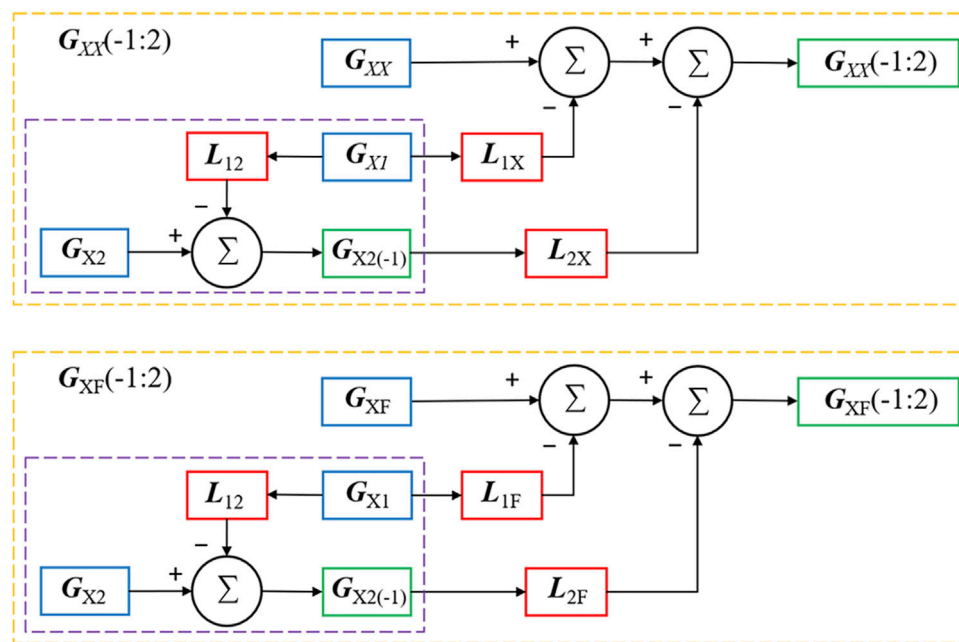$$L_{rj}^T = G_{rr(-1:\,r-1)}^{-1} G_{rj(-1:\,r-1)} \quad (4)$$

where G represents PSD or cPSD, when the matrix G has a bracket label, it signifies the cPSD, or conditioned PSD. Otherwise, it is the classic PSD in linear structural dynamics without any conditions. L is a transitional matrix. i and j are the labels related to response or excitation of underlying linear parts, and r is the label related to nonlinear response. Labels with brackets indicate the conditions. For instance, $(-1: r)$ represents the condition that the PSD is independent of the first to rth type of nonlinearities. Specifically, when $r = 1$, $(-1: 1)$ equals (-1), then the cPSD is the PSD separating the first type of nonlinearity, and $(-1: 0)$ is the unconditional PSD calculated by linear theory, $G_{ij(-1:0)} = G_{ij}$. After calculating the required cPSD, the cPSD-based underlying linear FRF estimation can be derived from the PSD-based linear FRF estimation theory (Bendat and Piersol, 2010),

$$H_{1(-1:\,r)} = G_{FF(-1:\,r)}^{-1} G_{FX(-1:\,r)}$$
$$H_{2(-1:\,r)} = G_{XF(-1:\,r)}^{-1} G_{XX(-1:\,r)} \quad (5)$$

where X and F are related to responses and excitations respectively similar to the counterparts in PSD-based FRF estimation theories in linear structural dynamics. The process of using the equations (4) and (5) to calculate the underlying linear FRFs will be further illustrated in case 1.

2.2 Correlation analysis for FRF

If underlying linear FRFs are obtained by the cRP method presented above, the FRF-based model updating methods are available to modify the linear parts of structures with local nonlinearities and conduct structural damage identification. Correlation analysis is an effective tool for evaluating the accuracy of numerical models and is also a common objective function in model updating. The correlation analysis methods for FRF data mainly including the frequency domain assurance criterion (FDAC) and the frequency response assurance criterion (FRAC) (Lee et al., 2018),

FIGURE 3
Calculation flow chart of cPSD.

FIGURE 4
Comparison between FRFs by cPSD and PSD and theoretical FRF.

$$\mathrm{FDAC}\bigl(\omega_i, \omega_j\bigr)$$

$$= \frac{\left|\sum_{k=1}^{N_p}\bigl(H_{1k}(\omega_i)^{\mathrm{H}} \cdot H_{2k}(\omega_j)\bigr)\right|^2}{\left[\sum_{k=1}^{N_p}\bigl(H_{1k}(\omega_i)^{\mathrm{H}} \cdot H_{1k}(\omega_i)\bigr)\right]\left[\sum_{k=1}^{N_p}\bigl(H_{2k}(\omega_j)^{\mathrm{H}} \cdot H_{2k}(\omega_j)\bigr)\right]}$$

$$\mathrm{FRAC} = \frac{\left|\sum_{j=1}^{N_f}\bigl(H_1(\omega_j)^{\mathrm{H}} \cdot H_2(\omega_j)\bigr)\right|^2}{\left[\sum_{j=1}^{N_f}\bigl(H_1(\omega_j)^{\mathrm{H}} \cdot H_1(\omega_j)\bigr)\right]\left[\sum_{j=1}^{N_f}\bigl(H_2(\omega_j)^{\mathrm{H}} \cdot H_2(\omega_j)\bigr)\right]}$$

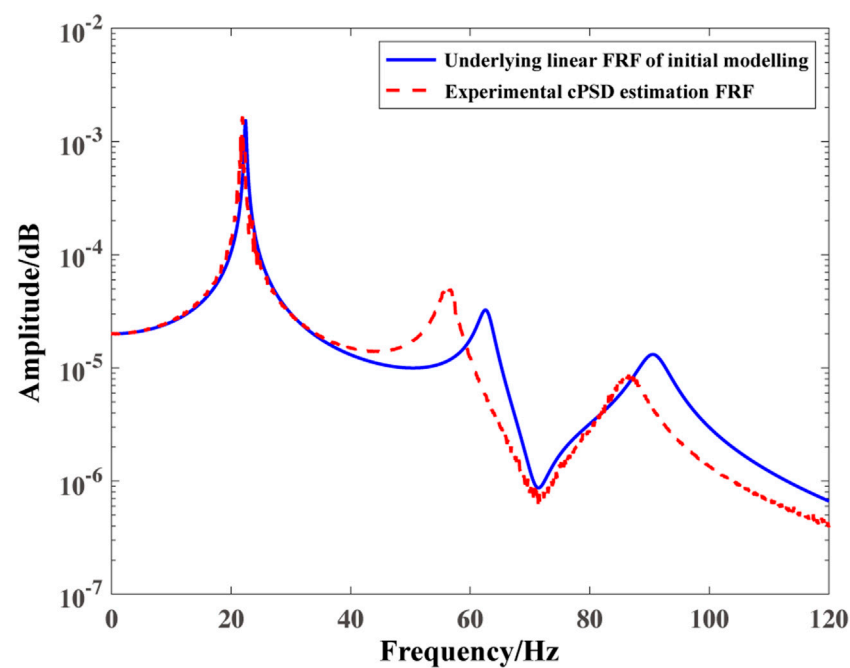(6)   (7)

FIGURE 5
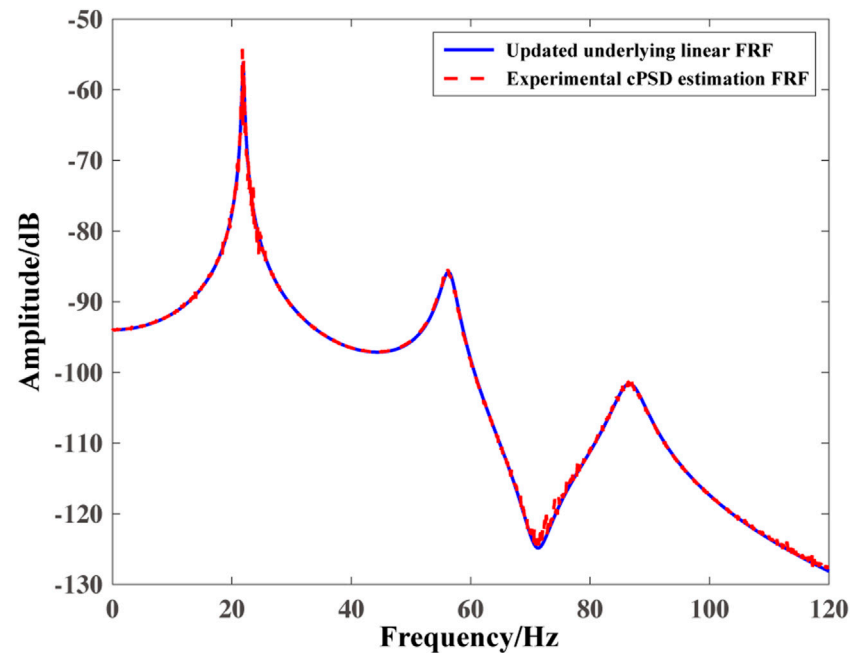Comparison of underlying linear FRFs before model updating.

FIGURE 6
Comparison of underlying linear FRFs after model updating.

where H_1, H_2 represents two different FRFs to be compared, N_p, N_f are the number of frequency points in the FRFs. FDAC, also known as frequency domain MAC, is widely used in frequency domain correlation analysis. However, FDAC is a frequency-dependent metric, which may lead to the issue of frequency points selection (Gang et al., 2014). FRAC describes the overall similarity between two FRFs by providing a single value in [0,1], which is more suitable for model updating as an objective function (Zhan et al., 2019). However,
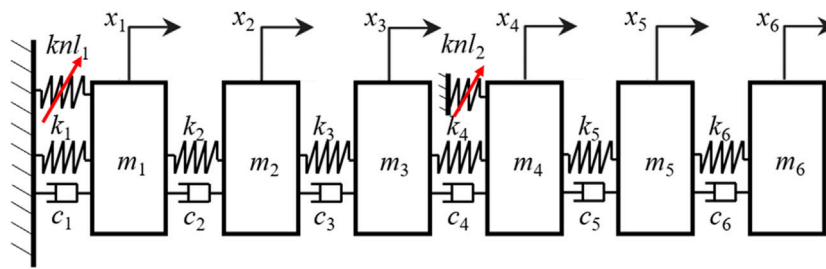
FIGURE 7
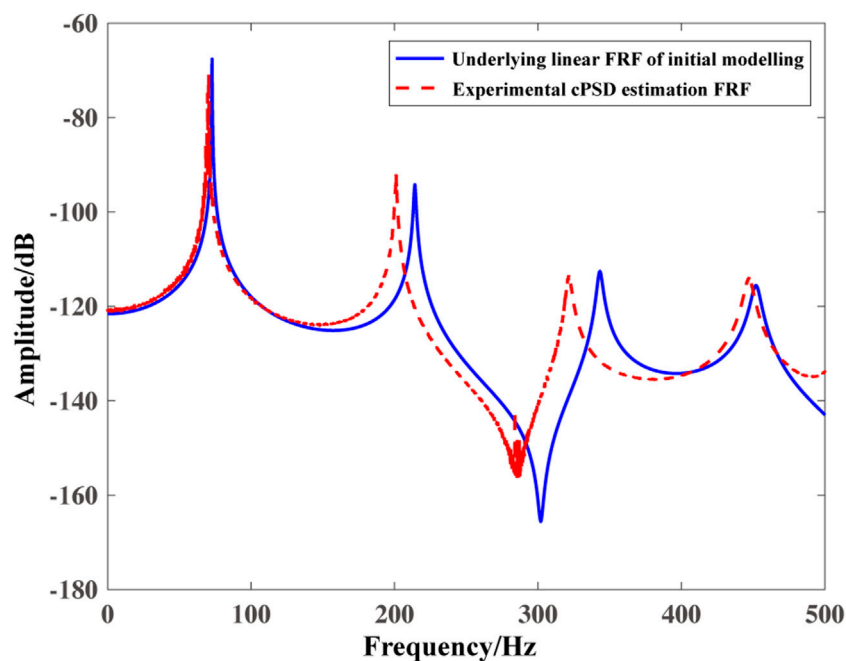Six DOFs mass-spring nonlinear structure.

FIGURE 8
Comparison of underlying linear FRFs before model updating.

FRAC is not sensitive to differences in the amplitudes of the FRFs. Therefore, Lee et al. (2018) proposed a new FRF correlation analysis metric named frequency response function similarity metric (FRFSM), which is also a single-valued metric in the interval of [0,1] applied for evaluating the overall similarity between FRFs but more sensitive to amplitude differences than FRAC. FRFSM is defined as follows,

$$S = \frac{1}{N}\sum_{j=1}^{N} \frac{f\left(\varepsilon_j; 0, \sigma_0^2\right)}{f_0} \tag{8}$$

where the function f represents the probability density function of the standard normal distribution,

$$f\left(x; \mu, \sigma^2\right) = \frac{1}{\sigma\sqrt{2\pi}} e^{-\frac{1}{2}\left(\frac{x-\mu}{\sigma}\right)^2} \tag{9}$$

ε_j represents the difference between FRFs, and f_0 represents the reference value when the difference is 0,

$$f_0 = f\left(0; 0, \sigma_0^2\right) \tag{10}$$

$$\varepsilon_j = \left| 10\log_{10}\left\|H_1\left(\omega_j\right)\right\|^2 - 10\log_{10}\left\|H_2\left(\omega_j\right)\right\|^2 \right| \tag{11}$$

where H_1 and H_2 can be understand as the FRFs calculated by the finite element model and the FRF data obtained from experiments respectively in model updating. From equations (8) to (11), it can be seen that FRFSM is equivalent to assigning weights to the differences between FRFs at the standard normal distribution probability density function scale. σ_0 is the standard deviation set by the researcher based on actual situation, and a smaller standard deviation will result in a smaller FRFSM value.
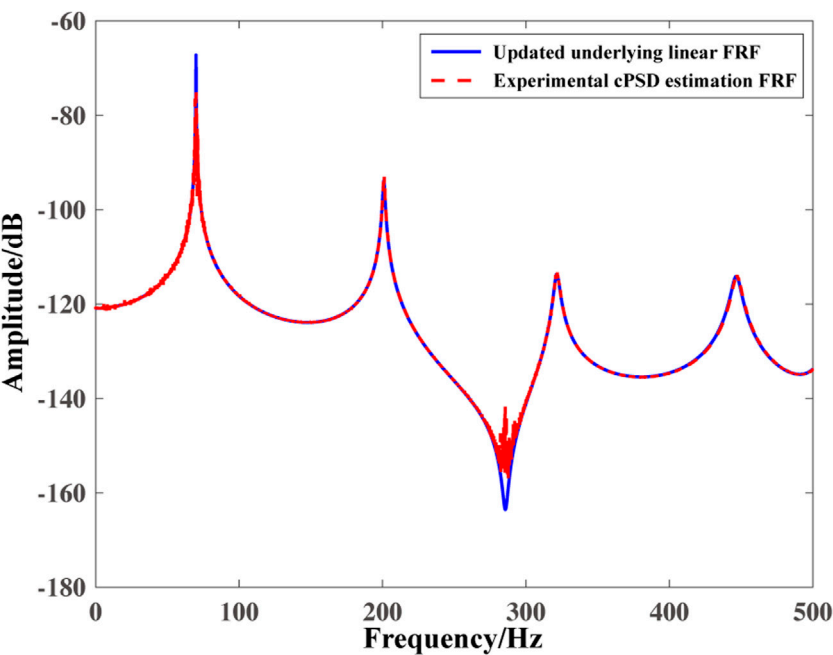
FIGURE 9
Comparison of underlying linear FRFs after model updating.

TABLE 1 Model updating results of submatrix parameters.

No. of submatrix parameters	2	3	4	5
Updated values	−0.002	−0.2003	−0.0060	−0.2997
Real values	0	−0.2000	0	−0.3000
Relative errors	—	0.15%	—	0.10%

3 The proposed model updating method

3.1 Model updating objective function

Based on the single-value similarity metric FRFSM, this paper defines the following model updating objective function,

$$obj = \left\| \left(1 - S_{ij} \right) \right\|^2 \qquad (12)$$

where i, j refers to the labels of the corresponding FRF curves used for model updating. For example, S_{21} describes the FRFs' similarity of 1 excitation and 2 responses between the FRF from the numerical model and the FRF from testing in the model updating framework. Complete FRF data measurement and frequency point selection are unnecessary.

3.2 SMW formulas

Like other conventional model updating methods, FRF-based model updating may encounter the issue of computational efficiency due to reusing the initial numerical model in the iterative optimization mechanism. Structural reanalysis theories aim to achieve fast calculation by utilizing initial structural information once and calculating subsequent responses after structural modification (Li et al., 2023). Therefore, this paper combines structural reanalysis theories with model updating to avoid
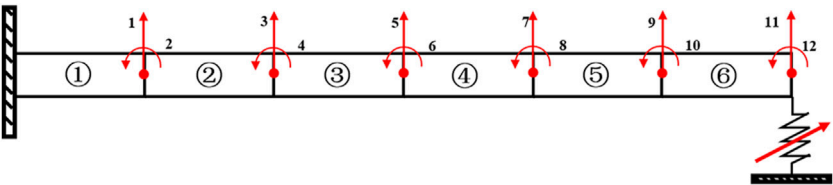
FIGURE 10
Nonlinear cantilever beam structure.

TABLE 2 Numerical model parameters for the nonlinear cantilever beam model.

Length m)	Section width m)	Section thickness m)	Elastic modulus (Pa)	Density (kg/m³)	*knl* (N/m³)
0.5	0.025	0.005	7.17×10^{10}	2.7×10^{3}	1×10^{8}

FIGURE 11
Comparison of underlying linear FRFs before model updating.

FIGURE 12
Comparison of underlying linear FRFs after model updating.

TABLE 3 Model updating results of sub-matrix parameters.

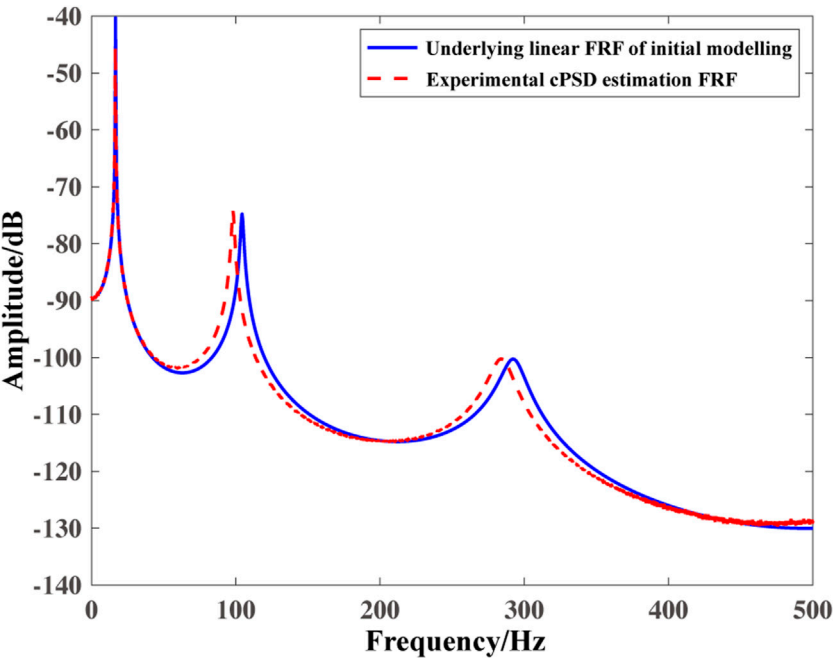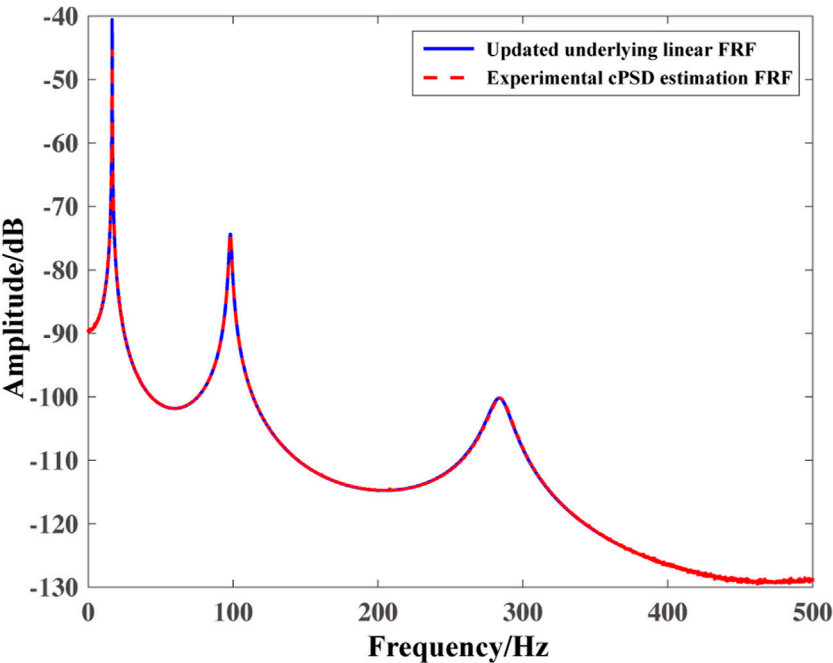| No. of submatrix parameters	3	4	5
Updated values	−0.0001	−0.2965	−0.0130
Real values	0	−0.3	0
Relative errors	—	1.17%	—

recalling the initial model, thereby improving the computational efficiency of model updating process.

The SMW formula is widely used in structural reanalysis. Akgun et al. (2001) have investigated that several common structural reanalysis methods are actually equivalent to the SMW formula under certain conditions. The SMW formula mainly solves the issue of taking inverse matrices of locally modified matrices. Fortunately, the dynamic stiffness matrix of Equation 3 and FRF matrices are exactly a pair of inverse matrices, $H(\omega) = B(\omega)^{-1}$, and dynamic stiffness matrix includes structural characteristic matrices. Therefore, the SMW formula can be reasonably combined with FRF-based model updating. If the dynamic stiffness B is modified by ΔB with rank p, and $\Delta B = UV^T$, the mathematical expression of the SMW formula is (Akgun et al., 2001)

$$\left(B + UV^T\right)^{-1} = B^{-1} - B^{-1}U\left(I + V^TB^{-1}U\right)^{-1}V^TB^{-1} \quad (13)$$

If the rank of ΔB is 1 and $\Delta B = uv^T$, the SMW formula degenerates into the Sherman-Morrison (SM) formula, which is mathematically expressed as (Akgun et al., 2001)

$$\left(B + uv^T\right)^{-1} = B^{-1} - B^{-1}u\left(1 + v^TB^{-1}u\right)^{-1}v^TB^{-1} \quad (14)$$

It can be seen that if this formula is applied to FRF-based model updating, it can avoid repeatedly calling the overall finite element model and only the initial model is used to calculate the FRFs after each modification.

Additionally, it should be noted that when applying the SMW formula to FRF-based model updating, a key step is how to decompose the dynamic stiffness modification matrix ΔB in a reasonable manner to satisfy Eq. 13 or (14). This paper selects sub-matrix parameterization for the parameters to be updated (Friswell and Mottershead, 1995). Taking the stiffness matrix as an example, the modified stiffness matrix K_u can be represented as,

$$K_u = K_0 + \sum_i^l p_i K_i^e \quad (15)$$

where p_i is the sub-matrix parameter, and each sub-matrix K_i^e can be composed of one certain element matrix or the sum of several element matrices. K_0 is the stiffness matrix of initial modelling. It can be seen that for structural damage identification problems, the sub-matrix parameters should be real numbers within the range of [-1,0], where 0 represents the undamaged condition and −1 represents complete failure. Therefore, the modification matrix ΔB is a real symmetric matrix, which can be represented by the symmetric Schur decomposition theorem as (Golub and van Loan, 2013),

$$\Delta B = Q\Lambda Q^T \quad (16)$$

where matrix Q is a real orthogonal matrix, and each column is composed of the eigenvectors of matrix ΔB. Matrix Λ is a diagonal

matrix composed of eigenvalues of matrix ΔB. Therefore, take: $U = Q\Lambda$, $V = Q$ in Equation 13 in this paper.

3.3 Summary

This paper establishes a two-stage model updating method for the linear parts of structures with local nonlinearities. Firstly, cRP method is employed to separate nonlinear effects to obtain the underlying linear FRFs. Secondly, the FRFSM metric is utilized to establish the model updating objective function. Meanwhile, based on the relationship of inverse matrices between FRF and dynamic stiffness matrix, the symmetric Schur decomposition of the structural sub-matrix is taken as the modification matrix in the SMW formula, and the SMW formula is reasonably integrated into the model updating process. The flowchart of the proposed method as seen in Figure 1. To further illustrate the details of the method and validate its efficacy in model updating and structural damage identification, three numerical examples are provided below.

4 Numerical verification

4.1 Case 1

This example is primarily employed to demonstrate the intricate details of the proposed method, with the model data being sourced from reference (Richards and Singh, 1998). The three DOFs spring-mass structure shown in Figure 2 is a structure with local nonlinearities of single location and multiple types. Quadratic and cubic types of nonlinearities are positioned between the second and third DOFs. The underlying linear structural mass M, damping C, and stiffness K matrices are

$$M = \begin{bmatrix} 1 & 0 & 0 \\ 0 & 1 & 0 \\ 0 & 0 & 1 \end{bmatrix}, C = \begin{bmatrix} 10 & -10 & 0 \\ -10 & 20 & -10 \\ 0 & -10 & 20 \end{bmatrix}, K = \begin{bmatrix} 1 & -1 & 0 \\ -1 & 2 & -1 \\ 0 & -1 & 2 \end{bmatrix} \times 10^5 \quad (17)$$

The restoring force between the second and the third DOF is expressed as,

$$f_{nl23} = -8 \times 10^6 \times (x_2 - x_3)^2 + 5 \times 10^8 \times (x_2 - x_3)^3 \quad (18)$$

The first step is to extract the underlying linear FRFs using the cRP method. Convert Equation 4 into a block diagram as shown in Figure 3, and take the H_2 estimation of Equation 5 as an example. Based on this block diagram, cPSD can be hierarchically solved. Due to the existence of two types of nonlinearities, it is necessary to firstly calculate the cPSD that is independent of the first type of nonlinearity, i.e., cPSD with the condition of (−1), and then further calculate the cPSD independent of the second type of nonlinearity, i.e., cPSD with the condition of (−1:2). The subscripts 1 and 2 in Figure 3 represent nonlinearity, and the labels between the two types of nonlinearities can be arbitrarily assigned. All PSD are solved according to relevant linear theories. It is worth noting that the calculation of the L matrix of the first layer in the block diagram only requires conventional PSD data,

while the L matrix of the second layer in the block diagram requires the corresponding cPSD. The calculation of L matrix process is similar to the block diagram shown in Figure 3 and will not be repeated.

A zero-mean Gaussian white noise excitation with a mean square value of 5 kN is applied at the first DOF. Taking the FRF calculated from the response of the second DOF as an example, the FRF calculated using PSD data directly, namely, H_{21} and the FRF calculated using cPSD data using the cRP method, namely, Hc_{21} are compared with the underlying linear FRF calculated theoretically, as shown in Figure 4. It can be seen that the presence of nonlinearities causes significant distortion in the estimated FRF. In contrast, the conditioned FRF after cRP operation is very close to the theoretical FRF, indicating that the cRP method can effectively extract the underlying linear FRF of structures with local nonlinearities.

Subsequently, the model updating method proposed in this paper is applied for structural damage identification. Assuming that there is 30% damage to k_1. Then the damaged FRF is taken as the experimental data, and the undamaged FRF is taken as the numerical data. Taking the FRF data excited at the first and the second DOF as an example, before the process of model updating, the comparison between the experimental FRF estimated by cPSD and the theoretically calculated FRF is shown in Figure 5. The difference between the FRF curves indicates the need for model updating. Taking the standard deviation σ_0 in Equation 8 as 1, and the FRFSM value at this time is 0.6362. The *fmincon* function in the The Mathworks, Inc., (2021) optimization toolbox is used to optimize Equation 12. The frequency range is [0, 120] Hz, and the experimental FRF data used is the first column representing the overall FRF matrix of the structure excited at the first DOF, namely, Hc_{11}, Hc_{21} and Hc_{31}. Taking Hc_{21} as an example, the comparison between the updated FRF and the experimental FRF is shown in Figure 6, and the two curves are already very close with a FRFSM value of 0.9930. And the updated sub-matrix parameter of the first element is −0.2958 with an error of only 1.4% between the true value −0.3 of the sub-matrix parameter corresponding to the 30% damage of k_1. The results show that the model updating method proposed in this paper can effectively quantify the damages extent and identify their locations for structures with local nonlinearities. Notably, all response data and excitation data are used for the cRP calculation, and only one element in overall FRF matrix at one frequency point is employed for model updating. The same applies to following cases. It should be noted that the data requirement of the cRP method is not higher than that of other common nonlinear identification methods.

4.2 Case 2

The six DOFs spring-mass structure depicted in Figure 7 constitutes a multi-type multi-location nonlinear system, where the cubic and quadratic nonlinearities located at the first and the fourth DOFs respectively, both of which are grounded nonlinear springs. The model data comes from the reference (Zhang et al., 2017), and the stiffness coefficients of the two nonlinear springs are $k_{nl1} = 10^{10}$ N/m³, $k_{nl2} = 10^7$ N/m², respectively. The elements of the underlying linear structural mass M, damping C, and stiffness K matrices are,

$$
\begin{cases}
m_1 = m_2 = m_3 = m_4 = m_5 = m_6 = 1\,\text{kg} \\
k_1 = k_2 = k_3 = k_4 = k_5 = k_6 = 3.6 \times 10^5\,N/m \\
c_1 = c_2 = c_3 = c_4 = c_5 = c_6 = 18\,N \cdot s/m
\end{cases} \tag{19}
$$

Assuming that k_3 and k_5 sustain 20% and 30% damage, respectively. Apply a zero-mean Gaussian white noise excitation with a mean square value of 5 kN at the sixth DOF. Similarly, the cRP method is first used to estimate the experimental FRF from cPSD. Taking the FRF calculated from the response of the third DOF as an example, the comparison between the initial modeling FRF and the experimental FRF is shown in Figure 8, where the FRFSM value is 0.6368. Take the second to fifth sub-matrix parameters as the parameters to be updated. The experimental FRF data used is the sixth column of the overall FRF matrix representing the excitation at the sixth DOF within the frequency range of [0, 500] Hz; Similarly, the *fmincon* function in the Matlab (2021a) optimization toolbox is used to optimize Equation 12, and the standard deviation σ_0 in Equation 12 is still taken as 1. Figure 9 indicates that the two FRF curves of updated and experimental FRFs are very close, with a FRFSM value of 0.9818. The updated second to fifth sub-matrices parameters are listed in Table 1. The results show that the proposed method can locate the damage and qualify the extent of the damages.

4.3 Case 3

Figure 10 is a widely used numerical model for nonlinear system identification (Kerschen et al., 2003), which represents a nonlinear cantilever beam structure consisting of 6 Euler beam elements and 12 DOFs. At the beam end, there is a cubic stiffness grounded spring with a stiffness coefficient of 108 N/m³. An excitation of zero-mean Gaussian white noise with a mean square value of 50 N is imposed at the 11th DOF of the beam end. The basic parameters of the model are presented in Table 2, and the data is adopted from the reference (da Silva et al., 2010).

Assuming a 30% stiffness damage occurs at the fourth element, and the sub-matrix parameters of the third to fifth elements are used as the parameters to be updated. Taking the FRF from the response of the third DOF as an example, before model updating, the comparison between the FRF estimated by the cPSD of the damaged model and the FRF from the initial modeling without damage is shown in Figure 11. The frequency band is taken as [0.500] Hz, and the FRFSM value at this time is 0.8970; The comparison of the two FRFs after model updating is shown in Figure 12. Under the same frequency range for analysis, the FRFSM value is 0.9994. The stiffness sub-matrix parameters of the third to fifth elements after updating are shown in Table 3. It can be seen that the proposed method in this paper accurately identifies the location and the extent of damages for structures with local nonlinearity.

5 Conclusion

This paper proposes a novel two-stage model updating method for structures with local nonlinearities and applies it to structural

damage identification. In the first stage, the method utilize the cRP method to extract the underlying linear FRF of tested structures, and then uses the FRFSM-based model updating objective function to conduct the constrained optimization process as the second stage. Simultaneously, based on the theoretical relationship between the FRF and the dynamic stiffness matrix, which is the inverse matrix of each other, the SMW formula is appropriately integrated into the model updating constrained optimization process. Owing to utilization of the sub-matrix parameterization and the symmetric Shur decomposition theorem in this paper, modification matrices at each iterative step during the optimization process can consistently meet the requirement of the SMW equation. Three numerical cases demonstrate that the proposed method can accurately identify the location and extent of damages in the presence of nonlinearities. Meanwhile, as an FRF-based model updating method, it has the advantages of not requiring frequency point selection, not depending on sensitivity, not recalling the initial finite element model, which avoids ill-conditioned issues and has high computational efficiency. Furthermore, benefiting from the excellent performance of the objective function for model updating, the proposed method is capable of achieving satisfactory results using even incomplete FRF data. Therefore, the method proposed in this paper can effectively and reliably conduct the tasks of model updating and damage identification in the structural health monitoring framework, and its application to more complex actual structures will be further expanded in subsequent research. Notably, nonlinearities discussed in this paper are belong to the weak nonlinearities. Additionally, research on the impact of noise is beyond the scope of this paper due to its involvement in nonlinear random vibration issues, but will also be a focus of future study.

Data availability statement

The raw data supporting the conclusions of this article will be made available by the authors, without undue reservation.

Author contributions

HZ: Conceptualization, Data curation, Formal Analysis, Funding acquisition, Investigation, Methodology, Project administration, Resources, Software, Supervision, Writing–original draft, Writing–review and editing. DW: Formal Analysis, Resources, Supervision, Writing–review and editing. LZ: Project administration, Supervision, Writing–review and editing. LH: Project administration, Supervision, Writing–review and editing. LL: Funding acquisition, Supervision, Writing–review and editing. HQ: Funding acquisition, Supervision, Writing–review and editing. DL: Supervision, Writing–review and editing. JF: Supervision, Writing–review and editing.

Funding

Conflict of interest

Authors HZ, DW, LZ, LH, LL, and HQ were employed by China Construction Second Engineering Bureau Co., Ltd.

The remaining authors declare that the research was conducted in the absence of any commercial or financial relationships that could be construed as a potential conflict of interest.

The handling editor CXQ declared a past co-authorship with the author DL.

Publisher's note

All claims expressed in this article are solely those of the authors and do not necessarily represent those of their affiliated organizations, or those of the publisher, the editors and the reviewers. Any product that may be evaluated in this article, or claim that may be made by its manufacturer, is not guaranteed or endorsed by the publisher.

References

Akgun, M. A., Garcelon, J. H., and Haftka, R. T. (2001). Fast exact linear and non-linear structural reanalysis and the Sherman-Morrison-Woodbury formulas. *Int. J. Numer. Methods Eng.* 50, 1587–1606. doi:10.1002/nme.87

Arora, V., Adhikari, S., and Vijayan, K. (2023). FRF-based finite element model updating for non-viscous and non-proportionally damped systems. *J. Sound. Vib.* 552, 117639. doi:10.1016/j.jsv.2023.117639

Bendat, J. S., and Piersol, A. G. (2010). *Random data: analysis and measurement procedures*. Hoboken: John Wiley and Sons.

Cong, S., Hu, S., and Li, H. J. (2022). FRF-based pole-zero method for finite element model updating. *Mech. Syst. Signal Process.* 177, 109206. doi:10.1016/j.ymssp.2022.109206

da Silva, S., Cogan, S., and Foltête, E. (2010). Nonlinear identification in structural dynamics based on Wiener series and Kautz filters. *Mech. Syst. Signal Process.* 24, 52–58. doi:10.1016/j.ymssp.2009.05.017

Ewins, D. J., Weekes, B., and delli Carri, A. (2015). Modal testing for model validation of structures with discrete nonlinearities. *Philos. Trans. R. Soc. A* 373, 20140410. doi:10.1098/rsta.2014.0410

Friswell, M. I., and Mottershead, J. E. (1995). *Finite element model updating in structural dynamics*. Dordrecht: Springer-Science+Business Media.

Gang, X. Y., Chai, S., Allemang, R. J., and Li, L. (2014). A new iterative model updating method using incomplete frequency response function data. *J. Sound. Vib.* 333 (9), 2443–2453. doi:10.1016/j.jsv.2013.12.008

Golub, G. H., and van Loan, C. F. (2013). *Matrix computations*. 4th Edition. Baltimore: The Johns Hopkins University Press, 439–512.

Hassani, S., and Shadan, F. (2022). Using incomplete FRF measurements for damage detection of structures with closely-spaced eigenvalues. *Measurement* 188, 110388. doi:10.1016/j.measurement.2021.110388

Hou, R. R., and Xia, Y. (2022). Review on the new development of vibration-based damage identification for civil engineering structures: 2010-2019. *J. Sound. Vib.* 491, 115741. doi:10.1016/j.jsv.2020.115741

Huang, Y., and Ferguson, N. S. (2018). Identification of biomechanical nonlinearity in whole-body vibration using a reverse path multi-input-single-output method. *J. Sound. Vib.* 419, 337–351. doi:10.1016/j.jsv.2018.01.002

Kerschen, G., Lenaerts, V., and Golinval, J. C. (2003). VTT benchmark: application of the restoring force surface method. *Mech. Syst. Signal Process.* 17 (1), 189–193. doi:10.1006/mssp.2002.1558

Kerschen, G., Worden, K., Vakakis, A. F., and Golinval, J. C. (2006). Past, present and future of nonlinear system identification in structural dynamics. *Mech. Syst. Signal Process.* 20 (3), 505–592. doi:10.1016/j.ymssp.2005.04.008

Lee, D., Ahn, T. S., and Kim, H. S. (2018). A metric on the similarity between two frequency response functions. *J. Sound. Vib.* 436, 32–45. doi:10.1016/j.jsv.2018.08.051

Li, Q. K., Liao, M. F., and Jing, X. J. (2021). Transmissibility function-based fault diagnosis methods for beam-like engineering structures: a review of theory and properties. *Nonlinear Dynam* 106 (3), 2131–2163. doi:10.1007/s11071-021-06883-5

Li, W. X., Chen, S. Y., and Huang, H. (2023). System reduction-based approximate reanalysis method for statically indeterminate structures with high-rank modification. *Structures* 55, 1423–1436. doi:10.1016/j.istruc.2023.06.063

Lin, R. M. (2017). Function-weighted frequency response function sensitivity method for analytical model updating. *J. Sound. Vib.* 403, 59–74. doi:10.1016/j.jsv.2017.05.031

Lin, R. M., and Ewins, D. J. (1994). Analytical model improvement using frequency response functions. *Mech. Syst. Signal Process.* 8 (4), 437–458. doi:10.1006/mssp.1994.1032

Lin, R. M., and Zhu, J. (2006). Model updating of damped structures using FRF data. *Mech. Syst. Signal Process.* 20 (8), 2200–2218. doi:10.1016/j.ymssp.2006.05.008

Moaveni, B., He, X., Conte, J. P., and Restrepo, J. I. (2010). Damage identification study of a seven-story full-scale building slice tested on the UCSD-NEES shake table. *Struct. Saf.* 32 (5), 347–356. doi:10.1016/j.strusafe.2010.03.006

Noel, J. P., and Kerschen, G. (2017). Nonlinear system identification in structural dynamics: 10 more years of progress. *Mech. Syst. Signal Process.* 83, 2–35. doi:10.1016/j.ymssp.2016.07.020

Richards, C. M., and Singh, R. (1998). Identification of multi-degree-of-freedom nonlinear systems under random excitations by the "reverse path" spectral method. *J. Sound. Vib.* 213 (4), 673–708. doi:10.1006/jsvi.1998.1522

The Mathworks, Inc. (2021). MATLAB version (2021a), Natick, Massachusetts.

Wang, X., Hill, T. L., Neild, S. A., Shaw, A. D., Haddad Khodaparast, H., and Friswell, M. I. (2018). Model updating strategy for structures with localised nonlinearities using frequency response measurements. *Mech. Syst. Signal Process.* 100, 940–961. doi:10.1016/j.ymssp.2017.08.004

Wu, Z. G., Yang, N., and Yang, C. (2015). Identification of nonlinear structures by the conditioned reverse path method. *J. Aircr.* 52 (2), 373–386. doi:10.2514/1.C032424

Zhan, M., Guo, Q. T., Yue, L., and Baoqiang, Z. (2019). Finite element model updating of jointed structure based on modal and strain frequency response function. *J. Mech. Sci. Technol.* 33 (10), 4583–4593. doi:10.1007/s12206-019-0902-0

Zhang, H., Li, D. S., and Li, H. N. (2020). Novel criterion for evaluation of stationarity in nonlinear structural dynamics. *J. Aerosp. Eng.* 33 (4), 06020001. doi:10.1061/(ASCE)AS.1943-5525.0001141

Zhang, M. W., Wei, S., Peng, Z. K., Dong, X., and Zhang, W. (2017). A two-stage time domain subspace method for identification of nonlinear vibrating structures. *Int. J. Mech. Sci.* 120, 81–90. doi:10.1016/j.ijmecsci.2016.11.008

Zhu, T. X., Zhang, G. B., and Zang, C. P. (2022). Frequency-domain nonlinear model updating based on analytical sensitivity and the Multi-Harmonic balance method. *Mech. Syst. Signal Process.* 163, 108169. doi:10.1016/j.ymssp.2021.108169

![frontiers] Frontiers in Materials

Study on mechanical properties and self-sensing properties of sprayed high-performance concrete containing glass aggregate

Jing Wang, Tianren Wang, Yunlong Zhang* and Xuesong Qian*

School of Transportation Science and Engineering, Jilin Jianzhu University, Changchun, China

Using glass sand as a substitute for sand in high-performance concrete not only conserves resources but also helps protect the environment. This study replaced manufactured sand with glass sand and added carbon fiber to prepare high-performance shotcrete. Its mechanical and self-sensing properties were then tested separately. The findings suggest that with an increase in glass sand content, the compressive strength of high-performance shotcrete initially rises and subsequently declines. When the replacement ratio of glass sand is 75%, the compressive strength exhibits its maximum value, whereas an increase in the glass sand content leads to a reduction in both splitting tensile strength and flexural strength. Although increasing carbon fiber content does not significantly contribute to compressive strength, it significantly improves flexural strength and splitting tensile strength. In addition, when testing the self-sensing performance of the material, it was found that its self-sensing performance increased significantly with increasing carbon fiber content but decreased with increasing glass sand content. Finally, an Ansys APDL simulation using the relevant parameters of the optimal group of mechanical properties was performed to model a tunnel and verify its feasibility and validity. This study provides a theoretical and practical reference for future engineering applications.

1 Introduction

Concrete stands as one of the most extensively employed construction materials in contemporary building practices. Its numerous benefits encompass ease of shaping, minimal energy requirements, exceptional longevity, cost-effectiveness, and strong compatibility with steel. Nevertheless, concrete does exhibit certain drawbacks, including brittleness and relatively limited tensile strength, constraining its extensive application in specific domains. Shotcrete is one of the more typical engineering applications of concrete. In tunnel construction, traffic tunnels are usually lined with a composite lining, with the initial ground support being of the sprayed anchor type and the secondary lining serving as a safety reserve. Although the composite lining in the bearing mechanism is reasonable and reflects the "first time, after the stiffness" principle, its conservative engineering measures lead to slow construction speed and also increase the cost of the entire project. Therefore, attention is

beginning to focus on the use of a single shotcrete lining as a permanent lining (Larive et al., 2020; Neuner et al., 2020; Shi et al., 2023). To meet relevant technical requirements and realistic demands, high-performance concrete (HPC) was developed. High-performance concrete has better workability, mechanical properties, and durability than conventional concrete (Biolzi et al., 1997; Song and Hwang, 2004; Lim and Ozbakkaloglu, 2014; Kou and Poon, 2015).

High-performance shotcrete (HPS) refers to the enhancement of the properties of conventional shotcrete, including workability, strength, and durability, in order to confer it with excellent pumpable and sprayable characteristics, high strength, and exceptional durability. Different mineral admixtures like fly ash, silica fume, slag, and various other substances are frequently utilized in the fabrication of high-performance concrete (Cong et al., 1992; Gražulytė et al., 2020). The utilization of these admixtures improves the mechanical properties of concrete by promoting pozzolanic reactivity, reducing permeability, and enhancing durability. The incorporation of fibers in sprayed concrete can effectively enhance its strength and toughness while mitigating the risk of cracking (Juan, 2009; Khooshechin and Tanzadeh, 2018). However, this can also influence the fluidity of the concrete, thereby partially constraining the advancement of fiber-reinforced shotcrete. Reactive powder concrete, an ultra-high-strength concrete, is created by blending active materials like cement and mineral admixtures, in addition to the inclusion of fibers (Richard and Marcel, 1995). Although notable progress has been made in the realm of high-performance shotcrete, the field of sprayed reactive powder concrete is still in its nascent stages. Wang (Zhang et al., 2022), for the first time, amalgamated reactive powder concrete with sprayed concrete to produce ultra-high performance concrete with a strength exceeding 110 MPa.

However, both reactive powder concrete and reactive powder shotcrete contain river sand, manufactured sand, or quartz sand (Helmi et al., 2016; Ji et al., 2021). Sand can play the role of lubrication, skeleton, and filler in concrete. Quartz sand not only causes environmental pollution, but its dust is so fine that it can be suspended in the air. Prolonged inhalation of dust containing quartz sand may lead to silicosis, impacting respiratory function. River sand has long been subjected to water erosion and has a smooth surface. Compared with manufactured sand, it can make concrete more mobile. However, river sand resources are very limited and the mining process can seriously damage the ecological balance of the river, harm the living environment of aquatic organisms, and some regions have banned mining of river sand. Manufactured sand is made by mechanically crushing mountain rock. Compared with river sand, the raw materials for manufactured sand are easy to obtain. However, because it is mechanically crushed, the particles are angular, have rough surfaces, and have poor mobility. Its mining process also directly destroys the structure of the mountain and disrupts the ecological balance. Glass is regarded as a favorable alternative to sand due to its favorable chemical and physical attributes (Du and Tan, 2013). Relevant scholars have successfully produced glass sand from recycled waste glass to partially or completely replace sand in concrete, confirming the feasibility of using glass sand in concrete (Tamanna et al., 2020). Although there are many studies on the use of glass sand to replace manufactured sand in normal concrete and all have achieved positive results,

there are fewer studies related to the use of glass sand in RPC and no application in sprayed activated powder concrete has been found so far. Therefore, there is a need to carry out relevant characterization studies on reactive powder shotcrete with glass aggregate.

As the project advances, the performance criteria for concrete tunnel linings are becoming increasingly intricate and diverse. Concrete is mandated to exhibit high fluidity, self-compaction, elevated strength, exceptional durability, enhanced serviceability, and an extended service life. Therefore, there is a need to inspect the concrete in real-time and to check the deformation and damage of the structure during its life cycle. This practice is known as Structural Health Monitoring (SHM). According to the results of related literature (Huang et al., 2007; Chen and Ansari, 2010; Imai and Feng, 2012; Ai et al., 2016), conventional monitoring systems often use supplementary or embedded sensors for the detection of damage and cracks in structural systems. However, the longevity of these supplementary or embedded sensors is notably constrained when measured against the expected service life of the infrastructure. Consequently, frequent replacements are necessitated, resulting in escalated costs. To address these inherent limitations in monitoring systems dependent on such additional or embedded sensors, extensive research has been dedicated to the investigation of smart building materials endowed with innate self-sensing capabilities in recent years (Fu et al., 1998; Chung, 1999; Han et al., 2015; Erdem et al., 2017). These self-sensing smart building materials can detect stress/strain, damage, and crack formation by monitoring changes in electrical resistivity during mechanical loading (Han et al., 2015). It has been shown that carbon fiber-reinforced composite materials (Chen and Chung, 1996; Wen and Chung, 2001; Chung, 2002), cementitious composites containing functional nanofillers (Han et al., 2009; Han et al., 2011; Azhari and Banthia, 2012), and self-sensing fiber-reinforced cementitious composites (Lin et al., 2011; Ranade et al., 2014; Downey et al., 2017) exhibit this self-sensing capability. This provides a basis for realizing self-monitoring of tunnel linings. Sun (Yunlong et al., 2022) used carbon fibers to successfully prepare reactive powder concrete with self-sensing capability, which possessed self-sensing capability while reaching a compressive strength of more than 100 MPa. Although the self-sensing capability of carbon fiber concrete has been quite studied and certain results have been achieved, the self-sensing capability of carbon fiber in sprayed high-performance concrete is still relatively low, hence, there is a compelling need for conducting future research in this area.

This study explores the application of glass sand in high-performance shotcrete. The use of this technology can protect the environment, reduce pollution, and contribute to the sustainable development of high-performance shotcrete. Considering the unclear impact of glass sand on high-performance shotcrete properties, this study investigates how varying glass sand replacement ratios affect the mechanical characteristics of concrete materials in high-performance shotcrete by substituting different quantities of glass sand for manufactured sand. Carbon fibers and different admixtures are also added to provide the self-sensing capability of the tunnel while ensuring toughness and strength. Based on this, mechanical indices such as compressive strength, splitting tensile strength, and flexural strength were used in this

study to evaluate the physical properties of the components. The pressure sensitivity was tested by plugging the specimens into a circuit as an evaluation criterion for self-sensing capability. A tunnel model was then simulated using Ansys APDL to verify its feasibility in project conditions.

2 Materials and methods

2.1 Raw materials

In this test, cement with a compressive strength of 52.5 MPa according to the standard (GB 175-2007, 2007) (GB175-2020, 2020) was used to produce all the concrete mixtures. Manufactured sand was screened to ensure a continuous particle size distribution. The gradation curves are shown in Figure 1. Silica fume was tested by Gansu Sanyuan Silica Material Co., fly ash was produced by Hebei Shengyi Mineral Products Trading Co., metakaolin was K-1300W type high activity metakaolin purchased from Inner Mongolia Chao Brand New Material Co. Glass sand aggregate was 100 mesh (0.15 mm), glass sand produced by Ningbo Hongyang Washing Equipment Co. Tables 1, 2 provides an in-depth analysis of the chemical and physical attributes of cement, silica fume, fly ash, manufactured sand, metakaolin, and glass sand. Throughout the experimental phase, carbon fibers, measuring 6 mm in length, boasting an aspect ratio of 1000, and possessing an impressive tensile strength of 3,950 MPa, were systematically incorporated into all mixtures. Furthermore, a polycarboxylate superplasticizer with a solid content of 38% was consistently employed in all concrete compositions. Figure 2 visually portrays the characteristics of glass sand, manufactured sand and carbon fiber.

2.2 Proportion of mixes

In this study, cement, silica fume, fly ash, metakaolin, manufactured sand, glass sand, and carbon fiber are used as raw materials to produce high-performance concrete with shotcrete properties. Glass sand (0%, 25%, 50%, 75%, 100%) was used as a replacement for manufactured sand in the shotcrete. Carbon fibers

FIGURE 1
Gradation curve of manufactured sand in HPS.
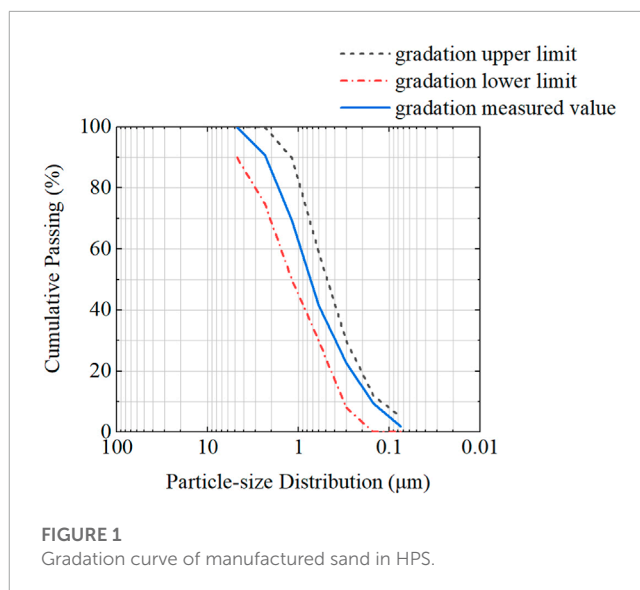
were also added in different proportions (0.5%, 0.7%, and 0.9%) to obtain better mechanical properties and self-sensing performance. The experimental water-cement ratio was 0.2, the sand-to-binder ratio was 0.7, and the polycarboxylate superplasticizer content was 1.8%. There are a total of 15 groups of mix proportions, and the carbon fiber content and glass sand replacement rate are shown in Table 3.

2.3 Specimen preparation

Carbon fibers may clump in concrete as the mixture. To ensure their even distribution in the concrete, it is essential to initially blend cement, silica fume, fly ash, manufactured sand, and glass sand in a concrete mixing pan, and continue mixing for a duration of 2 min. Then, the carbon fibers were sieved using a sieve with an aperture of 10 mm and mixed again for 2 min. Next, superplasticizer and water were added and mixing was continued for 3 min. At the end of the concrete paste mixing, it was quickly poured into the moist-mix concrete spraying machine, and the concrete paste was sprayed

TABLE 1 Chemical composition of raw materials.

Chemical composition identification (%)	Cement	Silica fume	Fly ash	Metakaolin	Glass sand
Silicon dioxide (SiO_2)	—	90.14	—	54.31	72.81
Potassium oxide (K_2O)	—	—	—	0.3	0.72
Sodium oxide (Na_2O)	—	—	—		—
Calcium oxide (CaO)	—	—	0.68	—	8.74
Magnesium oxide (MgO)	1.03	—	—	—	1.15
Ferric oxide (Fe_2O_3)	—	—	—	—	0.18
Aluminium oxide (Al_2O_3)	—	—	—	44.23	2.62
Chloride ion (Cl-)	0.009	0.125	—	—	—

TABLE 2 Physical characteristics of raw materials.

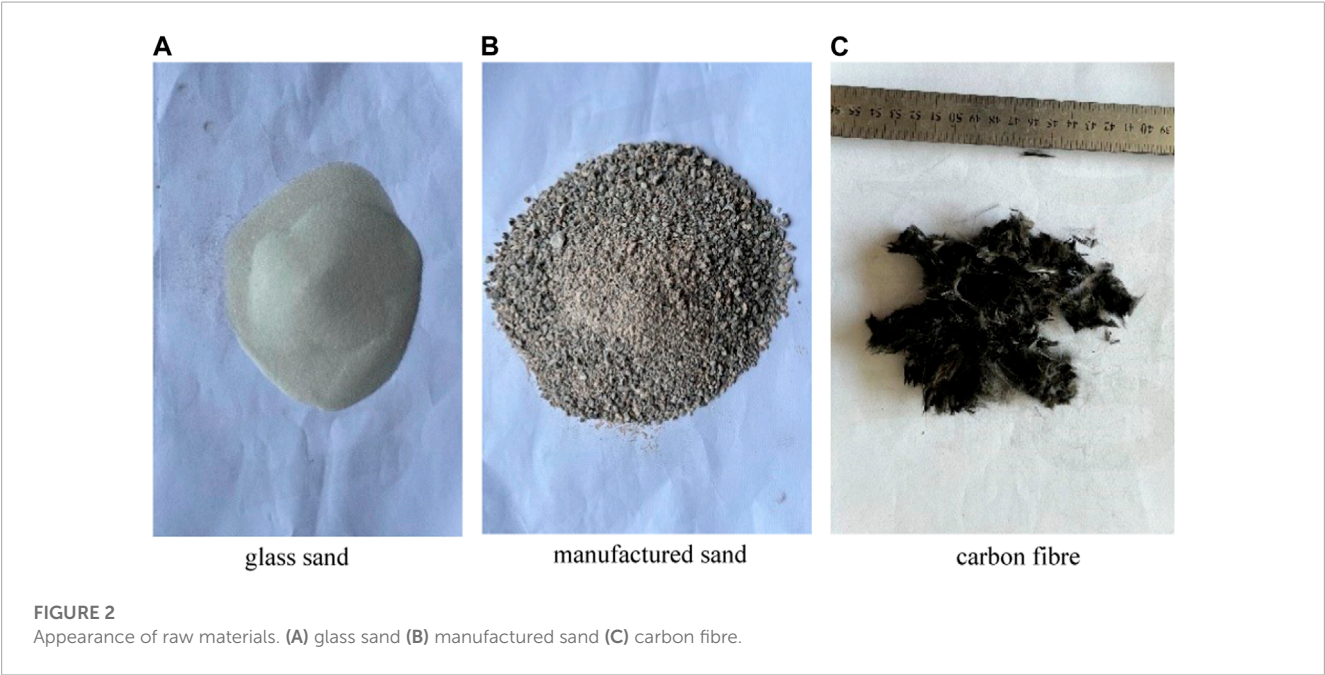| Physical properties identification	Cement	Silica fume	Fly ash	Metakaolin	Glass sand
Density	—	—	—	—	2.4–2.6 kg/m^3
Activity Index	—	74	—	123	—
Water Content	—	0.65	0.11	0.22	—
Ignition Loss	1.43	1.37	0.77	—	—
Fineness	—	—	10.6	—	—

FIGURE 2
Appearance of raw materials. **(A)** glass sand **(B)** manufactured sand **(C)** carbon fibre.

TABLE 3 Concrete mix design (%).

Name	0GS100S (%)	25GS75S (%)	50GS50S (%)	75GS15S (%)	100GS0S (%)
	0.50	0.50	0.50	0.50	0.50
Carbon fiber	0.70	0.70	0.70	0.70	0.70
	0.90	0.90	0.90	0.90	0.90

onto the plate through the moist-mix concrete spraying machine. After the spraying is stable, the slurry is then sprayed into the mold layer by layer. During the spraying process, the mold is at an angle of 80°with the ground, and sprayed layer by layer from the bottom upward.

After the specimens were sprayed, they were placed in a natural environment and demolded after 1 day of natural curing. After that, they were continued to be cured until they reached the standard age specified by the test. The curing environment temperature was 20°C ± 2°C. During the curing process, water was sprayed twice a day to ensure that the specimens could fully maintain the required moisture content.

2.4 Test procedure

1) Compressive strength test

According to the standard specification (GB/T50081-20192019), this experiment successfully prepared cubic specimens of 100 mm × 100 mm × 100 mm for compressive strength test. Throughout the testing process, a WAW-1000B electro-hydraulic servo universal material testing machine was employed to apply a load at a rate ranging from 0.3 to 1 MPa/s. The loading process is shown in Figure 3. To determine the effect of different curing times on the strength of the specimens, the compressive strengths were

FIGURE 3
Compressive strength test.

FIGURE 5
Flexural strength test.

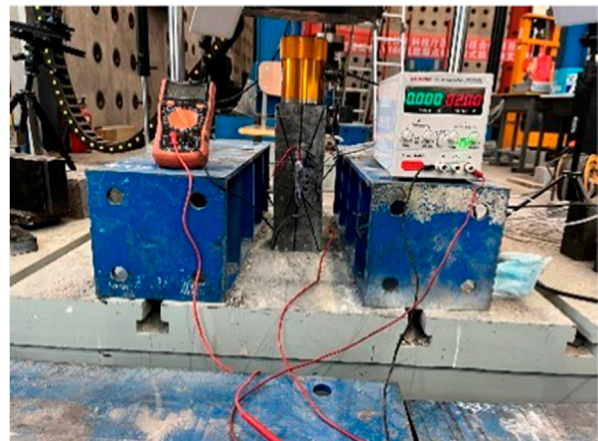

FIGURE 4
Splitting tensile strength test.

FIGURE 6
Pressure sensitivity test.

tested at ages of 1, 3, 7, 14, 28, and 56 days, respectively. There were three specimens for each age group. The compressive strength was calculated using Eq. 1.

$$f_{cc} = \frac{F}{A} \qquad (1)$$

where f_{cc} is the compressive strength of the concrete specimen, MPa; F is the ultimate load of the specimen, N; and A is the compressed area of the concrete specimen, mm^2.

2) Splitting tensile strength test

The splitting tensile test of concrete is shown in Figure 4. 100 mm × 100 mm × 100 mm cubic specimens were subjected to compression testing until failure using a YAW-1000 microcomputer-controlled fully automatic compression testing machine, following a loading rate of 0.1 MPa/s in compliance with the specified standard (GB/T50081-20192019). Three specimens were taken from each group. Before conducting the tests, wooden blocks

were affixed to the midpoint of the opposing sides of both the upper and lower surfaces of the specimen. Subsequently, the specimen was positioned between two semicircular steel plates and properly aligned. The test tensile strength was calculated using Eq. 2.

$$f_{ts} = \frac{2F}{\pi A} = 0.637 \frac{F}{A} \qquad (2)$$

where f_{ts} is the concrete splitting tensile strength, MPa; F is the destructive load of the specimen, N; A is the area of the splitting surface of the specimen, mm^2.

3) Flexural strength test

The flexural test of concrete is shown in Figure 5. In compliance with the standard (GB/T50081-20192019), rectangular concrete beams measuring 100 mm × 100 mm × 400 mm underwent a four-point bending test under a constant load of 0.08 MPa/s using
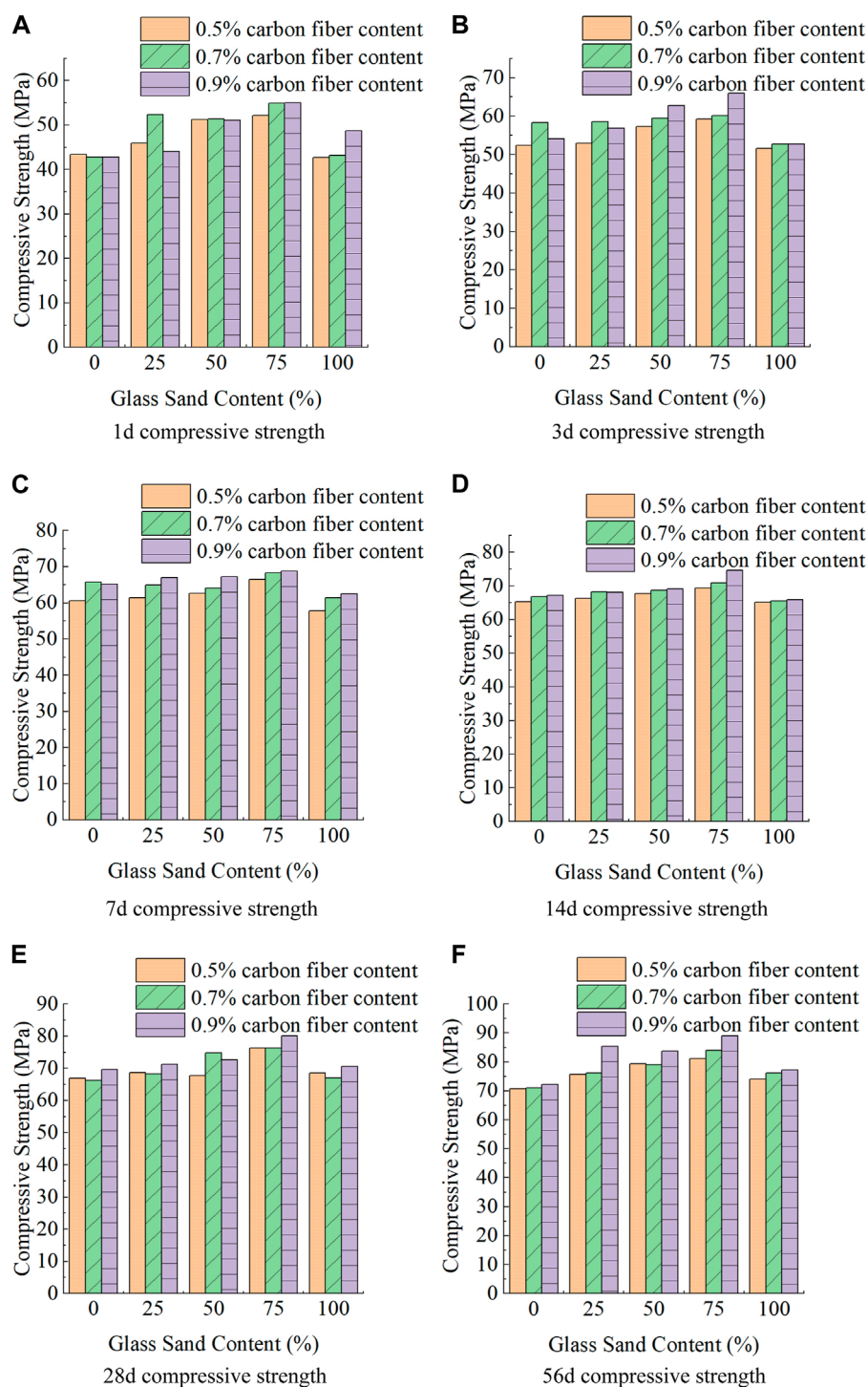
FIGURE 7
Compressive strength of concrete at different ages. **(A)** 1 days compressive strength **(B)** 3 days compressive strength **(C)** 7 days compressive strength **(D)** 14 days compressive strength **(E)** 28 days compressive strength **(F)** 56 days compressive strength.

an MAS-500 hydraulic testing machine until failure. The flexural strength was calculated using Eq. 3 as follows:

$$f_f = \frac{Fl}{bh^2} \qquad (3)$$

Where f_{ts} is the flexural strength of concrete, MPa; F is the breaking load of the specimen, N; l is the span between supports,

mm; h is the height of the specimen, mm; and b is the width of the specimen, mm.

4) Electrical measurements

The pressure sensitivity of the specimens was tested using the two-electrode method, as shown in Figure 6. Specimens with

FIGURE.8
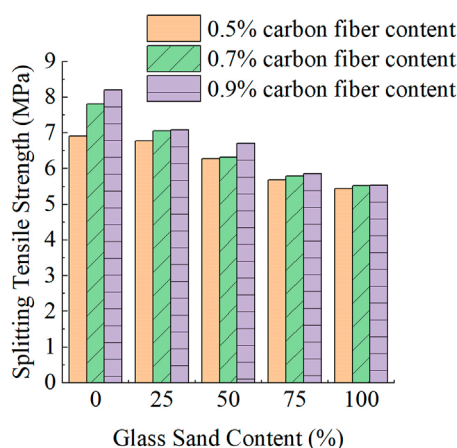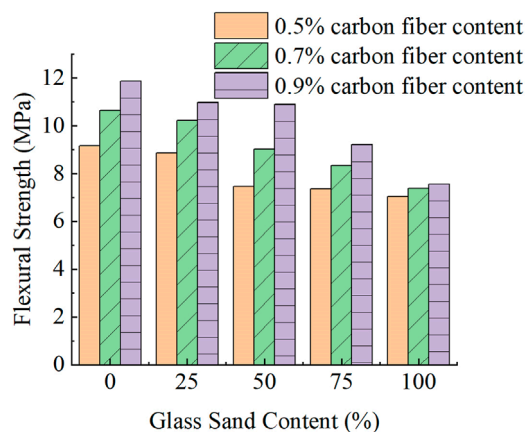28 days split tensile strength of concrete.

FIGURE 9
28 days flexural strength of concrete.

dimensions of 100 mm × 100 mm × 300 mm and 100 mm × 100 mm × 400 mm were tested using MAS-500 hydraulic presses, respectively, and subjected to a cyclic load of 1 kN/s. To prevent the specimen from tipping over when unloaded, the load was maintained at a minimum of 5 kN and the current at that moment was recorded. It should be noted that before each load test, in order to eliminate the effect of polarization, it is necessary to wait for the current to stabilize, with an equilibrium time of 30 ± 5 min, and record the initial current value. The calculation of the pressure sensitivity of the specimen is shown in Eqs. 4–6.

$$R = \frac{U}{I} \tag{4}$$

$$\rho = R\frac{S}{L} = \frac{US}{IL} \tag{5}$$

$$FCR = \left| \frac{\rho_i - \rho_{i-1}}{\rho_0} \right| \times 100\% \tag{6}$$

where R is the resistance, U is the voltage, I is the current, ρ is the resistivity, L is the length of the specimen, S is the cross-sectional area of the specimen, ρ_i is the resistivity at any instant, ρ_{i-1} is the resistivity at the previous instant, and ρ_0 is the resistivity at the initial instant; The fractional change in resistance (FCR) is an acronym for the rate of change of resistivity, which is used to determine the linear and nonlinear behavior of the change of resistivity in the interval. In addition, a larger *FCR* value indicates a more significant change in resistivity under the same load, indicating better conductivity within the sample, which is used to evaluate the self-sensing performance.

3 Results and discussions

3.1 Compressive strength

Figures 7A–F shows the compressive strength of high-performance shotcrete containing glass sand at different ages (1, 3, 7, 14, 28, 56 days) under natural curing conditions. Analyzing the figure data reveals a consistent increase in compressive strength over an extended curing period, regardless of fluctuations in glass sand content. When the carbon fiber content is 0.5% and the glass sand replacement rate is 0%, the compressive strengths of 1, 3, 7, 14, 28, and 56 days are 43.36, 52.4, 60.58, 65.24, 68.89, and 70.751 MPa, respectively. Although the compressive strength increases with the increase of the curing age, the growth rate decreases over time. The growth rate of each group of specimens is calculated as the percentage of strength increase compared with the previous age. The growth rates are 20.85%, 15.61%, 7.69%, 5.59%, and 2.7%, respectively. The possible reason for this phenomenon can be attributed to the rapid progress of concrete hydration reactions during the initial stages. This phase generates numerous products, such as calcium silicate hydrate (C-S-H), contributing to the early strength development of the cement. However, as the hydration reactions progress and consume a significant portion of calcium silicate, the subsequent stages exhibit less pronounced strength gains (Zheng, 2011). It is evident that the compressive strength of concrete specimens incorporating glass sand demonstrates an initial upward trend followed by a subsequent decline as the glass sand content increases. When the carbon fiber content is 0.9%, with the increase of glass sand replacement rate, the compressive strength at 28 days increases from 69.67 to 80.06 MPa, and then decreases to 70.54 MPa. The possible reason for this situation is that glass sand has a very small particle size, and adding glass sand to manufactured sand can improve the gradation of aggregate, fill the voids inside the concrete, and make the compressive strength show an upward trend. But when the glass sand replacement rate reaches 100%, there is no manufactured sand inside the specimen, destroying the original gradation, and reducing the strength. The optimum content was 75% of glass sand, which was consistent with the conclusion of Yubo Jiao who used glass sand to replace quartz sand in UHPC (Jiao et al., 2020).

As the carbon fiber doping proportion rises, there is a general upward trend in compressive strength. Nevertheless, it is worth noting that the overall impact of carbon fiber doping on compressive strength does not appear to be particularly substantial. It is worth mentioning that with the change in glass sand content, the change in carbon fiber content has a different
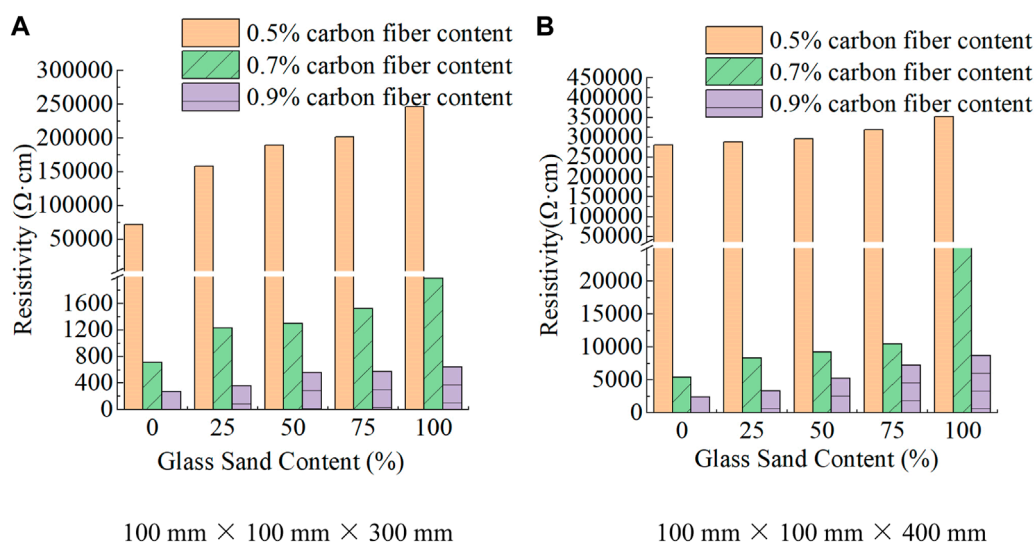
FIGURE 10
Initial resistivity of specimen of different sizes. **(A)** 100 mm × 100 mm × 300 mm **(B)** 100 mm × 100 mm × 400 mm.

impact on compressive strength. Figure 7 illustrates a noticeable trend: when the glass sand content is low, there is an initial tendency for the compressive strength to decrease as the carbon fiber content increases. However, with an increase in glass sand dosage, this tendency gradually diminishes, resulting in higher fiber content and, consequently, greater compressive strength. The reason for this phenomenon may be due to the particle size of 0.15 mm glass beads. This size of glass beads is conducive to the dispersion of fibers in concrete, which can create some gaps between the fibers to reduce their entanglement and aggregation, and promote their free flow and random orientation in the base material.

3.2 Splitting tensile strength

Figure 8 displays the splitting tensile strength of concrete specimens with different levels of glass sand content. It can be seen from the figure that the splitting tensile strength of concrete specimens decreases with the increase of glass sand content. The specimens containing 0.9% carbon fiber showed that the splitting tensile strength of each group decreased by 13.64%, 5.3%, 12.76%, and 5.46%, respectively, as the glass sand content increased, compared with the previous group of glass sand content. This may be due to the particle size of the selected glass sand being too small and the surface being smooth. From the microscopic level, their shape is spherical, without edges and corners. As the glass sand content increases, the friction force between the original manufactured sand gradually decreases, which affects the splitting tensile performance of the specimens. The test results unequivocally demonstrate that the incorporation of carbon fiber leads to a marked improvement in the concrete's splitting tensile performance. The cohesion between carbon fiber and concrete can resist the tensile stress inside the concrete. At the same time, the fibers bridge each other, which is conducive to the transmission of internal force in concrete, and also can prevent the generation

and development of cracks. During a splitting test, stress will be transmitted through the interface between fiber and matrix until the fiber reaches its maximum tensile strength and breaks. This is in line with the test results of Sahar Y. Ghanem (Ghanem and Bowling, 2019).

3.3 Flexural strength

Figure 9 displays the flexural strength exhibited by the concrete specimens. It is evident that both the flexural strength and splitting tensile strength of the specimens display a corresponding pattern, characterized by a decline in flexural strength as the content of glass sand increases. The figure also shows that for each group of concrete specimens with 0.9% carbon fiber content, their flexural strength decreased by 7.5%, 0.79%, 15.42%, and 17.87% respectively compared to the previous group with lower glass sand content. The other groups with different carbon fiber content exhibited similar patterns. The reason for this phenomenon might be the same as the reason for the reduction in splitting tensile strength. The glass sand particles used had fine and smooth surfaces, and their microscopic shape resembled microspheres without any sharp edges or corners. When the amount of glass sand increased, the friction force between the manufactured sand aggregates gradually weakened, resulting in a negative impact on the tensile performance of the specimens. Likewise, with an increase in carbon fiber content, the flexural strength and the splitting tensile strength showed similar patterns, which were an increase in both strengths with an increase in carbon fiber content. The reason for this situation is that the bond force between carbon fiber and concrete can resist the tensile stress within the concrete, and the fibers are interconnected, which facilitates the transfer of internal force in the concrete and can also effectively prevent the generation and spread of cracks. When the concrete underwent a tensile test, the pressure was transferred through the pressure was transferred by the interaction at the fiber-matrix interface and continued until the fiber reached its ultimate tensile
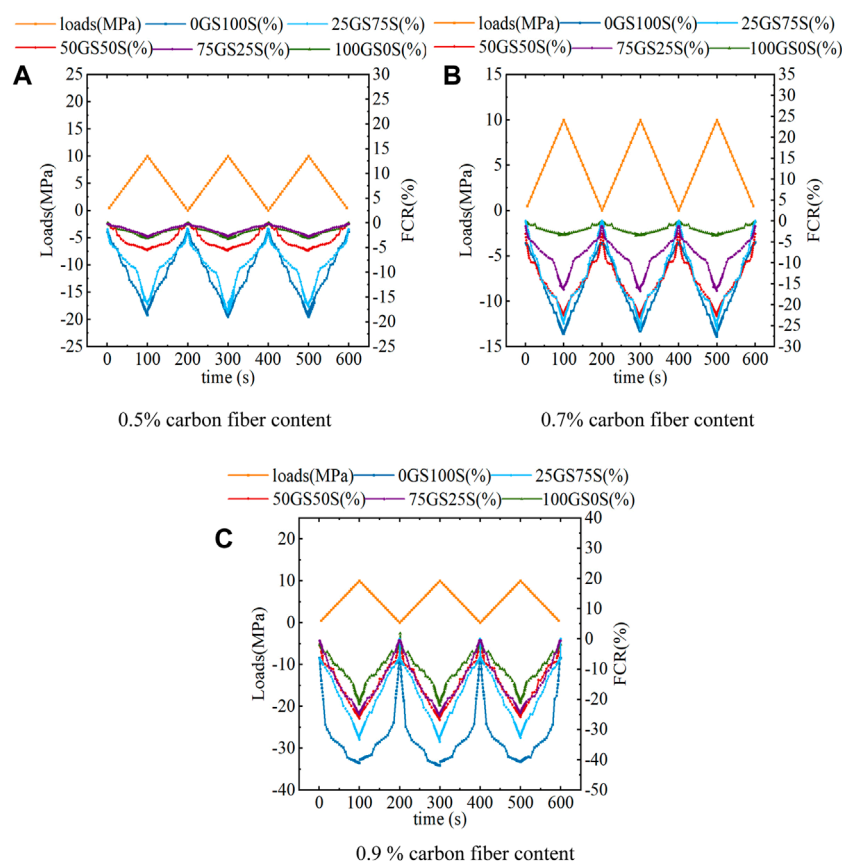
FIGURE 11
Resistivity Change of 100 mm × 100 mm × 300 mm Specimen under Cyclic Load **(A)** 0.5% carbon fiber content **(B)** 0.7% carbon fiber content. **(C)** 0.9 % carbon fiber content.

strength and eventually fractured. E. Mello (Mello et al., 2014) also reached similar conclusions.

3.4 Electrical resistivity

3.4.1 Electrical resistance before loading

The initial resistivity of the 100 mm × 100 mm × 300 mm and 100 mm × 100 mm × 400 mm specimens was tested, as depicted in Figures 10A, B. The figure clearly shows that when the carbon fiber content is 0.9%, as the glass sand content increases, the resistivity of each group of specimens increases by 1.03%, 1.64%, 1.82%, and 2.44%, respectively, compared to the specimens without glass sand. The reason for this situation might be that glass sand is a non-conductive material with very high resistivity, much higher than cement, water, and manufactured sand. Therefore, there is a trend of increasing resistivity with an increase in content. Also, the sand-to-binder ratio in this experiment is relatively large, so the change in glass sand content has a more pronounced impact on the resistivity.

However, as the carbon fiber content increases, the conductivity of concrete increases significantly. The proportion of carbon fiber increased from 0.5% to 0.7% and then to 0.9%, and its resistivity decreased from 71,505.38 to 715 Ω cm and then to 275.7 Ω cm, showing a clear decreasing trend. It is worth mentioning that when

the carbon fiber content increased from 0.5% to 0.7%, the resistivity decreased significantly; while from 0.7% to 0.9%, although there was also a decreasing trend, its decrease in resistivity was far less than the previous stage. The reason for this situation might be that with an increase in carbon fiber, the conductivity of carbon fiber cement-based materials gradually increases, and the number of fibers overlapping each other also gradually increases. When a certain fiber content (percolation threshold) is reached, the conductivity of the material no longer increases significantly. This is because, at this point, the fibers form a completely overlapping network structure, which makes the conductivity reach a relatively stable state (Chiarello and Zinno, 2005).

By comparing the results, it can be seen that as the specimen size changes, the resistivity of specimens containing 0.5% carbon fiber content increases from initial values of 71,505.38, 15,833.33, 189,046.7, 201,515.22, and 246,296.3 Ω cm to 280,590.7, 287,878.96, 295,567.6, 318,887.7, and 351,851.9 Ω cm respectively. A possible reason for this phenomenon is that concrete is a porous medium with pores and cracks of different scales inside. As the size of the concrete specimen increases, its internal pores and cracks also increase, thus affecting its conductivity performance. Generally speaking, the more pores and cracks there are, the worse the conductivity performance of concrete and the higher its resistivity. This is consistent with Heydar Dehghanpour's conclusion (Dehghanpour and Yilmaz, 2020).
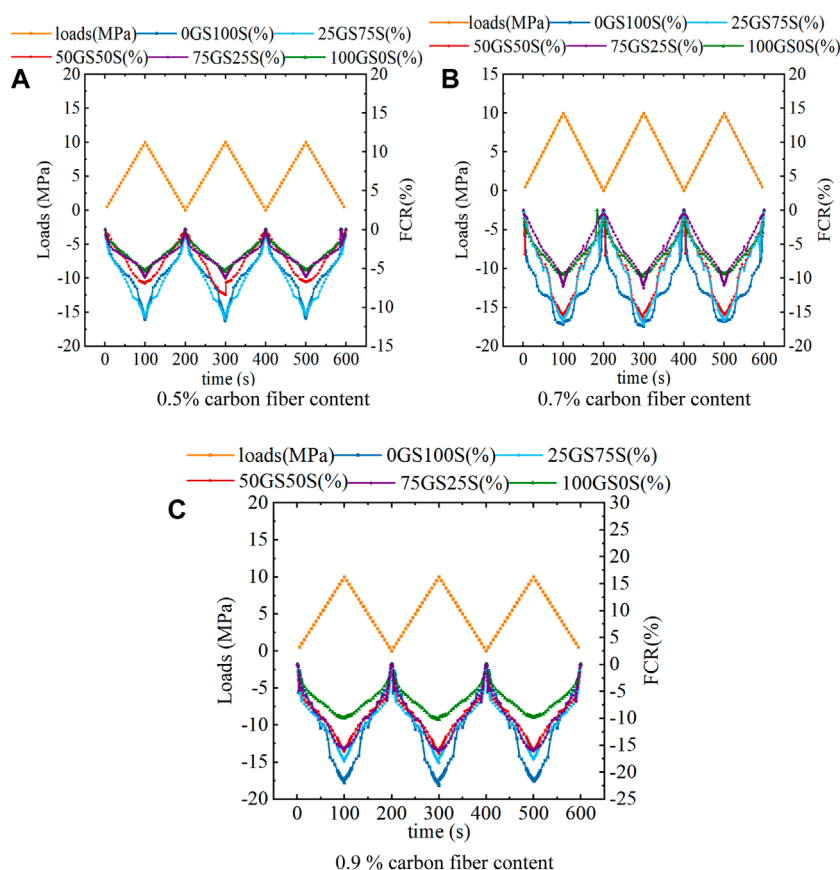
FIGURE 12
Resistivity change of 100 mm × 100 mm × 400 mm specimen under cyclic load. **(A)** 0.5% carbon fiber content **(B)** 0.7% carbon fiber content **(C)** 0.9 % carbon fiber content.
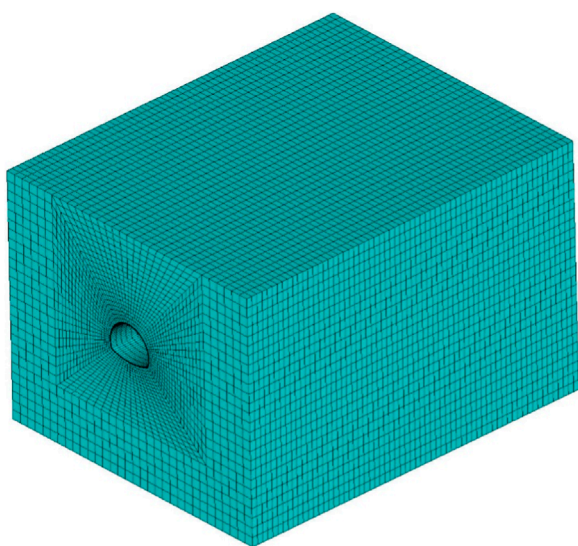

FIGURE 13
Finite element model of overall structure.

3.4.2 Fractional variation of real impedance under compression loads

The results of the sample's pressure sensitivity are displayed in Figures 11, 12. As displayed in the figure, as the load changes, the FCR also changes accordingly, showing a good correspondence and pressure sensitivity. That is, when the load increases and then decreases, the FCR has an opposite trend. When an external force is applied to the composite, it induces changes in the spacing among the conductive filler particles, resulting in a change in electrical resistance. In this study, the initial spacing of the carbon fibers under compressive loading decreases or becomes zero due to forceful deformation; therefore, the resistance decreases. A similar phenomenon was observed by (Dadkhah and Tulliani, 2022). By comparing the FCR at different glass sand contents, it is clear that the trend of decreasing FCR becomes moderate with increasing glass sand contents. This is because glass sand has a high resistivity and can hinder the conduction of current in the specimen, thus reducing the change in concrete resistivity. In addition, the glass sand selected in this study has a smaller grain size, which improves concrete compactness, so that concrete specimens are less deformed by force, thus reducing the FCR.

The FCR curves of the 100 mm × 100 mm × 300 mm (Figure 12) and 100 mm × 100 mm × 400 mm (Figure 13) specimens show a similar pattern. However, due to the size effect, the network of conductive materials is well connected and there are fewer tiny cracks and other disturbances in the conduction path when the specimen length is short, allowing the specimen to show the effect of the change more completely. However, as the sample size and the applied forces increase, damage occurs first in longer samples, resulting in an increase in insulating walls in the current path. This further increases the difficulty for electrons to traverse the insulating walls, reducing the signal efficiency and decreasing the rate of change magnitude. Therefore, to effectively and accurately ensure the self-monitoring function of the structure, a deeper study of the sample size should be carried out to further explore the self-sensing performance of large-size components. This indicates a direction for further research.

4 Finite element modeling of tunnel

Since there are not many examples of using shotcrete as permanent lining, Ansys APDL was used to simulate and verify the feasibility of HPS single-layer tunnel lining with glass sand (GHPSS). The research results will provide valuable references for future research on sprayed HPC single-layer tunnel lining.

4.1 Module selection and modeling

In this simulation, the rock unit surrounding the tunnel is modeled by the solid45 element, while the concrete is modeled by the solid65 element.

The specimen with 0.9% carbon fiber doping and 75% glass sand substitution rate was selected as the simulation object, and its relevant material parameters, such as compressive strength and splitting tensile strength, were adopted from the above experimental results. However, the simulation of the specimen's behavior uses the design value of the specimen's compressive strength and splitting tensile strength. According to the formula provided by GB50010-2010 (GB50010-2010, 2015), the compressive strength and splitting tensile strength are converted to their design values, which are calculated as shown in Eqs 7–12. The design value of the specimen's compressive strength is calculated as 34.107 MPa, and the design value of splitting tensile strength is 3.76 MPa. The specimen's density is calculated as 2,200.3 kg/m^3, its Poisson's ratio is 0.21, and the perimeter rock adopts the perimeter rock quality of V, with a density of 2,000 kg/m^3, Young's modulus of 1.2GPa, Poisson's ratio of 0.4, an angle of internal friction of 23.7°, and cohesion of 0.17°. The Drucker-Prager yield criterion was chosen for the perimeter rock, which is an approximation of the Mohr-Coulomb criterion and a modification of the von Mises yield criterion and is consistent with geotechnical materials simulations.

$$f_{cu,150} = 0.95f_{cu,100} \tag{7}$$

$$f_{ck} = 0.85\alpha_{c1}\alpha_{c2}f_{cu,150} \tag{8}$$

$$f_{cd} = \frac{f_{ck}}{k} \tag{9}$$

$$f_{ts,150} = 0.85f_{ts,100} \tag{10}$$

$$f_{tk} = 0.9f_{ts,150} \tag{11}$$

$$f_{td} = \frac{f_{tk}}{k} \tag{12}$$

$f_{cu,100}$—— cube compressive strength of HPS with an edge length of 100 mm, MPa;

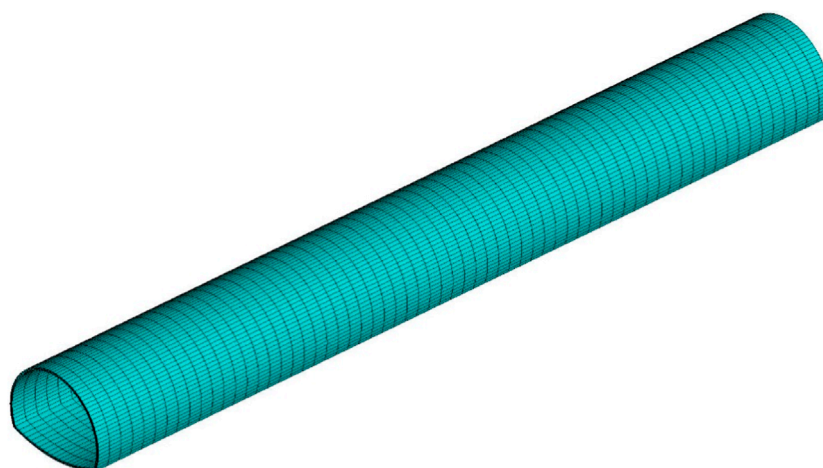$f_{cu,150}$—— cube compressive strength of HPS with an edge length of 150 mm, MPa;

FIGURE 14
Finite element model of single lining.
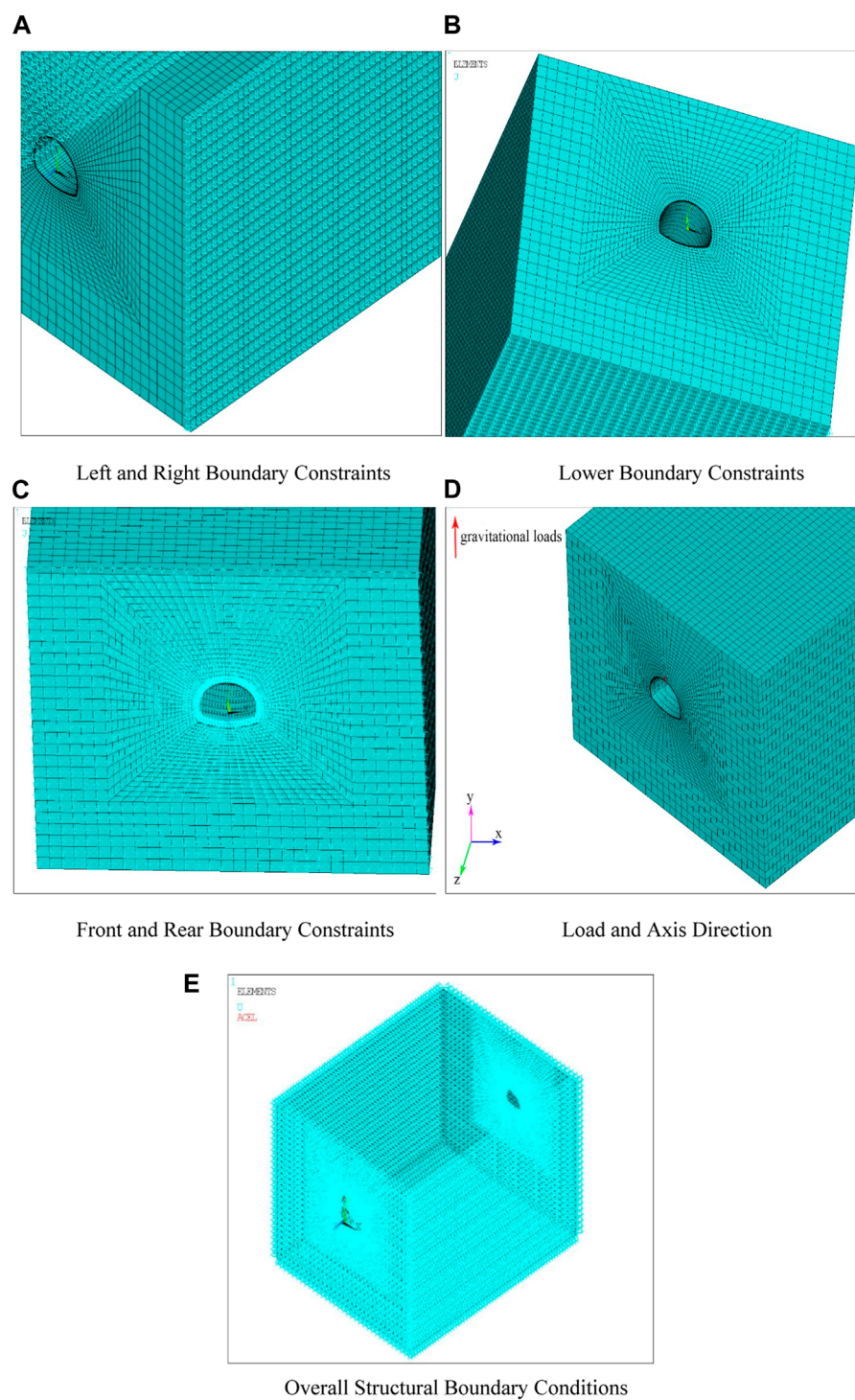
$f_{ts,100}$—— cube split tensile strength of HPS with an edge length of 100 mm, MPa;

$f_{ts,150}$—— cube split tensile strength of HPS with an edge length of 150 mm, MPa;

f_{ck}—— the standard value of HPS compressive strength, MPa;

f_{cd}—— the design value of HPS compressive strength, MPa;

f_{tk}—— the standard value of HPS tensile strength, MPa;

f_{td}—— the design value of HPS tensile strength, MPa;

α_{c1}—— the ratio of compressive strength between HPS prism and cube, $\alpha_{c1} = 0.82$.

FIGURE 16
Tunnel strain **(A)** and stress **(B)** clouds chart. **(A)** tunnel strain cloud chart **(B)** tunnel stress cloud chart.
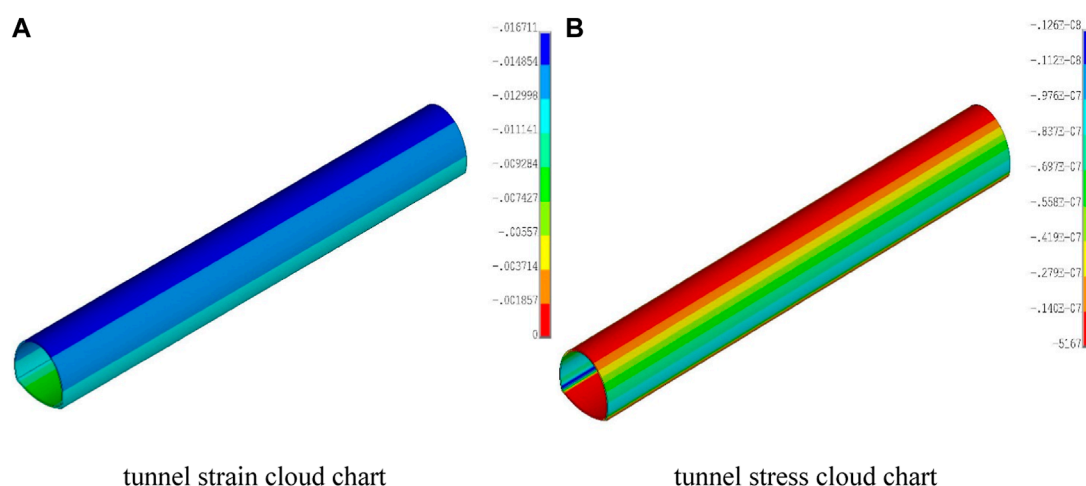
α_{c2}—— HPC brittleness reduction coefficient, α_{c2} = 0.87;

k——concrete partial coefficient, k = 1.4.

It should be noted that in this simulation, the surrounding rock and the lining concrete are both assumed to be isotropic homogeneous materials, and no relative slip occurs between them by default. The lining structure is considered as an integral whole with the surrounding rock, subject to the same stresses and deformations by external forces. In other words, the lining structure bonds well with the surrounding rock and deforms uniformly under external forces.

Based on computing time and result accuracy, the length of the tunnel is selected to be 100 m. In the simulation process, the lateral dimensions of the surrounding rock are 2.5 times the width of the tunnel, and the lower surrounding rock is three times the height of the tunnel. In summary, the dimensions of the surrounding rock in this simulation are 80 m × 65 m × 100 m. The shotcrete is modeled by a nonlinear constitutive model of concrete: The Multilinear Isotropic Hardening Model (MISO), which obeys the Von Mises yield criterion. The obtained model is shown in Figures 13, 14.

4.2 Establishment of boundary conditions and simulation calculation of models

During the construction and operation of the tunnel, different constraints are applied to different boundaries to limit the deformation of the mountain. The horizontal displacement at the mountain's left and right boundaries is small due to the distance from the tunnel, so only a modest amount of settling will occur. To limit the horizontal deformation, these boundaries must be subjected to horizontal constraints. The lower boundary of the mountain is connected to the ground and will not produce any vertical displacement, so vertical constraints must be applied to this boundary. As for the upper boundary of the mountain, it is a free surface and no constraints are applied. The length

of the tunnel will also be affected by the deformation of the mountain. If the deformation is large, it will directly affect the operation of the tunnel; therefore, horizontal constraints are set at the front and rear boundaries of the tunnel to limit the deformation.

After the tunnel is put into operation, the lining structure must withstand the pressure from the vehicles in addition to the pressure of the mountain and its own gravity. However, the external force exerted by vehicles is negligible compared to the mountain and its own gravity. Hence, only the gravitational force of the mountain needs to be considered when simulating the tunnel. However, since the surrounding rock is a compressed and non-tensile material, the direction of gravity acceleration is usually assumed to be vertically upward to prevent the surrounding rock from undergoing tension. Based on the comprehensive analysis, this study imposed constraint conditions in the y-direction at the lower boundary of the model, x-direction constraints at the left and right boundaries, and z-direction constraints at the front and back boundaries. Additionally, the coordinate system used in this simulation follows the standard ANSYS Cartesian coordinate system. A vertical upward gravitational acceleration was applied throughout the entire model to prevent tensile occurrences in the surrounding rock The results of the constraint and loading are shown in Figure 15. (Constraints and loads are shown separately for different directions to provide a clearer view.)

It can be concluded from the above constraints that the lining structure will only experience vertical displacement under the self-weight of the mountain, and will bear significant stress in the vertical direction. Therefore, this article will focus on analyzing the vertical deformation and stress of the lining structure. Figures 16A, B show the strain and stress diagrams.

It can be noticed from Figure 16 that the vertical displacement at the tunnel vault is the largest of the entire structure, followed by the side walls, and the vertical displacement at the inverted arch is the smallest. It is worth noting that the vertical displacement of the tunnel vault is approximately 16.7 mm. The stress cloud

diagram shows that all parts of the lining are under compression, which is the result of the combined effects of the surrounding rock pressure, the lateral soil pressure, and the gravity of the lining structure itself. In the entire lining structure, the vertical stress at the inside of the arch foot is the highest in the lining structure, reaching 12.6 Mpa. The reason for the maximum stress at the arch foot may be partly determined by the stress and displacement characteristics of the surrounding rock. After tunnel excavation, the surrounding rock will undergo elastic and plastic deformation, resulting in stress redistribution. Therefore, the surrounding rock at the arch foot is affected by both the weight of the tunnel and the gravity of the strata and is constrained by that at the crown of the arch, making it unable to sink freely. On the other hand, it is due to the fact that the location is at the junction of the lateral and inverted arches during modeling, and the curvature of the curve changes too much, resulting in stress concentration at this location.

By comparing the data, it is clear that the stresses in the Ansys APDL simulation are much smaller than the design strength of the specimens in the experiment. This offers theoretical guidance for high-performance shotcrete containing glass sand and a possibility for its application in engineering. Additionally, the use of glass sand has a lower environmental impact than the use of materials such as manufactured sand or quartz sand.

5 Conclusion

In this paper, the glass sand was used to replace manufactured sand at dif-ferent proportions of 0%, 25%, 50%, 75%, and 100%, and carbon fiber reinforced high-performance shotcrete was prepared and its praying performance was verified by an experiment. The basic mechanical properties and self-sensing abilities of the concrete were also investigated. Then, the experimental parameters were used to perform a simulation analysis, and the following results can be concluded:

- In high-performance shotcrete, the compressive strength tended to first increase and then decrease with increasing glass sand content. The optimum content was 75% of glass sand. Carbon fiber had a positive effect on the compressive perfor-mance of concrete, but the overall strength improvement was relatively limited. Therefore, the optimum group was when the glass sand content was 75% and the carbon fiber content was 0.9%, and its 28 days compressive strength was 80.06 MPa. A notable point was that the compressive strength fell at one point as the carbon fi-ber content increased, which could be caused by agglomeration of the carbon fiber. However, this phenomenon disappeared with the increase of glass sand content, which also confirmed that glass sand was beneficial for fiber dispersion.
- The splitting tensile strength and the compressive strength show opposite trends. As the glass sand content increases, the splitting tensile strength decreases linearly. This is because the glass sand particles are small and smooth, with a microstruc-ture similar to microspheres, without obvious edges and corners. Increasing the amount of glass sand gradually reduces the friction between the mechanism sand aggregates, thus affecting the tensile performance of the specimens to some extent.

Similarly, carbon fibers play a very important role in resisting the splitting tensile test. With increasing carbon fiber content, the splitting tensile strength tends to in-crease. The optimum group is the specimen with the lowest glass sand content but the highest carbon fiber content, that is, when the glass sand content is 0% and the carbon fiber content is 0.9%, its strength is 6.975 MPa.

- The flexural strength and the splitting tensile strength show similar patterns. As the glass sand content rises, the flexural strength tends to decrease, while as the carbon fiber content rises, the flexural strength tends to increase. This pattern may be due to both reflecting the tensile performance and crack resistance of concrete. Whereas both the splitting tensile strength test and the flexural strength test cause the expansion and failure of concrete cracks by applying different types of tensile forces.
- By studying the self-sensing performance of the specimens, it was found that the concrete specimens had good pressure sensitivity. The pressure sensitivity de-creased significantly as the glass sand content increased, and the resistivity also increased significantly. The explanation might be that the glass sand has a high re-sistivity, which impedes the current and causes the change in concrete resistivity to decrease. As the carbon fiber content gradually rose, its self-sensing ability im-proved significantly. As the carbon fiber content increased from 0.5%, 0.7%–0.9%, the resistivity of the specimens without glass sand was 71,505.38, 715, and 275 Ω cm, respectively. It is evident that a significant decrease in resistivity occurs as the fiber content varies from 0.5% to 0.7%. Hence, it can be deduced that there potentially exists a percolation threshold within the range of 0.5%–0.7%. It was also found that due to the size effect, the pressure sensitivity changed as the specimen size changed. Therefore, further research is needed with a focus on larger components.
- When using the optimal group of compressive strength, the vertical displacement of the arch crown is the largest, the vertical displacement of the side wall is the second, and the vertical displacement of the inverted arch is the smallest, with a maximum of 16.7 mm, when modeling and simulating with Ansys APDL. In terms of stress, all parts of the lining are subjected to pressure, and the vertical stress at the inner side of the arch foot is the most significant, reaching 12.6 MPa. This has practical significance for engineering projects.

Data availability statement

The raw data supporting the conclusion of this article will be made available by the authors, without undue reservation.

Author contributions

JW: Conceptualization, Formal Analysis, Investigation, Project administration, Writing–review and editing. Tianren Wang: Conceptualization, Formal Analysis, Methodology,

Writing–original draft. YZ: Investigation, Methodology, Writing–review and editing. XQ: Writing–review and editing.

Funding

Acknowledgments

Conflict of interest

The authors declare that the research was conducted in the absence of any commercial or financial relationships that could be construed as a potential conflict of interest.

Publisher's note

All claims expressed in this article are solely those of the authors and do not necessarily represent those of their affiliated organizations, or those of the publisher, the editors and the reviewers. Any product that may be evaluated in this article, or claim that may be made by its manufacturer, is not guaranteed or endorsed by the publisher.

References

Ai, D., Zhu, H., and Luo, H. (2016). Sensitivity of embedded active PZT sensor for concrete structural impact damage detection. *Constr. Build. Mater.* 111, 348–357. doi:10.1016/j.conbuildmat.2016.02.094

Azhari, F., and Banthia, N. (2012). Cement-based sensors with carbon fibers and carbon nanotubes for piezoresistive sensing. *Cem. Concr. Compos.* 34, 866–873. doi:10.1016/j.cemconcomp.2012.04.007

Biolzi, L., Guerrini, G. L., and Rosati, G. (1997). Overall structural behavior of high strength concrete specimens. *Constr. Build. Mater.* 11, 57–63. doi:10.1016/S0950-0618(96)00026-8

Chen, P. W., and Chung, D. D. L. (1996). Concrete as a new strain/stress sensor. *Compos. Part B Eng.* 27, 11–23. doi:10.1016/1359-8368(95)00002-X

Chen, Z., and Ansari, F. (2010). Fiber optic acoustic emission distributed crack sensor for large structures. *J. Struct. Control* 7, 119–129. doi:10.1002/stc.4300070108

Chiarello, M., and Zinno, R. (2005). Electrical conductivity of self-monitoring CFRC. *Cem. Concr. Compos.* 27, 463–469. doi:10.1016/j.cemconcomp.2004.09.001

Chung, D. D. L. (2002). Piezoresistive cement-based materials for strain sensing. *J. Intelligent Material Syst. Struct.* 13, 599–609. doi:10.1106/104538902031861

Chung, Z. Q. S. D. L., and Chung, D. (1999). Carbon fiber-reinforced concrete for traffic monitoring and weighing in motion. *Cem. Concr. Res.* 29 (3), 435–439. doi:10.1016/S0008-8846(98)00204-X

Cong, X., Darwin, D., and Mccabe, S. L. (1992). *Role of silica fume in compressive strength of cement paste, mortar, and concrete.* Lawrence, KS: University of Kansas Center for Research, Inc. doi:10.1007/BF02472261

Dadkhah, M., and Tulliani, J. M. (2022). Damage management of concrete structures with engineered cementitious materials and natural fibers: a review of potential uses. *Sustainability* 14, 3917. doi:10.3390/su14073917

Dehghanpour, H., and Yilmaz, K. (2020). Investigation of specimen size, geometry and temperature effects on resistivity of electrically conductive concretes. *Constr. Build. Mater.* 250, 118864. doi:10.1016/j.conbuildmat.2020.118864

Downey, A., D'alessandro, A., Ubertini, F., and Laflamme, S. (2017). Automated crack detection in conductive smart-concrete structures using a resistor mesh model. *Meas. Sci. Technol.* 29, 035107. doi:10.1088/1361-6501/aa9fb8

Du, H., and Tan, K. H. (2013). Use of waste glass as sand in mortar: Part II – alkali–silica reaction and mitigation methods. *Cem. Concr. Compos.* 35, 118–126. doi:10.1016/j.cemconcomp.2012.08.029

Erdem, S., Hanbay, S., and Blankson, M. A. (2017). Self-sensing damage assessment and image-based surface crack quantification of carbon nanofibre reinforced concrete. *Constr. Build. Mater.* 134, 520–529. doi:10.1016/j.conbuildmat.2016.12.197

Fu, X., Lu, W., and Chung, D. D. L. (1998). Improving the strain-sensing ability of carbon fiber-reinforced cement by ozone treatment of the fibers 11Communicated by D.M. Roy. *Cem. Concr. Res.* 28, 183–187. doi:10.1016/s0008-8846(97)00265-2

Gb175-2020 (2020). *Common portland cement.* Beijing, China: Springer.

Gb50010-2010 (2015). *Code for design of concrete structures.* Beijing, China: Springer.

Gb/T50081-2019 (2019). *Standard for test methods of concrete physical and mechanical properties Beijing.* China: Beijing, China: Springer.

Ghanem, S. Y., and Bowling, J. (2019). Mechanical properties of carbon fiber reinforced concrete. *Adv. Civ. Eng. Mater.* 8, 20180089. doi:10.1520/ACEM20180089

Gražulytė, J., Vaitkus, A., Šernas, O., and Čygas, D. (2020). "Effect of silica fume on high-strength concrete performance," in Proceedings of the 5th World Congress on Civil, Structural, and Environmental Engineering, Orléans, ON, Canada, October 2020.

Han, B., Ding, S., and Yu, X. (2015). Intrinsic self-sensing concrete and structures: a review. *Measurement* 59, 110–128. doi:10.1016/j.measurement.2014.09.048

Han, B., Yu, X., and Kwon, E. (2009). A self-sensing carbon nanotube/cement composite for traffic monitoring. *Nanotechnology* 20, 445501. doi:10.1088/0957-4484/20/44/445501

Han, B., Zhang, K., Yu, X., Kwon, E., and Ou, J. (2011). Nickel particle-based self-sensing pavement for vehicle detection. *Measurement* 44, 1645–1650. doi:10.1016/j.measurement.2011.06.014

Helmi, M. R., Stevens, L. A., and Rigby, S. P. (2016). Effects of high-pressure/temperature curing on reactive powder concrete microstructure formation. *Constr. Build. Mater.* 105, 554–562. doi:10.1016/j.conbuildmat.2015.12.147

Huang, S. C., Lin, W. W., Tsai, M. T., and Chen, M. H. (2007). Fiber optic in-line distributed sensor for detection and localization of the pipeline leaks. *Sensors Actuators A Phys.* 135, 570–579. doi:10.1016/j.sna.2006.10.010

Imai, M., and Feng, M. (2012). Sensing optical fiber installation study for crack identification using a stimulated Brillouin-based strain sensor. *Struct. Health Monit.* 11, 501–509. doi:10.1177/1475921712442440

Ji, J., Kang, W., Jiang, L., Li, Y., Ren, H., Hao, S., et al. (2021). Mechanical behavior of reactive powder concrete made from local material subjected to axial pressure. *Front. Mater.* 8, 737646. doi:10.3389/fmats.2021.737646

Jiao, Y., Zhang, Y., Guo, M., Zhang, L., and Liu, S. (2020). Mechanical and fracture properties of ultra-high performance concrete (UHPC) containing waste glass sand as partial replacement material. *J. Clean. Prod.* 277, 123501. doi:10.1016/j.jclepro.2020.123501

Juan, C. (2009). *Experimental study on the steel fiber shotcrete.*

Khooshechin, M., and Tanzadeh, J. (2018). Experimental and mechanical performance of shotcrete made with nanomaterials and fiber reinforcement. *Constr. Build. Mater.* 165, 199–205. doi:10.1016/j.conbuildmat.2017.12.199

Kou, S.-C., and Poon, C.-S. (2015). Effect of the quality of parent concrete on the properties of high performance recycled aggregate concrete. *Constr. Build. Mater.* 77, 501–508. doi:10.1016/j.conbuildmat.2014.12.035

Larive, C., Bouteille, S., Berthoz, N., and Zappelli, S. (2020). Fiber-reinforced sprayed concrete as a permanent tunnel lining. *Struct. Eng. Int.* 30, 498–505. doi:10.1080/10168664.2020.1735981

Lim, J. C., and Ozbakkaloglu, T. (2014). Influence of silica fume on stress–strain behavior of FRP-confined HSC. *Constr. Build. Mater.* 63, 11–24. doi:10.1016/j.conbuildmat.2014.03.044

Lin, V. W. J., Mo, L., Lynch, J. P., et al. (2011). "Mechanical and electrical characterization of self-sensing carbon black ECC," in International Society for Optics and Photonics), Australia, December, 2011.

Mello, E., Ribellato, C., and Mohamedelhassan, E. (2014). Improving concrete properties with fibers addition. *Int. J. Civ. Environ. Eng.* 8, 249–254. doi:10.5281/ZENODO.1091168

Neuner, M., Dummer, A., Schreter, M., Hofstetter, G., Cordes, T., and Bergmeister, K. (2020). Nonlinear time-dependent analysis of the load-bearing capacity of a single permanent shotcrete lining at the brenner base tunnel. *Struct. Eng. Int.* 30, 475–483. doi:10.1080/10168664.2020.1735979

Ranade, R., Zhang, J., Lynch, J. P., and Li, V. C. (2014). Influence of micro-cracking on the composite resistivity of engineered cementitious composites. *Cem. Concr. Res.* 58, 1–12. doi:10.1016/J.CEMCONRES.2014.01.002

Richard, P., and Marcel, C. (1995). Composition of reactive powder concretes. *Cem. Concr. Res.* 25 (7), 1501–1511. doi:10.1016/0008-8846(95)00144-2

Shi, D., Chen, X., Ning, Y., Bai, L., and Yu, X. (2023). Understanding the compression failure mechanism of rock–shotcrete composites using X-CT and DIC technologies. *Acta Geotech.* 1, 5213–5230. doi:10.1007/s11440-023-01884-7

Song, P. S., and Hwang, S. (2004). Mechanical properties of high-strength steel fiber-reinforced concrete. *Constr. Build. Mater.* 18, 669–673. doi:10.1016/j.conbuildmat.2004.04.027

Tamanna, N., Tuladhar, R., and Sivakugan, N. (2020). Performance of recycled waste glass sand as partial replacement of sand in concrete. *Constr. Build. Mater.* 239, 117804. doi:10.1016/j.conbuildmat.2019.117804

Wen, S., and Chung, D. D. L. (2001). Uniaxial tension in carbon fiber reinforced cement, sensed by electrical resistivity measurement in longitudinal and transverse directions. *Cem. Concr. Res.* 30, 1289–1294. doi:10.1016/s0008-8846(00)00304-5

Yunlong, Z. J. S., Jing, W., Xuesong, Q., and Qian, X. (2022). Optimization of performance index of self-sensing spray reactive powder concrete based on response surface methodology. *Mater. Lett. X* 13, 100120. doi:10.1016/j.mlblux.2021.100120

Zhang, Y., Wang, J., Wang, J., and Qian, X. (2022). Preparation, mechanics and self-sensing performance of sprayed reactive powder concrete. *Sci. Rep.* 12, 7787. doi:10.1038/s41598-022-11836-y

Zheng, Z. (2011). Proportion design and strength regularity of high strength concrete. *Concrete* 3. doi:10.1111/j.1759-6831.2010.00113.x

Frontiers in
Materials

Investigates the discovery and design of materials for future application

A multidisciplinary journal that explores the breadth of materials science, engineering and mechanics - from carbon-based materials to smart materials.

Discover the latest Research Topics

See more →

frontiers

Frontiers in
Materials

frontiers | Research Topics